

Copyright  
by  
Daniel Anthony Evans  
2015

**The Dissertation Committee for Daniel Anthony Evans Certifies that this is the approved version of the following dissertation:**

**Applications of Bis(imino)acenaphthene and Investigation of Boron Arsenide as a High Thermal Conductivity Material**

**Committee:**

---

Alan H. Cowley, Supervisor

---

Richard A. Jones

---

Simon M. Humphrey

---

Eric V. Anslyn

---

John G. Ekerdt

**Applications of Bis(imino)acenaphthene and Investigation of Boron  
Arsenide as a High Thermal Conductivity Material**

**by**

**Daniel Anthony Evans, B.A.**

**Dissertation**

Presented to the Faculty of the Graduate School of

The University of Texas at Austin

in Partial Fulfillment

of the Requirements

for the Degree of

**Doctor of Philosophy**

**The University of Texas at Austin**

**May 2015**

## **Dedication**

For my family, who have always pushed me to be my best.

## Acknowledgements

I would like to acknowledge my family, who have been very supportive during my education. My parents have both inspired me to achieve the highest education possible and to be diligent and dedicated to my studies. My brother, Greg, has always been my best friend and a supportive companion. I would also like to thank Professor Linda Doerrer at Boston University for instilling in me a strong work ethic during my two years of undergraduate research. I am thankful for the opportunity to have performed research in Professor Cowley's lab at the University of Texas at Austin. It has been a fulfilling and enjoyable experience.

I am also grateful for the guidance and aid I have received from all the members of the Inorganic Division in the Chemistry Department. Professors Jones, Holliday, Humphrey, Rose, and Que have always been open and helpful during my years as a graduate student. Dr. Vince Lynch has also been very helpful and has imparted some of his vast X-ray crystallography knowledge to me. I thank Dr. Shoulders for his assistance in performing and analyzing NMR spectroscopy experiments. Also, I thank Professor Li Shi, Dr. Daniel Sellan, and Jaehyun Kim for their wonderful collaborative effort in the boron arsenide project. Furthermore, I have thoroughly enjoyed our collaboration with Professor Ignacio Vargas-Baca. The calculations he performed for my compounds provided invaluable insight.

I would also like to thank my fellow graduate students in the Cowley lab and other labs in the department for providing companionship. Lastly, I would like to thank my wife Amy for providing support and encouragement during my years as a graduate student.

# **Applications of Bis(imino)acenaphthene and Investigation of Boron Arsenide as a High Thermal Conductivity Material**

Daniel Anthony Evans, Ph.D.

The University of Texas at Austin, 2015

Supervisor: Alan H. Cowley

**Abstract:** Functionalization of the ubiquitous bis(imino)acenaphthene ligand class has been explored. The successful functionalization of this ligand type was found to be dependent upon the steric congestion encompassing the N-C-C-N fragment of the aryl substituted BIAN ligand. The sterically directed functionalization was found to proceed via either a radical backbone dearomatization route or a nucleophilic imine C-alkylation pathway. The structures of each of the functionalized BIAN derivatives were examined by means of single crystal X-ray crystallography. The foregoing reactions were also probed by EPR spectroscopy and DFT-D calculations in order to help elucidate the nature of the driving forces that are involved in BIAN functionalization.

A series of aryl substituted BIAN zinc(II) chloride complexes were also prepared and their photophysical properties were investigated. Initially, four different methylated aryl substituents were examined, namely the 4-methylphenyl, 3,5-dimethylphenyl, 2,4,6-trimethylphenyl, and 2-methylphenyl derivatives. Examination of these four complexes revealed them to be non-emissive in solution. However, it was also determined that the 4-methylphenyl and 3,5-dimethylphenyl substituted complexes were emissive in the solid state. On the other hand, the 2,4,6-trimethylphenyl, and 2-methylphenyl complexes were

found to be non-emissive in the solid state. The origins of the emissions of the foregoing complexes were also probed by means of TD-DFT calculations.

The tuning of the stereoelectronic properties of a series of *para*-substituted aryl BIAN zinc(II) chloride complexes was undertaken with the view to modifying their solid state photophysical properties. For example, changing the electronic properties of the flanking *para*-substituted aryl substituents permitted tunability within the range of the red-orange-yellow emissions. Tunability was also achieved by employing a variety of different recrystallization techniques for growing the various structures, polymorphs, and solvatomorphs of each BIAN zinc(II) chloride complex.

Boron arsenide, a somewhat neglected semiconductor compound, has been examined for its potential use as a high thermal conductivity material. High quality single crystal BAs microstructures have been synthesized and characterized by means of powder X-ray diffraction, X-ray photoelectron spectroscopy, Raman spectroscopy, and scanning electron microscopy. The thermal conductivity properties of the BAs microstructures have been probed using microheater devices.

## Table of Contents

List of Tables .....	xiii
List of Figures .....	xxii
List of Schemes.....	xxxvii
Chapter 1: Functionalization of the Bis(imino)acenaphthene Ligand* .....	1
1.1 Introduction.....	1
1.1.1 History and Properties.....	1
1.1.2 Functionalization of the BIAN Ligand Class via Imine C-alkylation: Syntheses and Applications of BIAN* Derivatives.....	5
1.1.3 Backbone Dearomatization: Synthesis and Applications of the BIAN** Ligand. ....	24
1.1.4 BIAN* and BIAN**: An Overview of BIAN Functionalization	32
1.2 Results and Discussion .....	32
1.2.1 dpp-BIAN Radical Dearomatization.....	33
1.2.2 Sterically Directed Functionalization: Nucleophilic Imine C- Alkylation vs. Radical Backbone Dearomatization .....	39
1.2.3 Pathway Differentiation of BIAN Functionalization.....	46
1.2.4 X-Ray Diffraction Studies of 1-9b.....	55
1.2.4.1 [Li <sub>4</sub> ][(1,2-di-( <i>t</i> -Bu)-dpp-BIAN) <sub>2</sub> ] (1).....	56
1.2.4.2 1,2-di-( <i>t</i> -Bu)-dpp-BIAN (2) .....	58
1.2.4.3 1-( <i>t</i> -Bu)-2-(OH)-dpp-BIAN (3) .....	59
1.2.4.4 1,2-di-( <i>t</i> -Bu)-mes-BIAN (4) .....	60
1.2.4.5 <i>t</i> -Bu-(4-F)-BIAN* (5) .....	61
1.2.4.6 <i>t</i> -Bu-(4-OMe)-BIAN* (6) .....	62
1.2.4.7 TMS-CH <sub>2</sub> -(mes)-BIAN* (7).....	63
1.2.4.8 TMS-CH <sub>2</sub> -(4-F)-BIAN* (8a) .....	64
1.2.4.9 TMS-CH <sub>2</sub> -(4-F)-BIAN* (8b).....	66
1.2.4.10 TMS-CH <sub>2</sub> -(4-OMe)-BIAN* (9a) .....	68
1.2.4.11 TMS-CH <sub>2</sub> -(4-OMe)-BIAN* (9b).....	69



1.3 Conclusions.....	70
1.4 Experimental.....	71
1.4.1 General Procedures.....	71
1.4.2 Physical Measurements.....	71
1.4.3 Single Crystal X-ray Crystallography.....	72
1.4.4 Density Functional Theory.....	73
1.4.5 Synthesis of 1-9.....	73
1.4.5.1 [Li <sub>4</sub> ][(1,2-di-( <i>t</i> -Bu)-dpp-BIAN) <sub>2</sub> ] (1).....	73
1.4.5.2 1,2-di-( <i>t</i> -Bu)-dpp-BIAN (2).....	74
1.4.5.3 1-( <i>t</i> -Bu)-2-(OH)-dpp-BIAN (3).....	74
1.4.5.4 1,2-di-( <i>t</i> -Bu)-(mes)-BIAN (4).....	75
1.4.5.5 <i>t</i> -Bu-(4-F)-BIAN* (5).....	76
1.4.5.6 <i>t</i> -Bu-(4-OMe)-BIAN* (6).....	77
1.4.5.7 TMS-CH <sub>2</sub> -(mes)-BIAN* (7).....	78
1.4.5.8 TMS-CH <sub>2</sub> -(4-F)-BIAN* (8).....	79
1.4.5.9 TMS-CH <sub>2</sub> -(4-OMe)-BIAN* (9).....	80
Chapter 2: Solid State Photoluminescent Bis(imino)acenaphthene Zinc Chloride Complexes: An Aggregation-Induced Emission, Emission Tunability, and Solvatomorphic Study*.....	81
2.1 Introduction.....	81
2.1.1 Bis(imino)acenaphthene as a Ligand in Photoluminescent Complexes.....	81
2.1.2 Solid State Emissions: Aggregation-Caused Quenching (ACQ) vs. Aggregation-Induced Emission (AIE).....	86
2.1.3 Tuning of Solid State Emissions via Chemical Modifications, Polymorphism, and Solvatomorphism.....	94
2.2 Results and Discussion.....	111
2.2.1 Photophysical Properties of Bis(imino)acenaphthene Zinc Chloride Complexes: Tuning via Methylation of the Flanking Aryl Substituents.....	112
2.2.2 Photophysical Properties of Bis(imino)acenaphthene Zinc Chloride Complexes: Tuning via Modification of the Electronics of the <i>para</i> - Substituted Flanking Aryl Substituents.....	127

2.2.3 X-Ray Diffraction Studies of 10-21-DCM .....	146
2.2.3.1 4-methylphenyl-BIAN Zinc Chloride (10) .....	146
2.2.3.2 3,5-dimethylphenyl-BIAN Zinc Chloride (11) .....	147
2.2.3.3 2,4,6-trimethylphenyl-BIAN Zinc Chloride (12).....	148
2.2.3.4 2-methylphenyl-BIAN Zinc Chloride (13) .....	149
2.2.3.5 4-methylphenyl-BIAN Zinc Chloride · CHCl <sub>3</sub> (10-CHCl <sub>3</sub> )..	150
2.2.3.6 4-methylphenyl-BIAN Zinc Chloride · THF (10-THF) .....	151
2.2.3.7 4-methylphenyl-BIAN Zinc Chloride · DCM (10-DCM) .....	152
2.2.3.8 4-methylphenyl-BIAN Zinc Chloride · MeCN (10-MeCN)..	153
2.2.3.9 3,5-dimethylphenyl-BIAN Zinc Chloride · CHCl <sub>3</sub> (11-CHCl <sub>3</sub> )	154
2.2.3.10 3,5-dimethylphenyl-BIAN Zinc Chloride · THF (11-THF)	155
2.2.3.11 3,5-dimethylphenyl-BIAN Zinc Chloride · DCM (11-DCM)	156
2.2.3.12 3,5-dimethylphenyl-BIAN Zinc Chloride · MeCN (11-MeCN)	157
2.2.3.13 4-butoxyphenyl-BIAN Zinc Chloride (14) .....	158
2.2.3.14 4-methoxyphenyl-BIAN Zinc Chloride · CH <sub>3</sub> COOH (15)..	159
2.2.3.15 4-(methylthio)phenyl-BIAN Zinc Chloride · CH <sub>3</sub> COOH (16)	160
2.2.3.16 4-phenoxyphenyl-BIAN Zinc Chloride (17) .....	161
2.2.3.17 4-fluorophenyl-BIAN Zinc Chloride (18) .....	162
2.2.3.18 4-(trifluoromethoxy)phenyl-BIAN Zinc Chloride (20) .....	163
2.2.3.19 4-(trifluoromethyl)phenyl-BIAN Zinc Chloride (21) .....	164
2.2.3.20 4-butoxyphenyl-BIAN Zinc Chloride · DCM (14-DCM) ...	165
2.2.3.21 4-methoxyphenyl-BIAN Zinc Chloride · DCM (15-DCM)	166
2.2.3.22 4-(methylthio)phenyl-BIAN Zinc Chloride · DCM (16-DCM)	167
2.2.3.23 4-phenoxyphenyl-BIAN Zinc Chloride · DCM (17-DCM).	168
2.2.3.24 4-fluorophenyl-BIAN Zinc Chloride · THF (18-THF).....	169
2.2.3.25 4-bromophenyl-BIAN Zinc Chloride · DCM (19-DCM)....	170
2.2.3.26 4-(trifluoromethoxy)phenyl-BIAN Zinc Chloride · DCM (20- DCM) .....	171
2.2.3.27 4-(trifluoromethyl)phenyl-BIAN Zinc Chloride · DCM (21- DCM) .....	172
2.2.3.28 X-ray Powder Patterns for Complexes 10-13 .....	173

2.2.3.29 X-ray Powder Patterns for Complexes 10-CHCl <sub>3</sub> -10-MeCN	174
2.2.3.30 X-ray Powder Patterns for Complexes 11-CHCl <sub>3</sub> -11-MeCN	175
2.2.3.31 X-ray Powder Patterns for Complexes 14-17	176
2.2.3.32 X-ray Powder Patterns for Complexes 18, 20, and 21	177
2.2.3.33 X-ray Powder Patterns for Complexes 14-DCM-17-DCM	178
2.2.3.34 X-ray Powder Patterns for Complexes 18-THF-21-DCM	179
2.3 Conclusions	180
2.4 Experimental	180
2.4.1 General Procedures	180
2.4.2 Physical Measurements	181
2.4.3 Fluorescence Spectroscopy	181
2.4.4 Single Crystal and Powder X-ray Crystallography	182
2.4.5 Diffuse Reflectance and UV/vis Absorption Spectroscopy	183
2.4.6 Density Functional Theory	184
2.4.7 Fluorescent Microscopy	184
2.4.8 Synthesis of 10-21	184
2.4.8.1 4-methylphenyl-BIAN Zinc Chloride (10)	184
2.4.8.2 3,5-dimethylphenyl-BIAN zinc chloride (11)	185
2.4.8.3 2,4,6-trimethylphenyl-BIAN zinc chloride (12)	186
2.4.8.4 2-methylphenyl-BIAN zinc chloride (13)	186
2.4.8.5 4-butoxyphenyl-BIAN zinc chloride (14)	187
2.4.8.6 4-methoxyphenyl-BIAN zinc chloride (15)	188
2.4.8.7 4-(methylthio)phenyl-BIAN zinc chloride (16)	188
2.4.8.8 4-phenoxyphenyl-BIAN zinc chloride (17)	189
2.4.8.9 4-fluorophenyl-BIAN zinc chloride (18)	190
2.4.8.10 4-bromophenyl-BIAN zinc chloride (19)	191
2.4.8.11 4-(trifluoromethoxy)phenyl-BIAN zinc chloride (20)	191
2.4.8.12 4-(trifluoromethyl)phenyl-BIAN zinc chloride (21)	192

Chapter 3: Investigation of Boron Arsenide as a High Thermal Conductivity Material .....	193
3.1 Introduction.....	193
3.1.1 Predicted High Thermal Conductivity.....	193
3.1.2 Thermal Measurement of BAs.....	198
3.2 Results and Discussion .....	201
3.2.1 Synthesis and Characterization of BAs Material.....	202
3.2.2 Experimental Measurement of Thermal Conductivity of BAs Microstructures .....	209
3.3 Conclusions.....	216
3.4 Experimental .....	216
3.4.1 General Procedures .....	216
3.4.2 Raman Spectroscopy.....	217
3.4.3 X-ray Powder Diffraction .....	217
3.4.4 Scanning Electron Microscopy .....	217
3.4.5 X-ray Photoelectron Spectroscopy .....	217
3.4.6 Synthesis of BAs materials .....	218
Appendix A: X-Ray Diffraction Data for 1-9b.....	219
Appendix B: X-Ray Diffraction Data for 10-21-DCM.....	288
References.....	424

## List of Tables

Table 1: Polymerization data for the ROP of $\epsilon$ -CL using <b>X</b> and <b>Y</b> as initiators. <sup>27</sup>	15
Table 2: Hydroamination/hydroarylation of anilines with phenylacetylene catalyzed by complex <b>T</b> . <sup>13</sup>	17
Table 3: Intramolecular hydroamination of substituted aminoalkenes using dpp-BIAN** complex <b>AV</b> as a catalyst. <sup>33</sup>	27
Table 4: Intramolecular hydroamination of substituted aminoalkenes using dpp-BIAN** complexes <b>AU</b> , <b>AV</b> , and <b>AW</b> as catalysts in deuterated benzene solution. <sup>34</sup>	30
Table 5: Summary of the UV/vis absorption data for complexes <b>10-13</b> in DCM solution at room temperature. <sup>82</sup>	115
Table 6: Summary of the solid state photoluminescent data for complexes <b>10-13</b> . <sup>82</sup>	117
Table 7: Calculated crystallographic metrical parameters between the $\pi$ -stacked dimers of the ten emissive complexes <b>10-11-MeCN</b> . <sup>82</sup>	124
Table 8: Solid state photoluminescent data for the eight solvatomorphs <b>10-CHCl<sub>3</sub>-11-MeCN</b> . <sup>82</sup> *The relative quantum yield values were calculated based on the ratio of the emission intensities. The intensity of the emission peak for each solvatomorph was integrated and compared with that of the non-solvated complex for which the absolute quantum yield had been measured directly.	127
Table 9: Summary of the UV/vis absorption data for complexes <b>14-21</b> in DCM solution at room temperature.	129
Table 10: Summary of the solid state diffuse reflectance data for complexes <b>14-21</b> .	130

Table 11: Solid state photoluminescent data for complexes <b>14-21</b> . .....	132
Table 12: Hammett parameter ( $\sigma_p$ ) for the substituents of complexes <b>14-21</b> . <sup>86</sup> ..	133
Table 13: Solid state photoluminescent data for solvatomorphs <b>14-DCM-17-DCM</b> , <b>18-THF</b> , and <b>19-DCM-21-DCM</b> . .....	142
Table 14: Calculated crystallographic metrical parameters between the $\pi$ -stacked dimers of the 13 emissive complexes <b>14-21-DCM</b> . .....	144
Table 15: Average molecular weight, calculated natural thermal conductivity with experimental values in parenthesis, calculated isotopically pure thermal conductivity, and percent increase between isotopically pure and natural thermal conductivities. <sup>104</sup> .....	196
Table 16: Crystallographic Data and Structure Refinement of <b>1</b> . .....	219
Table 17: Atomic coordinates ( $\times 10^4$ ) and equivalent isotropic displacement parameters ( $\text{\AA}^2 \times 10^3$ ) for <b>1</b> . U(eq) is defined as one third of the trace of the orthogonalized $U^{ij}$ tensor.....	220
Table 18: Bond Lengths [ $\text{\AA}$ ] and Bond Angles [ $^\circ$ ] for <b>1</b> . .....	223
Table 19: Crystallographic Data and Structure Refinement of <b>2</b> . .....	232
Table 20: Atomic coordinates ( $\times 10^4$ ) and equivalent isotropic displacement parameters ( $\text{\AA}^2 \times 10^3$ ) for <b>2</b> . U(eq) is defined as one third of the trace of the orthogonalized $U^{ij}$ tensor.....	233
Table 21: Bond Lengths [ $\text{\AA}$ ] and Bond Angles [ $^\circ$ ] for <b>2</b> . .....	234
Table 22: Crystallographic Data and Structure Refinement of <b>3</b> . .....	237
Table 23: Atomic coordinates ( $\times 10^4$ ) and equivalent isotropic displacement parameters ( $\text{\AA}^2 \times 10^3$ ) for <b>3</b> . U(eq) is defined as one third of the trace of the orthogonalized $U^{ij}$ tensor.....	238
Table 24: Bond Lengths [ $\text{\AA}$ ] and Bond Angles [ $^\circ$ ] for <b>3</b> . .....	239

Table 25: Crystallographic Data and Structure Refinement of <b>4</b> .....	242
Table 26: Atomic coordinates ( x 10 <sup>4</sup> ) and equivalent isotropic displacement parameters (Å <sup>2</sup> x 10 <sup>3</sup> ) for <b>4</b> . U(eq) is defined as one third of the trace of the orthogonalized U <sup>ij</sup> tensor.....	243
Table 27: Bond Lengths [Å] and Bond Angles [°] for <b>4</b> . ....	245
Table 28: Crystallographic Data and Structure Refinement of <b>5</b> .....	250
Table 29: Atomic coordinates ( x 10 <sup>4</sup> ) and equivalent isotropic displacement parameters (Å <sup>2</sup> x 10 <sup>3</sup> ) for <b>5</b> . U(eq) is defined as one third of the trace of the orthogonalized U <sup>ij</sup> tensor.....	251
Table 30: Bond Lengths [Å] and Bond Angles [°] for <b>5</b> . ....	252
Table 31: Crystallographic Data and Structure Refinement of <b>6</b> .....	254
Table 32: Atomic coordinates ( x 10 <sup>4</sup> ) and equivalent isotropic displacement parameters (Å <sup>2</sup> x 10 <sup>3</sup> ) for <b>6</b> . U(eq) is defined as one third of the trace of the orthogonalized U <sup>ij</sup> tensor.....	255
Table 33: Bond Lengths [Å] angles [°] for <b>6</b> .....	256
Table 34: Crystallographic Data and Structure Refinement of <b>7</b> .....	258
Table 35: Atomic coordinates ( x 10 <sup>4</sup> ) and equivalent isotropic displacement parameters (Å <sup>2</sup> x 10 <sup>3</sup> ) for <b>7</b> . U(eq) is defined as one third of the trace of the orthogonalized U <sup>ij</sup> tensor.....	259
Table 36: Bond Lengths [Å]and Bond Angles [°] for <b>7</b> .....	260
Table 37: Crystallographic Data and Structure Refinement of <b>8a</b> .....	263
Table 38: Atomic coordinates ( x 10 <sup>4</sup> ) and equivalent isotropic displacement parameters (Å <sup>2</sup> x 10 <sup>3</sup> ) for <b>8a</b> . U(eq) is defined as one third of the trace of the orthogonalized U <sup>ij</sup> tensor.....	264
Table 39: Bond Lengths [Å] and Bond Angles [°] for <b>8a</b> . ....	266

Table 40: Crystallographic Data and Structure Refinement of <b>8b</b> .	270
Table 41: Atomic coordinates ( $\times 10^4$ ) and equivalent isotropic displacement parameters ( $\text{\AA}^2 \times 10^3$ ) for <b>8b</b> . U(eq) is defined as one third of the trace of the orthogonalized $U^{ij}$ tensor.	271
Table 42: Bond Lengths [ $\text{\AA}$ ] and Bond Angles [ $^\circ$ ] for <b>8b</b> .	272
Table 43: Crystallographic Data and Structure Refinement of <b>9a</b> .	274
Table 44: Atomic coordinates ( $\times 10^4$ ) and equivalent isotropic displacement parameters ( $\text{\AA}^2 \times 10^3$ ) for <b>9a</b> . U(eq) is defined as one third of the trace of the orthogonalized $U^{ij}$ tensor.	275
Table 45: Bond Lengths [ $\text{\AA}$ ] and Bond Angles [ $^\circ$ ] for <b>9a</b> .	277
Table 46: Crystallographic Data and Structure Refinement of <b>9b</b> .	281
Table 47: Atomic coordinates ( $\times 10^4$ ) and equivalent isotropic displacement parameters ( $\text{\AA}^2 \times 10^3$ ) for <b>9b</b> . U(eq) is defined as one third of the trace of the orthogonalized $U^{ij}$ tensor.	282
Table 48: Bond Lengths [ $\text{\AA}$ ] and Bond Angles [ $^\circ$ ] for <b>9b</b> .	284
Table 49: Crystallographic Data and Structure Refinement of <b>10</b> .	288
Table 50: Atomic coordinates ( $\times 10^4$ ) and equivalent isotropic displacement parameters ( $\text{\AA}^2 \times 10^3$ ) for <b>10</b> . U(eq) is defined as one third of the trace of the orthogonalized $U^{ij}$ tensor.	289
Table 51: Bond Lengths [ $\text{\AA}$ ] and Bond Angles [ $^\circ$ ] for <b>10</b> .	290
Table 52: Crystallographic Data and Structure Refinement of <b>11</b> .	292
Table 53: Atomic coordinates ( $\times 10^4$ ) and equivalent isotropic displacement parameters ( $\text{\AA}^2 \times 10^3$ ) for <b>11</b> . U(eq) is defined as one third of the trace of the orthogonalized $U^{ij}$ tensor.	293
Table 54: Bond Lengths [ $\text{\AA}$ ] and Bond Angles [ $^\circ$ ] for <b>11</b> .	295



Table 55: Crystallographic Data and Structure Refinement of <b>12</b> .....	299
Table 56: Atomic coordinates ( x 10 <sup>4</sup> ) and equivalent isotropic displacement parameters (Å <sup>2</sup> x 10 <sup>3</sup> ) for <b>12</b> . U(eq) is defined as one third of the trace of the orthogonalized U <sup>ij</sup> tensor.....	300
Table 57: Bond Lengths [Å] and Bond Angles [°] for <b>12</b> . ....	301
Table 58: Crystallographic Data and Structure Refinement of <b>13</b> .....	304
Table 59: Atomic coordinates ( x 10 <sup>4</sup> ) and equivalent isotropic displacement parameters (Å <sup>2</sup> x 10 <sup>3</sup> ) for <b>13</b> . U(eq) is defined as one third of the trace of the orthogonalized U <sup>ij</sup> tensor.....	305
Table 60: Bond Lengths [Å] and Bond Angles [°] for <b>13</b> . ....	306
Table 61: Crystallographic Data and Structure Refinement of <b>10-CHCl<sub>3</sub></b> . ....	309
Table 62: Atomic coordinates ( x 10 <sup>4</sup> ) and equivalent isotropic displacement parameters (Å <sup>2</sup> x 10 <sup>3</sup> ) for <b>10-CHCl<sub>3</sub></b> . U(eq) is defined as one third of the trace of the orthogonalized U <sup>ij</sup> tensor. ....	310
Table 63: Bond Lengths [Å] and Bond Angles [°] for <b>10-CHCl<sub>3</sub></b> .....	311
Table 64: Crystallographic Data and Structure Refinement of <b>10-THF</b> . ....	314
Table 65: Atomic coordinates ( x 10 <sup>4</sup> ) and equivalent isotropic displacement parameters (Å <sup>2</sup> x 10 <sup>3</sup> ) for <b>10-THF</b> . U(eq) is defined as one third of the trace of the orthogonalized U <sup>ij</sup> tensor. ....	315
Table 66: Bond Lengths [Å] and Bond Angles [°] for <b>10-THF</b> .....	316
Table 67: Crystallographic Data and Structure Refinement of <b>10-DCM</b> .....	319
Table 68: Atomic coordinates ( x 10 <sup>4</sup> ) and equivalent isotropic displacement parameters (Å <sup>2</sup> x 10 <sup>3</sup> ) for <b>10-DCM</b> . U(eq) is defined as one third of the trace of the orthogonalized U <sup>ij</sup> tensor. ....	320
Table 69: Bond Lengths [Å] and Bond Angles [°] for <b>10-DCM</b> .....	321

Table 70: Crystallographic Data and Structure Refinement of <b>10-MeCN</b> .....	323
Table 71: Atomic coordinates ( x 10 <sup>4</sup> ) and equivalent isotropic displacement parameters (Å <sup>2</sup> x 10 <sup>3</sup> ) for <b>10-MeCN</b> . U(eq) is defined as one third of the trace of the orthogonalized U <sup>ij</sup> tensor. ....	324
Table 72: Bond Lengths [Å] and Bond Angles [°] for <b>10-MeCN</b> .....	325
Table 73: Crystallographic Data and Structure Refinement of <b>11-CHCl<sub>3</sub></b> .....	327
Table 74: Atomic coordinates ( x 10 <sup>4</sup> ) and equivalent isotropic displacement parameters (Å <sup>2</sup> x 10 <sup>3</sup> ) for <b>11-CHCl<sub>3</sub></b> . U(eq) is defined as one third of the trace of the orthogonalized U <sup>ij</sup> tensor. ....	328
Table 75: Bond Lengths [Å] and Bond Angles [°] for <b>11-CHCl<sub>3</sub></b> .....	329
Table 76: Crystallographic Data and Structure Refinement of <b>11-THF</b> .....	332
Table 77: Atomic coordinates ( x 10 <sup>4</sup> ) and equivalent isotropic displacement parameters (Å <sup>2</sup> x 10 <sup>3</sup> ) for <b>11-THF</b> . U(eq) is defined as one third of the trace of the orthogonalized U <sup>ij</sup> tensor. ....	333
Table 78: Bond Lengths [Å] and Bond Angles [°] for <b>11-THF</b> .....	334
Table 79: Crystallographic Data and Structure Refinement of <b>11-DCM</b> .....	337
Table 80: Atomic coordinates ( x 10 <sup>4</sup> ) and equivalent isotropic displacement parameters (Å <sup>2</sup> x 10 <sup>3</sup> ) for <b>11-DCM</b> . U(eq) is defined as one third of the trace of the orthogonalized U <sup>ij</sup> tensor. ....	338
Table 81: Bond Lengths [Å] and Bond Angles [°] for <b>11-DCM</b> .....	339
Table 82: Crystallographic Data and Structure Refinement of <b>11-MeCN</b> .....	341
Table 83: Atomic coordinates ( x 10 <sup>4</sup> ) and equivalent isotropic displacement parameters (Å <sup>2</sup> x 10 <sup>3</sup> ) for <b>11-MeCN</b> . U(eq) is defined as one third of the trace of the orthogonalized U <sup>ij</sup> tensor. ....	342
Table 84: Bond Lengths [Å] and Bond Angles [°] for <b>11-MeCN</b> .....	343

Table 85: Crystallographic Data and Structure Refinement of <b>14</b> .....	345
Table 86: Atomic coordinates ( $\times 10^4$ ) and equivalent isotropic displacement parameters ( $\text{\AA}^2 \times 10^3$ ) for <b>14</b> . U(eq) is defined as one third of the trace of the orthogonalized $U^{ij}$ tensor.....	346
Table 87: Bond Lengths [ $\text{\AA}$ ] and Bond Angles [ $^\circ$ ] for <b>14</b> . .....	347
Table 88: Crystallographic Data and Structure Refinement of <b>15</b> .....	350
Table 89: Atomic coordinates ( $\times 10^4$ ) and equivalent isotropic displacement parameters ( $\text{\AA}^2 \times 10^3$ ) for <b>15</b> . U(eq) is defined as one third of the trace of the orthogonalized $U^{ij}$ tensor.....	351
Table 90: Bond Lengths [ $\text{\AA}$ ] and Bond Angles [ $^\circ$ ] for <b>15</b> . .....	352
Table 91: Crystallographic Data and Structure Refinement of <b>16</b> .....	355
Table 92: Atomic coordinates ( $\times 10^4$ ) and equivalent isotropic displacement parameters ( $\text{\AA}^2 \times 10^3$ ) for <b>16</b> . U(eq) is defined as one third of the trace of the orthogonalized $U^{ij}$ tensor.....	356
Table 93: Bond Lengths [ $\text{\AA}$ ] and Bond Angles [ $^\circ$ ] for <b>16</b> . .....	357
Table 94: Crystallographic Data and Structure Refinement of <b>17</b> .....	360
Table 95: Atomic coordinates ( $\times 10^4$ ) and equivalent isotropic displacement parameters ( $\text{\AA}^2 \times 10^3$ ) for <b>17</b> . U(eq) is defined as one third of the trace of the orthogonalized $U^{ij}$ tensor.....	361
Table 96: Bond Lengths [ $\text{\AA}$ ] and Bond Angles [ $^\circ$ ] for <b>17</b> . .....	362
Table 97: Crystallographic Data and Structure Refinement of <b>18</b> .....	365
Table 98: Atomic coordinates ( $\times 10^4$ ) and equivalent isotropic displacement parameters ( $\text{\AA}^2 \times 10^3$ ) for <b>18</b> . U(eq) is defined as one third of the trace of the orthogonalized $U^{ij}$ tensor.....	366
Table 99: Bond Lengths [ $\text{\AA}$ ] and Bond Angles [ $^\circ$ ] for <b>18</b> . .....	367

Table 100: Crystallographic Data and Structure Refinement of <b>20</b> .....	369
Table 101: Atomic coordinates ( $\times 10^4$ ) and equivalent isotropic displacement parameters ( $\text{\AA}^2 \times 10^3$ ) for <b>20</b> . U(eq) is defined as one third of the trace of the orthogonalized $U^{ij}$ tensor.....	370
Table 102: Bond Lengths [ $\text{\AA}$ ] and Bond Angles [ $^\circ$ ] for <b>20</b> . ....	371
Table 103: Crystallographic Data and Structure Refinement of <b>21</b> .....	374
Table 104: Atomic coordinates ( $\times 10^4$ ) and equivalent isotropic displacement parameters ( $\text{\AA}^2 \times 10^3$ ) for <b>21</b> . U(eq) is defined as one third of the trace of the orthogonalized $U^{ij}$ tensor.....	375
Table 105: Bond Lengths [ $\text{\AA}$ ] and Bond Angles [ $^\circ$ ] for <b>21</b> . ....	377
Table 106: Crystallographic Data and Structure Refinement of <b>14-DCM</b> .....	382
Table 107: Atomic coordinates ( $\times 10^4$ ) and equivalent isotropic displacement parameters ( $\text{\AA}^2 \times 10^3$ ) for <b>14-DCM</b> . U(eq) is defined as one third of the trace of the orthogonalized $U^{ij}$ tensor. ....	383
Table 108: Bond Lengths [ $\text{\AA}$ ] and Bond Angles [ $^\circ$ ] for <b>14-DCM</b> .....	384
Table 109: Crystallographic Data and Structure Refinement of <b>15-DCM</b> .....	387
Table 110: Atomic coordinates ( $\times 10^4$ ) and equivalent isotropic displacement parameters ( $\text{\AA}^2 \times 10^3$ ) for <b>15-DCM</b> . U(eq) is defined as one third of the trace of the orthogonalized $U^{ij}$ tensor. ....	388
Table 111: Bond Lengths [ $\text{\AA}$ ] and Bond Angles [ $^\circ$ ] for <b>15-DCM</b> .....	389
Table 112: Crystallographic Data and Structure Refinement of <b>16-DCM</b> .....	391
Table 113: Atomic coordinates ( $\times 10^4$ ) and equivalent isotropic displacement parameters ( $\text{\AA}^2 \times 10^3$ ) for <b>16-DCM</b> . U(eq) is defined as one third of the trace of the orthogonalized $U^{ij}$ tensor. ....	392
Table 114: Bond Lengths [ $\text{\AA}$ ] and Bond Angles [ $^\circ$ ] for <b>16-DCM</b> .....	393

Table 115: Crystallographic Data and Structure Refinement of <b>17-DCM</b> .....	396
Table 116: Atomic coordinates ( x 10 <sup>4</sup> ) and equivalent isotropic displacement parameters (Å <sup>2</sup> x 10 <sup>3</sup> ) for <b>17-DCM</b> . U(eq) is defined as one third of the trace of the orthogonalized U <sup>ij</sup> tensor. ....	397
Table 117: Bond Lengths [Å] and Bond Angles [°] for <b>17-DCM</b> .....	399
Table 118: Crystallographic Data and Structure Refinement of <b>18-THF</b> .....	402
Table 119: Atomic coordinates ( x 10 <sup>4</sup> ) and equivalent isotropic displacement parameters (Å <sup>2</sup> x 10 <sup>3</sup> ) for <b>18-THF</b> . U(eq) is defined as one third of the trace of the orthogonalized U <sup>ij</sup> tensor. ....	403
Table 120: Bond Lengths [Å] and Bond Angles [°] for <b>18-THF</b> .....	404
Table 121: Crystallographic Data and Structure Refinement of <b>19-DCM</b> .....	407
Table 122: Atomic coordinates ( x 10 <sup>4</sup> ) and equivalent isotropic displacement parameters (Å <sup>2</sup> x 10 <sup>3</sup> ) for <b>19-DCM</b> . U(eq) is defined as one third of the trace of the orthogonalized U <sup>ij</sup> tensor. ....	408
Table 123: Bond Lengths [Å] and Bond Angles [°] for <b>19-DCM</b> .....	409
Table 124: Crystallographic Data and Structure Refinement of <b>20-DCM</b> .....	411
Table 125: Atomic coordinates ( x 10 <sup>4</sup> ) and equivalent isotropic displacement parameters (Å <sup>2</sup> x 10 <sup>3</sup> ) for <b>20-DCM</b> . U(eq) is defined as one third of the trace of the orthogonalized U <sup>ij</sup> tensor. ....	412
Table 126: Bond Lengths [Å] and Bond Angles [°] for <b>20-DCM</b> .....	414
Table 127: Crystallographic Data and Structure Refinement of <b>21-DCM</b> .....	419
Table 128: Atomic coordinates ( x 10 <sup>4</sup> ) and equivalent isotropic displacement parameters (Å <sup>2</sup> x 10 <sup>3</sup> ) for <b>21-DCM</b> . U(eq) is defined as one third of the trace of the orthogonalized U <sup>ij</sup> tensor. ....	420
Table 129: Bond Lengths [Å] and Bond Angles [°] for <b>21-DCM</b> .....	421

## List of Figures

Figure 1: R-DAB and R-BIAN ligands. ....	1
Figure 2: BIAN* and BIAN** as new additions to nitrogen donor ligand family.	32
Figure 3: (Left) Experimental (a) and simulated (b) EPR spectra for the dearomatization radical intermediate in toluene solution at room temperature. (Right) Proposed radical intermediate structure for the radical dearomatization. <sup>35</sup> .....	38
Figure 4: BIAN derivatives selected for the investigation of BIAN functionalization pathways. <sup>38</sup> .....	41
Figure 5: Experimental (a) and simulated (b) EPR spectra of the radical intermediate in toluene solution at room temperature for dpp-BIAN (Left) and mes-BIAN (Right) with proposed radical intermediate structure (Center). <sup>35,38</sup> .....	43
Figure 6: (Left) Fukui functions for Ph-BIAN (Upper) and [Ph-BIAN] <sup>-</sup> (Lower). (Right) Labels used to identify the different positions on the BIAN ligand. <sup>38</sup> .....	49
Figure 7: Relative stabilities of the alkylation isomers for the radical dianionic [Ph-BIAN-Me] <sup>2-</sup> intermediate (Left) and the monoanionic [Ph-BIAN-Me] <sup>-</sup> intermediate (Right). <sup>38</sup> .....	50
Figure 8: SOMOs for the monoalkylated radical dianionic [Ph-BIAN-Me] <sup>2-</sup> . <sup>38</sup> ...	53
Figure 9: POV-Ray diagram of the Li-N antiprismatic core and appended BIAN C(1)-C(12) and C(45)-C(56) fragments of <b>1</b> . Thermal ellipsoids shown at 50% probability. <sup>35</sup> .....	56

Figure 10: POV-Ray diagram of complex <b>1</b> . All hydrogen atoms, benzene molecules, and all aryl isopropyl groups have been removed for clarity. Thermal ellipsoids shown at 50% probability. <sup>35</sup>	57
Figure 11: POV-Ray diagram of compound <b>2</b> . All hydrogen atoms have been removed for clarity. Thermal ellipsoids shown at 50% probability. <sup>35</sup>	58
Figure 12: POV-Ray diagram of compound <b>3</b> . All hydrogen atoms and one molecule of toluene have been removed for clarity. Thermal ellipsoids shown at 50% probability. <sup>35</sup>	59
Figure 13: POV-Ray diagram of compound <b>4</b> . All hydrogen atoms have been removed for clarity. Compound <b>4</b> crystallized with two independent molecules in the asymmetric unit; only one of which is displayed for clarity. Thermal ellipsoids shown at 50% probability. <sup>38</sup>	60
Figure 14: POV-Ray diagram of compound <b>5</b> . All hydrogen atoms have been removed for clarity with the exception of the amino hydrogen. Thermal ellipsoids shown at 50% probability. <sup>38</sup>	61
Figure 15: POV-Ray diagram of compound <b>6</b> . All hydrogen atoms have been removed for clarity with the exception of the amino hydrogen. Thermal ellipsoids shown at 50% probability. <sup>38</sup>	62
Figure 16: POV-Ray diagram of compound <b>7</b> . All hydrogen atoms have been removed for clarity with the exception of the amino hydrogen. Thermal ellipsoids shown at 50% probability. <sup>38</sup>	63
Figure 17: POV-Ray diagram of compound <b>8a</b> . All hydrogen atoms have been removed for clarity with the exception of the amino hydrogens. Thermal ellipsoids shown at 50% probability. <sup>38</sup>	64

Figure 18: POV-Ray diagram of compound <b>8b</b> . All hydrogen atoms have been removed for clarity with the exception of the amino hydrogens. Thermal ellipsoids shown at 50% probability. Compound <b>8b</b> crystallized with one molecule in the asymmetric unit. The expanded hydrogen bond dimer is displayed for clarity. <sup>38</sup>	66
Figure 19: POV-Ray diagram of the overlay of polymorphs <b>8a</b> and <b>8b</b> . All hydrogen atoms have been removed for clarity. Thermal ellipsoids shown at 50% probability. <sup>38</sup>	67
Figure 20: POV-Ray diagram of compound <b>9a</b> . All hydrogen atoms have been removed for clarity with the exception of the amino hydrogen. Thermal ellipsoids shown at 50% probability. <sup>38</sup>	68
Figure 21: POV-Ray diagram of compound <b>9b</b> . All hydrogen atoms have been removed for clarity with the exception of the amino hydrogen. Thermal ellipsoids shown at 50% probability. <sup>38</sup>	69
Figure 22: POV-Ray diagram of the overlay of polymorphs <b>9a</b> and <b>9b</b> . All hydrogen atoms have been removed for clarity. Thermal ellipsoids shown at 50% probability.	70
Figure 23: Non-luminescent <i>para</i> -substituted Re(Ar-BIAN)(CO) <sub>3</sub> (Cl) complexes <b>A-E</b> . <sup>50</sup>	81
Figure 24: Photoluminescent platinum(II) BIAN complexes ( <b>F, G, H</b> ). <sup>51</sup>	82
Figure 25: (Left) Photoluminescent platinum BIAN complexes featuring substituted acetylide ligands ( <b>I-M</b> ). (Right) Emission spectra of <b>I-M</b> in DCM solution at room temperature. <sup>52</sup>	83
Figure 26: Photoluminescent emission of ruthenium BIAN complexes <b>N, O, and P</b> at room temperature in DCM solution. <sup>53</sup>	84



Figure 27: Photoluminescent emissions of Cu(I) dimeric BIAN complexes <b>Q</b> , <b>R</b> , and <b>S</b> at room temperature in DCM solution. <sup>54</sup>	85
Figure 28: Phenyl substituted silole <b>T</b> displayed with twisted and coplanar orientations. <sup>61</sup>	87
Figure 29: (Left) Photoluminescent spectra for a 90:10 % water/ethanol volumetric mixture of <b>T</b> , pure ethanol solution of <b>T</b> , and solid film of <b>T</b> . (Right) Plot of the quantum yields of silole <b>T</b> with different water/ethanol volumetric mixtures. <sup>61</sup>	88
Figure 30: (Top) Hexaphenylsilole <b>U</b> is AIE active in acetonitrile/water volumetric mixtures. <sup>62</sup> (Bottom) N,N-Dicyclohexyl-3,4,9,10-perylenetetracarboxylic diimide <b>V</b> demonstrates ACQ in THF/water volumetric mixtures. <sup>63</sup>	89
Figure 31: (Left) AIE experiment of HPS ( <b>U</b> ) with acetone/water volumetric fractions. (Right) Photoluminescent (PL) intensity of silole HPS <b>U</b> increased with increasing viscosity of methanol/glycerol volumetric mixtures. <sup>64</sup>	91
Figure 32: (Left) Piezochromism experiment of HPS ( <b>U</b> ) displaying increasing PL (photoluminescent) intensity with increasing applied pressure. (Right) Piezochromic behavior of the intensity of HPS and AlQ <sub>3</sub> with increasing applied pressure. <sup>65</sup>	92
Figure 33: (Left) Thermochromism experiment of HPS ( <b>U</b> ) in THF solution displaying the increase of PL intensity with decreasing temperature. (Right) Dynamic <sup>1</sup> H NMR experiment displaying RIR with decreasing temperature in a deuterated dichloromethane solution of <b>U</b> . <sup>64</sup>	93

Figure 34: Butter-fly shaped cholesteryl substituted pyran compound <b>W</b> exhibiting green, yellow, and red emissions. <sup>71</sup> .....	95
Figure 35: Multicolor tuning of the AIE active substituted diphenyl- <i>o</i> -carborane compounds. <sup>72</sup> .....	96
Figure 36: (Left) Crystal structure of compound <b>Z</b> . (Right) Viscochromism study of compound <b>Z</b> in methanol/glycerol volumetric mixtures <sup>72</sup> .....	97
Figure 37: (Left) Thermochromism experiment of <b>Z</b> in 2-Me-THF solution. (Right) Dynamic <sup>1</sup> H NMR experiment of <b>Z</b> in deuterated dichloromethane solution. <sup>72</sup> .....	98
Figure 38: Multicolor tuning of pyrene luminophore via acylation. <sup>73</sup> .....	99
Figure 39: Progressive acylation lead to an increase in intermolecular orbital overlap between pyrene units and an overall red shift in the emission. <sup>73</sup> ....	100
Figure 40: Emission spectra of the five polymorphs of compound <b>AE</b> . <sup>75</sup> .....	101
Figure 41: Packing interactions of the five polymorphs of compound <b>AE</b> with photographs of each crystal under UV irradiation. <sup>75</sup> .....	102
Figure 42: Solid state emissions from two polymorphs of 1,4,7,10-tetra( <i>n</i> -butyl)tetracene compound <b>AF</b> . <sup>77</sup> .....	103
Figure 43: Packing environments of polymorphs <b>AF1</b> and <b>AF2</b> featuring herringbone and slipped-stacked arrangements, respectively. <sup>77</sup> .....	104
Figure 44: Emission spectra for the polymorph and pseudopolymorphs of <b>AG</b> . The solution based emission spectrum of <b>AG</b> was performed in a dilute chloroform solution. <sup>78</sup> .....	105
Figure 45: Stacking interactions of the polymorph and pseudopolymorph structures of <b>AG</b> with <i>d</i> = distance between quinacridone rings and $\theta$ = angle between quinacridone centroids. <sup>78</sup> .....	106

Figure 46: Crystal packing diagrams for polymorphs <b>AH1</b> and <b>AH2</b> for [Re <sub>2</sub> (μ-Cl) <sub>2</sub> (CO) <sub>6</sub> (μ-4,5(SiMe <sub>3</sub> ) <sub>2</sub> -pyridazine)] complex <b>AH</b> . <sup>79</sup>	107
Figure 47: Emission spectra and photographs displaying the solid state emissions from polymorphs <b>AH1</b> and <b>AH2</b> for [Re <sub>2</sub> (μ-Cl) <sub>2</sub> (CO) <sub>6</sub> (μ-4,5(SiMe <sub>3</sub> ) <sub>2</sub> -pyridazine)] complex <b>AH</b> . <sup>79</sup>	108
Figure 48: Various crystal packing diagrams for polymorphs <b>AI1</b> , <b>AI2</b> , and <b>AI3</b> for 9,10-Bis((E)-2(pyrid-2-yl)vinyl)anthracene ( <b>AI</b> ). <sup>80</sup>	109
Figure 49: Progressive red shift in emission with respect to degree of π-stacking interactions for polymorphs <b>AI1</b> , <b>AI2</b> , and <b>AI3</b> for 9,10-Bis((E)-2(pyrid-2-yl)vinyl)anthracene ( <b>AI</b> ). <sup>80</sup>	110
Figure 50: Polymorph structures <b>AJ1</b> and <b>AJ2</b> featuring <i>anti</i> and <i>syn</i> relationships between methoxy groups. <sup>81</sup>	111
Figure 51: Methyl substituted Ar-BIAN zinc complexes <b>10-13</b> . <sup>82</sup>	113
Figure 52: UV/vis absorption spectra for complexes <b>10-13</b> in DCM solution at room temperature. <sup>82</sup>	114
Figure 53: (Top) Solid state absorption spectra with optical images of complexes <b>10-13</b> in DCM solution and in the solid state under ambient light and UV irradiation. Solid state emission (Bottom-Left) and excitation (Bottom-Right) spectra for complexes <b>10-13</b> . BaSO <sub>4</sub> was used as a background scan material for the solid state emission scans. <sup>82</sup>	116
Figure 54: AIE experiment of <b>10</b> in DCM/hexanes volumetric mixtures along with photographs of each fraction under ambient light and UV irradiation (the percentage values above are relative to the DCM content). <sup>82</sup>	117

Figure 55: AIE experiment of <b>11</b> in THF/hexanes volumetric mixtures along with photographs of each fraction under ambient light and UV irradiation (the percentage values above are relative to the THF content). <sup>82</sup> .....	118
Figure 56: POV-Ray diagrams for complexes <b>10-13</b> with thermal ellipsoids displayed at 50% probability. All hydrogen atoms have been removed for clarity. Note however, that complex <b>11</b> crystallized with two molecules in the asymmetric unit. One of these molecules has been removed for clarity. All four complexes crystallized without any solvent in the crystal lattice. <sup>82</sup> .....	120
Figure 57: Crystal packing diagrams for complexes <b>10-13</b> . <sup>82</sup> .....	121
Figure 58: Transition density of the radiative decay from the $T_1 \rightarrow S_0$ transition for complex <b>10</b> . <sup>82</sup> .....	122
Figure 59: Stacking interactions of solvatomorphs for complexes <b>10</b> and <b>11</b> (Top). Slipped stacked $\pi$ - $\pi$ interactions (Bottom): a = interplanar distance, b = slip distance of naphthalene centroids, c = distance between naphthalene centroids, $\theta$ = slip angle between naphthalene centriods. <sup>82</sup> .....	123
Figure 60: (Top) Emission spectra, optical images (Middle), and fluorescent images (Bottom) for solvatomorphs <b>10-11-MeCN</b> . <sup>82</sup> .....	126
Figure 61: Excitation spectra for all ten emissive complexes <b>10-11-MeCN</b> . <sup>82</sup> ...	126
Figure 62: UV/vis spectra of Ar-BIAN zinc chloride complexes <b>14-21</b> in DCM solution at room temperature with photographs of each complex in DCM solution under ambient light and UV irradiation. ....	129
Figure 63: Solid state diffuse reflectance spectra for complexes <b>14-21</b> . ....	130

Figure 64: Solid state emission (Top-Left) and excitation (Top-Right) spectra for <b>14-21</b> along with a photograph of each complex under ambient light and UV irradiation. ....	131
Figure 65: (Left) Hammett relationship between the $\lambda_{\max}$ values vs. the $\sigma_p$ values without outlier complex <b>16</b> . (Right) Hammett relationship with outlier complex <b>16</b> .....	134
Figure 66: AIE emission spectra and images of DCM/hexanes volumetric fractions of <b>14-19</b> in ambient light and under UV irradiation (the percentage values above are relative to the DCM content).....	136
Figure 67: POV-Ray diagrams for complexes <b>14-19</b> , <b>20</b> , and <b>21</b> with thermal ellipsoids displayed at 50% probability. All hydrogen atoms have been removed for clarity. Note however, that complexes <b>20</b> and <b>21</b> crystallized with only half of the dimeric complex in the asymmetric unit. The expanded complex is displayed for clarity. ....	137
Figure 68: POV-Ray diagrams of the solvatomorphs <b>14-DCM-17-DCM</b> , <b>18</b> , and <b>19-DCM-21-DCM</b> with thermal ellipsoids displayed at 50% probability. All hydrogen atoms have been removed for clarity. Note however, that solvatomorph <b>20-DCM</b> crystallized with two complexes in the asymmetric unit, only one of which is displayed for clarity.....	140
Figure 69: Solid state emission (Top-Left) and excitation (Top-Right) spectra of the solvatomorphs <b>14-DCM-17-DCM</b> , <b>18</b> , and <b>19-DCM-21-DCM</b> with photograph of solvatomorphs under ambient light and UV irradiation. ....	141

Figure 70: POV-Ray diagrams of <b>18</b> (Left), <b>18-THF</b> (Center), and an overlay image (Right) of both crystal structures with thermal ellipsoids displayed at 50% probability. All hydrogen atoms have been removed for clarity.	143
Figure 71: Solid state emission spectra for <b>18</b> and <b>18-THF</b> with each complex under a fluorescent microscope, ambient light, and UV irradiation.	143
Figure 72: POV-Ray diagram of complex <b>10</b> with thermal ellipsoids displayed at 50% probability. All hydrogen atoms have been removed for clarity. <sup>82</sup>	146
Figure 73: POV-Ray diagram of complex <b>11</b> with thermal ellipsoids displayed at 50% probability. All hydrogen atoms have been removed for clarity. Complex <b>11</b> crystallized with two complexes in the asymmetric unit, only one of which is presented above. <sup>82</sup>	147
Figure 74: POV-Ray diagram of complex <b>12</b> with thermal ellipsoids displayed at 50% probability. All hydrogen atoms have been removed for clarity. <sup>82</sup>	148
Figure 75: POV-Ray diagram of complex <b>13</b> with thermal ellipsoids displayed at 50% probability. All hydrogen atoms have been removed for clarity. <sup>82</sup>	149
Figure 76: POV-Ray diagram of complex <b>10-CHCl<sub>3</sub></b> with thermal ellipsoids displayed at 50% probability. All hydrogen atoms have been removed for clarity. <sup>82</sup>	150
Figure 77: POV-Ray diagram of complex <b>10-THF</b> with thermal ellipsoids displayed at 50% probability. All hydrogen atoms have been removed for clarity. <sup>82</sup>	151
Figure 78: POV-Ray diagram of complex <b>10-DCM</b> with thermal ellipsoids displayed at 50% probability. All hydrogen atoms have been removed for clarity. <sup>82</sup>	152

Figure 79: POV-Ray diagram of complex <b>10-MeCN</b> with thermal ellipsoids displayed at 50% probability. All hydrogen atoms have been removed for clarity. <sup>82</sup> .....	153
Figure 80: POV-Ray diagram of complex <b>11-CHCl<sub>3</sub></b> with thermal ellipsoids displayed at 50% probability. All hydrogen atoms have been removed for clarity. <sup>82</sup> .....	154
Figure 81: POV-Ray diagram of complex <b>11-THF</b> with thermal ellipsoids displayed at 50% probability. All hydrogen atoms have been removed for clarity. <sup>82</sup> .....	155
Figure 82: POV-Ray diagram of complex <b>11-DCM</b> with thermal ellipsoids displayed at 50% probability. All hydrogen atoms have been removed for clarity. <sup>82</sup> .....	156
Figure 83: POV-Ray diagram of complex <b>11-MeCN</b> with thermal ellipsoids displayed at 50% probability. All hydrogen atoms have been removed for clarity. <sup>82</sup> .....	157
Figure 84: POV-Ray diagram of complex <b>14</b> with thermal ellipsoids displayed at 50% probability. All hydrogen atoms have been removed for clarity. ...	158
Figure 85: POV-Ray diagram of complex <b>15</b> with thermal ellipsoids displayed at 50% probability. All hydrogen atoms have been removed for clarity. ...	159
Figure 86: POV-Ray diagram of complex <b>16</b> with thermal ellipsoids displayed at 50% probability. All hydrogen atoms have been removed for clarity. ...	160
Figure 87: POV-Ray diagram of complex <b>17</b> with thermal ellipsoids displayed at 50% probability. All hydrogen atoms have been removed for clarity. ...	161
Figure 88: POV-Ray diagram of complex <b>18</b> with thermal ellipsoids displayed at 50% probability. All hydrogen atoms have been removed for clarity. ...	162

Figure 89: POV-Ray diagram of complex <b>20</b> with thermal ellipsoids displayed at 50% probability. All hydrogen atoms have been removed for clarity. Note however, complex <b>20</b> crystallized with half of the dimeric complex in the asymmetric unit. The expanded complex is displayed for clarity.	163
Figure 90: POV-Ray diagram of complex <b>21</b> with thermal ellipsoids displayed at 50% probability. All hydrogen atoms have been removed for clarity. Note however, complex <b>21</b> crystallized with two complexes in the asymmetric unit.	164
Figure 91: POV-Ray diagram of complex <b>14-DCM</b> with thermal ellipsoids displayed at 50% probability. All hydrogen atoms have been removed for clarity.	165
Figure 92: POV-Ray diagram of complex <b>15-DCM</b> with thermal ellipsoids displayed at 50% probability. All hydrogen atoms have been removed for clarity.	166
Figure 93: POV-Ray diagram of complex <b>16-DCM</b> with thermal ellipsoids displayed at 50% probability. All hydrogen atoms have been removed for clarity.	167
Figure 94: POV-Ray diagram of complex <b>17-DCM</b> with thermal ellipsoids displayed at 50% probability. All hydrogen atoms have been removed for clarity.	168
Figure 95: POV-Ray diagram of complex <b>18-THF</b> with thermal ellipsoids displayed at 50% probability. All hydrogen atoms have been removed for clarity.	169



Figure 96: POV-Ray diagram of complex <b>19-DCM</b> with thermal ellipsoids displayed at 50% probability. All hydrogen atoms have been removed for clarity. .....	170
Figure 97: POV-Ray diagram of complex <b>20-DCM</b> with thermal ellipsoids displayed at 50% probability. All hydrogen atoms have been removed for clarity. Note however, complex <b>20-DCM</b> crystallized with two complexes and two DCM solvent molecules in the asymmetric unit. Only one DCM and one complex are displayed for clarity. ....	171
Figure 98: POV-Ray diagram of complex <b>21-DCM</b> with thermal ellipsoids displayed at 50% probability. All hydrogen atoms have been removed for clarity. .....	172
Figure 99: Experimental (black) and simulated (blue) X-ray powder pattern for complexes <b>10-13</b> . Experimental and simulated powder patterns are in acceptable agreement. <sup>82</sup> .....	173
Figure 100: Experimental (black) and simulated (blue) X-ray powder pattern for complexes <b>10-CHCl<sub>3</sub>-10-MeCN</b> . Experimental and simulated powder patterns are in acceptable agreement. <sup>82</sup> .....	174
Figure 101: Experimental (black) and simulated (blue) X-ray powder pattern for complexes <b>11-CHCl<sub>3</sub>-11-MeCN</b> . Experimental and simulated powder patterns are in acceptable agreement. <sup>82</sup> .....	175
Figure 102: Experimental (black) and simulated (blue) X-ray powder pattern for complexes <b>14-17</b> . Experimental and simulated powder patterns are in acceptable agreement. <sup>82</sup> .....	176

Figure 103: Experimental (black) and simulated (blue) X-ray powder pattern for complexes <b>18</b> , <b>20</b> , and <b>21</b> . Experimental and simulated powder patterns are in acceptable agreement. <sup>82</sup> .....	177
Figure 104: Experimental (black) and simulated (blue) X-ray powder pattern for complexes <b>14-DCM-17-DCM</b> . Experimental and simulated powder patterns are in acceptable agreement. <sup>82</sup> .....	178
Figure 105: Experimental (black) and simulated (blue) X-ray powder pattern for complexes <b>19-THF-21-DCM</b> . Experimental and simulated powder patterns are in acceptable agreement. <sup>82</sup> .....	179
Figure 106: Calculated thermal conductivity values vs. temperature for diamond, BN, BP, BAs, and BSb. Open shapes are experimental data points. Closed circles are for GaN(230 m <sup>-1</sup> K <sup>-1</sup> ), Al(240 m <sup>-1</sup> K <sup>-1</sup> ), AlN(285 m <sup>-1</sup> K <sup>-1</sup> ), Cu(400 m <sup>-1</sup> K <sup>-1</sup> ), SiC(490 m <sup>-1</sup> K <sup>-1</sup> ). <sup>104</sup> .....	195
Figure 107: Frequency of the phonon modes in silicon (Red) and BAs (Black). Large acoustic-optical frequency gap inhibits scattering between these phonons. Acoustic bunching of longitudinal (LA) and two transverse (TA) acoustic phonon branches inhibits scattering between these phonon modes. <sup>104</sup> .....	197
Figure 108: Powder X-ray diffraction pattern of cubic BAs with lattice constant of a = 4.7801(2) Å. <sup>110</sup> .....	199
Figure 109: SEM images of BAs crystals. <sup>110</sup> .....	200
Figure 110: Effect of arsenic deficiencies on thermal conductivity in BAs crystals. <sup>110</sup> .....	201
Figure 111: Post reaction quartz vessel with a large arsenic crystal and boron substrates that had visibly undergone a reaction.....	203

Figure 112: Boron substrate with visible BAs growth (silver color) on the surface as visualized by a conventional microscope (Left) and SEM (Right).	203
Figure 113: Powder X-ray diffraction data of a boron substrate with BAs surface growth: (Black) BAs growth on a boron substrate, (Red) theoretical cubic BAs, (Blue) unreacted boron substrate, and (Green) theoretical $\beta$ -rhombohedral boron. <sup>103,112</sup>	204
Figure 114: Raman spectra for the current experimental BAs sample (Blue) and previously reported BAs sample (Red). <sup>113</sup>	205
Figure 115: Full Raman spectrum for the experimental BAs material.	206
Figure 116: XPS peaks for B 1s electrons and As 3d electrons.	207
Figure 117: SEM images of three boron substrates obtained from the same growth. These images display poor (Left), medium (Center), and high (Right) surface coverage.	207
Figure 118: SEM images of different BAs morphologies.	208
Figure 119: SEM image of microheater device. <sup>115</sup>	209
Figure 120: SEM images of BAs morphologies that are potentially suitable for measurement with microheater devices.	210
Figure 121: SEM and microscope images of the BAs microstructure loaded onto a microheater device.	211
Figure 122: SEM images of 4-probe microheater device with suspended 240 nm thick silicon nanowire. <sup>116</sup>	213
Figure 123: SEM images of 4-probe microheater device with suspended BAs microstructure.	214

Figure 124: (Top) Experimental value of the thermal conductivity of the BAs  
microstructure. (Bottom) SEM image displaying contact resistance  
between the heater lines and BAs the microstructure.....215

## List of Schemes

Scheme 1: General synthesis of aryl substituted BIAN ligands. <sup>5</sup> .....	2
Scheme 2: Mono-, di-, tri-, and tetranionic dpp-BIAN species. <sup>15</sup> .....	3
Scheme 3: Syntheses of imine C-alkylated dpp-BIAN* compounds <b>B</b> and <b>C</b> . <sup>16</sup> .....	5
Scheme 4: Syntheses of imine C-ethylated dpp-BIAN* magnesium complexes <b>D</b> , <b>E</b> , and <b>F</b> . <sup>17</sup> .....	6
Scheme 5: Imine C-butylation of free dpp-BIAN with <i>n</i> -BuLi. <sup>18</sup> .....	7
Scheme 6: Hydrolysis of the imine C-butyated lithium BIAN* complex <b>G</b> to yield free amino-imine BIAN* ligand <b>I</b> . <sup>18</sup> .....	8
Scheme 7: Salt metathesis reaction of imine C-butyated lithium BIAN* complex <b>G</b> to yield BIAN* Ge(II) complex <b>J</b> . <sup>18</sup> .....	8
Scheme 8: Syntheses of dpp-BIAN* zinc complexes ( <b>K</b> , <b>L</b> , <b>M</b> ). <sup>19</sup> .....	9
Scheme 9: Syntheses of BIAN* group 13 alkyl complexes <b>N</b> , <b>O</b> , and <b>P</b> . <sup>20</sup> .....	10
Scheme 10: Synthesis of the allyl substituted BIAN* aluminum complex <b>R</b> and the imine C-allylated BIAN* ligand <b>S</b> . <sup>20</sup> .....	10
Scheme 11: Formation of the gallium-zinc bonded complex <b>V</b> using the dpp-BIAN* ligand as a support. <sup>21</sup> .....	11
Scheme 12: Syntheses of mes-BIAN alkyl zinc complexes <b>W</b> , <b>X</b> , and <b>Y</b> . <sup>27</sup> .....	13
Scheme 13: $\epsilon$ -Caprolactone polymerization using the mes-BIAN alkyl zinc salt catalyst <b>X</b> and mes-BIAN* neutral alkyl zinc catalyst <b>Y</b> . <sup>27</sup> .....	14
Scheme 14: Reversible addition of alkynes to digallane BIAN complex <b>T</b> . <sup>28</sup> .....	16
Scheme 15: Mechanism for the hydroamination of alkynes catalyzed by digallane BIAN complex <b>T</b> . <sup>13</sup> .....	18

Scheme 16: Reactions of alkynes with dialane BIAN complex <b>AF</b> and thermal instability of complex <b>AH</b> . <sup>29</sup>	19
Scheme 17: Reaction 1-phenyl-1-propyne with dialane BIAN complex <b>AF</b> and thermal decomposition of <b>AJ</b> . <sup>29</sup>	20
Scheme 18: Reaction of diphenylacetylene and methyvinylketone with dpp-BIAN aluminum complex <b>AL</b> . <sup>30</sup>	21
Scheme 19: Hydroamination/hydroarylation reactions of diphenylamine with phenylacetylene using <b>AM</b> as a catalyst. <sup>30</sup>	22
Scheme 20: Formation of the dpp-BIAN* Re(I) complex <b>AP</b> by reaction of <b>AO</b> with KN(SiMe <sub>3</sub> ) <sub>2</sub> . <sup>31</sup>	23
Scheme 21: Reaction of digallane complex <b>T</b> with benzylideneacetone. <sup>32</sup>	24
Scheme 22: Thermal decomposition of complex <b>AQ</b> to form <b>AR</b> and dpp-BIAN* ligand <b>AS</b> . <sup>32</sup>	24
Scheme 23: Dearomatization reaction of dpp-BIAN K(CH(SiMe <sub>3</sub> ) <sub>2</sub> ) in deuterated benzene solution. <sup>33</sup>	25
Scheme 24: Dearomatization reaction of dpp-BIAN with bis(trimethylsilyl)methyl alkaline earth complexes. <sup>33</sup>	26
Scheme 25: Dearomatization reaction of dpp-BIAN with K[CH(SiMe <sub>3</sub> )(2-NMe <sub>2</sub> )C <sub>6</sub> H <sub>4</sub> ]. <sup>34</sup>	28
Scheme 26: Formation of Ba dpp-BIAN** complexes ( <b>AY</b> , <b>AZ</b> ) and the unexpected backbone dearomatized dimeric BIAN species <b>AAA</b> . <sup>34</sup>	29
Scheme 27: Formation of Ca dpp-BIAN** complex <b>AAB</b> . <sup>34</sup>	29
Scheme 28: Synthesis of vicinal di- <i>t</i> -butylated dearomatized dpp-BIAN lithium antiprismatic complex ( <b>1</b> ). <sup>35</sup>	33

Scheme 29: Formation of vicinal di- <i>t</i> -butylated, dearomatized free dpp-BIAN ligand <b>2</b> . <sup>35</sup> .....	35
Scheme 30: Nucleophilic dearomatization of naphthalene with <i>t</i> -BuLi. <sup>37</sup> .....	36
Scheme 31: Formation mono- <i>t</i> -butyl-hydroxy dearomatized free dpp-BIAN ligand <b>3</b> . <sup>35</sup> .....	37
Scheme 32: Versatile pathways for BIAN functionalization. <sup>18,33,35</sup> .....	40
Scheme 33: <i>mes</i> -BIAN and dpp-BIAN reactivity with <i>t</i> -BuLi. <sup>38</sup> .....	42
Scheme 34: 4-F-BIAN and 4-OMe-BIAN reactivity with <i>t</i> -BuLi. <sup>38</sup> .....	44
Scheme 35: Backbone dearomatization and imine C-alkylation of <i>mes</i> -BIAN. <sup>38</sup> .....	45
Scheme 36: Imine C-alkylation of 4-F-BIAN and 4-OMe-BIAN. <sup>38</sup> .....	46
Scheme 37: Proposed mechanism for the formation of the monoalkylated radical dianionic intermediate. <sup>38</sup> .....	48
Scheme 38: Pathways for the nucleophilic imine C-alkylation and radical dearomatization functionalization reactions of the Ar-BIAN ligand. <sup>38</sup> .....	54
Scheme 39: Syntheses of methyl substituted Ar-BIAN zinc complexes. <sup>82</sup> .....	112
Scheme 40: Syntheses of <i>para</i> -substituted Ar-BIAN zinc chloride complexes <b>14-21</b> . .....	128

# Chapter 1: Functionalization of the Bis(imino)acenaphthene Ligand\*

## 1.1 INTRODUCTION

### 1.1.1 History and Properties

The bis(imino)acenaphthene (BIAN) ligand was first synthesized and reported in the early 1960s. This work was pioneered by Matei *et al.* and Dvolaitzky who described the first condensation reactions of aminophenols with acenaphthenequinone.<sup>1-4</sup> However, BIAN research remained dormant until the 1990s, at which point it became more widely researched.<sup>5</sup> Currently, the most prevalent application of R-BIAN is as a ligand support for polymerization catalysts. In 1995, Brookhart *et al.* reported the use of 1,4-diaza-1,3-butadiene (R-DAB) and R-BIAN as ligand supports for Pd(II) and Ni(II) olefin polymerization catalysts.<sup>6</sup> Subsequently, the use of R-BIAN as a support for polymerization catalysts was expanded to include a vast array of different polymerization processes that include: lactide,<sup>7</sup> ethylene,<sup>8</sup> 1-hexene and 1-decene,<sup>9</sup> polyketones,<sup>10</sup> dienes,<sup>11</sup> and atom-transfer radical-polymerization of styrene.<sup>12</sup> To date the neutral BIAN ligand has been used in over 1200 d-block metal complexes.<sup>13</sup>

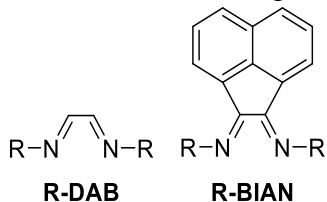


Figure 1: R-DAB and R-BIAN ligands.

---

\* Evans, D. A.; Cowley, A. H. *J. Am. Chem. Soc.* **2012**, *134*, 15676-15675.

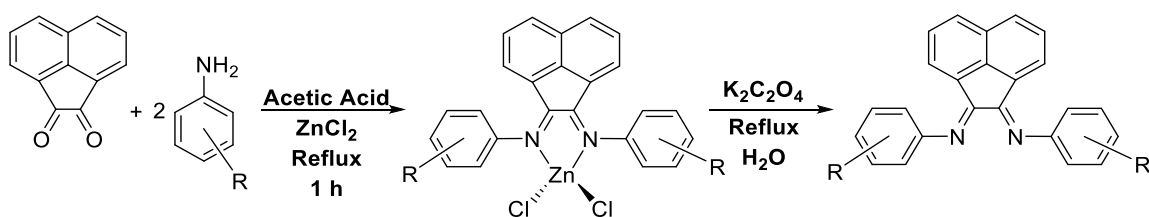
Acknowledgement is made to A. H. Cowley for supervision.

\* Evans, D. A.; Vargas-Baca, I.; Cowley, A. H. *J. Am. Chem. Soc.* **2013**, *135*, 13939-13946.



Acknowledgments are made to I. Vargas-Baca for his computational modeling contributions and A. H. Cowley for supervision.

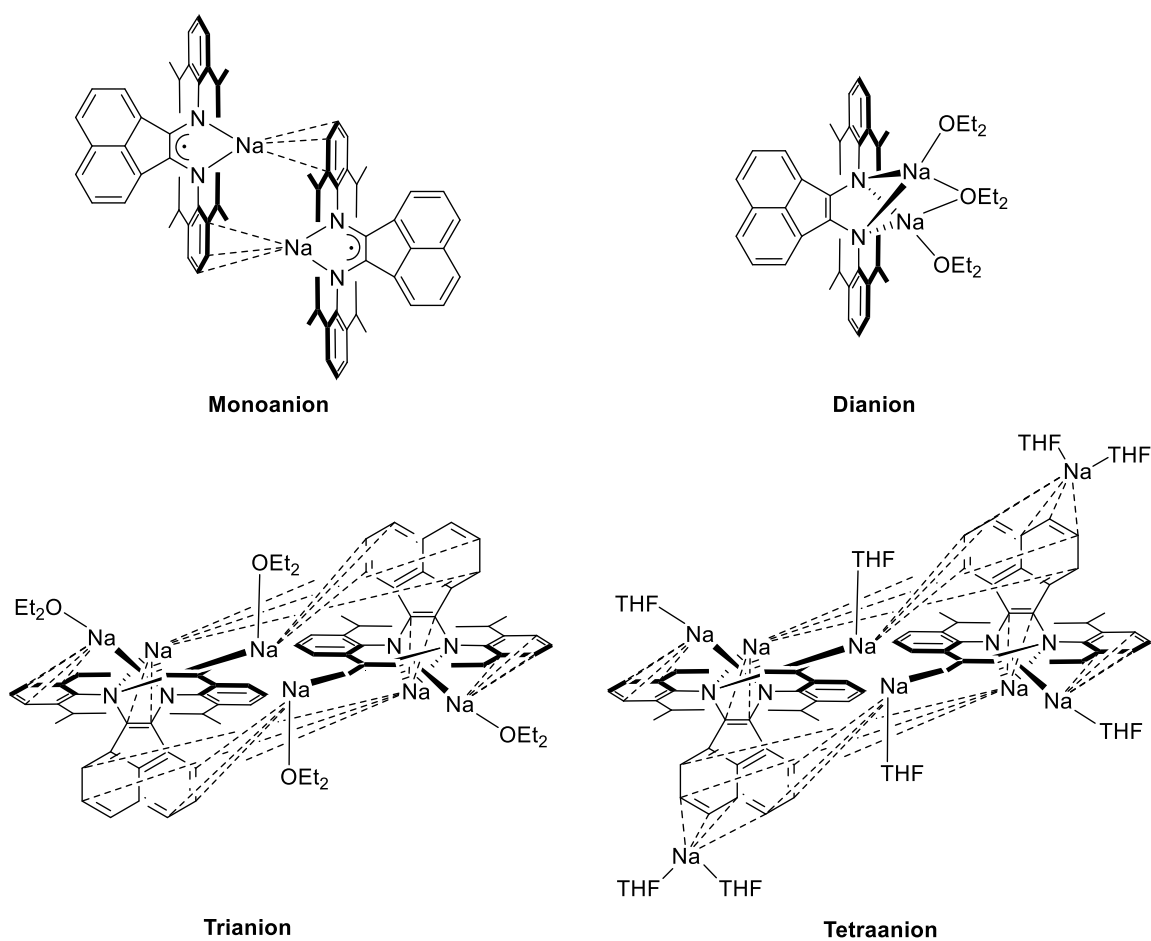
As displayed in Figure 1, the R-BIAN ligand can be visualized as the fusion of the R-DAB structure to a naphthalene unit. While the R-DAB ligand has the freedom of rotation of the N-C-C-N fragment, the R-BIAN ligand features a naphthalene backbone unit that inhibits this rotation. Overall, this structural change results in a more rigid ligand and locks the N-C-C-N bidentate chelation unit into the *s-cis* conformation. A study performed by Ragaini *et al.* displayed the robust and strong donicity of the R-BIAN ligand class by comparing the formation constants of Pd(0) and Pd(II) complexes of R-BIAN with other strong well known bidentate nitrogen donor ligands.<sup>14</sup> On the basis of this study, it was determined that the donicity strength of BIAN was akin to that of the ubiquitous phenanthroline and bipyridine.



Scheme 1: General synthesis of aryl substituted BIAN ligands.<sup>5</sup>

Another advantageous property of this robust bidentate nitrogen donor ligand relates to the ability to tune the stereoelectronic properties of the flanking aryl substituents by judicious choice of the aniline that was used for the synthesis of BIAN. As exhibited in Scheme 1, the synthesis of aryl substituted BIAN ligands (Ar-BIAN) is performed by refluxing an acetic acid solution of acenaphthenequinone with two equivalents of aniline in the presence of anhydrous zinc chloride. The foregoing condensation reaction results in the formation of the Ar-BIAN zinc(II) chloride complex.

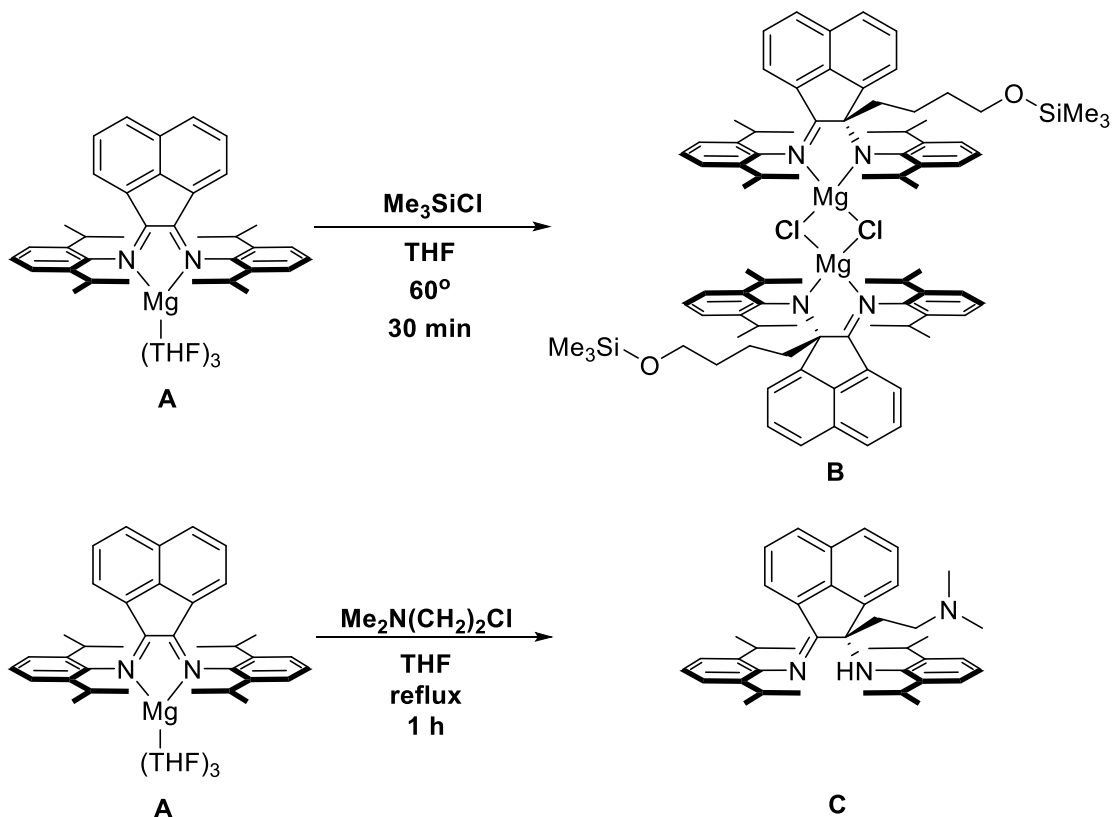
Subsequent decomplexation can be easily achieved by reflux in an aqueous potassium oxalate solution, thereby generating the free Ar-BIAN ligand. The versatility of this reaction is evident from the large variety of substituents on the aniline starting material. By employing different aniline reactants, installation of various electronic or steric protecting groups into the Ar-BIAN ligand framework can be readily achieved, thus yielding the desired ligand properties.



Scheme 2: Mono-, di-, tri-, and tetranionic dpp-BIAN species.<sup>15</sup>

Yet another advantageous and fascinating aspect of Ar-BIAN is its rich redox chemistry. This aspect was elegantly demonstrated by Fedushkin *et al.*, who treated 2,6-diisopropylphenyl (dpp) BIAN with sodium metal, thereby sequentially reducing the dpp-BIAN to the mono-, di-, tri-, and tetranions.<sup>15</sup> As displayed in Scheme 2, the first reduction event occurred in the N-C-C-N fragment to form the delocalized radical monoanion. The subsequent reduction also occurred in the N-C-C-N fragment resulting in the formation of the diamagnetic dianionic species. The next reduction event took place in the one of the rings of the naphthalene backbone to produce the trianionic species. Finally, the fourth reduction event took place in the other naphthalene ring, thus generating the tetraanionic species.

### 1.1.2 Functionalization of the BIAN Ligand Class via Imine C-alkylation: Syntheses and Applications of BIAN\* Derivatives

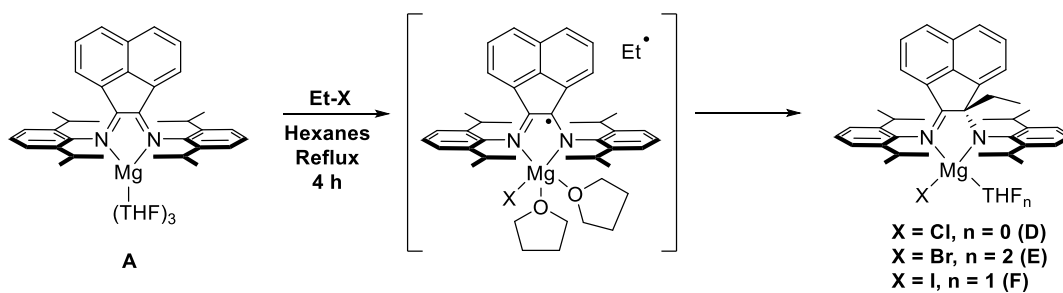


Scheme 3: Syntheses of imine C-alkylated dpp-BIAN\* compounds **B** and **C**.<sup>16</sup>

Recently, several research groups have chosen to focus on the functionalization of BIAN with the objective of modifying the properties of this ligand class. This type of functionalization was initially observed serendipitously by Fedushkin *et al.* in 2004.<sup>16</sup> In this work, the reactivity of the dianionic (dpp-BIAN) $\text{Mg}(\text{THF})_3$  complex **A** was under investigation. Interestingly, Fedushkin *et al.* encountered an unexpected reactivity of **A** with  $\text{Me}_3\text{SiCl}$  in THF solution. As displayed in Scheme 3, this reaction involved the cleavage of the THF solvent molecule and alkylation of the imine moiety of the dpp-

BIAN ligand. Furthermore, the Cl atom migrated to the magnesium metal center thus forming the imine C-alkylated, bridged dichloro species **B**. This class of imine C-alkylated derivatives of BIAN will henceforth be referred to as BIAN\* derivatives.

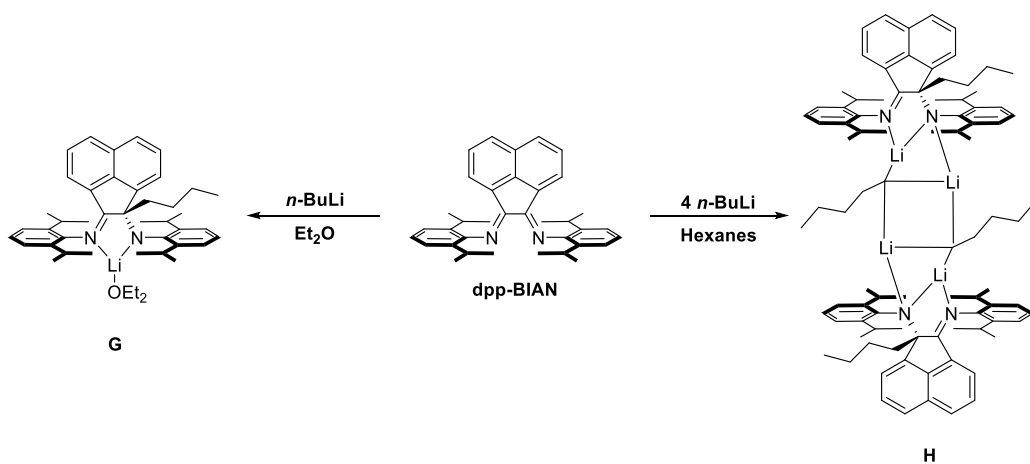
A similar reactivity was observed upon reaction of the same (dpp-BIAN)Mg(THF)<sub>3</sub> complex **A** with 2-(dimethyl-amino)ethyl chloride.<sup>16</sup> Presumably, a similar reaction took place in which the chloro species migrated to the magnesium metal center and the BIAN ligand underwent an analogous imine C-alkylation reaction. However, the authors surmised that the isolation of the hydrolyzed form of the amino-imine product **C** could be due to the presence of residual water or HCl in the reaction mixture. In fact, the 2-(dimethyl-amino)ethyl chloride that was used in the above reaction, had been synthesized previously via the reaction of the HCl salt of 2-(dimethyl-amino)ethyl chloride with sodium hydroxide, thus causing the proposed water or HCl contamination.



Scheme 4: Syntheses of imine C-ethylated dpp-BIAN\* magnesium complexes **D**, **E**, and **F**.<sup>17</sup>

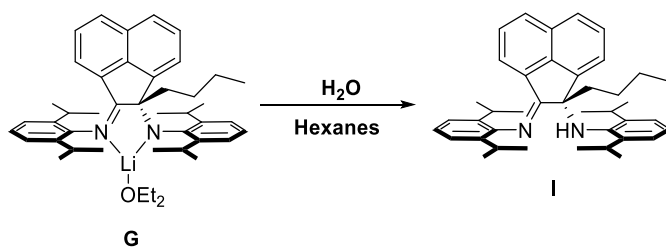
In a subsequent study performed by Fedushkin *et al.* in 2006, the (dpp-BIAN)Mg(THF)<sub>3</sub> complex **A** was treated with ethyl halides.<sup>17</sup> In this study, three imine C-ethylated magnesium BIAN\* complexes were synthesized (**D**, **E**, **F**) and isolated

(Scheme 4). The reaction was proposed to proceed through a single-electron transfer (SET) pathway resulting in the formation of a magnesium-chlorine bond along with the formation of both the dpp-BIAN radical and ethyl radical intermediates. The imine C-ethylation step was proposed to form upon radical recombination, although no EPR spectroscopic evidence was given to support this claim.



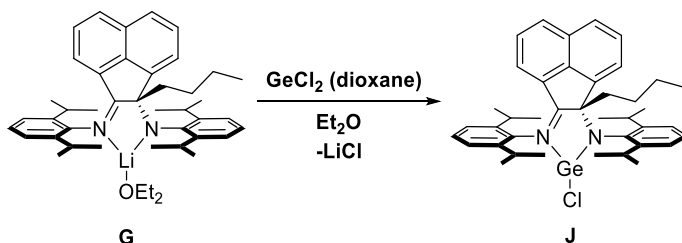
Scheme 5: Imine C-butylation of free dpp-BIAN with *n*-BuLi.<sup>18</sup>

Inspired by the imine C-alkylation reactions of (dpp-BIAN)Mg(THF)<sub>3</sub>, Fedushkin *et al.*, chose to investigate the reaction of free dpp-BIAN with *n*-BuLi.<sup>18</sup> As displayed in Scheme 5, the reaction of free dpp-BIAN with *n*-BuLi in diethyl ether solution yielded the C-butylation lithium BIAN\* etherate complex **G**. Furthermore, when the same reaction was performed in hexanes solution, a similar imine C-butylation BIAN\* lithium dimeric species (**H**) was formed and confirmed by means of single crystal X-ray crystallography.



Scheme 6: Hydrolysis of the imine C-butylated lithium BIAN\* complex **G** to yield free amino-imine BIAN\* ligand **I**.<sup>18</sup>

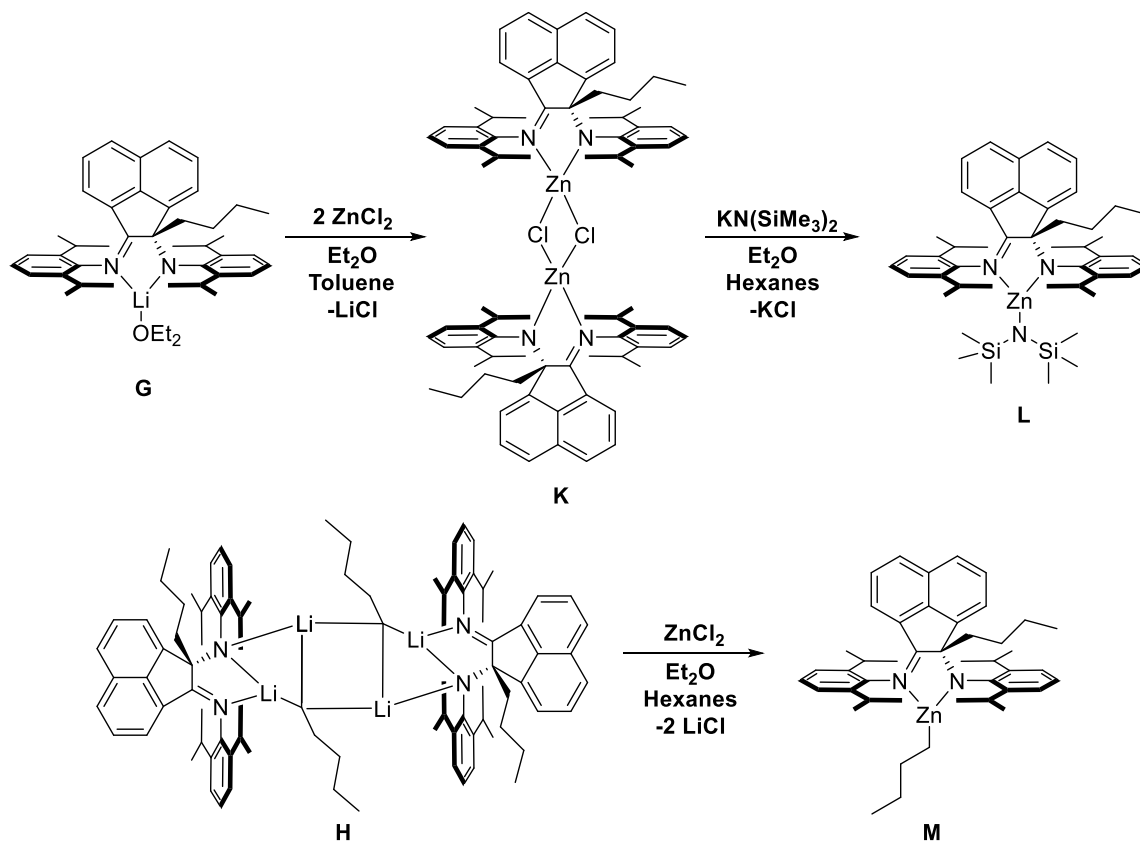
Hydrolysis of the imine C-butylated BIAN\* lithium etherate complex **G** was achieved by exposure of **G** to a water/hexanes mixture. As displayed in Scheme 6, this reaction resulted in the isolation of the free BIAN\* ligand **I**. Furthermore, as displayed in Scheme 7, the new dpp-BIAN\* lithium salt **G** was utilized effectively for salt metathesis reactions. This was confirmed by the reaction of the aforementioned BIAN\* lithium complex (**G**) with  $\text{GeCl}_2$ , resulting in the formation of the three-coordinate BIAN\* Ge(II) complex **J**.



Scheme 7: Salt metathesis reaction of imine C-butylated lithium BIAN\* complex **G** to yield BIAN\* Ge(II) complex **J**.<sup>18</sup>

In a study performed in 2008, Fedushkin *et al.* expanded the use of their novel BIAN\* lithium complex (**G**) for the generation of three new BIAN\* zinc complexes.<sup>19</sup> As displayed in Scheme 7, the reaction of an equimolar amount of the aforementioned lithium etherate complex **G** with zinc chloride in an ether/toluene solution produced the

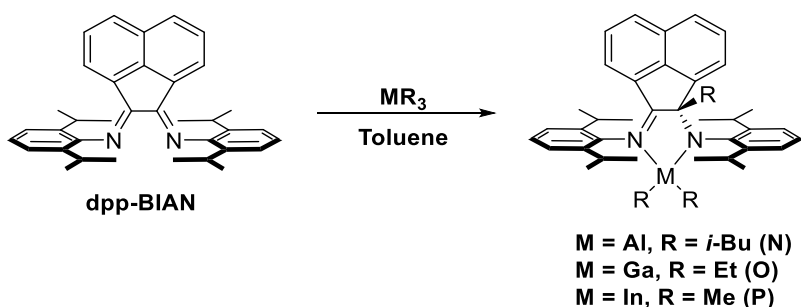
dimeric dpp-BIAN\* zinc chloride species **K**. Furthermore, the reaction of this zinc chloride species **K** with potassium bis(trimethylsilyl)amide yielded the bis(trimethylsilyl)amide adduct of the dpp-BIAN\* zinc complex **L**. However, if the dimeric lithium dpp-BIAN\* complex **H** was treated with zinc chloride in an ether/hexanes mixture, the outcome of the reaction was the elimination of two equivalents of lithium chloride and the formation of the dpp-BIAN\* alkylzinc complex **M**, as displayed in Scheme 8.



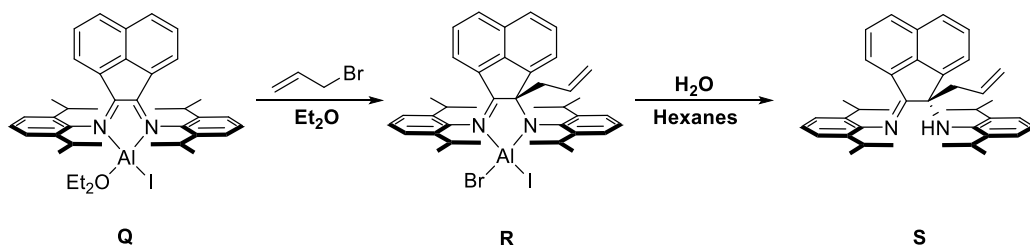
Scheme 8: Syntheses of dpp-BIAN\* zinc complexes (**K**, **L**, **M**).<sup>19</sup>



In a report from 2010, Fedushkin *et al.* probed the reactivity of dpp-BIAN with group 13 alkyl complexes, namely triisobutylaluminum, triethylgallium, and trimethylindium.<sup>20</sup> Fedushkin *et al.* demonstrated that treatment of the free dpp-BIAN ligand with the previous group 13 alkyl complexes generated the imine C-*iso*-butylated aluminum BIAN\* complex **N**, the imine C-ethylated gallium BIAN\* complex **O**, and the imine C-methylated indium BIAN\* complex **P**. (Scheme 9).



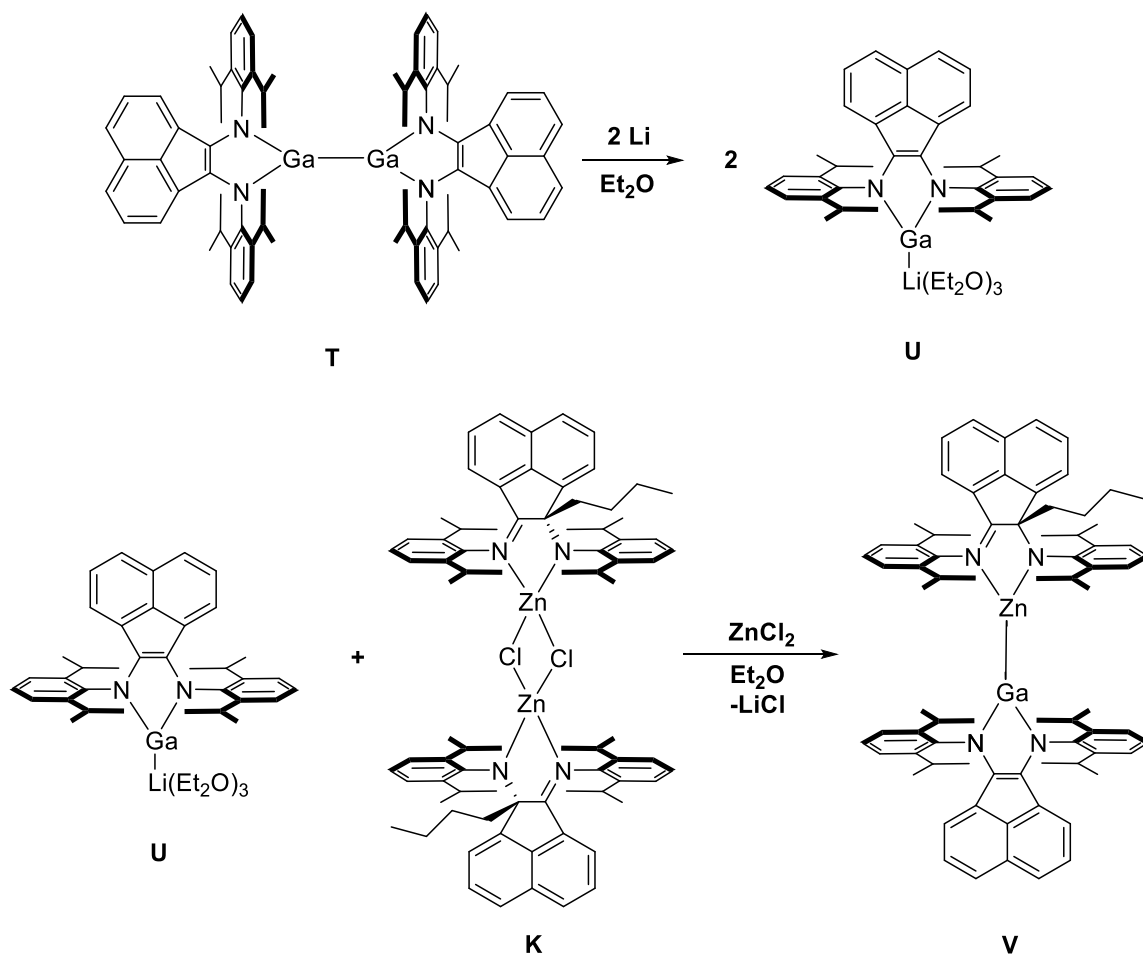
Scheme 9: Syntheses of BIAN\* group 13 alkyl complexes **N**, **O**, and **P**.<sup>20</sup>



Scheme 10: Synthesis of the allyl substituted BIAN\* aluminum complex **R** and the imine C-allylated BIAN\* ligand **S**.<sup>20</sup>

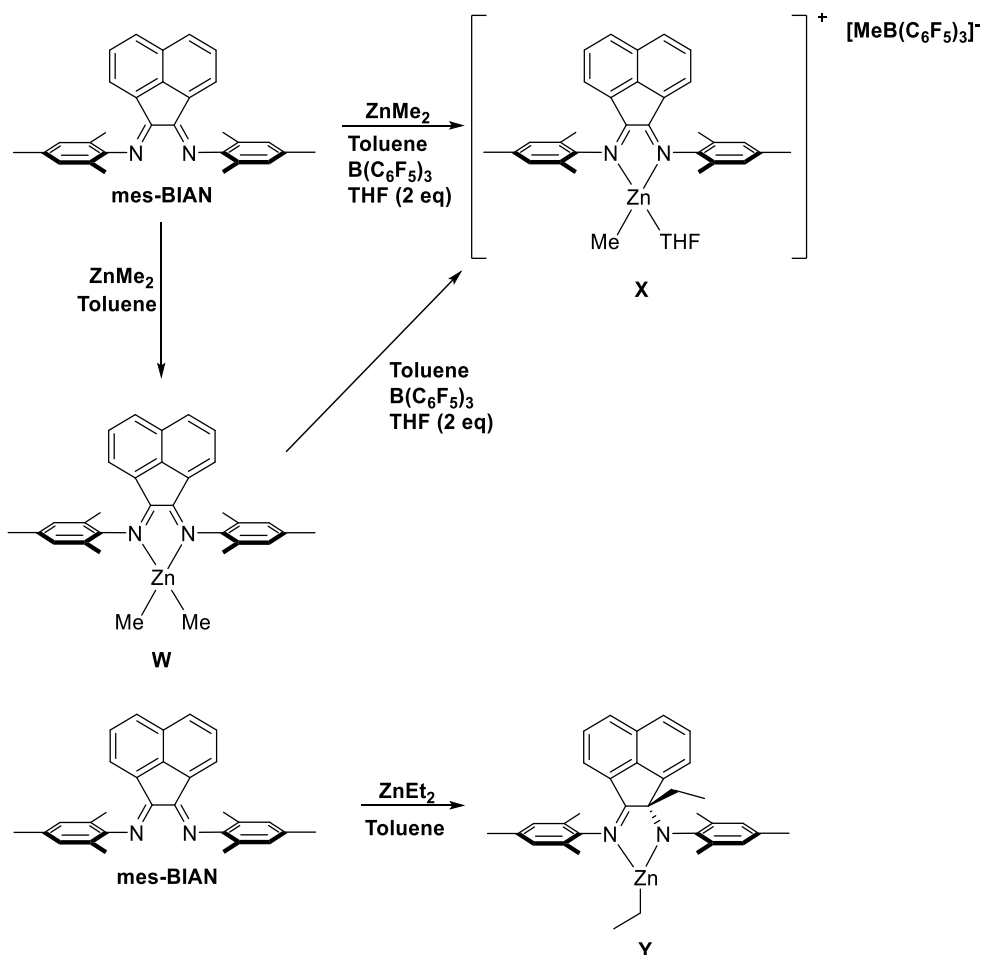
In addition to the direct reaction of group 13 alkyl complexes with dpp-BIAN to generate the respective BIAN\* complexes (**N**, **O**, **P**), Fedushkin *et al.* also demonstrated that reaction of the dianionic aluminum BIAN complex **Q** with alkyl halides resulted in

formation of the BIAN\* derivatives **R** and **S** via an alternate route.<sup>20</sup> As displayed in Scheme 10, reaction of **Q** with allyl bromide in diethyl ether solution resulted in the formation of an allyl substituted BIAN\* aluminum complex **R**. Exposure of complex **R** to a water/hexanes mixture resulted in hydrolysis of the aluminum complex **R** and formation of the free BIAN\* ligand **S**.



Scheme 11: Formation of the gallium-zinc bonded complex **V** using the dpp-BIAN\* ligand as a support.<sup>21</sup>

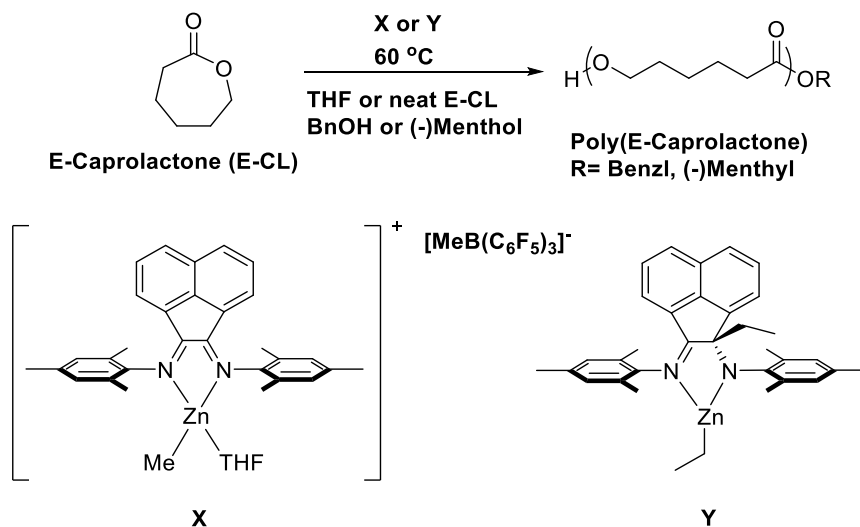
In a report from 2011, Fedushkin *et al.* utilized the new BIAN\* ligand as a support for formation of an interesting gallium-zinc bonded complex.<sup>21</sup> Such gallium-zinc bonded organometallic complexes are rarely observed, with only a few citations of such complexes in the literature.<sup>22-25</sup> Nevertheless, the dpp-BIAN\* ligand was used to stabilize the gallium-zinc complex **V**. Initially, digallane **T** was reacted with two equivalents of lithium metal in diethyl ether solution thereby producing complex **U**. Complex **V** was synthesized (Scheme 11). via a salt elimination reaction that used the previously synthesized gallium-lithium dpp-BIAN complex **U**<sup>26</sup> and the dimeric dpp-BIAN\* zinc chloride species **K**<sup>19</sup>.



Scheme 12: Syntheses of mes-BIAN alkyl zinc complexes **W**, **X**, and **Y**.<sup>27</sup>

In a 2012 study by Dagorne and Avilés *et al.*, 2,4,6-trimethylphenyl (mes) BIAN was used to synthesize the neutral alkyl zinc complex **W** directly from the reaction of dimethylzinc in toluene solution.<sup>27</sup> Moreover, upon exposure of free mes-BIAN to dimethylzinc, B(C<sub>6</sub>F<sub>5</sub>)<sub>3</sub>, and 2 equivalents of THF, the zinc mes-BIAN salt **X** was generated. Salt **X** can also be generated indirectly by reaction of **W** with B(C<sub>6</sub>F<sub>5</sub>)<sub>3</sub> and 2 equivalents of THF. Interestingly, exposure of mes-BIAN to diethylzinc did not result in

the formation of a neutral BIAN alkyl zinc complex. As displayed in Scheme 12, this reaction afforded an imine C-ethylated BIAN\* alkyl zinc complex **Y**.



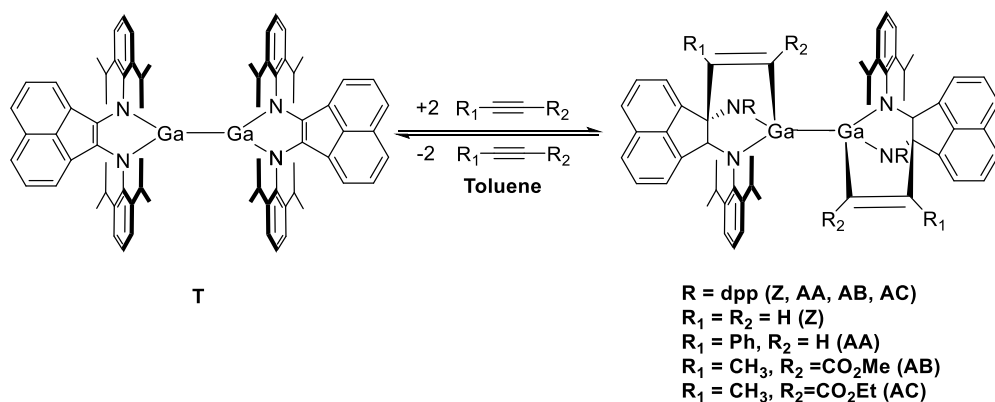
Scheme 13:  $\epsilon$ -Caprolactone polymerization using the mes-BIAN alkyl zinc salt catalyst **X** and mes-BIAN\* neutral alkyl zinc catalyst **Y**.<sup>27</sup>

Dagorne and Avilés *et al.* utilized the aforementioned mes-BIAN alkyl zinc complexes **X** and **Y** as initiators for the ring-opening polymerization (ROP) of  $\epsilon$ -caprolactone ( $\epsilon$ -CL) (Scheme 13). The living cationic ring-opening polymerization reactions were performed in either THF solution or neat  $\epsilon$ -caprolactone. As displayed in Table 1, complex **X** was found to be both highly active for the ROP of  $\epsilon$ -CL in addition to featuring high percent conversion and PDI values. The BIAN\* complex **Y** was also found to be active for the ROP of  $\epsilon$ -CL, albeit with less desirable percent conversion and PDI values.

Table 1: Polymerization data for the ROP of  $\epsilon$ -CL using **X** and **Y** as initiators.<sup>27</sup>

Initiator	Init./BnOH/ ( $\epsilon$ -CL)	Solvent	Time (h)	Conversion (%)	$M_n(\text{corr.})$	$M_n(\text{theor.})$	PDI
<b>X</b>	1/3/300	THF	2	90	11,550	11,400	1.08
<b>X</b>	1/3/1000	THF	6	91	32,250	34,580	1.13
<b>X</b>	1/3/1500	Neat ( $\epsilon$ -CL)	2	67	37,950	34,360	1.12
<b>X</b>	1/50/5000	Neat ( $\epsilon$ -CL)	2	100	13,600	11,400	1.14
<b>Y</b>	1/3/1500	Neat ( $\epsilon$ -CL)	2	49	27,960	29,990	1.27

In 2010, Fedushkin *et al.* reported the reversible addition of alkynes to the dianionic dpp-BIAN digallane complex **T**.<sup>28</sup> As exhibited in Scheme 14, the alkyne cycloaddition formed a C-C bond with the imine fragment resulting in the formation of a new Ga-C-C-C-N five membered ring. Gallium complexes **Z**, **AA**, **AB**, and **AC** represented novel additions to the BIAN\* ligand class. Surprisingly, the formation of all four BIAN\* gallium complexes was found to be reversible. Complexes **Z** and **AA** were found to revert back to the initial digallane complex **T** and the respective alkyne species at temperatures below 100 °C. Furthermore, complexes **AB** and **AC** displayed similar reversibilities with respect to conversion back to the initial gallium complex **T** and the respective alkyne at elevated temperatures of approximately 200 °C.



Scheme 14: Reversible addition of alkynes to digallane BIAN complex **T**.<sup>28</sup>

In a subsequent 2012 report, Fedushkin *et al.* examined the possibility of expanding the versatility of the interesting cycloaddition reactions that took place between the various substrates and the digallane BIAN complex **T**.<sup>13</sup> For example, the reactions of digallane **T** with  $\text{H}_2\text{C}=\text{C}(\text{Me})\text{CO}_2\text{Me}$ ,  $\text{Me}_2\text{C}=\text{O}$ ,  $\text{RC}\equiv\text{N}$ , ( $\text{R} = \text{Me}, \text{Ph}$ ) and  $\text{PhNC}$  were investigated. However, none of these substrates was found to be reactive with complex **T**. Despite the lack of reactivity with these substrates, Fedushkin *et al.* expanded the utility of complex **T** by employing it as a catalyst for the hydroamination of phenylacetylene with a wide variety of anilines. As displayed in Table 2, digallane complex **T** was shown to be effective for this transformation. Each catalytic reaction was performed with 2 mol % catalyst in a deuterated benzene solution. Interestingly, the reaction of phenylacetylene with 1-aminonaphthalene resulted in not only the hydroamination product but also in the formation of the hydroarylation product. Furthermore, the reaction of complex **T** with 1-aminoanthracene resulted in the exclusive formation of the hydroarylation product, as displayed in Table 2. A summary of the catalytic data can be found in the aforementioned Table.

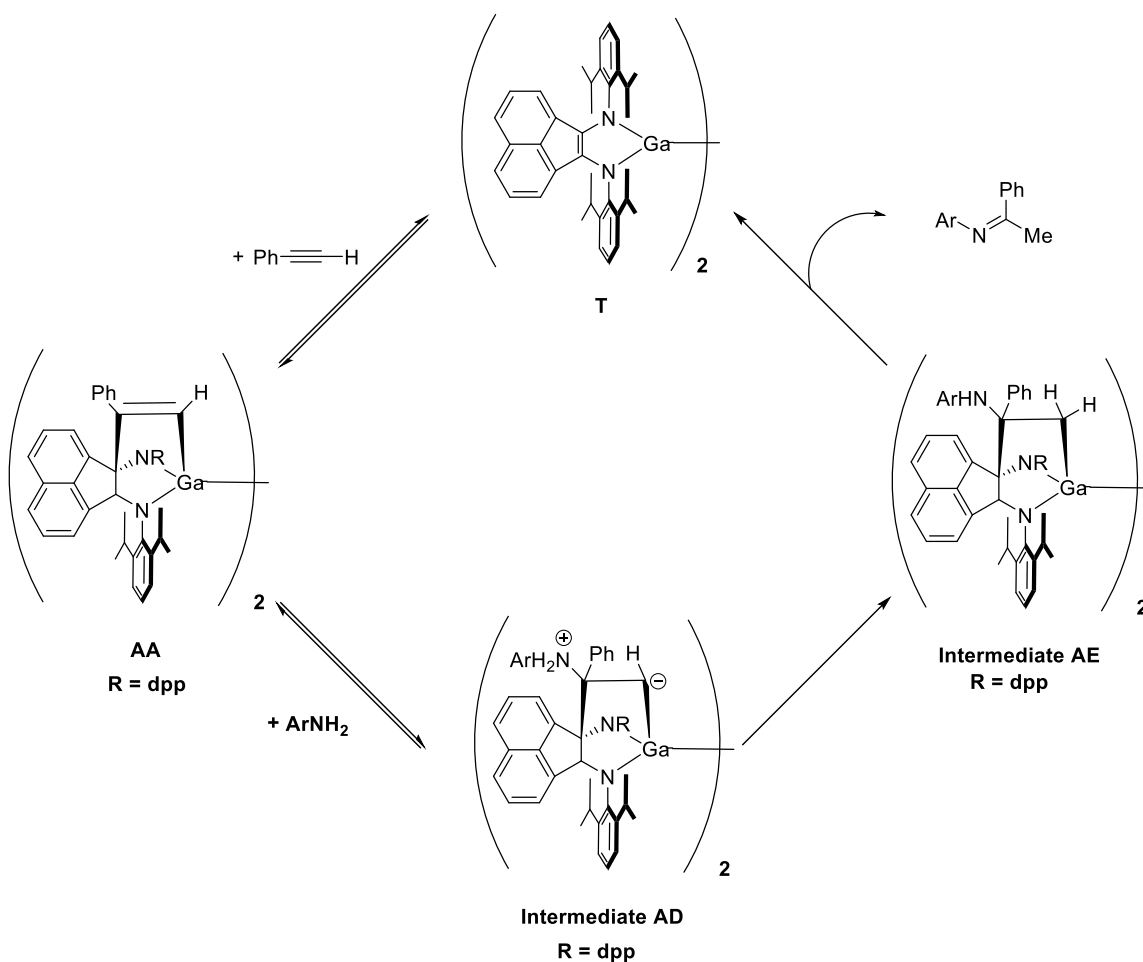
Table 2: Hydroamination/hydroarylation of anilines with phenylacetylene catalyzed by complex **T**.<sup>13</sup>

Cat.	Aniline	Product	Time (h)	Temp. (°C)	Yield (%)
<b>T</b>			16	90	> 99
<b>T</b>			6	110	> 99
<b>T</b>			90	110	19
<b>T</b>			50	110	98
<b>T</b>			200	110	95
<b>T</b>			18	110	92
<b>T</b>			66	90	13
<b>T</b>			12	90	48
<b>T</b>					52
<b>T</b>			18	90	>99

The reaction mechanism for the hydroamination of phenylacetylene with the various aniline substrates was proposed by Fedushkin *et al.* to proceed through the

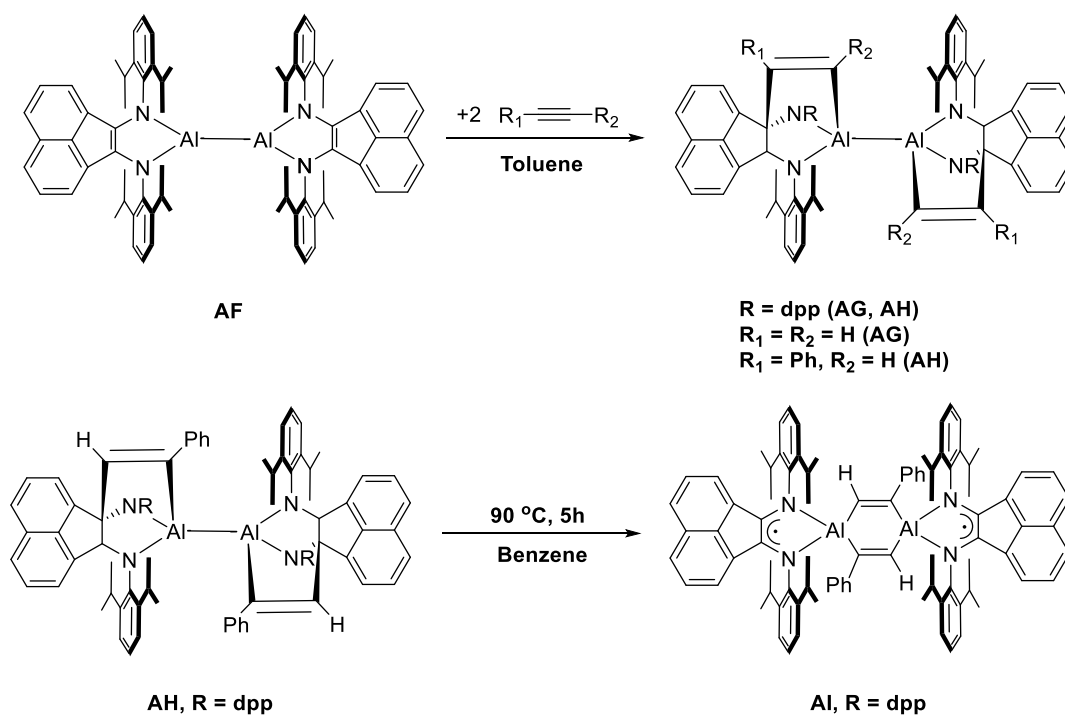


mechanism that is outlined in Scheme 15.<sup>13</sup> The initial step of the hydroamination process is the imine C-alkylation step to generate the stable cycloaddition product **AA**. Following this cycloaddition, the aniline substrate attacks the phenyl substituted carbon atom of the double bond in the Ga-N-C-C-C five membered ring to form **Intermediate AD**. Next, a proton transfer step takes place, thereby producing **Intermediate AE**. Lastly, elimination of the  $\alpha$ -aminoolefin regenerates the digallane BIAN complex **T**.



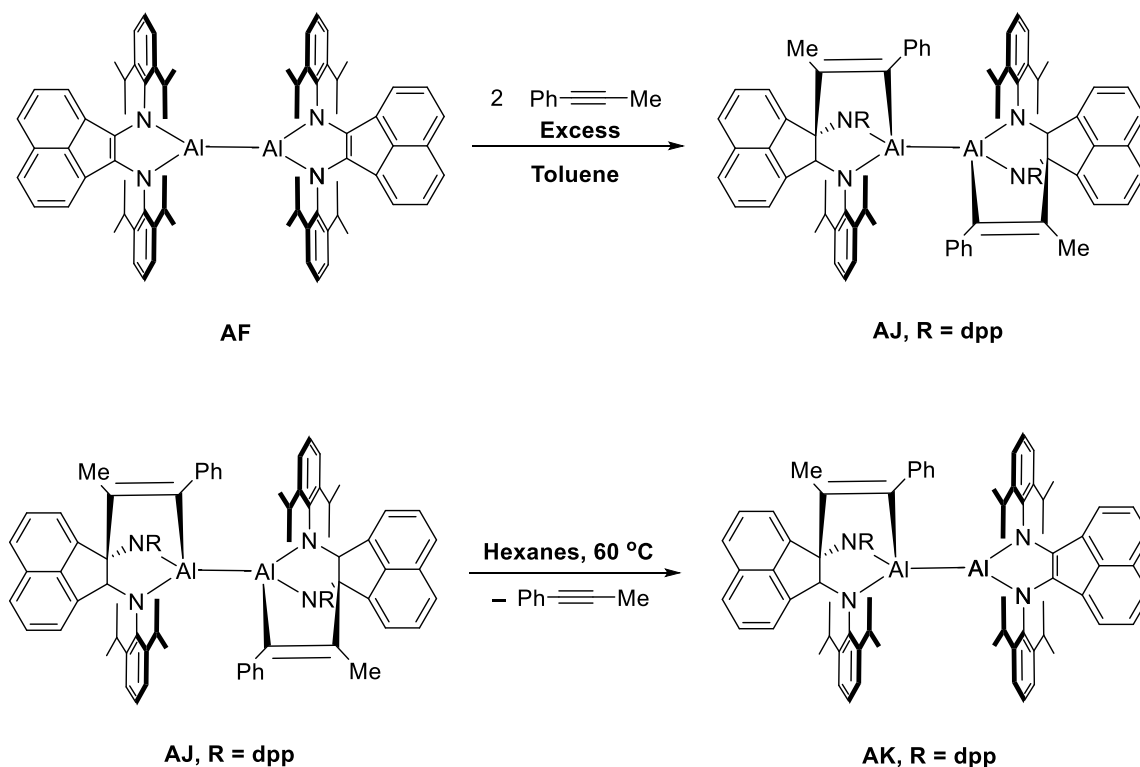
Scheme 15: Mechanism for the hydroamination of alkynes catalyzed by digallane BIAN complex **T**.<sup>13</sup>

Following the study of the reversible addition of alkynes to digallane BIAN complexes, Fedushkin *et al.* performed a subsequent investigation of alkyne addition to dialane BIAN complexes.<sup>29</sup> As exhibited in Scheme 16, the reaction of the dialane BIAN complex **AF** resulted in the cycloaddition of the alkyne to the dialane species, reminiscent of the digallane reactions discussed above. The cycloaddition dpp-BIAN dialane products, **AG** and **AH**, both featured new Al-C-C-C-N five membered rings. The cycloaddition products, **AG** and **AH**, also exhibited thermal instability. This was demonstrated by heating a benzene solution of **AH** to 90 °C for 5 hours, which resulted in the rearrangement reaction of **AH** to form a di-radical bridged species **AI**, as displayed in Scheme 16.



Scheme 16: Reactions of alkynes with dialane BIAN complex **AF** and thermal instability of complex **AH**.<sup>29</sup>

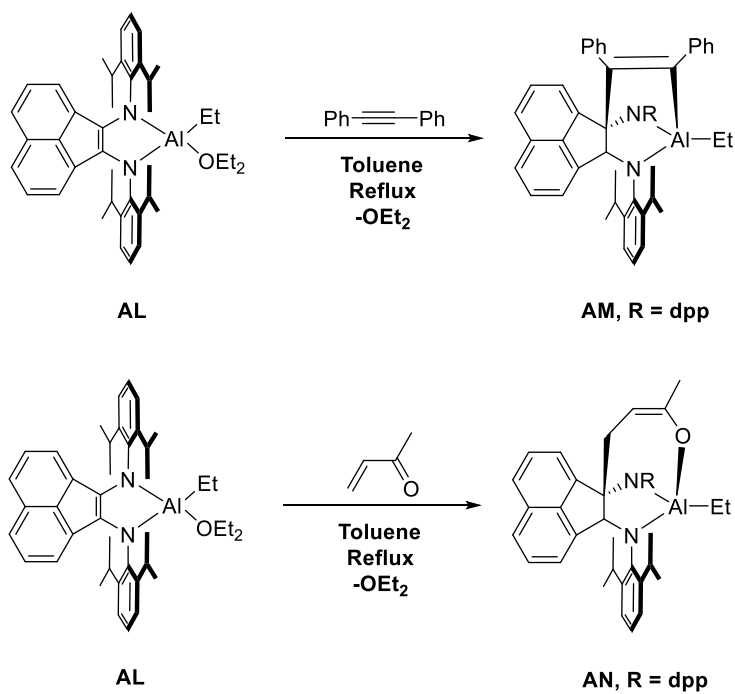
It was determined that **AF** was less reactive toward internal alkynes such as 1-phenyl-1-propyne. However, the cycloaddition of 1-phenyl-1-propyne was made possible by employing an excess of this reagent. As displayed in Scheme 17, the use of an excess of 1-phenyl-1-propyne, enabled the formation of the cycloaddition product **AJ**. Akin to dialane complex **AH**, dialane complex **AJ** was also shown to be thermally unstable. Heating a hexanes solution of **AJ** at 60 °C resulted in the elimination of only one of the alkyne species, which in turn, generated the asymmetric mono cycloaddition product **AK**.



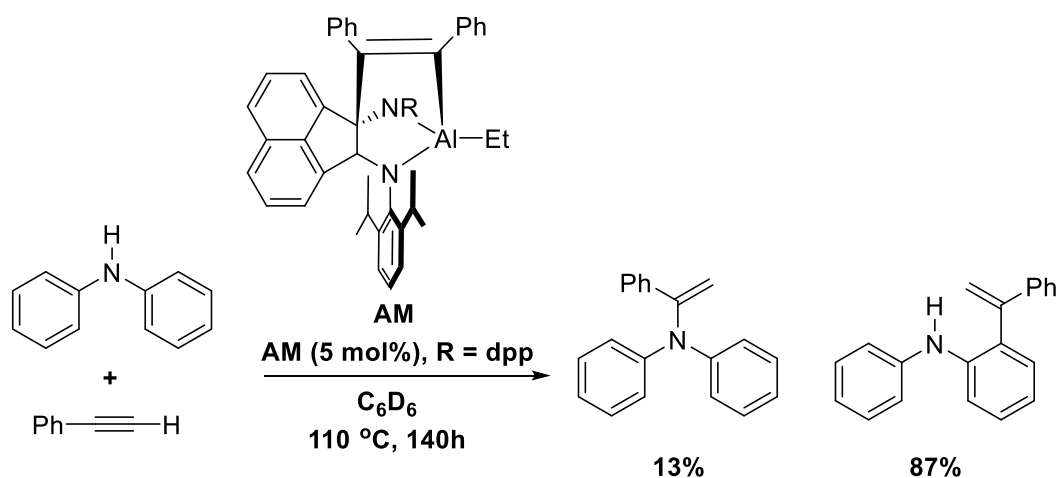
Scheme 17: Reaction 1-phenyl-1-propyne with dialane BIAN complex **AF** and thermal decomposition of **AJ**.<sup>29</sup>

Expanding on the foregoing dialane BIAN research, Fedushkin *et al.* published a report on the addition of diphenylacetylene and methyvinylketone to the dpp-BIAN

aluminum complex **AL**.<sup>30</sup> The imine C-alkylated cycloaddition products, as displayed in Scheme 18, were synthesized in a similar fashion to that reported for the dialane cycloaddition products.<sup>29</sup> Complex **AM** was used in a preliminary catalytic hydroamination/hydroarylation trial reaction of diphenylamine with phenylacetylene (Scheme 19). Interestingly, complex **AM** was found to be more active for the hydroarylation than the hydroamination reaction. This result was contrary to what was observed for the catalytic trials using digallane complex **T**.<sup>13</sup>

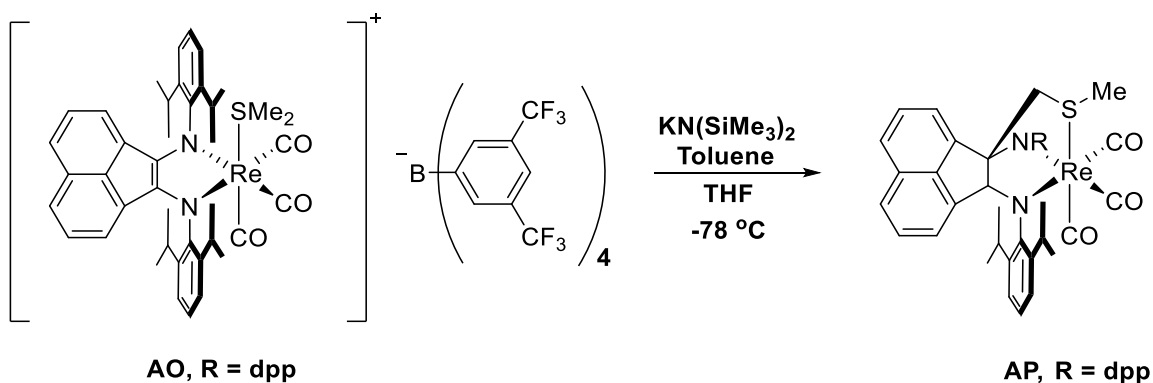


Scheme 18: Reaction of diphenylacetylene and methylvinylketone with dpp-BIAN aluminum complex **AL**.<sup>30</sup>



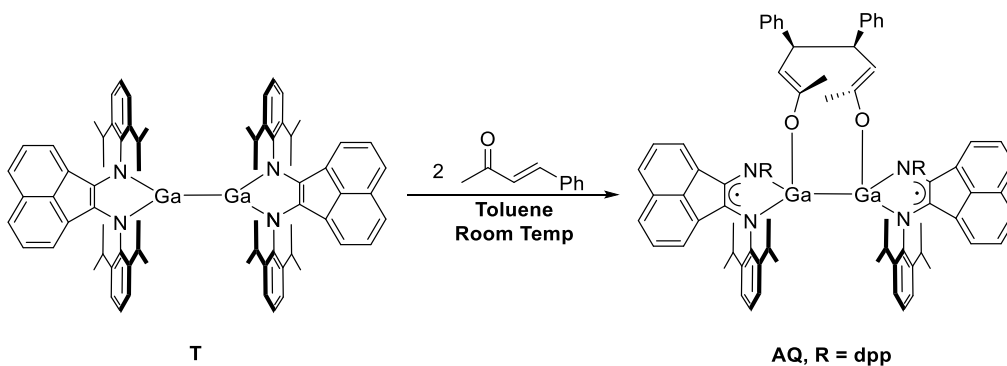
Scheme 19: Hydroamination/hydroarylation reactions of diphenylamine with phenylacetylene using **AM** as a catalyst.<sup>30</sup>

In 2013, Perez *et al.* reported the interesting reaction of the  $[\text{Re}(\text{dpp-BIAN})(\text{CO})_3(\text{SMe}_2)]^+[\text{BAR}^2_4]^-$  complex **AO** with  $\text{KN}(\text{SiMe}_3)_2$  (Scheme 20).<sup>31</sup> In this reaction, the  $\text{KN}(\text{SiMe}_3)_2$  base deprotonated one proton from the dimethyl sulfide ligand, and the resulting carbanion performed nucleophilic imine C-alkylation, generating the Re(I) BIAN\* complex **AP**. The resulting Re-N-C-C-S five membered ring structure was confirmed on the basis of a single crystal X-ray crystallography study. Unexpectedly, Perez *et al.* discovered that the reaction of  $[\text{Re}(\text{bpy})(\text{CO})_3(\text{SMe}_2)]^+[\text{OTf}]^-$  with  $\text{KN}(\text{SiMe}_3)_2$  resulted in a similar outcome.

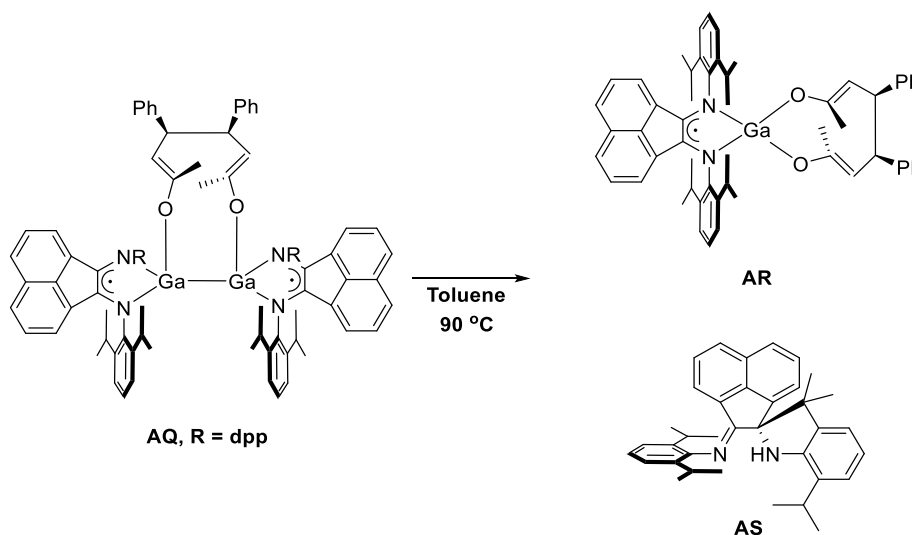


Scheme 20: Formation of the dpp-BIAN\* Re(I) complex **AP** by reaction of **AO** with  $\text{KN}(\text{SiMe}_3)_2$ .<sup>31</sup>

In a 2014 report, Fedushkin *et al.* expanded the research that had been performed on the dpp-BIAN digallane complex **T**.<sup>32</sup> It was found that the reaction of complex **T** with benzylideneacetone resulted in oxidation of the dianionic dpp-BIAN ligand framework. Furthermore, this reaction formed a bridged dimeric radical digallane dpp-BIAN complex **AQ**, as exhibited in Scheme 21. The thermal stability of complex **AQ** was tested by heating a toluene solution of **AQ** for 10 minutes at 95 °C. The thermal decomposition products, as displayed in Scheme 22, were both the monomeric radical gallium dpp-BIAN complex **AR** and the intramolecular imine C-alkylated free dpp-BIAN\* ligand **AS**.



Scheme 21: Reaction of digallane complex **T** with benzylideneacetone.<sup>32</sup>

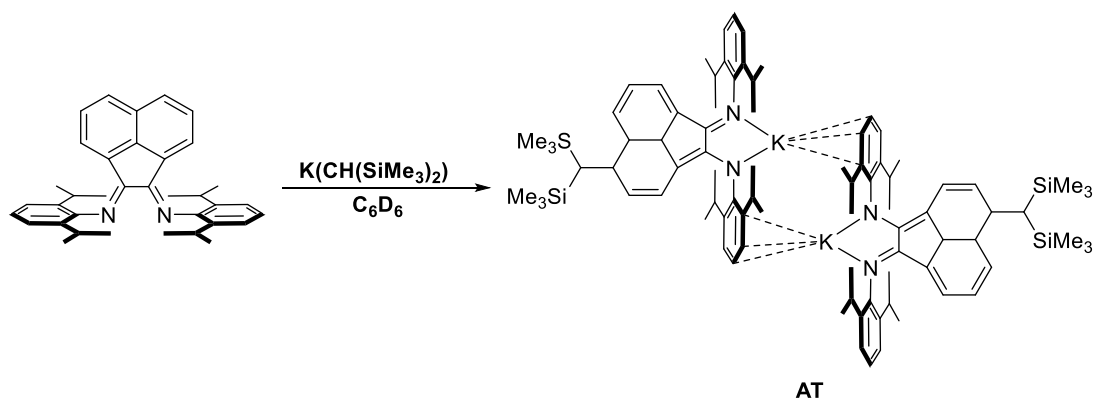


Scheme 22: Thermal decomposition of complex **AQ** to form **AR** and dpp-BIAN\* ligand **AS**.<sup>32</sup>

### 1.1.3 Backbone Dearomatization: Synthesis and Applications of the BIAN\*\* Ligand.

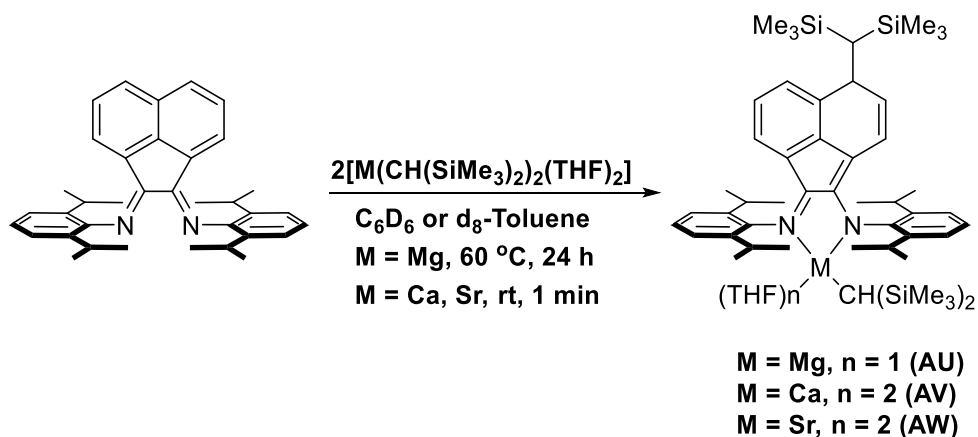
BIAN\* ligand types are formed via an imine C-alkylation process. As discussed in Section 1.1.2, there are numerous examples of the syntheses and applications of BIAN\* ligands. Interestingly, a study performed in 2011 by Hill *et al.* led to the discovery of an alternate backbone dearomatized form of the dpp-BIAN\* ligand.<sup>33</sup> Reaction of dpp-BIAN with  $\text{K}(\text{CH}(\text{SiMe}_3)_2)$  in deuterated benzene solution resulted in

both alkylation of the backbone naphthalene moiety of the dpp-BIAN ligand and removal of the aromaticity from one of the naphthalene rings. Overall, the dearomatization process shifted the electron density from the broken C=C double bond to form an alternate amido-imine BIAN\* potassium complex **AT**, as displayed in Scheme 23. The formation of this unexpected product was confirmed by means of a single crystal X-ray crystallography study. This class of dearomatized BIAN\* variants will be referred to as BIAN\*\* henceforth.



Scheme 23: Dearomatization reaction of dpp-BIAN  $\text{K}(\text{CH}(\text{SiMe}_3)_2)$  in deuterated benzene solution.<sup>33</sup>



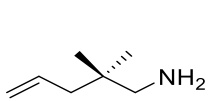
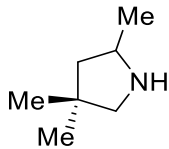
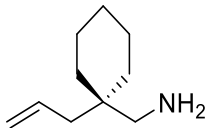
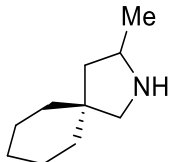
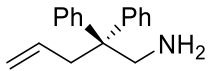
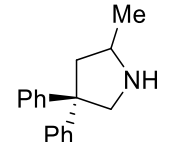
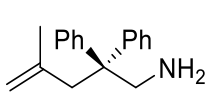
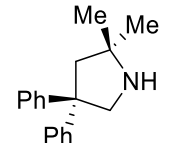
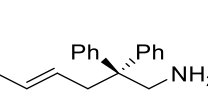
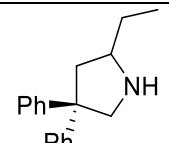
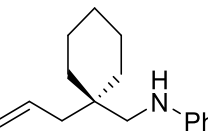
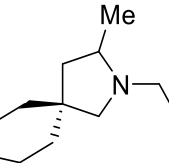


Scheme 24: Dearomatization reaction of dpp-BIAN with bis(trimethylsilyl)methyl alkaline earth complexes.<sup>33</sup>

Hill *et al.* expanded the scope of the previous reaction to include reactions of dpp-BIAN with bis(trimethylsilyl)methyl alkaline earth complexes to yield three different alkaline earth dpp-BIAN\*\* complexes (AU, AV, AW), as displayed in Scheme 24. Surprisingly, attempts to generate the free dpp-BIAN\*\* amino-imine ligand via hydrolysis of the metal complexes was not possible. In contrast to BIAN\*, where generation of the free BIAN\* amino-imine ligand was possible, hydrolysis of the dpp-BIAN\*\* metal complexes only resulted in isolation of the rearomatized free dpp-BIAN ligand and the formation of bis(trimethylsilyl)methane. Although the authors do not give an explanation for the mechanism of the foregoing transformation, they surmise that, in the absence of an electropositive metal center in the N-C-C-N chelation unit, the energy gained by the formation of the bis(trimethylsilyl)methane alkane could be the driving force for the dealkylation process. Overall, rearomatization of the dpp-BIAN ligand would also be energetically favorable. Hill *et al.* utilized the dpp-BIAN\*\* complex AV as a catalyst for intramolecular hydroamination of substituted aminoalkenes in deuterated

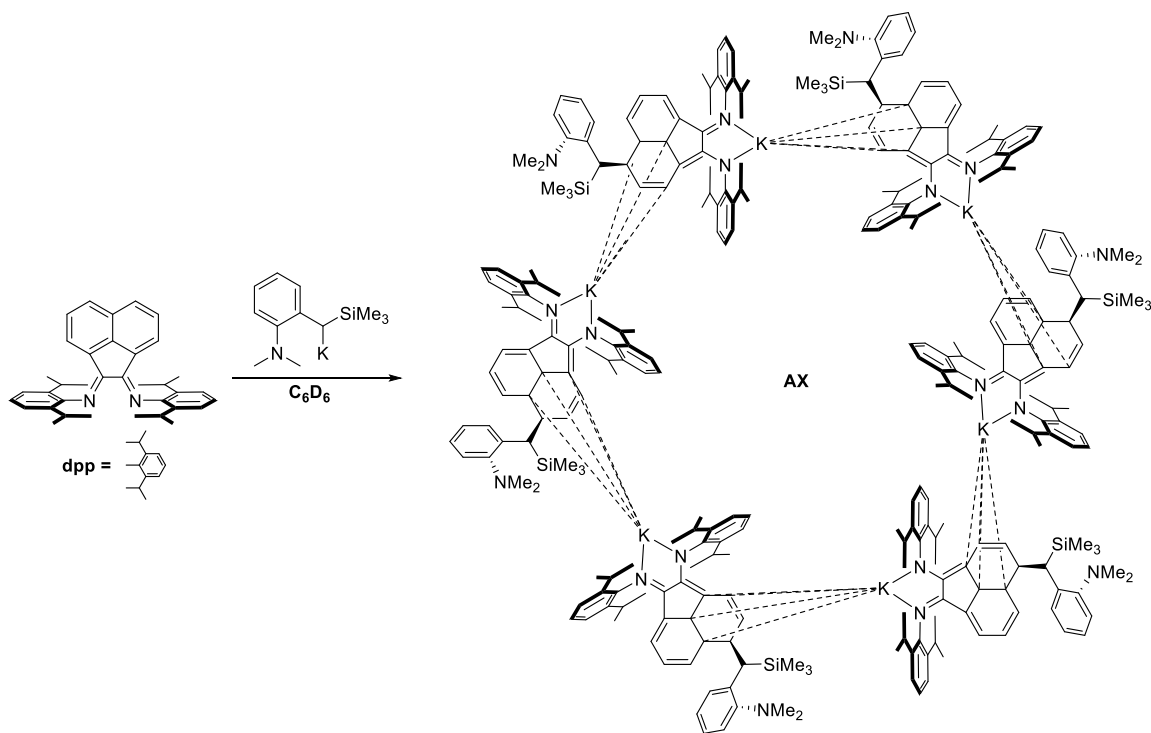
benzene or toluene solution on an NMR scale. As displayed in Table 3, complex **AV** was shown to be an effective catalyst for the aforementioned hydroamination reactions.

Table 3: Intramolecular hydroamination of substituted aminoalkenes using dpp-BIAN\*\* complex **AV** as a catalyst.<sup>33</sup>

Aminoalkene	Product	Cat. Loading (% Mol)	Time (h)	Temp. (°C)	Yield (%)
		2	1	25	95
		1	0.3	25	99
		0.5	0.25	25	> 99
		2	1	25	98
		5	5	25	95
		5	3.5 days	60	92

In a subsequent publication from 2014, Hill *et al.*, further examined the unusual dearomatized dpp-BIAN\*\* ligand.<sup>34</sup> As previously mentioned, reaction of  $K(\text{CH}(\text{SiMe}_3)_2)$  in deuterated benzene solution generated the unusual backbone

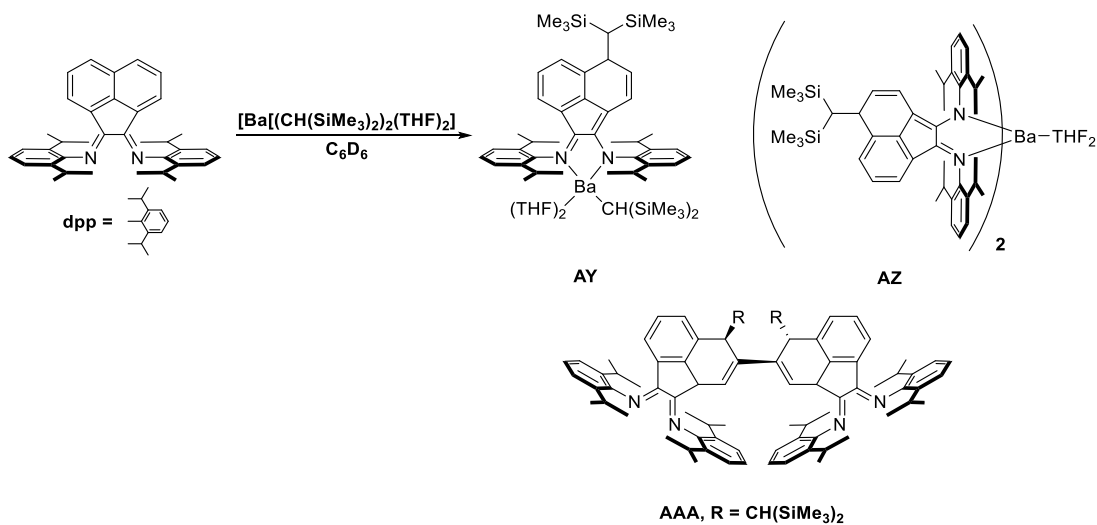
dearomatized complex **AT**, as confirmed by the dimeric structure obtained via a single crystal X-ray diffraction study. In the 2014 report, reaction of dpp-BIAN with  $\text{K}[\text{CH}(\text{SiMe}_3)((2\text{-NMe}_2)\text{C}_6\text{H}_4)]$  yielded a similar backbone dearomatized BIAN\*\* potassium complex **AX** as displayed in Scheme 25. Complex **AX** was found to be hexameric in structure, as confirmed by means of a single crystal X-ray diffraction study.



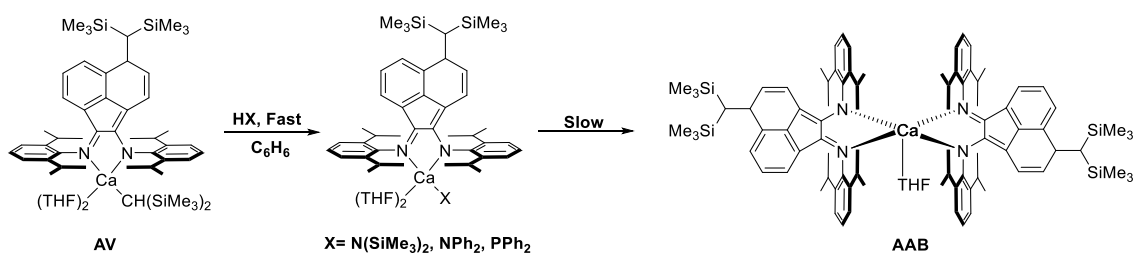
Scheme 25: Dearomatization reaction of dpp-BIAN with  $\text{K}[\text{CH}(\text{SiMe}_3)((2\text{-NMe}_2)\text{C}_6\text{H}_4)]$ .<sup>34</sup>

In the 2011 report from Hill *et al.*, Mg(II), Ca(II), and Sr(II) dpp-BIAN\*\* complexes were synthesized.<sup>33</sup> In the 2014 report, both homo- and heteroleptic Ba(II) dpp-BIAN\*\* complexes were synthesized via reaction of dpp-BIAN with  $\text{K}[(\text{CH}(\text{SiMe}_3)_2)(\text{THF})_2]$  in deuterated benzene solution. As displayed in Scheme 26, this

reaction yielded three different products, namely, the heteroleptic Ba(II) dpp-BIAN\*\* complex **AY**, the homoleptic Ba(II) dpp-BIAN\*\* complex **AZ**, and the unexpected backbone dearomatized dimeric BIAN species **AAA**. Furthermore, it was discovered that the homoleptic Ca(II) complex **AAB** could be generated in a similar manner, as displayed in Scheme 27.



Scheme 26: Formation of Ba dpp-BIAN\*\* complexes (**AY**, **AZ**) and the unexpected backbone dearomatized dimeric BIAN species **AAA**.<sup>34</sup>



Scheme 27: Formation of Ca dpp-BIAN\*\* complex **AAB**.<sup>34</sup>

In 2014, Hill *et al.* revisited the use of the dpp-BIAN\*\* alkaline earth complexes for use as catalysts in intramolecular hydroamination transformations. As displayed in

Table 4, the hydroamination trials were performed using not only the calcium dpp-BIAN\*\* complex **AV** but also the magnesium (**AU**) and strontium (**AW**) analogues, as well. The details of this catalytic study can be found in Table 4.

Table 4: Intramolecular hydroamination of substituted aminoalkenes using dpp-BIAN\*\* complexes **AU**, **AV**, and **AW** as catalysts in deuterated benzene solution.<sup>34</sup>

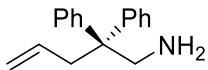
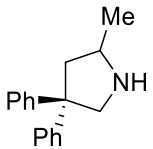
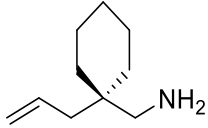
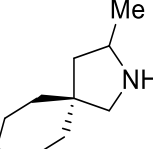
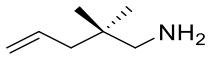
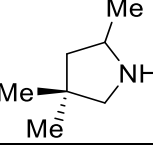
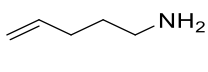
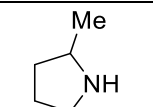
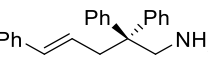
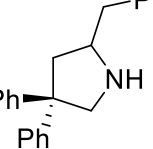
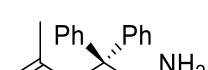
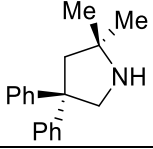
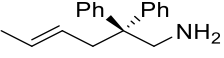
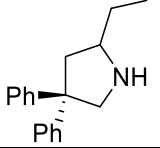
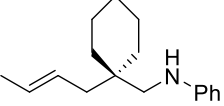
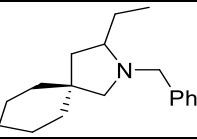

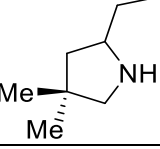
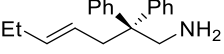
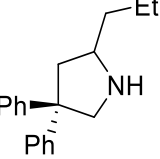
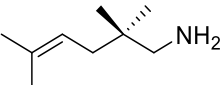
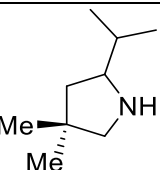
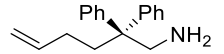
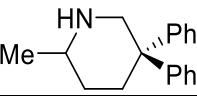
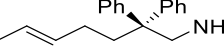
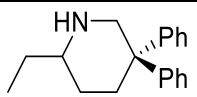
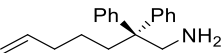
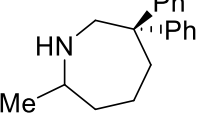
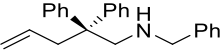
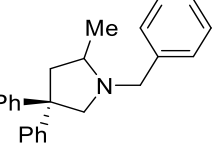
Aminoalkene	Product	Cat. Loading (% Mol)	Time (h)	Temp. (°C)	Yield (%)
		0.5 ( <b>AU</b> ) 0.5 ( <b>AV</b> ) 0.5 ( <b>AW</b> )	18 0.25 1	60 25 25	< 5 > 99 76
		1 ( <b>AV</b> )	0.3	25	99
		2 ( <b>AV</b> )	1	25	95
		2 ( <b>AV</b> )	24	80	0
		0.25 ( <b>AV</b> )	0.1	25	98
		2 ( <b>AV</b> )	1	25	98

Table 4: continued.

		5 (AV)	5	25	95
		10 (AV)	18	60	93
		10 (AV)	48	80	0
		12 (AV)	40	60	98
		20 (AV)	80	80	0
		5.0 (AU) 2.0 (AV)	18 1	60 25	> 99 85
		20 (AV)	48	80	0
		20 (AU) 20 (AV)	24 48	80 80	95 0
		1.0 (AV)	0.5	25	98

### 1.1.4 BIAN\* and BIAN\*\*: An Overview of BIAN Functionalization

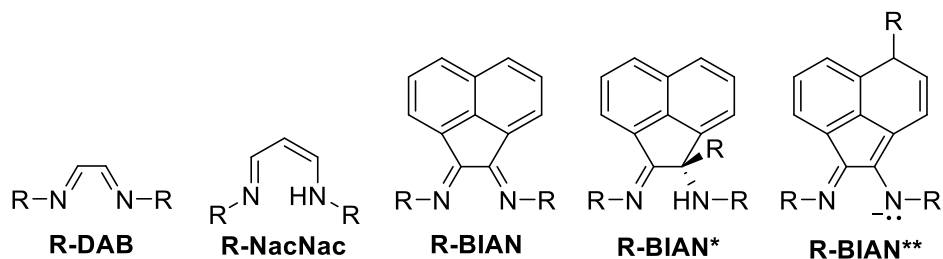


Figure 2: BIAN\* and BIAN\*\* as new additions to nitrogen donor ligand family.

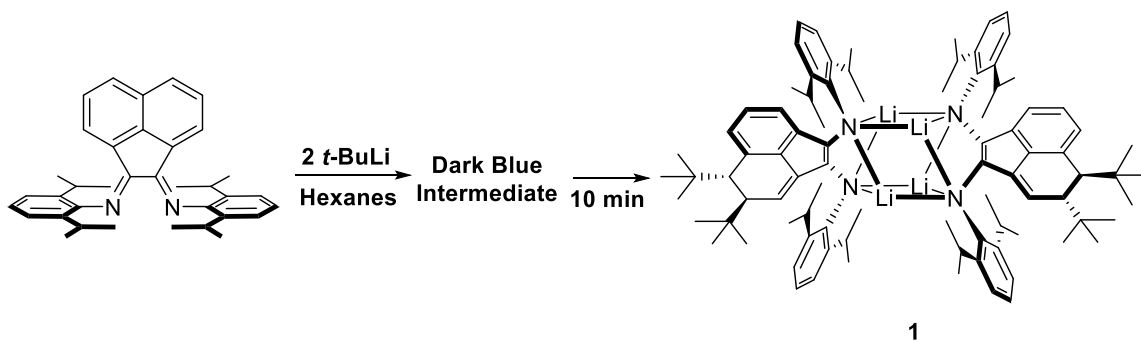
The synthesis, development, and application of both BIAN\* and BIAN\*\* represent exciting new additions to the nitrogen donor ligand family (Figure 2). Both the BIAN\* and BIAN\*\* ligands can be viewed as hybrid ligand combinations of the BIAN and the NacNac ligand systems. Since the field of BIAN functionalization is in its relative infancy, challenges still remain as to what forces dictate the aforementioned functionalization reactions described in both Sections 1.1.2 and 1.1.3.

## 1.2 RESULTS AND DISCUSSION

In Section 1.2, the driving forces of functionalization of the BIAN ligand class will be discussed, specifically those that involve the reaction of sterically demanding alkyllithium nucleophiles. In this section the sterically directed functionalization reactions that were explored by Evans and Cowley will be discussed. Moreover, the experimental results that were obtained will be supplemented by DFT calculations performed by our collaborator Professor Ignacio Vargas-Baca at McMaster University. Overall, by utilizing both experimental and theoretical data, the pathways of BIAN functionalization were differentiated.

### 1.2.1 dpp-BIAN Radical Dearomatization

As discussed above, the BIAN\* and BIAN\*\* ligand classes represent interesting additions to the nitrogen donor family. Particular interest was generated in the functionalization of the Ar-BIAN ligand system using sterically demanding attacking nucleophiles. For this purpose, the reaction of dpp-BIAN with *t*-butyllithium (*t*-BuLi) in hexanes solution at ambient temperature was investigated by Evans and Cowley.<sup>35</sup> Upon addition of *t*-BuLi to the yellow dpp-BIAN hexanes solution in a 1:1 molar ratio, there was an instant color change to an intense deep blue color. This solution remained deep blue for approximately 10 minutes, after which the solution changed to a deep purple hue. The deep purple solution was concentrated to yield a deep purple powder. This purple powder was subsequently recrystallized using dry benzene solution in an inert atmosphere of a glove box. Inspection of the crystal structure revealed the identity of the purple powder to be the unexpected  $[\text{Li}_4][(\text{1,2-di-}(t\text{-Bu})\text{-dpp-BIAN})_2]$  complex **1**, as displayed Scheme 28.



Scheme 28: Synthesis of vicinal di-*t*-butylated dearomatized dpp-BIAN lithium antiprismatic complex (**1**).<sup>35</sup>

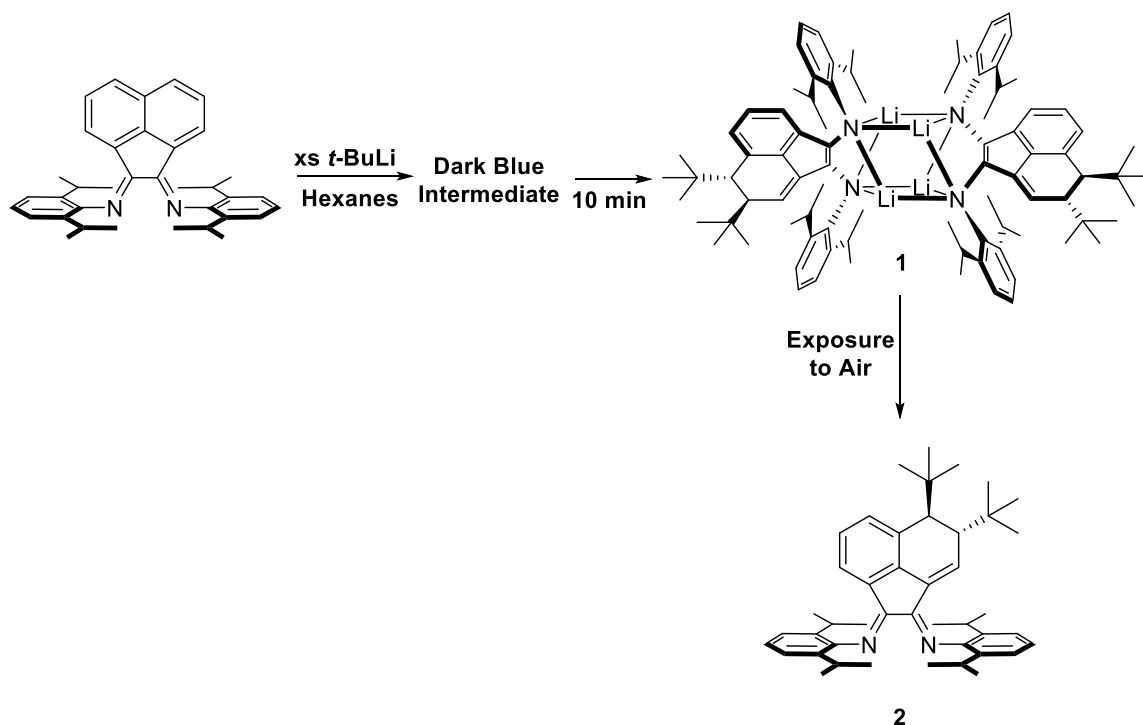


The unexpected structure of **1** comprised a Li-N distorted antiprismatic core structure. Moreover, each dpp-BIAN ligand had undergone vicinal di-*t*-butylation in one of the naphthalene backbone rings. This di-*t*-butylation resulted in dearomatization of one of the rings of the naphthalene backbone. Furthermore, as a function of dearomatization and vicinal di-*t*-butylation, the dpp-BIAN ligand had been reduced by two electrons, thus generating a diamido functionality. Lastly, vicinal di-*t*-butylation of the backbone yielded two chiral centers at the carbon  $\alpha$  to each *t*-butyl group. Moreover, the formation of **1** occurred with high stereoselectivity with only the *trans*-stereoisomer isolated.

The initial synthesis of **1** was performed using a 1:1 molar ratio of *t*-BuLi to dpp-BIAN. However, as previously discussed, the product stoichiometry requires a 1:2 molar ratio of dpp-BIAN to *t*-BuLi. Subsequently, the reaction was performed with a 1:2 molar ratio of dpp-BIAN to *t*-BuLi resulting in an overall 87% yield. Interestingly, this reaction proceeded independently of the initial stoichiometry of the reactants. An excess or deficiency of *t*-BuLi solely resulted in formation of **1**.

Exposure of a hexanes solution of the di-*t*-butylated complex **1** to ambient air and water resulted in an immediate color change from dark purple to red. Concentration of the red hexanes solution yielded a crystalline red powder in almost quantitative yield. The structure of the crystalline red powder was elucidated by means of a single crystal X-ray diffraction study. The structure was determined to be the vicinal di-*t*-butylated, dearomatized free dpp-BIAN ligand **2**, as displayed in Scheme 29. Compound **2** had undergone an overall two electron oxidation transforming the diamido functionality back to an initial diimine. This transformation was reminiscent of the report by Fedushkin *et al.*, where a hydrolyzed diamine compound underwent a facile oxidation back to a diimine moiety.<sup>36</sup> However, the above reaction differed from that observed during the

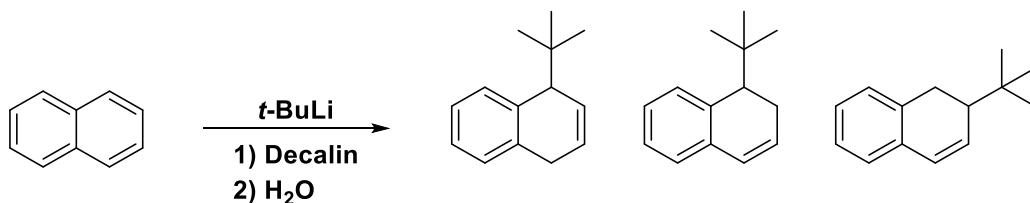
hydrolysis reactions involving BIAN\*\* in the work by Hill *et al.*<sup>33</sup> The hydrolysis of **1** resulted in formation of the dearomatized free dpp-BIAN ligand **2** and not a dealkylation/rearomatization reaction that was observed by Hill *et al.*



Scheme 29: Formation of vicinal di-*t*-butylated, dearomatized free dpp-BIAN ligand **2**.<sup>35</sup>

After inspection of **1** and **2**, it is clear that the foregoing reactions did not proceed through imine C-alkylation pathways akin to that reported by Fedushkin *et al.* for the reaction of *n*-BuLi with dpp-BIAN.<sup>18</sup> Thus, the mechanism for the unexpected dearomatization reaction was subsequently investigated by Evans and Cowley. Previously, it was found that the dearomatization of naphthalene is possible via the reaction of *t*-BuLi in decalin solution.<sup>37</sup> As displayed in Scheme 30, this reaction produced an array of mono-*t*-butylated, dearomatized products. This reaction proceeded

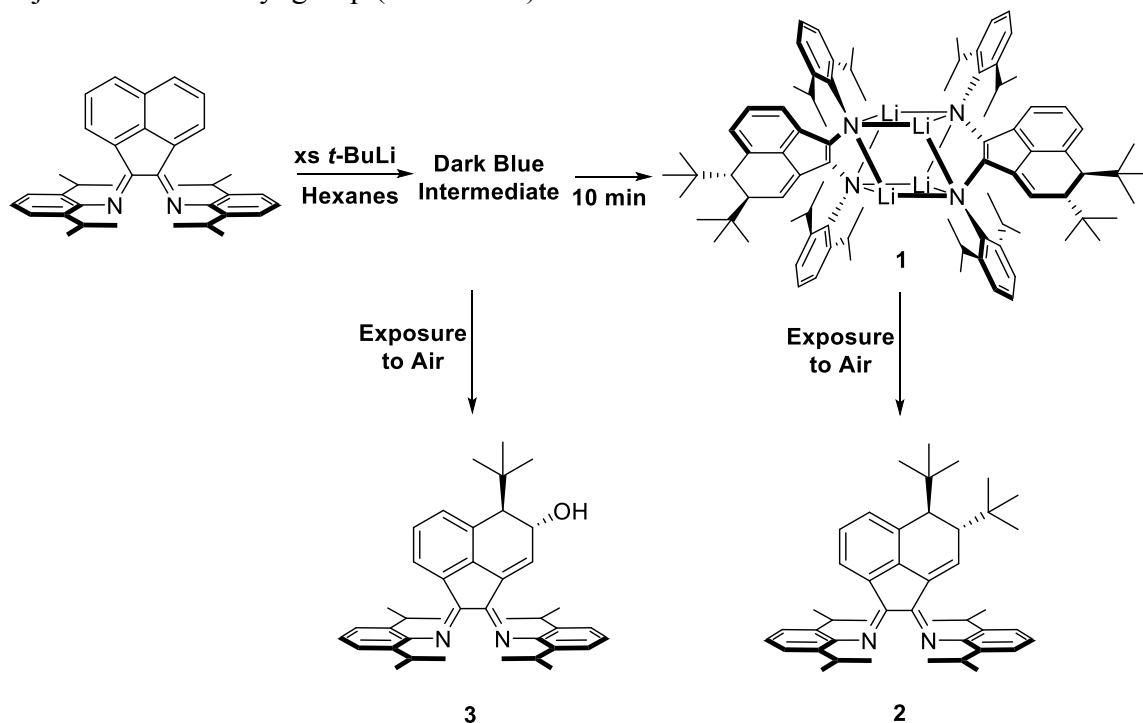
through a nucleophilic dearomatization pathway ( $D_NAr$ ).<sup>37</sup> A plausible mechanism for the formation of complex **1** comprises two successive nucleophilic dearomatization processes. If the reaction pathway for the synthesis of **1** had proceeded through this route, isolation of a mono-*t*-butylated compound akin to that described by Hill *et al.*<sup>33</sup> should be possible.



Scheme 30: Nucleophilic dearomatization of naphthalene with *t*-BuLi.<sup>37</sup>

In order to assess the viability of the nucleophilic dearomatization mechanism, the isolation of a mono-*t*-butylated compound was investigated. The synthesis of **1** was repeated. However, during the dark blue intermediate color stage, the reaction was not allowed to proceed to the dark purple color stage. Instead, the reaction was quenched with water at the dark blue colored stage. The addition of water generated a different purple color solution that slowly changed to dark red over a period of 24 hours. Subsequently, a red-orange precipitate was extracted from the red hexanes solution. Recrystallization of this precipitate from toluene solution resulted in a crop of suitable crystals for X-ray diffraction in a 34% yield. Surprisingly, a single crystal X-ray crystallography study revealed the identity of this compound to be that of a mono-*t*-butyl-hydroxy species. Formation of the mono-*t*-butyl-hydroxy dearomatized free dpp-BIAN ligand **3** was unexpected because a mono-*t*-butyl-dihydro compound was anticipated to form based on the premise of two subsequent nucleophilic dearomatization processes.

The structure of **3** was very similar to that of **2** with the exception of the hydroxyl species adjacent to the *t*-butyl group (Scheme 31).



Scheme 31: Formation mono-*t*-butyl-hydroxy dearomatized free dpp-BIAN ligand **3**.<sup>35</sup>

The foregoing experimental results were inconsistent with a typical nucleophilic dearomatization process. It was therefore hypothesized that the foregoing reactions could possibly be proceeding through a radical pathway. In order to assess the viability of a radical pathway, the dearomatization reaction was probed via EPR spectroscopy. A solution of dpp-BIAN in dry hexanes was prepared in the inert atmosphere of the glove box. Upon addition of *t*-BuLi, the reaction instantly turned deep blue at which point an aliquot of the reaction was diluted and loaded into a quartz EPR tube. The sample was then quickly probed by EPR spectroscopy in order to examine the transient intermediate species. The foregoing EPR experiment successfully detected a radical in solution,

although the hyperfine signal was very broadened. However, by performing the dearomatization reaction in toluene, a similar deep green intermediate colored solution was generated. The hyperfine signal detected in toluene solution was much more defined and detailed, as displayed in Figure 3.

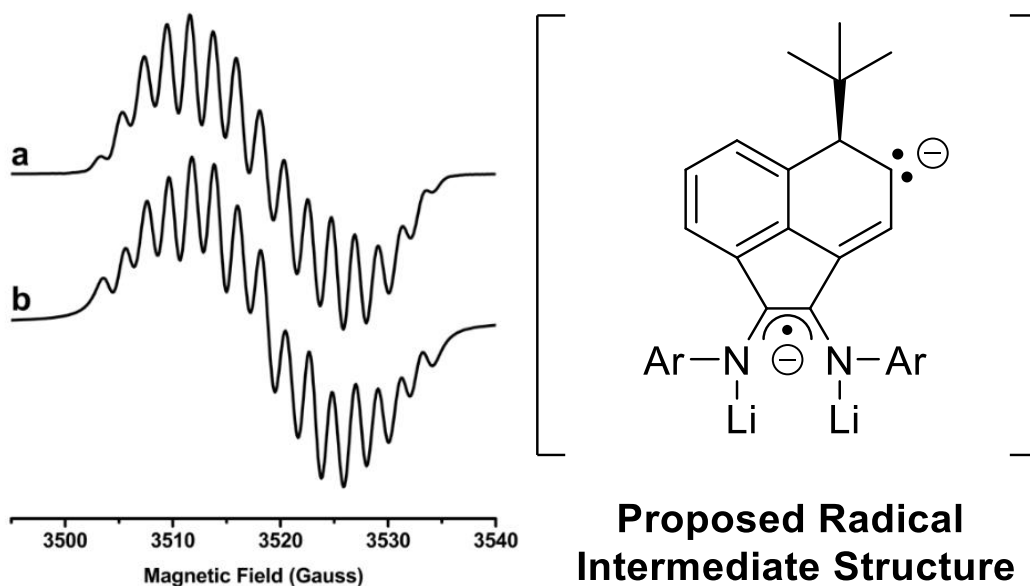


Figure 3: (Left) Experimental (a) and simulated (b) EPR spectra for the dearomatization radical intermediate in toluene solution at room temperature. (Right) Proposed radical intermediate structure for the radical dearomatization.<sup>35</sup>

The detailed hyperfine structure was modeled using simulation software. As mentioned previously in the work of Fedushkin *et al.*, the initial reduction of the dpp-BIAN ligand typically occurs in the N-C-C-N fragment.<sup>15</sup> With this in mind, the 15 lined hyperfine structure was modeled using two <sup>14</sup>N nuclei ( $I = 1$ , natural abundance 99.64%) and two <sup>7</sup>Li nuclei ( $I = 3/2$ , natural abundance 92.58%). The foregoing nuclei were chosen based on the fact that the final product **1** was a dianionic species with two lithium atoms per dpp-BIAN ligand. Interestingly, however, the simulation matched the

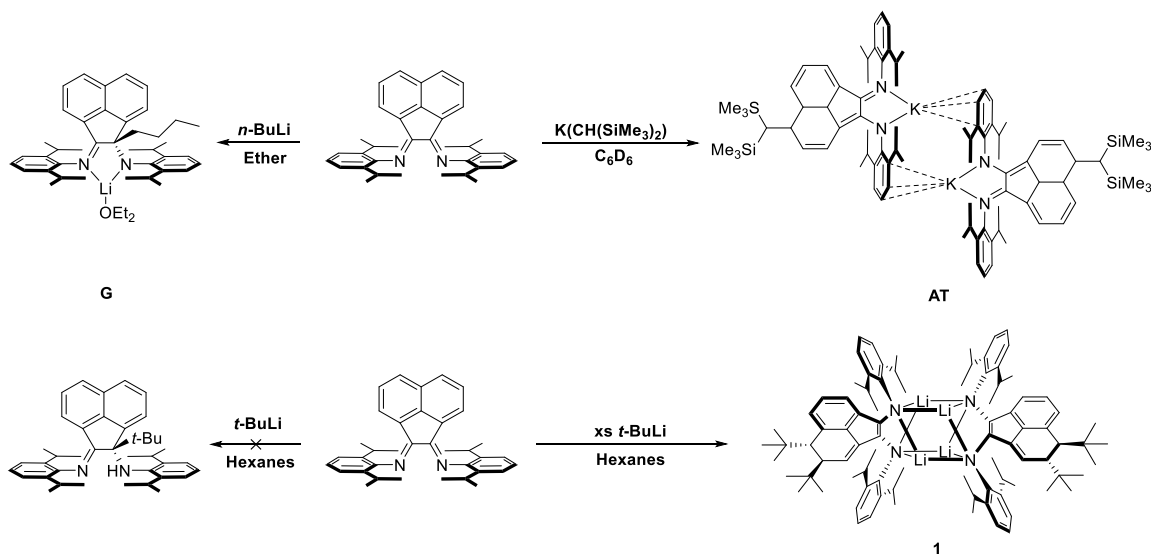
experimental spectrum using nonequivalent lithium and nitrogen nuclei. This gave some structural insight into the radical intermediate structure. The nonequivalence could be a result of mono-*t*-butylation of the backbone, which would break the C<sub>2v</sub> symmetry of the dpp-BIAN ligand, thus resulting in nonequivalent hyperfine coupling constants for each nitrogen and lithium nuclei. Overall, the spectrum was simulated using the following parameters:  $g = 2.003286$ ,  $A_N = 4.67$  G and 4.20 G,  $A_{Li} = 2.0$  G and 1.9 G.

With a satisfactory simulation of the experimental EPR spectrum, the identity of the radical intermediate structure could be proposed. The proposed radical intermediate structure features a single *t*-butyl group on the naphthalene backbone and two lithium atoms coordinated to the N-C-C-N fragment. This structure was in accord with that observed in the formation of compound **3**, where the mono-*t*-butyl group was located at the same position adjacent to the hydroxyl group that was subsequently added during hydrolysis. The formation of **3** clearly indicates that each *t*-butylation occurred in distinct steps during the dearomatization pathway. With all things considered, the radical intermediate was proposed to be the mono-*t*-butylated radical dianionic dpp-BIAN dilithium species, as displayed in Figure 3.

### **1.2.2 Sterically Directed Functionalization: Nucleophilic Imine C-Alkylation vs. Radical Backbone Dearomatization**

The study performed on the unexpected radical dearomatization of dpp-BIAN with *t*-BuLi raised several synthetic and mechanistic questions involving the functionalization of the BIAN ligand.<sup>35</sup> As exhibited in Scheme 32, the functionalization of dpp-BIAN can proceed through several different pathways with relatively similar reagents. Fedushkin *et al.* demonstrated imine C-alkylation pathways with *n*-BuLi,<sup>18</sup> Hill *et al.* discovered the interesting backbone dearomatization reaction using

$\text{K}[\text{CH}(\text{SiMe}_3)_2]$ ,<sup>33</sup> and, as discussed in Section 1.2.1, the radical backbone dearomatization using *t*-BuLi.<sup>35</sup> The answers to three specific questions were sought in the following study. First, what is the thermodynamic driving force that dictates the pathway for BIAN functionalization that is described above? Is it possible to control the regioselectivity of the foregoing reactions? Is the synthesis of a *t*-butylated BIAN\* derivative possible, akin to that described by Fedushkin *et al.*,<sup>18</sup> or does *t*-BuLi exclusively adopt the radical dearomatization pathway? The objective of the subsequent study by Evans and Cowley was to perform a comprehensive investigation of the functionalization reactions of the BIAN ligand in order to address the foregoing questions.<sup>38</sup>



Scheme 32: Versatile pathways for BIAN functionalization.<sup>18,33,35</sup>

As discussed extensively in Section 1.1, the majority of the research performed on the BIAN ligand has been carried out using the dpp group as the flanking aryl substituent. As a result, interest was generated in using an array of different flanking aryl substituents

to probe the effects of changing both the steric and the electronic properties of these substituents. Accordingly, the scope of the BIAN functionalization was expanded to include the 2,4,6-trimethylphenyl (mes) BIAN, 4-fluorophenyl (4-F) BIAN, and 4-methoxyphenyl (4-OMe) BIAN derivatives, as displayed in Figure 4. The mes-BIAN derivative, while slightly less sterically encumbered than the dpp-BIAN ligand, was predicted to behave in a similar fashion to the latter. On the other hand, the flanking imino aryl groups of the 4-fluorophenyl (4-F) and 4-methoxyphenyl (4-OMe) derivatives were selected to probe the electronic effects of the methoxy and fluoro group located in the *para*-position. Furthermore, both 4-F BIAN and 4-OMe BIAN provide less steric protection of the N-C-C-N fragment of the BIAN ligand in comparison to their dpp-BIAN and mes-BIAN counterparts.

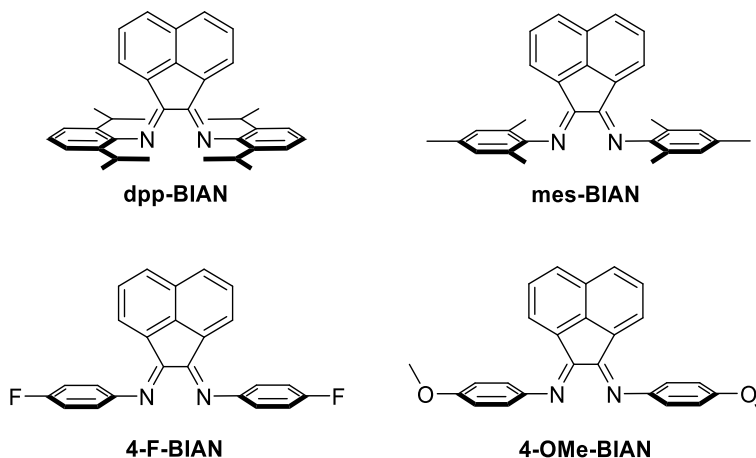
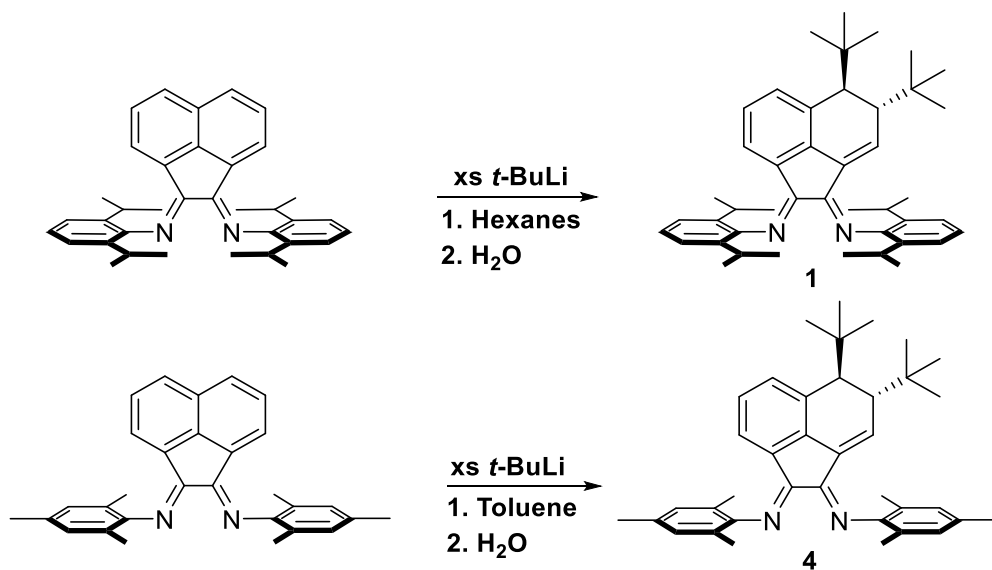


Figure 4: BIAN derivatives selected for the investigation of BIAN functionalization pathways.<sup>38</sup>

First, the reaction of mes-BIAN and *t*-BuLi was investigated. A red toluene solution of mes-BIAN was treated with *t*-BuLi, thereby generating a deep green colored



solution that gradually became dark purple over time. After 48 hours, the reaction was quenched by exposure to air and the addition of water resulting in the formation of a dark red colored solution. This solution was concentrated, and the red powder sample **4** was recrystallized and subsequently studied by means of a single crystal X-ray diffraction study. The identity of **4** was determined to be an analogous vicinal *t*-butylated backbone dearomatized mes-BIAN ligand akin to that reported for the reaction of dpp-BIAN with *t*-BuLi (Scheme 33). The formation of **4** was of significant importance because it confirmed that the dearomatization of the BIAN ligand was not strictly confined to dpp-BIAN.



Scheme 33: mes-BIAN and dpp-BIAN reactivity with *t*-BuLi.<sup>38</sup>

In order to confirm that the reactions that produced **1** and **4** were both proceeding through analogous radical dearomatization pathways, the synthesis of **4** was probed via EPR spectroscopy. The reaction and acquisition of the EPR spectrum was performed in a

similar fashion to that described previously. Upon examination with EPR spectroscopy, the intermediate deep green colored solution exhibited a detailed hyperfine coupling structure akin to that described above for the radical intermediate detected in the dearomatization reaction of dpp-BIAN with *t*-BuLi. The hyperfine structure was successfully simulated with hyperfine coupling constants that were similar to that used for the simulation of the radical intermediate of dpp-BIAN (Figure 5). The experimental spectrum of the green intermediate of **4** was simulated using the following parameters: ( $g = 2.003376$ ,  $A_N = 4.50$  G and 4.20 G,  $A_{Li} = 2.0$  G and 1.9 G).

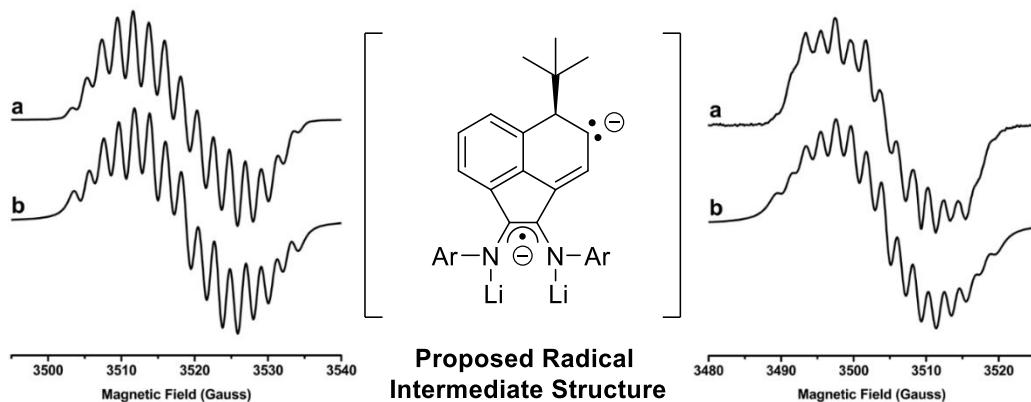
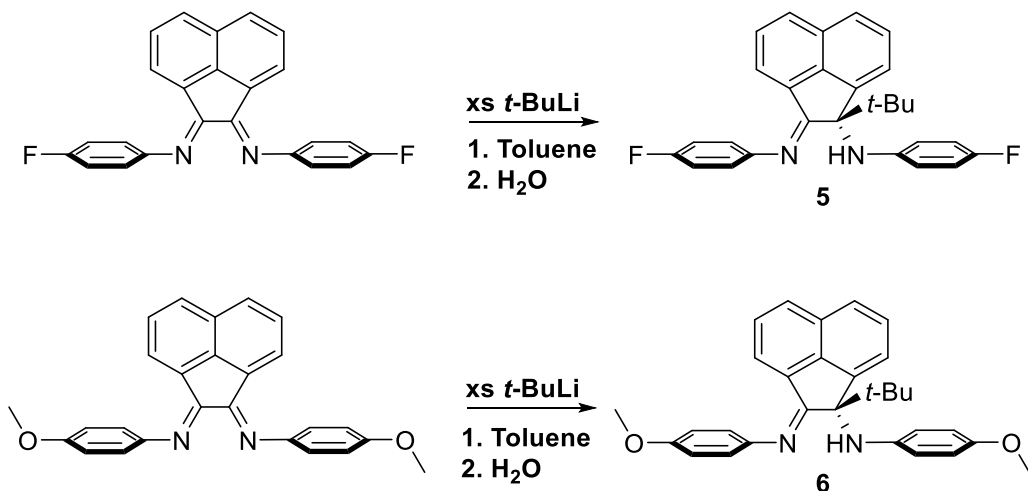


Figure 5: Experimental (a) and simulated (b) EPR spectra of the radical intermediate in toluene solution at room temperature for dpp-BIAN (Left) and mes-BIAN (Right) with proposed radical intermediate structure (Center).<sup>35,38</sup>

After confirming the radical nature of the functionalization reaction of mes-BIAN with *t*-BuLi, the focus was shifted towards the reactivity of 4-F and 4-OMe BIAN with *t*-BuLi. The reactivity of 4-F and 4-OMe was examined in order to determine whether a further reduction in steric bulk and an introduction of electronic effects would have an impact on their reactivities toward *t*-BuLi. As displayed in Scheme 34, toluene solutions of 4-F and 4-OMe BIAN were both treated with *t*-BuLi resulting in immediate color

changes of the reaction mixtures from orange to dark purple-brown and red to dark green-yellow, respectively. Over time, the later reaction mixtures assumed dark yellow (4-F) and dark green (4-OMe) hues. Hydrolysis of each reaction mixture resulted in color changes from dark yellow to amber (4-F) and from dark green to dark red-brown (4-OMe), respectively. Concentration and recrystallization led to the formation of suitable crystalline samples of **5** (4-F) and **6** (4-OMe). The structures of both compounds were determined by a single-crystal X-ray diffraction study, which revealed their identities to be those of *t*-butylated BIAN\* derivatives **5** (4-F) and **6** (4-OMe).

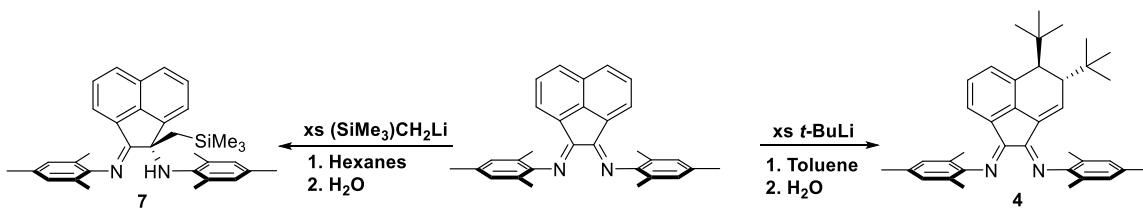


Scheme 34: 4-F-BIAN and 4-OMe-BIAN reactivity with *t*-BuLi.<sup>38</sup>

Clearly, a distinct structural dichotomy exists between the backbone dearomatized compounds **2** and **4** and the imine *C*-*t*-butylated compounds **5** and **6**. Interestingly, the mode of attack of *t*-BuLi was dependent on the nature of the flanking aryl substituents of the BIAN ligands. This unanticipated and exciting observation prompted further investigation into explaining the driving forces of BIAN functionalization. For this

purpose, a similar large alkyl lithium reagent, namely, (trimethylsilyl)methyl lithium (TMS-CH<sub>2</sub>-Li) was investigated for comparison with the reactivity observed with *t*-BuLi.

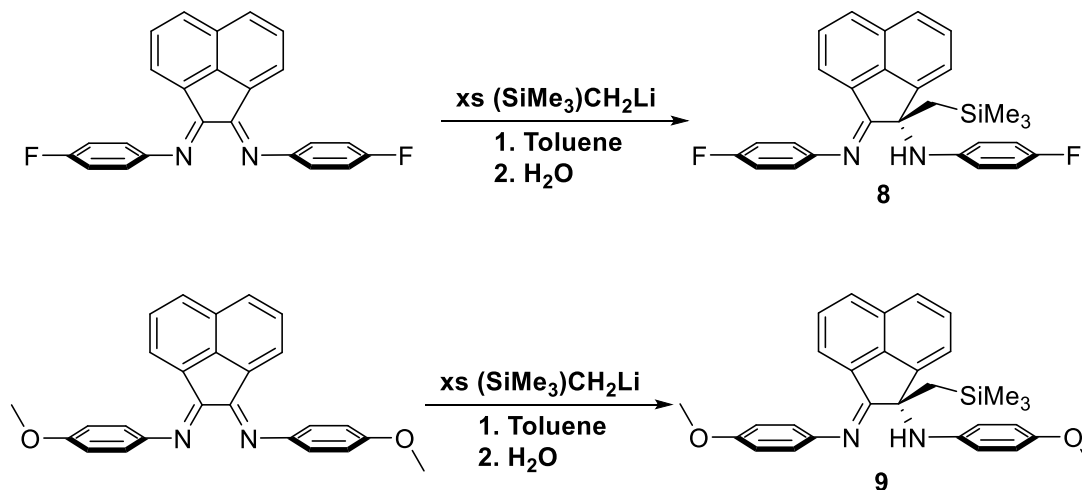
Reaction of a red hexanes solution of mes-BIAN with TMS-CH<sub>2</sub>-Li resulted in the development of a dark-amber brown solution. In contrast to the color changes observed in the reaction of *t*-BuLi with mes-BIAN, this dark-amber brown solution remained the same color for several hours. Following hydrolysis, the dark-amber brown solution changed to an orange-yellow color. Concentration and recrystallization led to the formation of product **7**. On the basis of a single-crystal X-ray diffraction study, the identity of **7** was determined to be the (trimethylsilyl)methyl substituted mes-BIAN\* compound. Surprisingly, the reaction of mes-BIAN with *t*-BuLi and TMS-CH<sub>2</sub>-Li, which are both comparably large alkyl lithium reagents, resulted in the formation of two distinctly different BIAN compounds (**4** and **7**), as exhibited in Scheme 35.



Scheme 35: Backbone dearomatization and imine C-alkylation of mes-BIAN.<sup>38</sup>

Next, the reactions of 4-F and 4-OMe BIAN with TMS-CH<sub>2</sub>-Li were explored. Toluene solutions of 4-F and 4-OMe BIAN were treated with TMS-CH<sub>2</sub>-Li and resulted in color changes of the reaction mixtures from orange to purple-red and from red to dark purple, respectively. Overtime, the 4-F and 4-OMe reaction mixtures slowly assumed a bright red and a dark red-brown color, respectively. Hydrolysis of these reaction mixtures afforded a dark yellow solution (4-F) and a light red-orange solution (4-OMe).

Concentration of these solutions and recrystallization led to the formation of compounds **8** (4-F) and **9** (4-OMe), as displayed in Scheme 36. A single crystal X-ray diffraction study revealed the identities of **8** (4-F) and **9** (4-OMe) to be that of (trimethylsilyl)methyl substituted BIAN\* derivatives.



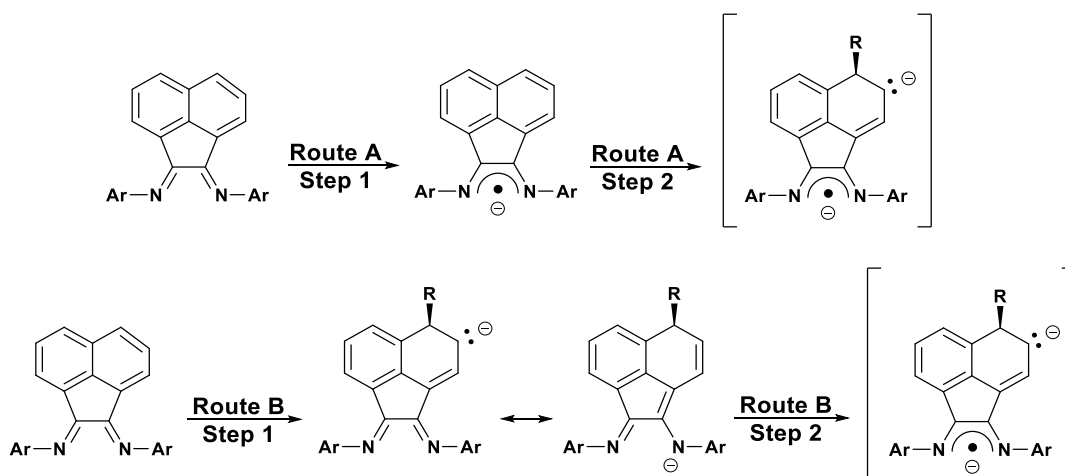
Scheme 36: Imine C-alkylation of 4-F-BIAN and 4-OMe-BIAN.<sup>38</sup>

The reactions for the formation of all imine C-alkylated BIAN\* derivatives were probed via EPR spectroscopy in order to determine if they proceed through radical pathways as well. However, no radical intermediates were detected via EPR spectroscopy. Only the syntheses of **1** and **4** led to detection of radical intermediates. This finding led to the proposition that imine C-alkylation was proceeding through a nucleophilic pathway in contrast to the radical pathway of backbone dearomatization.

### 1.2.3 Pathway Differentiation of BIAN Functionalization

As previously mentioned, there is a significant difference in reactivity of mes-BIAN with the similar alkyllithium reagents *t*-BuLi and TMS-CH<sub>2</sub>-Li. The difference is

displayed in Scheme 35, with a clear pathway distinction of nucleophilic imine C-alkylation versus radical backbone dearomatization. As demonstrated by the EPR spectroscopy experiments, the formation of the monoalkylated radical dianionic intermediate (coordinated to lithium) represents a key intermediate step along the dearomatization pathway. The generation of such a species would take place along one of two alternative two-stage routes, namely, Routes A and B, as displayed in Scheme 37. Step 1 of Route A would comprise electron transfer from R-Li to Ar-BIAN to generate a radical monoanionic species. After reduction, Step 2 would consist of nucleophilic addition of the second equivalent of R-Li to the backbone of the reduced radical monoanionic species resulting in the formation of the monoalkylated radical dianionic intermediate. On the other hand, Route B would comprise initial nucleophilic addition of R<sup>-</sup> on the backbone of free dpp-BIAN to generate a monoalkylated monoanionic intermediate. This transient monoanionic species would be resonance stabilized. Following nucleophilic addition, Step 2 would consist of a single-electron transfer from a second equivalent of R-Li to generate the monoalkylated radical dianionic intermediate. Both Route A and Route B would involve the formation of a •R radical species, which would be more readily generated from *t*-BuLi than from *n*-BuLi or TMS-CH<sub>2</sub>-Li. Such a radical would couple in the final step of the process to generate the dialkylated dianionic species akin to complex **1**.



Scheme 37: Proposed mechanism for the formation of the monoalkylated radical dianionic intermediate.<sup>38</sup>

It was decided that density functional theory (DFT) calculations could be employed to assess the factors that govern the competition between imine C-alkylation and backbone dearomatization pathways. Accordingly, the aforementioned calculations were performed in a collaborative effort with Professor Ignacio Vargas-Baca of McMaster University performing the theoretical calculations.<sup>38</sup> Initially, the electron affinities were examined for Ph-BIAN (as a model for dpp- and mes-BIAN), 4-F-BIAN, and 4-OMe-BIAN. The electron affinities were determined to be -165.6, -152.3, and -139.3 kJ/mol, respectively. These exothermic values are consistent with the well-known electron accepting redox properties of the BIAN ligand system.<sup>15</sup> Next, the most electrophilic sites of the BIAN ligand were identified by using the Fukui function<sup>39,40</sup>, which provided a map of the most electrophilic regions of the Ph-BIAN and  $[\text{Ph-BIAN}]^{\cdot-}$  radical anion. The electrophilic regions can be viewed in Figure 6.

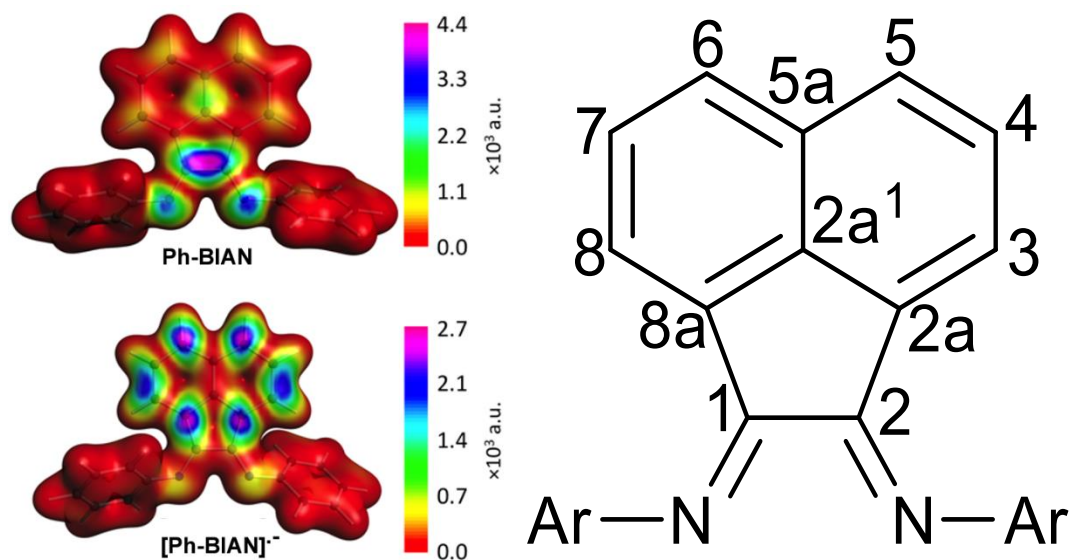


Figure 6: (Left) Fukui functions for Ph-BIAN (Upper) and [Ph-BIAN] $\cdot^-$  (Lower). (Right) Labels used to identify the different positions on the BIAN ligand.<sup>38</sup>

As displayed by the Fukui function, the region, where nucleophilic attack would take place on neutral Ph-BIAN, is at the imino carbon atoms. This Fukui function represents the primary reason why the reaction of alkyllithium reagents with Ar-BIAN compounds results in nucleophilic imine C-alkylation with the less sterically demanding flanking aryl substituents. Presumably, if the incoming nucleophile can access the electrophilic imino carbon atom, imine C-alkylation occurs. In contrast, inspection of the Fukui function for the radical monoanion [Ph-BIAN] $\cdot^-$  indicates that the primary electrophilic sites are the naphthalenic carbon atoms, specifically at the 5 position. Position 4 and 3 would also be candidates for nucleophile addition; however, 5 was found to be the most electrophilic naphthalenic carbon atom overall.



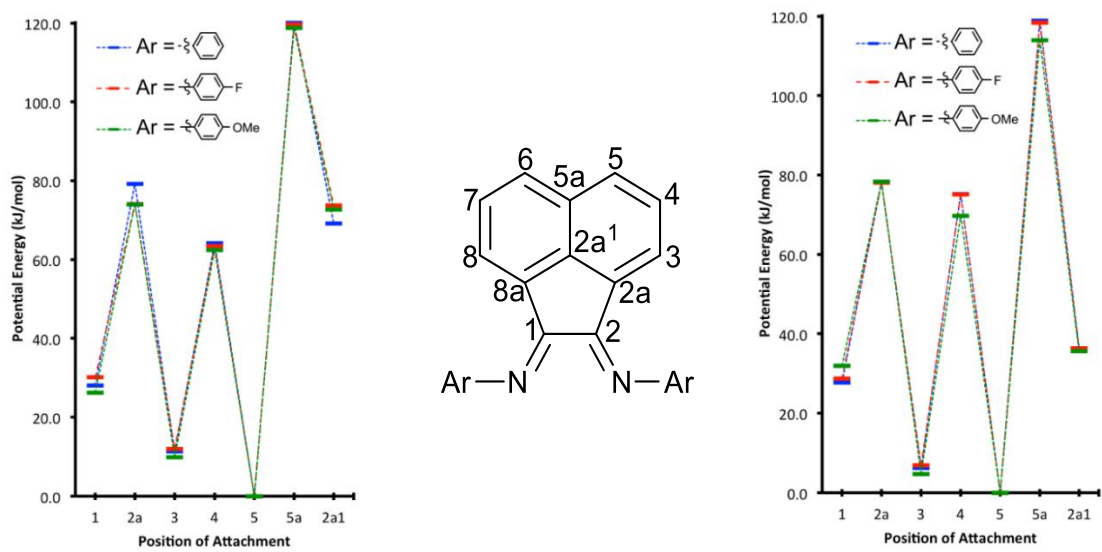


Figure 7: Relative stabilities of the alkylation isomers for the radical dianionic  $[\text{Ph-BIAN-Me}]^{2-}$  intermediate (Left) and the monoanionic  $[\text{Ph-BIAN-Me}]^-$  intermediate (Right).<sup>38</sup>

Next, the relative stabilities of the alkylation isomers of the monoalkylated radical dianion  $[\text{Ph-BIAN-R}]^{2-}$  (detected by EPR spectroscopy) and the monoalkylated monoanionic  $[\text{Ph-BIAN-R}]^-$  species (step 1 of Route B) were probed. The calculations were performed on Ph-BIAN, 4-F-BIAN, and 4-OMe-BIAN in order to examine the effect that electronics would have on the stabilities of the different alkylation isomers. In order to reduce calculation time, the incoming nucleophile R was chosen to be a methyl group for the theoretical model. Interestingly, the relative stabilities for all alkylation isomers for both the radical dianion  $[\text{Ph-BIAN-R}]^{2-}$  and monoanion  $[\text{Ph-BIAN-R}]^-$  were determined to be almost entirely independent of the electronics of the flanking aryl substituents. As displayed in Figure 7, alkylation at each location of the BIAN ligand resulted in essentially the same energy for Ph-BIAN, 4-F-BIAN, and 4-OMe-BIAN. This

was unexpected because the electronics of the flanking substituents have a significant impact on the electron affinities of each respective BIAN ligand, as discussed above.

After inspection of the relative stabilities of the alkylation isomers of both the radical dianionic  $[\text{Ph-BIAN-Me}]^{2-}$  and the monoanionic  $[\text{Ph-BIAN-Me}]^-$ , it is clear that alkylation at position 5 is the most thermodynamically stable alkylation isomer for both functionalization intermediates. This theoretical model is in good agreement not only with the crystal structure of the mono-*t*-butyl-hydroxy compound **3** but also with the proposed radical intermediate structure that was determined by means of EPR spectroscopy. As displayed in Figure 7, alkylation at positions 2a, 2a<sup>1</sup>, 4, and 5a, would be energetically unfavorable as compared to alkylation at positions 1, 3, and 5. However, the Fukui function shows that position 5 is more electrophilic than position 3. Therefore, alkylation at position 5 is favored over alkylation at position 3.

Although alkylation at position 1 was determined to be thermodynamically less stable than alkylation at position 5, alkylation at position 1 was still observed experimentally with the imine C-alkylation reactions discussed above. However, the Fukui function provided a kinetic rationale for imine C-alkylation with neutral Ph-BIAN because the imino carbon atoms in this case are highly electrophilic. Moreover, the model used to calculate the relative stabilities of the alkylation isomers did not initially incorporate the energy that would be gained by chelation of a lithium cation in the N-C-C-N fragment after imine C-alkylation was performed at position 1. This energetic correction was employed and reduced the potential energy by 14.8 kJ/mol for alkylation at position 1 for both  $[\text{Ph-BIAN-Me}]^-$  and  $[\text{Ph-BIAN-Me}]^{2-}$ . Considering these two factors, imine C-alkylation becomes a more plausible route for BIAN functionalization.

Next, the calculations were performed in a similar fashion with alkylation with the *t*-butyl group to give [Ph-BIAN-*t*-Bu]<sup>-</sup> and [Ph-BIAN-*t*-Bu]<sup>-2</sup>. The exchange of methyl for *t*-butyl was expected to introduce some destabilizing effects from steric repulsion of the flanking phenyl groups and the *t*-butyl group. However, the potential energies decreased by 10.4 and 8.4 kJ/mol for the monoanion and dianion, respectively. (Although, significant steric repulsion would be expected for imine C-alkylation with flanking dpp-groups).

Next, the SOMOs were calculated for the monoalkylated radical dianion [Ph-BIAN-R]<sup>-2</sup> that was detected by EPR spectroscopy (Figure 8). With the exception of the imine C-alkylated product, which would break conjugation in the N-C-C-N fragment, all alkylation isomers featured spin delocalization over the N-C-C-N fragment in good agreement with the experimental EPR hyperfine structure. The alkylation isomer that is particularly relevant is the SOMO of isomer 5, for which the Mulliken spin density was determined to be 0.33 and 0.37, which are in accord with the experimental hyperfine coupling constants discussed above.

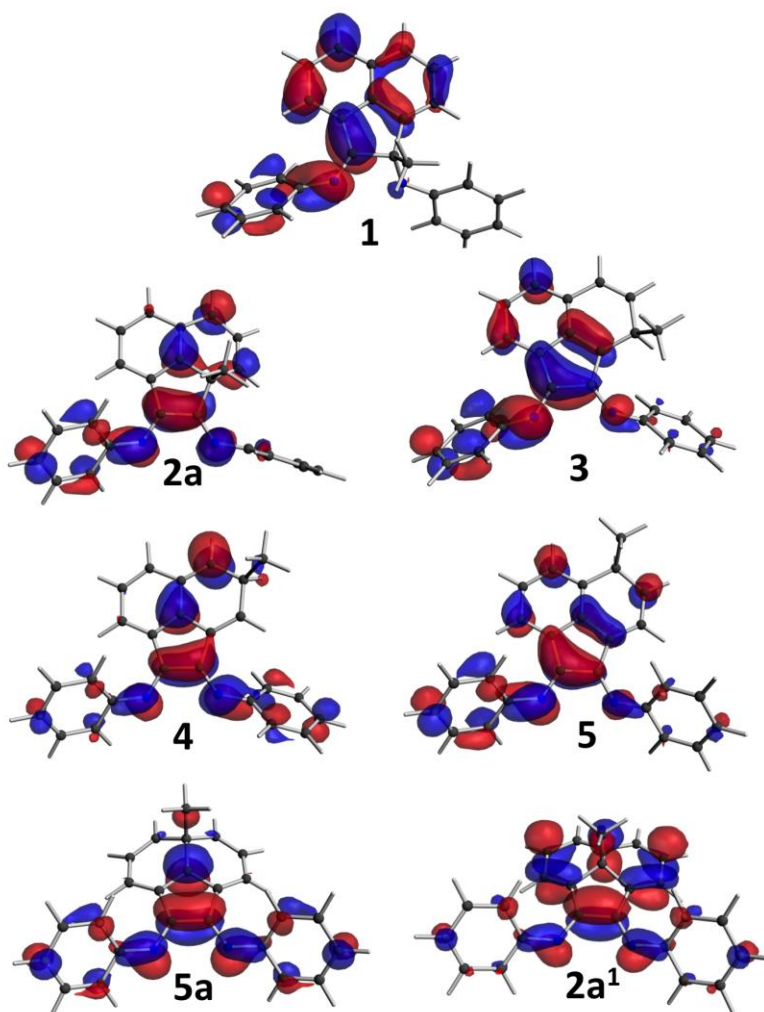
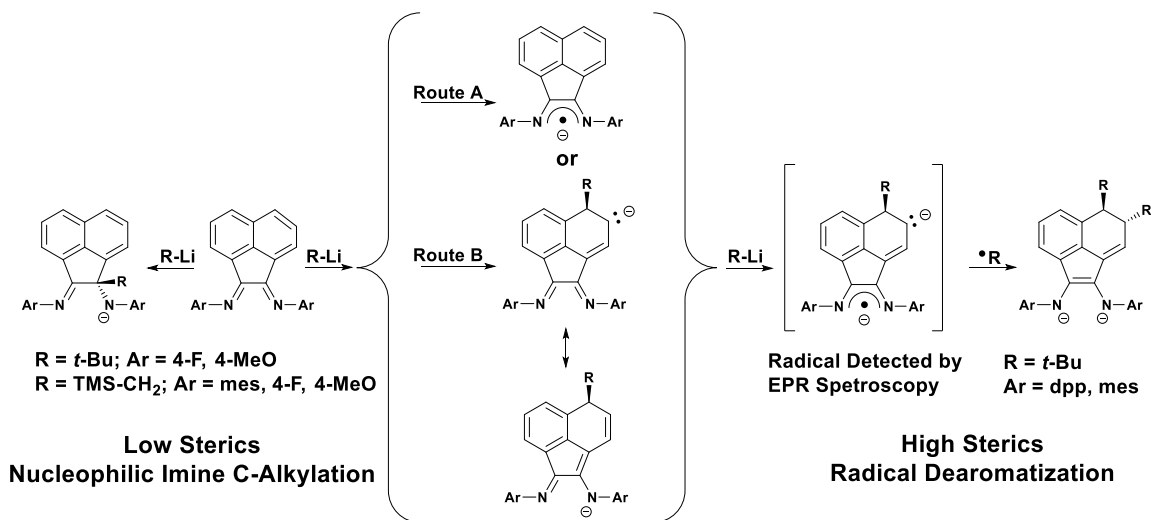


Figure 8: SOMOs for the monoalkylated radical dianionic  $[\text{Ph-BIAN-Me}]^{2-}$ .<sup>38</sup>

Considering the experimental and theoretical data collected in this study, pathway differentiation became possible for the proposed routes of BIAN functionalization (Scheme 38). First, if the incoming nucleophile can access the electrophilic imino carbon atoms of the BIAN ligand, then imine C-alkylation occurs. This occurs not only with the reaction of *t*-BuLi with 4-F-BIAN and 4-OMe-BIAN but also with the reaction of TMS-CH<sub>2</sub>-Li with 4-F-BIAN, 4-OMe-BIAN, and mes-BIAN. However, if the incoming

nucleophile was sufficiently bulky and could not access the imino carbon atom, radical backbone dearomatization was observed. As previously mentioned, the radical dearomatization would proceed through either Route A or Route B. However, the electron affinity calculated for the monoalkylated monoanion [Ph-BIAN-Me]<sup>-</sup>, which would be formed during Route B, was found to be highly endothermic (>150 kJ/mol). The foregoing endothermic electron affinity is an obstacle along the functionalization pathway of Route B from an energetic point of view. This is due to the fact that the next step along Route B would comprise a single electron transfer from R-Li to [Ph-BIAN-Me]<sup>-</sup> to generate the monoalkylated radical dianion that was detected by EPR spectroscopy. Also, Route B is very reminiscent of the reaction observed in the report by Hill *et al.*<sup>33</sup> However, the species reported from Hill *et al.* was a final product as opposed to an intermediate species described in the functionalization pathway Route B.



Scheme 38: Pathways for the nucleophilic imine C-alkylation and radical dearomatization functionalization reactions of the Ar-BIAN ligand.<sup>38</sup>

Considering these factors, the more likely pathway for BIAN functionalization was proposed to be Route A. Route A would comprise a single electron transfer event to generate the radical monoanion [Ar-BIAN]<sup>•-</sup>. This initial step would be expected to be exothermic as determined by the previously calculated electron affinities of the neutral BIAN ligand. Next, alkylation of a second equivalent of R-Li would generate the monoalkylated radical dianionic species that was detected by EPR spectroscopy. This alkylation event would be favorable upon consideration of the foregoing DFT results, namely, the relative stabilities of the alkylation isomers and the Fukui function of the radical monoanion [Ph-BIAN]<sup>•-</sup>. After formation of the monoalkylated radical dianion species, the last step of the radical dearomatization would consist of a coupling with •R to generate the vicinal *t*-butylated dearomatized BIAN species.

#### **1.2.4 X-Ray Diffraction Studies of 1-9b**

In this Section, each crystal structure that was discussed above was analyzed and interpreted. Full crystallographic data for compounds **1-9b** can be found in Appendix A with refinement details, atom positions, and tables of bond lengths and bond angles.

#### 1.2.4.1 [Li<sub>4</sub>][(1,2-di-(*t*-Bu)-dpp-BIAN)<sub>2</sub>] (1)

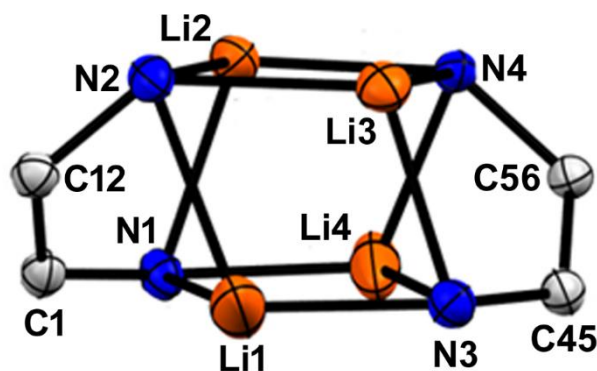


Figure 9: POV-Ray diagram of the Li-N antiprismatic core and appended BIAN C(1)-C(12) and C(45)-C(56) fragments of **1**. Thermal ellipsoids shown at 50% probability.<sup>35</sup>

Purple crystals of complex **1** were grown in an inert atmosphere from slow evaporation of a benzene solution. Complex **1** crystallized in the triclinic crystal system in the P-1 space group. The asymmetric unit featured two molecules of benzene in addition to one [Li<sub>4</sub>][(1,2-di-(*t*-Bu)-dpp-BIAN)<sub>2</sub>] complex. The Li-N antiprismatic core structure featured a significantly asymmetric structure such that each lithium and nitrogen atom resided in a unique bonding environment (Figure 9). Three faces of the antiprism are somewhat regular. However, the other three faces were found to be much less symmetric, particularly the distorted Li(4)-N(1)-Li(1)-N(3) face. This aforementioned distorted face featured a long Li(1)-N(1) bond distance of 2.887(7) Å, which is significantly longer than the rest of the Li-N bonds in the antiprismatic structure (1.977(6)-2.265(7) Å). Moreover, short contacts were found for each lithium atom and the C(1)-C(12) and C(45)-C(56) double bonds which are found in the range of 2.160(6) to 2.667(5) Å.

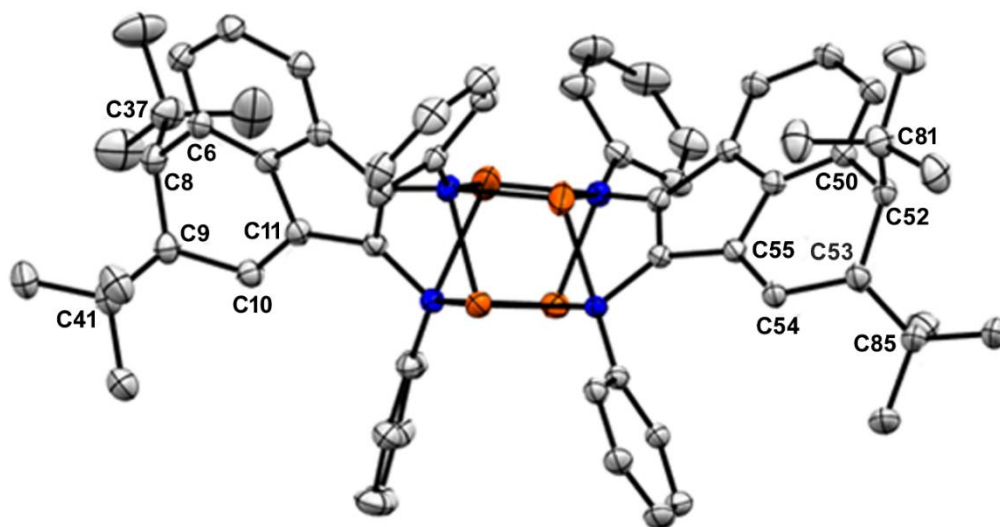


Figure 10: POV-Ray diagram of complex **1**. All hydrogen atoms, benzene molecules, and all aryl isopropyl groups have been removed for clarity. Thermal ellipsoids shown at 50% probability.<sup>35</sup>

The reduction of the N-C-C-N fragment was evident from the single bond lengths for the C(1)-N(1), C(45)-N(3), C(12)-N(2), and C(56)-N(4) bonds, which were found to be 1.402(3) Å, 1.405(3) Å, 1.430(3) Å, and 1.405(3) Å, respectively (Figure 10). Furthermore, the C(1)-C(12) and C(45)-C(56) bonds were found to be double bonds as indicated by their short bond lengths of 1.401(3) Å and 1.394(3) Å, respectively. The dearomatization of the naphthalene backbone was evident in the average C-C single bond of the C(6)-C(8)-C(9)-C(10) and C(50)-C(52)-C(53)-C(54) fragments of 1.539(4) Å. However, double bonding was retained for the C(10)-C(11) and C(54)-C(55) bonds, which feature bond lengths of 1.347(3) Å and 1.347(4) Å, respectively. The torsion angle between the vicinal *t*-butyl groups of the C(37)-C(8)-C(9)-C(41) and C(81)-C(52)-C(53)-C(85) fragments were determined to be -134.3(2) and -141.7(2) degrees, respectively. As previously mentioned, only the *trans*-stereoisomer was observed in the crystal structure for complex **1**.



#### 1.2.4.2 1,2-di-(*t*-Bu)-dpp-BIAN (**2**)

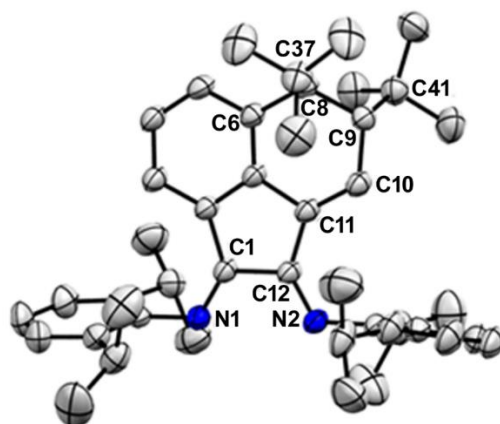


Figure 11: POV-Ray diagram of compound **2**. All hydrogen atoms have been removed for clarity. Thermal ellipsoids shown at 50% probability.<sup>35</sup>

Red crystals of **2** were grown by slow evaporation of a hexanes solution. Compound **2** crystallized in the monoclinic crystal system in the  $P2_1/c$  space group. Compound **2** contained only one molecule in the asymmetric unit (Figure 11). The bond lengths and angles of the BIAN backbone were found to be very similar to complex **1**. The dearomatization of the naphthalene backbone was evident from the average C-C single bond lengths in the C(6)-C(8)-C(9)-C(10) fragment of 1.538(3) Å. The double bond between C(10)-C(11) exhibited a bond length of 1.338(3) Å. However, formation of compound **2** was accompanied by a two electron oxidation in the N-C-C-N fragment resulting in conversion of the diamido functionality to a diimine moiety. This was evident after inspection of the C(1)-N(1), and C(12)-N(2) double bond lengths of 1.280(3) Å and 1.277(3) Å, respectively. Furthermore, the C(1)-C(12) bond length of 1.521(3) Å was indicative of a C-C single bond. The torsion angle between *t*-butyl groups in the C(37)-C(8)-C(9)-C(41) fragment was determined to be -138.9(2) degrees. As discussed above, compound **2** featured only the *trans*-stereoisomer.

### 1.2.4.3 1-(*t*-Bu)-2-(OH)-dpp-BIAN (**3**)

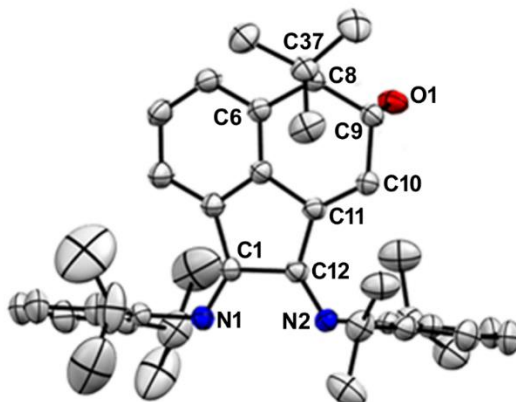


Figure 12: POV-Ray diagram of compound **3**. All hydrogen atoms and one molecule of toluene have been removed for clarity. Thermal ellipsoids shown at 50% probability.<sup>35</sup>

Red crystals of **3** were grown by slow evaporation of a toluene solution. Compound **3** crystallized in the monoclinic crystal system in the  $P2_1/n$  space group (Figure 12). The asymmetric unit of **3** contained one molecule of toluene in addition to one BIAN ligand. Not surprisingly, the bond lengths and angles of the BIAN backbone were very similar to both complex **1** and compound **2**. The dearomatization of the naphthalene backbone was exhibited in the average C-C single bond lengths in the C(6)-C(8)-C(9)-C(10) fragment of 1.527(2) Å. The double bond between the C(10)-C(11) bond exhibited a bond length of 1.340(2) Å. Akin to compound **2**, the N-C-C-N fragment exhibited a diimine moiety. This was evident in the C(1)-N(1), and C(12)-N(2) double bond lengths of 1.278(2) Å and 1.274(2) Å, respectively. The C(1)-C(12) single bond length was found to be 1.519(2) Å. The C(9)-O(1) bond length of 1.428(2) Å was indicative of a C-O single bond. The torsion angle between the C(37)-C(8)-C(9)-O(1) fragment was determined to be -153.65(13) degrees. Compound **3** only featured the *trans*-stereoisomer.

#### 1.2.4.4 1,2-di-(*t*-Bu)-*mes*-BIAN (**4**)

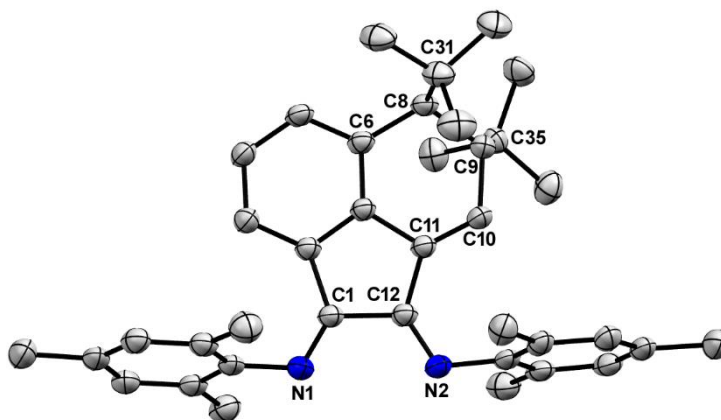


Figure 13: POV-Ray diagram of compound **4**. All hydrogen atoms have been removed for clarity. Compound **4** crystallized with two independent molecules in the asymmetric unit; only one of which is displayed for clarity. Thermal ellipsoids shown at 50% probability.<sup>38</sup>

Red crystals of **4** were grown from slow vapor diffusion of hexanes into a dichloromethane solution. Compound **4** crystallized in the triclinic crystal system in the P-1 space group (Figure 13). Compound **4** crystallized with two independent molecules in the asymmetric unit. Akin to that observed for compound **2**, compound **4** exhibited an imine functionality as evidenced by the average C=N double bond length of 1.277(2) Å. The average C-C single bond length in the N-C-C-N fragment was found to be 1.518(3) Å. Dearomatization was confirmed in the C(6)-C(8)-C(9)-C(10) and C(44)-C(46)-C(47)-C(48) fragments by the distance of the average C-C bond length of 1.531(3) Å. A localized double bond was evident between the C(10)-C(11) and C(48)-C(49) bonds, as indicated by the average C=C bond length of 1.331(3) (Å). The average torsion angle between the *t*-butyl groups was determined to be 142.60(18) degrees. Lastly, similar high stereoselectivity was observed in this transformation with only isolation of the *trans*-stereoisomer.

#### 1.2.4.5 *t*-Bu-(4-F)-BIAN\* (**5**)

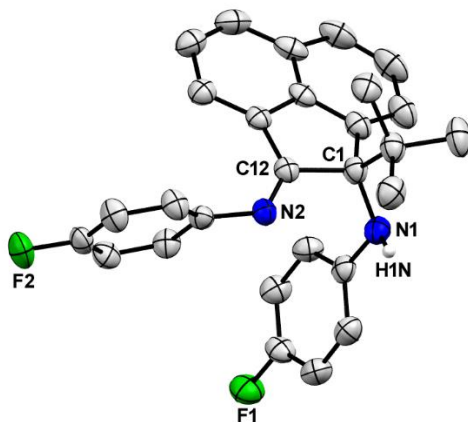


Figure 14: POV-Ray diagram of compound **5**. All hydrogen atoms have been removed for clarity with the exception of the amino hydrogen. Thermal ellipsoids shown at 50% probability.<sup>38</sup>

Dark yellow crystals of **5** were grown from slow vapor diffusion of hexanes into a dichloromethane solution. Compound **5** crystallized in the monoclinic crystal system in the  $P2_1/c$  space group (Figure 14). Compound **5** crystallized with one molecule in the asymmetric unit. The metrical parameters of the N-C-C-N fragment revealed the formation of a *t*-butylated BIAN\* ligand. The N(1)-C(1) and C(1)-C(12) bonds were both found to be single C-N and C-C bonds as evident from the bond lengths of 1.465(3) Å and 1.564(3) Å, respectively. The C(12)-N(2) bond retained the imine functionality as indicated from the C=N double bond length of 1.270(3) Å. The bond angles in the N-C-C-N fragment involving the C(1)-N(1)-H(1N), N(1)-C(1)-C(12), and N(2)-C(12)-C(1) fragments were found to be 109.7(17), 112.65(18), and 119.5(2) degrees, respectively. There was no intermolecular hydrogen bonds detected between the amino hydrogen and the imine moiety in the crystal lattice. This is indicative of the high steric bulk encompassing the N-C-C-N fragment, which inhibited this favorable crystal packing arrangement.

#### 1.2.4.6 *t*-Bu-(4-OMe)-BIAN\* (**6**)

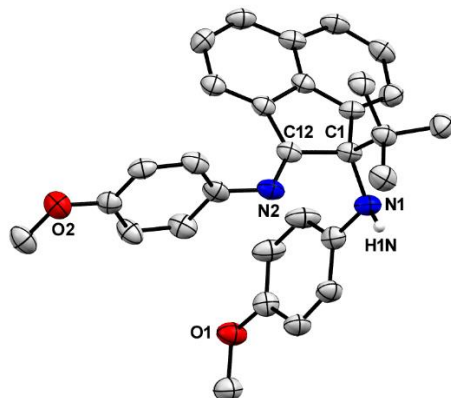


Figure 15: POV-Ray diagram of compound **6**. All hydrogen atoms have been removed for clarity with the exception of the amino hydrogen. Thermal ellipsoids shown at 50% probability.<sup>38</sup>

Red-brown crystals of **6** were grown from slow evaporation of a chloroform solution. Compound **6** crystallized in the triclinic crystal system in the P-1 space group (Figure 15). Compound **6** crystallized with one molecule in the asymmetric unit. The metrical parameters of the N-C-C-N fragment confirmed the formation of a *t*-butylated BIAN\* derivative. The N(1)-C(1) and C(1)-C(12) bonds were confirmed to be single C-N and C-C bonds as evident from the bond lengths of 1.486(4) Å and 1.564(5) Å, respectively. The C(12)-N(2) bond was found to be an imine functionality as indicated from the C=N double bond length of 1.278(4) Å. The bond angles in the N-C-C-N fragment involving the C(1)-N(1)-H(1N), N(1)-C(1)-C(12), and N(2)-C(12)-C(1) fragments were found to be 111(2), 112.3(3), and 119.3(3) degrees, respectively. Akin to that observed for compound **5**, there was no intermolecular hydrogen bonding between the amino hydrogen and the imine moiety in the crystal lattice. As mentioned above, this is indicative of the steric bulk encompassing the N-C-C-N fragment, which inhibits this favorable crystal packing arrangement.

#### 1.2.4.7 TMS-CH<sub>2</sub>-(mes)-BIAN\* (7)

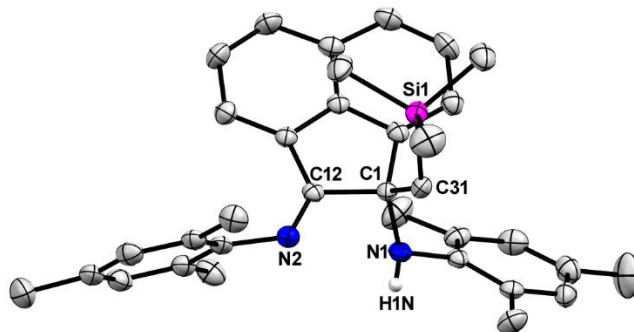


Figure 16: POV-Ray diagram of compound **7**. All hydrogen atoms have been removed for clarity with the exception of the amino hydrogen. Thermal ellipsoids shown at 50% probability.<sup>38</sup>

Yellow-brown crystals of **7** were grown from slow evaporation of a hexanes solution. Compound **7** crystallized in the monoclinic crystal system in the  $P2_1/c$  space group (Figure 16). Compound **7** crystallized with one molecule in the asymmetric unit. The metrical parameters of the N-C-C-N fragment confirmed the formation of the imine C-alkylated BIAN\* derivative. The N(1)-C(1) and C(1)-C(12) bonds were confirmed to be single C-N and C-C bonds as evident from the bond lengths of 1.501(3) Å and 1.557(3) Å, respectively. The C(12)-N(2) bond was confirmed to be an imine functionality as indicated from the C=N double bond length of 1.272(3) Å. The bond angles in the N-C-C-N fragment involving the C(1)-N(1)-H(1N), N(1)-C(1)-C(12), and N(2)-C(12)-C(1) fragments were found to be 108.3(16), 103.73(16), and 118.80(19) degrees, respectively. Akin to that observed for both compound **5** and compound **6**, no intermolecular hydrogen bonding between the amino hydrogen and the imine moiety was found. This indicated that, although the TMS-CH<sub>2</sub> is less sterically encumbered compared to *t*-Bu, it is still sufficiently bulky to inhibit intramolecular hydrogen bonding interactions within the crystal lattice of the mes-BIAN\* compound.

#### 1.2.4.8 TMS-CH<sub>2</sub>-(4-F)-BIAN\* (**8a**)

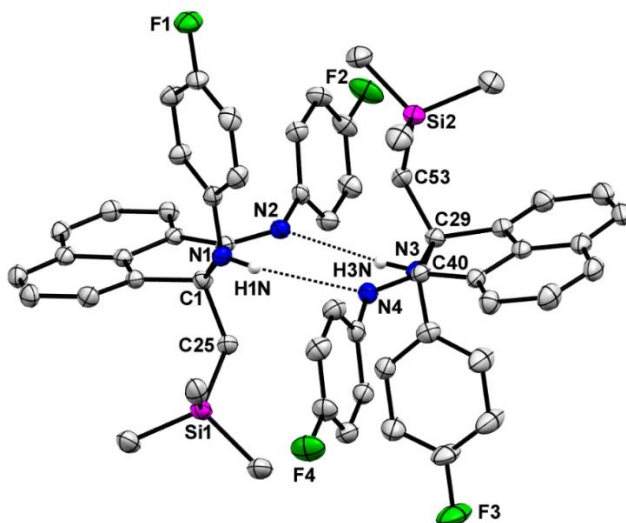


Figure 17: POV-Ray diagram of compound **8a**. All hydrogen atoms have been removed for clarity with the exception of the amino hydrogens. Thermal ellipsoids shown at 50% probability.<sup>38</sup>

Orange-yellow crystals of **8a** were grown from slow evaporation of a hexanes solution. Compound **8a** crystallized in the triclinic crystal system in the P-1 space group (Figure 17). Compound **8a** crystallized with two molecules in the asymmetric unit. The metrical parameters of the N-C-C-N fragment confirmed the formation of an imine C-alkylated BIAN\* derivative. The average N-C and C-C single bonds were found to have bond lengths of 1.461(3) Å and 1.519(3) Å, respectively. The average C-N double bonds were confirmed by the average bond length of 1.276(3) Å. The bond angles in the N-C-C-N fragment involving the C(1)-N(1)-H(1N), N(1)-C(1)-C(12), N(2)-C(12)-C(1), C(29)-N(3)-H(3N), N(3)-C(29)-C(40), and N(4)-C(40)-C(29) fragments were found to be 111.7(18), 114.16(17), 119.85(17), 108.4(16), 118.85(16), 119.80(18) degrees, respectively. Compound **8a** crystallized as hydrogen-bonded dimers as shown in Figure

17. This intramolecular hydrogen bonding interaction is a favorable crystal packing arrangement that was absent in the structures of **5**, **6**, and **7**. The existence of this hydrogen-bound dimeric interaction is indicative of a diminished steric encumbrance encompassing the N-C-C-N fragment of **8a**. The difference in structure between both 4-F BIAN\* derivatives **5** and **8a** highlights the difference between the *t*-Bu and TMS-CH<sub>2</sub> substituents. Also, the steric differences between the mes-BIAN\* compound **6** (which did not exhibit intermolecular hydrogen bonding) and the 4-F BIAN\* compound **8a** (which did exhibit intermolecular hydrogen bonding) were emphasized after analyzing each structure.



#### 1.2.4.9 TMS-CH<sub>2</sub>-(4-F)-BIAN\* (**8b**)

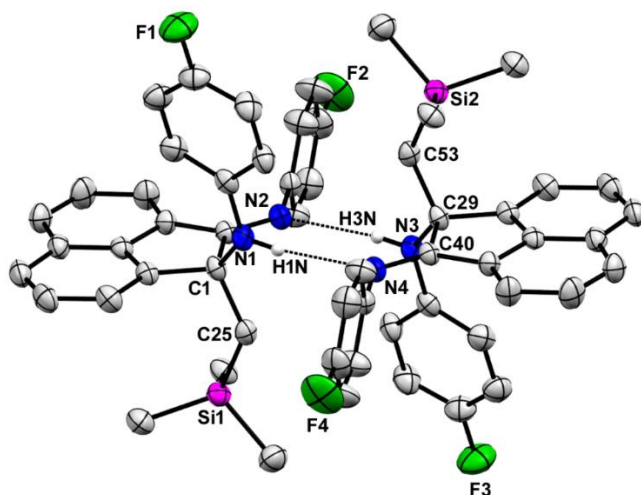


Figure 18: POV-Ray diagram of compound **8b**. All hydrogen atoms have been removed for clarity with the exception of the amino hydrogens. Thermal ellipsoids shown at 50% probability. Compound **8b** crystallized with one molecule in the asymmetric unit. The expanded hydrogen bond dimer is displayed for clarity.<sup>38</sup>

An alternate yellow crystal polymorph (**8b**) of compound **8a** was grown from the same recrystallization vial as **8a** by slow evaporation of a hexanes solution. Compound **8b** also crystallized in the triclinic crystal system in the P-1 space group (Figure 18). Compound **8b** crystallized with only one molecule in the asymmetric unit. The metrical parameters of the N-C-C-N fragment confirmed the formation of an imine C-alkylated BIAN\* derivative. The N(1)-C(1) and C(1)-C(12) bonds were confirmed to be single C-N and C-C bonds as evident from the bond lengths of 1.456(3) Å and 1.567(3) Å, respectively. The C(12)-N(2) bond was confirmed to be an imine functionality as indicated from the C=N double bond length of 1.280(3) Å. The bond angles in the N-C-C-N fragment involving the C(1)-N(1)-H(1N), N(1)-C(1)-C(12), and N(2)-C(12)-C(1)

fragments were found to be 112.6(16), 112.57(16), and 119.54(17) degrees, respectively. Compound **8b** crystallized in a hydrogen-bound dimer similar to **8a**, as shown in the structure overlay in Figure 19.

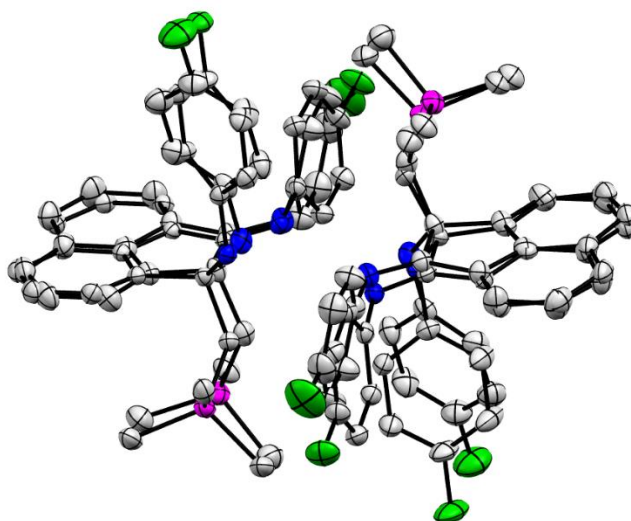


Figure 19: POV-Ray diagram of the overlay of polymorphs **8a** and **8b**. All hydrogen atoms have been removed for clarity. Thermal ellipsoids shown at 50% probability.<sup>38</sup>

#### 1.2.4.10 TMS-CH<sub>2</sub>-(4-OMe)-BIAN\* (9a)

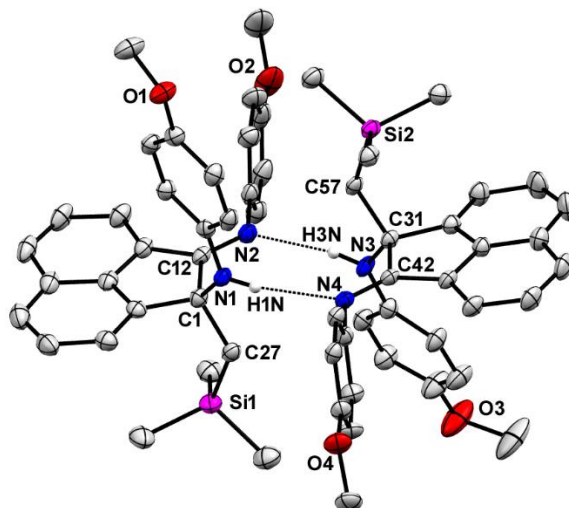


Figure 20: POV-Ray diagram of compound **9a**. All hydrogen atoms have been removed for clarity with the exception of the amino hydrogen. Thermal ellipsoids shown at 50% probability.<sup>38</sup>

Orange-yellow crystals of **9a** were grown from slow vapor diffusion of hexanes into a dichloromethane solution. Compound **9a** crystallized in the triclinic crystal system in the P-1 space group (Figure 20). Compound **9a** crystallized with two molecules in the asymmetric unit. The metrical parameters of the N-C-C-N fragment confirmed the formation of an imine C-alkylated BIAN\* derivative. The average N-C and C-C single bonds were found to have bond lengths of 1.453(3) Å and 1.561(4) Å, respectively. The average C-N double bonds were confirmed by the average bond length of 1.271(3) Å. The bond angles in the N-C-C-N fragment involving the C(1)-N(1)-H(1N), N(1)-C(1)-C(12), N(2)-C(12)-C(1), C(31)-N(3)-H(3N), N(3)-C(31)-C(42), and N(4)-C(42)-C(31) fragments were found to be 112(2), 114.4(2), 120.1(2), 112(2), 113.1(2), 120.0(2) degrees, respectively. Compound **9a** crystallized as hydrogen-bond dimers akin to that described for **8a** and **8b** as shown in Figure 20.

#### 1.2.4.11 TMS-CH<sub>2</sub>-(4-OMe)-BIAN\* (**9b**)

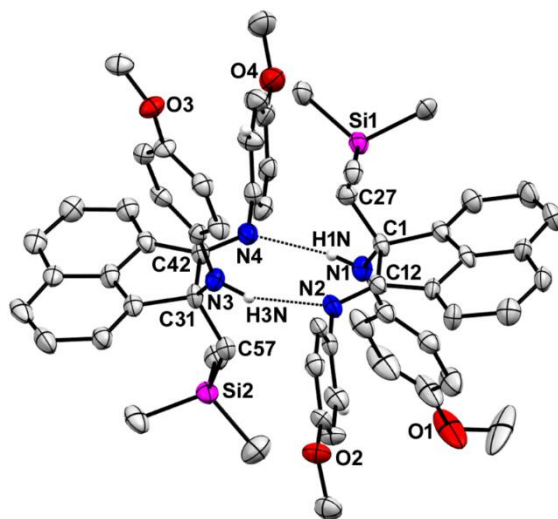


Figure 21: POV-Ray diagram of compound **9b**. All hydrogen atoms have been removed for clarity with the exception of the amino hydrogen. Thermal ellipsoids shown at 50% probability.<sup>38</sup>

An alternate yellow crystal polymorph (**9b**) of compound **9a** was grown from slow evaporation of a dichloromethane solution. Compound **9b** crystallized in the monoclinic crystal system in the  $P2_1/c$  space group (Figure 21). Compound **9b** crystallized with two molecules in the asymmetric unit. The metrical parameters of the N-C-C-N fragment confirmed the formation of an imine C-alkylated BIAN\* derivative. The average N-C and C-C single bonds were found to have bond lengths of 1.473(8) Å and 1.569(10) Å, respectively. The average C-N double bonds were confirmed by the average bond length of 1.289(8) Å. The bond angles in the N-C-C-N fragment involving the C(1)-N(1)-H(1N), N(1)-C(1)-C(12), N(2)-C(12)-C(1), C(31)-N(3)-H(3N), N(3)-C(31)-C(42), and N(4)-C(42)-C(31) fragments were found to be 115(4), 112.6(5), 120.2(6), 113(5), 114.9(6), and 118.4(6) degrees, respectively. Compound **9b** crystallized in a similar

hydrogen-bound dimer akin to **8a**, **8b**, and **9a** as shown in the structure overlay in Figure 22.

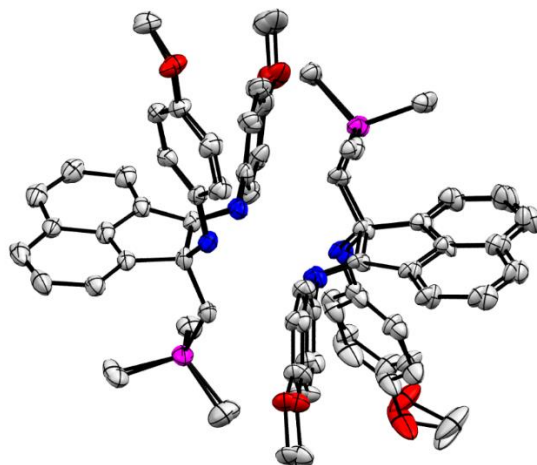


Figure 22: POV-Ray diagram of the overlay of polymorphs **9a** and **9b**. All hydrogen atoms have been removed for clarity. Thermal ellipsoids shown at 50% probability.

### 1.3 CONCLUSIONS

In conclusion, the previous Section (Section 1.2) described the sterically directed functionalization of the redox-active Ar-BIAN ligand class with bulky alkyllithium reagents. The pathways for nucleophilic imine C-alkylation and radical backbone dearomatization were differentiated based on the steric bulk encompassing the N-C-C-N fragment. On one hand, if the steric bulk of the flanking aryl groups was modest and the incoming nucleophile could access the electrophilic imino carbon, imine C-alkylation would take place. On the other hand, if the steric bulk was sufficiently large and the incoming nucleophile could not access the imino carbon, the functionalization reaction proceeded through the radical backbone dearomatization pathway. Each pathway was examined using single crystal X-ray crystallography, EPR spectroscopy, and computational modeling. After analysis, it was proposed that the most likely route for

dearomatization was Route A, namely single-electron transfer to neutral BIAN followed by a nucleophilic attack on the naphthalenic carbon atom 5. This nucleophilic attack generated the monoalkylated radical dianion observed during the EPR spectroscopy experiments. Lastly, this radical dianion would couple with  $\bullet R$  to generate the backbone dearomatized Ar-BIAN product.

## 1.4 EXPERIMENTAL

### 1.4.1 General Procedures

All reactions were performed under a dry, oxygen-free argon atmosphere using standard Schlenk techniques or in a Vacuum Atmospheres dry box. All glassware was oven dried and flushed with argon gas prior to use. All solvents were distilled and dried over sodium benzophenone and degassed prior to use. The dpp-BIAN,<sup>41</sup> mes-BIAN,<sup>41</sup> 4-F-BIAN,<sup>42</sup> and 4-OMe-BIAN<sup>43</sup> compounds were synthesized according to the pertinent literature procedures.

### 1.4.2 Physical Measurements

All of the NMR spectra were recorded at 298 K on either a Varian DirectDrive instrument (<sup>1</sup>H NMR, 599.75 MHz; <sup>13</sup>C NMR, 150.82 MHz), a Varian INOVA instrument (<sup>1</sup>H NMR, 499.87 MHz; <sup>13</sup>C NMR, 125.71 MHz, <sup>19</sup>F 469.85 MHz), or a Varian AS400 spectrometer (<sup>1</sup>H NMR, 399.80 MHz; <sup>13</sup>C NMR, 100.53 MHz) using residual solvent as the internal reference. The deuterated chloroform, benzene, and methylene chloride solvents were procured from Cambridge Isotopes Laboratories, Inc. and stored over 4 Å molecular sieves prior to use. The high-resolution electrospray ionization mass spectral data (HRMS-ESI) were collected on an Agilent 6530 Accurate Mass Q-TOF LC/MS mass spectrometer, and the high-resolution chemical ionization

mass spectral data (HRMS-CI) were collected on a Micromass Autospec Ultima mass spectrometer. All of the EPR experiments were recorded on a Bruker EMX-Plus X-band spectrometer and simulated using the Bruker Win EPR SimFonia simulation software Version 1.26. The melting points of **1-9** were determined using a Mel-Temp apparatus.

### 1.4.3 Single Crystal X-ray Crystallography

In the cases of compounds **1-9b**, suitable single crystals of all compounds were obtained by conventional recrystallization techniques. The single crystals were removed from their respective vials, covered with mineral oil, and mounted on a nylon thread loop. The X-ray diffraction data were collected on either a Rigaku AFC12 Saturn 724+ CCD diffractometer equipped with a Rigaku XStream low temperature device that operated at 100 K for crystals **1**, **4**, **8a**, **9a**, and **9b** or on a Rigaku SCX-Mini diffractometer equipped with a Rigaku XStream low temperature device that operated at either 163 K for crystals **5**, **6**, **7**, and **8b** or at 153 K for crystals **2** and **3**. Both instruments used a graphite-monochromated Mo K $\alpha$  radiation source ( $\lambda = 0.71075 \text{ \AA}$ ). Corrections were applied for Lorentz and polarization effects. The structures were solved by direct methods and refined by full-matrix least-squares cycles on  $F^2$  using the Siemens SHELXTL PLUS 5.0 (PC) software package<sup>44</sup> and PLATON<sup>45</sup>. All non-hydrogen atoms were refined anisotropically. The hydrogen atoms were placed in fixed, calculated positions using a riding model with the exception of all the amino hydrogen atoms, which were observed in a  $\Delta F$  map and refined with isotropic displacement parameters. The POV-Ray images were created using the Mercury version 3.3 program.

#### 1.4.4 Density Functional Theory

The density functional theory calculations were performed by our collaborator Professor Ignacio Vargas-Baca at McMaster University using the ADF DFT package (SCM, version 2013.01).<sup>46-48</sup> All-electron Slater-type basis sets were of triple- $\zeta$  quality with double polarization. Geometry optimizations were performed without constraints. General visualization was performed with the ADF-GUI.<sup>49</sup>

#### 1.4.5 Synthesis of 1-9

##### 1.4.5.1 [Li<sub>4</sub>][(1,2-di-(*t*-Bu)-dpp-BIAN)<sub>2</sub>] (1)

A 1.6 M pentane solution of *t*-BuLi (2.50 mL, 3.9944 mmol) was added to a hexanes (150 mL) solution of dpp-BIAN (1.00 g, 1.9972 mmol), thereby creating a dark blue solution. This dark blue solution quickly assumed a dark purple color over a period of approximately 10 minutes. The resulting dark purple colored solution was allowed to react for 48 hours. Concentration of this solution, followed by recrystallization from benzene, afforded purple crystals of **1** in 87.1 % yield (1.093 g, 1.740 mmol). <sup>1</sup>H NMR (C<sub>6</sub>D<sub>6</sub>):  $\delta$  0.53 (d, 3H, CH<sub>3</sub>,  $J$  = 7.0 Hz) 0.68 (s, 9H, *t*-Bu), 0.78 (d, 3H, CH<sub>3</sub>,  $J$  = 6.6 Hz), 0.82 (s, 9H, *t*-Bu), 0.91 (d, 3H, CH<sub>3</sub>,  $J$  = 6.6 Hz), 0.98 (d, 3H, CH<sub>3</sub>,  $J$  = 6.5), 1.01 (d, 3H, CH<sub>3</sub>,  $J$  = 7.0 Hz), 1.27 (m, 9H, CH<sub>3</sub>), 2.16 (d, 1H, CH,  $J$  = 6.0 Hz), 2.48 (s, 1H, CH), 2.75 (sept, 1H, *i*-Pr CH,  $J$  = 6.5 Hz), 3.46 (sept, 1H, *i*-Pr CH,  $J$  = 6.8 Hz), 3.58 (sept, 1H, *i*-Pr CH,  $J$  = 6.7 Hz), 3.86 (sept, 1H,  $J$  = 6.7 Hz), 4.49 (d, 1H, CH,  $J$  = 5.9 Hz), 6.12 (d, 1H, CH,  $J$  = 7.3 Hz), 6.57 (d, 1H, CH,  $J$  = 7.7 Hz), 6.64 (t, 1H, CH,  $J$  = 7.5 Hz), 7.02 (m, 6H, CH), 7.12 (d, 1H, CH,  $J$  = 7.3 Hz). <sup>13</sup>C NMR (C<sub>6</sub>D<sub>6</sub>):  $\delta$  22.31, 23.95, 24.53, 25.48, 25.53, 26.40, 26.46, 26.65, 27.56, 27.85, 28.11, 28.88, 29.14, 30.99, 35.94, 37.45, 45.40, 47.69, 115.37, 121.83, 122.94, 123.45, 124.05, 124.37, 124.49, 125.40, 125.62, 125.80,



128.70, 129.34, 133.60, 134.63, 136.26, 138.90, 140.95, 143.19, 145.02, 146.54, 148.81, 151.27. MP = 220 °C (decomp).

#### 1.4.5.2 1,2-di-(*t*-Bu)-dpp-BIAN (2)

A 1.6 M pentane solution of *t*-BuLi (2.50 mL, 3.9944 mmol) was added to a hexanes (150 mL) solution of dpp-BIAN (1.00 g, 1.9972 mmol), thereby creating a dark blue solution. This dark blue solution quickly assumed a dark purple color over a period of approximately 10 minutes. The resulting purple solution was allowed to react for 48 hours. Subsequent exposure to air resulted in an immediate color change of the reaction mixture from purple to red. Concentration of this red hexanes solution afforded red crystals of **2** in 87.1 % yield (1.069 g, 1.740 mmol). HRMS (ESI): calcd for [M + H]<sup>+</sup> C<sub>44</sub>H<sub>58</sub>N<sub>2</sub> *m/z* 615.46730; found 615.46700; <sup>1</sup>H NMR (CDCl<sub>3</sub>): δ 0.64 (s, 9H, *t*-Bu), 0.75 (s, 9H, *t*-Bu), 0.95 (d, 6H, CH<sub>3</sub> *J* = 6.78 Hz), 1.14-1.27 (m, 18H, CH<sub>3</sub>), 2.27 (d, 1H, CH, *J* = 5.8 Hz), 2.59 (s, 1H, CH) 2.91-3.07 (m, 4H, *i*-Pr CH), 5.35 (d, 1H, CH, *J* = 5.6 Hz), 6.17 (d, 1H, CH, *J* = 7.8 Hz), 6.85 (t, 1H, CH, *J* = 7.6 Hz), 7.03 (d, 1H, CH, *J* = 7.3 Hz), 7.03-7.26 (m, 6H, CH). <sup>13</sup>C NMR (CDCl<sub>3</sub>): δ 22.46, 22.54, 23.02, 23.07, 23.32, 23.38, 23.43, 23.54, 27.11, 27.62, 28.15, 28.42, 28.59, 28.79, 35.73, 36.87, 45.57, 46.32, 122.92, 123.26, 123.35, 123.75, 123.87, 127.54, 128.46, 129.02, 131.98, 132.97, 133.67, 134.51, 135.32, 135.38, 135.57, 141.04, 147.56, 147.87, 159.46, 161.83. MP = 184 °C.

#### 1.4.5.3 1-(*t*-Bu)-2-(OH)-dpp-BIAN (3)

A 1.6 M pentane solution of *t*-BuLi (0.65 mL, 0.9986 mmol) was added to a hexanes (40 mL) solution of dpp-BIAN (0.250 g, 0.4993 mmol), thereby creating a dark blue solution. Exposure of air to this blue solution resulted in the formation of a different dark purple solution. This dark purple solution faded to a dark red color over a period of

approximately 24 hours, following which a red-orange precipitate was extracted from the hexanes solution and recrystallized from toluene solution to yield red-orange crystals of **3** in 34.4% yield (0.0987 g, 0.172 mmol). HRMS (ESI): calcd for  $[M + H]^+$   $C_{40}H_{50}N_2O$   $m/z$  575.39960; found 575.39920;  $^1H$  NMR ( $CD_2Cl_2$ ):  $\delta$  0.78 (s, 9H, t-Bu), 0.97 (d, 3H,  $CH_3$ ,  $J = 6.66$  Hz), 1.07 (d, 3H,  $CH_3$ ,  $J = 6.7$  Hz), 1.11 (d, 3H,  $CH_3$ ,  $J = 6.9$  Hz), 1.19 (m, 15H,  $CH_3$ ), 2.75 (s, 1H, CH), 2.88 (m, 4H, i-Pr CH), 4.38 (dd, 1H, CH,  $J = 6.1, 6.8$  Hz), 5.50 (d, 1H, CH,  $J = 5.7$  Hz), 6.38 (d, 1H, CH,  $J = 7.8$  Hz), 7.00 (t, 1H, CH,  $J = 7.4$  Hz), 7.21 (m, 7 H, CH).  $^{13}C$  NMR ( $CD_2Cl_2$ ):  $\delta$  22.46, 22.80, 23.01, 23.20, 28.25, 28.85, 28.98, 29.05, 34.75, 54.40, 66.01, 123.57, 123.69, 123.90, 124.36, 124.50, 127.57, 128.71, 129.84, 130.00, 132.07, 134.39, 135.23, 135.31, 135.40, 140.00, 147.67, 147.85, 160.14, 160.77. MP = 158 °C.

#### 1.4.5.4 1,2-di-(*t*-Bu)-(mes)-BIAN (**4**)

Mes-BIAN (1.00 g, 2.40 mmol) was dissolved in 300 mL of toluene, thereby generating a red solution. A solution of *t*-BuLi in pentane (1.7 M) (3.54 mL, 6.01 mmol) was added to the foregoing solution, thereby immediately forming a dark green solution. Over a period of several hours, the dark green solution gradually assumed a dark purple color. After 48 hours, the addition of water to the dark purple solution resulted in the slow formation of a clear red colored solution. The toluene solution was extracted by means of a separatory funnel and dried over anhydrous magnesium sulfate. Concentration of the toluene solution afforded a mixture of products that was washed with pentane to remove impurities. The crude product was then extracted into a dichloromethane solution and recrystallized by slow vapor diffusion of hexanes into the dichloromethane solution, which in turn resulted in the formation of a crop of red crystals of **4** that were suitable for a single-crystal X-ray diffraction study. (0.354 g, 27.8%) HRMS (ESI): calcd for  $[M +$

$\text{H}]^+ \text{C}_{38}\text{H}_{47}\text{N}_2$   $m/z$  531.37338; found 531.37423;  $^1\text{H}$  NMR ( $\text{CDCl}_3$ ):  $\delta$  0.663 (s, 9H, t-Bu), 0.767 (s, 9H, t-Bu), 2.022 (s, 3H,  $\text{CH}_3$ ), 2.053 (s, 3H,  $\text{CH}_3$ ), 2.065 (s, 3H,  $\text{CH}_3$ ), 2.110 (s, 3H,  $\text{CH}_3$ ), 2.276 (d, 1H, CH,  $J = 6.1$  Hz), 2.316 (s, 3H,  $\text{CH}_3$ ), 2.340 (s, 3H,  $\text{CH}_3$ ), 2.585 (s, 1H, CH), 5.380 (d, 1H, CH,  $J = 5.9$  Hz), 6.354 (d, 1H, Ar-CH,  $J = 7.6$ ), 6.897 (m, 5H, Ar-H), 7.065 (d, 1H, Ar-H,  $J = 7.6$  Hz).  $^{13}\text{C}$  NMR ( $\text{CDCl}_3$ ):  $\delta$  17.41, 17.65, 17.67, 17.71, 20.85, 20.90, 27.24, 27.61, 35.86, 36.95, 45.76, 46.09, 122.84, 123.73, 124.37, 124.57, 124.69, 127.95, 128.42, 128.60, 128.75, 128.86, 129.01, 131.58, 132.30, 132.40, 133.10, 133.74, 140.85, 146.77, 147.31, 160.35, 161.63. MP = 217 °C.

#### 1.4.5.5 *t*-Bu-(4-F)-BIAN\* (5)

4-F-BIAN (0.150 g, 0.408 mmol) was dissolved in 80 mL of toluene, thereby generating an orange-red solution. A solution of *t*-BuLi in pentane (1.7 M) (0.360 mL, 0.611 mmol) was added to the foregoing solution, thereby immediately generating a dark purple-brown solution. This dark purple-brown solution assumed a dark yellow color over a period several hours. After 24 hours, the addition of water to this dark yellow solution resulted in the formation of an amber colored biphasic mixture. The toluene solution was extracted by means of a separatory funnel and dried over anhydrous magnesium sulfate. Concentration of this toluene solution, followed by extraction into a hexanes solution and subsequent recrystallization by slow evaporation of chloroform, resulted in the formation of a crop of dark yellow crystals of **5** that were suitable for single crystal X-ray diffraction. (0.113 g, 65.1 % yield). HRMS (CI,  $\text{CH}_4$ ) calcd for  $[\text{M} + \text{H}]^+ \text{C}_{28}\text{H}_{25}\text{N}_2\text{F}_2$   $m/z$  427.1986; found 427.2000;  $^1\text{H}$  NMR ( $\text{CDCl}_3$ ):  $\delta$  1.085 (s, 9H,  $(\text{CH}_3)_3$ ), 4.703 (s, (broad), 1H, NH), 6.049 (m, 2H, Ar-H, apparent complex coupling from fluorine), 6.534 (m, 2H, Ar-H, apparent complex coupling from fluorine), 6.584 (m, 3H, Ar-H, apparent complex coupling from fluorine), 7.025 (m, 2H, Ar-H, apparent

complex coupling from fluorine), 7.305 (t, 1H, Ar-H,  $J = 7.7$  Hz), 7.524 (d, 1H, Ar-H,  $J = 6.2$  Hz), 7.574 (t, 1H, Ar-H,  $J = 7.5$  Hz), 7.778 (d, 1H, Ar-H,  $J = 8.1$  Hz), 7.865 (d, 1H, Ar-H,  $J = 8.1$  Hz).  $^{13}\text{C}$  NMR ( $\text{CDCl}_3$ ):  $\delta$  25.41, 39.43, 73.41, 114.98 (d, 2C,  $J = 22$  Hz (F)), 116.24 (d, 2C,  $J = 22$  Hz (F)), 116.44 (d, 2C,  $J = 7$  Hz (F)), 119.26 (d, 2C,  $J = 8$  Hz (F)), 122.37, 122.73, 124.66, 127.36, 127.76, 128.86, 130.89, 131.60, 139.99, 140.58, 142.61 (d, 1C,  $J = 2$  Hz (F)), 147.95 (d, 1C,  $J = 3$  Hz (F)), 156.10 (d, 1C,  $J = 236$  Hz (F)), 159.58, (d, 1C,  $J = 242$  Hz (F)), 172.75.  $^{19}\text{F}$  NMR ( $\text{CDCl}_3$ ):  $\delta$  -121.04 (m (apparent septet), 1F), -127.59 (m (apparent septet), 1F). MP = 166 °C.

#### 1.4.5.6 *t*-Bu-(4-OMe)-BIAN\* (6)

4-OMe-BIAN (0.150 g, 0.383 mmol) was dissolved in 80 mL of toluene thereby, creating a red solution. A solution of *t*-BuLi in pentane (1.7 M) (0.338 mL, 0.574 mmol) was then added to the foregoing solution, thus immediately generating a dark green-yellow reaction mixture. The dark green-yellow reaction mixture gradually assumed a dark green color over a period several hours. After 24 hours, the addition of water to this dark green solution resulted in the formation of a dark red-brown colored biphasic mixture. The toluene solution was then extracted with a separatory funnel and dried over anhydrous magnesium sulfate. Concentration of this toluene solution, followed by extraction into a hexanes solution and recrystallization by slow evaporation of chloroform, resulted in the formation of a crop of X-ray suitable dark red-brown crystals of **6**. (0.152 g, 88.3%). HRMS (CI,  $\text{CH}_4$ ) calcd for  $[\text{M} + \text{H}]^+$   $\text{C}_{30}\text{H}_{31}\text{N}_2\text{O}_2$   $m/z$  451.2386; found 451.2372;  $^1\text{H}$  NMR ( $\text{CDCl}_3$ ):  $\delta$  1.106 (s, 9H,  $(\text{CH}_3)_3$ ), 3.593 (s, 3H,  $\text{CH}_3$ ), 3.831 (s, 3H,  $\text{CH}_3$ ), 4.587 (s, (broad), 1H, NH), 6.134 (m, 2H, Ar-H), 6.430 (m, 2H, Ar-H), 6.626 (m, 3H, Ar-H), 6.890 (d, 2H, Ar-H,  $J = 8.3$  Hz), 7.289 (t, 1H, Ar-H,  $J = 8.0$  Hz), 7.562 (m, 2H, Ar-H), 7.765 (dd, 1H, Ar-H,  $J = 6.8$  Hz, 2.2 Hz), 7.840 (d, 1H, Ar-H,  $J = 8.3$

Hz).  $^{13}\text{C}$  NMR ( $\text{CDCl}_3$ ):  $\delta$  25.47, 39.39, 55.50, 73.58, 114.03, 114.73, 117.41, 119.07, 122.43, 122.59, 124.38, 127.26, 127.59, 128.38, 130.82, 131.93, 140.11, 140.40, 141.19, 145.45, 152.42, 156.09, 172.60. MP = 148 °C.

#### 1.4.5.7 TMS-CH<sub>2</sub>-(mes)-BIAN\* (7)

Mes-BIAN (0.150 g, 0.361 mmol) was dissolved in 150 mL of hexanes, which resulted in the formation of a red solution. A solution of (trimethylsilyl)methyl lithium in hexanes (0.8 M) (0.676 mL, 0.541 mmol) was added to the foregoing solution, thus immediately generating a dark amber-brown solution. Over a period of several hours, the dark amber-brown solution assumed a light amber color. After 48 hours, the addition of water to the foregoing solution resulted in the immediate formation of a clear yellow-orange solution. This hexanes solution was extracted by means of a separatory funnel and dried over anhydrous magnesium sulfate. Concentration of the hexanes solution, followed by subsequent recrystallization via slow evaporation of hexanes, resulted in the formation of a crop of X-ray suitable yellow-brown crystals of **7**. (0.123 g, 67.7%). HRMS (CI,  $\text{CH}_4$ ) calcd for  $[\text{M} + \text{H}]^+$   $\text{C}_{34}\text{H}_{41}\text{N}_2\text{Si}$   $m/z$  505.3039; found 505.3046;  $^1\text{H}$  NMR ( $\text{CDCl}_3$ ):  $\delta$  -0.508 (s, 9H,  $(\text{CH}_3)_3$ ), 1.842 (s, 6H,  $\text{CH}_3$ ), 1.900 (s, 3H,  $\text{CH}_3$ ), 2.114 (AB quartet, 2H,  $\text{CH}_2$ ,  $J = 13.7$  Hz), 2.239 (s, 3H,  $\text{CH}_3$ ), 2.248 (s, 3H,  $\text{CH}_3$ ), 2.375 (s, 3H,  $\text{CH}_3$ ), 3.748 (s (broad), 1H, NH), 6.762 (s, 2H, Ar-H), 6.813 (d, 1H, Ar-H,  $J = 7.1$  Hz), 6.908 (s, 1H, Ar-H), 6.965 (d, 1H, Ar-H,  $J = 6.8$  Hz), 6.990 (s, 1H, Ar-H), 7.338 (t, 1H, Ar-H,  $J = 7.7$  Hz), 7.448 (t, 1H, Ar-H,  $J = 7.7$  Hz), 7.750 (d, 1H, Ar-H,  $J = 8.1$  Hz), 7.838 (d, 1H, Ar-H,  $J = 8.0$  Hz).  $^{13}\text{C}$  NMR ( $\text{CDCl}_3$ ):  $\delta$  0.033, 17.70, 18.48, 19.72, 20.63, 20.83, 31.03, 70.92, 122.36, 122.71, 124.22, 125.67, 126.29, 127.47, 128.03, 128.56, 128.90, 129.07, 129.29, 130.71, 131.59, 132.51, 132.74, 135.21, 139.24, 140.13, 142.56, 145.82, 174.32. MP 151 °C.

#### 1.4.5.8 TMS-CH<sub>2</sub>-(4-F)-BIAN\* (**8**)

4-F-BIAN (0.150 g, 0.408 mmol) was dissolved in 80 mL of toluene, which resulted in the formation of an orange-red solution. A solution of (trimethylsilyl)methyl lithium in hexanes (0.8 M) (0.765 mL, 0.612 mmol) was added to the foregoing solution, thereby immediately generating a dark purple-red solution. The dark purple-red solution subsequently assumed a bright red-orange color over a period of several hours. After 24 hours, the addition of water to this solution resulted in the formation of a dark yellow colored biphasic mixture. In turn, this dark yellow toluene solution was extracted by means of a separatory funnel and subsequently dried over anhydrous magnesium sulfate. Concentration of this toluene solution, followed by extraction into a hexanes solution and subsequent recrystallization by slow evaporation of the hexanes solution, resulted in the formation of a crop of X-ray suitable orange-yellow crystals of **8**. (0.167 g, 89.8 % yield). HRMS (CI, CH<sub>4</sub>) calcd for [M + H]<sup>+</sup> C<sub>28</sub>H<sub>27</sub>N<sub>2</sub>F<sub>2</sub>Si *m/z* 457.1912; found 457.1920; <sup>1</sup>H NMR (CDCl<sub>3</sub>): δ -0.565 (s, 9H, (CH<sub>3</sub>)<sub>3</sub>), 1.753 (s, 2H, CH<sub>2</sub>), 4.636 (s, (broad), 1H, NH), 6.088 (m, 2H, Ar-H, apparent complex coupling from fluorine), 6.538 (m, 2H, Ar-H, apparent complex coupling from fluorine), 6.625 (m, 2H, Ar-H, apparent complex coupling from fluorine), 6.677 (d, 1H, Ar-H, *J* = 7.1 Hz), 7.027 (m, 2H, Ar-H, apparent complex coupling from fluorine), 7.345 (t, 1H, Ar-H, *J* = 8.8 Hz), 7.661 (m, 2H, Ar-H), 7.805 (dd, 1H, Ar-H, *J* = 7.5 Hz, 1.46 Hz), 7.899 (d, 1H, Ar-H, *J* = 8.2 Hz). <sup>13</sup>C NMR (CDCl<sub>3</sub>): δ -0.63, 33.60, 68.33, 115.107 (d, 2C, *J* = 22 Hz (F)), 116.31 (d, 2C, *J* = 22 Hz (F)), 117.32 (d, 2C, *J* = 7 Hz (F)), 119.55 (d, 2C, *J* = 8 Hz (F)), 120.31, 123.50, 124.81, 127.73, 128.65, 129.25, 130.58, 131.46, 138.69, 142.43 (d, 1C, *J* = 2 Hz (F)), 143.31, 147.87 (d, 1C, *J* = 3 Hz (F)), 156.52 (d, 1C, *J* = 237 Hz (F)), 159.72

(d, 1C,  $J = 242$  Hz (F)), 175.08.  $^{19}\text{F}$  NMR ( $\text{CDCl}_3$ ):  $\delta$  -120.68 (m (apparent septet), 1F), -126.50 (m (apparent septet), 1F). MP = 181 °C.

#### 1.4.5.9 TMS-CH<sub>2</sub>-(4-OMe)-BIAN\* (9)

4-OMe-BIAN (0.150 g, 0.383 mmol) was dissolved in 80 mL of toluene, which resulted in the formation of a red colored solution. A solution of (trimethylsilyl)methyl lithium in hexanes (0.8 M) (0.719 mL, 0.575 mmol) was added to the foregoing solution, which immediately assumed a dark purple color. The dark purple solution changed to a dark purple-red colored solution over a period several hours. After 24 hours, the addition of water to this dark purple-red solution resulted in the formation of a light red-orange colored biphasic mixture. The toluene solution was then extracted by means of a separatory funnel and dried over anhydrous magnesium sulfate. Concentration of this toluene solution, followed by extraction into a hexanes solution and subsequent recrystallization by slow vapor diffusion of hexanes into dichloromethane solution, resulted in the formation of a crop of X-ray suitable amber crystals of **9**. (0.127 g, 69.1%). HRMS (CI, CH<sub>4</sub>) calcd for  $[\text{M} + \text{H}]^+$  C<sub>30</sub>H<sub>33</sub>N<sub>2</sub>O<sub>2</sub>Si  $m/z$  481.2311; found 481.2292;  $^1\text{H}$  NMR ( $\text{CDCl}_3$ ):  $\delta$  -0.576 (s, 9H, (CH<sub>3</sub>)<sub>3</sub>), 1.763 (AB quartet, 2H, CH<sub>2</sub>,  $J = 14.5$  Hz), 3.581 (s, 3H, CH<sub>3</sub>), 3.814 (s, 3H, CH<sub>3</sub>), 4.492 (s (broad), 1H, NH), 6.173 (m, 2H, Ar-H), 6.412 (m, 2H, Ar-H), 6.644 (d (broad), 2H, Ar-H,  $J = 8.4$  Hz), 6.712 (d, 1H, Ar-H,  $J = 7.2$  Hz), 6.874 (d, 2H, Ar-H,  $J = 7.6$  Hz), 7.300 (t, 1H, Ar-H,  $J = 8.0$  Hz), 7.620 (m, 2H, Ar-H), 7.776 (dd, H, Ar-H,  $J = 7.2$  Hz,  $J = 2.0$  Hz), 7.848 (d, 1H, Ar-H,  $J = 7.9$  Hz).  $^{13}\text{C}$  NMR ( $\text{CDCl}_3$ ):  $\delta$  -0.610, 33.27, 55.43, 55.46, 68.51, 114.00, 114.75, 118.70, 119.44, 120.35, 123.29, 124.55, 127.60, 128.45, 128.73, 130.94, 131.36, 138.91, 139.97, 143.82, 145.21, 153.07, 156.29, 174.87. MP = 155 °C.

## Chapter 2: Solid State Photoluminescent Bis(imino)acenaphthene Zinc Chloride Complexes: An Aggregation-Induced Emission, Emission Tunability, and Solvatomorphic Study\*

### 2.1 INTRODUCTION

#### 2.1.1 Bis(imino)acenaphthene as a Ligand in Photoluminescent Complexes

As discussed extensively in Chapter 1, the bis(imino)acenaphthene (BIAN) ligand is a versatile bidentate nitrogen donor ligand. However, this ligand has rarely been employed as a ligand support for photoluminescent metal complexes. This is somewhat surprising, based on the fact that the BIAN ligand possesses many advantageous properties with respect to its use as a ligand for photoluminescent applications. For example, Ar-BIAN ligands feature a  $\pi$ -conjugated naphthalene backbone, overall structural rigidity, a bidentate nitrogen donor functionality (which is common to many photoluminescent ligands such as 2-2'-bipyridine), and the ability to tune the stereoelectronic properties of the flanking aryl substituents. Despite these potential advantages, the use of BIAN ligands for photoluminescent applications is quite rare with only four such literature reports, as discussed below.

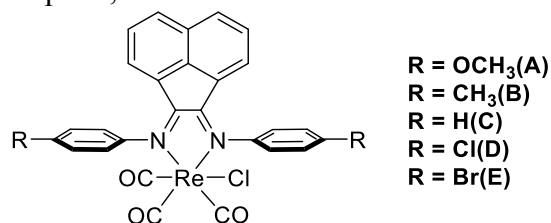


Figure 23: Non-luminescent *para*-substituted Re(Ar-BIAN)(CO)<sub>3</sub>(Cl) complexes A-E.<sup>50</sup>

\* Evans, D. A.; Lee, L. M.; Vargas-Baca, I.; Cowley, A. H. *Organometallics* **2015**. Acknowledgments are made to L. M. Lee for solid state diffuse reflectance measurements, I. Vargas-Baca for his computational modeling contributions, and A. H. Cowley for supervision



One literature study from 2000, reported the syntheses of a series of *para*-substituted rhenium BIAN complexes that were expected to display interesting photoluminescent properties.<sup>50</sup> As displayed in Figure 23, a series of rhenium(I) BIAN complexes (**A-E**) was synthesized with various functional groups in the *para*-position of the flanking aryl substituents. Unfortunately, this series of BIAN complexes was found to be nonemissive not only at room temperature but also at 77 K.

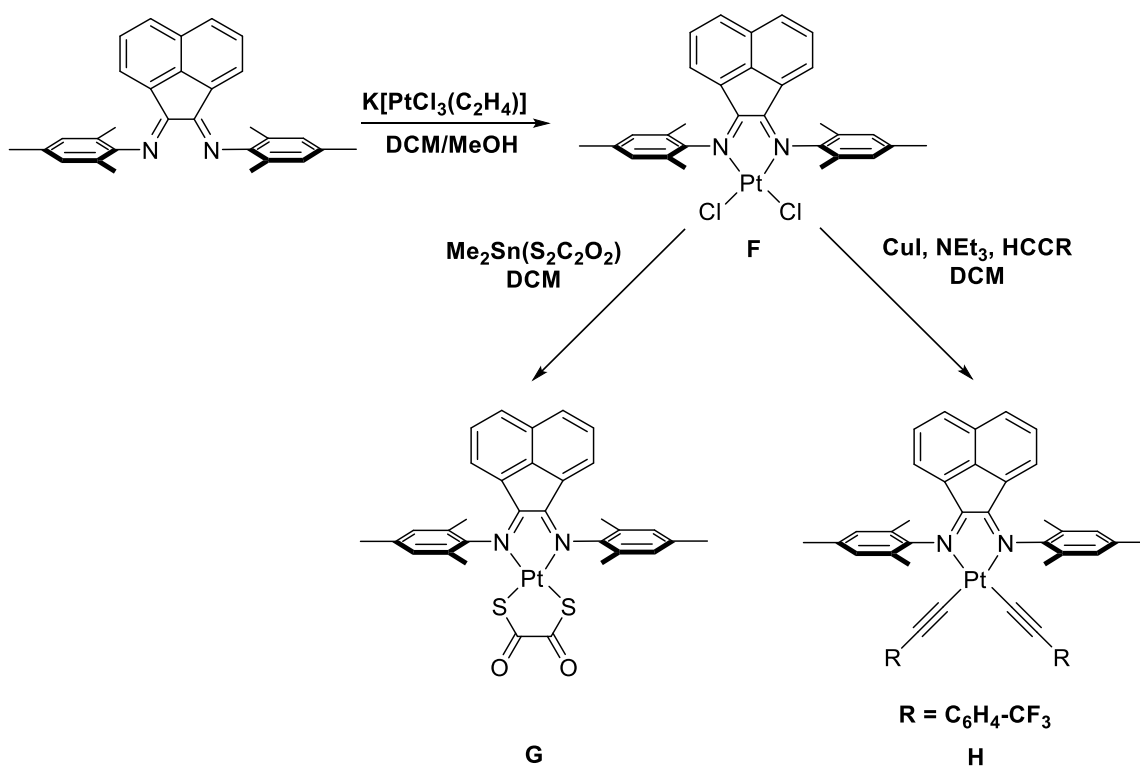


Figure 24: Photoluminescent platinum(II) BIAN complexes (**F**, **G**, **H**).<sup>51</sup>

A study from Weinstein *et al.* in 2006, reported the photoluminescent behavior of the three platinum(II) mes-BIAN complexes **F**, **G**, and **H** (Figure 24).<sup>51</sup> These complexes were found to be luminescent in DCM solution at room temperature. The emissions from

**F**, **G**, and **H** were found to exhibit low energies in the red/near-IR region of the spectrum with  $\lambda_{\text{max}}$  values of 777, 820, and 800 nm, respectively. The quantum yields of the platinum complexes **F**, **G**, and **H** were extremely low with values of 0.03 %, 0.004 %, and 0.08 %, respectively. Lastly, complexes **F**, **G**, and **H** exhibited emission lifetimes of 20, 17, and 30 nanoseconds, respectively. This report demonstrated the first photoluminescent platinum diimine dichloride complexes in solution at room temperature, albeit in a very low quantum yield.

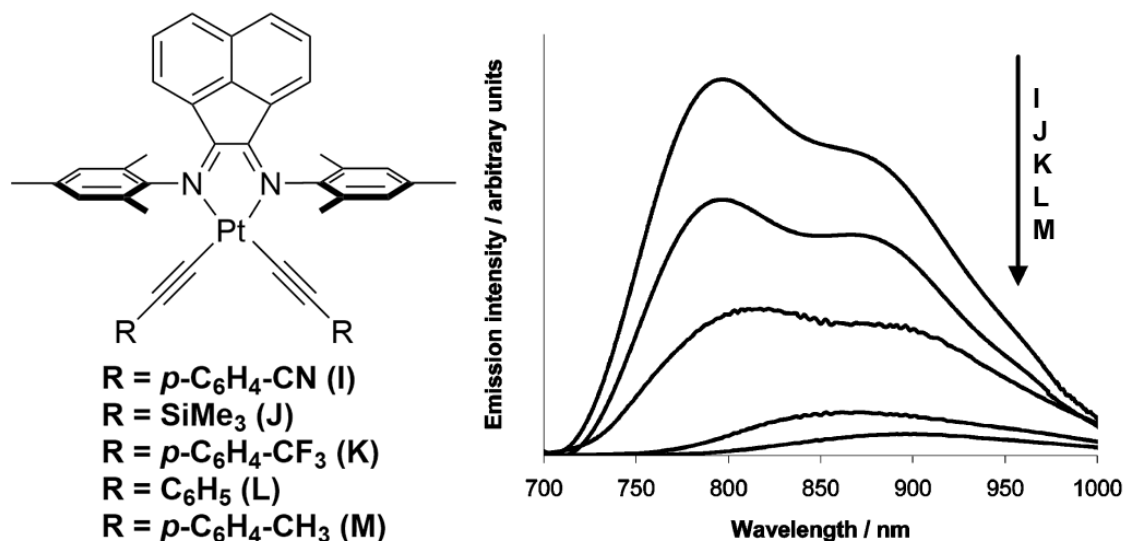


Figure 25: (Left) Photoluminescent platinum BIAN complexes featuring substituted acetylide ligands (**I-M**). (Right) Emission spectra of **I-M** in DCM solution at room temperature.<sup>52</sup>

A subsequent report from Weinstein *et al.* in 2008, expanded on the research of platinum(II) acetylide BIAN photoluminescent complexes.<sup>52</sup> By applying a similar synthetic route to that exhibited in Figure 24, a series of platinum BIAN complexes featuring substituted acetylide ligands was synthesized (**I-M**). As displayed in Figure 25, the  $\lambda_{\text{max}}$  values for complexes **I-M** were found to be 786, 790, 800, 848, and 896 nm,

respectively. Typical platinum acetylide complexes with 1,10-phenanthroline or 2,2'-bipyridine ligands emit in the region of 450-600 nm. In comparison, the emissions from the similar bidentate nitrogen donor BIAN supported platinum acetylide complexes were found to be significantly red shifted. The foregoing red shifted emissions were proposed to be due to the strong electron accepting ability of the mes-BIAN ligand, which in turn lowered the energy of the emissions. Also, akin to that described in the 2006 study<sup>51</sup>, the quantum yields for complexes **I-M** were found to be extremely low with values ranging from 0.53 % (**I**) to 0.009 % (**M**). The lifetimes of each complex were also similar to those described above, with emission lifetimes ranging from 36 ns (**I**) to 8 ns (**M**).

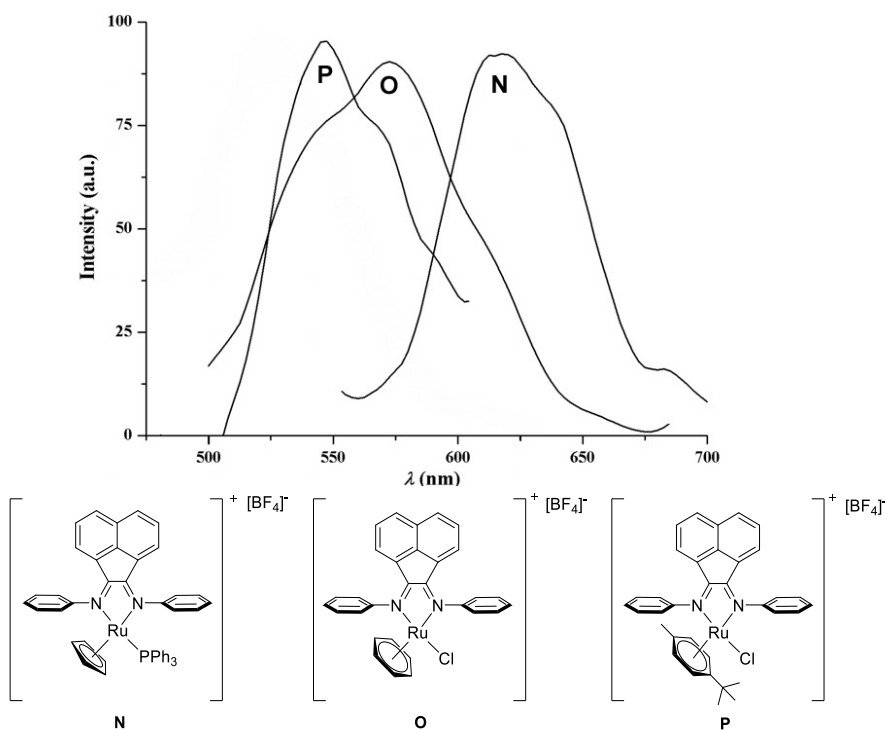


Figure 26: Photoluminescent emission of ruthenium BIAN complexes **N**, **O**, and **P** at room temperature in DCM solution.<sup>53</sup>

In 2008, Pandey *et al.* performed a study based on ruthenium(II), rhodium(III), and iridium(III) BIAN complexes for use as catalysts for the hydrogenation of terephthalaldehyde to 4-(hydroxymethyl)benzylaldehyde.<sup>53</sup> Although this work was concerned with hydrogenation catalysis, Pandey *et al.* reported that the ruthenium(II) BIAN complexes (**N**, **O**, **P**) were found to be emissive in DCM solution at room temperature (Figure 26). The emissions of complexes **N**, **O**, and **P** were centered at 617, 577, and 547 nm, respectively. However, no further details were presented in this study on the photoluminescent emission of these ruthenium complexes.

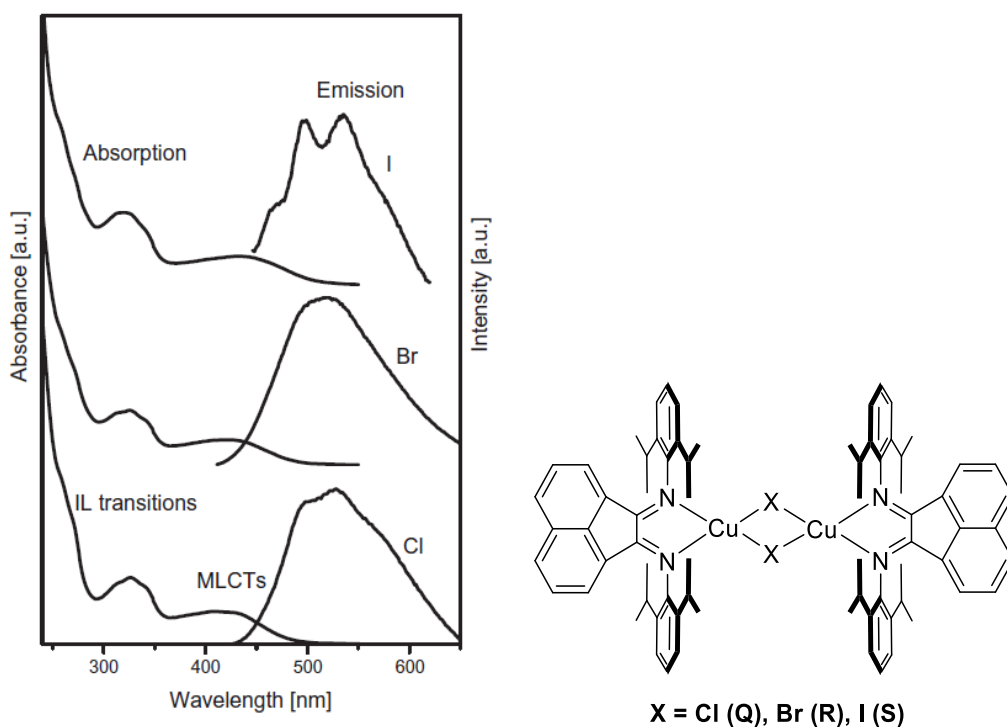


Figure 27: Photoluminescent emissions of Cu(I) dimeric BIAN complexes **Q**, **R**, and **S** at room temperature in DCM solution.<sup>54</sup>

Lastly, in 2011, Knör *et al.* published a study on dinuclear halide bridged copper(I) BIAN complexes **Q**, **R**, and **S**.<sup>54</sup> Upon irradiation in the UV region, these Cu(I) complexes exhibited “weak” luminescence with emissions centered at 510 nm (Figure 27). No other fluorescence spectroscopy data was provided in this study. The report of Knör *et al.* was primarily concerned with UV/vis and structural properties of the dinuclear Cu(I) BIAN complexes.

It is clear from the proceeding studies that the photoluminescent applications of the ubiquitous BIAN ligand remain relatively unexplored. Accordingly, interest was generated in the potential utilization of BIAN ligands as supports for photoluminescent complexes. In Section 2.2, the solid state photophysical properties of Ar-BIAN complexes will be explored. Specifically, the aggregation-induced emission (AIE) of a series of Ar-BIAN zinc chloride complexes will be discussed along with a detailed solvatomorphic investigation.

### **2.1.2 Solid State Emissions: Aggregation-Caused Quenching (ACQ) vs. Aggregation-Induced Emission (AIE)**

Organic light emitting diodes (OLEDs) are materials that have attracted significant attention since their conception by Tang and VanSlyke in 1987.<sup>55–57</sup> However, the intensities of most emissive materials is significantly reduced in the aggregated state when compared to those of the solution based emissions.<sup>58</sup> This deleterious type of quenching is referred to as aggregation-caused quenching (ACQ).<sup>59</sup> ACQ is typically manifested through intermolecular interactions that take place between emissive molecules such as  $\pi$ - $\pi$  stacking. ACQ represents a major obstacle for the fabrication of emissive materials for OLEDs because they operate in the condensed state and thus their emissions are quenched. Measures, such as the installation of sterically bulky groups that

will inhibit ACQ by blocking intermolecular interactions upon aggregation, have been taken to circumvent this obstacle.<sup>60</sup> However, the foregoing approach has not successfully overcome the problem that ACQ presents for OLEDs; in part, because aggregate formation is an inherent process upon formation of a solid state material.

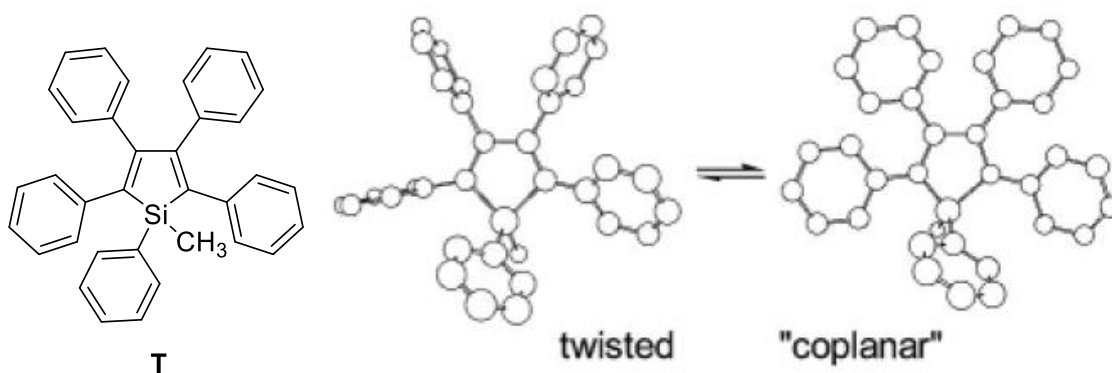


Figure 28: Phenyl substituted silole **T** displayed with twisted and coplanar orientations.<sup>61</sup>

In a pioneering report from 2001, Tang *et al.* discovered an emissive material that demonstrated properties that were the exact opposite of ACQ materials.<sup>61</sup> The 1-methyl-1,2,3,4,5-pentaphenylsilole material **T** was determined to be nonemissive in solution but became highly emissive in the aggregated state.<sup>61</sup> Upon inspection of Figure 28, two types or orientations can be visualized for the structure of silole **T**. It is clear that a twisted orientation for silole **T** would be preferred in solution. However, a coplanar orientation would follow the typical mechanism for ACQ materials by forming  $\pi$ -stacked columns upon aggregation.<sup>59</sup> The distinguishing feature of silole **T** is that the formation of a coplanar structure seems to be highly unlikely due to the substantial steric encumbrance of the five phenyl substituents on the silole ring. With the objective of

developing a more complete understanding of the properties of silole **T**, Tang *et al.* launched an investigation to determine the origin of this new phenomenon.

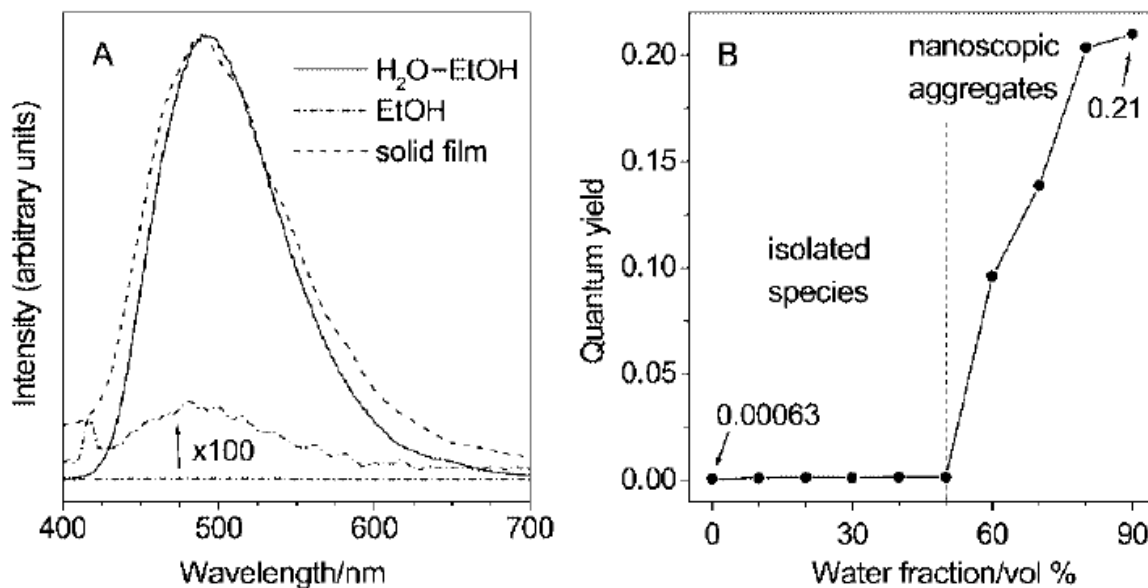


Figure 29: (Left) Photoluminescent spectra for a 90:10 % water/ethanol volumetric mixture of **T**, pure ethanol solution of **T**, and solid film of **T**. (Right) Plot of the quantum yields of silole **T** with different water/ethanol volumetric mixtures.<sup>61</sup>

To demonstrate the interesting emissive behavior of silole **T**, a series of volumetric fractions was prepared using ethanol and water. Silole **T** was soluble and nonemissive in ethanol solution, as displayed in Figure 29. However, upon addition of the poor solvent water, the hydrophobic silole materials began to aggregate and emission was detected. As previously mentioned, this outcome was the exact opposite behavior of most emissive materials, which quench upon aggregation. Accordingly, Tang *et al.* termed this peculiar phenomenon aggregation-induced emission (AIE). The definition of an AIE material has been described by Tang *et al.* as a material that is “non-luminescent in the

solution state but emissive in the aggregated state (as nanoparticle suspensions in poor solvents or as thin films in the solid state).<sup>61</sup> Tang *et al.* demonstrated the usefulness of AIE materials by utilizing silole **T** as the emissive layer in an effective and functioning OLED electroluminescent device.<sup>61</sup> The exciting and unexpected AIE phenomenon represented the start of a new class of emissive materials and prompted further investigation into the origins of such emissions.

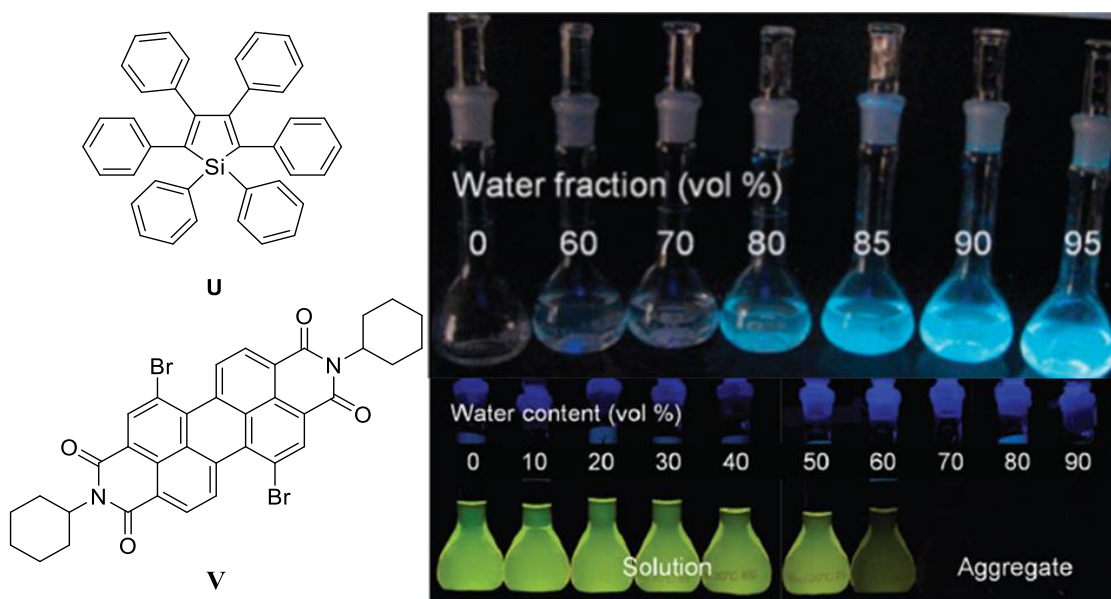


Figure 30: (Top) Hexaphenylsilole **U** is AIE active in acetonitrile/water volumetric mixtures.<sup>62</sup> (Bottom) N,N-Dicyclohexyl-3,4,9,10-perylenetetracarboxylic diimide **V** demonstrates ACQ in THF/water volumetric mixtures.<sup>63</sup>

The potential for AIE materials to overcome the obstacles that are typically encountered during solid state OLED device fabrication was immediately obvious. However, in the early 2000s, AIE materials were still in their infancy, and questions regarding how they functioned still remained unanswered. In a 2003 study by Tang *et al.*,



the mechanism of emission of these AIE silole materials was investigated.<sup>64</sup> The representative silole that was chosen for this investigation was hexaphenylsilole (HPS or **U**). As displayed in Figure 30, **U** was found to be AIE active and exhibited a vivid blue emission<sup>62</sup>, while the N,N-dicyclohexyl-3,4,9,10-perylenetetracarboxylic diimide **V** exhibited typical ACQ behavior.<sup>63</sup> A single crystal X-ray crystallographic study of **U** confirmed that the structure of **U** in the crystalline state adopted a twisted conformation.<sup>64</sup> This was important information for understanding the origins of the AIE for **U** because it confirmed that planarization did not occur upon aggregation of silole **U**. It was proposed that the dynamic intramolecular rotations of the six phenyl rotor substituents of silole **U** could be responsible for the quenching of the emissions in solution. It was hypothesized that, upon aggregation, the intramolecular rotations would be inhibited by the close steric interactions of the adjacent silole molecules. Accordingly, several experiments were performed in order to validate the theory that the restriction of the intramolecular rotations (RIR) was responsible for the AIE of the phenyl substituted silole materials.

As previously mentioned, aggregation in a poor solvent will cause silole **U** to exhibit AIE. However, Tang *et al.* proposed that solvent viscosity could produce similar results by inhibiting the intramolecular rotations.<sup>64</sup> For this purpose, a viscochromism study was performed on silole **U** using methanol/glycerol volumetric mixtures. Interestingly, the photoluminescent intensity increased with solvent viscosity, as displayed in Figure 31. The difference between the viscochromism study and a typical AIE experiment was evident in the volumetric fractions with < 50 % glycerol. In this region, the HPS silole **U** remained soluble yet emission linearly increased as the percentage of glycerol increased. This outcome was in contrast to the AIE experiment of acetone/water volumetric fractions, as displayed in Figure 31. In this latter experiment,

the emission was only observed upon aggregation in volumetric fractions with > 50 % water. Therefore, the emission detected in the visochromism experiment was proposed to originate from the partial restriction of the intramolecular rotations of the phenyl rotors of **U** by the viscous solvent media. Furthermore, at volumetric fractions of > 50 % glycerol, the intensity of the emission of **U** drastically increased based on typical AIE behavior.

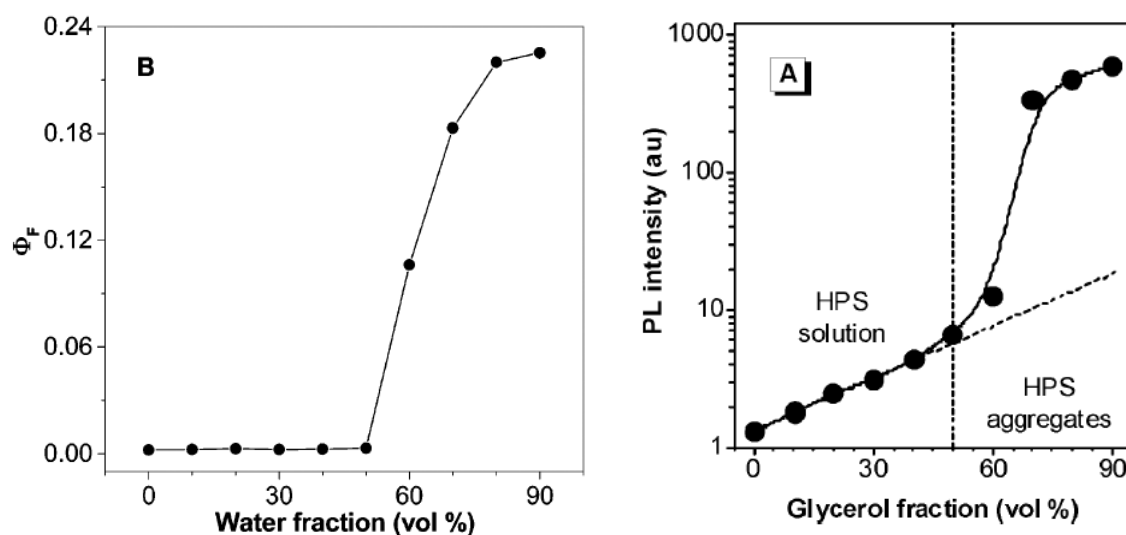


Figure 31: (Left) AIE experiment of HPS (**U**) with acetone/water volumetric fractions. (Right) Photoluminescent (PL) intensity of silole HPS **U** increased with increasing viscosity of methanol/glycerol volumetric mixtures.<sup>64</sup>

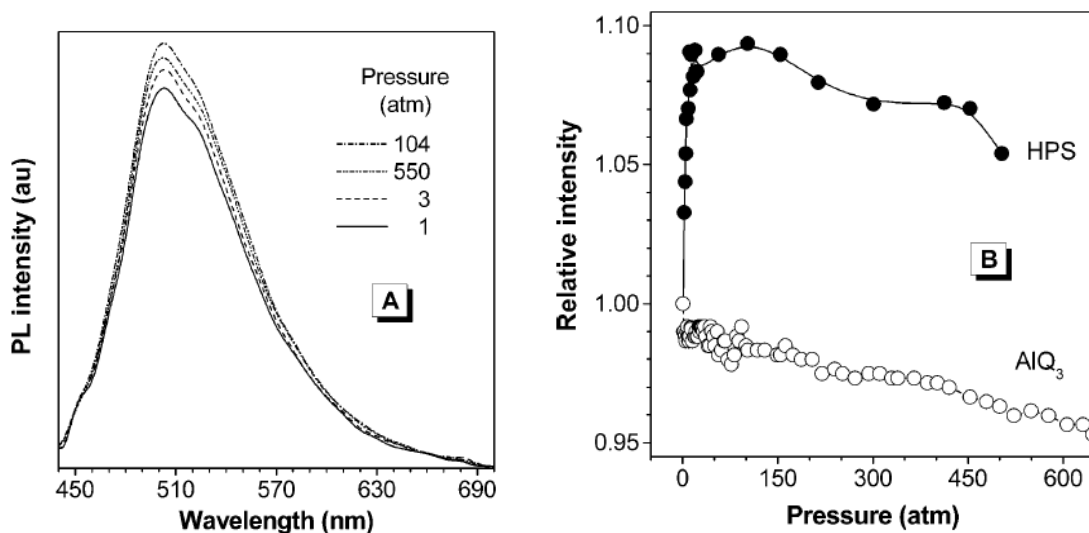


Figure 32: (Left) Piezochromism experiment of HPS (**U**) displaying increasing PL (photoluminescent) intensity with increasing applied pressure. (Right) Piezochromic behavior of the intensity of HPS and AlQ<sub>3</sub> with increasing applied pressure.<sup>65</sup>

In order to further verify the RIR mechanism for the AIE behavior of silole **U**, piezochromism experiments were explored by Tang *et al.*<sup>65</sup> In this study, the emission of silole **U** was measured under different applied pressures with the premise that an increase in pressure would further reduce the intramolecular rotations and increase the intensity of the emissions. The piezochromism study referred to above utilized the ubiquitous tris(8-hydroxyquinolato)aluminum (AlQ<sub>3</sub>) complex as a comparison with silole **U**. As displayed in Figure 32, the increase in pressure resulted in an increase in the emission intensity for silole **U**. This was based on the fact that, as pressure increased, the distance between the silole molecules decreased, thereby inhibiting the intramolecular rotations leading to enhanced emissions. However, as pressure further increased, the emission intensity of **U** began to drop. This drop in emission intensity was proposed to be caused by excimer formation.<sup>64</sup> As the pressure increased, there could conceivably be a drastic

shortening of the intermolecular distance between silole molecules, which could encourage excimer formation. This pressurized induced quenching is common in solid state luminescent materials.<sup>66,67</sup> As shown in Figure 32, the well-known AlQ<sub>3</sub> complex exhibited pressurized induced quenching with decreasing emission intensity as the applied pressure increased.

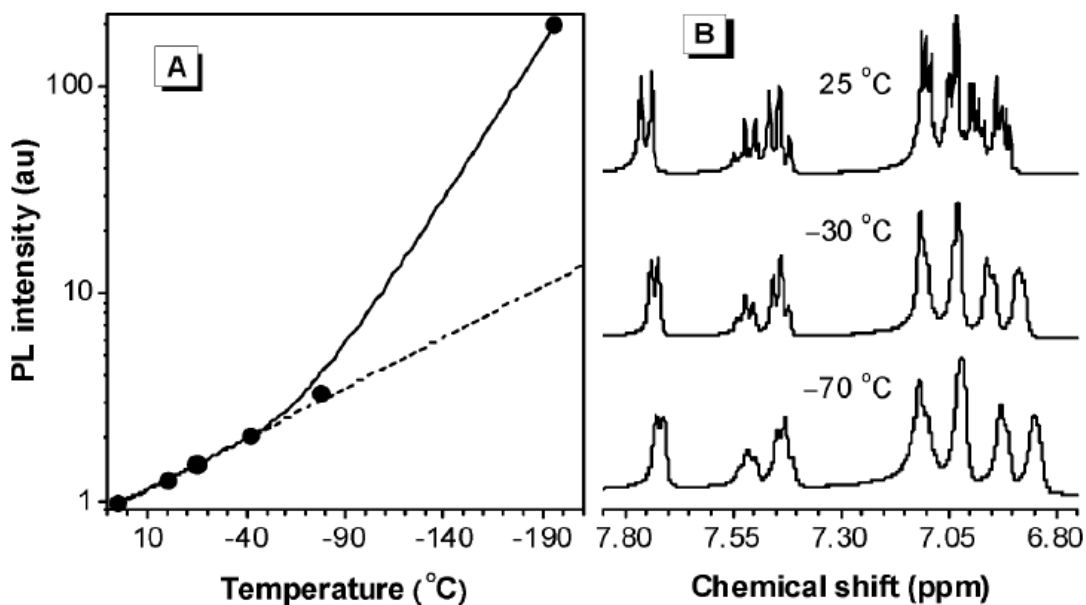


Figure 33: (Left) Thermochromism experiment of HPS (**U**) in THF solution displaying the increase of PL intensity with decreasing temperature. (Right) Dynamic <sup>1</sup>H NMR experiment displaying RIR with decreasing temperature in a deuterated dichloromethane solution of **U**.<sup>64</sup>

Thermochromism experiments were also employed to help strengthen the argument that RIR are responsible for the AIE behavior of silole **U**.<sup>64</sup> For this purpose, a THF solution of **U** was prepared by Tang *et al.* to measure the photoluminescent intensity of **U** vs. temperature. It was evident from Figure 33 that the emission of silole **U** increased with the decreasing temperature of the solution (but still above the melting

point of THF). However, below the melting point of THF, a solid glass was formed and the intensity drastically increased due to a typical AIE process. Regardless, this experiment confirmed the hypothesis that, with decreasing temperatures, the intramolecular rotations would be diminished and would result in an increased photoluminescent intensity. Furthermore, a dynamic  $^1\text{H}$  NMR experiment was performed in a deuterated dichloromethane solution on silole **U** to further confirm a decrease in the intramolecular rotations with decreasing temperature. At room temperature, the dynamic phenyl rotors of **U** were free to rotate and consequently gave a sharp NMR signal. However, upon cooling to  $-70\text{ }^\circ\text{C}$ , the NMR signals were broadened, thus indicating a restriction of the intramolecular rotations at low temperatures. Overall, Tang *et al.* pioneered and established a new category of emissive materials by their research with AIE compounds. Overall, the exploration of these materials is currently a rapidly growing field of research that has attracted the attention of many research groups and continues to grow to this day.<sup>62,63,68</sup>

### **2.1.3 Tuning of Solid State Emissions via Chemical Modifications, Polymorphism, and Solvatomorphism**

A distinct advantage that OLED technology has over traditional LED technology is the capacity for tuning of the emissive material.<sup>69,70</sup> LEDs consist of semiconductor materials that do not allow tunability of their emissive properties via solution based chemical modifications. On the other hand, the emissive layer in OLEDs are made up of small molecules that can be chemically modified to change their emissive properties. This type of modification of the solid state emissive materials is of special interest for the fabrication of new and versatile OLED devices.

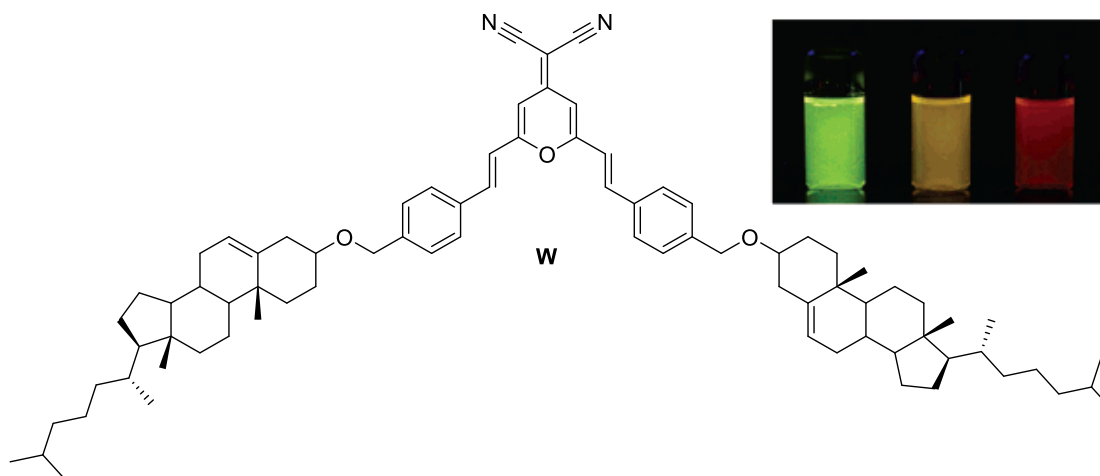


Figure 34: Butter-fly shaped cholesteryl substituted pyran compound **W** exhibiting green, yellow, and red emissions.<sup>71</sup>

As discussed in Section 2.1.2, AIE materials offer a new class of solid state emissive materials. However, the emissions typically observed for AIE materials were found in the blue and green regions of the visible spectrum.<sup>71</sup> Although color-tunable AIE materials are uncommon in the literature, there have recently been two published reports. The first report by Tang *et al.*, described an interesting color-tunable AIE material derived from a novel cholesteryl substituted pyran compound **W**, as displayed in Figure 34.<sup>71</sup> The emission of this “butterfly-shaped” pyran compound proved to be highly sensitive to the supermolecular assembly upon aggregation. This was demonstrated elegantly by an AIE experiment with THF/water volumetric mixtures. In THF solution **W** was found to be nonemissive; however, upon formation of the 60:40 THF/water volumetric mixture, compound **W** exhibited a green emission. Furthermore, formation of the 10:90 THF/water volumetric mixture resulted in a morphological change in the aggregated pyran derivative, yielding a yellow emission. Lastly, the 1:99 THF/water

volumetric mixture exhibited a red emission via a further change in the conformation of the aggregated compound **W**.

The different morphological phases were subsequently studied, and it was discovered that the green and yellow emissive fractions formed into crystalline nanoaggregates as confirmed by means of scanning electron microscopy (SEM), transmission electron microscopy (TEM), and electron diffraction. On the other hand, the red emissive fraction was confirmed to be amorphous via the same analytical techniques. The difference in structure was proposed to be due to the amount of water, which would influence how **W** formed in the aggregated state. It was proposed that the 99% water fraction would result in an immediate aggregation yielding an amorphous material.

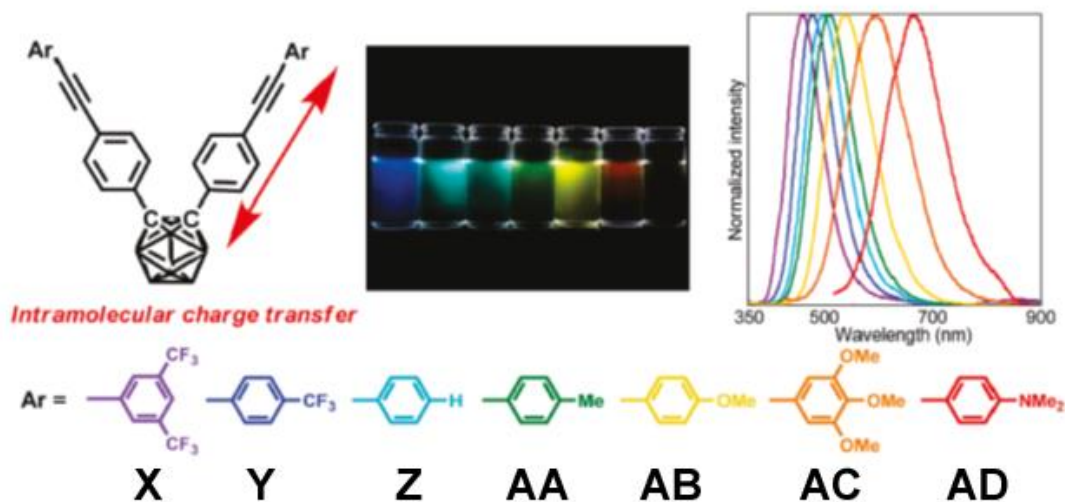


Figure 35: Multicolor tuning of the AIE active substituted diphenyl-*o*-carborane compounds.<sup>72</sup>

In a more recent study in 2011 by Kokado and Chujo, the multicolor tuning of the AIE active substituted diphenyl carborane was elegantly demonstrated.<sup>72</sup> This fascinating

study confirmed that chemical modifications of an emissive system can effectively tune the emission color. This systematic tunability spanned the range of electron withdrawing/electron donating groups from trifluoromethyl groups to methoxy and dimethylamino groups. Each of the seven compounds found in Figure 35 were nonemissive in solution. However, each compound was emissive in THF/water volumetric mixtures of 1:99 %, as displayed in Figure 35. This observation confirmed that the compounds **X-AD** were AIE active. Furthermore, a wide range of color tunability was achieved ranging from high energy blue emissions with a  $\lambda_{\text{max}} = 452$  nm to low energy red emissions with a  $\lambda_{\text{max}} = 662$  nm.

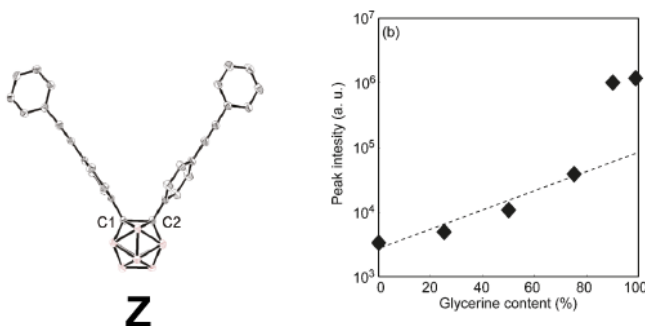


Figure 36: (Left) Crystal structure of compound **Z**. (Right) Viscochromism study of compound **Z** in methanol/glycerol volumetric mixtures<sup>72</sup>

Kokado and Chujo provided mechanistic insight into their AIE active compounds by means of viscochromism and thermochromism studies.<sup>72</sup> Volumetric ratios of methanol/glycerol were prepared in order confirm that compound **Z** emitted via a RIR mechanism that should be sensitive to solvent viscosity. Akin to the viscochromism study performed by Tang *et al.*,<sup>64</sup> Kokado and Chujo also observed a relationship between solvent viscosity and emission intensity, as displayed in Figure 36. The emission intensity of compound **Z** linearly increased with increasing solvent viscosity from 0-75 % glycerol



content. A drastic increase in emission intensity was observed in the volumetric fractions with more than 75 % glycerol, as expected for typical AIE behavior. This experiment helped to confirm the RIR mechanism of these AIE active materials.

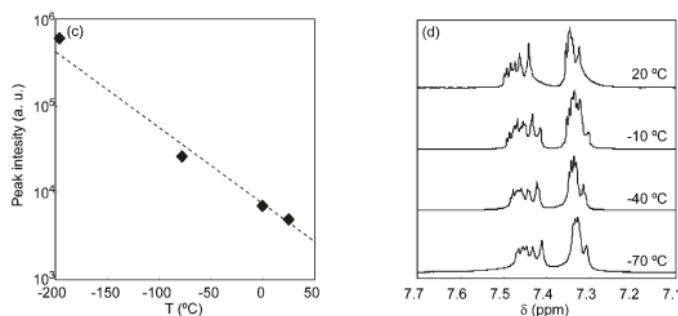


Figure 37: (Left) Thermochromism experiment of **Z** in 2-Me-THF solution. (Right) Dynamic <sup>1</sup>H NMR experiment of **Z** in deuterated dichloromethane solution.<sup>72</sup>

To further reinforce a RIR mechanism, a thermochromism study was performed by Kokado and Chujo. As displayed in Figure 37, there was a direct relationship between the temperature of the 2-Me-THF solution of **Z** with the emission intensity. There was a 6-fold increase in emission intensity between the room temperature data point and the -78 °C data point. This can be attributed to the RIR that was increasing the AIE effect leading to a more intense emission. The emission significantly increased upon formation of the 2-Me-THF glass below -136 °C, which is characteristic for AIE materials.<sup>64</sup> In order to achieve a more thorough understanding of the RIR mechanism, Kokado and Chujo performed a dynamic <sup>1</sup>H NMR experiment to directly probe the RIR of the diphenyl-*o*-carboranes. At room temperature, sharp resonances for the phenyl protons were attributed to dynamic rotations. However, upon cooling the deuterated dichloromethane solution of **Z**, there was a broadening of the peaks that is indicative of a restriction of the rotations of

the phenyl rotors. This dynamic  $^1\text{H}$  NMR experiment helped to validate the claim that compounds **X-AD** are AIE active via a RIR mechanism.

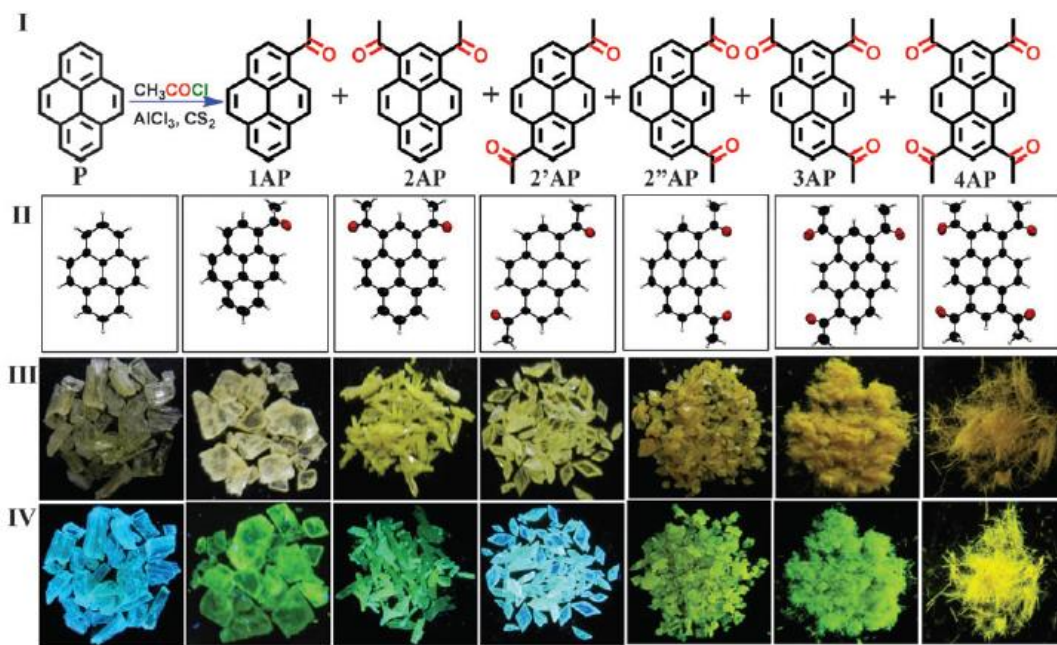


Figure 38: Multicolor tuning of pyrene luminophore via acylation.<sup>73</sup>

In a more recent report from 2014, Hariharan *et al.* described how the acylation of the pervasive pyrene compound could be an effective tool for the tuning of solid state pyrene based emissions.<sup>73</sup> Molecular crystal engineering is an effective way of modulating the solid state emissions of luminophores by chemical modifications. Chemical modifications can impact subtle changes in the crystal packing environments, which can slightly change the extent of orbital overlap between pyrene units and thus change the overall photophysical properties.<sup>74</sup> This type of molecular crystal engineering is vividly displayed in Figure 38, where the progressive acylation of pyrene resulted in different solid state photophysical properties.

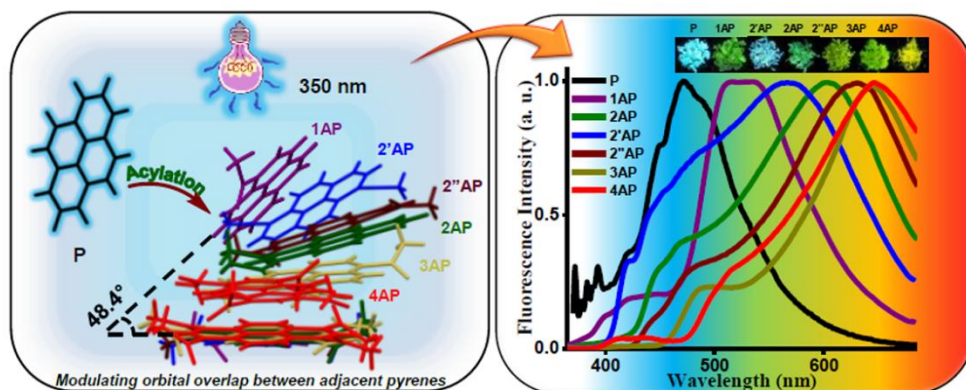


Figure 39: Progressive acylation lead to an increase in intermolecular orbital overlap between pyrene units and an overall red shift in the emission.<sup>73</sup>

Overall, the progressive acylation of the pyrene scaffold changed both the intermolecular interactions and the extent of orbital overlap between the adjacent pyrene units. This is effectively described in Figure 39, which displays the correlations between orbital overlap and acylation. As the number of acyl groups increased on the pyrene scaffold, the extent of orbital overlap increased thus leading to a red shift in the emission. The  $\lambda_{\text{max}}$  for pyrene and the tetra-acylated pyrene differed by 174 nm, which is a drastic red shift. Obviously, these types of chemical modifications can be quite effective for the tuning of solid state emissive materials.

In conjunction with color tunability via chemical modifications as described by the sophisticated studies of Tang *et al.*,<sup>64</sup> Kokado and Chujo,<sup>72</sup> and Hariharan *et al.*,<sup>73</sup> polymorphism can also be employed as a way to tune the color of emissive materials. By utilizing polymorphism, the crystal packing environments of solid state emissive materials can be modified thus changing the overall photophysical properties of the solid state material.

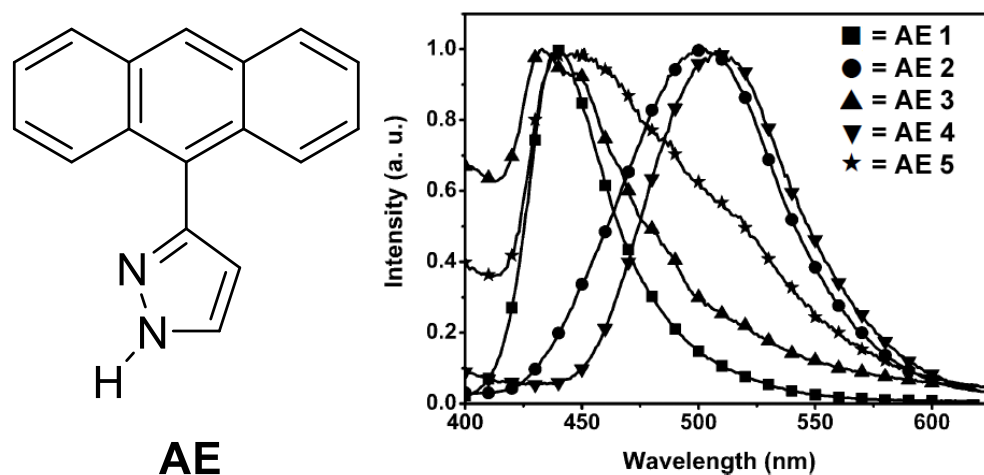


Figure 40: Emission spectra of the five polymorphs of compound **AE**.<sup>75</sup>

In 2006, Wang *et al.* published a study on the solid state emissive properties of several polymorphs of the 3(5)-(9-anthryl)pyrazole compound **AE** (Figure 40).<sup>75</sup> Polymorphs **AE1** and **AE2** were grown by means of vacuum sublimation at different temperatures. Polymorphs **AE3** and **AE4** were concomitant polymorphs that resulted from a slow vapor diffusion of diethyl ether into a chloroform solution of **AE**. Lastly, polymorph **AE5** was grown in a chloroform solution at 243 K. As displayed in Figure 41, the polymorphs emitted both blue and green light. Polymorphs **AE1** and **AE3** were found to emit blue light, while polymorphs **AE2** and **AE4** emitted green light. Polymorph **AE5** was determined to lie between the foregoing polymorphs with a blue-green emission.

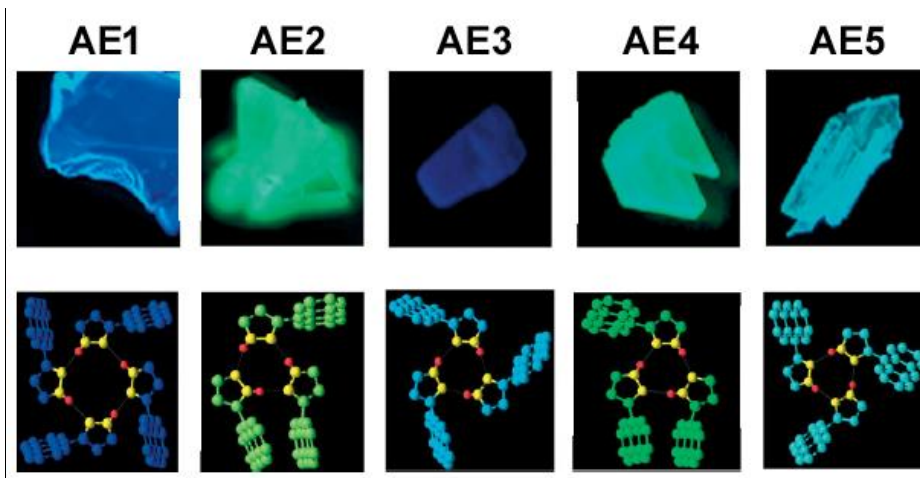


Figure 41: Packing interactions of the five polymorphs of compound **AE** with photographs of each crystal under UV irradiation.<sup>75</sup>

In order to determine the structure-property relationship between the crystal packing environments and the solid state emissive properties, a detailed single crystal X-ray diffraction study was performed by Wang *et al.*<sup>75</sup> Polymorph **AE1** was found to have a tetrameric paddlewheel formation featuring intermolecular hydrogen bonding between pyrole moieties. Polymorphs **AE2** and **AE4** featured a similar trimeric relationship that was held together by both intermolecular hydrogen bonding and intermolecular  $\pi$ - $\pi$  stacking between adjacent anthracene groups. Lastly, polymorph **AE5** packed in a trimeric paddlewheel formation that exhibited weaker intermolecular  $\pi$ - $\pi$  stacking between anthracene units in comparison with polymorphs **AE2** and **AE4**. Overall, the trend between the packing environment and the emissive properties can be understood on the basis of the intermolecular  $\pi$ - $\pi$  stacking between anthracene units. Polymorphs that did not feature intermolecular  $\pi$ - $\pi$  stacking emitted blue light, while the polymorphs that did feature intermolecular  $\pi$ - $\pi$  stacking had red shifted green emissions. Polymorph **AE5** was found to be a hybrid of these two packing environments with weak intermolecular  $\pi$ -

$\pi$  stacking interactions and thus was found to emit blue-green light. In summary, it was determined that face-to-face intermolecular  $\pi$ - $\pi$  stacking played an important role in the emissive properties resulting in more red shifted emissions with increasing intermolecular  $\pi$ - $\pi$  stacking interactions.<sup>76</sup>

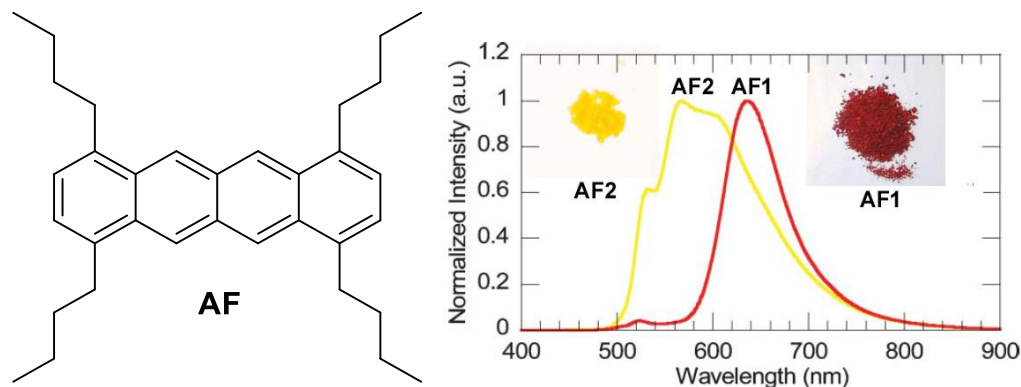


Figure 42: Solid state emissions from two polymorphs of 1,4,7,10-tetra(*n*-butyl)tetracene compound **AF**.<sup>77</sup>

A study by Kitamura *et al.* from 2007, was based on the tuning of the solid state emissions from two polymorphs of the 1,4,7,10-tetra(*n*-butyl)tetracene compound **AF**.<sup>77</sup> During the synthesis of this compound, the authors noted that two different colored products were formed during the work-up. This was dependent upon the solvent that was used during the rotary-evaporation procedure. Using chloroform for the rotary-evaporation procedure resulted in the formation of the mostly red polymorph **AF1**, the while utilization of *n*-hexane as the solvent in the rotary-evaporation procedure led to the formation of the yellow polymorph **AF2**. As displayed in Figure 42, polymorphs **AF1** and **AF2** were found to be emissive in the red and yellow regions, respectively.

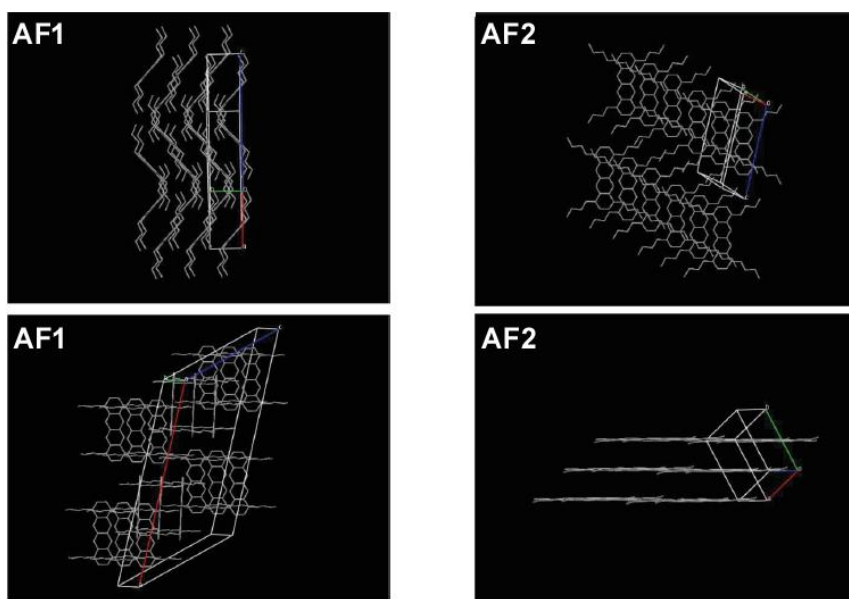


Figure 43: Packing environments of polymorphs **AF1** and **AF2** featuring herringbone and slipped-stacked arrangements, respectively.<sup>77</sup>

Analysis of each structure by means of X-ray crystallography, resulted in the isolation of the two different polymorph structures for **AF1** and **AF2**. The difference in packing arrangements between the two polymorphs was found to be significant. Polymorph **AF1** packed in a herringbone arrangement that was totally devoid of intermolecular  $\pi$ - $\pi$  stacking interactions. On the other hand, polymorph **AF2** was found to pack in a slipped-stacked arrangement that featured intermolecular  $\pi$ - $\pi$  stacking between tetracene units. Akin to that observed in the work of Wang *et al.*,<sup>75</sup> the extent of intermolecular  $\pi$ - $\pi$  stacking had a drastic effect on the solid state photophysical properties of polymorphs **AF1** and **AF2**. This difference is highlighted in Figure 43, which displays the packing environments of both polymorph structures.

In 2009, a subsequent study performed by Wang *et al.* was based on the solid state photophysical properties of N,N-di(*n*-butyl)quinacridone (**AG**).<sup>78</sup> The authors were

able to grow four different polymorph structures of **AG** by vacuum sublimation (**AG1**), slow evaporation of chloroform (**AG2**), slow vapor diffusion of diethyl ether into a chloroform solution of **AG** (**AG3**), and slow vapor diffusion of methanol into a chloroform solution of **AG** (**AG4**). Furthermore, two pseudopolymorphs or solvatomorphs of **AG** (**AG5** and **AG6**), which are polymorph structures that crystallize with different solvent molecules within the crystal lattice, were obtained. **AG5** was grown by slow evaporation of a chloroform/petroleum ether solution of **AG** and **AG6** was grown by slow vapor diffusion of petroleum ether into a chloroform solution of **AG**. Pseudopolymorphs **AG5** and **AG6** incorporated a water molecule and a chloroform molecule into their crystal lattices, respectively.

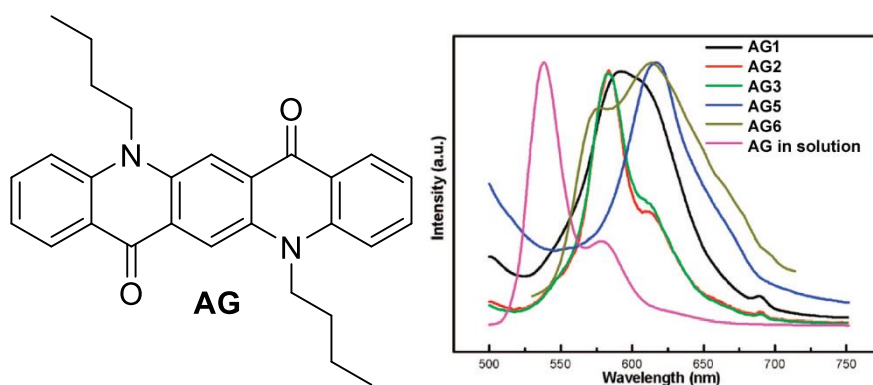


Figure 44: Emission spectra for the polymorph and pseudopolymorphs of **AG**. The solution based emission spectrum of **AG** was performed in a dilute chloroform solution.<sup>78</sup>



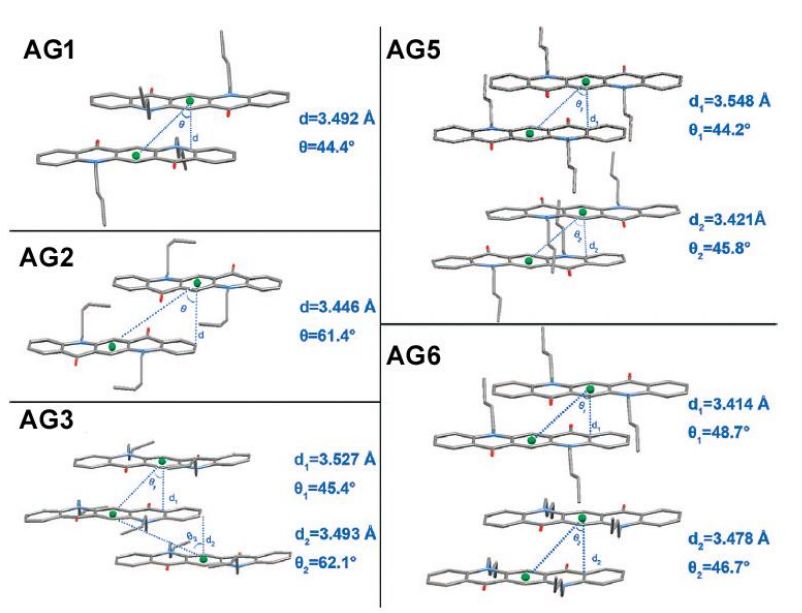


Figure 45: Stacking interactions of the polymorph and pseudopolymorph structures of **AG** with  $d$  = distance between quinacridone rings and  $\theta$  = angle between quinacridone centroids.<sup>78</sup>

As displayed in Figure 44, the emissive properties of each polymorph structure and **AG** in chloroform solution was investigated (Polymorph **AG4** was not able to be grown in sufficient quantities for a solid state photophysical study). As previously discussed, the difference in packing environments for each polymorph dictated the solid state photophysical properties. This was clearly demonstrated by Wang *et al.*, who performed an in depth analysis of the different  $\pi$ -stacking relationships between adjacent quinacridone units.<sup>78</sup> As displayed in Figure 45, the distance between quinacridone rings and the slip angle between quinacridone centroids was determined. For example, polymorphs **AG2** and **AG3** featured a larger slip angle between quinacridone centroids compared with those of the other three structures and consequently were found to have weaker  $\pi$ -stacking interactions and blue shifted emissions. Structures **AG1**, **AG5**, and

**AG6** were found to have stronger  $\pi$ -stacking interactions, and thus the emissions of the foregoing polymorphs and pseudopolymorphs were found to be red shifted.

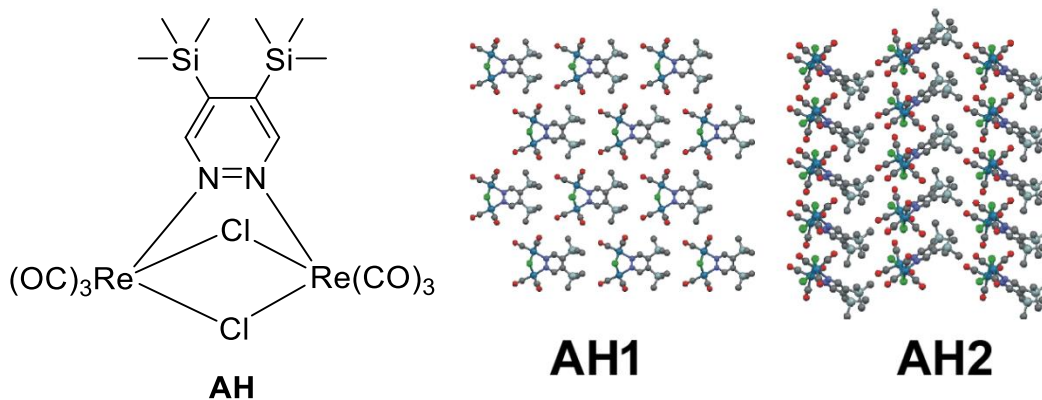


Figure 46: Crystal packing diagrams for polymorphs **AH1** and **AH2** for  $[\text{Re}_2(\mu\text{-Cl})_2(\text{CO})_6(\mu\text{-4,5}(\text{SiMe}_3)_2\text{-pyridazine})]$  complex **AH**.<sup>79</sup>

In a 2010 report by Panigati, Mercandelli, and De Cola *et al.*, the solid state photoluminescent behavior of two concomitant polymorphs of the  $[\text{Re}_2(\mu\text{-Cl})_2(\text{CO})_6(\mu\text{-4,5}(\text{SiMe}_3)_2\text{-pyridazine})]$  complex **AH** were investigated.<sup>79</sup> The concomitant polymorphs of **AH** were a yellow monoclinic polymorph **AH1** and an orange orthorhombic polymorph **AH2**. As displayed in Figure 46, no major difference was discernable in the crystal packing environments of either polymorph structure. Investigation of the solid state photophysical properties of polymorphs **AH1** and **AH2** revealed a significant red shift in the emission of **AH1** compared to **AH2**, with emission  $\lambda_{\text{max}}$  values of 534 nm and 570 nm, respectively. This red shift in emission was particularly interesting given that the crystal packing environments were very similar in nature. This study highlighted the importance of crystal packing on solid state emissive materials. This was evident from the fact that the difference between the crystal packing of polymorphs **AH1** and **AH2** was

miniscule, yet the emission changed from a green emission to a yellow-orange emission, respectively (Figure 47).

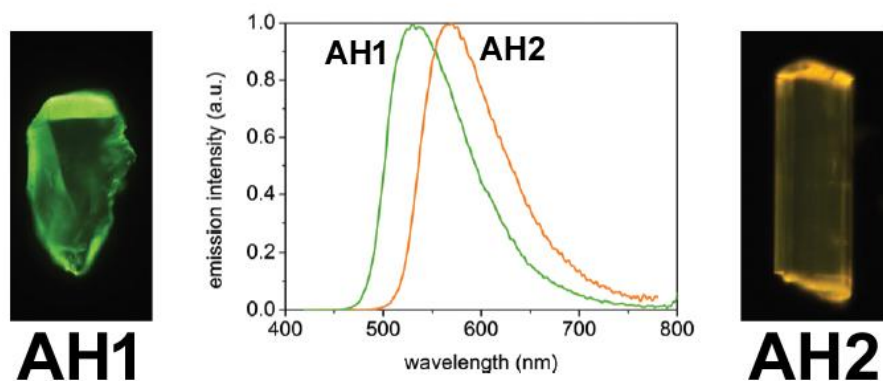


Figure 47: Emission spectra and photographs displaying the solid state emissions from polymorphs **AH1** and **AH2** for  $[\text{Re}_2(\mu\text{-Cl})_2(\text{CO})_6(\mu\text{-4,5}(\text{SiMe}_3)_2\text{-pyridazine})]$  complex **AH**.<sup>79</sup>

In 2012, Zou and Tian *et al.* published a paper on the different solid state photophysical properties of 9,10-Bis((E)-2(pyrid-2-yl)vinyl)anthracene (**AI**).<sup>80</sup> In contrast to those observed in the study by Panigati, Mercandelli, and De Cola *et al.*,<sup>79</sup> the crystal packing environments of polymorphs **AI1**, **AI2**, and **AI3** were all found to be very different (Figure 48). First, polymorph **AI1** was found to pack in a staircase fashion that did not involve any intermolecular  $\pi$ -stacking with a distance between anthracene rings of approximately 3.38 Å. Furthermore, polymorph **AI2** featured a slipped stacked staircase arrangement with weak intermolecular  $\pi$ -stacking with distances of approximately 3.65 Å. Lastly, the crystal packing environment of polymorph **AI3** was determined to be a face-to-face arrangement with strong intermolecular  $\pi$ -stacking interactions with distances of approximately 3.52 Å.

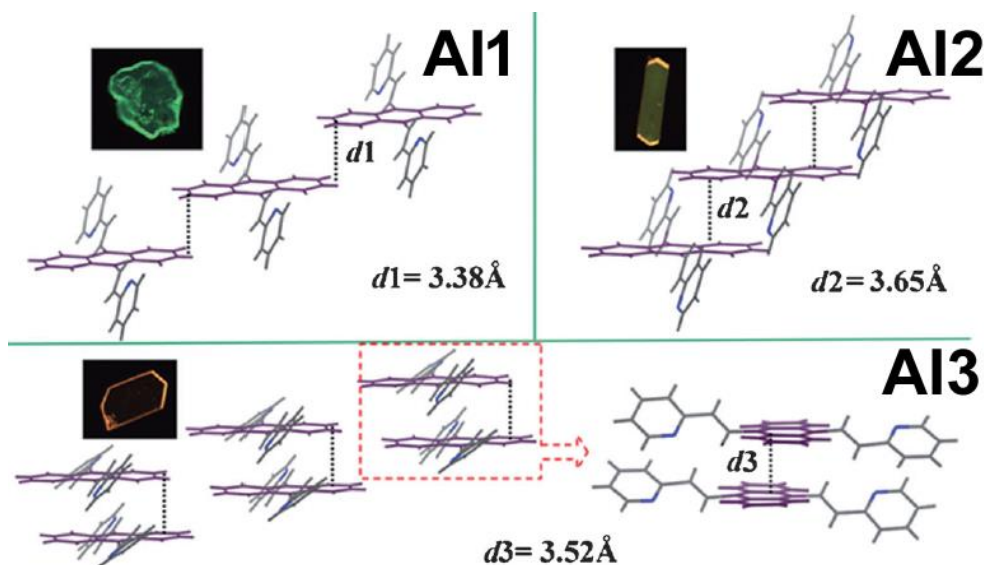


Figure 48: Various crystal packing diagrams for polymorphs **AI1**, **AI2**, and **AI3** for 9,10-Bis((E)-2(pyrid-2-yl)vinyl)anthracene (**AI**).<sup>80</sup>

The difference in crystal packing environments was clearly manifested in the solid state emissive properties of **AI1**, **AI2**, and **AI3**. As displayed in Figure 49, the emission displayed a drastic red shift of 91 nm between polymorphs **AI1** to **AI3**. The experimental fluorescence data for these complexes was in good agreement with the general trend that stronger intermolecular  $\pi$ -stacking interactions yields red shifted emissions. This certainly was true upon inspection of the emissive properties of **AI1**, **AI2**, and **AI3**, where polymorph **AI1** was found to be devoid of  $\pi$ -stacking interactions, polymorph **AI2** displayed weak  $\pi$ -stacking interactions, and polymorph **AI3** featured strong  $\pi$ -stacking interactions, resulting in progressive red shifted emissions of 527 nm, 579 nm, and 618 nm, respectively.

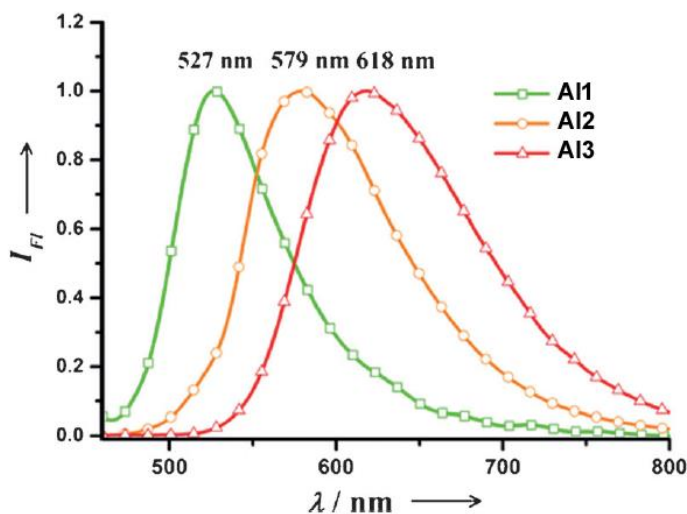


Figure 49: Progressive red shift in emission with respect to degree of  $\pi$ -stacking interactions for polymorphs **AI1**, **AI2**, and **AI3** for 9,10-Bis((E)-2-(pyrid-2-yl)vinyl)anthracene (**AI**).<sup>80</sup>

In a recent study from 2014 by Šket *et al.*, the emissions of two polymorphic structures of the  $\text{BF}_2$  complexes of 1-phenyl-3-(3,5-dimethoxyphenyl)-propane-1,3-dione (**AJ**) were investigated.<sup>81</sup> The polymorphs of **AJ** were concomitant polymorphs that formed during recrystallization of a DCM/hexanes mixtures of **AJ**. Polymorph **AJ1** was found to emit green-yellow light, while polymorph **AJ2** exhibited yellow emissions. A single crystal X-ray diffraction study revealed the difference in molecular structure between the two polymorphs. First, **AJ1** was found to have *meta*-methoxy groups pointing away from each other (*anti*), while polymorph **AJ2** featured *meta*-methoxy groups facing each other (*syn*), as displayed in Figure 50.

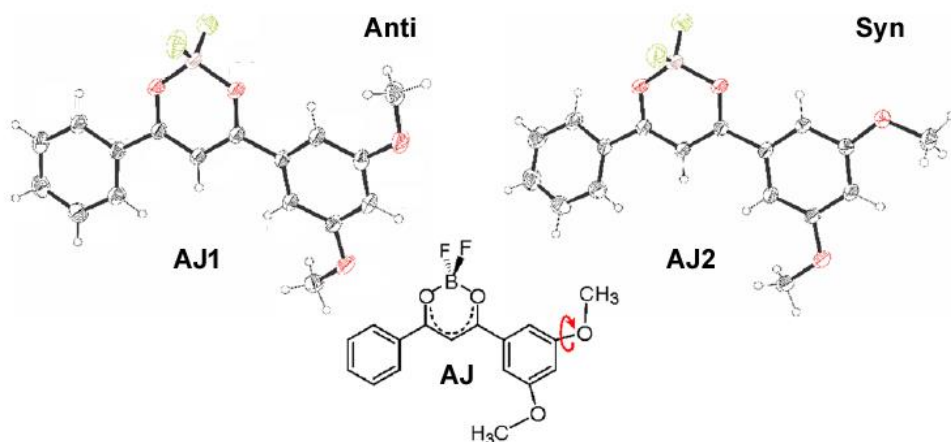


Figure 50: Polymorph structures **AJ1** and **AJ2** featuring *anti* and *syn* relationships between methoxy groups.<sup>81</sup>

This slight difference in orientation of the molecular structures resulted in two different crystal packing environments for polymorphs **AJ1** and **AJ2**. Polymorph **AJ1** featured several weak intermolecular  $\pi$ -stacking interactions in the range of 3.863-4.183 Å. Furthermore, these weak interactions were calculated to have low degree of ring overlap in the range of 6-13%. On the other hand, polymorph **AJ2** featured stronger intermolecular  $\pi$ -stacking interactions with stacking distances of 3.815-3.827 Å. Moreover, the packing of **AJ2** exhibited significant ring overlap in the range of 31-51%. Akin to previous reports, the major difference between the two polymorphs can be understood in terms of the degree of intermolecular  $\pi$ -stacking interactions. As the ring overlap increased, the stronger intermolecular  $\pi$ -stacking interactions gave rise to an overall red shift in the fluorescent emission of **AJ2** in comparison with **AJ1**.

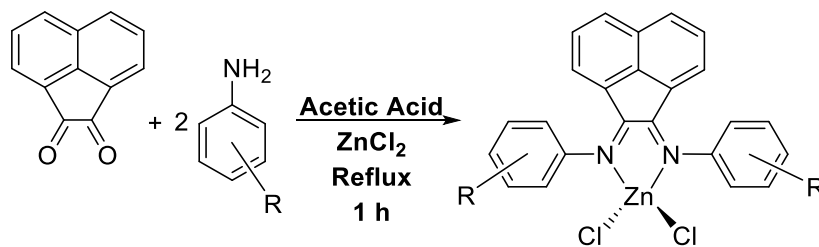
## 2.2 RESULTS AND DISCUSSION

In Section 2.2, a series of photoluminescent Ar-BIAN zinc(II) chloride complexes will be discussed. Initially, the flanking aryl substituents were confined to methylated

aryl groups with *ortho*-, *meta*-, and *para*-substituents in order to investigate steric effects while holding the electronic effects relatively constant. Furthermore, solvatomorphs were investigated as a way to tune the solid state photoluminescent properties of the Ar-BIAN zinc(II) chloride complexes. This particular study was aided by TD-DFT calculations performed by our collaborator Professor Ignacio Vargas-Baca at McMaster University. After concluding this study, tuning of the electronics of a series of *para*-substituted Ar-BIAN zinc(II) chloride complexes was investigated as a way to tune the color of emission via chemical modifications of the periphery of the Ar-BIAN ligand.

### 2.2.1 Photophysical Properties of Bis(imino)acenaphthene Zinc Chloride Complexes: Tuning via Methylation of the Flanking Aryl Substituents

As discussed in Section 2.1, the bis(imino)acenaphthene (BIAN) ligand framework has been used sparingly as a ligand support for photoluminescent complexes. However, it was discovered that Ar-BIAN zinc(II) chloride complexes exhibited interesting photoluminescent behavior. Consequently, a thorough investigation was launched in order to gain further insight into the origins of these emissions and to understand how tuning of the aryl substituents would affect the photophysical properties of the BIAN zinc complexes.<sup>82</sup>



R = 4-Me (10), 3,5-Me (11), 2,4,6-Me (12), 2-Me (13)

Scheme 39: Syntheses of methyl substituted Ar-BIAN zinc complexes.<sup>82</sup>

The syntheses of the methyl substituted Ar-BIAN zinc complexes were performed via facile condensation reactions of two equivalents of the appropriate methyl substituted aniline with acenaphthenequinone in the presence of zinc(II) chloride (Scheme 39).<sup>5</sup> The reaction mixture was refluxed in glacial acetic acid for one hour after which the BIAN zinc chloride complex formed as a precipitate. Typically, the BIAN zinc chloride complex is viewed as a valuable stepping stone along the pathway to synthesizing the more useful free BIAN ligand. However, it was discovered that the neglected BIAN zinc chloride complex displayed some very interesting and peculiar photoluminescent properties.

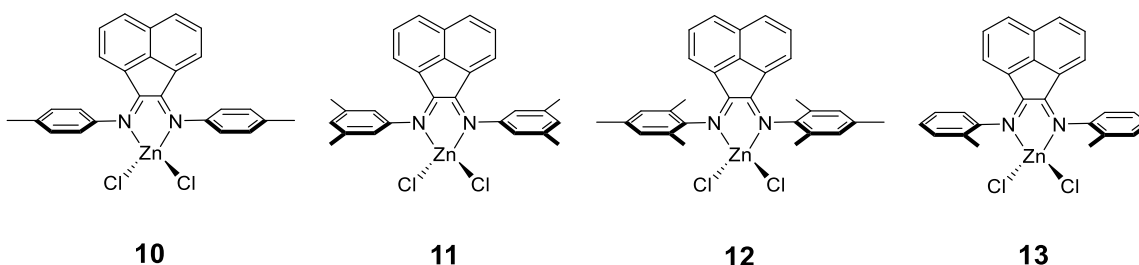


Figure 51: Methyl substituted Ar-BIAN zinc complexes **10-13**.<sup>82</sup>

As mentioned above, one advantageous feature of the BIAN ligand class is facile tunability of the stereoelectronic properties of the flanking aryl substituents. Initially, the investigation of the BIAN zinc chloride photoluminescent properties was confined to aryl groups bearing various methyl substituents namely, 4-methylphenyl (4-Me), 3,5-dimethylphenyl (3,5-Me), 2,4,6-trimethylphenyl (mes), and 2-methylphenyl (2-Me) substituents. These groups were selected in order to probe the photophysical properties of the system while keeping the electronics relatively constant between each BIAN



complex. Accordingly, the 4-Me (**10**), 3,5-Me (**11**), mes (**12**), and 2-Me (**13**) complexes were synthesized according to the methods described in the literature (Figure 51).<sup>5,14</sup>

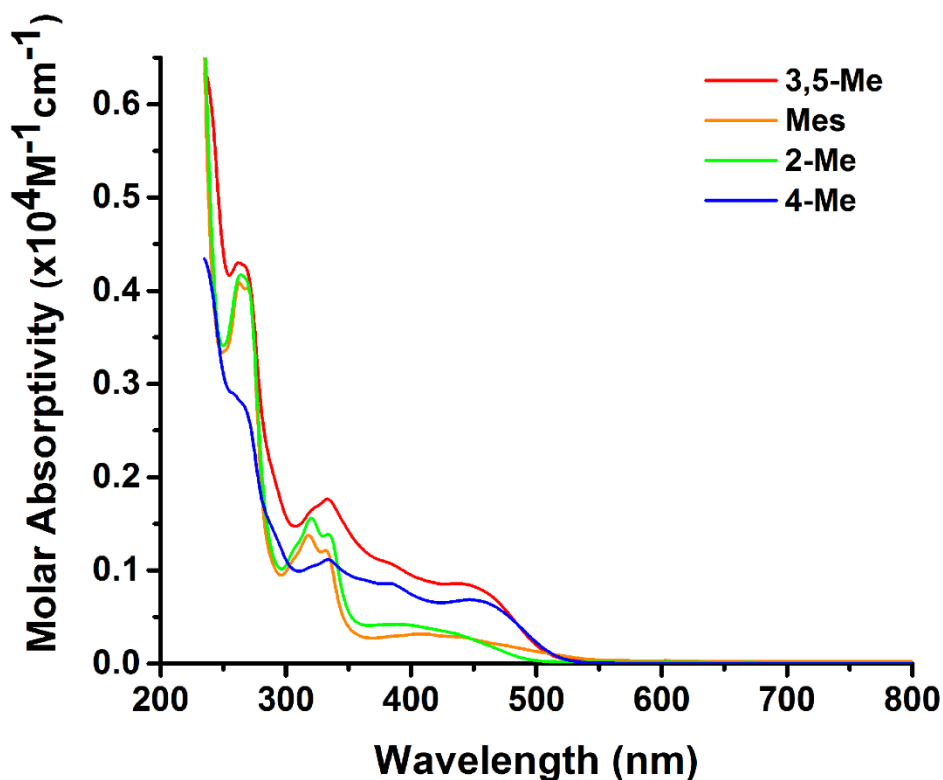


Figure 52: UV/vis absorption spectra for complexes **10-13** in DCM solution at room temperature.<sup>82</sup>

After complexes **10-13** were synthesized, the photophysical properties were subsequently investigated. First, a solution based UV/vis study was performed in DCM solution at room temperature. As displayed in Figure 52, complexes **10-13** featured very similar absorption bands. In accord with previous UV/vis studies on BIAN complexes, the high energy bands ( $> 350$  nm) were assigned to  $\pi$ - $\pi^*$  transitions that stem from both the flanking aryl groups and the acenaphthene backbone in accord with literature precedent.<sup>8,83,84</sup> Furthermore, the low energy bands were tentatively assigned to

intraligand charge transfers (<sup>1</sup>ILCT) between the flanking aryl substituents and the acenaphthene backbone. This assignment was based on a DFT study reported by Zysman-Colman and Hasan.<sup>85</sup> A summary of the UV/vis spectroscopic data for complexes **10-13** is displayed in Table 5.

Table 5: Summary of the UV/vis absorption data for complexes **10-13** in DCM solution at room temperature.<sup>82</sup>

Complex	$\lambda_{\max}$ (nm) ( $\epsilon \times 10^4 \text{ M}^{-1} \text{ cm}^{-1}$ )
10	447 (0.68), 334 (1.12), 259 (2.89)
11	437 (0.86), 333 (1.76), 262 (4.30)
12	408 (0.32), 332 (1.21), 318 (1.38) 263, (4.09)
13	387 (0.42), 334 (1.39), 321 (1.56), 264, (4.17)

Next, the focus was switched to probing the solid state diffuse reflectance properties of complexes **10-13**. The diffuse reflectance spectra for complexes **10-13** (Figure 53) displayed intense absorption bands between 450 and 550 nm. For complex **12**, there was an absorption shoulder at 520 nm. Interestingly, despite the similarities between complexes **10-13** observed in the solid state diffuse reflectance spectra, the emissive properties of all four complexes were found to be different. Specifically, the 4-Me (**10**) and 3,5-Me (**11**) substituted complexes were found to be emissive with  $\lambda_{\max}$  - values of 570 and 575 nm, respectively. The emissions of complexes **10** and **11** were identified as phosphorescent emissions based on their short microsecond lifetimes both at ambient temperature and at liquid nitrogen temperature (Table 5). Furthermore, complexes **10** and **11** exhibited relatively low absolute quantum yield values (Table 6). On the other hand, the mes (**12**) and 2-Me (**13**) substituted complexes were found to be

nonemissive in the solid state. Moreover, complexes **10-13** were found to be nonemissive in solution (Figure 53).

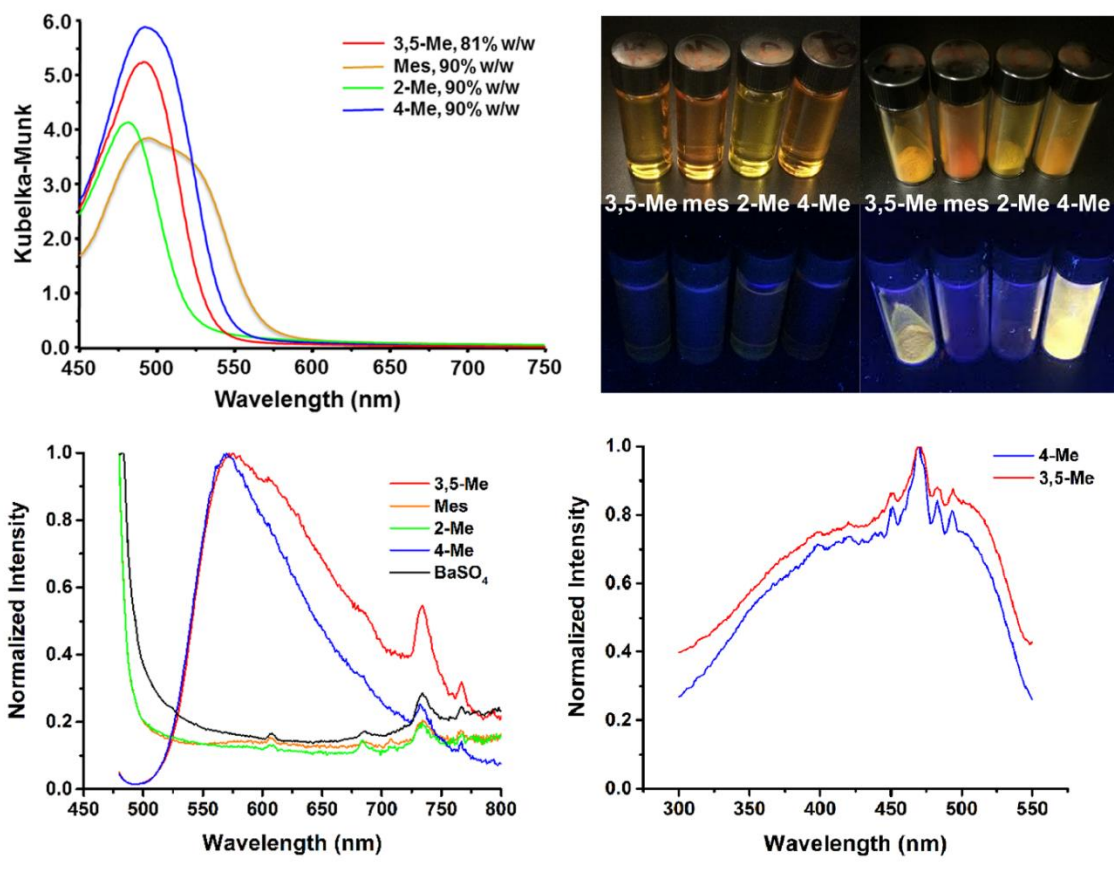


Figure 53: (Top) Solid state absorption spectra with optical images of complexes **10-13** in DCM solution and in the solid state under ambient light and UV irradiation. Solid state emission (Bottom-Left) and excitation (Bottom-Right) spectra for complexes **10-13**. BaSO<sub>4</sub> was used as a background scan material for the solid state emission scans.<sup>82</sup>

Table 6: Summary of the solid state photoluminescent data for complexes **10-13**.<sup>82</sup>

Complex	$\lambda_{em}$ (nm)	$\lambda_{ex}$ (nm)	$\tau$ ( $\mu s$ )	$\Phi$ (%) (Absolute)
1	570	470	$2.60 \pm 0.79$ (298 K) $3.99 \pm 1.26$ (77 K)	$1.69 \pm 0.06$
2	575	470	$6.21 \pm 0.70$ (298 K) $6.88 \pm 1.17$ (77K)	$1.01 \pm 0.13$

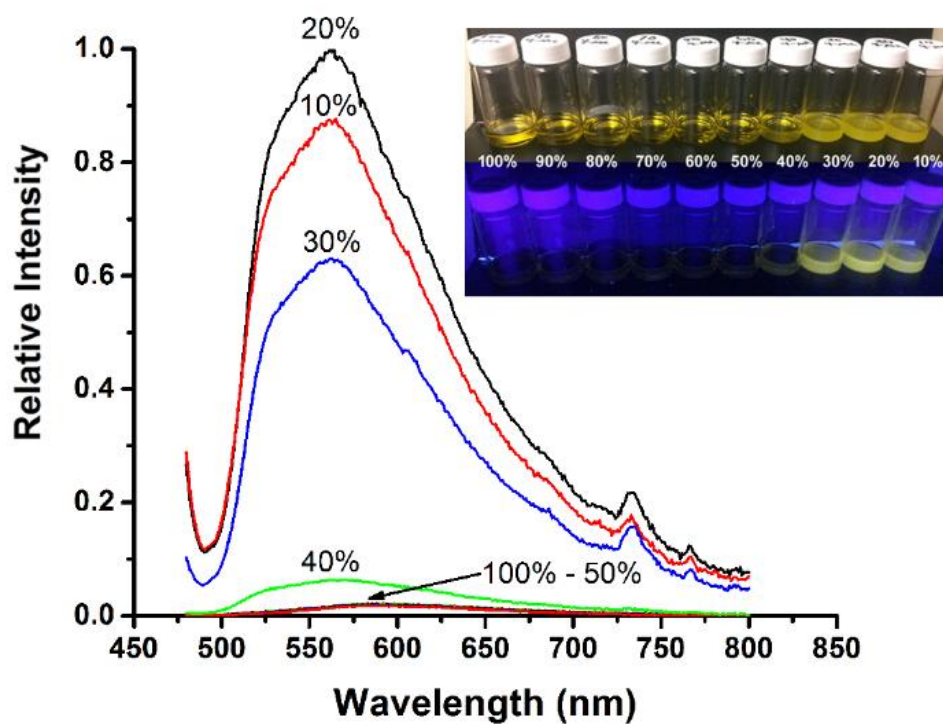


Figure 54: AIE experiment of **10** in DCM/hexanes volumetric mixtures along with photographs of each fraction under ambient light and UV irradiation (the percentage values above are relative to the DCM content).<sup>82</sup>

In order to gain further insight into the origins of the emissions of complexes **10** and **11**, aggregation-induced emission (AIE) experiments were performed. For this purpose, a  $\sim 10^{-4}$  M DCM stock solution of **10** was prepared and used to create

DCM/hexanes volumetric fractions. As exhibited in Figure 54, complex **10** was completely nonemissive in translucent DCM/hexanes volumetric mixtures up to the ratio of 50:50% DCM/hexanes. Upon formation of the 40:60% DCM/hexanes volumetric ratio, a faint emission was detected. The intensity of the emission drastically increased upon formation of the volumetric fractions in the range of 30-10% DCM. In these three volumetric fractions, complex **10** had aggregated and emission was evident from both the emission spectra and the photographs in Figure 54. An analogous AIE experiment was performed on complex **11** in a  $\sim 10^{-3}$  M THF stock solution. By using THF/hexanes volumetric fractions, a similar AIE behavior was detected for complex **11**, albeit with less intense emissions in the 20 and 10 % DCM fractions (Figure 55).

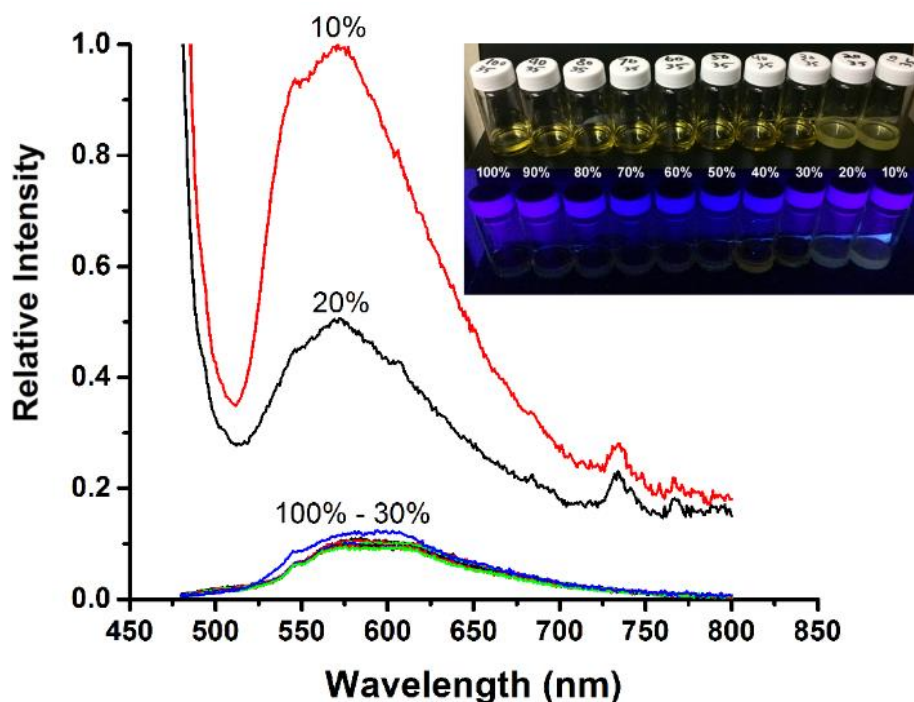


Figure 55: AIE experiment of **11** in THF/hexanes volumetric mixtures along with photographs of each fraction under ambient light and UV irradiation (the percentage values above are relative to the THF content).<sup>82</sup>

Although complexes **10** and **11** were found to be AIE active, the previous experiments did not answer the question as to why complexes **12** and **13** were nonemissive in both solution and the solid state. In order to gain further insight into the origins of the foregoing emissions, the structures of complexes **10-13** were investigated in a single crystal X-ray crystallography study. Surprisingly, single crystals of complexes **10-12** were able to be harvested directly from the precipitate that had formed during the condensation reaction. This was useful because it provided insight into the structures of the “as-synthesized” complexes. Unfortunately, this approach was not feasible for complex **13**; therefore, a suitable single crystal of complex **13** was grown by slow evaporation of a DCM solution.

Inspection of the four crystal structures of complexes **10-13** presented in Figure 56 revealed a clear structural distinction between the emissive complexes **10** and **11** vs. the nonemissive complexes **12** and **13**. The emissive complexes **10** and **11** were found to have average acenaphthene-aryl interplanar torsion angles of  $58.76^\circ$  and  $69.77^\circ$ , respectively. On the other hand, the nonemissive complexes **12** and **13** exhibited average acenaphthene-aryl interplanar torsion angles of  $80.47^\circ$  and  $81.79^\circ$ , respectively. Overall, the emissive complexes have torsion angles between the flanking aryl substituents and the acenaphthene backbone that are more acute compared to the torsion angles of the nonemissive complexes. The foregoing differences are most likely due to the presence of methyl groups on the 2- and/or 6-positions of the flanking aryl substituents of complexes **12** and **13**, which are absent in complexes **10** and **11**. The presence of these *ortho*-methyl groups restrict the intramolecular rotations of the aryl rings. Overall, the restricted intramolecular rotations orient the flanking aryl rings in a nearly orthogonal manner with respect to the acenaphthene backbone. This is not observed when the methyl groups are

located in the *para*- or *meta*-positions. During the intramolecular rotations, these methyl groups do not encounter the same steric repulsion that the *ortho*-methyl groups have with respect to the acenaphthene backbone.

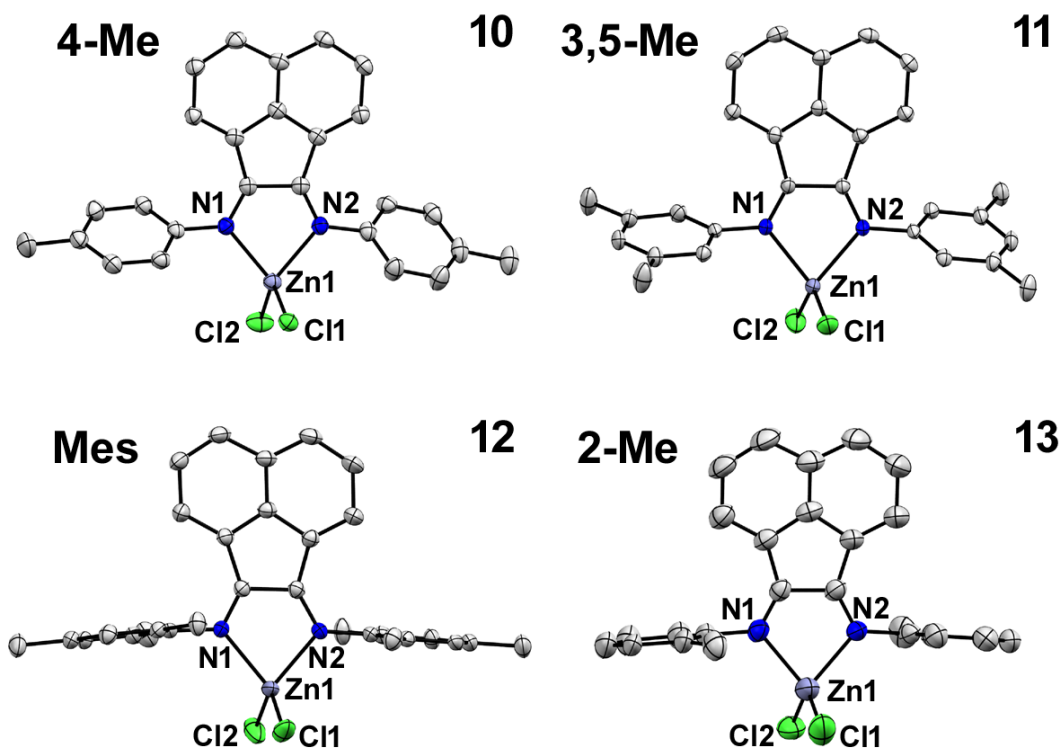


Figure 56: POV-Ray diagrams for complexes **10-13** with thermal ellipsoids displayed at 50% probability. All hydrogen atoms have been removed for clarity. Note however, that complex **11** crystallized with two molecules in the asymmetric unit. One of these molecules has been removed for clarity. All four complexes crystallized without any solvent in the crystal lattice.<sup>82</sup>

The difference in molecular structure had a drastic impact on the crystal packing environments of **10-13** (Figure 57). The crystal packing environments were separated into two distinct classes. First, the emissive complexes **10** and **11** are densely packed and

feature parallel displaced, head-to-tail  $\pi$ -stacking dimers. Complex **10** exhibited an extended array of  $\pi$ -stacking dimeric columns arranged in a slipped stacked staircase formation. This formation was based on  $\pi$ -stacking from two adjacent naphthalene rings in addition to a close contact interaction between a chloride ligand and both carbons of the N-C-C-N fragment. Complex **11** also featured parallel slipped  $\pi$ -stacking dimers, which are flanked on either side by two other BIAN complexes. However, complex **11** did not feature an extended staircase formation of  $\pi$ -stacking dimers akin to that of complex **10**. These types of face-to-face  $\pi$ -stacking interactions are known to be conducive to excimer formation.<sup>75</sup>

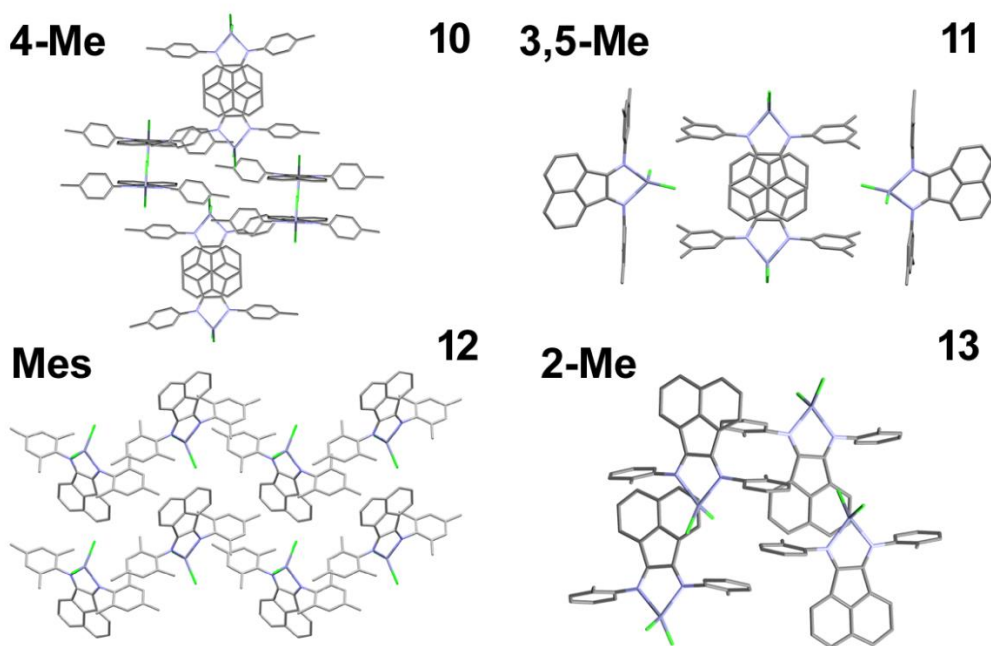


Figure 57: Crystal packing diagrams for complexes **10-13**.<sup>82</sup>

On the other hand, complexes **12** and **13** were found to pack in a less dense fashion and do not feature any intermolecular  $\pi$ -stacking interactions. As discussed



above, the presence of *ortho*-methyl groups oriented complexes **12** and **13** in a nearly orthogonal manner. This orthogonal orientation, in conjunction with the steric repulsion of the *ortho*-methyl groups, resulted in an absence of intermolecular  $\pi$ -stacking interactions within the crystal lattice. As a result, complexes **12** and **13** packed in a less dense herringbone arrangement. The absence of intermolecular  $\pi$ -stacking interactions could be responsible for the nonemissive behavior of complexes **12** and **13**.

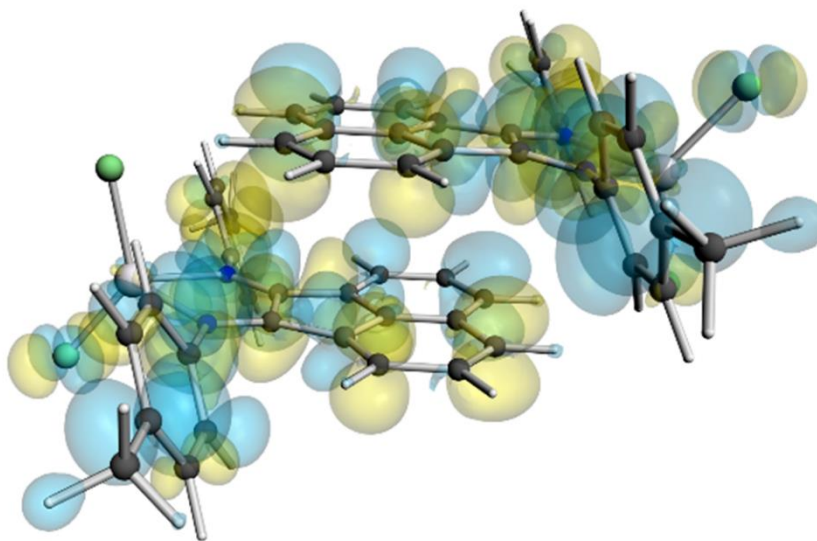


Figure 58: Transition density of the radiative decay from the  $T_1 \rightarrow S_0$  transition for complex **10**.<sup>82</sup>

In an effort to gain further insight into the emissive behavior of the BIAN zinc chloride complexes, TD-DFT calculations were performed by our collaborator Professor Ignacio Vargas-Baca of McMaster University.<sup>82</sup> Using TD-DFT, it was possible to confirm the viability of intermolecular electron excitations between a  $\pi$ -stacked dimer of complex **10**, as displayed in Figure 58. Furthermore, the radiative decay from the  $T_1 \rightarrow S_0$

transition was visualized by plotting the transition density. According to the results from the TD-DFT study, small perturbations of the crystal packing environments could change the degree of intermolecular  $\pi$ -stacking interactions and thus change the overall emission color. Accordingly, solvatomorphism was investigated as a method for tuning the emissions of the methylated Ar-BIAN zinc complexes.

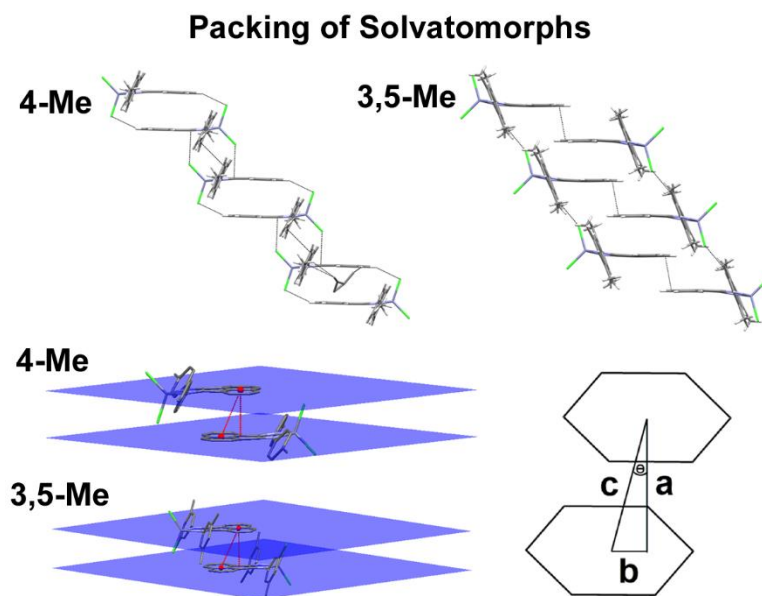


Figure 59: Stacking interactions of solvatomorphs for complexes **10** and **11** (Top). Slipped stacked  $\pi$ - $\pi$  interactions (Bottom): a = interplanar distance, b = slip distance of naphthalene centroids, c = distance between naphthalene centroids,  $\theta$  = slip angle between naphthalene centroids.<sup>82</sup>

For emissive complexes **10** and **11**, four solvatomorphs of each complex were grown using different solvents during recrystallization. These complexes featured the same general packing environments. However, each solvatomorph incorporated different solvent molecules into the crystal lattice. Crystals were obtained with  $\text{CHCl}_3$ , THF, DCM, and MeCN solvent molecules in the crystal lattice to form solvatomorphs **10-**

**CHCl<sub>3</sub>, 10-THF, 10-DCM, 10-MeCN, 11-CHCl<sub>3</sub>, 11-THF, 11-DCM, and 11-MeCN.** As displayed in Figure 59, the packing environments of solvatomorphs **10-CHCl<sub>3</sub>, 10-THF, 10-DCM, and 10-MeCN** were akin to that described for the non-solvated lattice of complex **10**. However, solvatomorphs **11-CHCl<sub>3</sub>, 11-THF, 11-DCM, and 11-MeCN** were found to exhibit parallel slipped  $\pi$ - $\pi$  stacking staircase formations, unlike that of the non-solvated complex **11**. These staircase formations formed as a result of both the  $\pi$ - $\pi$  contacts between the naphthalene units and the Cl-H contacts of the flanking aryl groups.

Table 7: Calculated crystallographic metrical parameters between the  $\pi$ -stacked dimers of the ten emissive complexes **10-11-MeCN**.<sup>82</sup>

Complex	a (Å)	b (Å)	c (Å)	$\theta$ (°)
10	3.504 Å	1.439 Å	3.788 Å	22.33 °
10-CHCl <sub>3</sub>	3.418 Å	1.266 Å	3.645 Å	20.33 °
10-THF	3.421 Å	1.415 Å	3.702 Å	22.47 °
10-DCM	3.569 Å	1.604 Å	3.787 Å	19.54 °
10-MeCN	3.549 Å	1.400 Å	3.815 Å	21.52 °
11	3.725 Å	1.763 Å	4.121 Å	25.32 °
11-CHCl <sub>3</sub>	3.431 Å	1.300 Å	3.668 Å	20.71 °
11-THF	3.404 Å	1.246 Å	3.625 Å	20.10 °
11-DCM	3.400 Å	1.328 Å	3.650 Å	21.33 °
11-MeCN	3.450 Å	1.228 Å	3.662 Å	19.59 °

As displayed in Figure 59, the extent of  $\pi$ -stacking can be understood by measurement of four specific metrical parameters: interplanar distance (a), slip distance

of naphthalene centroids (b), distance between naphthalene centroids (c), and slip angle between naphthalene centroids ( $\theta$ ). These crystallographic metrical parameters for all ten emissive solvatomorphs are summarized in Table 7. Each of the 10 solvatomorphs exhibited a slightly different crystal packing environment. A subsequent fluorescence spectroscopy experiment was performed in order to determine if slightly different crystal packing environments would result in different photoluminescent emissions.

As exhibited in Figure 60, each solvatomorph was shown to be emissive. Interestingly, in the case of the solvatomorphs of complex **10**, solvatomorph **10-CHCl<sub>3</sub>** was found to be unique. This solvatomorph exhibited a  $\lambda_{\text{max}}$  emission of 590 nm, while the other three solvatomorphs of complex **10** displayed  $\lambda_{\text{max}}$  values of 567-569 nm. This significant red shift in emission was presumably due to an increase in  $\pi$ - $\pi$  orbital overlap of solvatomorph **10-CHCl<sub>3</sub>** in comparison with the other solvatomorphs of complex **10**. Solvatomorph **10-CHCl<sub>3</sub>** exhibited shorter distances between the naphthalene rings and a smaller slip angle between naphthalene centroids. As previously discussed in numerous literature examples, there is a direct correlation between a red shift in emission and an increase in  $\pi$ - $\pi$  orbital overlap between adjacent  $\pi$ -stacking units. The solvatomorphs of complex **11** exhibited less significant shifts in photoluminescent emission. In this case, the **11-CHCl<sub>3</sub>** and **11-MeCN** solvatomorphs were found to be red shifted by approximately 10 nm with respect to the **11-THF** and **11-DCM** solvatomorphs. A summary of the photophysical data for all the solvatomorphs can be found in Figure 60, Figure 61, and Table 8.

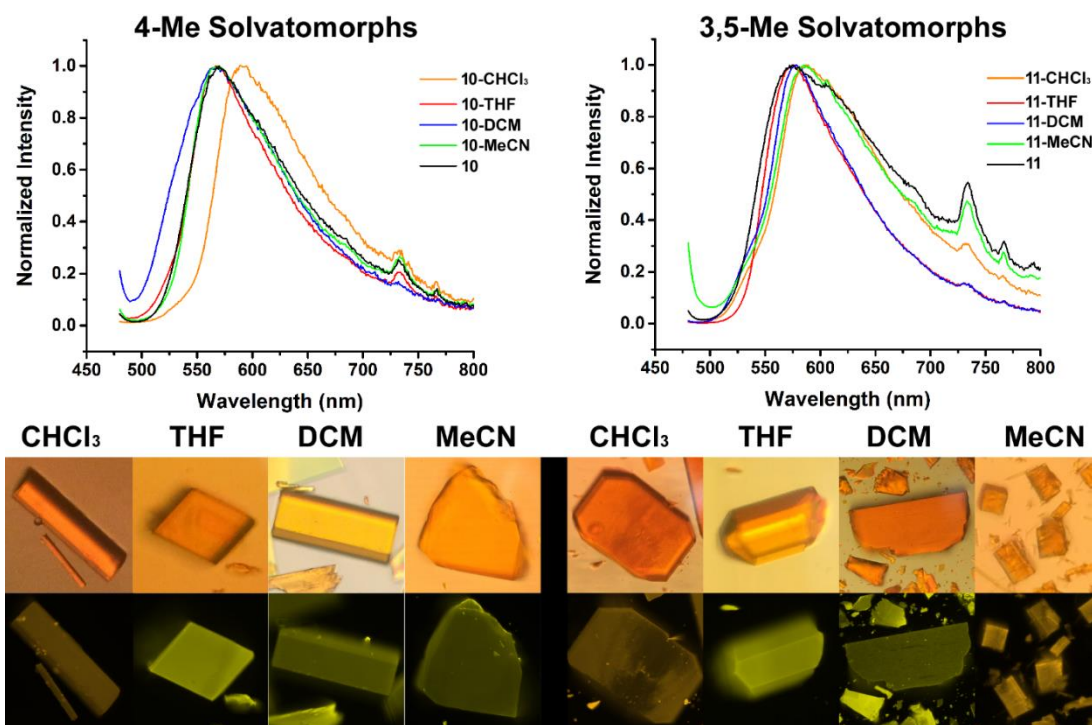


Figure 60: (Top) Emission spectra, optical images (Middle), and fluorescent images (Bottom) for solvatomorphs **10-11-MeCN**.<sup>82</sup>

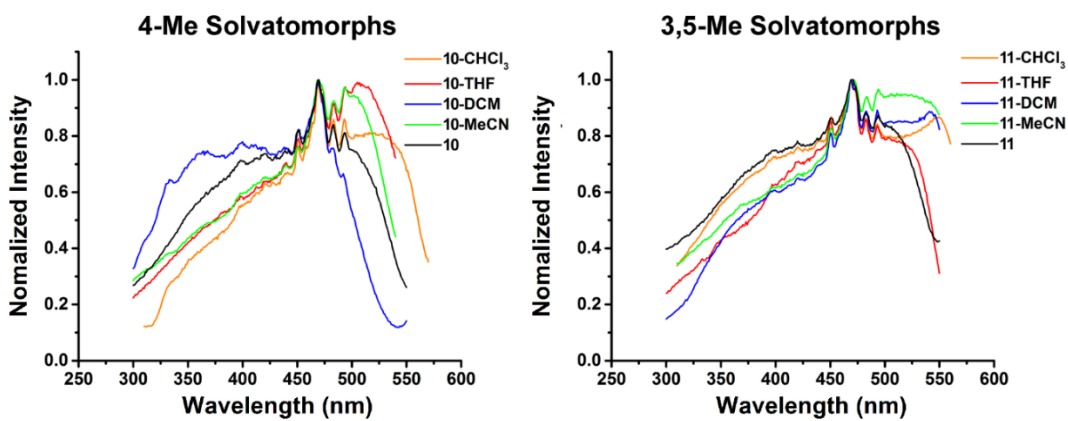


Figure 61: Excitation spectra for all ten emissive complexes **10-11-MeCN**.<sup>82</sup>

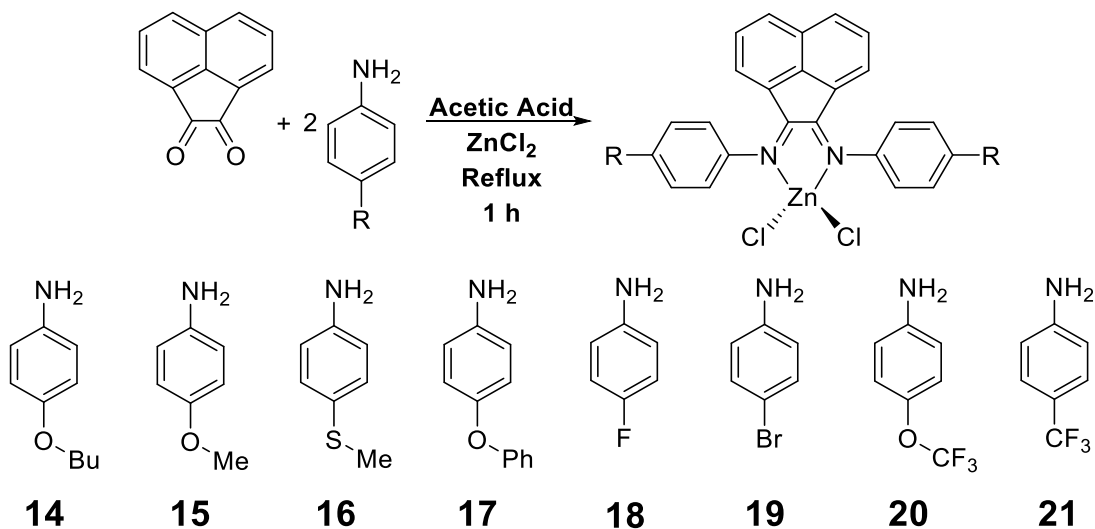
Table 8: Solid state photoluminescent data for the eight solvatomorphs **10-CHCl<sub>3</sub>-11-MeCN**.<sup>82</sup> \*The relative quantum yield values were calculated based on the ratio of the emission intensities. The intensity of the emission peak for each solvatomorph was integrated and compared with that of the non-solvated complex for which the absolute quantum yield had been measured directly.

Solvatomorph	$\lambda_{em}$ (nm)	$\lambda_{ex}$ (nm)	$\tau$ ( $\mu$ s)	$\Phi$ (%) (Relative)*
1-CHCl <sub>3</sub>	590	470	4.59 $\pm$ 1.12	3.78 $\pm$ 0.13
1-THF	567	470	2.97 $\pm$ 0.96	1.52 $\pm$ 0.14
1-DCM	569	470	6.23 $\pm$ 1.17	0.35 $\pm$ 0.01
1-MeCN	569	470	2.86 $\pm$ 0.57	0.63 $\pm$ 0.02
2-CHCl <sub>3</sub>	587	470	4.94 $\pm$ 0.09	1.03 $\pm$ 0.13
2-THF	576	470	4.51 $\pm$ 0.75	2.59 $\pm$ 0.32
2-DCM	578	470	4.54 $\pm$ 1.02	2.42 $\pm$ 0.30
2-MeCN	585	470	6.41 $\pm$ 1.33	0.84 $\pm$ 0.10

### 2.2.2 Photophysical Properties of Bis(imino)acenaphthene Zinc Chloride Complexes: Tuning via Modification of the Electronics of the *para*-Substituted Flanking Aryl Substituents

In Section 2.2.1, the methylated Ar-BIAN zinc(II) chloride complexes were investigated in order to determine the origins of their emissions while holding the electronic effects of the system relatively constant. After this study was accomplished, focus was shifted to probing the electronic effects of *para*-substituted aryl substituents. The substituents that were investigated in this particular study were the 4-butoxy (4-OBu, **14**), 4-methoxy (4-OMe, **15**), 4-methylthio (4-SMe, **16**), 4-phenoxy (4-OPh, **17**), 4-fluoro (4-F, **18**), 4-bromo (4-Br, **19**), 4-trifluoromethoxy (4-OCF<sub>3</sub>, **20**), and 4-trifluoromethyl (4-

CF<sub>3</sub>, **21**) substituents. As displayed in Scheme 40, the BIAN zinc complexes **14-21** were synthesized in an analogous manner to that described in the literature.<sup>5</sup>



Scheme 40: Syntheses of *para*-substituted Ar-BIAN zinc chloride complexes **14-21**.

First, the absorption properties of complexes **14-21** were examined by means of UV/vis spectroscopy in DCM solution at room temperature. As displayed in Figure 62, each complex exhibited a similarly structured absorption spectrum. As previously discussed in Section 2.2.1, the low energy bands are attributed to  $\pi$ - $\pi^*$  transitions that emanate from both the flanking aryl groups and the acenaphthene backbone, in accord with literature reports.<sup>8,83,84</sup> Also, the low energy bands were tentatively assigned to intraligand charge transfers (<sup>1</sup>ILCT) between the flanking aryl substituents and the acenaphthene backbone in agreement with the DFT study performed by Zysman-Colman and Hasan.<sup>85</sup> A summary of the solution based UV/vis spectroscopic data for complexes **14-21** is displayed in Table 9.

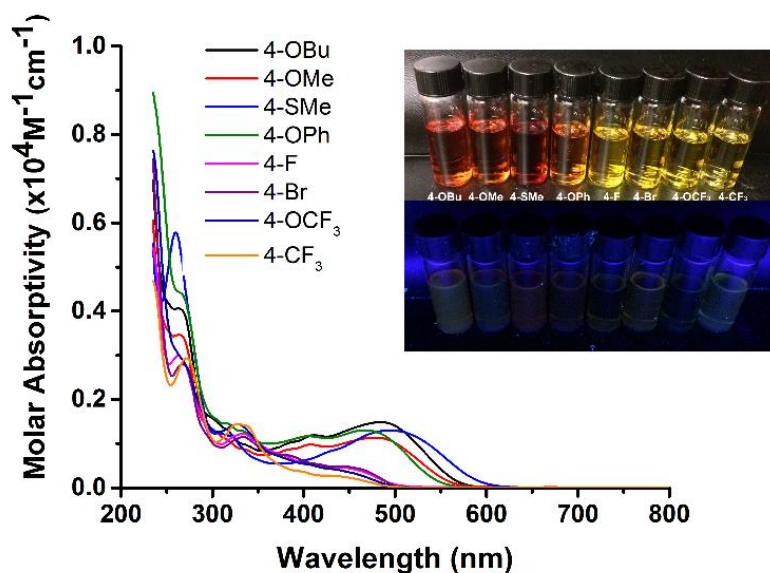


Figure 62: UV/vis spectra of Ar-BIAN zinc chloride complexes **14-21** in DCM solution at room temperature with photographs of each complex in DCM solution under ambient light and UV irradiation.

Table 9: Summary of the UV/vis absorption data for complexes **14-21** in DCM solution at room temperature.

Complex	$\lambda_{\max}$ (nm) ( $\epsilon \times 10^4 \text{ M}^{-1} \text{ cm}^{-1}$ )
14	484 (1.49), 411 (1.19) 298sh (1.60), 262 (4.06)
15	478 (1.14), 408 (0.98), 315sh, (1.10) 264 (3.46)
16	495 (1.30), 307 (1.24), 260 (5.78)
17	467 (1.30), 405 (1.17), 315 (1.46), 263sh (4.44)
18	435 (0.47), 333 (1.23), 263 (2.99)
19	439 (0.49), 333 (1.15), 267 (2.80)
20	428sh (0.43), 328 (1.44), 263sh (3.02)
21	423sh (0.28), 327, (1.44), 271 (2.93)



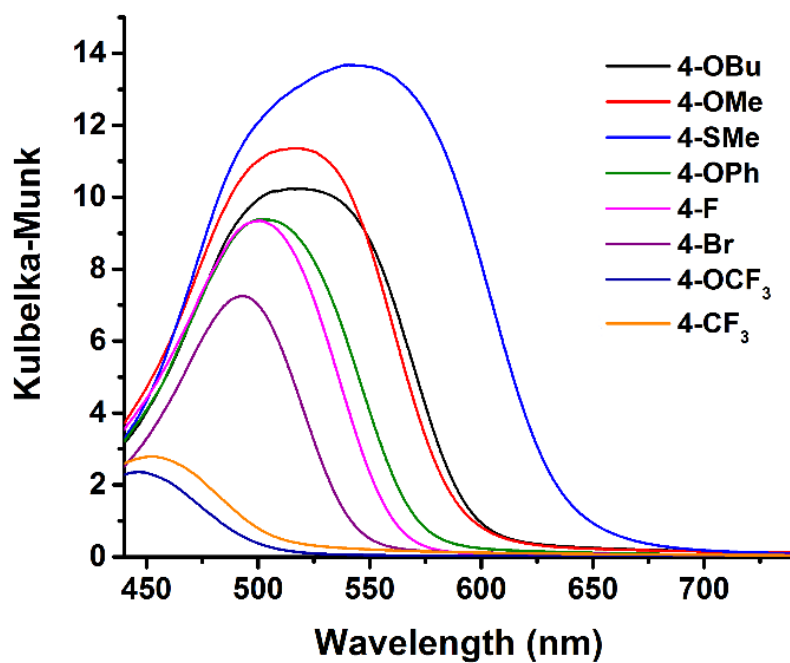


Figure 63: Solid state diffuse reflectance spectra for complexes **14-21**.

Table 10: Summary of the solid state diffuse reflectance data for complexes **14-21**.

Complex	$\lambda_{\max}$ (nm)	Kubelka-Munk
14	514	10.24
15	517	11.36
16	540	13.67
17	502	9.38
18	501	9.34
19	493	7.25
20	446	2.36
21	452	2.79

Subsequently, the solid state photophysical properties of **14-21** were studied. The solid state diffuse reflectance spectra, as displayed in Figure 63, exhibited intense absorption bands for complexes **14-19** and less intense blue shifted absorption bands for complexes **20** and **21**. With the exception of complex **16**, the foregoing absorption bands progressively blue shifted as the electron withdrawing character of the BIAN complex increased. A summary of the pertinent solid state diffuse reflectance spectroscopic data can be found in Table 10.

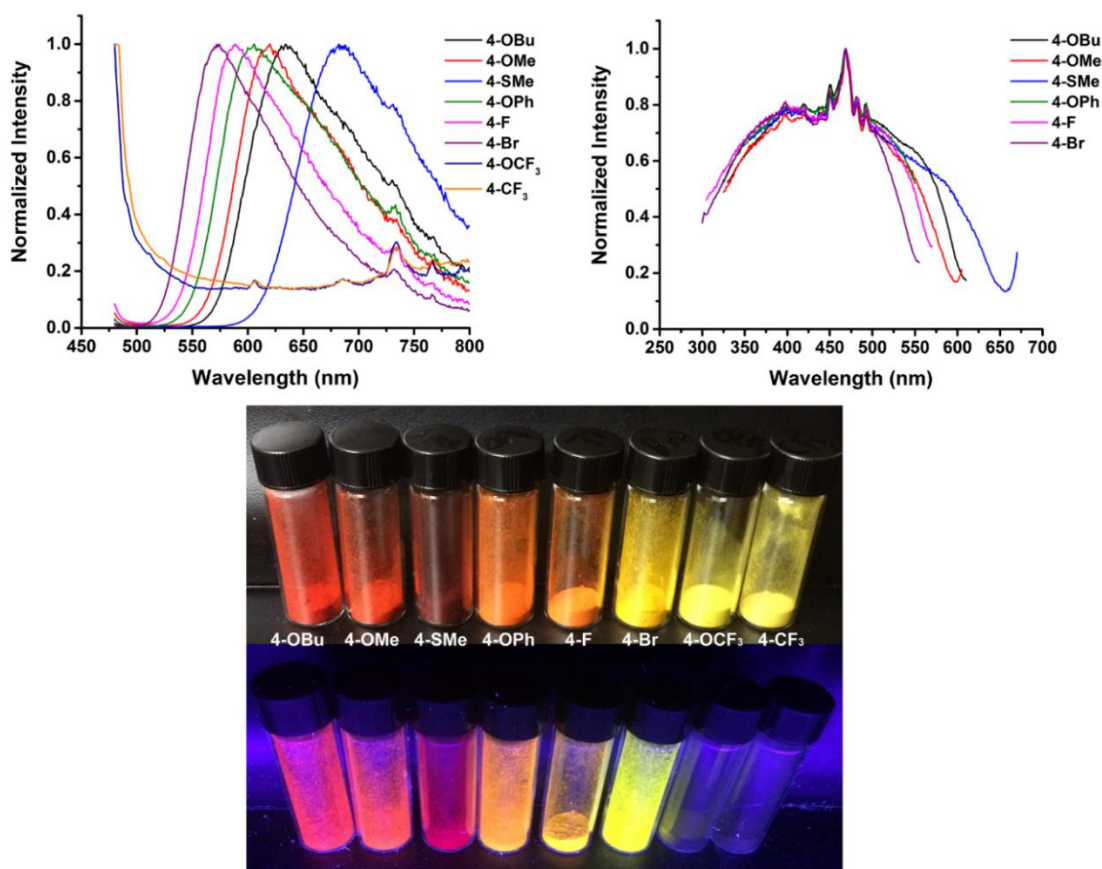


Figure 64: Solid state emission (Top-Left) and excitation (Top-Right) spectra for **14-21** along with a photograph of each complex under ambient light and UV irradiation.

After probing the solid state absorption properties, the solid state photoluminescent properties of **14-21** were investigated. As displayed in Figure 62, all eight complexes were found to be nonemissive in DCM solution. This was reminiscent of the behavior of complexes **10-13**, as previously discussed.<sup>82</sup> However, as exhibited in Figure 64, complexes **14-19** were found to be emissive in the solid state. Conversely, complexes **20** and **21** were determined to be nonemissive in the solid state. Akin to the complexes described above, complexes **14-19** displayed short phosphorescent microsecond lifetimes ( $\tau$ ). Furthermore, complexes **14-19** exhibited relatively low absolute quantum yields ( $\Phi$ ).

Table 11: Solid state photoluminescent data for complexes **14-21**.

Complex	$\lambda_{em}$ (nm)	$\lambda_{ex}$ (nm)	$\tau$ ( $\mu$ s)	$\Phi$ (%) (Absolute)
14	634	470	$3.12 \pm 0.70$	$1.06 \pm 0.09$
15	620	470	$4.04 \pm 0.96$	$1.20 \pm 0.05$
16	682	470	$1.24 \pm 0.66$	$1.33 \pm 0.18$
17	606	470	$4.01 \pm 1.39$	$1.30 \pm 0.08$
18	589	470	$4.38 \pm 1.29$	$1.72 \pm 0.03$
19	574	470	$2.43 \pm 0.66$	$1.80 \pm 0.06$
20	---	---	---	---
21	---	---	---	---

As presented in Table 11, the emissions that were detected for complexes **14-21** displayed overall color tunability that progressively changed from red to orange to yellow. The range of emissions spanned over 100 nm over all of the *para*-substituted

complexes. The color tunability was achieved by modifications of the periphery of the BIAN ligand by installing electron donating/withdrawing groups on the flanking aryl substituents. Overall, the strongly electron donating groups, such as 4-OBu, 4-OMe, and 4-SMe exhibited red emissions. The 4-OPh and 4-F substituted complexes featured orange emissions. Lastly, the 4-Br substituted complex displayed emission in the yellow region of the spectrum.

Table 12: Hammett parameter ( $\sigma_p$ ) for the substituents of complexes **14-21**.<sup>86</sup>

Substituent	Hammett parameter ( $\sigma_p$ )
4-OBu	-0.32
4-OMe	-0.27
4-SMe	0.00
4-OPh	-0.03
4-F	0.06
4-Br	0.23
4-OCF <sub>3</sub>	0.35
4-CF <sub>3</sub>	0.54

As described above, the emissions of the “as-synthesized” complexes **14-19** followed a general trend. Specifically, as the electron withdrawing strength of the *para*-substituted flanking aryl group increased, the emission was found to gradually blue shift. To quantify this observation, a Hammett relationship was investigated in order to see if a correlation existed between the emission maxima and the Hammett parameter ( $\sigma_p$ ) of each substituent (Table 12). For this purpose, a plot of  $\lambda_{\max}$  vs.  $\sigma_p$  was created. As

displayed in Figure 65, if complex **16** was omitted from the series, complexes **14**, **15**, **17**, **18**, and **19** exhibited a nearly linear relationship between emission maxima and the Hammett parameter ( $\sigma_p$ ) of each substituent. This was confirmed via the Pearson regression value of  $R^2 = 0.984$ . However, if complex **16** was included in the series, it was found to be an obvious outlier. This was confirmed from the new Pearson regression value of  $R^2 = 0.486$ . Interestingly, complex **16** was found to exhibit significantly red shifted emissions and absorptions both with respect to its  $\sigma_p$  value and also with respect to those of the other complexes in the series.

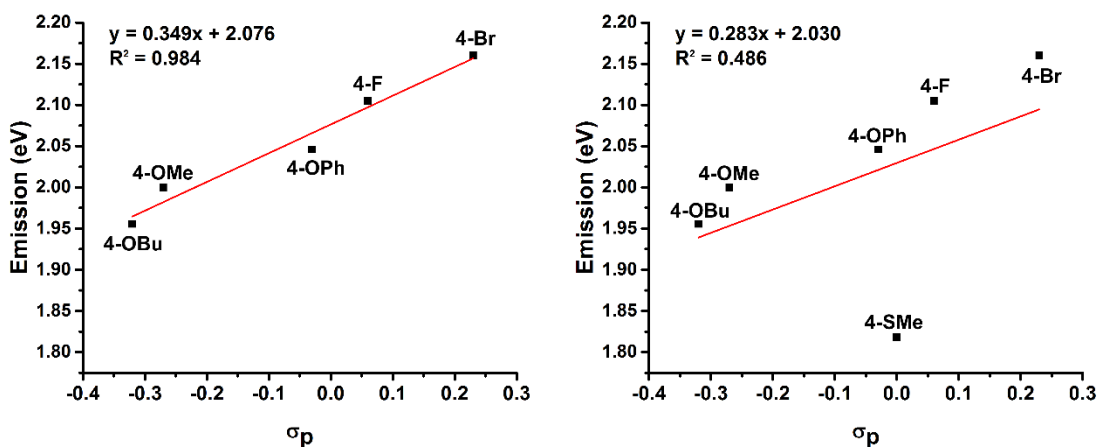


Figure 65: (Left) Hammett relationship between the  $\lambda_{\max}$  values vs. the  $\sigma_p$  values without outlier complex **16**. (Right) Hammett relationship with outlier complex **16**.

After confirming the color tunability of the foregoing series of Ar-BIAN zinc chloride complexes, investigation into the origins of the emission was performed. As in the case of the methylated Ar-BIAN zinc chloride complexes, a series of aggregation-induced emission (AIE) experiments was performed on complexes **14-19** in order to determine if they behaved in an analogous fashion to those that were described above. For this purpose, stock DCM ( $\sim 10^{-4}$  -  $10^{-3}$  M) solutions of each complex were prepared.

As shown in Figure 66, each of the six complexes was found to be AIE active. Furthermore, each complex was nonemissive in translucent solution and only became emissive upon aggregation.

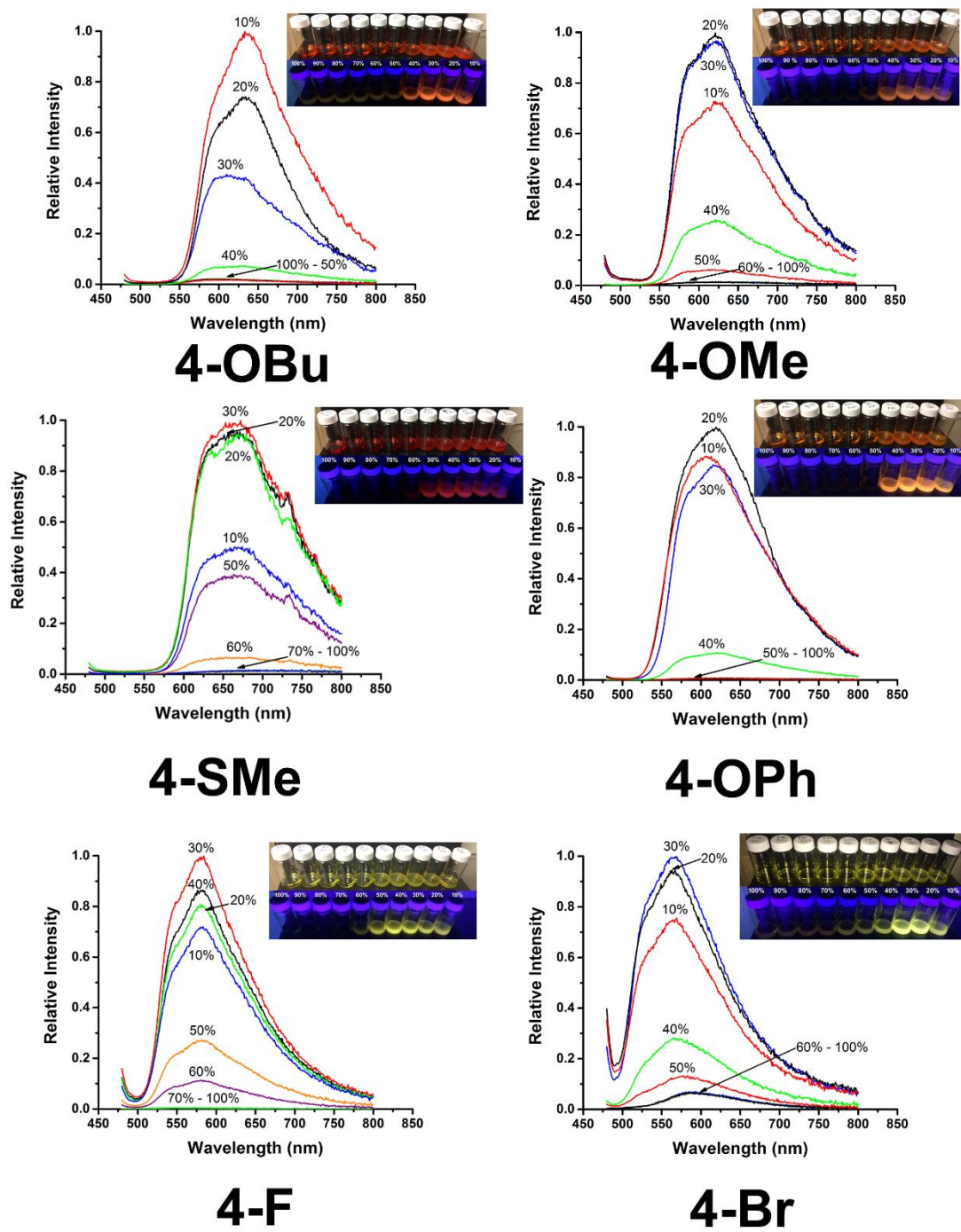


Figure 66: AIE emission spectra and images of DCM/hexanes volumetric fractions of **14-19** in ambient light and under UV irradiation (the percentage values above are relative to the DCM content).

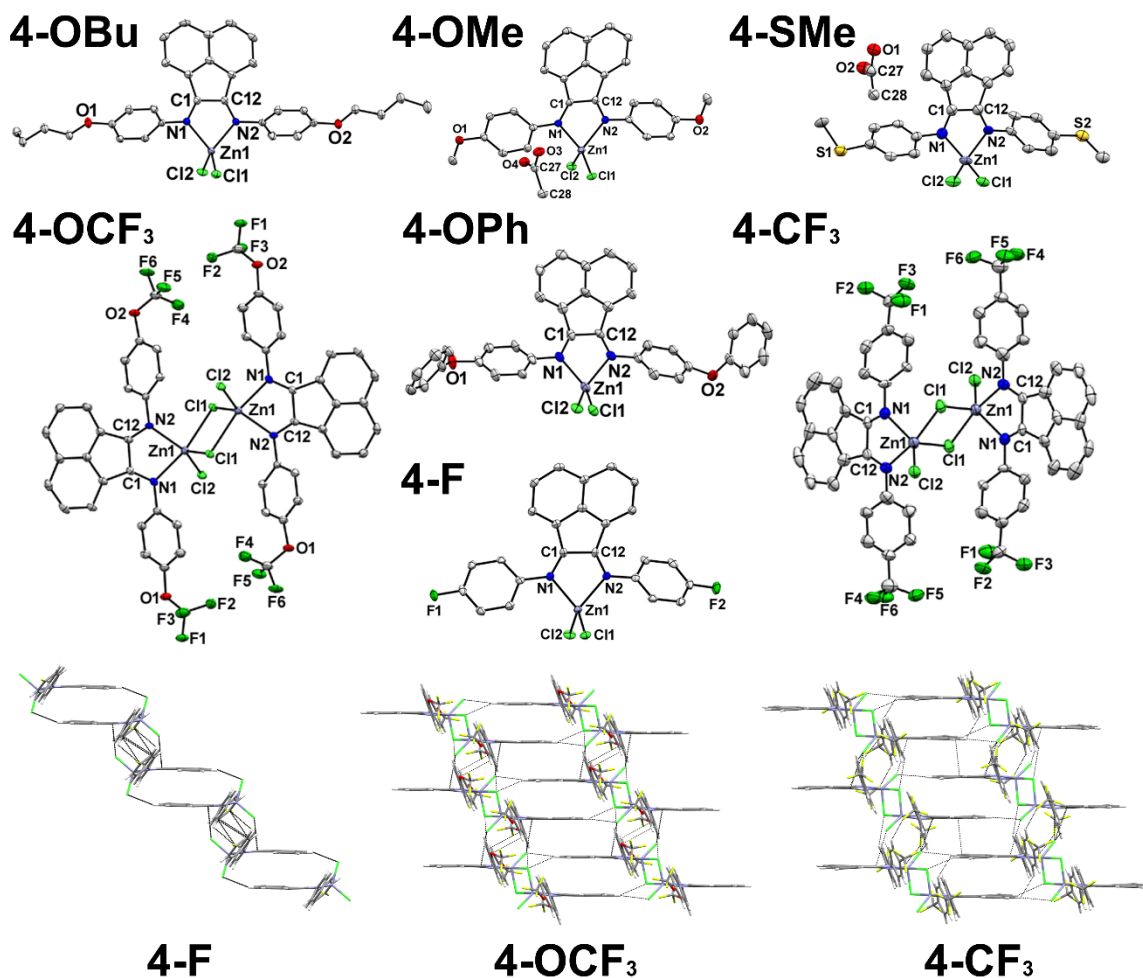


Figure 67: POV-Ray diagrams for complexes **14-19**, **20**, and **21** with thermal ellipsoids displayed at 50% probability. All hydrogen atoms have been removed for clarity. Note however, that complexes **20** and **21** crystallized with only half of the dimeric complex in the asymmetric unit. The expanded complex is displayed for clarity.

After examining the photophysical properties of each complex, the question as to why complexes **20** and **21** were nonemissive remained unanswered. As mentioned in Section 2.2.1, the solid state structure of the methylated Ar-BIAN complexes had a strong influence on the emissive properties of each complex.<sup>82</sup> Accordingly, the solid state



structure of each complex was investigated in order to determine if there were any discernable differences between complexes **14-21**. As previously mentioned, this class of complexes is very sensitive to the nature of the recrystallization technique. Fortunately, akin to the methylated Ar-BIAN complexes, the “as-synthesized” crystalline powders that had precipitated directly from the acetic acid reflux reaction were suitable for single crystal X-ray diffraction studies. However, since the “as-synthesized” crystalline powders could not be recrystallized for fear of altering their initial structure via solvatomorphism, the overall quality of some of the structures is less than desirable.

The crystal structures of the “as-synthesized” complexes **14-18**, **20**, and **21** were studied directly from the reaction precipitate. Unfortunately, complex **19** did not form a suitable crystalline powder from the precipitate reaction mixture and thus the “as-synthesized” structure was not able to be studied. As exhibited in Figure 67, complexes **14-18** featured tetrahedral geometries with respect to the zinc metal center. Furthermore, complexes **15** and **16** featured an acetic acid solvent molecule within the crystal lattice, while complexes **14**, **17**, and **18** were non-solvated. Surprisingly, complexes **20** and **21** did not feature tetrahedral geometries. Instead, these complexes formed a dimeric bridging trigonal bipyramidal structures around the zinc metal center featuring one bridging  $\mu^2$ -chloride ligand.

As discussed above, the packing environment of each BIAN zinc complex had a significant impact on the emissive properties of each complex. It was proposed that the nonemissive behavior of complexes **20** and **21** was a consequence of a different molecular geometry that resulted in an overall different crystal packing environment. A subsequent investigation of the crystal packing environments of complexes **14-18** and complexes **20** and **21** revealed a major difference in crystal packing environments. First,

complexes **14-18** featured packing environments that were very reminiscent of the emissive complexes **10** and **11** with slipped-stacked extended staircase arrays of intermolecular  $\pi$ - $\pi$  interactions between the adjacent naphthalene units, as discussed above. The foregoing staircase formations were a consequence of close contacts that involved the chloride ligand on the zinc metal center with both the carbon atoms of the N-C-C-N fragment and the naphthalenic hydrogen atoms. A representative crystal packing diagram of complex **18** is displayed in Figure 67. On the other hand, the crystal packing environments of complexes **20** and **21** did not feature an extended staircase array of intermolecular  $\pi$ - $\pi$  interactions. Instead, these complexes formed an extended  $\pi$ - $\pi$  stacking in a columnar fashion, which is an orientation that can be deleterious from the standpoint of emissions.<sup>59</sup>

Following the analysis of the “as-synthesized” crystalline powder complexes **14-21**, solvatomorphism was subsequently examined. As mentioned above in Section 2.2.1, solvatomorphism can be an effective way of tuning the solid state photophysical properties of this class of Ar-BIAN zinc chloride complexes. By recrystallizing each complex in DCM solution, seven solvatomorphs of each complex were able to be grown. Each of the solvatomorphs were grown via a slow vapor diffusion of hexanes into a DCM solution. As displayed in Figure 68, all of the solvatomorph structures, with the exception of complex **18**, featured a DCM solvent molecule in their respective crystal lattice. Surprisingly, complexes **20-DCM** and **21-DCM** were found not possess trigonal bipyramidal structures after recrystallization. Instead, these complexes exhibited monomeric tetrahedral structures.

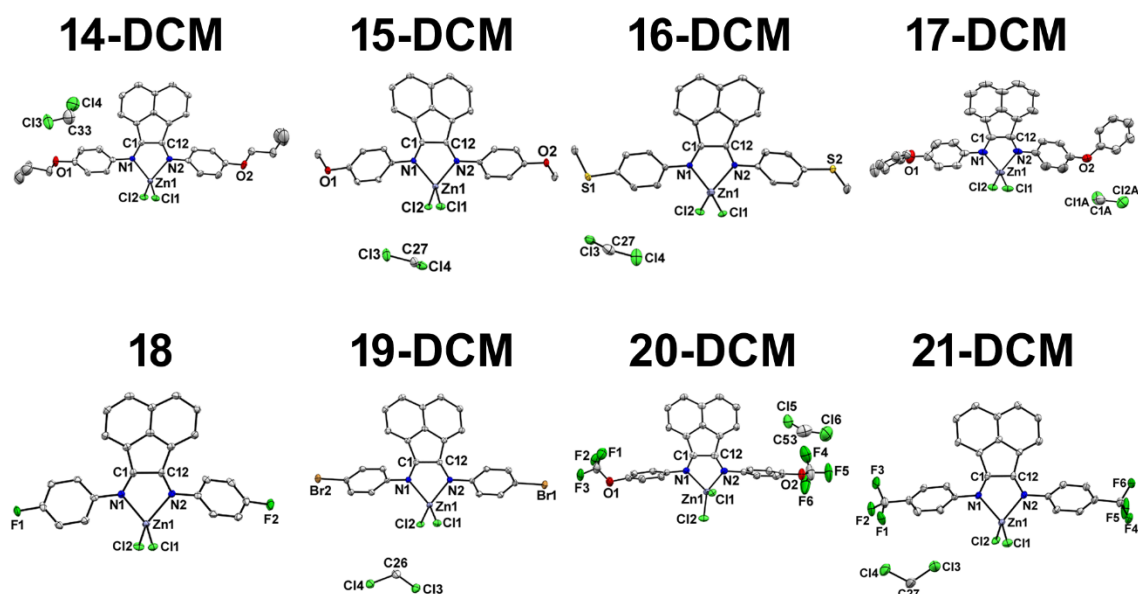


Figure 68: POV-Ray diagrams of the solvatomorphs **14-DCM-17-DCM**, **18**, and **19-DCM-21-DCM** with thermal ellipsoids displayed at 50% probability. All hydrogen atoms have been removed for clarity. Note however, that solvatomorph **20-DCM** crystallized with two complexes in the asymmetric unit, only one of which is displayed for clarity.

Following the foregoing structural study of the solvatomorphs, a photoluminescent investigation was performed to determine whether the solvatomorphs exhibited different solid state photoluminescent properties. As demonstrated in Figure 69 and Table 13, solvatomorphs **14-DCM-17-DCM** and **19-DCM** displayed relatively similar emissive properties to those of the non-solvated “as-synthesized” complexes, albeit with overall higher relative quantum yields ( $\Phi$ ). As previously mentioned, complex **18** did not incorporate a DCM solvent into the crystal lattice and therefore the photophysical properties were unchanged. Remarkably, the nonemissive complexes **20** and **21** were found to be emissive after recrystallization in DCM to form the solvatomorphs **20-DCM** and **21-DCM**. This outcome was presumably due to the formation of the slipped-stacked  $\pi$ -stacking staircase formation in the monomeric

tetrahedral DCM solvatomorphs of complexes **20-DCM** and **21-DCM**, which were absent in the corresponding “as-synthesized” crystalline lattices of **20** and **21**.

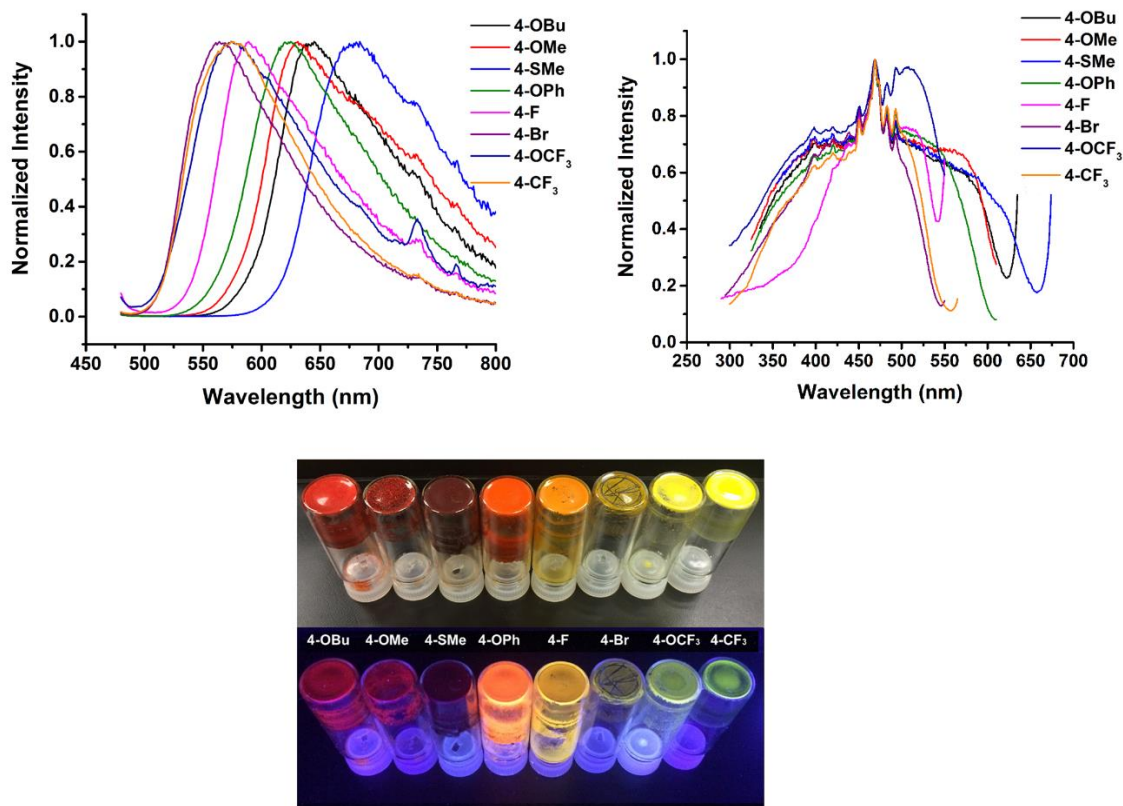


Figure 69: Solid state emission (Top-Left) and excitation (Top-Right) spectra of the solvatomorphs **14-DCM-17-DCM**, **18**, and **19-DCM-21-DCM** with photograph of solvatomorphs under ambient light and UV irradiation.

Table 13: Solid state photoluminescent data for solvatomorphs **14-DCM-17-DCM**, **18-THF**, and **19-DCM-21-DCM**.

Solvatomorph	$\lambda_{em}$ (nm)	$\lambda_{ex}$ (nm)	$\tau$ ( $\mu$ s)	$\Phi$ (%) (Relative)
14-DCM	645	470	$5.13 \pm 1.87$	$5.99 \pm 0.51$
15-DCM	631	470	$3.06 \pm 1.06$	$1.96 \pm 0.08$
16-DCM	684	470	$3.58 \pm 1.46$	$3.24 \pm 0.44$
17-DCM	625	470	$1.60 \pm 0.57$	$7.03 \pm 0.43$
18-THF	562	470	$2.12 \pm 0.83$	$2.89 \pm 0.05$
19-DCM	564	470	$6.16 \pm 1.37$	$2.57 \pm 0.09$
20-DCM	574	470	$3.71 \pm 0.83$	$1.80 \pm 0.06$
21-DCM	576	470	$4.12 \pm 0.70$	$9.54 \pm 0.32$

As discussed above, the recrystallization of complex **18** in DCM solution did not result in the formation of a DCM solvatomorphic structure. However, recrystallization via a slow vapor diffusion of hexanes into a THF solution generated a THF solvatomorph of complex (**18-THF**) (Figure 70). As shown in Figure 71, the incorporation of a THF molecule into the crystal lattice had a significant impact on the solid state photoluminescent properties. Specifically, the emission maximum for the THF solvatomorph **18-THF** was found to be blue shifted by approximately 30 nm in comparison with that of the non-solvated complex **18**. The inclusion of a THF molecule changed the color of the emission from orange to yellow. This shift was presumably due to the difference in crystal packing environments between the two lattices. For example, the average torsion angle between the acenaphthene backbone and the flanking aryl rings for complexes **18** and **18-THF** was found to be 53.90 and 65.21 degrees, respectively.

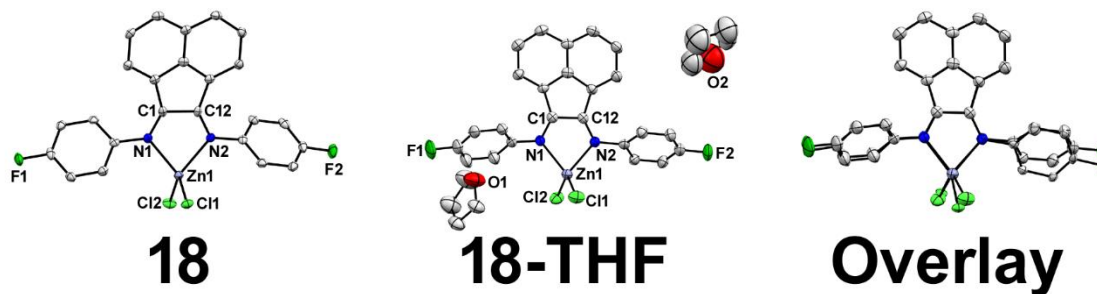


Figure 70: POV-Ray diagrams of **18** (Left), **18-THF** (Center), and an overlay image (Right) of both crystal structures with thermal ellipsoids displayed at 50% probability. All hydrogen atoms have been removed for clarity.

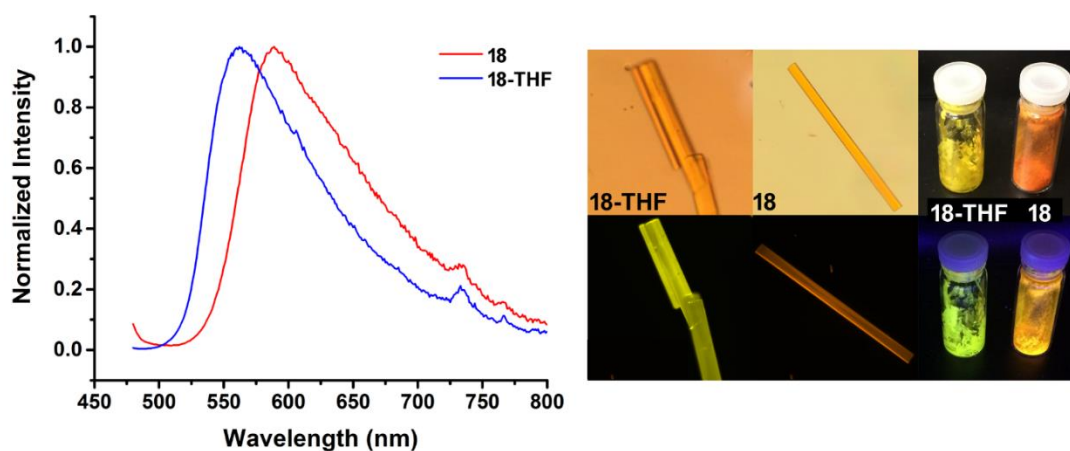


Figure 71: Solid state emission spectra for **18** and **18-THF** with each complex under a fluorescent microscope, ambient light, and UV irradiation.

Table 14: Calculated crystallographic metrical parameters between the  $\pi$ -stacked dimers of the 13 emissive complexes **14-21-DCM**.

Solvatomorph	a (Å)	b (Å)	c (Å)	$\theta$ (°)
14	3.440	1.766	3.867	27.18
14-DCM	3.484	1.419	3.762	22.16
15	3.522	1.293	3.752	20.17
15-DCM	3.445	1.366	3.706	21.63
16	3.517	1.363	3.772	21.19
16-DCM	3.575	1.252	3.788	19.31
17	3.561	1.620	3.912	24.46
17-DCM	3.450	1.394	3.721	22.00
18	3.435	1.207	3.641	19.37
18-THF	3.542	1.564	3.872	23.83
19-DCM	3.512	1.326	3.754	20.69
20-DCM	3.528	1.306	3.762	18.76
21-DCM	3.516	1.298	3.748	20.27

As previously discussed (Figure 70), the difference between the solvatomorphic structures can be quantified by inspection of the metrical parameters of the slipped stacked  $\pi$ - $\pi$  interactions that exist between adjacent naphthalene units. The metrical parameters of the  $\pi$ - $\pi$  interactions are separated into four components: the interplanar distance (a), the slip distance between naphthalene centroids (b), the distance between naphthalene centroids (c), and the slip angle between naphthalene centroids ( $\theta$ ). The most drastic and noticeable difference between the solvated and non-solvated structures was

between complex **18** and **18-THF**. The significant blue shift in the emission was presumably due to the decrease in orbital overlap as evidenced by the longer  $\pi$ - $\pi$  interactions and the larger slip angles, as shown in Table 14. Overall, the aforementioned calculated metrical parameters are summarized in this Table.



### 2.2.3 X-Ray Diffraction Studies of 10-21-DCM

Full crystallographic data for **10-21-DCM** can be found in Appendix B with refinement details, atom positions, and tables of bond lengths and bond angles.

#### 2.2.3.1 4-methylphenyl-BIAN Zinc Chloride (**10**)

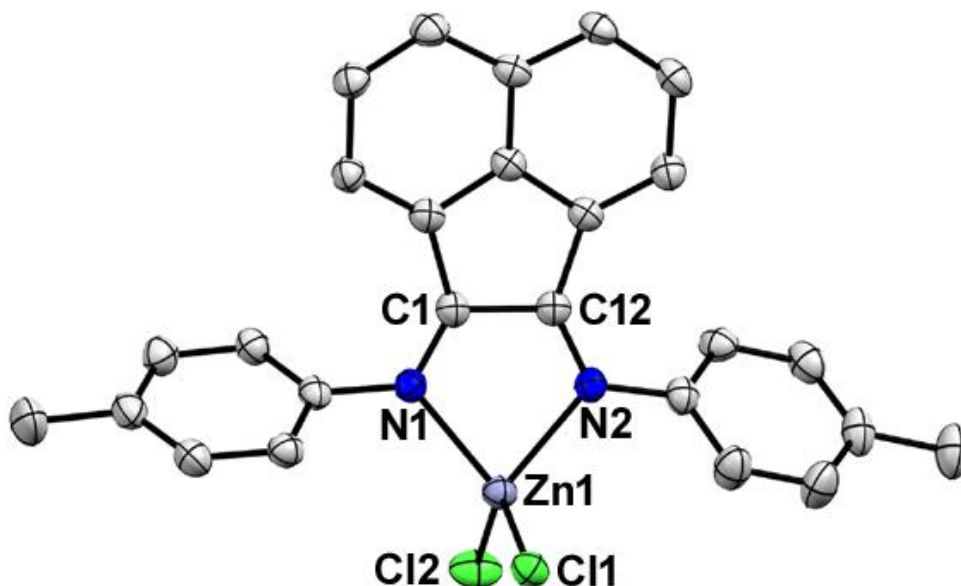


Figure 72: POV-Ray diagram of complex **10** with thermal ellipsoids displayed at 50% probability. All hydrogen atoms have been removed for clarity.<sup>82</sup>

Suitable crystals of complex **10** were obtained directly from the condensation precipitate. Complex **10** crystallized with one complex in the asymmetric unit in the monoclinic crystal system in the  $I2/a$  space group (Figure 72). Complex **10** featured average C=N double, Zn-N single, and Zn-Cl single bond lengths of 1.283(4) Å, 2.082(2) Å, and 2.206(1) Å, respectively. The average aryl-acenaphthene torsion angle was calculated to be 58.76°. Furthermore, the N(1)-Zn(1)-N(2) and Cl(1)-Zn(1)-Cl(2) angles were found to be 81.23(10)° and 118.33(3)°, respectively.

### 2.2.3.2 3,5-dimethylphenyl-BIAN Zinc Chloride (**11**)

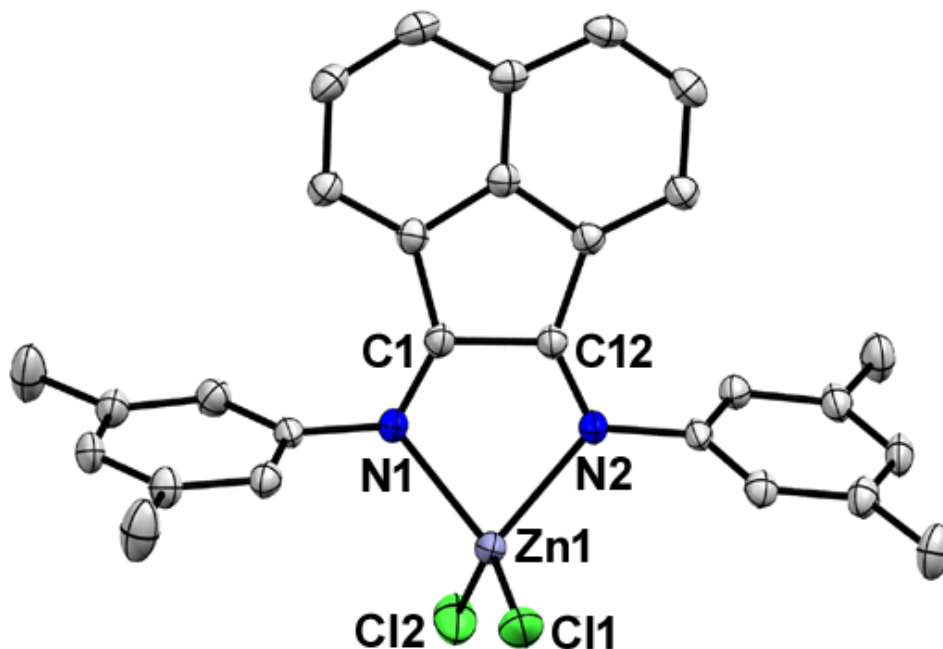


Figure 73: POV-Ray diagram of complex **11** with thermal ellipsoids displayed at 50% probability. All hydrogen atoms have been removed for clarity. Complex **11** crystallized with two complexes in the asymmetric unit, only one of which is presented above.<sup>82</sup>

As in the case of complex **10**, suitable crystals of complex **11** were obtained directly from the condensation precipitate. Complex **11** crystallized with two molecules in the asymmetric unit in the triclinic crystal system in the P-1 space group (Figure 73). Complex **11** featured average C=N double, Zn-N single, and Zn-Cl single bond lengths of 1.280(2) Å, 2.107(2) Å, and 2.196(1) Å, respectively. The average aryl-acenaphthene torsion angle was calculated to be 69.77°. Furthermore, complex **11** featured average N-Zn-N and Cl-Zn-Cl angles of 81.11(6)° and 125.35(3)°, respectively.

### 2.2.3.3 2,4,6-trimethylphenyl-BIAN Zinc Chloride (**12**)

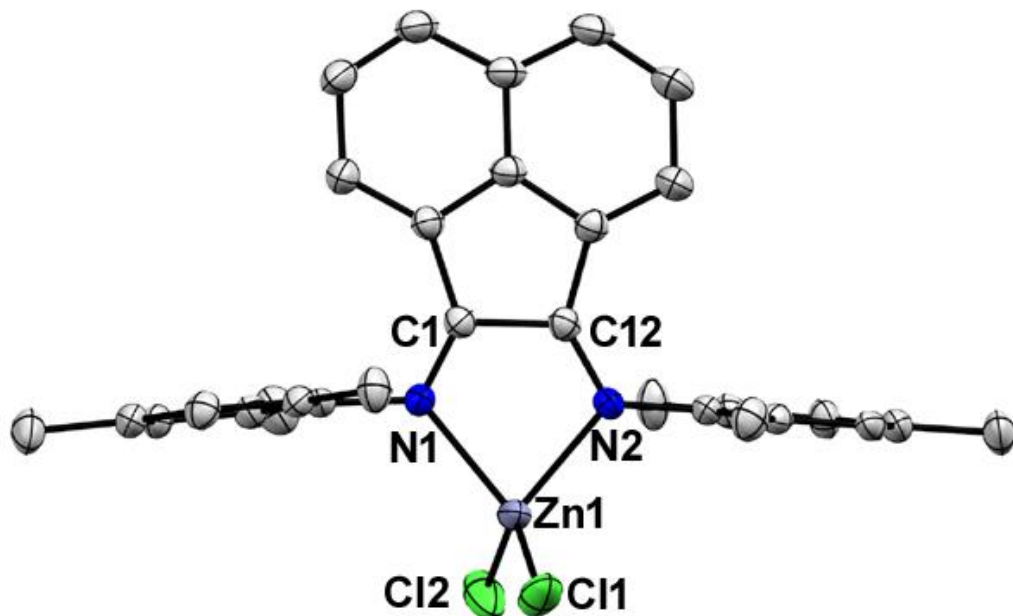


Figure 74: POV-Ray diagram of complex **12** with thermal ellipsoids displayed at 50% probability. All hydrogen atoms have been removed for clarity.<sup>82</sup>

Akin to complexes **10** and **11**, suitable crystals of complex **12** were also obtained directly from the condensation precipitate. Complex **12** crystallized with one molecule in the asymmetric unit in the monoclinic crystal system in the  $P2_1$  space group (Figure 74). Complex **12** featured average C=N double, Zn-N single, and Zn-Cl single bond lengths of 1.275(3) Å, 2.1034(2) Å, and 2.197(1) Å, respectively. The average aryl-acenaphthene torsion angle was calculated to be 80.47°. Furthermore, the N(1)-Zn(1)-N(2) and Cl(1)-Zn(1)-Cl(2) angles were found to be 81.26(7)° and 118.28(3)°, respectively.

#### 2.2.3.4 2-methylphenyl-BIAN Zinc Chloride (**13**)

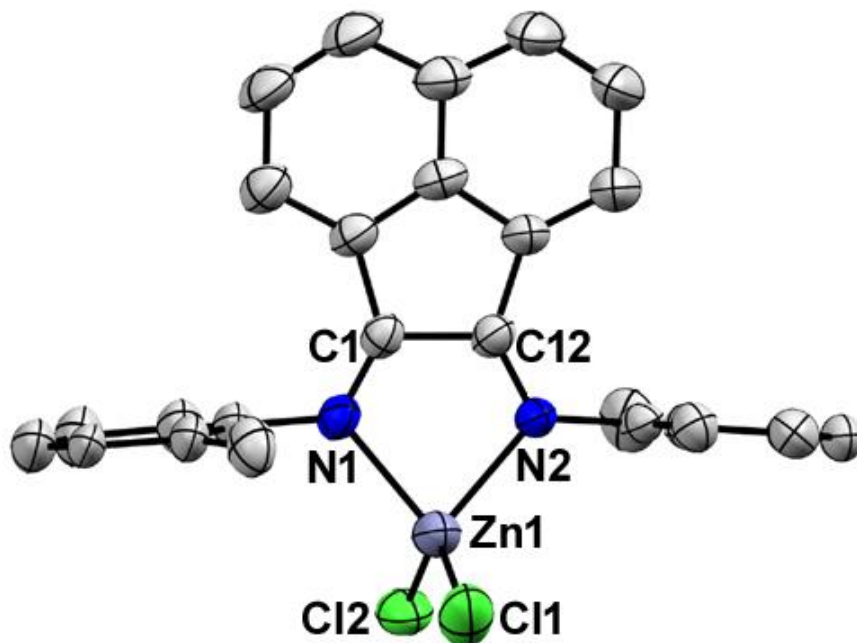


Figure 75: POV-Ray diagram of complex **13** with thermal ellipsoids displayed at 50% probability. All hydrogen atoms have been removed for clarity.<sup>82</sup>

In contrast to complexes **10**, **11**, and **12**, suitable crystals of complex **13** could not be obtained directly from the condensation precipitate. Suitable crystals of complex **13** were grown from a slow evaporation of a dichloromethane solution. Complex **13** crystallized with one molecule in the asymmetric unit in the orthorhombic crystal system in the  $P2_12_12_1$  space group (Figure 75). Complex **13** featured average C=N double, Zn-N single, and Zn-Cl single bond lengths of 1.269(6) Å, 2.103(3) Å, and 2.202(2) Å, respectively. The average aryl-acenaphthene torsion angle was calculated to be 81.79°. Furthermore, the N(1)-Zn(1)-N(2) and Cl(1)-Zn(1)-Cl(2) angles were found to be 80.80(14)° and 120.97(7)°, respectively.

### 2.2.3.5 4-methylphenyl-BIAN Zinc Chloride · CHCl<sub>3</sub> (10-CHCl<sub>3</sub>)

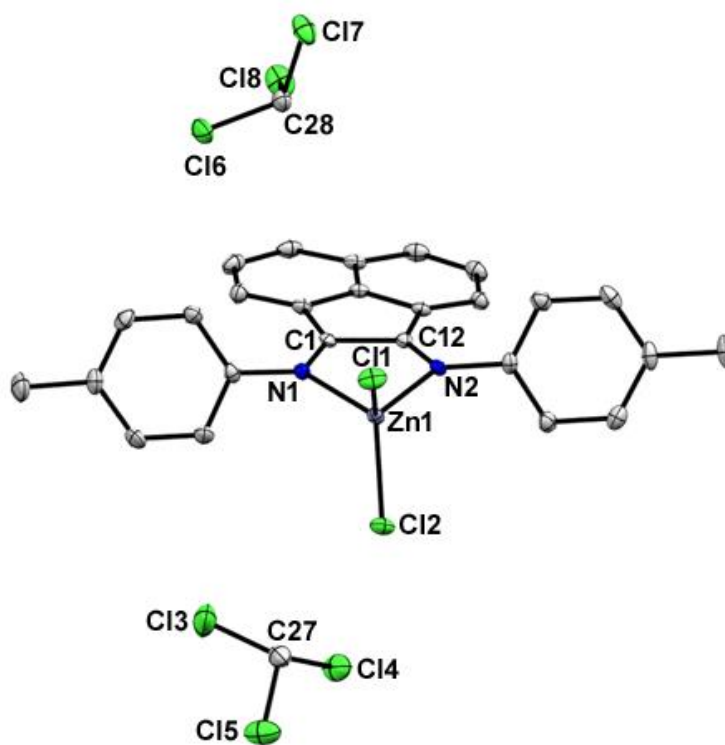


Figure 76: POV-Ray diagram of complex **10-CHCl<sub>3</sub>** with thermal ellipsoids displayed at 50% probability. All hydrogen atoms have been removed for clarity.<sup>82</sup>

Suitable crystals of complex **10-CHCl<sub>3</sub>** were grown from a slow vapor diffusion of hexanes into a chloroform solution. Complex **10-CHCl<sub>3</sub>** crystallized in the monoclinic crystal system in the  $P2_1/c$  space group with one BIAN complex and two chloroform solvent molecules in the asymmetric unit (Figure 76). Complex **10-CHCl<sub>3</sub>** featured average C=N double, Zn-N single, and Zn-Cl single bond lengths of 1.283(3) Å, 2.083(2) Å, and 2.213(1) Å, respectively. The average aryl-acenaphthene torsion angle was calculated to be 59.59°. Furthermore, the N(1)-Zn(1)-N(2) and Cl(1)-Zn(1)-Cl(2) angles were found to be 81.07(7)° and 119.60(2)°, respectively.

### 2.2.3.6 4-methylphenyl-BIAN Zinc Chloride · THF (10-THF)

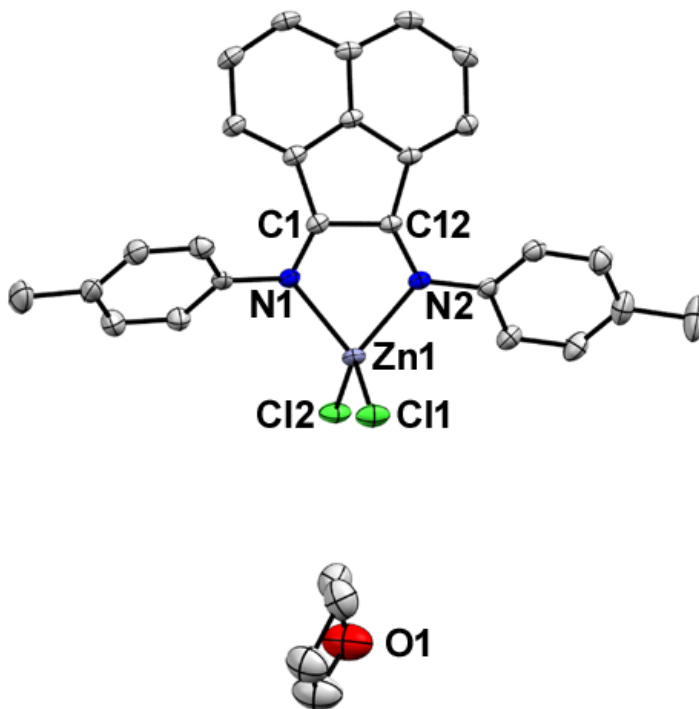


Figure 77: POV-Ray diagram of complex **10-THF** with thermal ellipsoids displayed at 50% probability. All hydrogen atoms have been removed for clarity.<sup>82</sup>

Suitable crystals of complex **10-THF** were grown from a slow vapor diffusion of hexanes into a tetrahydrofuran solution. Complex **10-THF** crystallized in the monoclinic crystal system in the  $C2/c$  space group with one BIAN complex and one tetrahydrofuran solvent molecule in the asymmetric unit (Figure 77). Complex **10-THF** featured average C=N double, Zn-N single, and Zn-Cl single bond lengths of 1.285(3) Å, 2.086(2) Å, and 2.206(6) Å, respectively. The average aryl-acenaphthene torsion angle was calculated to be 58.89°. Furthermore, the N(1)-Zn(1)-N(2) and Cl(1)-Zn(1)-Cl(2) angles were found to be 81.01(6)° and 116.37(2)°, respectively.

### 2.2.3.7 4-methylphenyl-BIAN Zinc Chloride · DCM (10-DCM)

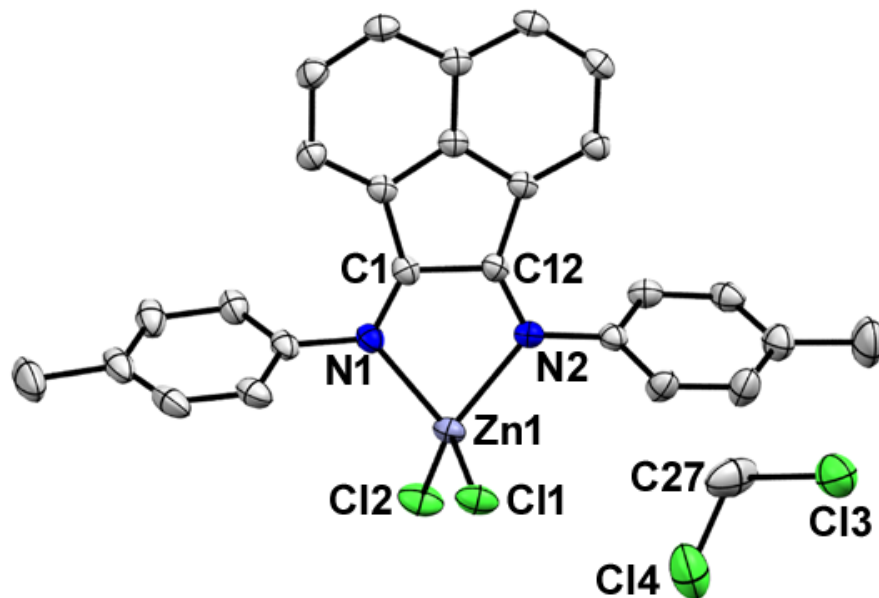


Figure 78: POV-Ray diagram of complex **10-DCM** with thermal ellipsoids displayed at 50% probability. All hydrogen atoms have been removed for clarity.<sup>82</sup>

Suitable crystals of complex **10-DCM** were grown from a slow vapor diffusion of hexanes into a dichloromethane solution. Complex **10-DCM** crystallized in the monoclinic crystal system in the  $P2_1/c$  space group with one BIAN complex and one dichloromethane solvent molecule in the asymmetric unit (Figure 78). Complex **10-DCM** featured average C=N double, Zn-N single, and Zn-Cl single bond lengths of 1.286(4) Å, 2.077(2) Å, and 2.208(8) Å, respectively. The average aryl-acenaphthene torsion angle was calculated to be 68.62°. Furthermore, the N(1)-Zn(1)-N(2) and Cl(1)-Zn(1)-Cl(2) angles were found to be 81.14(9)° and 116.98(3)°, respectively.

### 2.2.3.8 4-methylphenyl-BIAN Zinc Chloride · MeCN (10-MeCN)

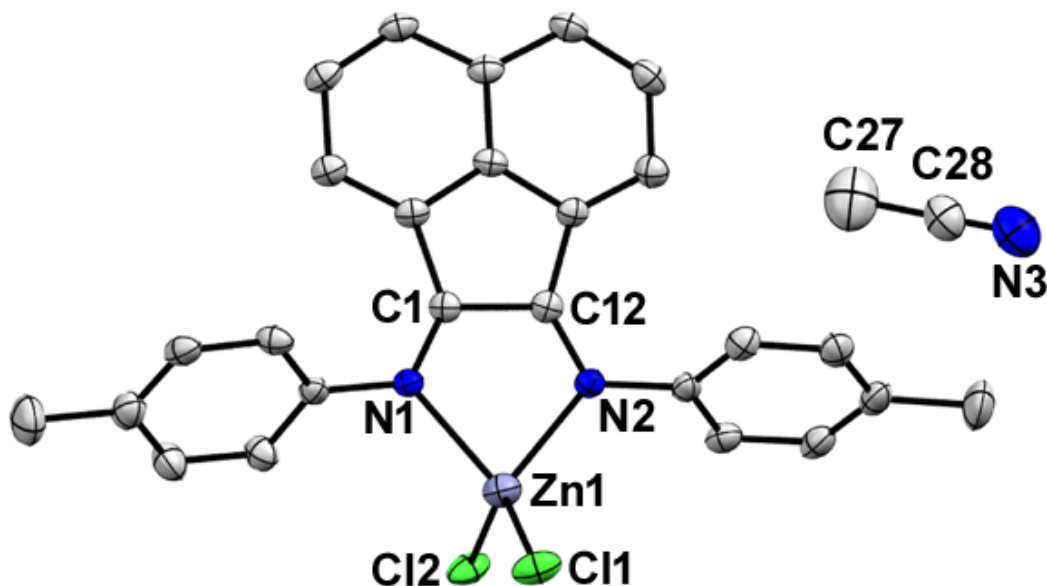


Figure 79: POV-Ray diagram of complex **10-MeCN** with thermal ellipsoids displayed at 50% probability. All hydrogen atoms have been removed for clarity.<sup>82</sup>

Suitable crystals of complex **10-MeCN** were grown from a slow vapor diffusion of diethyl ether into an acetonitrile solution. Complex **10-MeCN** crystallized in the monoclinic crystal system in the  $P2_1/c$  space group with one BIAN complex and one acetonitrile solvent molecule in the asymmetric unit (Figure 79). Complex **10-MeCN** featured average C=N double, Zn-N single, and Zn-Cl single bond lengths of 1.283(3) Å, 2.083(4) Å, and 2.206(2) Å, respectively. The average aryl-acenaphthene torsion angle was calculated to be 65.47°. Furthermore, the N(1)-Zn(1)-N(2) and Cl(1)-Zn(1)-Cl(2) angles were found to be 81.3(2)° and 117.69(8)°, respectively.



### 2.2.3.9 3,5-dimethylphenyl-BIAN Zinc Chloride · CHCl<sub>3</sub> (11-CHCl<sub>3</sub>)

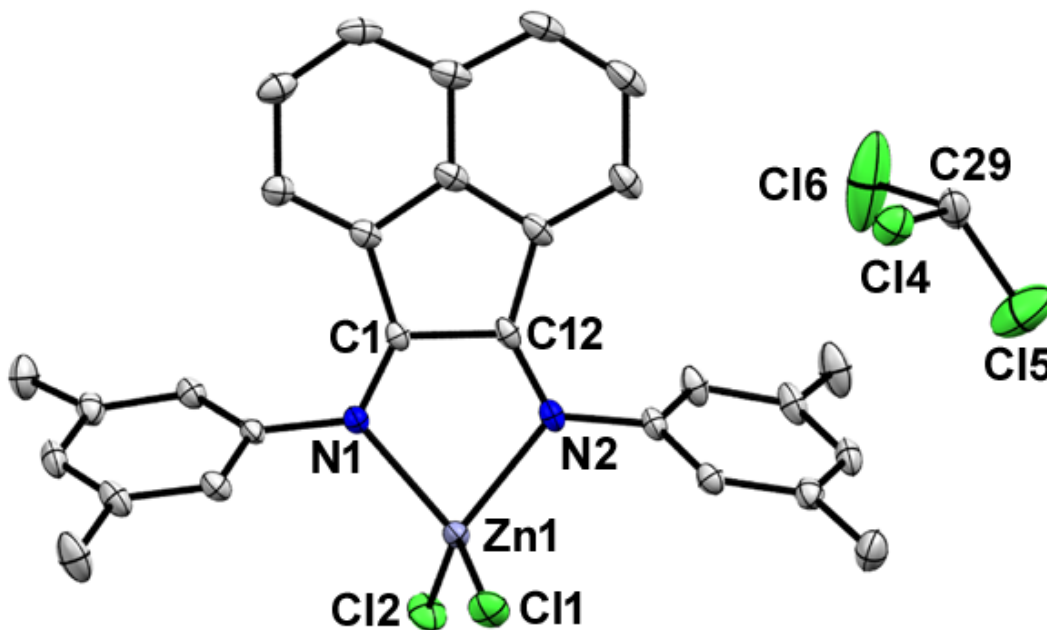


Figure 80: POV-Ray diagram of complex **11-CHCl<sub>3</sub>** with thermal ellipsoids displayed at 50% probability. All hydrogen atoms have been removed for clarity.<sup>82</sup>

Suitable crystals of complex **11-CHCl<sub>3</sub>** were grown from a slow vapor diffusion of hexanes into a chloroform solution. Complex **11-CHCl<sub>3</sub>** crystallized in the monoclinic crystal system in the  $P2_1/c$  space group with one BIAN complex and one chloroform solvent molecule in the asymmetric unit (Figure 80). Complex **11-CHCl<sub>3</sub>** featured average C=N double, Zn-N single, and Zn-Cl single bond lengths of 1.281(3) Å, 2.096(2) Å, and 2.196(1) Å, respectively. The average aryl-acenaphthene torsion angle was calculated to be 65.10°. Furthermore, the N(1)-Zn(1)-N(2) and Cl(1)-Zn(1)-Cl(2) angles were found to be 80.56(7)° and 123.12(3)°, respectively.

### 2.2.3.10 3,5-dimethylphenyl-BIAN Zinc Chloride · THF (11-THF)

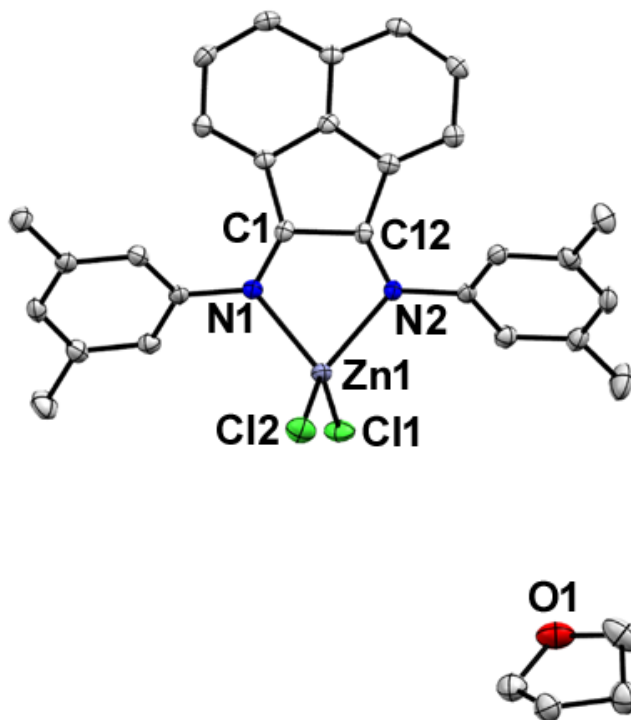


Figure 81: POV-Ray diagram of complex **11-THF** with thermal ellipsoids displayed at 50% probability. All hydrogen atoms have been removed for clarity.<sup>82</sup>

Suitable crystals of complex **11-THF** were grown from a slow vapor diffusion of hexanes into a tetrahydrofuran solution. Complex **11-THF** crystallized in the monoclinic crystal system in the  $P2_1/c$  space group with one BIAN complex and one tetrahydrofuran solvent molecule in the asymmetric unit (Figure 81). Complex **11-THF** featured average C=N double, Zn-N single, and Zn-Cl single bond lengths of 1.283(2) Å, 2.102(1) Å, and 2.202(1) Å, respectively. The average aryl-acenaphthene torsion angle was calculated to be 66.46°. Furthermore, the N(1)-Zn(1)-N(2) and Cl(1)-Zn(1)-Cl(2) angles were found to be 80.40(5)° and 119.75(2)°, respectively.

### 2.2.3.11 3,5-dimethylphenyl-BIAN Zinc Chloride · DCM (11-DCM)

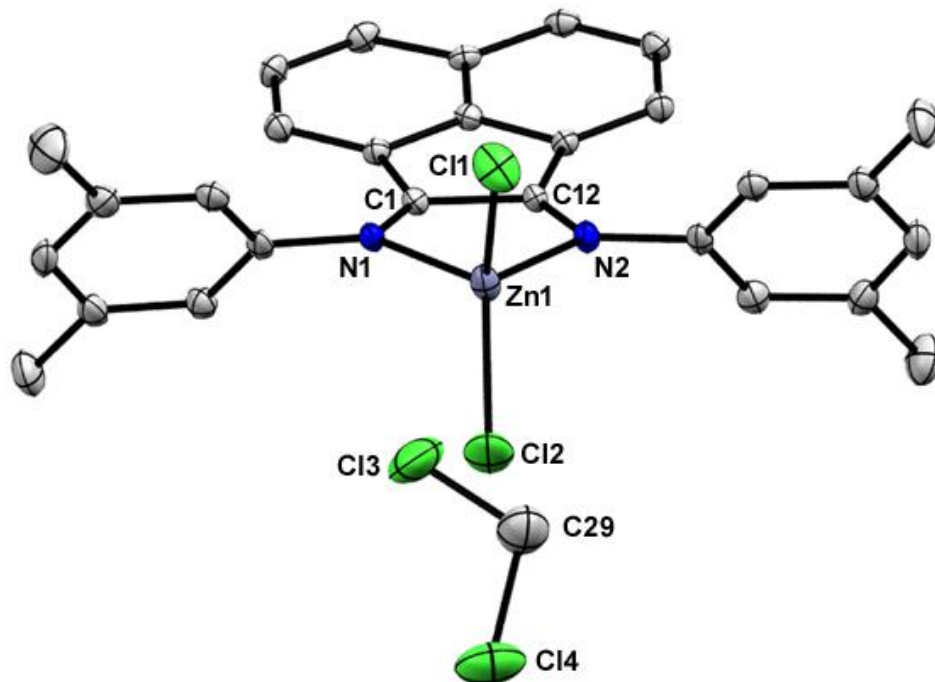


Figure 82: POV-Ray diagram of complex **11-DCM** with thermal ellipsoids displayed at 50% probability. All hydrogen atoms have been removed for clarity.<sup>82</sup>

Suitable crystals of complex **11-DCM** were grown from a slow vapor diffusion of hexanes into a dichloromethane solution. Complex **11-DCM** crystallized in the monoclinic crystal system in the  $P2_1/c$  space group with one BIAN complex and one dichloromethane solvent molecule in the asymmetric unit (Figure 82). Complex **11-DCM** featured average C=N double, Zn-N single, and Zn-Cl single bond lengths of 1.284(3) Å, 2.097(2) Å, and 2.199(1) Å, respectively. The average aryl-acenaphthene torsion angle was calculated to be 65.85°. Furthermore, the N(1)-Zn(1)-N(2) and Cl(1)-Zn(1)-Cl(2) angles were found to be 80.93(6)° and 121.24(3)°, respectively.

### 2.2.3.12 3,5-dimethylphenyl-BIAN Zinc Chloride · MeCN (11-MeCN)

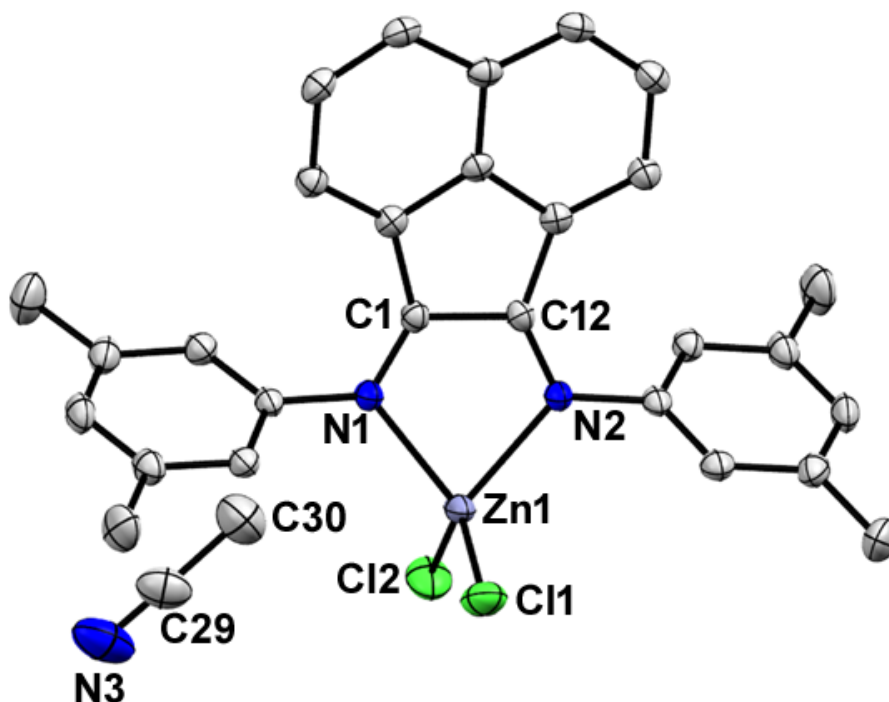


Figure 83: POV-Ray diagram of complex **11-MeCN** with thermal ellipsoids displayed at 50% probability. All hydrogen atoms have been removed for clarity.<sup>82</sup>

Suitable crystals of complex **11-MeCN** were grown from a slow vapor diffusion of diethyl ether into an acetonitrile solution. Complex **11-MeCN** crystallized in the monoclinic crystal system in the  $P2_1/n$  space group with one BIAN complex and one acetonitrile solvent molecule in the asymmetric unit (Figure 83). Complex **11-MeCN** featured average C=N double, Zn-N single, and Zn-Cl single bond lengths of 1.279(2) Å, 2.095(1) Å, and 2.204(1) Å, respectively. The average aryl-acenaphthene torsion angle was calculated to be 66.97°. Furthermore, the N(1)-Zn(1)-N(2) and Cl(1)-Zn(1)-Cl(2) angles were found to be 80.64(5)° and 119.24(2)°, respectively.

### 2.2.3.13 4-butoxyphenyl-BIAN Zinc Chloride (**14**)

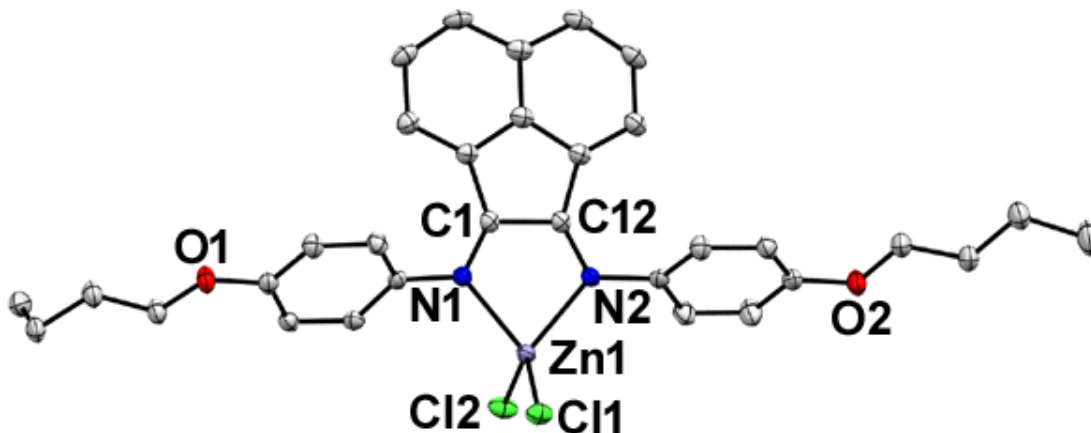


Figure 84: POV-Ray diagram of complex **14** with thermal ellipsoids displayed at 50% probability. All hydrogen atoms have been removed for clarity.

Suitable crystals of complex **14** were obtained directly from the condensation precipitate. Complex **14** crystallized with one complex in the asymmetric unit in the monoclinic crystal system in the  $I2/a$  space group (Figure 84). Complex **14** featured average C=N double, Zn-N single, and Zn-Cl single bond lengths of 1.284(2) Å, 2.088(1) Å, and 2.207(1) Å, respectively. The average aryl-acenaphthene torsion angle was calculated to be 63.72°. Furthermore, the N(1)-Zn(1)-N(2) and Cl(1)-Zn(1)-Cl(2) angles were found to be 81.28(6)° and 115.56(2)°, respectively.

### 2.2.3.14 4-methoxyphenyl-BIAN Zinc Chloride · CH<sub>3</sub>COOH (15)

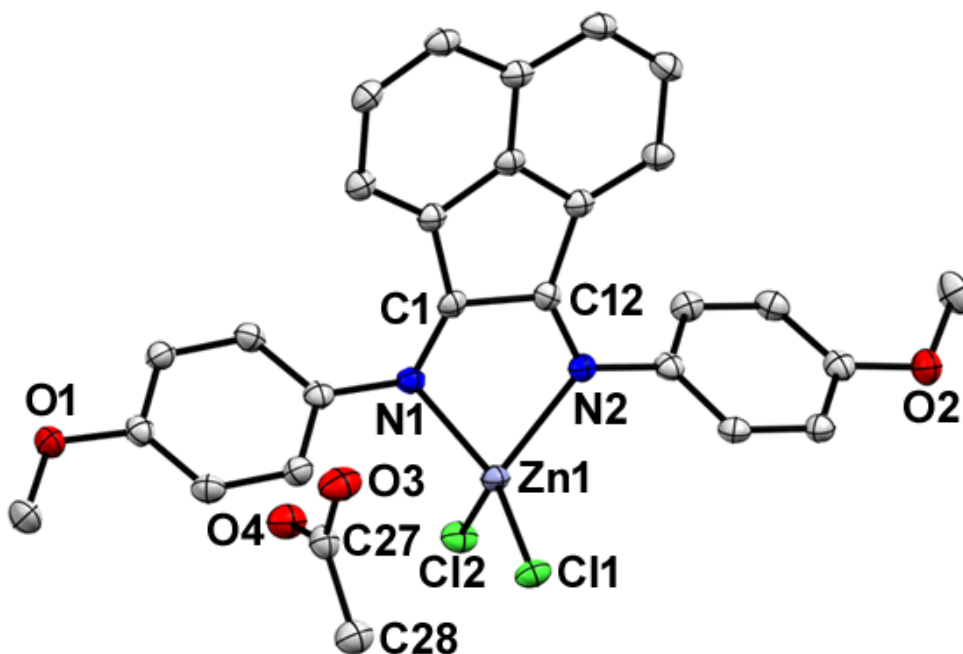


Figure 85: POV-Ray diagram of complex **15** with thermal ellipsoids displayed at 50% probability. All hydrogen atoms have been removed for clarity.

Suitable crystals of complex **15** were obtained directly from the condensation precipitate. Complex **15** crystallized with one complex and one acetic acid molecule in the asymmetric unit in the monoclinic crystal system in the  $P2_1/c$  space group (Figure 85). Complex **15** featured average C=N double, Zn-N single, and Zn-Cl single bond lengths of 1.285(2) Å, 2.078(2) Å, and 2.211(1) Å, respectively. The average aryl-acenaphthene torsion angle was calculated to be 60.25°. Furthermore, the N(1)-Zn(1)-N(2) and Cl(1)-Zn(1)-Cl(2) angles were found to be 81.42(6)° and 117.55(2)°, respectively.

### 2.2.3.15 4-(methylthio)phenyl-BIAN Zinc Chloride · CH<sub>3</sub>COOH (16)

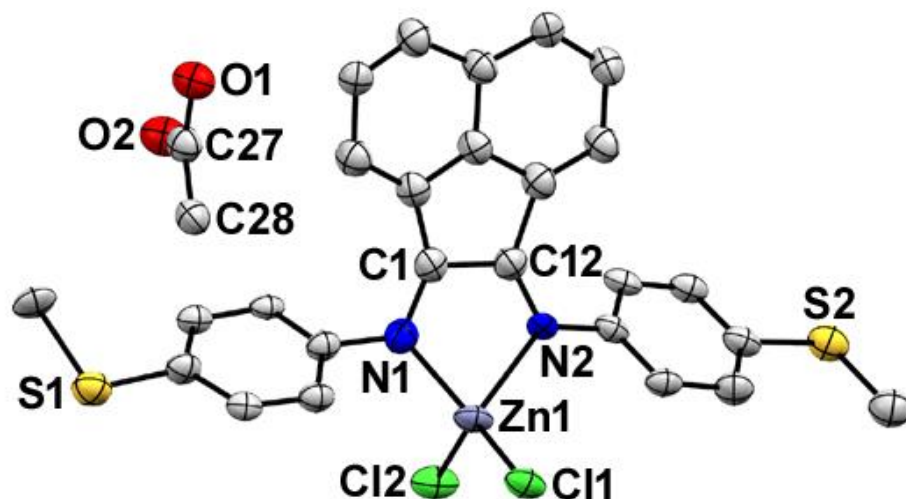


Figure 86: POV-Ray diagram of complex **16** with thermal ellipsoids displayed at 50% probability. All hydrogen atoms have been removed for clarity.

Suitable crystals of complex **16** were obtained directly from the condensation precipitate. Complex **16** crystallized with one complex and one acetic acid molecule in the asymmetric unit in the monoclinic crystal system in the  $P2_1/c$  space group (Figure 86). Complex **16** featured average C=N double, Zn-N single, and Zn-Cl single bond lengths of 1.33(4) Å, 2.08(3) Å, and 2.209(9) Å, respectively. The average aryl-acenaphthene torsion angle was calculated to be 60.36°. Furthermore, the N(1)-Zn(1)-N(2) and Cl(1)-Zn(1)-Cl(2) angles were found to be 83.0(10)° and 118.4(4)°, respectively.

### 2.2.3.16 4-phenoxyphenyl-BIAN Zinc Chloride (17)

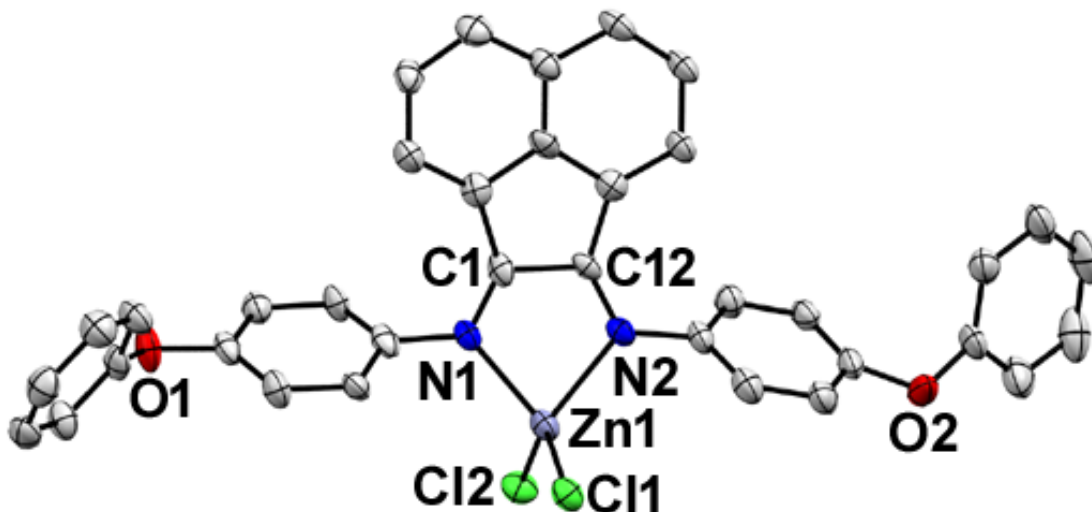


Figure 87: POV-Ray diagram of complex **17** with thermal ellipsoids displayed at 50% probability. All hydrogen atoms have been removed for clarity.

Suitable crystals of complex **17** were obtained directly from the condensation precipitate. Complex **17** crystallized with one complex in the asymmetric unit in the monoclinic crystal system in the  $P2_1/c$  space group (Figure 87). Complex **17** featured average C=N double, Zn-N single, and Zn-Cl single bond lengths of 1.279(13) Å, 2.085(8) Å, and 2.209(3) Å, respectively. The average aryl-acenaphthene torsion angle was calculated to be 64.45°. Furthermore, the N(1)-Zn(1)-N(2) and Cl(1)-Zn(1)-Cl(2) angles were found to be 80.6(3)° and 118.23(12)°, respectively.



### 2.2.3.17 4-fluorophenyl-BIAN Zinc Chloride (**18**)

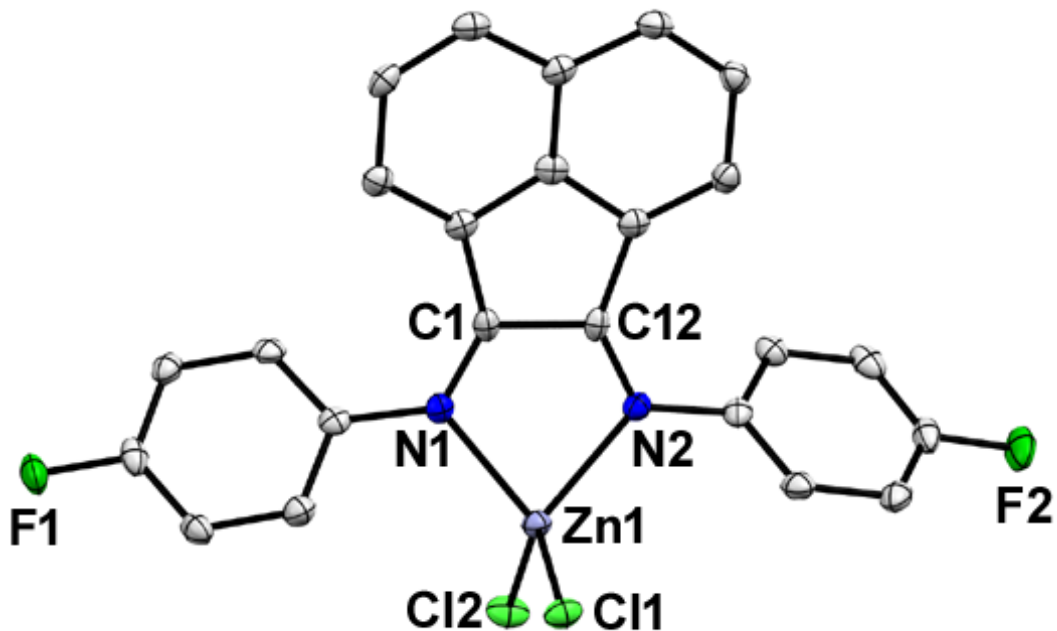


Figure 88: POV-Ray diagram of complex **18** with thermal ellipsoids displayed at 50% probability. All hydrogen atoms have been removed for clarity.

Suitable crystals of complex **18** were obtained directly from the condensation precipitate. Complex **18** crystallized with one complex in the asymmetric unit in the monoclinic crystal system in the  $P2_1/c$  space group (Figure 88). Complex **18** featured average C=N double, Zn-N single, and Zn-Cl single bond lengths of 1.293(5) Å, 2.081(3) Å, and 2.217(1) Å, respectively. The average aryl-acenaphthene torsion angle was calculated to be 53.9°. Furthermore, the N(1)-Zn(1)-N(2) and Cl(1)-Zn(1)-Cl(2) angles were found to be 81.06(11)° and 115.35(4)°, respectively.

### 2.2.3.18 4-(trifluoromethoxy)phenyl-BIAN Zinc Chloride (**20**)

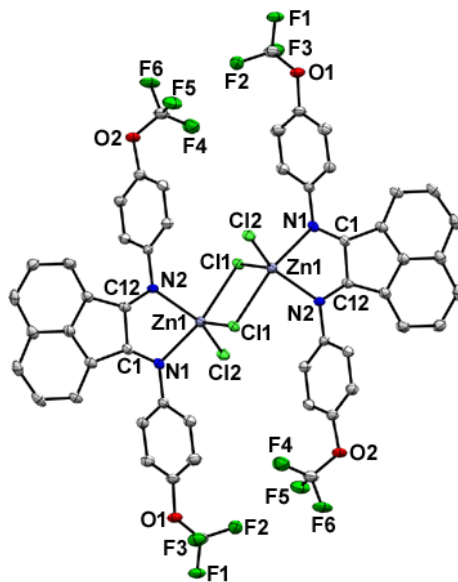


Figure 89: POV-Ray diagram of complex **20** with thermal ellipsoids displayed at 50% probability. All hydrogen atoms have been removed for clarity. Note however, complex **20** crystallized with half of the dimeric complex in the asymmetric unit. The expanded complex is displayed for clarity.

Suitable crystals of complex **20** were obtained directly from the condensation precipitate. Complex **20** crystallized with half of the dimeric complex in the asymmetric unit in the triclinic crystal system in the P-1 space group (Figure 89). Complex **20** featured average C=N double, average Zn-N single, axial Zn-Cl single, and bridging Zn-Cl single bond lengths of 1.281(4) Å, 2.157(3) Å, 2.241(1) Å, and 2.314(1) Å, respectively. The average aryl-acenaphthene torsion angle was calculated to be 67.82°. Furthermore, the axial N(1)-Zn(1)-Cl(1)#1 bond angle and equatorial N(2)-Zn(1)-Cl(2), Cl(1)-Zn(1)-Cl(2), N(2)-Zn(1)-Cl(1) trigonal bipyramidal bond angles in the zinc metal center were found to be 168.27(8)° and 135.57(8)°, 115.27(4)°, 109.09(8)°, respectively.

### 2.2.3.19 4-(trifluoromethyl)phenyl-BIAN Zinc Chloride (**21**)

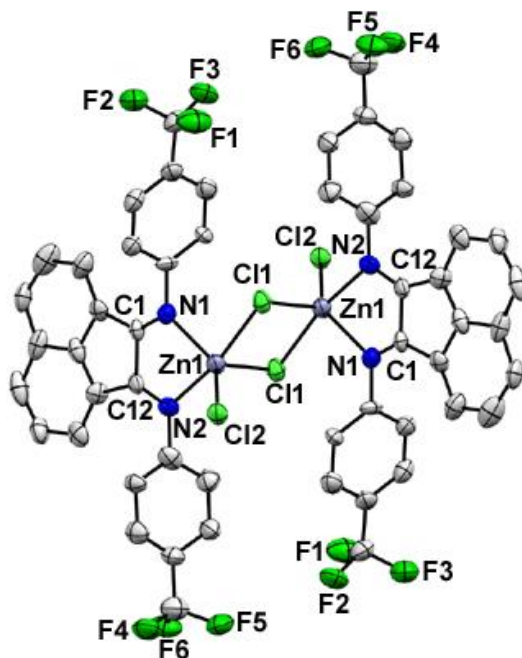


Figure 90: POV-Ray diagram of complex **21** with thermal ellipsoids displayed at 50% probability. All hydrogen atoms have been removed for clarity. Note however, complex **21** crystallized with two complexes in the asymmetric unit.

Suitable crystals of complex **21** were obtained directly from the condensation precipitate. Complex **21** crystallized with two complexes in the asymmetric unit in the triclinic crystal system in the P-1 space group (Figure 90). Complex **21** featured average C=N double, average Zn-N single, axial Zn-Cl single, and bridging Zn-Cl single bond lengths of 1.253(17) Å, 2.146(12) Å, 2.234(4) Å, and 2.337(4) Å, respectively. The average aryl-acenaphthene torsion angle was calculated to be 77.77°. Furthermore, the axial N(2)-Zn(1)-Cl(1)#1 bond angle and equatorial N(1)-Zn(1)-Cl(1), Cl(1)-Zn(1)-Cl(2), N(1)-Zn(1)-Cl(2) trigonal bipyramidal bond angles in the zinc metal center were found to be 169.2(3)° and 106.7(3)°, 118.11(14)°, 134.8(3)°, respectively.

### 2.2.3.20 4-butoxyphenyl-BIAN Zinc Chloride · DCM (14-DCM)

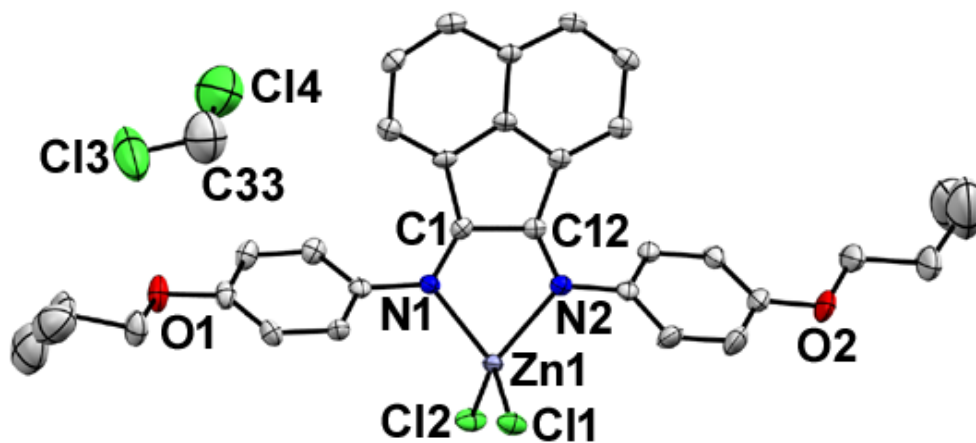


Figure 91: POV-Ray diagram of complex **14-DCM** with thermal ellipsoids displayed at 50% probability. All hydrogen atoms have been removed for clarity.

Suitable crystals of complex **14-DCM** were obtained directly from a slow vapor diffusion of hexanes into a dichloromethane solution. Complex **14-DCM** crystallized with one complex and one dichloromethane solvent molecule in the asymmetric unit in the monoclinic crystal system in the  $P2_1/n$  space group (Figure 91). Complex **14-DCM** featured average C=N double, Zn-N single, and Zn-Cl single bond lengths of 1.289(7) Å, 2.086(4) Å, and 2.215(2) Å, respectively. The average aryl-acenaphthene torsion angle was calculated to be 62.69°. Furthermore, the N(1)-Zn(1)-N(2) and Cl(1)-Zn(1)-Cl(2) angles were found to be 81.24(16)° and 116.43(5)°, respectively.

### 2.2.3.21 4-methoxyphenyl-BIAN Zinc Chloride · DCM (15-DCM)

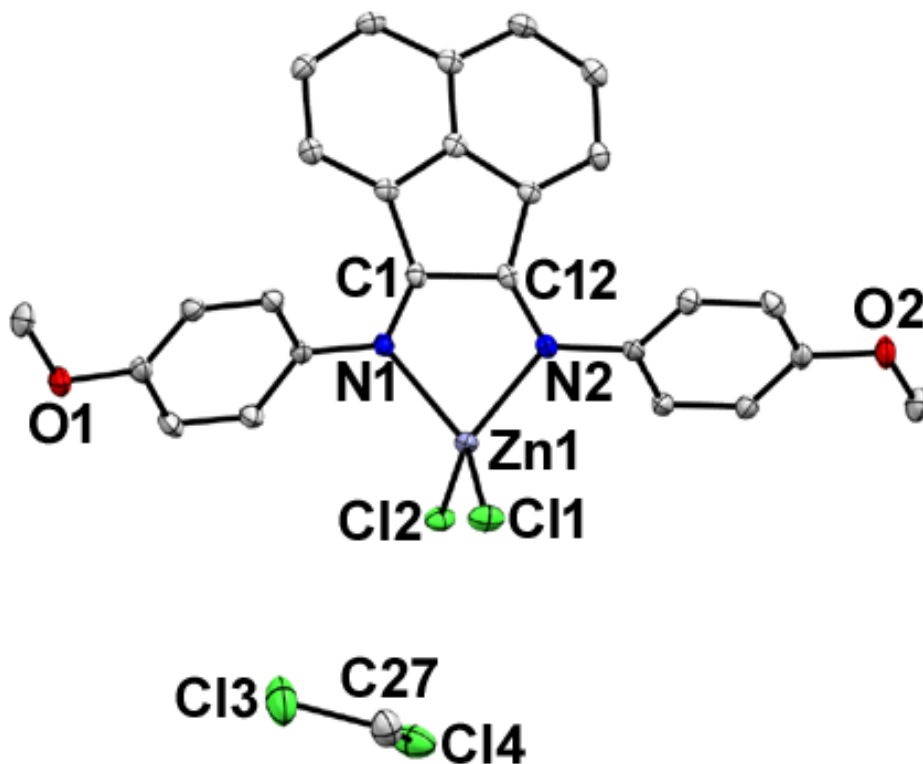


Figure 92: POV-Ray diagram of complex **15-DCM** with thermal ellipsoids displayed at 50% probability. All hydrogen atoms have been removed for clarity.

Suitable crystals of complex **15-DCM** were obtained directly from a slow vapor diffusion of hexanes into a dichloromethane solution. Complex **15-DCM** crystallized with one complex and one dichloromethane solvent molecule in the asymmetric unit in the monoclinic crystal system in the  $P2_1/c$  space group (Figure 92). Complex **15-DCM** featured average C=N double, Zn-N single, and Zn-Cl single bond lengths of 1.285(2) Å, 2.076(2) Å, and 2.211(1) Å, respectively. The average aryl-acenaphthene torsion angle was calculated to be 60.36°. Furthermore, the N(1)-Zn(1)-N(2) and Cl(1)-Zn(1)-Cl(2) angles were found to be 81.34(6)° and 113.20(2)°, respectively.

### 2.2.3.22 4-(methylthio)phenyl-BIAN Zinc Chloride · DCM (16-DCM)

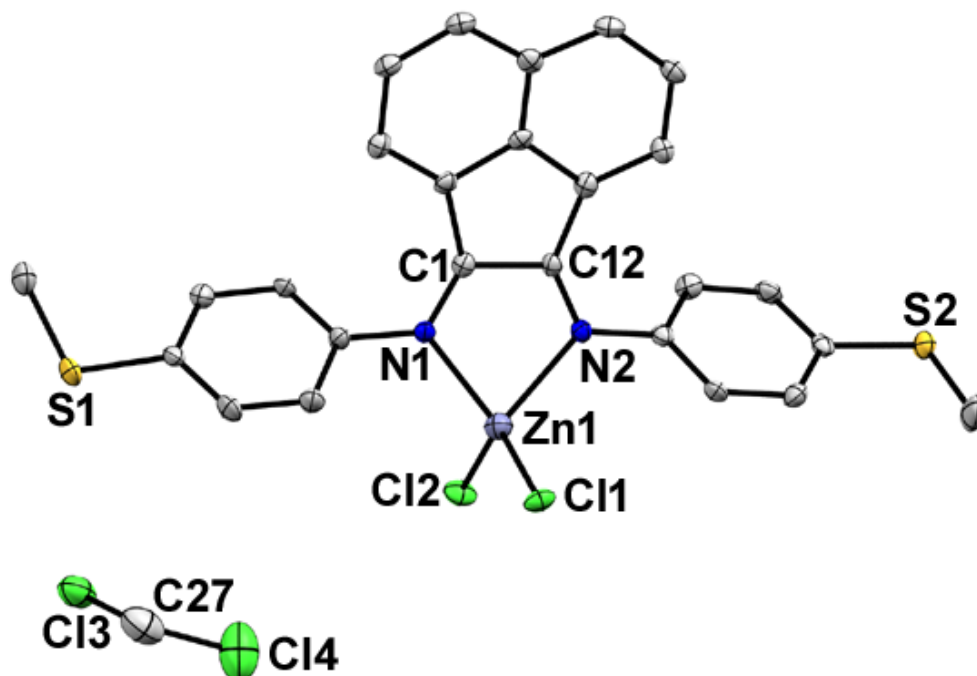


Figure 93: POV-Ray diagram of complex **16-DCM** with thermal ellipsoids displayed at 50% probability. All hydrogen atoms have been removed for clarity.

Suitable crystals of complex **16-DCM** were obtained directly from a slow vapor diffusion of hexanes into a dichloromethane solution. Complex **16-DCM** crystallized with one complex and one dichloromethane solvent molecule in the asymmetric unit in the monoclinic crystal system in the  $P2_1/c$  space group (Figure 93). Complex **16-DCM** featured average C=N double, Zn-N single, and Zn-Cl single bond lengths of 1.281(7) Å, 2.082(5) Å, and 2.210(2) Å, respectively. The average aryl-acenaphthene torsion angle was calculated to be 64.11°. Furthermore, the N(1)-Zn(1)-N(2) and Cl(1)-Zn(1)-Cl(2) angles were found to be 81.35(18)° and 116.80(6)°, respectively.

### 2.2.3.23 4-phenoxyphenyl-BIAN Zinc Chloride · DCM (17-DCM)

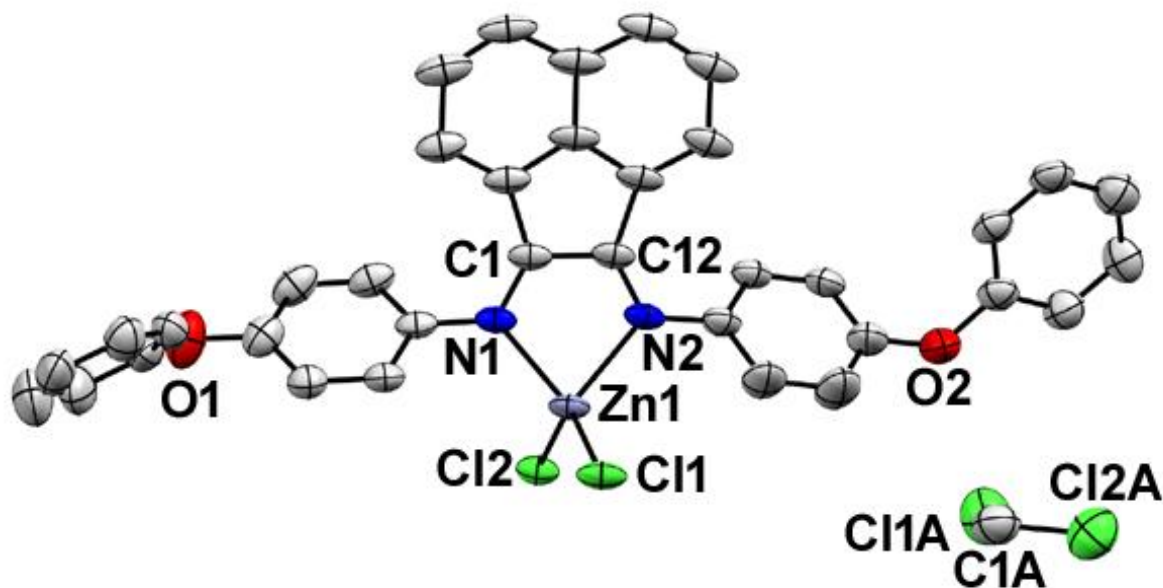


Figure 94: POV-Ray diagram of complex **17-DCM** with thermal ellipsoids displayed at 50% probability. All hydrogen atoms have been removed for clarity.

Suitable crystals of complex **17-DCM** were obtained directly from a slow vapor diffusion of hexanes into a dichloromethane solution. Complex **17-DCM** crystallized with one complex and one dichloromethane solvent molecule in the asymmetric unit in the monoclinic crystal system in the  $I2/a$  space group (Figure 94). Complex **17-DCM** featured average C=N double, Zn-N single, and Zn-Cl single bond lengths of 1.285(5) Å, 2.093(4) Å, and 2.217(2) Å, respectively. The average aryl-acenaphthene torsion angle was calculated to be 58.08°. Furthermore, the N(1)-Zn(1)-N(2) and Cl(1)-Zn(1)-Cl(2) angles were found to be 81.01(14)° and 115.82(4)°, respectively.

### 2.2.3.24 4-fluorophenyl-BIAN Zinc Chloride · THF (18-THF)

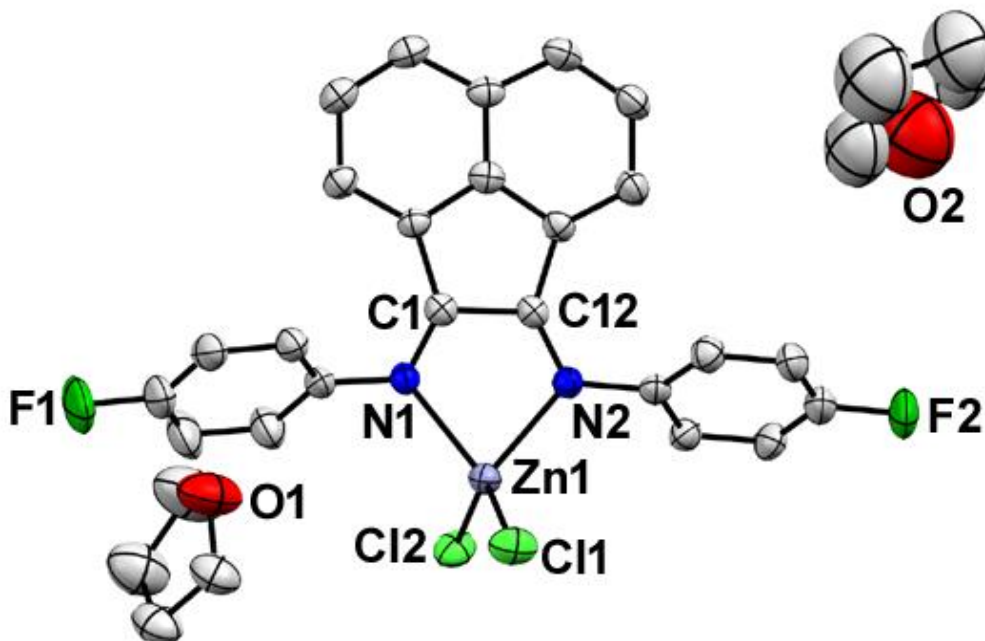


Figure 95: POV-Ray diagram of complex **18-THF** with thermal ellipsoids displayed at 50% probability. All hydrogen atoms have been removed for clarity.

Suitable crystals of complex **18-THF** were obtained directly from a slow vapor diffusion of hexanes into a tetrahydrofuran solution. Complex **18-THF** crystallized with one complex and two tetrahydrofuran solvent molecules in the asymmetric unit in the monoclinic crystal system in the  $P2_1/c$  space group (Figure 95). Complex **18-THF** featured average C=N double, Zn-N single, and Zn-Cl single bond lengths of 1.282(4) Å, 2.092(2) Å, and 2.204(1) Å, respectively. The average aryl-acenaphthene torsion angle was calculated to be 65.21°. Furthermore, the N(1)-Zn(1)-N(2) and Cl(1)-Zn(1)-Cl(2) angles were found to be 80.73(10)° and 119.00(4)°, respectively.



### 2.2.3.25 4-bromophenyl-BIAN Zinc Chloride · DCM (19-DCM)

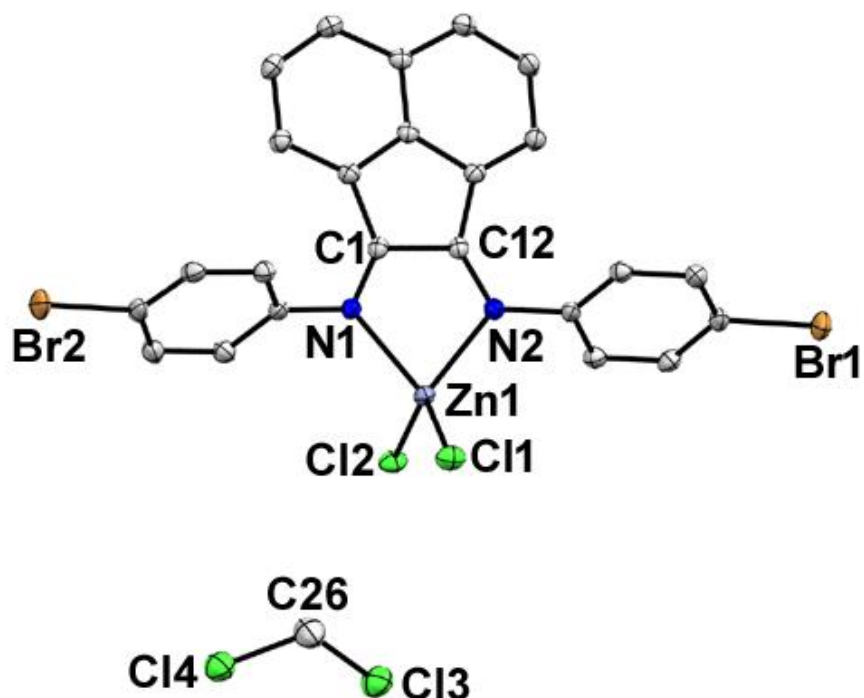


Figure 96: POV-Ray diagram of complex **19-DCM** with thermal ellipsoids displayed at 50% probability. All hydrogen atoms have been removed for clarity.

Suitable crystals of complex **19-DCM** were obtained directly from a slow vapor diffusion of hexanes into a dichloromethane solution. Complex **19-DCM** crystallized with one complex and one dichloromethane solvent molecule in the asymmetric unit in the monoclinic crystal system in the  $P2_1/c$  space group (Figure 96). Complex **19-DCM** featured average C=N double, Zn-N single, and Zn-Cl single bond lengths of 1.281(2) Å, 2.090(2) Å, and 2.204(1) Å, respectively. The average aryl-acenaphthene torsion angle was calculated to be 69.65°. Furthermore, the N(1)-Zn(1)-N(2) and Cl(1)-Zn(1)-Cl(2) angles were found to be 80.98(6)° and 116.24(2)°, respectively.

### 2.2.3.26 4-(trifluoromethoxy)phenyl-BIAN Zinc Chloride · DCM (20-DCM)

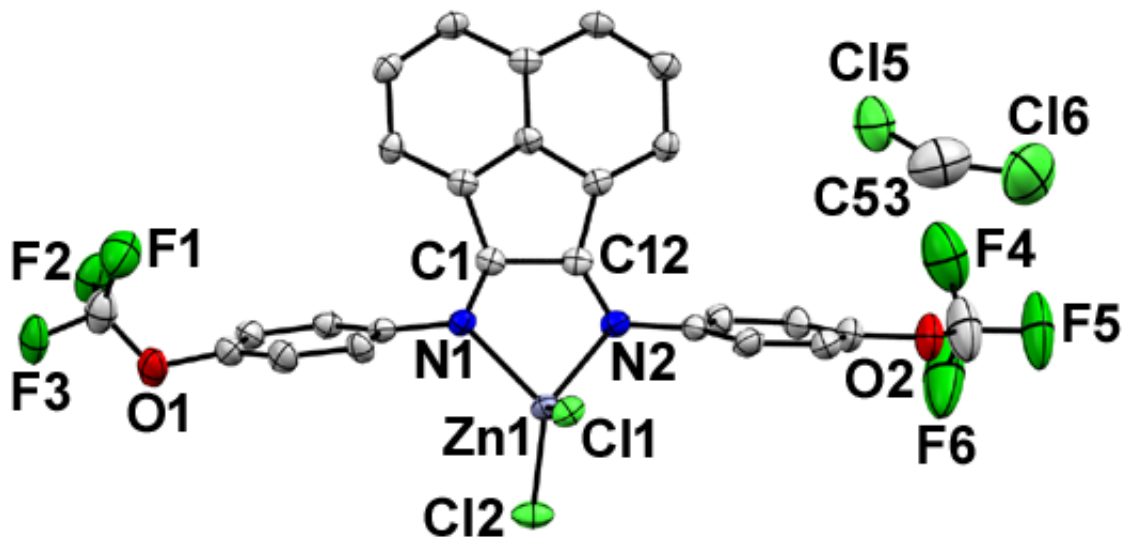


Figure 97: POV-Ray diagram of complex **20-DCM** with thermal ellipsoids displayed at 50% probability. All hydrogen atoms have been removed for clarity. Note however, complex **20-DCM** crystallized with two complexes and two DCM solvent molecules in the asymmetric unit. Only one DCM and one complex are displayed for clarity.

Suitable crystals of complex **20-DCM** were obtained directly from a slow vapor diffusion of hexanes into a dichloromethane solution. Complex **20-DCM** crystallized with two complexes and two dichloromethane solvent molecule in the asymmetric unit in the triclinic crystal system in the P-1 space group (Figure 97). Complex **20-DCM** featured average C=N double, Zn-N single, and Zn-Cl single bond lengths of 1.287(7) Å, 2.086(5) Å, and 2.207(2) Å, respectively. The average aryl-acenaphthene torsion angle was calculated to be 64.68°. Furthermore, the N(1)-Zn(1)-N(2) and Cl(1)-Zn(1)-Cl(2) angles were found to be 81.36(17)° and 118.33(6)°, respectively.

### 2.2.3.27 4-(trifluoromethyl)phenyl-BIAN Zinc Chloride · DCM (21-DCM)

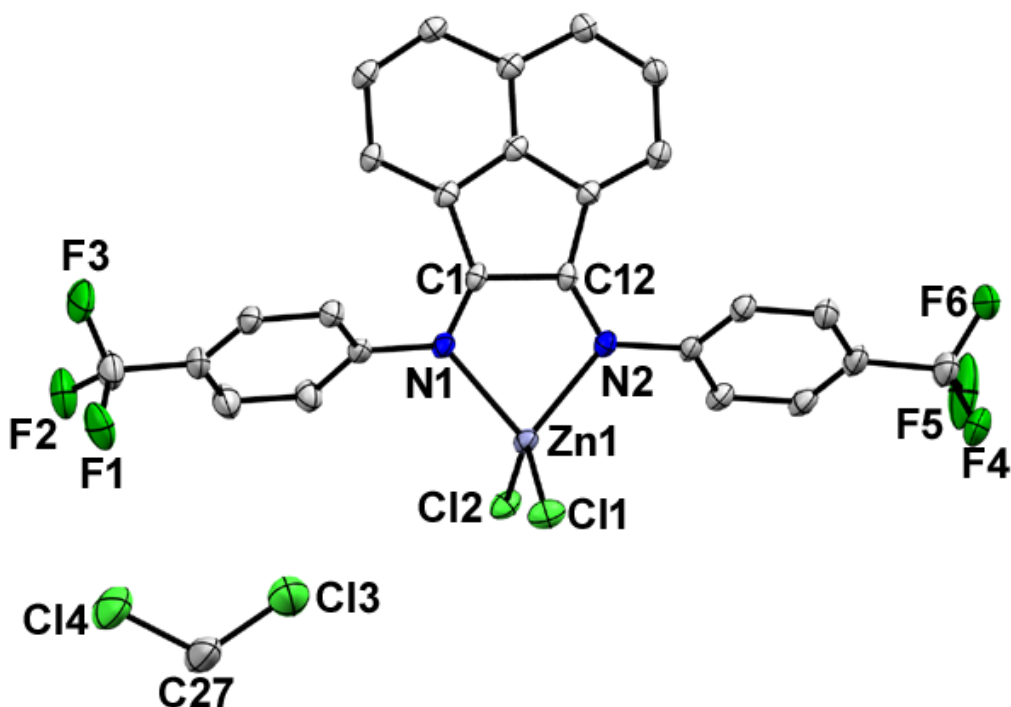


Figure 98: POV-Ray diagram of complex **21-DCM** with thermal ellipsoids displayed at 50% probability. All hydrogen atoms have been removed for clarity.

Suitable crystals of complex **21-DCM** were obtained directly from a slow vapor diffusion of hexanes into a dichloromethane solution. Complex **21-DCM** crystallized with one complex and one dichloromethane solvent molecule in the asymmetric unit in the monoclinic crystal system in the  $P2_1/c$  space group (Figure 98). Complex **21-DCM** featured average C=N double, Zn-N single, and Zn-Cl single bond lengths of 1.280(3) Å, 2.092(2) Å, and 2.203(1) Å, respectively. The average aryl-acenaphthene torsion angle was calculated to be 68.47°. Furthermore, the N(1)-Zn(1)-N(2) and Cl(1)-Zn(1)-Cl(2) angles were found to be 80.89(7)° and 118.10(2)°, respectively.

### 2.2.3.28 X-ray Powder Patterns for Complexes 10-13

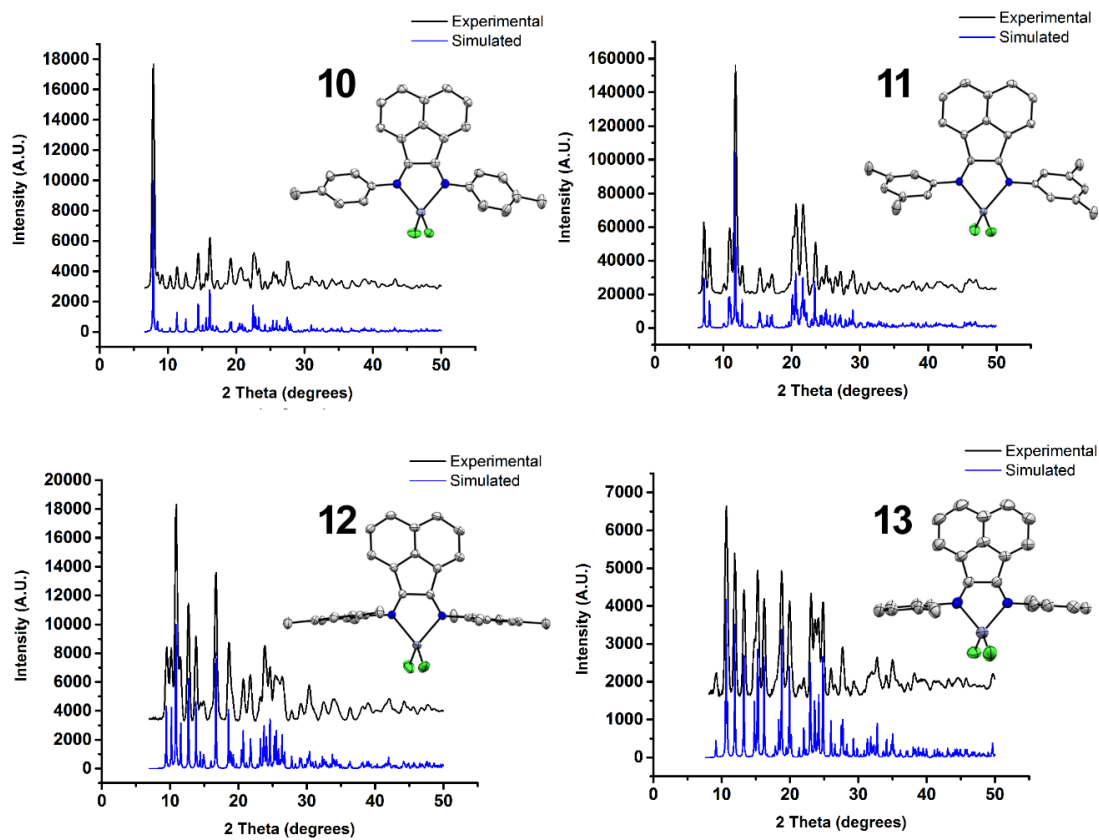


Figure 99: Experimental (black) and simulated (blue) X-ray powder pattern for complexes **10-13**. Experimental and simulated powder patterns are in acceptable agreement.<sup>82</sup>

### 2.2.3.29 X-ray Powder Patterns for Complexes 10-CHCl<sub>3</sub>-10-MeCN

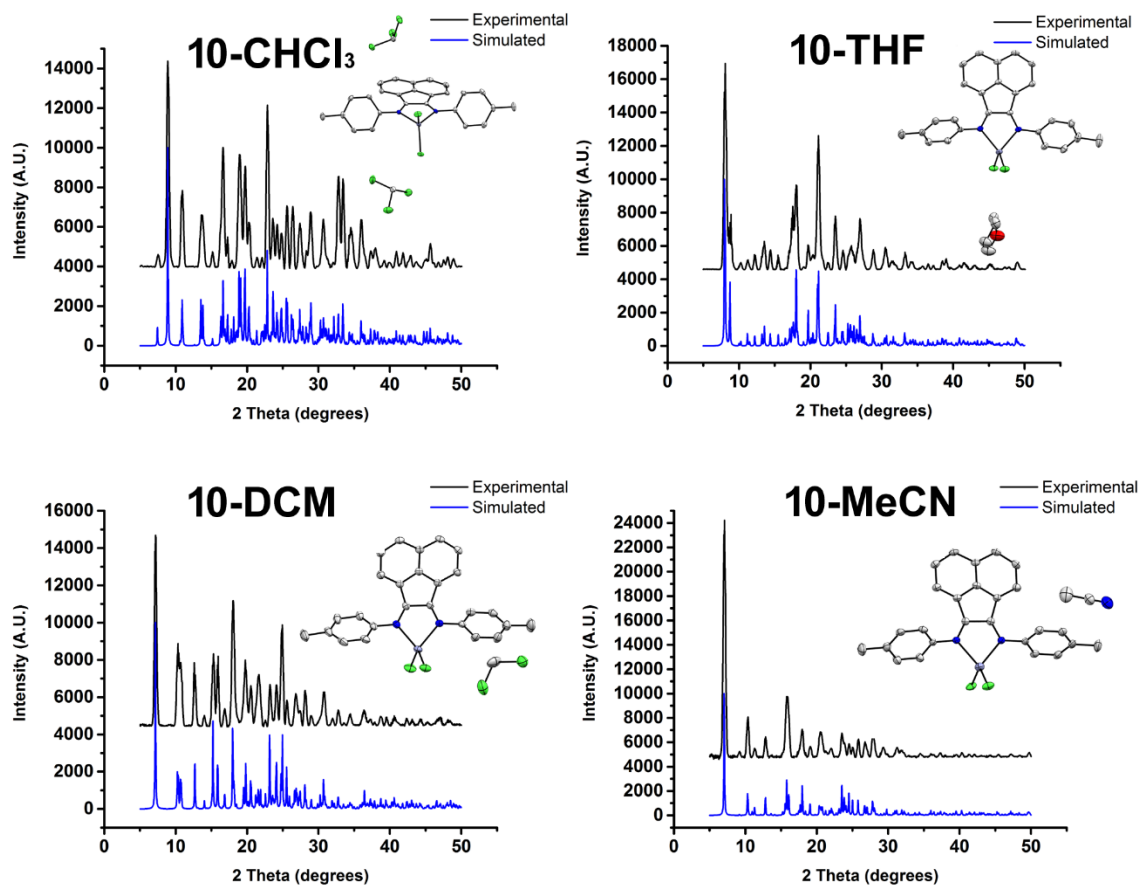


Figure 100: Experimental (black) and simulated (blue) X-ray powder pattern for complexes **10-CHCl<sub>3</sub>-10-MeCN**. Experimental and simulated powder patterns are in acceptable agreement.<sup>82</sup>

### 2.2.3.30 X-ray Powder Patterns for Complexes 11-CHCl<sub>3</sub>-11-MeCN

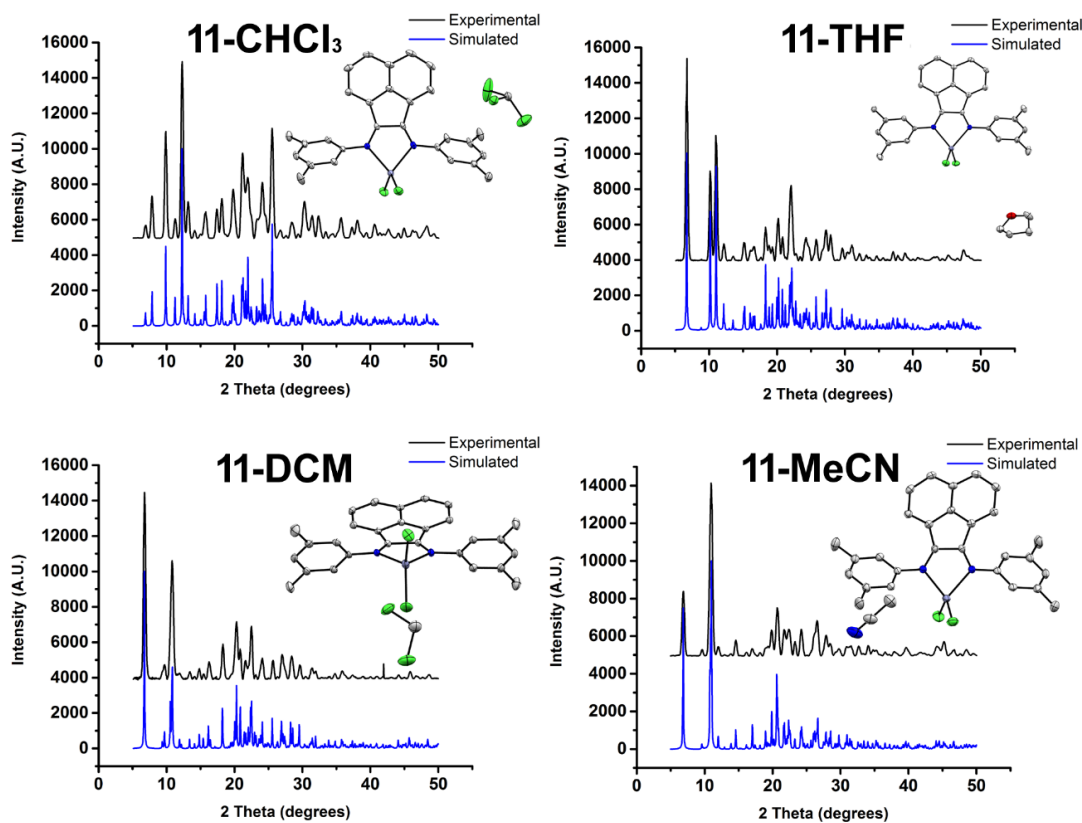


Figure 101: Experimental (black) and simulated (blue) X-ray powder pattern for complexes 11-CHCl<sub>3</sub>-11-MeCN. Experimental and simulated powder patterns are in acceptable agreement.<sup>82</sup>

### 2.2.3.31 X-ray Powder Patterns for Complexes 14-17

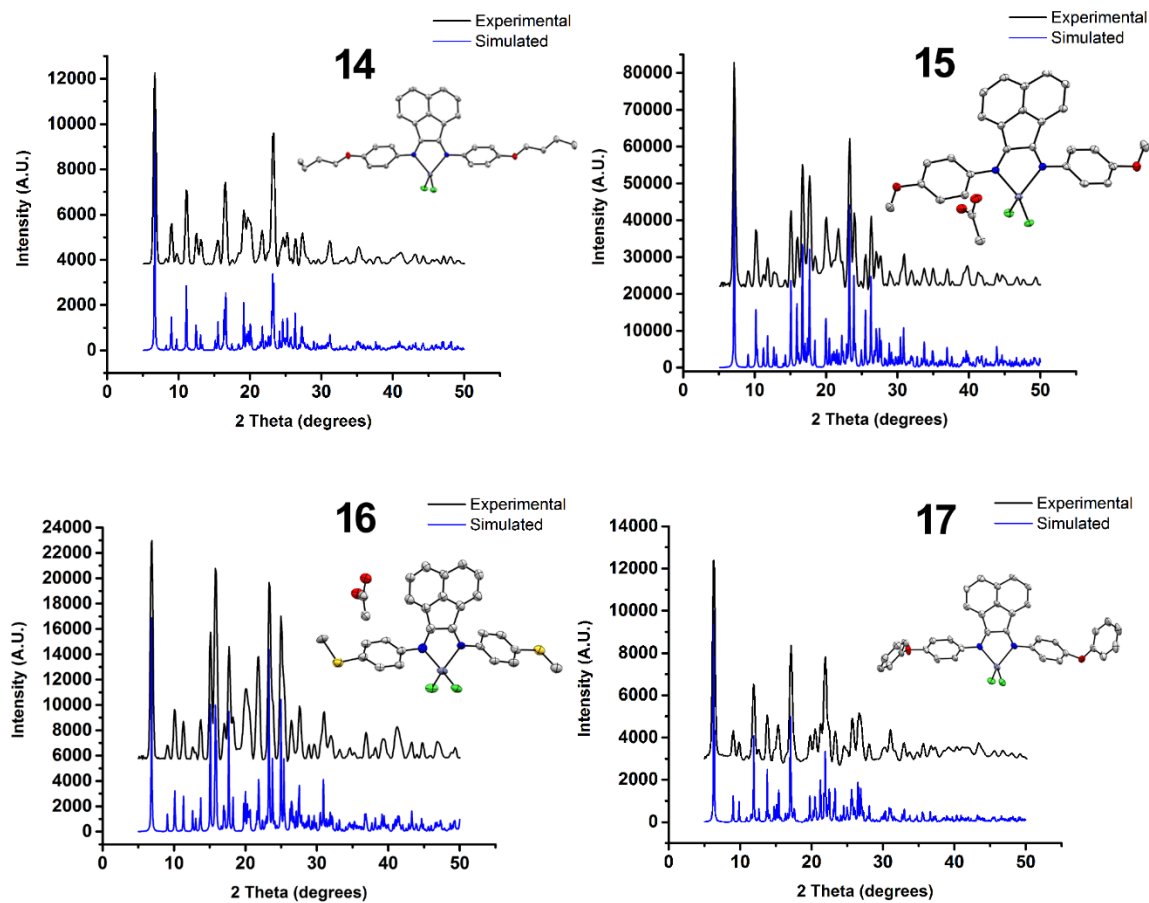


Figure 102: Experimental (black) and simulated (blue) X-ray powder pattern for complexes **14-17**. Experimental and simulated powder patterns are in acceptable agreement.<sup>82</sup>

### 2.2.3.32 X-ray Powder Patterns for Complexes 18, 20, and 21

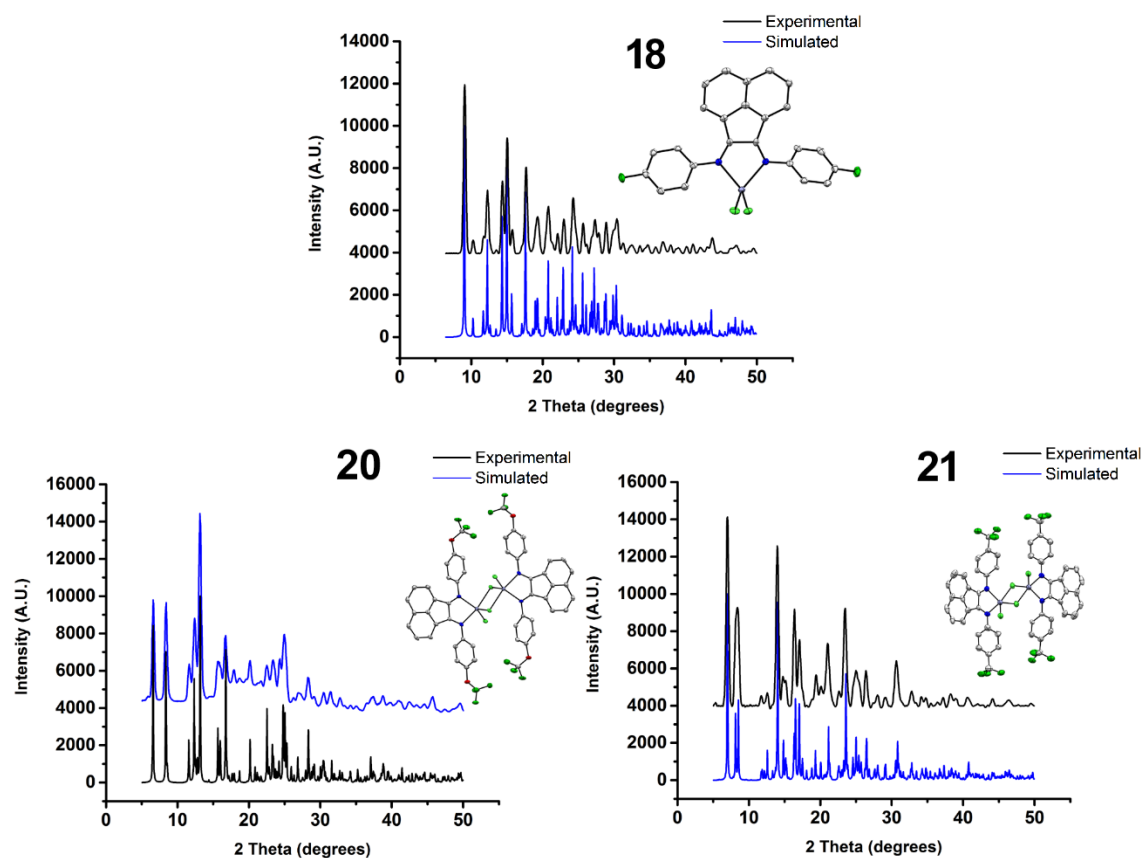


Figure 103: Experimental (black) and simulated (blue) X-ray powder pattern for complexes **18**, **20**, and **21**. Experimental and simulated powder patterns are in acceptable agreement.<sup>82</sup>



### 2.2.3.33 X-ray Powder Patterns for Complexes 14-DCM-17-DCM

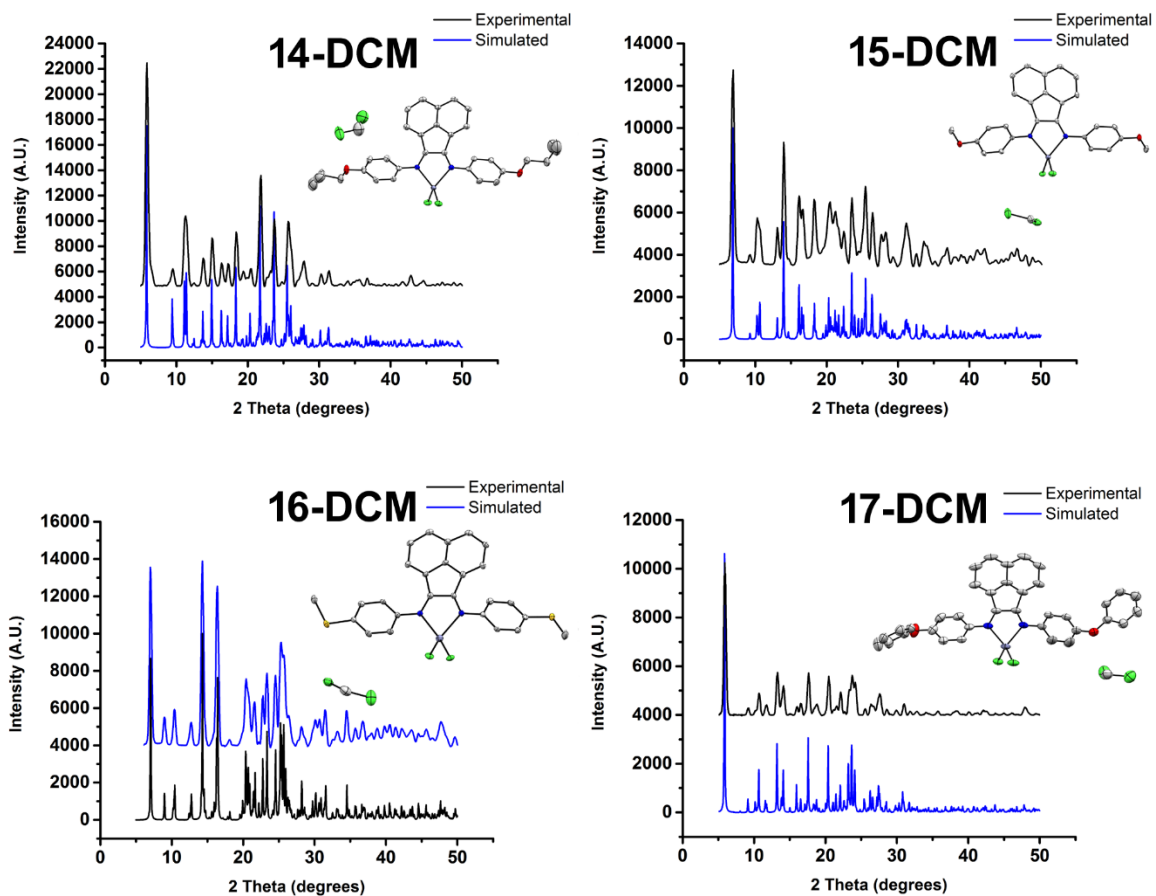


Figure 104: Experimental (black) and simulated (blue) X-ray powder pattern for complexes **14-DCM-17-DCM**. Experimental and simulated powder patterns are in acceptable agreement.<sup>82</sup>

### 2.2.3.34 X-ray Powder Patterns for Complexes 18-THF-21-DCM

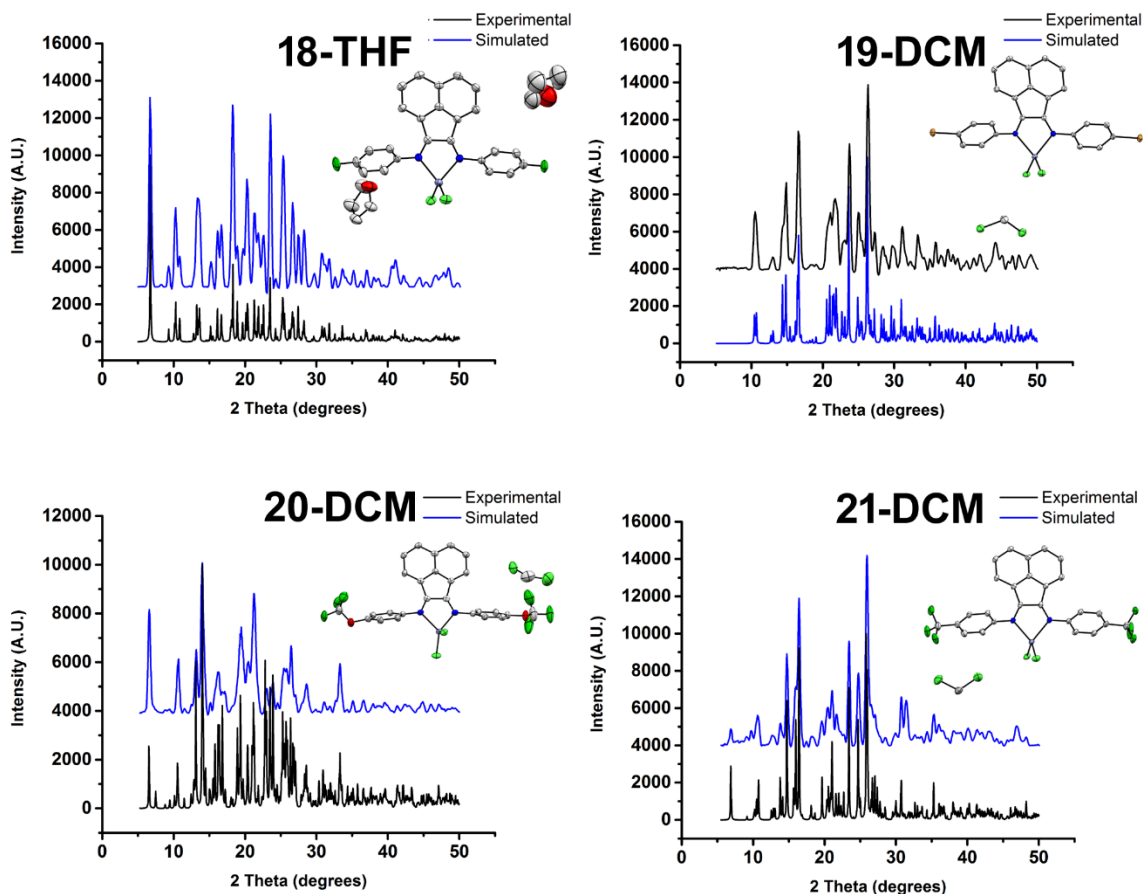


Figure 105: Experimental (black) and simulated (blue) X-ray powder pattern for complexes **19-THF-21-DCM**. Experimental and simulated powder patterns are in acceptable agreement.<sup>82</sup>

## 2.3 CONCLUSIONS

In conclusion, the solid state photophysical properties of a series of Ar-BIAN zinc chloride complexes were investigated. Initially, four methylated aryl substituents were chosen to gain a further understanding of the origin of the solid state emissions from the Ar-BIAN zinc chloride complexes. As a result of different crystal packing environments, Ar-BIAN zinc complexes that had *para*- and *meta*-substituted methyl substituents were found to be emissive in the solid state. On the other hand, Ar-BIAN zinc chloride complexes featuring methyl substituents in the *ortho*-position were found to be nonemissive. These results were confirmed on the basis of a detailed crystallographic study in conjunction with TD-DFT calculations.

A subsequent study of a series of *para*-substituted Ar-BIAN zinc complexes, demonstrated that the tunability of color was possible via modification of the electronic properties at the periphery of the BIAN ligand. Electron donating groups were shown to exhibit red and orange emissions, while electron withdrawing groups displayed yellow emissions. Solvatomorphism was also employed in order to further tune the solid state photophysical properties of the Ar-BIAN zinc complexes. This was highlighted by the difference between complexes **18** and **18-THF**, which displayed an approximate 30 nm shift in the emission color from orange to yellow, respectively.

## 2.4 EXPERIMENTAL

### 2.4.1 General Procedures

All reactions were performed in the ambient atmosphere with glassware that was oven dried and flushed with argon gas prior to use. Each BIAN zinc complex was synthesized according to the pertinent literature procedures (**10**<sup>5</sup>, **11**<sup>5</sup>, **12**<sup>5</sup>, **13**<sup>14</sup>, **15**<sup>87</sup>, **18**<sup>42</sup>,

**19**<sup>50</sup>, and **21**<sup>88</sup>). The BIAN complexes **14**, **16**, **17**, and **20** are new complexes first reported in this work.

#### **2.4.2 Physical Measurements**

All of the NMR spectra were recorded at 298 K on either a Varian DirectDrive instrument (<sup>1</sup>H NMR, 599.75 MHz; <sup>13</sup>C NMR, 150.82 MHz), a Varian INOVA instrument (<sup>1</sup>H NMR, 499.87 MHz; <sup>13</sup>C NMR, 125.71 MHz; <sup>19</sup>F 469.85 MHz), an Agilent MR instrument (<sup>1</sup>H NMR, 399.77 MHz; <sup>13</sup>C NMR, 100.52 MHz; <sup>19</sup>F 469.85 MHz), or a Varian Unity Instrument (<sup>1</sup>H NMR, 399.14 MHz; <sup>13</sup>C NMR, 75.47 MHz; <sup>19</sup>F 282.41 MHz) using residual solvent as the internal reference. The deuterated chloroform, dichloromethane, and dimethylsulfoxide solvents were purchased from Cambridge Isotopes Laboratories, Inc. and stored over 4 Å molecular sieves. The high-resolution chemical ionization mass spectral data (HRMS-CI) were collected on a Micromass Autospec Ultima mass spectrometer. The melting points of **10-21** were determined using a Mel-Temp apparatus. Samples of complexes **10-21** were sent to Midwest Microlab, LLC for C, H, and N elemental analyses.

#### **2.4.3 Fluorescence Spectroscopy**

All of the solid state fluorescence spectroscopy experiments were performed on a Photon Technology International QM 4 spectrophotometer equipped with a 6-inch diameter K Sphere-B integrating sphere. The crystalline powders of **10-21** were loaded into quartz EPR tubes for measurement purposes, and their chemical identities were confirmed by powder X-ray crystallography. All solvatomorph samples were loaded into quartz EPR tubes and subsequently covered with mineral oil to maintain crystallinity, with the exception of the 4-OCF<sub>3</sub> crystals which were kept in their mother liquor in order

to retain crystallinity. The absolute quantum yield measurements were made by using a 6-inch diameter K Sphere-B integrating sphere. The absolute quantum yield values were calculated by dividing the integrated area under each emission curve by the respective excitation peak of each sample.  $[(\text{Area}_{\text{sample emission}} / (\text{Area}_{\text{BaSO}_4 \text{ blank excitation}} - \text{Area}_{\text{sample excitation}}))]$ . The relative quantum yield values were calculated based on the ratio of the emission intensities. The intensity of the emission peak for each solvatomorph was integrated and compared with that of the non-solvated complex for which the absolute quantum yield had been measured directly. All graphs were constructed using the OriginPro 9.1 Student Version 64bit program.

#### 2.4.4 Single Crystal and Powder X-ray Crystallography

In the cases of compounds **10-12**, **14-18**, **20**, and **21** suitable single crystals could be obtained directly from each reaction mixture. Suitable crystals of complex **13** were grown via slow evaporation of a dichloromethane solution of this complex. Each solvatomorph crystal (**14-DCM-21-DCM**) was grown from the appropriate solvent. In each case, the single crystals were removed from their respective vials, covered with mineral oil, and mounted separately on nylon thread loops. The X-ray diffraction data were collected on either an Agilent Technologies SuperNova Dual Source diffractometer using a  $\mu$ -focus Cu K $\alpha$  radiation source ( $\lambda = 1.5418 \text{ \AA}$ ) equipped with collimating mirror monochromators that operated at 147 K, 133K, or 100K, or on a Rigaku AFC12 Saturn 724+ CCD diffractometer equipped with a Rigaku XStream low temperature device that operated at 100 K, or on a Rigaku SCX-Mini diffractometer equipped with a Rigaku XStream low temperature device that operated at 153 K. Both Rigaku instruments used a graphite-monochromated Mo K $\alpha$  radiation source ( $\lambda = 0.71075 \text{ \AA}$ ). All powder X-ray diffraction data were collected on an Agilent Technologies SuperNova Dual Source

diffractometer. Data collection, unit cell refinement, and data reduction were performed using the Agilent Technologies CrysAlisPro V 1.171.37.31 program.<sup>89</sup> The structures were solved by direct methods and refined by full-matrix least-squares cycles on  $F^2$  using the Siemens SHELXTL PLUS 5.0 (PC) software package<sup>44</sup> and PLATON<sup>45</sup>. All non-hydrogen atoms were refined anisotropically. The hydrogen atoms were placed in fixed, calculated positions using a riding model, which were observed in a  $\Delta F$  map and refined with isotropic displacement parameters. The POV-Ray images were created using the Mercury version 3.3 program. The crystallographic details concerning the solvatomorph  $\pi$ - $\pi$  interactions were calculated using the Mercury version 3.3 program. All powder X-ray diffraction (XRD) graphs were constructed using the OriginPro 9.1 Student Version 64 bit program and the Eva program version 15.0.0.0. All simulated powder XRD graphs were created using Mercury version 3.3 program.

#### **2.4.5 Diffuse Reflectance and UV/vis Absorption Spectroscopy**

All diffuse-reflectance measurements were performed by our collaborator Professor Ignacio Vargas-Baca at McMaster University using an illuminated (tungsten-halogen light source) integrating sphere (Ocean Optics ISP-REF) attached to a photodiode array spectrophotometer (Ocean Optics SD 2000). All data were reported relative to a  $\text{BaSO}_4$  standard. Each measurement was integrated over 3 ms and corrected for stray light and dark current. The raw data were used to calculate the reflectance ( $R$ ) using Grams/AI (version 8.0). The Kubelka-Munk function ( $[1-R]^2/2R$ ) was evaluated in Excel. All UV/vis absorption experiments were performed at the University of Texas at Austin using a Varian Cary 6000i UV-VIS-NIR spectrophotometer. All UV/vis graphs were constructed using the OriginPro 9.1 Student Version 64bit program.

## 2.4.6 Density Functional Theory

The density functional theory calculations were performed by our collaborator Professor Ignacio Vargas-Baca at McMaster using the ADF DFT package (version 2013).<sup>46,47</sup> A model of the pi-stacked dimer of complex **10** was built from the crystallographic coordinates and the positions of all non-carbon atoms were optimized using the exchange-correlation functional of Perdew, Burke, and Ernzerhof<sup>90</sup> and corrected for dispersion<sup>91</sup> with a triple- $\zeta$  all-electron basis set with two polarization functions and applying the Zeroth Order Regular Approximation (ZORA)<sup>92-96</sup> formalism with specially adapted basis sets. In the interest of expediency, the lowest 80 singlet-singlet and lowest 80 singlet-triplet electronic excitations<sup>97,98</sup> were calculated using time-dependent density functional theory (TD-DFT) under the Statistical Average of different model Potentials for occupied KS Orbitals (SAOP).<sup>99-101</sup>

## 2.4.7 Fluorescent Microscopy

The fluorescent microscopy was performed on a Zeiss Axiovert200M Epifluorescent Microscope. The crystalline solvatomorph samples were excited using a FITC filter cube. The fluorescent microscopy images were created using the program Axiovision 4.6.

## 2.4.8 Synthesis of 10-21

### 2.4.8.1 4-methylphenyl-BIAN Zinc Chloride (10)

A mixture of acenaphthenequinone (1.00 g, 5.49 mmol) and anhydrous zinc chloride (2.02 g, 14.82 mmol) was suspended in 10 mL of glacial acetic acid, thereby generating a yellow suspension. The yellow suspension was heated to 60 °C and *p*-toluidine (1.42 mL, 12.63 mmol) was added, following which the resulting solution was

refluxed for 1 hour. The precipitate that had formed during the reaction was filtered off and washed sequentially with water and diethyl ether. The resulting crystalline yellow-orange powder was collected and used without further purification for a single crystal X-ray diffraction study (2.18 g, 80%).

HRMS (CI, CH<sub>4</sub>): calcd for [M - Cl]<sup>+</sup> [C<sub>26</sub>H<sub>20</sub>N<sub>2</sub>ZnCl]<sup>+</sup> *m/z* 459.0606; found 459.0605; <sup>1</sup>H NMR (CDCl<sub>3</sub>): δ 2.464 (s, 6H, CH<sub>3</sub>), 7.363 (d, 4H, Ar-H, *J* = 8.0 Hz), 7.511 (d, 4H, Ar-H, *J* = 8.0 Hz), 7.598 (t, 2H, Ar-H, *J* = 7.7 Hz), 7.650 (d, 2H, Ar-H, *J* = 7.2 Hz), 8.132 (d, 2H, Ar-H, *J* = 8.1 Hz). <sup>13</sup>C NMR (CDCl<sub>3</sub>): δ 21.35, 121.69, 125.33, 125.96, 128.56, 130.66, 131.14, 132.26, 139.20, 141.07, 144.88, 161.85. MP = 344 °C. Anal. Calcd. for C<sub>26</sub>H<sub>20</sub>N<sub>2</sub>ZnCl<sub>2</sub>: C, 62.87; H, 4.06; N, 5.64. Found: C, 62.84; H, 3.99; N, 5.54.

#### 2.4.8.2 3,5-dimethylphenyl-BIAN zinc chloride (11)

A mixture of acenaphthenequinone (1.00 g, 5.49 mmol) and anhydrous zinc chloride (2.02 g, 14.82 mmol) was suspended in 10 mL glacial acetic acid, thereby generating a yellow suspension. The yellow suspension was heated to 60 °C and 3,5-dimethylaniline (1.49 mL, 12.63 mmol) was added, following which the resulting solution was refluxed for 1 hour. The precipitate that had formed during the reaction was filtered off and washed sequentially with water and diethyl ether. The resulting crystalline yellow powder was collected and used without further purification for a single crystal X-ray diffraction study (1.84 g, 64%).

HRMS (CI, CH<sub>4</sub>): calcd for [M - Cl]<sup>+</sup> [C<sub>28</sub>H<sub>24</sub>N<sub>2</sub>ZnCl]<sup>+</sup> *m/z* 487.0919; found 487.0913; <sup>1</sup>H NMR (CDCl<sub>3</sub>): δ 2.404 (s, 12H, CH<sub>3</sub>), 7.102 (s, 2H, Ar-CH<sub>3</sub>), 7.179 (s, 4H, Ar-CH<sub>3</sub>), 7.536 (d, 2H, Ar-H, *J* = 6.5 Hz), 7.607 (d, 2H, Ar-H, *J* = 7.8 Hz), 8.147 (d, 2H, Ar-H, *J* = 8.2 Hz). <sup>13</sup>C NMR (CDCl<sub>3</sub>): δ 21.38, 118.82, 125.27, 126.05, 128.60, 130.37,



131.08, 132.19, 140.03, 162.12. MP = 321 °C. Anal. Calcd. for C<sub>28</sub>H<sub>24</sub>N<sub>2</sub>ZnCl<sub>2</sub>: C, 64.08; H, 4.61; N, 5.34. Found: C, 64.06; H, 4.62; N, 5.28.

#### 2.4.8.3 2,4,6-trimethylphenyl-BIAN zinc chloride (12)

A mixture of acenaphthenequinone (1.00 g, 5.49 mmol) and anhydrous zinc chloride (2.02 g, 14.82 mmol) was suspended in 10 mL of glacial acetic acid, thereby generating a yellow suspension. The yellow suspension was heated to 60 °C and 2,4,6-trimethylphenylaniline (1.64 mL, 12.63 mmol) was added, following which the resulting solution was refluxed for 1 hour. The precipitate that had formed during the reaction was filtered off and washed sequentially with water and diethyl ether. The resulting crystalline red powder was collected and used without further purification for a single crystal X-ray diffraction study (2.69 g, 89%).

HRMS (CI, CH<sub>4</sub>): calcd for [M - Cl]<sup>+</sup> [C<sub>30</sub>H<sub>28</sub>N<sub>2</sub>ZnCl]<sup>+</sup> *m/z* 515.1232; found 515.1237; <sup>1</sup>H NMR (CDCl<sub>3</sub>): δ 2.313 (s, 12H, CH<sub>3</sub>), 2.405 (s, 6H, CH<sub>3</sub>), 6.936 (d, 2H, Ar-H, *J* = 7.4 Hz), 7.063 (s, 4H, Ar-H), 7.602 (dd, 2H, Ar-H, *J* = 7.8 Hz, 1.0 Hz), 8.153 (d, 2H, Ar-H, *J* = 8.0 Hz). <sup>13</sup>C NMR (CDCl<sub>3</sub>): δ 18.36, 21.02, 125.57, 125.87, 128.36, 129.33, 129.97, 130.97, 132.36, 137.24, 140.28, 144.43, 164.20. MP = 384°C. Anal. Calcd. for C<sub>30</sub>H<sub>28</sub>N<sub>2</sub>ZnCl<sub>2</sub>: C, 65.18; H, 5.11; N, 5.07. Found: C, 65.18; H, 5.13; N, 5.02.

#### 2.4.8.4 2-methylphenyl-BIAN zinc chloride (13)

A mixture of acenaphthenequinone (1.00 g, 5.49 mmol) and anhydrous zinc chloride (2.02 g, 14.82 mmol) was suspended in 10 mL of glacial acetic acid, thereby generating a yellow suspension. The yellow suspension was heated to 60 °C and *o*-toluidine (1.35 mL, 12.63 mmol) was added, following which the resulting solution was refluxed for 1 hour. The precipitate that had formed during the reaction was filtered off

and washed sequentially with water and diethyl ether. The resulting crystalline yellow powder was collected and subsequently recrystallized using dichloromethane. The resulting crop of crystals proved to be suitable for a single crystal X-ray diffraction study. (1.47 g, 53%).

HRMS (CI, CH<sub>4</sub>): calcd for [M - Cl]<sup>+</sup> [C<sub>26</sub>H<sub>20</sub>N<sub>2</sub>ZnCl]<sup>+</sup> *m/z* 459.0606; found 459.0610; <sup>1</sup>H NMR (CDCl<sub>3</sub>): δ 2.355 (s, 6H, CH<sub>3</sub>), 6.974 (apparent dd, 2H, Ar-H, *J* = 7.2 Hz), 7.391 (m, 8H, Ar-H), 7.573 (dd, 2H, Ar-H, *J* = 8.3 Hz, *J* = 1.0 Hz), 8.133 (d, 2H, Ar-H, *J* = 8.1 Hz). <sup>13</sup>C NMR (CDCl<sub>3</sub>): δ 18.04, 18.28, 120.63, 120.93, 125.50, 125.51, 126.10, 127.74, 127.83, 128.08, 128.11, 128.76, 128.94, 129.12, 131.00, 132.02, 131.66, 131.68, 132.40, 132.42, 143.37, 143.41, 144.85, 144.89, 163.51, 163.52. MP 359 °C. Anal. Calcd. for C<sub>26</sub>H<sub>20</sub>N<sub>2</sub>ZnCl<sub>2</sub>: C, 62.87; H, 4.06; N, 5.64. Found: C, 62.80; H, 4.13; N, 5.59.

#### 2.4.8.5 4-butoxyphenyl-BIAN zinc chloride (14)

A mixture of acenaphthenequinone (1.00 g, 5.49 mmol) and anhydrous zinc chloride (2.02 g, 14.82 mmol) was suspended in 10 mL of glacial acetic acid, thereby generating a yellow suspension. The yellow suspension was heated to 60 °C and 4-butoxyaniline (2.10 mL, 12.63 mmol) was added, following which the resulting solution was refluxed for 1 hour. The red precipitate that had formed during the reaction was filtered off and washed sequentially with water and diethyl ether. The resulting red crystalline powder was collected and used without further purification for a single crystal X-ray diffraction study (2.94 g, 88%).

HRMS (CI, CH<sub>4</sub>): calcd for [M - Cl]<sup>+</sup> [C<sub>32</sub>H<sub>32</sub>N<sub>2</sub>O<sub>2</sub>ZnCl]<sup>+</sup> *m/z* 575.1444; found 575.1434; <sup>1</sup>H NMR (CD<sub>2</sub>Cl<sub>2</sub>): δ 1.023 (t, 6H, CH<sub>3</sub>, *J* = 7.4 Hz), 1.542 (m, 4H, CH<sub>2</sub>), 1.840 (m, 4H, CH<sub>2</sub>), 4.095 (t, 4H, CH<sub>2</sub>, *J* = 6.5 Hz), 7.122 (d, 4H, Ar-H, *J* = 9.0 Hz),

7.632 (m, 6H, Ar-H), 7.844 (d, 2H, Ar-H,  $J = 7.4$  Hz), 8.191 (d, 2H, Ar-H,  $J = 7.8$  Hz).  $^{13}\text{C}$  NMR ( $\text{CD}_2\text{Cl}_2$ ):  $\delta$  13.58, 19.20, 31.22, 68.30, 115.68, 123.65, 125.39, 125.61, 128.44, 131.18, 132.26, 136.22, 144.62, 159.96, 161.41. Anal. Calcd. for  $\text{C}_{32}\text{H}_{32}\text{N}_2\text{O}_2\text{ZnCl}_2$ : C, 62.71; H, 5.26; N, 4.57. Found: C, 62.72; H, 5.24; N, 4.62. MP = 310 °C (decomp).

#### 2.4.8.6 4-methoxyphenyl-BIAN zinc chloride (15)

A mixture of acenaphthenequinone (1.00 g, 5.49 mmol) and anhydrous zinc chloride (2.02 g, 14.82 mmol) was suspended in 10 mL of glacial acetic acid, thereby generating a yellow suspension. The yellow suspension was heated to 60 °C and *p*-anisidine (1.55 g, 12.63 mmol) was added, following which the resulting solution was refluxed for 1 hour. The red precipitate that had formed during the reaction was filtered off and washed sequentially with water and diethyl ether. The resulting red crystalline powder was collected and used without further purification for a single crystal X-ray diffraction study (2.17 g, 75%).

HRMS (CI,  $\text{CH}_4$ ): calcd for  $[\text{M} - \text{Cl}]^+ [\text{C}_{26}\text{H}_{20}\text{N}_2\text{O}_2\text{ZnCl}]^+ m/z$  491.0505; found 491.0497;  $^1\text{H}$  NMR ( $\text{CDCl}_3$ ):  $\delta$  3.923 (s, 6H,  $\text{CH}_3$ ), 7.095 (d, 4H, Ar-H,  $J = 6.8$  Hz), 7.642 (m, 6H, Ar-H), 7.818 (d, 2H, Ar-H,  $J = 7.3$  Hz), 8.158 (d, 2H, Ar-H,  $J = 8.3$  Hz).  $^{13}\text{C}$  NMR ( $\text{CDCl}_3$ ):  $\delta$  56.11, 115.63, 124.02, 125.74, 126.07, 128.88, 131.60, 132.72, 136.85, 145.09, 160.72, 161.99. Anal. Calcd. for  $\text{C}_{26}\text{H}_{20}\text{N}_2\text{O}_2\text{ZnCl}_2 \cdot \text{C}_2\text{H}_4\text{O}_2$ : C, 57.12; H, 4.11; N, 4.76. Found: C, 57.19; H, 3.94; N, 4.67. MP = 299 °C (decomp).

#### 2.4.8.7 4-(methylthio)phenyl-BIAN zinc chloride (16)

A mixture of acenaphthenequinone (1.00 g, 5.49 mmol) and anhydrous zinc chloride (2.02 g, 14.82 mmol) was suspended in 10 mL of glacial acetic acid, thereby

generating a yellow suspension. The yellow suspension was heated to 60 °C and 4-(methylthio)aniline (1.57 mL, 12.63 mmol) was added, following which the resulting solution was refluxed for 1 hour. The dark red precipitate that had formed during the reaction was filtered off and washed sequentially with water and diethyl ether. The resulting dark red crystalline powder was collected and used without further purification for a single crystal X-ray diffraction study (2.86 g, 93%).

HRMS (CI, CH<sub>4</sub>): calcd for [M - Cl]<sup>+</sup> [C<sub>26</sub>H<sub>20</sub>N<sub>2</sub>S<sub>2</sub>ZnCl]<sup>+</sup> *m/z* 523.0048; found 523.0032; <sup>1</sup>H NMR (CDCl<sub>3</sub>): δ 2.566 (s, 6H, CH<sub>3</sub>), 7.409 (d, 2H, Ar-H, *J* = 8.6 Hz), 7.580 (d, 2H, Ar-H, *J* = 9.0 Hz), 7.628 (t, 2H, Ar-H, *J* = 8.1 Hz), 7.409 (d, 2H, Ar-H, *J* = 8.6 Hz), 8.158 (d, 2H, Ar-H, *J* = 8.6 Hz). <sup>13</sup>C NMR (CDCl<sub>3</sub>): δ 15.56, 122.56, 125.23, 125.94, 127.82, 128.66, 131.19, 132.48, 140.27, 140.75, 144.81, 161.72. Anal. Calcd. for C<sub>26</sub>H<sub>20</sub>N<sub>2</sub>S<sub>2</sub>ZnCl<sub>2</sub>·C<sub>2</sub>H<sub>4</sub>O<sub>2</sub>: C, 54.16; H, 3.90; N, 4.51. Found: C, 54.22; H, 3.75; N, 4.80. MP = 314 °C (decomp).

#### 2.4.8.8 4-phenoxyphenyl-BIAN zinc chloride (17)

A mixture of acenaphthenequinone (1.00 g, 5.49 mmol) and anhydrous zinc chloride (2.02 g, 14.82 mmol) was suspended in 10 mL of glacial acetic acid, thereby generating a yellow suspension. The yellow suspension was heated to 60 °C and 4-phenoxyaniline (2.34 g, 12.63 mmol) was added, following which the resulting solution was refluxed for 1 hour. The orange-red precipitate that had formed during the reaction was filtered off and washed sequentially with water and diethyl ether. The resulting orange-red crystalline powder was collected and used without further purification for a single crystal X-ray diffraction study (2.41 g, 67%).

HRMS (CI, CH<sub>4</sub>): calcd for [M - Cl]<sup>+</sup> [C<sub>36</sub>H<sub>24</sub>N<sub>2</sub>O<sub>2</sub>ZnCl]<sup>+</sup> *m/z* 615.0818; found 615.0816; <sup>1</sup>H NMR (CDCl<sub>3</sub>): 7.196 (m, 10H, Ar-H) 7.432 (t-d, 4H, Ar-H, *J* = 7.1 Hz, *J* =

1.8 Hz), 7.636 (dd, 4H, Ar-H,  $J = 6.8$  Hz,  $J = 2.2$  Hz), 7.666 (t, 2H, Ar-H,  $J = 7.8$  Hz), 7.773 (d, 2H, Ar-H,  $J = 7.1$  Hz), 8.186 (d, 2H, Ar-H,  $J = 8.3$  Hz).  $^{13}\text{C}$  NMR ( $\text{CDCl}_3$ ):  $\delta$  119.40, 119.80, 123.69, 124.40, 125.26, 125.87, 128.65, 130.09, 131.23, 132.59, 138.20, 144.86, 156.02, 158.37, 161.83. Anal. Calcd. for  $\text{C}_{36}\text{H}_{24}\text{N}_2\text{O}_2\text{ZnCl}_2$ : C, 66.23; H, 3.71; N, 4.29. Found: C, 66.23; H, 3.61; N, 4.30. MP = 316 °C (decomp).

#### 2.4.8.9 4-fluorophenyl-BIAN zinc chloride (18)

A mixture of acenaphthenequinone (1.00 g, 5.49 mmol) and anhydrous zinc chloride (2.02 g, 14.82 mmol) was suspended in 10 mL of glacial acetic acid, thereby generating a yellow suspension. The yellow suspension was heated to 60 °C and 4-fluoroaniline (1.20 mL, 12.63 mmol) was added, following which the resulting solution was refluxed for 1 hour. The orange precipitate that had formed during the reaction was filtered off and washed sequentially with water and diethyl ether. The resulting orange crystalline powder was collected and used without further purification for a single crystal X-ray diffraction study (2.33 g, 84%).

HRMS (CI,  $\text{CH}_4$ ): calcd for  $[\text{M} - \text{Cl}]^+ [\text{C}_{24}\text{H}_{14}\text{N}_2\text{F}_2\text{ZnCl}]^+ m/z$  467.0105; found 467.012;  $^1\text{H}$  NMR ( $\text{D}_6$ -DMSO):  $\delta$  6.823 (d, 2H, Ar-H,  $J = 7.3$  Hz), 7.141 (m, 4H, Ar-H, apparent complex coupling from fluorine), 7.360 (m, 4H, Ar-H, apparent complex coupling from fluorine), 7.559 (t, 2H, Ar-H,  $J = 7.8$  Hz), 8.115 (d, 2H, Ar-H,  $J = 8.3$  Hz).  $^{19}\text{F}$  NMR ( $\text{D}_6$ -DMSO):  $\delta$  -119.83 (m (apparent septet), Ar-F, 2F).  $^{13}\text{C}$  NMR ( $\text{D}_6$ -DMSO):  $\delta$  116.53 (d, 4C,  $J = 22.54$  Hz (F)), 119.91, 123.48, 127.65, 128.12, 129.77, 130.97, 141.17, 147.17, 159.60 (d, 2C,  $J = 240.19$  Hz (F)), 160.70. Anal. Calcd. for  $\text{C}_{24}\text{H}_{14}\text{N}_2\text{F}_2\text{ZnCl}_2$ : C, 57.12; H, 2.80; N, 5.55. Found: C, 56.83; H, 2.94; N, 5.44. MP = 362 °C (decomp).

#### 2.4.8.10 4-bromophenyl-BIAN zinc chloride (19)

A mixture of acenaphthenequinone (1.00 g, 5.49 mmol) and anhydrous zinc chloride (2.02 g, 14.82 mmol) was suspended in 10 mL of glacial acetic acid, thereby generating a yellow suspension. This yellow suspension was heated to 60 °C and 4-bromoaniline (2.17 g, 12.63 mmol) was added, following which the resulting solution was refluxed for 1 hour. The dark yellow precipitate that had formed during the reaction was filtered off and washed sequentially with water and diethyl ether. The resulting dark yellow crystalline powder was collected and recrystallized using dichloromethane to obtain yellow crystals of **19**. (2.92 g, 85%).

HRMS (CI, CH<sub>4</sub>): calcd for [M - Cl]<sup>+</sup> [C<sub>24</sub>H<sub>14</sub>N<sub>2</sub>Br<sub>2</sub>ZnCl]<sup>+</sup> *m/z* 586.8504; found 586.8515; <sup>1</sup>H NMR (D<sub>6</sub>-DMSO): 6.493 (d, 4H, Ar-H, *J* = 6.7 Hz), 7.090 (d, 4H, Ar-H, *J* = 6.7 Hz), 7.886 (t, 2H, Ar-H, *J* = 7.5 Hz), 8.043 (d, 2H, Ar-H, *J* = 7.0 Hz), 8.401 (d, 2H, Ar-H, *J* = 8.2 Hz). <sup>13</sup>C NMR (D<sub>6</sub>-DMSO): δ 106.84, 116.47, 121.88, 129.01, 129.06, 130.92, 131.79, 132.91, 144.88, 148.17, 173.26. Anal. Calcd. for C<sub>24</sub>H<sub>14</sub>N<sub>2</sub>Br<sub>2</sub>ZnCl<sub>2</sub>: C, 46.01; H, 2.25; N, 4.47. Found: C, 45.96; H, 2.24; N, 4.36. MP = 352 °C (decomp).

#### 2.4.8.11 4-(trifluoromethoxy)phenyl-BIAN zinc chloride (20)

A mixture of acenaphthenequinone (1.00 g, 5.49 mmol) and anhydrous zinc chloride (2.02 g, 14.82 mmol) was suspended in 10 mL of glacial acetic acid, thereby generating a yellow suspension. The yellow suspension was heated to 60 °C and 4-(trifluoromethoxy)aniline (1.69 mL, 12.63 mmol) was added, following which the resulting solution was refluxed for 1 hour. The yellow precipitate that had formed during the reaction was filtered off and washed sequentially with water and diethyl ether. The resulting yellow crystalline powder was collected and used without further purification for a single crystal X-ray diffraction study (2.44 g, 70%).

HRMS (CI, CH<sub>4</sub>): calcd for [M - Cl]<sup>+</sup> [C<sub>26</sub>H<sub>14</sub>N<sub>2</sub>O<sub>2</sub>F<sub>6</sub>ZnCl]<sup>+</sup> *m/z* 598.9939; found 598.9929; <sup>1</sup>H NMR (CDCl<sub>3</sub>): δ 7.461 (d, 4H, Ar-H, *J* = 8.3 Hz), 7.526 (d, 2H, Ar-H, *J* = 7.3 Hz), 7.669 (m, 6H, Ar-H), 8.228 (d, 2H, Ar-H, *J* = 8.3 Hz). <sup>19</sup>F NMR (CDCl<sub>3</sub>): δ -58.18 (s, -OCF<sub>3</sub>, 6F). <sup>13</sup>C NMR (CDCl<sub>3</sub>): δ 120.42 (q, 2C, -CF<sub>3</sub>, *J* = 258.2 Hz), 122.67, 123.25, 124.73, 126.30, 128.94, 131.30, 133.06, 141.76, 145.42, 149.20, 163.02. Anal. Calcd. for C<sub>26</sub>H<sub>14</sub>N<sub>2</sub>O<sub>2</sub>F<sub>6</sub>ZnCl<sub>2</sub>: C, 49.05; H, 2.22; N, 4.40. Found: C, 49.40; H, 2.07; N, 4.39. MP = 291 °C (decomp).

#### 2.4.8.12 4-(trifluoromethyl)phenyl-BIAN zinc chloride (21)

A mixture of acenaphthenequinone (1.00 g, 5.49 mmol) and anhydrous zinc chloride (2.02 g, 14.82 mmol) was suspended in 10 mL of glacial acetic acid and 2 mL of toluene, thereby generating a yellow suspension. The yellow suspension was heated to 60 °C and 4-(trifluoromethyl)aniline (1.59 mL, 12.63 mmol) was added, following which the resulting solution was refluxed for 1 hour. The yellow precipitate that had formed during the reaction was filtered off and washed sequentially with water and diethyl ether. The resulting yellow crystalline powder was collected and used without further purification for a single crystal X-ray diffraction study (2.29 g, 69%).

HRMS (CI, CH<sub>4</sub>): calcd for [M - Cl]<sup>+</sup> [C<sub>26</sub>H<sub>14</sub>N<sub>2</sub>F<sub>6</sub>ZnCl]<sup>+</sup> *m/z* 567.0041; found 567.0046; <sup>1</sup>H NMR (CD<sub>2</sub>Cl<sub>2</sub>): δ 7.438 (d, 2H, Ar-H, *J* = 7.4 Hz), 7.679 (t, 2H, Ar-H, *J* = 7.8 Hz), 7.732 (d, 4H, Ar-H, *J* = 8.2 Hz), 7.935 (d, 4H, Ar-H, *J* = 8.2 Hz), 8.259 (d, 2H, Ar-H, *J* = 8.2 Hz). <sup>19</sup>F NMR (CD<sub>2</sub>Cl<sub>2</sub>): δ -62.83 (s, Ar-F, 6F). <sup>13</sup>C NMR (CD<sub>2</sub>Cl<sub>2</sub>): δ 122.27, 124.24 (q, 2C, *J* = 272.50 Hz (F)), 124.88, 127.06, 128.03 (q, 4C, *J* = 4.14 Hz (F)), 129.37, 130.97 (q, 2C, *J* = 33.60 Hz (F)), 131.70, 133.71, 146.02, 147.28, 164.00. Anal. Calcd. for C<sub>26</sub>H<sub>14</sub>N<sub>2</sub>F<sub>6</sub>ZnCl<sub>2</sub>: C, 51.64; H, 2.33; N, 4.63. Found: C, 52.04; H, 2.27; N, 4.64. MP = 370 °C (decomp).

## **Chapter 3: Investigation of Boron Arsenide as a High Thermal Conductivity Material**

### **3.1 INTRODUCTION**

#### **3.1.1 Predicted High Thermal Conductivity**

Group III-V semiconductors are very useful materials and have a wide range of applications in the microelectronics industry.<sup>102</sup> However, of the group III-V semiconductors, boron arsenide (BAs) has been somewhat neglected. This is primarily due to the difficulties that are encountered during the synthesis of this compound. The first report on the synthesis and characterization of BAs was published in 1958.<sup>103</sup> In this study, BAs was synthesized using the very harsh reaction conditions of heating elemental arsenic and elemental boron to in a sealed quartz tube at 700-800 °C. However, this synthetic approach only produced a small amount of crystalline BAs that was not adequate for materials applications. As a result, of the difficulty of synthesis, research and applications of BAs has remained insignificant in comparison with the other members of the group III-V semiconductor family.

However, a recent theoretical report published in 2013 has revitalized interest in the BAs material.<sup>104</sup> In this report by Lindsay, Broido, and Reinecke, the thermal conductivity ( $\kappa$ ) properties of BAs and other boron semiconductor materials were investigated and compared with that of diamond. Diamond and other carbon based materials, such as graphite, have the highest thermal conductivities of any bulk materials to date. In the bulk, the thermal conductivity of diamond is approximately  $2270 \text{ W m}^{-1} \text{ K}^{-1}$ .<sup>105</sup> The high thermal conductivity of diamond is 4 to 5 times larger than other high thermal conductivity materials such as copper.<sup>106</sup> However, despite the advantageous thermal properties of diamond, the fabrication of devices that utilize



diamond is very problematic. Furthermore, diamond is an electrical insulator and, therefore, cannot be used in microelectronic devices. However, in the report by Lindsay, Broido, and Reinecke, BAs was predicted to have comparable thermal conductivity properties to diamond at room temperature.

Thermal management in the microelectronics industry represents an increasingly taxing problem. As microelectronics become smaller and smaller, the issue of thermal management becomes magnified and increasingly challenging.<sup>107</sup> Therefore, the discovery of new high thermal conductivity materials that can address the thermal management issue is particularly exciting. BAs is a semiconductor material with electronic properties that are similar to silicon.<sup>108</sup> So unlike diamond, BAs could conceivably be utilized in the microelectronics industry as a high thermal conductivity replacement for silicon that could mitigate the thermal management problem.

As displayed in Figure 106 and Table 15, the calculated room temperature thermal conductivity of BAs was determined to be  $2240 \text{ W m}^{-1} \text{ K}^{-1}$ . This value was comparable to the calculated thermal conductivity of diamond at room temperature. Surprisingly, BAs does not follow the general trend that is displayed in both Figure 106 and Table 15, namely that, as average atomic weight increases, the thermal conductivity decreases. This trend holds true for the calculated values of BN, BP, and BSb. However, BAs was found to be a significant outlier with a very high predicted thermal conductivity.

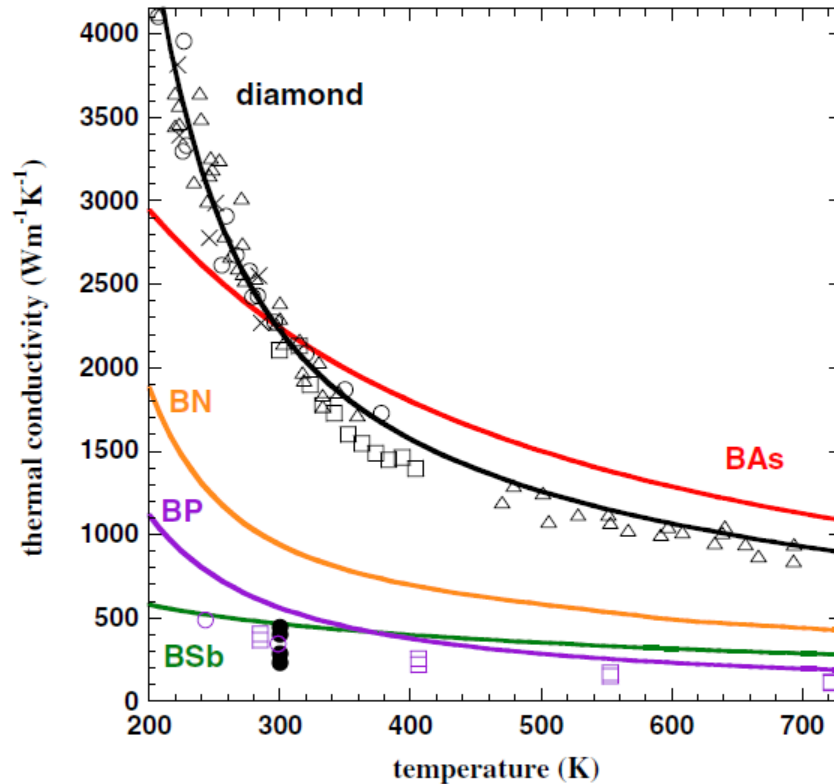


Figure 106: Calculated thermal conductivity values vs. temperature for diamond, BN, BP, BAs, and BSb. Open shapes are experimental data points. Closed circles are for GaN( $230 \text{ m}^{-1} \text{ K}^{-1}$ ), Al( $240 \text{ m}^{-1} \text{ K}^{-1}$ ), AlN( $285 \text{ m}^{-1} \text{ K}^{-1}$ ), Cu( $400 \text{ m}^{-1} \text{ K}^{-1}$ ), SiC( $490 \text{ m}^{-1} \text{ K}^{-1}$ ).<sup>104</sup>

Why does BAs possess this theoretical high thermal conductivity property? The common properties of many high thermal conductivity materials are: a simple crystal structure, a low average atomic mass, strong interatomic bonding, and a low anharmonicity.<sup>104</sup> Although BAs fits into several of these categories, such as simple a crystal structure and strong interatomic bonding, it does not feature a low average atomic mass. In fact, in comparison with other high thermal conductivity materials (such as diamond or cubic boron nitride), the average atomic mass of BAs is significantly larger.

One unique feature of BAs is the almost perfectly covalent bond between boron and arsenic. The other members of the III-V series are more polar covalent or ionic in nature. In contrast, however, the B-As bond is almost entirely covalent.<sup>109</sup> In this respect, BAs is more like diamond. However, the factor that most contributes to the predicted high thermal conductivity of BAs lies in the energies of the optical and acoustic phonon branches of BAs.

Table 15: Average molecular weight, calculated natural thermal conductivity with experimental values in parenthesis, calculated isotopically pure thermal conductivity, and percent increase between isotopically pure and natural thermal conductivities.<sup>104</sup>

Material	Average Molecular Weight	$K_{\text{natural}}$ ( $\text{W m}^{-1} \text{K}^{-1}$ )	$K_{\text{pure}}$ ( $\text{W m}^{-1} \text{K}^{-1}$ )	Percent enhancement of $K_{\text{pure}}$ VS. $K_{\text{natural}}$
Cubic BN	12.41	940 (768)	2145	130
BP	20.89	580 (400)	665	15
BAs	42.87	2240	3170	40
BSb	66.28	465	1180	155
Diamond	12.01	2290 (2270)	3450	50
Silicon	28.09	145 (142)	155	7
Germanium	72.59	60 (59)	75	23

Semiconductor materials transport heat primarily through lattice vibrations or phonons. Thermal resistance is often a result of phonon scattering, which in turn inhibits thermal transport. Interestingly, the energies of the optical and acoustic phonon branches are such that phonon-phonon scattering is almost entirely forbidden. This unusual

outcome is due to the presence of both a large acoustic and optical phonon energy gap and bunching of the acoustic phonon branches, as displayed in Figure 107.

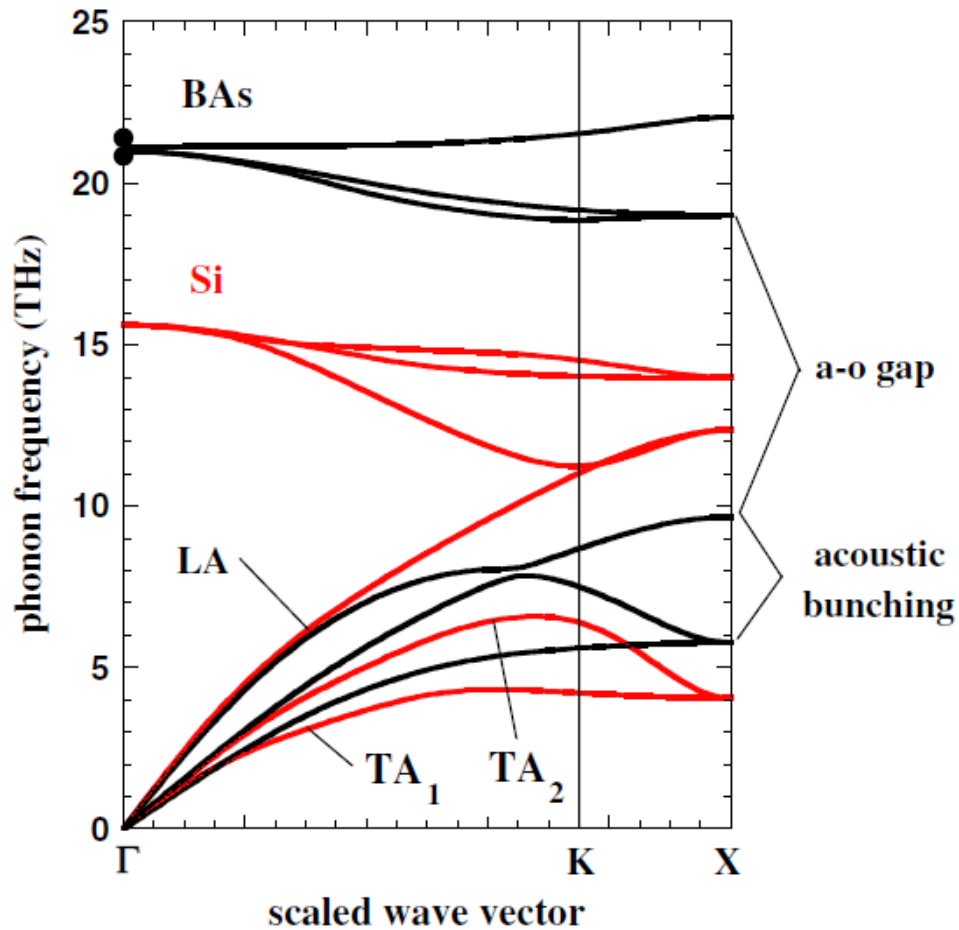


Figure 107: Frequency of the phonon modes in silicon (Red) and BAs (Black). Large acoustic-optical frequency gap inhibits scattering between these phonons. Acoustic bunching of longitudinal (LA) and two transverse (TA) acoustic phonon branches inhibits scattering between these phonon modes.<sup>104</sup>

### 3.1.2 Thermal Measurement of BAs

As a result of the elegant work of Lindsay, Broido, and Reinecke, interest has been generated in BAs as a potentially very useful material.<sup>104</sup> As a result, several research groups are trying to confirm the theoretical calculations and measure the predicted high thermal conductivity of BAs. Very recently, in January 2015, an experimental study by Ren, Chu, and coworkers was published on a measurement of the thermal conductivity of BAs.<sup>110</sup> In this report, the BAs materials were synthesized by means of a chemical vapor transport method, which involved heating elemental B and elemental As in a 1:1.8 molar ratio in a sealed quartz tube. Initially, the tube was heated at 500 °C for 10 hours and subsequently heated at 800 °C for a period of 3 days. After the reaction had finished, the excess arsenic was separated from the BAs samples and ground up, and the foregoing reaction was repeated with the same heating parameters. This process was repeated several times until a homogenous BAs powder was produced, as confirmed by the absence of As peaks in the X-ray powder patterns (Figure 108). The resulting BAs was confirmed to be cubic with a lattice constant of  $a = 4.7801(2) \text{ \AA}$ , which was in accord with previous experimental results.<sup>103</sup>

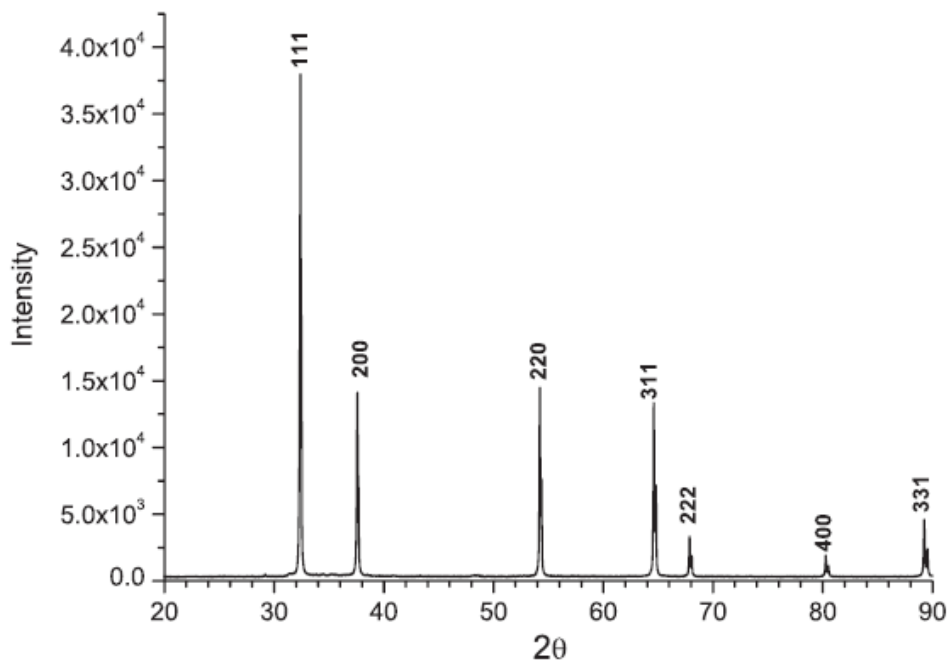


Figure 108: Powder X-ray diffraction pattern of cubic BAs with lattice constant of  $a = 4.7801(2) \text{ \AA}$ .<sup>110</sup>

The BAs powder sample was subsequently measured by means of scanning electron microscopy (SEM) and determined to have a typical grain size of 5 microns ( $\mu\text{m}$ ). Next, single crystals of BAs were grown from the powder precursor via chemical vapor transport using iodine. For this purpose, the BAs powder, excess As, and elemental iodide were placed at one end of a tube furnace that was heated to approximately 900 °C. Crystals of BAs were then collected at the cooler end of the tube at approximately 650 °C. For purification purposes, the crystals were washed with concentrated HCl, thereby removing any residual arsenic. The single crystals were then studied by X-ray photoelectron spectroscopy (XPS), which indicated a B to As elemental ratio of 50.7:49.3%. After XPS analysis, the single crystals were studied using SEM, as displayed

in Figure 109. Subsequently, single crystal X-ray diffraction was attempted. However, the crystals were found to have complex twinned structures.

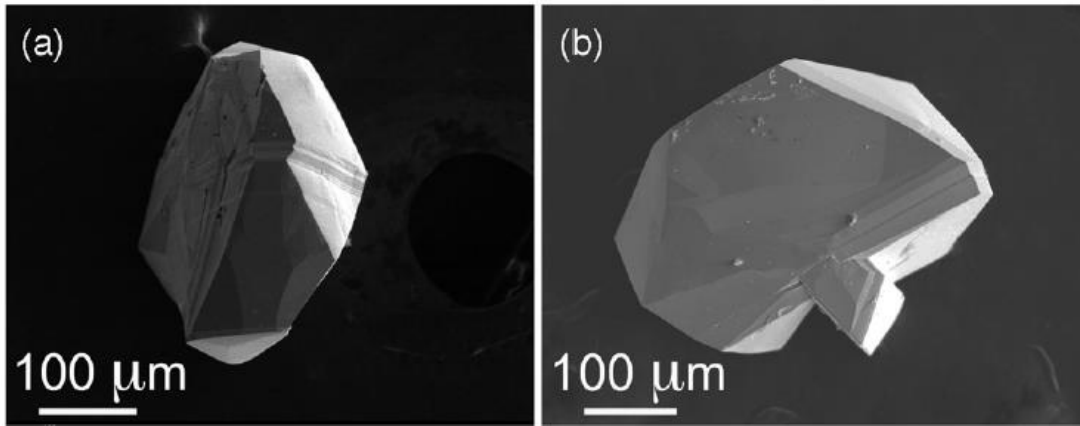


Figure 109: SEM images of BAs crystals.<sup>110</sup>

Following characterization, thermal conductivity measurements were subsequently attempted using the time-domain thermoreflectance technique (TDTR). This technique is reliable for measurement of the thermal conductivity of small samples. This method uses one laser to heat the surface of the sample, while a probe laser measures the temperature dependent reflectance of the surface. The resulting reflectivity is measured versus time and, hence, the thermal conductivity value can be obtained. Using this method, a value of  $196 \text{ W m}^{-1} \text{ K}^{-1}$  was obtained for a 300 micron sample. This result, although not comparable to the theoretical value of  $2000 \text{ W m}^{-1} \text{ K}^{-1}$ , was very promising in that a high value of  $196 \text{ W m}^{-1} \text{ K}^{-1}$  was obtained despite the presence of such impediments as arsenic deficiencies, crystal defects, and an overall twinned structure.

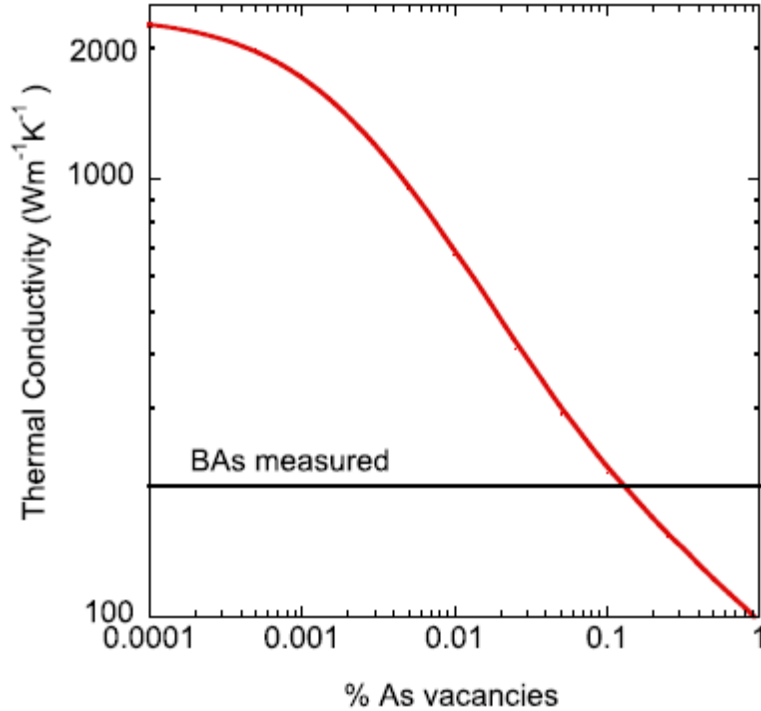


Figure 110: Effect of arsenic deficiencies on thermal conductivity in BAs crystals.<sup>110</sup>

Theoretical methods were employed in order to assess the impact that arsenic deficiencies would have on the predicted thermal conductivity of BAs. Unfortunately, as displayed in Figure 110, even a 0.1% As deficiency could decrease the thermal conductivity value by an order of magnitude. Therefore, the As deficiency in the BAs material could be a significant factor leading to the lower thermal conductivity value obtained experimentally.

### 3.2 RESULTS AND DISCUSSION

The BAs material had been investigated previously in the Cowley research group. Swingle, Cowley, Bard, and coworkers published a report in 2012 on the application of the neglected semiconductor BAs as a photoelectrode material.<sup>111</sup> In Section 3.2, the



status of the ongoing effort to measure the thermal conductivity of BAs microstructures will be discussed. The ongoing study is a collaborative effort with the Shi Group in the Mechanical Engineering Department at the University of Texas at Austin, a group that specializes in the thermal measurement of nanostructures. The synthesis and characterization of the BAs microstructures has been completed. However, as will be discussed later, the thermal measurements are still being optimized.

### **3.2.1 Synthesis and Characterization of BAs Material**

As discussed in Section 3.1, BAs has been predicted to have exceptional thermal transport properties. The neglected semiconductor BAs continues to be focal point in the Cowley research group over the past few years. Accordingly, it was decided that a collaborative effort with the Shi group at University of Texas at Austin would be appropriate for measuring the predicted thermal conductivity of BAs.

Consequently, BAs materials were synthesized according to the route described in 1958.<sup>103</sup> For this purpose, elemental arsenic and elemental boron were loaded in a 2.1:1 molar ratio into quartz tubes (which had been previously dried at 1000 °C in a furnace). These quartz reaction vessels were then evacuated on a Schlenk line for one hour, following which, the quartz reaction vessels were sealed and loaded into a furnace that was heated at 800 °C for three days. At this temperature arsenic exists in the vapor phase, while boron remains in the solid phase. After the appropriate reaction time, the reaction vessel was slowly cooled at the rate of 0.1 °C/min. As displayed in Figure 111, the completed reaction typically features the deposition of a large coalesced polycrystalline arsenic crystal along with small boron pellets that had visibly undergone reaction. As displayed in Figure 112, the surface growth of BAs is clearly apparent not only from SEM imaging but also from a conventional microscope.



Figure 111: Post reaction quartz vessel with a large arsenic crystal and boron substrates that had visibly undergone a reaction.

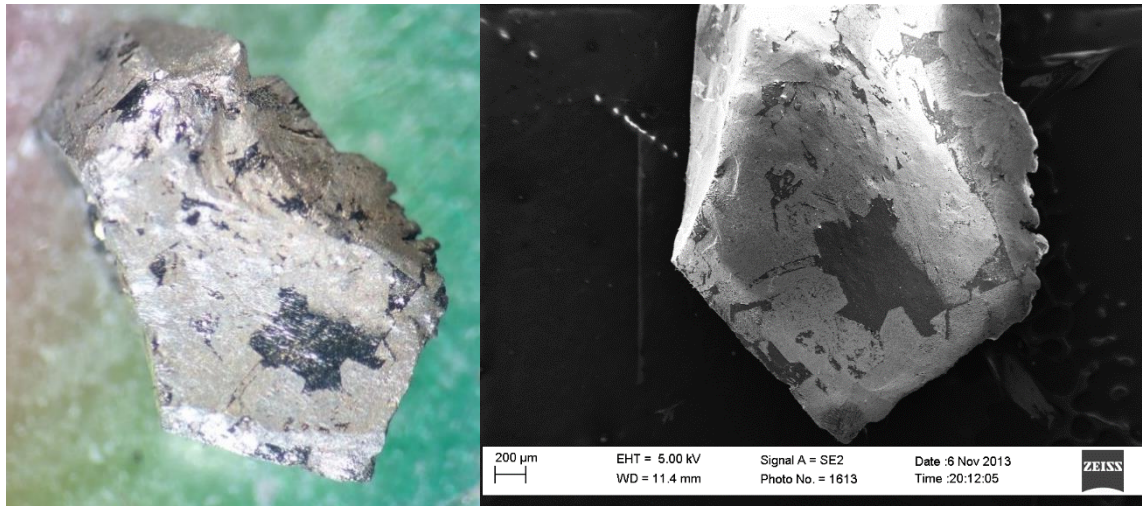


Figure 112: Boron substrate with visible BAs growth (silver color) on the surface as visualized by a conventional microscope (Left) and SEM (Right).

The surface reaction was characterized using several analytical techniques. First, the BAs samples were examined by means of powder X-ray diffraction (XRD). Initially, the boron substrate was examined in order to obtain a background scan. The boron substrate, as displayed in Figure 113, matched the  $\beta$ -rhombohedral boron allotrope. The pertinent lattice parameters were  $a = 10.92500 \text{ \AA}$ ,  $b = 10.92500 \text{ \AA}$ ,  $c = 23.81400 \text{ \AA}$ ,  $\alpha = 90.000^\circ$ ,  $\beta = 90.000^\circ$ , and  $\gamma = 120.000^\circ$ .<sup>112</sup>

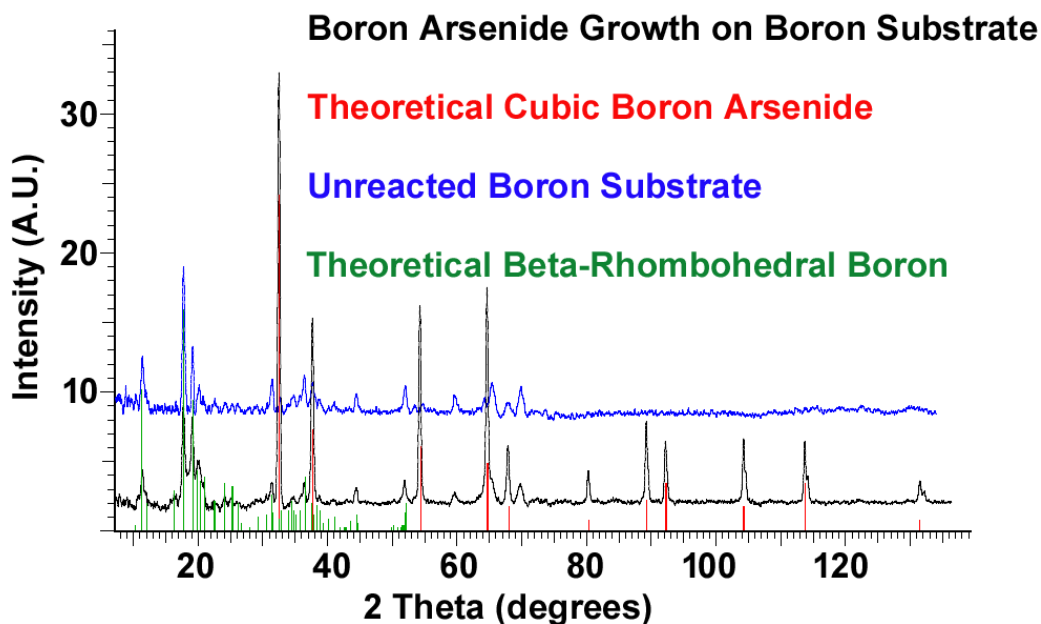


Figure 113: Powder X-ray diffraction data of a boron substrate with BAs surface growth: (Black) BAs growth on a boron substrate, (Red) theoretical cubic BAs, (Blue) unreacted boron substrate, and (Green) theoretical  $\beta$ -rhombohedral boron.<sup>103,112</sup>

Subsequently, a sample with BAs surface growth was crushed and examined by means of powder X-ray diffraction. As exhibited in Figure 113, the powder pattern retained the peaks that had been assigned to the  $\beta$ -rhombohedral boron substrate. However, the new sharp peaks were attributed to cubic boron arsenide that had grown on the surface of the boron substrate. These peaks matched the literature values for the lattice parameters of  $a = 4.77700 \text{ \AA}$ ,  $b = 4.77700 \text{ \AA}$ ,  $c = 4.7770 \text{ \AA}$ ,  $\alpha = 90.000^\circ$ ,  $\beta = 90.000^\circ$ , and  $\gamma = 90.000^\circ$ .<sup>103</sup> Furthermore, the peaks that were attributed to BAs were found to be in good agreement with that reported by Ren, Chu, and coworkers.<sup>110</sup>

Following completion of the powder X-ray diffraction analysis, the BAs samples were probed by Raman spectroscopy. In 1994, Ruoff *et al.* reported a study of the

pressure induced amorphization of BAs.<sup>113</sup> In this study, the Raman spectrum of boron arsenide was reported. As displayed in Figure 114, the Raman spectrum for our experimental BAs sample perfectly matched that of the Ruoff sample from 1994. Furthermore, the full Raman spectrum presented in Figure 115 confirms that the signal detected at  $698\text{ cm}^{-1}$  was the only Raman peak detected for the BAs material.

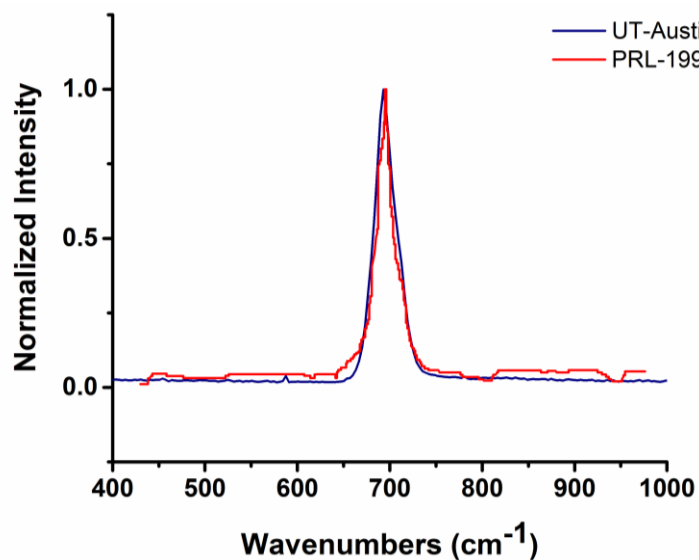


Figure 114: Raman spectra for the current experimental BAs sample (Blue) and previously reported BAs sample (Red).<sup>113</sup>

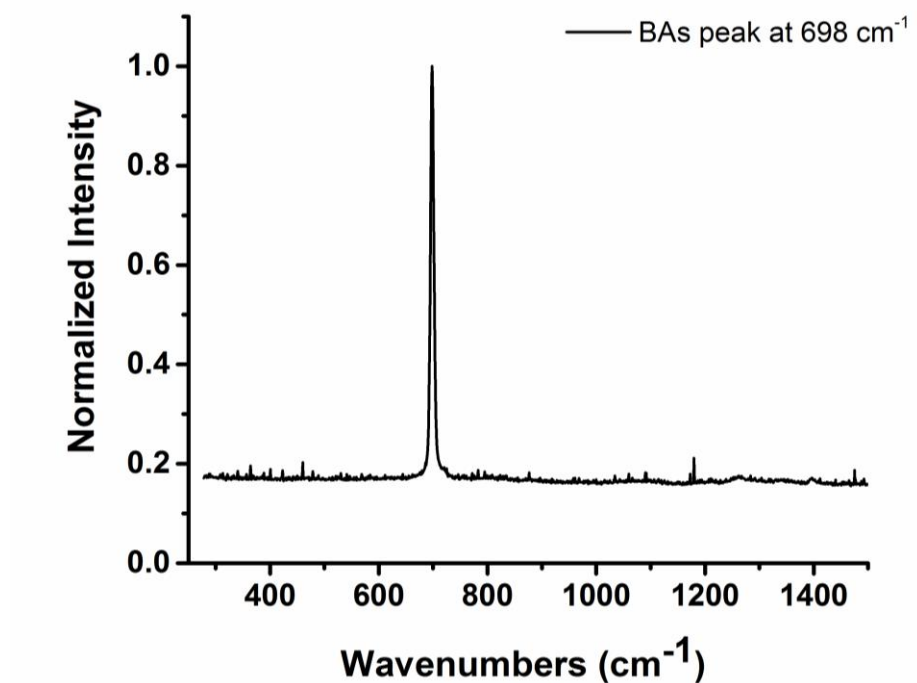


Figure 115: Full Raman spectrum for the experimental BAs material.

Subsequently, X-ray photoelectron spectroscopy (XPS) was used in order to determine the molecular composition of the BAs materials that were present on the surface of the boron substrate. As exhibited in Figure 116, the XPS spectrum displayed both the boron 1s and arsenic 3d peaks. The molecular composition of the BAs material was found to be 49.91% boron : 50.09 % arsenic. Note, the smaller arsenic peak at 43-46 eV is indicative of the presence of arsenic oxide.<sup>114</sup>

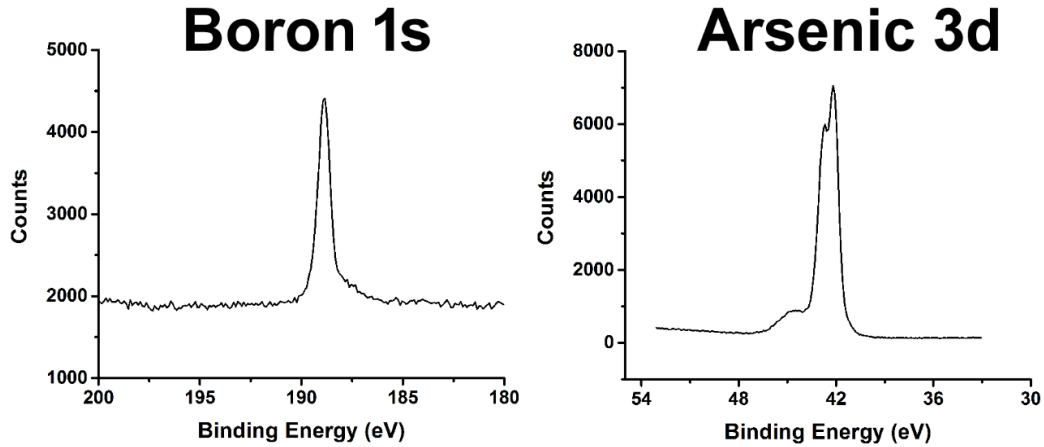


Figure 116: XPS peaks for B 1s electrons and As 3d electrons.

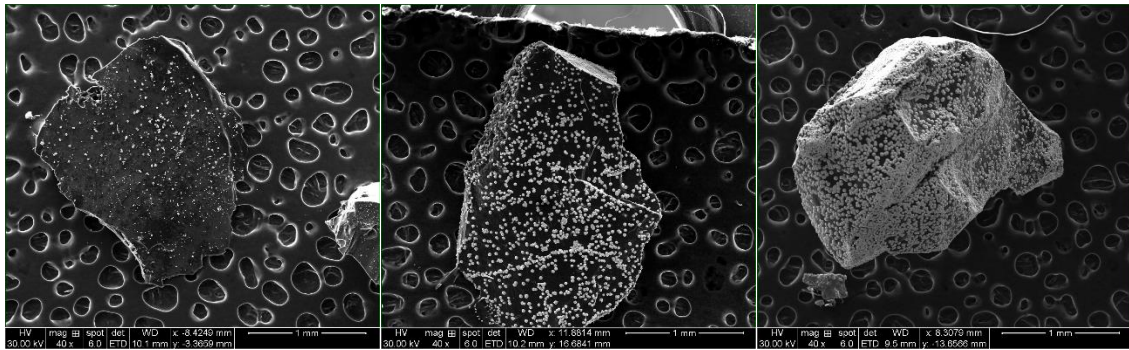


Figure 117: SEM images of three boron substrates obtained from the same growth. These images display poor (Left), medium (Center), and high (Right) surface coverage.

Finally, the surface growth morphologies of the BAs materials were examined using SEM. The BAs surface growth process turned out to be very unpredictable. The three boron substrates that are displayed in Figure 117, were obtained from the same reaction vessel. However, it is evident that the surface coverage of the three samples was very different, ranging from poor to very high. Furthermore, the differences in growth morphologies of the BAs microstructures that were encountered were vast. As displayed in Figure 118, BAs microstructures featured extended growth on the surface, dendritic

growths, nanowire growths, platelet growths, needle microstructures, and large pellet growths.

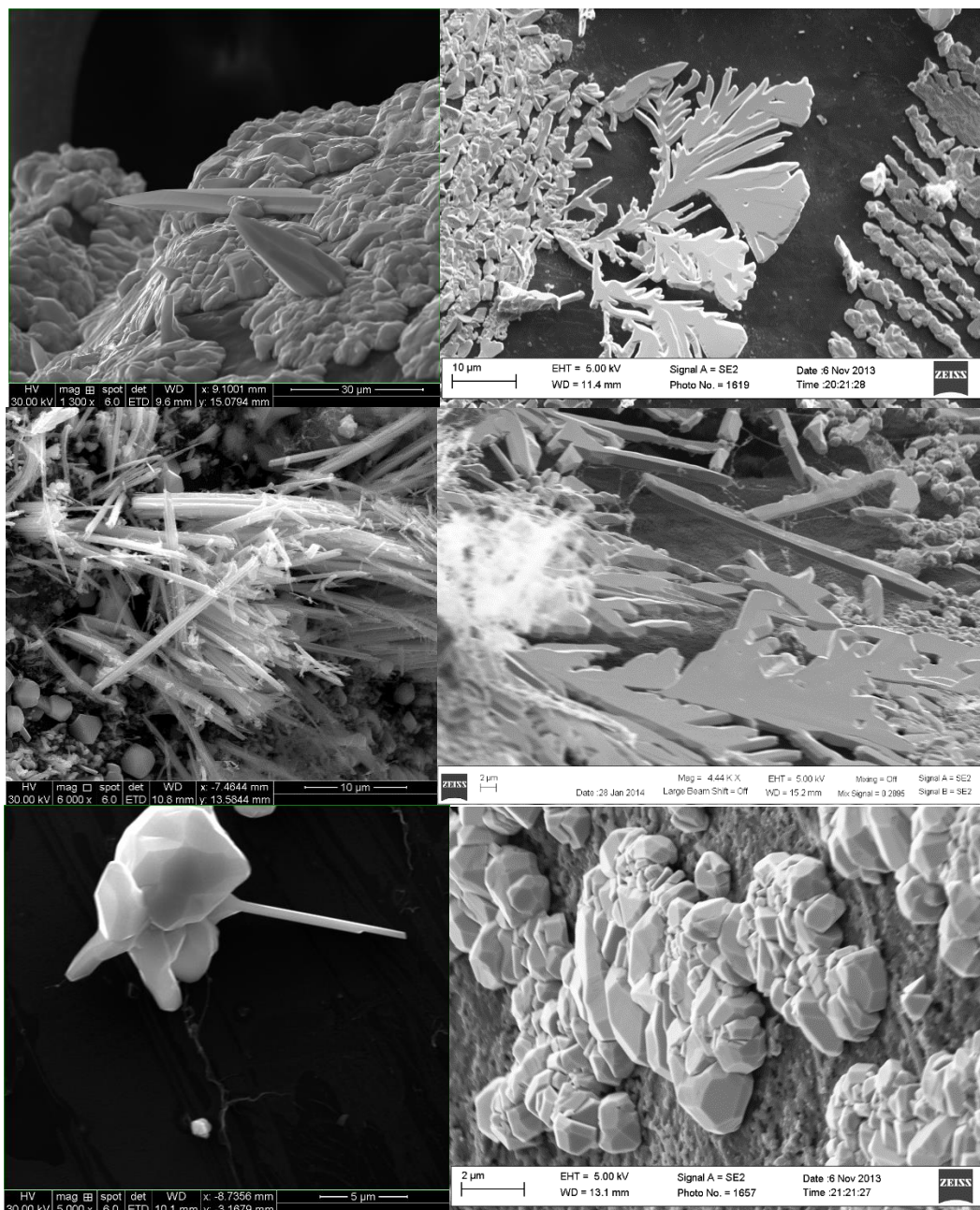


Figure 118: SEM images of different BAs morphologies.

### 3.2.2 Experimental Measurement of Thermal Conductivity of BAs Microstructures

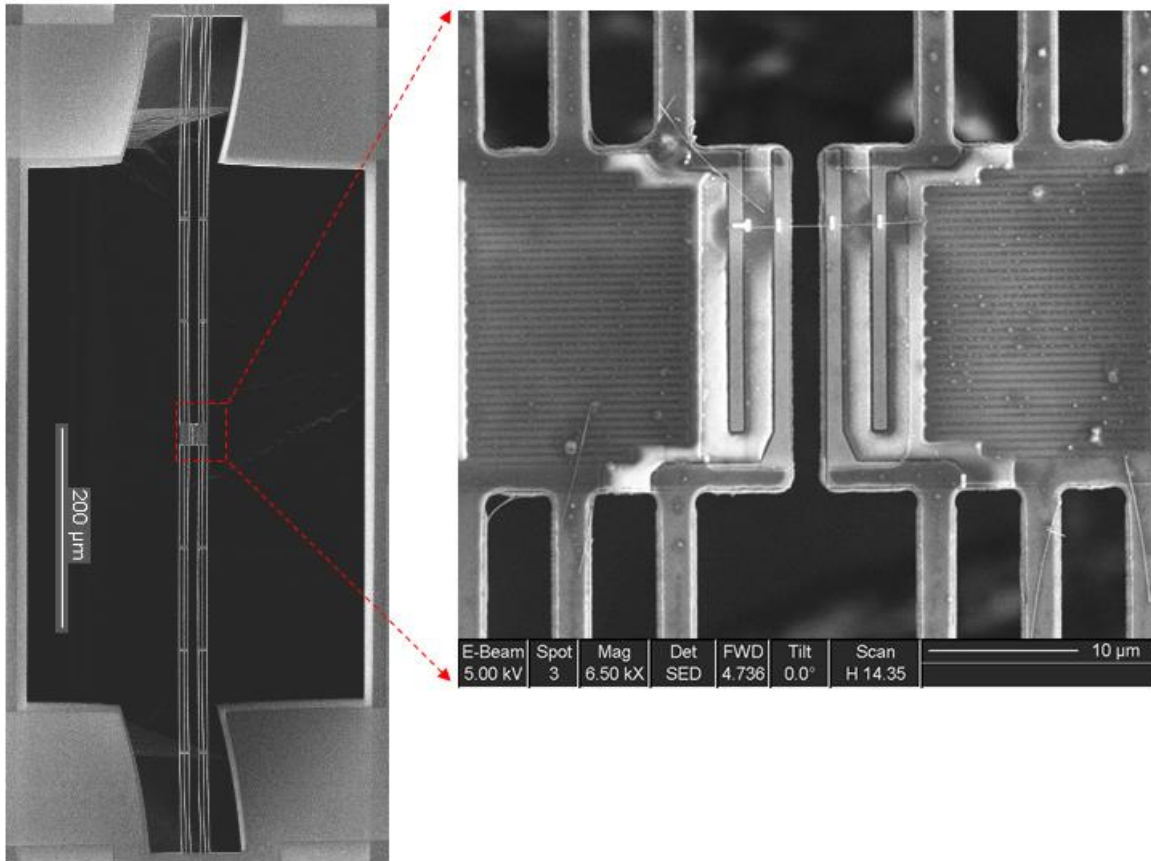


Figure 119: SEM image of microheater device.<sup>115</sup>

Although the BAs material had been successfully synthesized and characterized, the challenge of measuring the thermal properties of BAs remained. Upon initial inspection, such small BAs microstructures appear to be unsuitable for thermal measurement experiments. Fortunately, however, the Shi research group in the Mechanical Engineering Department at the University of Texas at Austin specializes in the measurement of the thermal transport of nanostructures. In 2003, Shi *et al.* developed a microheater device that was capable of measuring the thermal properties of nanostructures.<sup>115</sup> The device functions by placing a nanostructure across a suspended



microheater device under high vacuum ( $1 \times 10^{-5}$  Torr), as displayed in Figure 119. One side of the device features a heating membrane that transfers heat through the nanostructure to the opposite side, which acts as the sensing membrane.

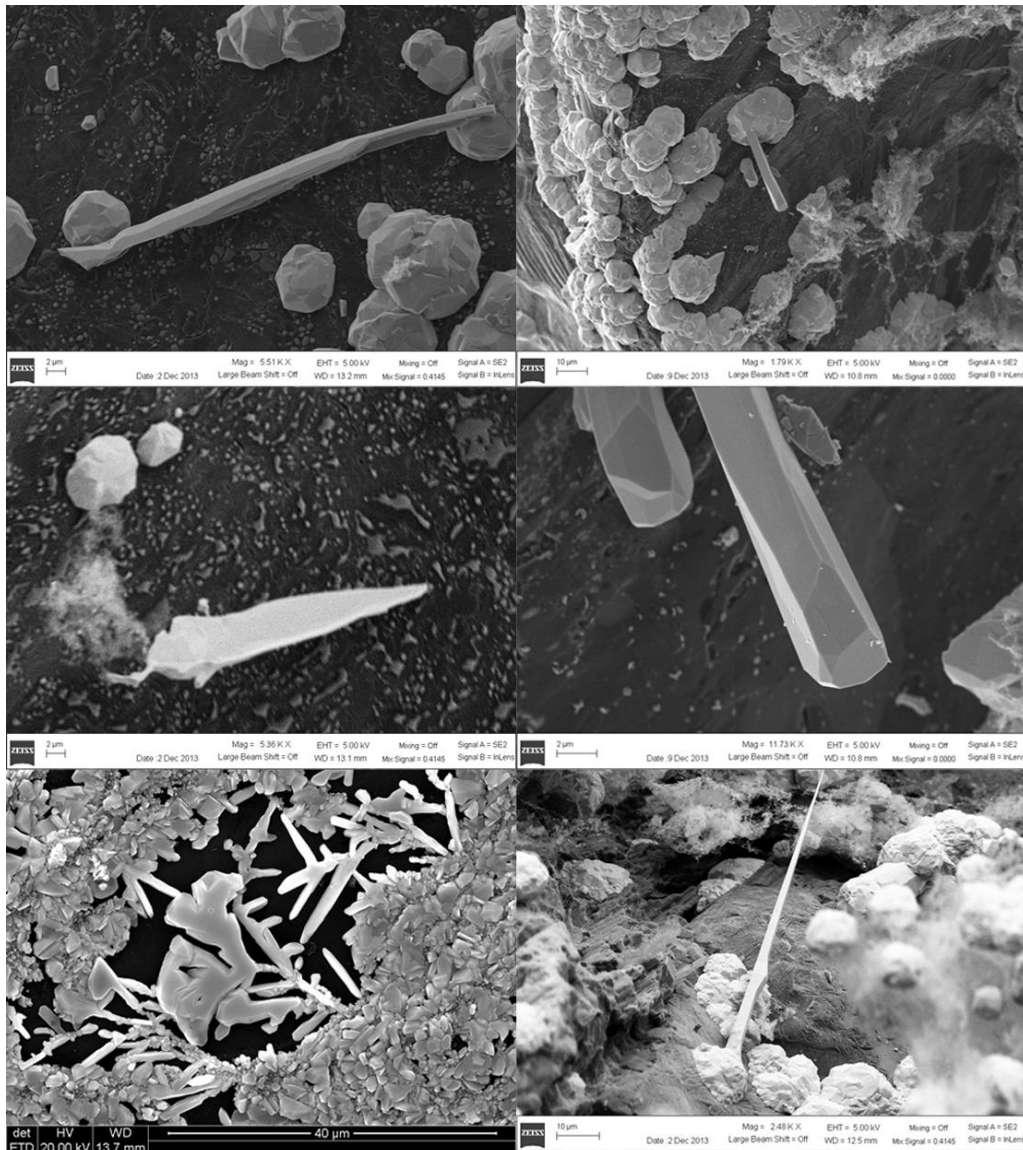


Figure 120: SEM images of BAs morphologies that are potentially suitable for measurement with microheater devices.

Using this approach, the measurement of the BAs materials could be achieved using the microheater device technologies developed in the Shi group. Accordingly, BAs microstructures that could be suspended across the microheater device were sought on the surface of the boron substrates. As displayed in Figure 120, potentially suitable BAs microstructures were found on the surface of the boron substrate. These BAs microstructures were harvested off the boron substrate and subsequently placed onto the microheater devices for thermal conductivity measurement purposes (Figure 121).

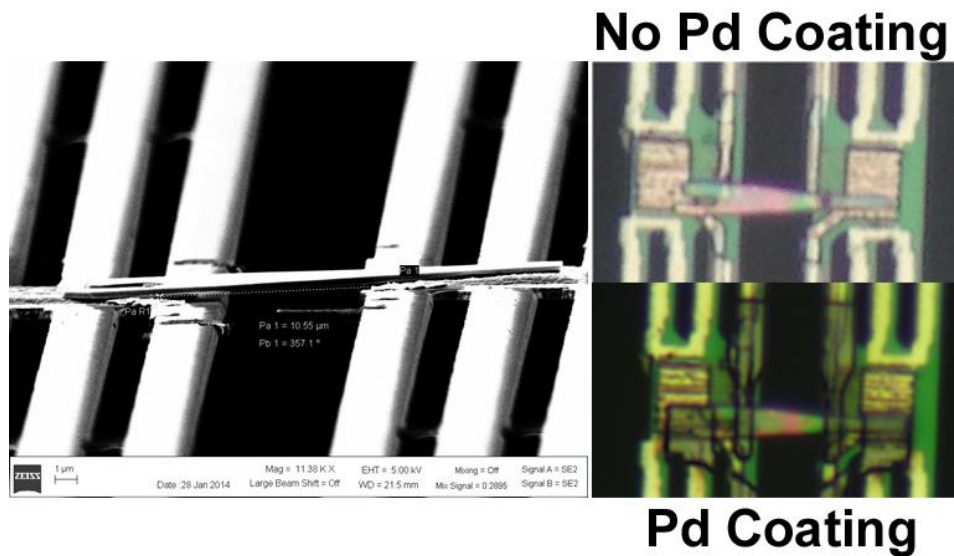


Figure 121: SEM and microscope images of the BAs microstructure loaded onto a microheater device.

The first measurement was attempted with a microheater device displayed in Figure 121. Initially, the sample measurement was attempted without any palladium metal deposition on the BAs sample. However, this experiment failed due to the presence of significant contact thermal resistance between the sample and the heater pads of the microheater device. This became apparent after inspection of the SEM of the BAs

microstructure. This rigid microstructure appears to be in poor contact with the heater pads, and hence it was clear that this measurement had a thermal contact resistance problem. In order to overcome this problem, a coating of Pd metal was deposited onto the BAs microstructure to eliminate the contact resistance between the sample and the heating pad. This modification was successful in removing the thermal contact resistance problems from the system. Unfortunately, after the Pd metal coating was deposited, the device failed due to the fact that the sensing part of the device did not experience any observable thermal delay. Essentially, the high thermal conductivity BAs sample created a thermal short circuit after the contact resistance problem was resolved. The heating pad and the sensing pad were found to be always at the same temperature during measurement. Typically, there is a delay between heating on one side of the device and sensing the temperature rise on the other side of the device as the heat transfers through the sample. However, this was not the case in our relatively large BAs sample. Normally, the microheater devices that are fabricated in the Shi research group, are designed for materials on the nano scale. Therefore, it was determined that these “6-beam” microheater devices, which are displayed in Figure 121, are not sufficiently sensitive for use with relatively large, high thermal conductivity samples.

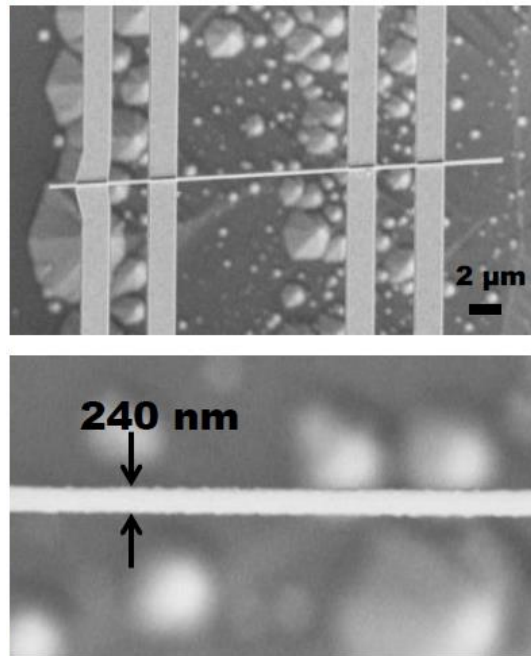


Figure 122: SEM images of 4-probe microheater device with suspended 240 nm thick silicon nanowire.<sup>116</sup>

Fortunately, however, the Shi research group has very recently developed a new 4-probe microheater device, which is considerably more sensitive than the “6-beam” devices discussed above.<sup>116</sup> This device was calibrated using silicon, a material with well-known thermal conductivity properties (Figure 122). Using this device, excellent agreement was obtained for the literature values of the thermal conductivity of silicon. Subsequently, the more sensitive 4-probe microheater device was utilized in an attempt to measure the thermal conductivity of our BAs microstructures.

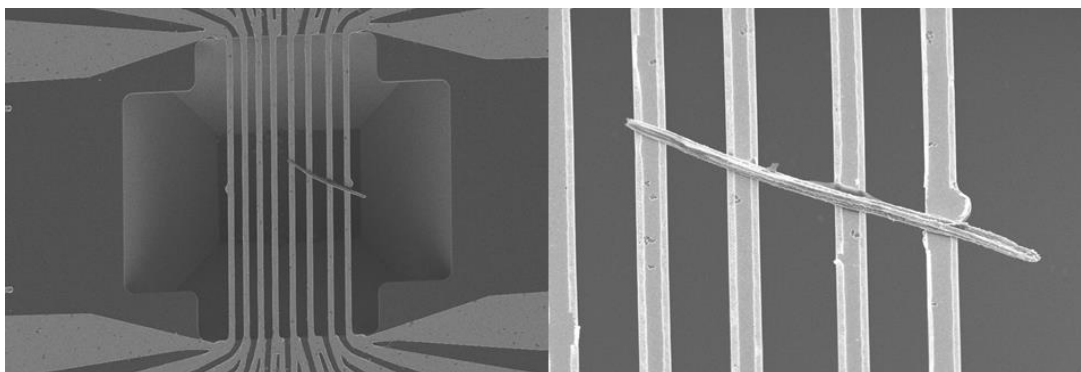


Figure 123: SEM images of 4-probe microheater device with suspended BAS microstructure.

As exhibited in Figure 123, a BAS microstructure was loaded onto a new 4-probe microheater device. Although, eight heater lines were fabricated in this device, only 4 of them are used for the experiment. The presence of eight lines makes the transfer of the BAS sample to the microheater significantly easier. Overall, the 4-probe microheater device functioned properly; however, the preliminary results that were obtained for the thermal conductivity of this BAS microstructure were disappointing. As displayed in Figure 124, the thermal conductivity of this sample was determined to be  $\sim 6.5 \text{ W/ m}^{-1} \text{ K}^{-1}$  at 300 K, which represents a value that is below expectations.

## Thermal Conductivity of BAs Microstructure

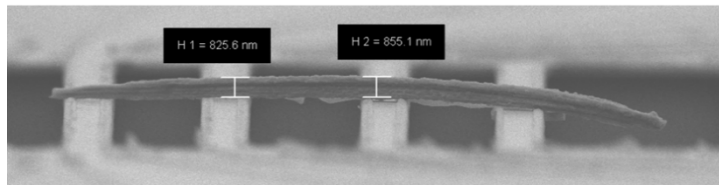
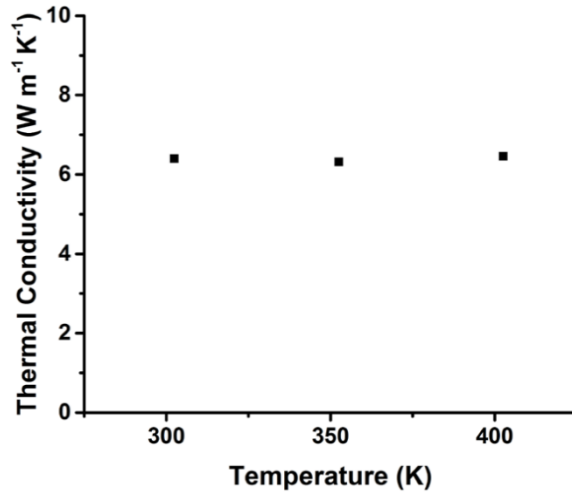


Figure 124: (Top) Experimental value of the thermal conductivity of the BAs microstructure. (Bottom) SEM image displaying contact resistance between the heater lines and BAs the microstructure.

Although this value was very low, there are expectations of drastically increasing the measured thermal conductivity. These expectations are motivated by the following considerations. First, the sample suffered from thermal contact resistance problems. This is displayed in Figure 124, where the “U” shaped heater lines might not be heating the sample in an effective, uniform manner. Accordingly, future efforts will be focused on Pd metal depositions to overcome this obstacle. Second, the sample was very thick (825-850 nm). The thickness of the sample could be problematic because the microheater device functions based on the idea of uniform heating of the sample in one direction from heater

line to heater line. However, if the sample is too thick, the heating would not be uniform and would interfere with an accurate measurement. With this in mind, future efforts will also be focused on obtaining the thinnest high quality BAs microstructure sample possible and loading this sample onto the 4-probe microheater device.

### **3.3 CONCLUSIONS**

In conclusion, high quality crystalline BAs materials were synthesized and characterized using Raman spectroscopy, XPS, powder X-ray diffraction, and SEM. Initially, the BAs microstructures were loaded onto “6-beam” microheater devices. However, these devices were determined to be insufficiently sensitive enough for measurement of the thermal conductivity of large BAs microstructures. Subsequently, a new 4-probe microheater device was developed by the Shi group and used to measure the thermal conductivity of BAs. However, problems were encountered during this measurement and only a modest value of  $\sim 6.5 \text{ W m}^{-1} \text{ K}^{-1}$  was obtained for the thermal conductivity of the BAs microstructure. Future efforts will be focused on the optimization of the 4-probe microheater device and the isolation of thin high quality BAs microstructures.

### **3.4 EXPERIMENTAL**

#### **3.4.1 General Procedures**

The synthesis of the BAs materials was prepared in an argon containing glove box. The quartz tubes were dried in an oven at 1000 °C for 12 hours prior to use. Boron powder (crystalline,  $\sim 4 + 40$  mesh, puratonic 99.9999%) and arsenic (polycrystalline lump, 2-8 mm, puratonic 99.9999%) were purchased from Alfa Aesar.

### **3.4.2 Raman Spectroscopy**

The Raman spectroscopy experiments were performed using the WITec Alpha 300RS confocal Raman imaging and scanning near-field optical microscope. The instrument was equipped with a 488 nm excitation laser and was operated using the WITec Control Version 1.60.

### **3.4.3 X-ray Powder Diffraction**

The X-ray powder diffraction data were collected on a Rigaku R-Axis Spider diffractometer equipped with an image plate detector. This instrument was also equipped with a monochromator and a Cu K $\alpha$  radiation source (1.51418 Å). The instrument utilized the Rapid/XRD Version 2.3.8 diffractometer program from the Rigaku Americas Corporation, The Woodlands, TX. The integration of the powder patterns was performed using the 2DP Version 1.0 program, which was also obtained from the Rigaku Americas Corporation, The Woodlands, TX. The experimental spectrum was created using the Eva Version 15.0.0.0 program.

### **3.4.4 Scanning Electron Microscopy**

The scanning electron microscopy (SEM) experiments were performed on a FEI Quanta 650 ESEM instrument.

### **3.4.5 X-ray Photoelectron Spectroscopy**

The X-ray photoelectron spectroscopy (XPS) experiments were performed on a Kratos Axis Ultra X-ray photoelectron spectrometer utilizing a monochromated Al K $\alpha$  radiation source ( $\lambda = 8.3401$  Å). All spectra were collected using 80 eV pass energy. The spectra were integrated using the CasaXPS software version 2.3.16 with the relative sensitivity factors of 0.159 and 0.677 for B 1s and As 3d, respectively.



### **3.4.6 Synthesis of BAs materials**

The BAs materials were synthesized according to the route described in the report from 1958.<sup>103</sup> Elemental arsenic (0.73 g, 9.71 mmol) and elemental boron (0.50 g, 4.62 mmol) were loaded into quartz tubes (which had been previously dried at 1000 °C in a furnace). The quartz reaction vessels were then evacuated on a Schlenk line for one hour. Following this, the quartz reaction vessels were sealed and loaded into a furnace and heated at 800 °C for three days. After this reaction time had been completed, the reaction vessel was slowly cooled at 0.1 °C/min. The elemental arsenic was removed manually from the boron substrates after completion of the reaction.

## Appendix A: X-Ray Diffraction Data for 1-9b

Table 16: Crystallographic Data and Structure Refinement of 1.

Empirical formula	C <sub>94</sub> H <sub>122</sub> Li <sub>4</sub> N <sub>4</sub>	
Formula weight	1335.72	
Temperature	100(2) K	
Wavelength	0.71075 Å	
Crystal system	Triclinic	
Space group	P-1	
Unit cell dimensions	a = 12.916(2) Å	α = 100.698(9)°.
	b = 13.320(3) Å	β = 99.299(10)°.
	c = 25.385(5) Å	γ = 105.796(9)°.
Volume	4024(2) Å <sup>3</sup>	
Z	2	
Density (calculated)	1.102 Mg/m <sup>3</sup>	
Absorption coefficient	0.062 mm <sup>-1</sup>	
F(000)	1452	
Crystal size	0.25 x 0.12 x 0.10 mm <sup>3</sup>	
Theta range for data collection	1.70 to 27.50°.	
Index ranges	-16<=h<=16, -17<=k<=17, -32<=l<=32	
Reflections collected	85689	
Independent reflections	18485 [R(int) = 0.0897]	
Completeness to theta = 27.50°	99.9 %	
Absorption correction	Semi-empirical from equivalents	
Max. and min. transmission	1.00000 and 0.8241	
Refinement method	Full-matrix least-squares on F <sup>2</sup>	
Data / restraints / parameters	18485 / 0 / 970	
Goodness-of-fit on F <sup>2</sup>	1.095	
Final R indices [I>2sigma(I)]	R1 = 0.0953, wR2 = 0.2224	
R indices (all data)	R1 = 0.1214, wR2 = 0.2397	
Largest diff. peak and hole	0.388 and -0.337 e.Å <sup>-3</sup>	

Table 17: Atomic coordinates ( $\times 10^4$ ) and equivalent isotropic displacement parameters ( $\text{\AA}^2 \times 10^3$ ) for **1**. U(eq) is defined as one third of the trace of the orthogonalized  $U^{ij}$  tensor.

	x	y	z	U(eq)
C(1)	3449(2)	2013(2)	1582(1)	19(1)
C(2)	3306(2)	2531(2)	1118(1)	19(1)
C(1A)	10731(3)	5897(3)	5383(1)	44(1)
C(3A)	10341(3)	4514(3)	4560(1)	47(1)
C(2A)	11068(3)	5399(3)	4943(1)	44(1)
C(3)	2479(2)	2335(2)	652(1)	24(1)
C(4)	2675(2)	2996(2)	283(1)	28(1)
C(4A)	9409(4)	3928(3)	-201(2)	65(1)
C(5)	3653(2)	3840(2)	382(1)	28(1)
C(6A)	10871(4)	5322(4)	450(2)	63(1)
C(6)	4469(2)	4083(2)	864(1)	23(1)
C(5A)	10286(4)	4249(4)	248(2)	64(1)
C(7)	4273(2)	3402(2)	1208(1)	20(1)
C(8)	5527(2)	5042(2)	1028(1)	24(1)
C(9)	6464(2)	4860(2)	1442(1)	25(1)
C(10)	6061(2)	4174(2)	1832(1)	22(1)
C(11)	5034(2)	3475(2)	1720(1)	19(1)
C(12)	4445(2)	2614(2)	1956(1)	18(1)
C(13)	1997(2)	358(2)	1166(1)	23(1)
C(14)	840(2)	111(2)	1119(1)	31(1)
C(15)	114(2)	-654(3)	664(1)	40(1)
C(16)	496(3)	-1150(3)	247(1)	43(1)
C(17)	1621(3)	-887(2)	278(1)	36(1)
C(18)	2384(2)	-151(2)	728(1)	27(1)
C(19)	350(2)	694(2)	1541(1)	34(1)
C(20)	-416(3)	1252(3)	1272(2)	50(1)

C(21)	-247(3)	-46(3)	1863(1)	46(1)
C(22)	3607(2)	59(2)	728(1)	32(1)
C(23)	3938(3)	-972(3)	679(2)	44(1)
C(24)	3940(3)	587(3)	265(2)	55(1)
C(25)	5919(2)	2759(2)	2701(1)	20(1)
C(26)	6387(2)	3642(2)	3165(1)	22(1)
C(27)	7531(2)	3988(2)	3371(1)	26(1)
C(28)	8205(2)	3488(2)	3132(1)	30(1)
C(29)	7748(2)	2606(2)	2691(1)	26(1)
C(30)	6614(2)	2223(2)	2471(1)	22(1)
C(31)	5677(2)	4233(2)	3439(1)	24(1)
C(32)	5278(2)	4957(2)	3099(1)	29(1)
C(33)	6235(2)	4915(2)	4025(1)	34(1)
C(34)	6116(2)	1210(2)	2006(1)	26(1)
C(35)	5798(3)	212(2)	2242(1)	37(1)
C(36)	6864(3)	1046(3)	1608(1)	36(1)
C(41)	7315(2)	4450(3)	1156(1)	32(1)
C(42)	7920(3)	5297(3)	878(2)	46(1)
C(43)	8207(2)	4308(3)	1593(1)	38(1)
C(44)	6743(3)	3381(3)	734(1)	40(1)
C(37)	5314(2)	6141(2)	1237(1)	31(1)
C(40)	6351(3)	7087(2)	1280(1)	39(1)
C(39)	4381(3)	6285(3)	829(2)	45(1)
C(38)	5012(3)	6218(3)	1799(1)	43(1)
C(45)	1947(2)	1403(2)	3144(1)	19(1)
C(46)	899(2)	1245(2)	3329(1)	21(1)
C(47)	199(2)	1863(2)	3408(1)	25(1)
C(48)	-746(2)	1427(2)	3601(1)	28(1)
C(49)	-991(2)	415(2)	3708(1)	28(1)
C(50)	-311(2)	-232(2)	3612(1)	25(1)
C(51)	620(2)	221(2)	3434(1)	22(1)
C(52)	-532(2)	-1384(2)	3668(1)	29(1)

C(53)	563(2)	-1672(2)	3799(1)	28(1)
C(54)	1430(2)	-1197(2)	3496(1)	24(1)
C(55)	1462(2)	-292(2)	3325(1)	21(1)
C(56)	2247(2)	467(2)	3104(1)	19(1)
C(57)	2577(2)	3336(2)	3317(1)	22(1)
C(58)	2308(2)	4079(2)	3026(1)	26(1)
C(59)	2495(2)	5142(2)	3308(1)	32(1)
C(60)	2907(3)	5481(2)	3869(1)	36(1)
C(61)	3099(2)	4737(2)	4160(1)	32(1)
C(62)	2939(2)	3672(2)	3902(1)	24(1)
C(63)	1757(2)	3743(2)	2416(1)	29(1)
C(64)	2421(3)	4337(2)	2060(1)	35(1)
C(65)	600(3)	3883(3)	2323(2)	48(1)
C(66)	3148(2)	2919(2)	4265(1)	27(1)
C(67)	2344(3)	2792(3)	4652(1)	34(1)
C(68)	4339(2)	3288(2)	4608(1)	33(1)
C(69)	3573(2)	-492(2)	3002(1)	22(1)
C(70)	3122(2)	-1531(2)	2648(1)	28(1)
C(71)	3614(2)	-2317(2)	2731(1)	33(1)
C(72)	4520(3)	-2109(2)	3153(1)	38(1)
C(73)	4936(3)	-1112(2)	3509(1)	37(1)
C(74)	4473(2)	-292(2)	3449(1)	27(1)
C(75)	2091(3)	-1826(2)	2190(1)	38(1)
C(76)	1265(3)	-2950(3)	2147(2)	48(1)
C(77)	2405(3)	-1803(3)	1647(2)	51(1)
C(78)	4961(2)	784(2)	3871(1)	32(1)
C(79)	6142(3)	1377(3)	3850(1)	42(1)
C(80)	4916(3)	644(3)	4454(1)	40(1)
C(81)	-1414(2)	-2209(2)	3164(1)	37(1)
C(82)	-1068(3)	-2161(3)	2625(2)	61(1)
C(83)	-2522(3)	-1980(3)	3130(2)	57(1)
C(84)	-1616(3)	-3359(3)	3240(2)	57(1)

C(85)	1078(2)	-1438(2)	4431(1)	33(1)
C(86)	245(3)	-2065(3)	4719(1)	43(1)
C(87)	2085(3)	-1849(3)	4507(1)	40(1)
C(88)	1439(3)	-239(3)	4710(1)	42(1)
N(1)	2738(2)	1073(2)	1657(1)	21(1)
N(2)	4749(2)	2380(2)	2476(1)	18(1)
N(3)	2587(2)	2322(2)	3015(1)	19(1)
N(4)	3172(2)	382(2)	2896(1)	21(1)
Li(1)	3465(5)	3013(5)	2528(3)	51(2)
Li(2)	3871(4)	727(3)	2217(2)	25(1)
Li(3)	4072(3)	1950(4)	3101(2)	24(1)
Li(4)	2065(4)	872(6)	2292(2)	52(2)

Table 18: Bond Lengths [Å] and Bond Angles [°] for **1**.

C(1)-C(12)	1.401(3)	C(6)-C(7)	1.377(3)
C(1)-N(1)	1.402(3)	C(6)-C(8)	1.529(4)
C(1)-C(2)	1.483(3)	C(7)-C(11)	1.466(3)
C(1)-Li(1)	2.514(7)	C(8)-C(9)	1.572(4)
C(1)-Li(2)	2.660(5)	C(8)-C(37)	1.574(4)
C(2)-C(3)	1.391(3)	C(9)-C(10)	1.525(3)
C(2)-C(7)	1.406(3)	C(9)-C(41)	1.572(4)
C(1A)-C(3A)#1	1.384(5)	C(10)-C(11)	1.347(3)
C(1A)-C(2A)	1.385(5)	C(11)-C(12)	1.478(3)
C(3A)-C(2A)	1.376(5)	C(12)-N(2)	1.430(3)
C(3A)-C(1A)#1	1.384(5)	C(12)-Li(1)	2.160(6)
C(3)-C(4)	1.405(4)	C(12)-Li(2)	2.659(5)
C(4)-C(5)	1.394(4)	C(13)-C(14)	1.420(4)
C(4A)-C(6A)#2	1.375(7)	C(13)-C(18)	1.425(4)
C(4A)-C(5A)	1.378(7)	C(13)-N(1)	1.433(3)
C(5)-C(6)	1.400(4)	C(14)-C(15)	1.394(4)
C(6A)-C(5A)	1.375(6)	C(14)-C(19)	1.526(4)
C(6A)-C(4A)#2	1.375(7)	C(15)-C(16)	1.372(5)

C(16)-C(17)	1.385(5)	C(45)-Li(4)	2.192(6)
C(17)-C(18)	1.389(4)	C(45)-Li(3)	2.667(5)
C(18)-C(22)	1.528(4)	C(46)-C(47)	1.391(4)
C(19)-C(21)	1.525(4)	C(46)-C(51)	1.401(3)
C(19)-C(20)	1.539(4)	C(47)-C(48)	1.409(4)
C(19)-Li(4)	2.604(6)	C(48)-C(49)	1.385(4)
C(22)-C(23)	1.535(4)	C(49)-C(50)	1.407(4)
C(22)-C(24)	1.539(5)	C(50)-C(51)	1.376(3)
C(25)-C(26)	1.417(4)	C(50)-C(52)	1.520(4)
C(25)-C(30)	1.421(4)	C(51)-C(55)	1.470(4)
C(25)-N(2)	1.436(3)	C(52)-C(53)	1.566(4)
C(25)-Li(3)	2.770(5)	C(52)-C(81)	1.571(4)
C(26)-C(27)	1.400(4)	C(53)-C(54)	1.524(4)
C(26)-C(31)	1.530(4)	C(53)-C(85)	1.571(4)
C(27)-C(28)	1.381(4)	C(54)-C(55)	1.347(4)
C(28)-C(29)	1.379(4)	C(55)-C(56)	1.483(3)
C(29)-C(30)	1.393(4)	C(56)-N(4)	1.405(3)
C(30)-C(34)	1.522(4)	C(56)-Li(4)	2.219(6)
C(31)-C(33)	1.533(4)	C(56)-Li(3)	2.634(5)
C(31)-C(32)	1.541(4)	C(57)-C(58)	1.422(4)
C(34)-C(36)	1.534(4)	C(57)-C(62)	1.428(4)
C(34)-C(35)	1.540(4)	C(57)-N(3)	1.429(3)
C(35)-Li(2)	2.750(5)	C(57)-Li(1)	2.491(6)
C(41)-C(44)	1.525(5)	C(58)-C(59)	1.399(4)
C(41)-C(43)	1.541(4)	C(58)-C(63)	1.524(4)
C(41)-C(42)	1.542(4)	C(58)-Li(1)	2.637(6)
C(37)-C(38)	1.530(4)	C(59)-C(60)	1.378(4)
C(37)-C(39)	1.537(4)	C(60)-C(61)	1.391(4)
C(37)-C(40)	1.542(4)	C(61)-C(62)	1.390(4)
C(45)-C(56)	1.394(3)	C(62)-C(66)	1.530(4)
C(45)-N(3)	1.405(3)	C(63)-C(64)	1.525(4)
C(45)-C(46)	1.477(3)	C(63)-C(65)	1.542(4)

C(63)-Li(1)	2.639(6)	N(4)-Li(4)	2.234(6)
C(66)-C(68)	1.536(4)	Li(1)-Li(3)	2.393(7)
C(66)-C(67)	1.540(4)	Li(1)-Li(4)	2.823(10)
C(69)-C(70)	1.411(4)	Li(1)-Li(2)	3.206(7)
C(69)-C(74)	1.416(4)	Li(2)-Li(4)	2.427(7)
C(69)-N(4)	1.447(3)	Li(2)-Li(3)	2.446(6)
C(70)-C(71)	1.394(4)	Li(3)-Li(4)	2.856(7)
C(70)-C(75)	1.525(4)		
C(71)-C(72)	1.380(4)	C(12)-C(1)-N(1)	123.1(2)
C(72)-C(73)	1.371(5)	C(12)-C(1)-C(2)	109.0(2)
C(73)-C(74)	1.399(4)	N(1)-C(1)-C(2)	127.9(2)
C(74)-C(78)	1.524(4)	C(12)-C(1)-Li(1)	59.10(19)
C(75)-C(77)	1.502(5)	N(1)-C(1)-Li(1)	90.4(2)
C(75)-C(76)	1.556(5)	C(2)-C(1)-Li(1)	118.7(2)
C(78)-C(79)	1.530(4)	C(12)-C(1)-Li(2)	74.68(17)
C(78)-C(80)	1.534(4)	N(1)-C(1)-Li(2)	50.62(15)
C(81)-C(82)	1.513(5)	C(2)-C(1)-Li(2)	164.3(2)
C(81)-C(83)	1.535(5)	Li(1)-C(1)-Li(2)	76.51(17)
C(81)-C(84)	1.536(5)	C(3)-C(2)-C(7)	118.6(2)
C(85)-C(88)	1.530(5)	C(3)-C(2)-C(1)	134.9(2)
C(85)-C(87)	1.540(4)	C(7)-C(2)-C(1)	106.5(2)
C(85)-C(86)	1.543(4)	C(3A)#1-C(1A)-C(2A)	119.4(4)
N(1)-Li(4)	1.977(6)	C(2A)-C(3A)-C(1A)#1	120.2(3)
N(1)-Li(2)	2.076(5)	C(3A)-C(2A)-C(1A)	120.4(4)
N(2)-Li(3)	2.030(5)	C(2)-C(3)-C(4)	118.0(2)
N(2)-Li(1)	2.066(6)	C(5)-C(4)-C(3)	121.7(2)
N(2)-Li(2)	2.104(5)	C(6A)#2-C(4A)-C(5A)	120.0(4)
N(3)-Li(1)	1.991(6)	C(4)-C(5)-C(6)	121.0(2)
N(3)-Li(3)	2.095(5)	C(5A)-C(6A)-C(4A)#2	119.9(5)
N(3)-Li(4)	2.265(7)	C(7)-C(6)-C(5)	116.0(2)
N(4)-Li(3)	2.016(5)	C(7)-C(6)-C(8)	119.2(2)
N(4)-Li(2)	2.137(5)	C(5)-C(6)-C(8)	124.8(2)



C(6A)-C(5A)-C(4A)	120.0(4)	C(16)-C(17)-C(18)	121.8(3)
C(6)-C(7)-C(2)	124.5(2)	C(17)-C(18)-C(13)	119.1(3)
C(6)-C(7)-C(11)	125.2(2)	C(17)-C(18)-C(22)	117.6(3)
C(2)-C(7)-C(11)	110.2(2)	C(13)-C(18)-C(22)	123.3(2)
C(6)-C(8)-C(9)	112.2(2)	C(21)-C(19)-C(14)	112.4(3)
C(6)-C(8)-C(37)	112.7(2)	C(21)-C(19)-C(20)	110.7(3)
C(9)-C(8)-C(37)	112.5(2)	C(14)-C(19)-C(20)	111.6(3)
C(10)-C(9)-C(41)	110.9(2)	C(21)-C(19)-Li(4)	82.5(2)
C(10)-C(9)-C(8)	115.1(2)	C(14)-C(19)-Li(4)	88.4(2)
C(41)-C(9)-C(8)	113.4(2)	C(20)-C(19)-Li(4)	147.6(3)
C(11)-C(10)-C(9)	122.6(2)	C(18)-C(22)-C(23)	112.2(2)
C(10)-C(11)-C(7)	118.0(2)	C(18)-C(22)-C(24)	112.5(3)
C(10)-C(11)-C(12)	136.1(2)	C(23)-C(22)-C(24)	108.5(3)
C(7)-C(11)-C(12)	105.4(2)	C(26)-C(25)-C(30)	119.3(2)
C(1)-C(12)-N(2)	121.8(2)	C(26)-C(25)-N(2)	120.6(2)
C(1)-C(12)-C(11)	108.5(2)	C(30)-C(25)-N(2)	120.1(2)
N(2)-C(12)-C(11)	129.7(2)	C(26)-C(25)-Li(3)	92.95(18)
C(1)-C(12)-Li(1)	87.1(2)	C(30)-C(25)-Li(3)	129.78(19)
N(2)-C(12)-Li(1)	66.71(19)	N(2)-C(25)-Li(3)	45.12(14)
C(11)-C(12)-Li(1)	117.9(2)	C(27)-C(26)-C(25)	118.8(2)
C(1)-C(12)-Li(2)	74.78(17)	C(27)-C(26)-C(31)	119.6(2)
N(2)-C(12)-Li(2)	51.96(15)	C(25)-C(26)-C(31)	121.6(2)
C(11)-C(12)-Li(2)	159.00(19)	C(28)-C(27)-C(26)	121.5(3)
Li(1)-C(12)-Li(2)	82.7(2)	C(29)-C(28)-C(27)	119.8(2)
C(14)-C(13)-C(18)	118.4(2)	C(28)-C(29)-C(30)	121.1(3)
C(14)-C(13)-N(1)	119.6(2)	C(29)-C(30)-C(25)	119.4(2)
C(18)-C(13)-N(1)	122.0(2)	C(29)-C(30)-C(34)	120.4(2)
C(15)-C(14)-C(13)	119.9(3)	C(25)-C(30)-C(34)	120.2(2)
C(15)-C(14)-C(19)	118.0(3)	C(26)-C(31)-C(33)	114.3(2)
C(13)-C(14)-C(19)	122.0(2)	C(26)-C(31)-C(32)	112.8(2)
C(16)-C(15)-C(14)	121.2(3)	C(33)-C(31)-C(32)	108.2(2)
C(15)-C(16)-C(17)	119.5(3)	C(30)-C(34)-C(36)	114.4(2)

C(30)-C(34)-C(35)	110.3(2)	C(51)-C(50)-C(52)	117.9(2)
C(36)-C(34)-C(35)	109.1(2)	C(49)-C(50)-C(52)	126.1(2)
C(34)-C(35)-Li(2)	81.79(19)	C(50)-C(51)-C(46)	124.6(2)
C(44)-C(41)-C(43)	109.2(3)	C(50)-C(51)-C(55)	125.4(2)
C(44)-C(41)-C(42)	110.1(3)	C(46)-C(51)-C(55)	110.0(2)
C(43)-C(41)-C(42)	106.4(2)	C(50)-C(52)-C(53)	111.8(2)
C(44)-C(41)-C(9)	111.2(2)	C(50)-C(52)-C(81)	112.1(2)
C(43)-C(41)-C(9)	109.8(2)	C(53)-C(52)-C(81)	113.5(2)
C(42)-C(41)-C(9)	110.1(3)	C(54)-C(53)-C(52)	114.2(2)
C(38)-C(37)-C(39)	108.6(3)	C(54)-C(53)-C(85)	110.9(2)
C(38)-C(37)-C(40)	109.3(3)	C(52)-C(53)-C(85)	113.9(2)
C(39)-C(37)-C(40)	106.0(2)	C(55)-C(54)-C(53)	121.6(2)
C(38)-C(37)-C(8)	111.3(2)	C(54)-C(55)-C(51)	117.8(2)
C(39)-C(37)-C(8)	111.3(2)	C(54)-C(55)-C(56)	136.1(2)
C(40)-C(37)-C(8)	110.1(2)	C(51)-C(55)-C(56)	105.5(2)
C(56)-C(45)-N(3)	122.0(2)	C(45)-C(56)-N(4)	120.8(2)
C(56)-C(45)-C(46)	109.7(2)	C(45)-C(56)-C(55)	107.7(2)
N(3)-C(45)-C(46)	128.2(2)	N(4)-C(56)-C(55)	131.4(2)
C(56)-C(45)-Li(4)	72.6(2)	C(45)-C(56)-Li(4)	70.5(2)
N(3)-C(45)-Li(4)	74.5(2)	N(4)-C(56)-Li(4)	72.2(2)
C(46)-C(45)-Li(4)	124.4(2)	C(55)-C(56)-Li(4)	130.5(2)
C(56)-C(45)-Li(3)	73.43(17)	C(45)-C(56)-Li(3)	76.07(17)
N(3)-C(45)-Li(3)	51.20(15)	N(4)-C(56)-Li(3)	49.12(15)
C(46)-C(45)-Li(3)	164.3(2)	C(55)-C(56)-Li(3)	157.93(19)
Li(4)-C(45)-Li(3)	71.25(18)	Li(4)-C(56)-Li(3)	71.54(19)
C(47)-C(46)-C(51)	118.7(2)	C(58)-C(57)-C(62)	118.6(2)
C(47)-C(46)-C(45)	134.7(2)	C(58)-C(57)-N(3)	119.2(2)
C(51)-C(46)-C(45)	106.6(2)	C(62)-C(57)-N(3)	121.9(2)
C(46)-C(47)-C(48)	117.8(2)	C(58)-C(57)-Li(1)	79.6(2)
C(49)-C(48)-C(47)	122.0(2)	C(62)-C(57)-Li(1)	135.9(2)
C(48)-C(49)-C(50)	120.8(2)	N(3)-C(57)-Li(1)	53.03(19)
C(51)-C(50)-C(49)	116.0(2)	C(59)-C(58)-C(57)	119.8(3)

C(59)-C(58)-C(63)	118.0(2)	C(77)-C(75)-C(70)	110.3(3)
C(57)-C(58)-C(63)	122.0(2)	C(77)-C(75)-C(76)	109.2(3)
C(59)-C(58)-Li(1)	135.7(2)	C(70)-C(75)-C(76)	112.9(3)
C(57)-C(58)-Li(1)	68.33(18)	C(74)-C(78)-C(79)	112.8(3)
C(63)-C(58)-Li(1)	73.3(2)	C(74)-C(78)-C(80)	111.1(2)
C(60)-C(59)-C(58)	121.2(3)	C(79)-C(78)-C(80)	110.2(2)
C(59)-C(60)-C(61)	119.0(3)	C(82)-C(81)-C(83)	108.8(3)
C(62)-C(61)-C(60)	122.4(3)	C(82)-C(81)-C(84)	108.8(3)
C(61)-C(62)-C(57)	118.6(3)	C(83)-C(81)-C(84)	106.7(3)
C(61)-C(62)-C(66)	117.9(2)	C(82)-C(81)-C(52)	112.3(2)
C(57)-C(62)-C(66)	123.5(2)	C(83)-C(81)-C(52)	109.8(3)
C(58)-C(63)-C(64)	114.3(2)	C(84)-C(81)-C(52)	110.3(3)
C(58)-C(63)-C(65)	110.7(3)	C(88)-C(85)-C(87)	109.2(3)
C(64)-C(63)-C(65)	108.9(2)	C(88)-C(85)-C(86)	109.4(3)
C(58)-C(63)-Li(1)	73.1(2)	C(87)-C(85)-C(86)	106.6(2)
C(64)-C(63)-Li(1)	80.1(2)	C(88)-C(85)-C(53)	112.0(2)
C(65)-C(63)-Li(1)	166.3(3)	C(87)-C(85)-C(53)	109.0(2)
C(62)-C(66)-C(68)	113.0(2)	C(86)-C(85)-C(53)	110.4(2)
C(62)-C(66)-C(67)	111.0(2)	C(1)-N(1)-C(13)	115.3(2)
C(68)-C(66)-C(67)	109.1(2)	C(1)-N(1)-Li(4)	128.5(3)
C(70)-C(69)-C(74)	119.1(2)	C(13)-N(1)-Li(4)	108.9(2)
C(70)-C(69)-N(4)	121.1(2)	C(1)-N(1)-Li(2)	97.91(19)
C(74)-C(69)-N(4)	119.7(2)	C(13)-N(1)-Li(2)	127.6(2)
C(71)-C(70)-C(69)	119.1(3)	Li(4)-N(1)-Li(2)	73.5(2)
C(71)-C(70)-C(75)	119.1(3)	C(12)-N(2)-C(25)	113.34(19)
C(69)-C(70)-C(75)	121.8(2)	C(12)-N(2)-Li(3)	140.3(2)
C(72)-C(71)-C(70)	121.7(3)	C(25)-N(2)-Li(3)	104.80(19)
C(73)-C(72)-C(71)	119.3(3)	C(12)-N(2)-Li(1)	73.8(2)
C(72)-C(73)-C(74)	121.6(3)	C(25)-N(2)-Li(1)	135.2(3)
C(73)-C(74)-C(69)	119.1(3)	Li(3)-N(2)-Li(1)	71.5(2)
C(73)-C(74)-C(78)	118.4(3)	C(12)-N(2)-Li(2)	95.70(18)
C(69)-C(74)-C(78)	122.5(2)	C(25)-N(2)-Li(2)	121.49(19)

Li(3)-N(2)-Li(2)	72.50(19)	N(3)-Li(1)-C(1)	122.3(3)
Li(1)-N(2)-Li(2)	100.5(2)	N(2)-Li(1)-C(1)	64.49(18)
C(45)-N(3)-C(57)	116.5(2)	C(12)-Li(1)-C(1)	33.80(13)
C(45)-N(3)-Li(1)	150.9(3)	Li(3)-Li(1)-C(1)	102.6(2)
C(57)-N(3)-Li(1)	92.0(2)	C(57)-Li(1)-C(1)	151.9(3)
C(45)-N(3)-Li(3)	97.28(19)	N(3)-Li(1)-C(58)	62.39(16)
C(57)-N(3)-Li(3)	119.1(2)	N(2)-Li(1)-C(58)	155.8(3)
Li(1)-N(3)-Li(3)	71.6(2)	C(12)-Li(1)-C(58)	158.2(3)
C(45)-N(3)-Li(4)	68.82(19)	Li(3)-Li(1)-C(58)	109.3(2)
C(57)-N(3)-Li(4)	155.8(2)	C(57)-Li(1)-C(58)	32.05(11)
Li(1)-N(3)-Li(4)	82.8(3)	C(1)-Li(1)-C(58)	139.7(3)
Li(3)-N(3)-Li(4)	81.7(2)	N(3)-Li(1)-C(63)	77.72(19)
C(56)-N(4)-C(69)	115.84(19)	N(2)-Li(1)-C(63)	170.5(3)
C(56)-N(4)-Li(3)	99.10(19)	C(12)-Li(1)-C(63)	131.4(3)
C(69)-N(4)-Li(3)	125.7(2)	Li(3)-Li(1)-C(63)	133.7(2)
C(56)-N(4)-Li(2)	138.1(2)	C(57)-Li(1)-C(63)	60.24(15)
C(69)-N(4)-Li(2)	101.17(18)	C(1)-Li(1)-C(63)	106.2(3)
Li(3)-N(4)-Li(2)	72.08(18)	C(58)-Li(1)-C(63)	33.58(11)
C(56)-N(4)-Li(4)	71.01(19)	N(3)-Li(1)-Li(4)	52.8(2)
C(69)-N(4)-Li(4)	144.4(3)	N(2)-Li(1)-Li(4)	86.9(3)
Li(3)-N(4)-Li(4)	84.3(2)	C(12)-Li(1)-Li(4)	92.9(3)
Li(2)-N(4)-Li(4)	67.40(19)	Li(3)-Li(1)-Li(4)	65.8(2)
N(3)-Li(1)-N(2)	108.4(3)	C(57)-Li(1)-Li(4)	85.5(2)
N(3)-Li(1)-C(12)	138.7(3)	C(1)-Li(1)-Li(4)	69.5(2)
N(2)-Li(1)-C(12)	39.46(13)	C(58)-Li(1)-Li(4)	101.8(2)
N(3)-Li(1)-Li(3)	56.20(18)	C(63)-Li(1)-Li(4)	91.4(2)
N(2)-Li(1)-Li(3)	53.56(17)	N(3)-Li(1)-Li(2)	83.4(2)
C(12)-Li(1)-Li(3)	91.3(2)	N(2)-Li(1)-Li(2)	40.20(15)
N(3)-Li(1)-C(57)	34.99(12)	C(12)-Li(1)-Li(2)	55.35(17)
N(2)-Li(1)-C(57)	128.8(3)	Li(3)-Li(1)-Li(2)	49.21(17)
C(12)-Li(1)-C(57)	168.3(3)	C(57)-Li(1)-Li(2)	117.0(2)
Li(3)-Li(1)-C(57)	77.5(2)	C(1)-Li(1)-Li(2)	53.79(15)

C(58)-Li(1)-Li(2)	145.0(2)	N(2)-Li(2)-Li(1)	39.32(15)
C(63)-Li(1)-Li(2)	136.5(3)	N(4)-Li(2)-Li(1)	86.04(17)
Li(4)-Li(1)-Li(2)	46.94(18)	Li(4)-Li(2)-Li(1)	58.2(2)
N(1)-Li(2)-N(2)	88.73(18)	Li(3)-Li(2)-Li(1)	47.80(17)
N(1)-Li(2)-N(4)	109.5(2)	C(12)-Li(2)-Li(1)	41.94(12)
N(2)-Li(2)-N(4)	104.0(2)	C(1)-Li(2)-Li(1)	49.70(14)
N(1)-Li(2)-Li(4)	51.36(17)	C(35)-Li(2)-Li(1)	130.7(2)
N(2)-Li(2)-Li(4)	97.3(2)	N(4)-Li(3)-N(2)	111.4(2)
N(4)-Li(2)-Li(4)	58.22(18)	N(4)-Li(3)-N(3)	88.16(18)
N(1)-Li(2)-Li(3)	105.7(2)	N(2)-Li(3)-N(3)	105.8(2)
N(2)-Li(2)-Li(3)	52.35(15)	N(4)-Li(3)-Li(1)	115.2(3)
N(4)-Li(2)-Li(3)	51.68(15)	N(2)-Li(3)-Li(1)	54.95(17)
Li(4)-Li(2)-Li(3)	71.8(2)	N(3)-Li(3)-Li(1)	52.17(17)
N(1)-Li(2)-C(12)	61.25(13)	N(4)-Li(3)-Li(2)	56.24(16)
N(2)-Li(2)-C(12)	32.34(10)	N(2)-Li(3)-Li(2)	55.15(16)
N(4)-Li(2)-C(12)	127.0(2)	N(3)-Li(3)-Li(2)	103.5(2)
Li(4)-Li(2)-C(12)	91.3(2)	Li(1)-Li(3)-Li(2)	83.0(2)
Li(3)-Li(2)-C(12)	79.28(17)	N(4)-Li(3)-C(56)	31.78(10)
N(1)-Li(2)-C(1)	31.46(10)	N(2)-Li(3)-C(56)	131.7(2)
N(2)-Li(2)-C(1)	61.23(13)	N(3)-Li(3)-C(56)	61.13(13)
N(4)-Li(2)-C(1)	127.8(2)	Li(1)-Li(3)-C(56)	104.4(2)
Li(4)-Li(2)-C(1)	73.61(19)	Li(2)-Li(3)-C(56)	81.48(17)
Li(3)-Li(2)-C(1)	97.10(18)	N(4)-Li(3)-C(45)	60.77(13)
C(12)-Li(2)-C(1)	30.54(9)	N(2)-Li(3)-C(45)	128.0(2)
N(1)-Li(2)-C(35)	137.8(2)	N(3)-Li(3)-C(45)	31.51(10)
N(2)-Li(2)-C(35)	91.45(18)	Li(1)-Li(3)-C(45)	81.0(2)
N(4)-Li(2)-C(35)	111.37(19)	Li(2)-Li(3)-C(45)	97.73(19)
Li(4)-Li(2)-C(35)	167.8(3)	C(56)-Li(3)-C(45)	30.50(9)
Li(3)-Li(2)-C(35)	107.6(2)	N(4)-Li(3)-C(25)	123.4(2)
C(12)-Li(2)-C(35)	100.56(17)	N(2)-Li(3)-C(25)	30.09(9)
C(1)-Li(2)-C(35)	118.29(18)	N(3)-Li(3)-C(25)	129.3(2)
N(1)-Li(2)-Li(1)	61.98(17)	Li(1)-Li(3)-C(25)	77.54(19)

Li(2)-Li(3)-C(25)	72.80(16)	N(4)-Li(4)-Li(2)	54.38(18)
C(56)-Li(3)-C(25)	153.8(2)	N(3)-Li(4)-Li(2)	99.2(2)
C(45)-Li(3)-C(25)	157.36(19)	N(1)-Li(4)-C(19)	78.7(2)
N(4)-Li(3)-Li(4)	51.11(18)	C(45)-Li(4)-C(19)	115.6(3)
N(2)-Li(3)-Li(4)	86.68(19)	C(56)-Li(4)-C(19)	132.8(3)
N(3)-Li(3)-Li(4)	51.70(18)	N(4)-Li(4)-C(19)	158.5(3)
Li(1)-Li(3)-Li(4)	64.4(3)	N(3)-Li(4)-C(19)	116.3(3)
Li(2)-Li(3)-Li(4)	53.80(19)	Li(2)-Li(4)-C(19)	131.1(3)
C(56)-Li(3)-Li(4)	47.47(15)	N(1)-Li(4)-Li(1)	71.5(2)
C(45)-Li(3)-Li(4)	46.61(14)	C(45)-Li(4)-Li(1)	81.0(3)
C(25)-Li(3)-Li(4)	115.81(19)	C(56)-Li(4)-Li(1)	103.4(3)
N(1)-Li(4)-C(45)	152.0(4)	N(4)-Li(4)-Li(1)	94.3(2)
N(1)-Li(4)-C(56)	146.1(3)	N(3)-Li(4)-Li(1)	44.42(18)
C(45)-Li(4)-C(56)	36.85(13)	Li(2)-Li(4)-Li(1)	74.9(2)
N(1)-Li(4)-N(4)	109.4(3)	C(19)-Li(4)-Li(1)	107.3(3)
C(45)-Li(4)-N(4)	66.72(18)	N(1)-Li(4)-Li(3)	94.9(2)
C(56)-Li(4)-N(4)	36.77(12)	C(45)-Li(4)-Li(3)	62.14(18)
N(1)-Li(4)-N(3)	115.9(3)	C(56)-Li(4)-Li(3)	61.00(17)
C(45)-Li(4)-N(3)	36.71(13)	N(4)-Li(4)-Li(3)	44.62(15)
C(56)-Li(4)-N(3)	66.20(18)	N(3)-Li(4)-Li(3)	46.55(15)
N(4)-Li(4)-N(3)	79.0(2)	Li(2)-Li(4)-Li(3)	54.42(18)
N(1)-Li(4)-Li(2)	55.12(18)	C(19)-Li(4)-Li(3)	156.7(3)
C(45)-Li(4)-Li(2)	113.0(3)	Li(1)-Li(4)-Li(3)	49.84(18)
C(56)-Li(4)-Li(2)	91.0(2)		

---

Table 19: Crystallographic Data and Structure Refinement of **2**.

Empirical formula	C <sub>44</sub> H <sub>58</sub> N <sub>2</sub>	
Formula weight	614.92	
Temperature	153(2) K	
Wavelength	0.71075 Å	
Crystal system	Monoclinic	
Space group	P2 <sub>1</sub> /c	
Unit cell dimensions	a = 9.841(4) Å	α = 90°.
	b = 25.042(8) Å	β = 103.111(4)°.
	c = 16.187(6) Å	γ = 90°.
Volume	3885(2) Å <sup>3</sup>	
Z	4	
Density (calculated)	1.051 Mg/m <sup>3</sup>	
Absorption coefficient	0.060 mm <sup>-1</sup>	
F(000)	1344	
Crystal size	0.29 x 0.23 x 0.19 mm <sup>3</sup>	
Theta range for data collection	1.53 to 25.09°.	
Index ranges	-11 ≤ h ≤ 11, -29 ≤ k ≤ 27, -19 ≤ l ≤ 19	
Reflections collected	29416	
Independent reflections	6859 [R(int) = 0.0591]	
Completeness to theta = 25.09°	99.3 %	
Absorption correction	Semi-empirical from equivalents	
Max. and min. transmission	1.00000 and 0.8626	
Refinement method	Full-matrix least-squares on F <sup>2</sup>	
Data / restraints / parameters	6859 / 56 / 461	
Goodness-of-fit on F <sup>2</sup>	1.064	
Final R indices [I > 2σ(I)]	R1 = 0.0621, wR2 = 0.1465	
R indices (all data)	R1 = 0.0880, wR2 = 0.1731	
Largest diff. peak and hole	0.184 and -0.260 e.Å <sup>-3</sup>	

Table 20: Atomic coordinates ( $\times 10^4$ ) and equivalent isotropic displacement parameters ( $\text{\AA}^2 \times 10^3$ ) for **2**. U(eq) is defined as one third of the trace of the orthogonalized  $U^{ij}$  tensor.

	x	y	z	U(eq)
C(1)	2630(2)	2670(1)	8340(1)	34(1)
C(2)	2475(2)	2741(1)	7410(1)	35(1)
C(3)	1972(3)	2410(1)	6709(1)	41(1)
C(4)	2027(3)	2605(1)	5913(1)	43(1)
C(5)	2496(2)	3119(1)	5798(1)	40(1)
C(6)	2956(2)	3463(1)	6484(1)	34(1)
C(7)	2984(2)	3248(1)	7283(1)	33(1)
C(8)	3407(2)	4040(1)	6426(1)	38(1)
C(9)	4536(2)	4215(1)	7233(1)	37(1)
C(10)	4331(2)	3974(1)	8056(1)	37(1)
C(11)	3602(2)	3524(1)	8073(1)	34(1)
C(12)	3312(2)	3176(1)	8761(1)	33(1)
C(13)	1656(2)	1813(1)	8393(1)	36(1)
C(14)	220(3)	1743(1)	8348(2)	43(1)
C(15)	-411(3)	1276(1)	7984(2)	53(1)
C(16)	350(3)	886(1)	7700(2)	59(1)
C(17)	1773(3)	947(1)	7785(2)	53(1)
C(18)	2469(3)	1410(1)	8136(1)	40(1)
C(19)	-591(3)	2176(1)	8689(2)	54(1)
C(20)	-1041(4)	2624(1)	8049(2)	82(1)
C(21)	-1837(4)	1955(2)	9003(3)	97(1)
C(22)	4045(3)	1466(1)	8270(2)	45(1)
C(23)	4636(3)	1175(1)	7600(2)	66(1)
C(24)	4749(3)	1263(1)	9156(2)	66(1)
C(25)	4167(3)	3702(1)	9984(1)	39(1)
C(26)	3371(3)	4151(1)	10082(2)	50(1)



C(27)	4050(3)	4574(1)	10568(2)	58(1)
C(28)	5446(3)	4553(1)	10940(2)	56(1)
C(29)	6218(3)	4106(1)	10839(2)	51(1)
C(30)	5601(3)	3669(1)	10359(1)	43(1)
C(31)	1763(7)	4115(5)	9856(5)	57(3)
C(32)	1185(9)	4506(5)	9129(5)	99(3)
C(33)	1099(8)	4216(5)	10594(6)	94(3)
C(31A)	1847(6)	4200(4)	9583(5)	50(2)
C(32A)	1364(6)	4757(2)	9370(4)	54(2)
C(33A)	948(6)	3912(3)	10110(5)	91(2)
C(34)	6413(3)	3164(1)	10267(2)	54(1)
C(35)	6043(4)	2717(1)	10818(2)	84(1)
C(36)	7990(3)	3244(2)	10452(3)	86(1)
C(37)	2132(3)	4434(1)	6200(2)	51(1)
C(38)	1105(3)	4243(1)	5392(2)	74(1)
C(39)	1364(3)	4472(1)	6919(2)	72(1)
C(40)	2637(4)	4992(1)	6006(2)	82(1)
C(41)	6076(3)	4135(1)	7128(2)	45(1)
C(42)	6338(3)	3555(1)	6907(2)	58(1)
C(43)	6355(3)	4503(1)	6421(2)	60(1)
C(44)	7119(3)	4294(1)	7950(2)	65(1)
N(1)	2297(2)	2289(1)	8784(1)	35(1)
N(2)	3496(2)	3238(1)	9562(1)	39(1)

Table 21: Bond Lengths [ $\text{\AA}$ ] and Bond Angles [ $^\circ$ ] for **2**.

C(1)-N(1)	1.280(3)	C(5)-C(6)	1.399(3)
C(1)-C(2)	1.488(3)	C(6)-C(7)	1.395(3)
C(1)-C(12)	1.521(3)	C(6)-C(8)	1.521(3)
C(2)-C(7)	1.397(3)	C(7)-C(11)	1.460(3)
C(2)-C(3)	1.401(3)	C(8)-C(37)	1.572(3)
C(3)-C(4)	1.391(3)	C(8)-C(9)	1.574(3)
C(4)-C(5)	1.394(3)	C(9)-C(10)	1.518(3)

C(9)-C(41)	1.575(3)	C(34)-C(35)	1.526(4)
C(10)-C(11)	1.338(3)	C(37)-C(39)	1.528(4)
C(11)-C(12)	1.493(3)	C(37)-C(38)	1.537(4)
C(12)-N(2)	1.277(3)	C(37)-C(40)	1.540(4)
C(13)-C(18)	1.408(3)	C(41)-C(42)	1.532(4)
C(13)-C(14)	1.410(3)	C(41)-C(44)	1.537(4)
C(13)-N(1)	1.428(3)	C(41)-C(43)	1.543(4)
C(14)-C(15)	1.392(4)		
C(14)-C(19)	1.522(4)	N(1)-C(1)-C(2)	132.6(2)
C(15)-C(16)	1.372(4)	N(1)-C(1)-C(12)	120.72(19)
C(16)-C(17)	1.384(4)	C(2)-C(1)-C(12)	106.71(18)
C(17)-C(18)	1.401(3)	C(7)-C(2)-C(3)	119.3(2)
C(18)-C(22)	1.522(3)	C(7)-C(2)-C(1)	107.48(18)
C(19)-C(20)	1.524(4)	C(3)-C(2)-C(1)	133.2(2)
C(19)-C(21)	1.532(4)	C(4)-C(3)-C(2)	117.6(2)
C(22)-C(23)	1.526(3)	C(3)-C(4)-C(5)	122.1(2)
C(22)-C(24)	1.531(3)	C(4)-C(5)-C(6)	121.4(2)
C(25)-C(26)	1.401(3)	C(7)-C(6)-C(5)	115.6(2)
C(25)-C(30)	1.406(4)	C(7)-C(6)-C(8)	118.75(19)
C(25)-N(2)	1.430(3)	C(5)-C(6)-C(8)	125.7(2)
C(26)-C(27)	1.395(4)	C(6)-C(7)-C(2)	123.8(2)
C(26)-C(31A)	1.539(6)	C(6)-C(7)-C(11)	123.0(2)
C(26)-C(31)	1.545(8)	C(2)-C(7)-C(11)	113.15(19)
C(27)-C(28)	1.370(4)	C(6)-C(8)-C(37)	112.4(2)
C(28)-C(29)	1.382(4)	C(6)-C(8)-C(9)	111.94(18)
C(29)-C(30)	1.399(3)	C(37)-C(8)-C(9)	113.26(19)
C(30)-C(34)	1.523(4)	C(10)-C(9)-C(8)	114.13(19)
C(31)-C(33)	1.507(7)	C(10)-C(9)-C(41)	111.47(19)
C(31)-C(32)	1.538(7)	C(8)-C(9)-C(41)	112.98(19)
C(31A)-C(32A)	1.489(10)	C(11)-C(10)-C(9)	122.1(2)
C(31A)-C(33A)	1.541(8)	C(10)-C(11)-C(7)	120.0(2)
C(34)-C(36)	1.526(4)	C(10)-C(11)-C(12)	134.5(2)

C(7)-C(11)-C(12)	105.35(18)	C(31A)-C(26)-C(31)	19.2(4)
N(2)-C(12)-C(11)	132.8(2)	C(28)-C(27)-C(26)	121.5(3)
N(2)-C(12)-C(1)	120.25(19)	C(27)-C(28)-C(29)	120.2(2)
C(11)-C(12)-C(1)	106.93(17)	C(28)-C(29)-C(30)	121.1(3)
C(18)-C(13)-C(14)	121.7(2)	C(29)-C(30)-C(25)	117.5(2)
C(18)-C(13)-N(1)	120.4(2)	C(29)-C(30)-C(34)	122.3(2)
C(14)-C(13)-N(1)	117.6(2)	C(25)-C(30)-C(34)	120.2(2)
C(15)-C(14)-C(13)	118.2(2)	C(33)-C(31)-C(32)	110.4(7)
C(15)-C(14)-C(19)	122.1(2)	C(33)-C(31)-C(26)	114.0(6)
C(13)-C(14)-C(19)	119.7(2)	C(32)-C(31)-C(26)	109.0(6)
C(16)-C(15)-C(14)	121.1(3)	C(32A)-C(31A)-C(26)	114.8(6)
C(15)-C(16)-C(17)	120.3(2)	C(32A)-C(31A)-C(33A)	112.0(6)
C(16)-C(17)-C(18)	121.5(3)	C(26)-C(31A)-C(33A)	106.6(5)
C(17)-C(18)-C(13)	117.1(2)	C(30)-C(34)-C(36)	113.8(2)
C(17)-C(18)-C(22)	121.4(2)	C(30)-C(34)-C(35)	110.6(2)
C(13)-C(18)-C(22)	121.4(2)	C(36)-C(34)-C(35)	110.5(3)
C(14)-C(19)-C(20)	111.9(2)	C(39)-C(37)-C(38)	108.9(3)
C(14)-C(19)-C(21)	112.9(3)	C(39)-C(37)-C(40)	109.7(3)
C(20)-C(19)-C(21)	111.1(3)	C(38)-C(37)-C(40)	106.9(2)
C(18)-C(22)-C(23)	113.3(2)	C(39)-C(37)-C(8)	111.6(2)
C(18)-C(22)-C(24)	109.5(2)	C(38)-C(37)-C(8)	109.8(2)
C(23)-C(22)-C(24)	110.1(2)	C(40)-C(37)-C(8)	109.8(2)
C(26)-C(25)-C(30)	121.9(2)	C(42)-C(41)-C(44)	109.4(2)
C(26)-C(25)-N(2)	119.8(2)	C(42)-C(41)-C(43)	109.0(2)
C(30)-C(25)-N(2)	118.0(2)	C(44)-C(41)-C(43)	106.9(2)
C(27)-C(26)-C(25)	117.7(3)	C(42)-C(41)-C(9)	111.3(2)
C(27)-C(26)-C(31A)	121.3(4)	C(44)-C(41)-C(9)	110.1(2)
C(25)-C(26)-C(31A)	120.6(4)	C(43)-C(41)-C(9)	110.0(2)
C(27)-C(26)-C(31)	120.8(5)	C(1)-N(1)-C(13)	121.07(18)
C(25)-C(26)-C(31)	119.7(5)	C(12)-N(2)-C(25)	121.85(19)

---

Table 22: Crystallographic Data and Structure Refinement of **3**.

Empirical formula	C <sub>43.50</sub> H <sub>54</sub> N <sub>2</sub> O	
Formula weight	620.89	
Temperature	153(2) K	
Wavelength	0.71075 Å	
Crystal system	Monoclinic	
Space group	P2 <sub>1</sub> /n	
Unit cell dimensions	a = 10.840(3) Å	α = 90°.
	b = 15.555(4) Å	β = 91.876(3)°.
	c = 23.010(6) Å	γ = 90°.
Volume	3877.8(18) Å <sup>3</sup>	
Z	4	
Density (calculated)	1.064 Mg/m <sup>3</sup>	
Absorption coefficient	0.062 mm <sup>-1</sup>	
F(000)	1348	
Crystal size	0.33 x 0.31 x 0.09 mm <sup>3</sup>	
Theta range for data collection	2.20 to 27.50°.	
Index ranges	-14 ≤ h ≤ 14, -20 ≤ k ≤ 20, -29 ≤ l ≤ 29	
Reflections collected	40438	
Independent reflections	8888 [R(int) = 0.0461]	
Completeness to theta = 27.50°	99.9 %	
Absorption correction	Semi-empirical from equivalents	
Max. and min. transmission	1.00000 and 0.8715	
Refinement method	Full-matrix least-squares on F <sup>2</sup>	
Data / restraints / parameters	8888 / 105 / 467	
Goodness-of-fit on F <sup>2</sup>	1.062	
Final R indices [I > 2σ(I)]	R1 = 0.0642, wR2 = 0.1589	
R indices (all data)	R1 = 0.0867, wR2 = 0.1785	
Largest diff. peak and hole	0.257 and -0.280 e.Å <sup>-3</sup>	

Table 23: Atomic coordinates ( $\times 10^4$ ) and equivalent isotropic displacement parameters ( $\text{\AA}^2 \times 10^3$ ) for **3**. U(eq) is defined as one third of the trace of the orthogonalized  $U^{ij}$  tensor.

	x	y	z	U(eq)
C(1)	2195(2)	9054(1)	8300(1)	29(1)
C(2)	2686(2)	9860(1)	8562(1)	33(1)
C(3)	2618(2)	10224(1)	9115(1)	41(1)
C(4)	3161(2)	11023(1)	9206(1)	43(1)
C(5)	3792(2)	11450(1)	8771(1)	37(1)
C(6)	3897(2)	11088(1)	8219(1)	31(1)
C(7)	3295(2)	10306(1)	8127(1)	30(1)
C(8)	4580(2)	11481(1)	7719(1)	30(1)
C(9)	3956(2)	11229(1)	7128(1)	31(1)
C(10)	3483(2)	10315(1)	7077(1)	30(1)
C(11)	3146(1)	9897(1)	7556(1)	28(1)
C(12)	2421(1)	9101(1)	7653(1)	28(1)
C(13)	1508(2)	8352(1)	9128(1)	30(1)
C(14)	2477(2)	8109(1)	9507(1)	43(1)
C(15)	2237(2)	8090(1)	10101(1)	53(1)
C(16)	1106(2)	8295(1)	10303(1)	54(1)
C(17)	147(2)	8494(1)	9920(1)	50(1)
C(18)	321(2)	8517(1)	9320(1)	38(1)
C(19)	3733(2)	7857(2)	9297(1)	73(1)
C(20)	4753(3)	8374(3)	9594(2)	142(2)
C(21)	3965(4)	6898(3)	9378(2)	118(2)
C(22)	-714(2)	8735(2)	8886(1)	55(1)
C(23)	-801(3)	9703(2)	8788(2)	106(1)
C(24)	-1950(2)	8342(3)	9043(2)	106(1)
C(25)	2117(2)	8588(1)	6700(1)	29(1)
C(26)	3218(2)	8285(1)	6467(1)	35(1)

C(27)	3292(2)	8276(1)	5862(1)	47(1)
C(28)	2333(2)	8561(2)	5506(1)	54(1)
C(29)	1254(2)	8857(1)	5742(1)	47(1)
C(30)	1112(2)	8867(1)	6343(1)	35(1)
C(31)	4294(2)	7960(1)	6851(1)	43(1)
C(32)	4319(2)	6976(2)	6869(1)	60(1)
C(33)	5532(2)	8312(1)	6661(1)	55(1)
C(34)	-64(2)	9182(1)	6616(1)	42(1)
C(35)	42(2)	10115(1)	6818(1)	60(1)
C(36)	-1216(2)	9081(2)	6219(1)	63(1)
C(37)	6002(2)	11291(1)	7749(1)	36(1)
C(38)	6646(2)	11885(2)	7316(1)	56(1)
C(39)	6294(2)	10354(1)	7608(1)	51(1)
C(40)	6555(2)	11498(1)	8356(1)	49(1)
N(1)	1695(1)	8387(1)	8514(1)	29(1)
N(2)	1935(1)	8547(1)	7308(1)	29(1)
O(1)	2873(1)	11729(1)	7006(1)	40(1)
C(41)	4895(5)	10372(3)	5154(2)	63(1)
C(42)	5848(7)	9829(4)	5300(4)	81(3)
C(43)	6032(7)	9128(4)	4968(3)	104(2)
C(44)	5265(7)	8974(7)	4498(4)	112(4)
C(45)	4313(7)	9510(4)	4340(3)	93(2)
C(46)	4130(7)	10225(4)	4684(3)	69(3)
C(47)	4701(8)	11139(5)	5520(3)	111(4)

Table 24: Bond Lengths [ $\text{\AA}$ ] and Bond Angles [ $^\circ$ ] for **3**.

C(1)-N(1)	1.278(2)	C(4)-C(5)	1.398(3)
C(1)-C(2)	1.481(2)	C(5)-C(6)	1.397(2)
C(1)-C(12)	1.519(2)	C(6)-C(7)	1.394(2)
C(2)-C(3)	1.398(2)	C(6)-C(8)	1.517(2)
C(2)-C(7)	1.400(2)	C(7)-C(11)	1.464(2)
C(3)-C(4)	1.388(3)	C(8)-C(9)	1.549(2)

C(8)-C(37)	1.569(2)	C(37)-C(39)	1.529(3)
C(9)-O(1)	1.428(2)	C(37)-C(40)	1.537(3)
C(9)-C(10)	1.515(2)	C(37)-C(38)	1.541(3)
C(10)-C(11)	1.340(2)	C(41)-C(46)	1.360(6)
C(11)-C(12)	1.487(2)	C(41)-C(42)	1.368(6)
C(12)-N(2)	1.274(2)	C(41)-C(47)	1.480(8)
C(13)-C(14)	1.394(3)	C(42)-C(43)	1.350(7)
C(13)-C(18)	1.399(2)	C(43)-C(44)	1.362(7)
C(13)-N(1)	1.434(2)	C(44)-C(45)	1.367(7)
C(14)-C(15)	1.400(3)	C(45)-C(46)	1.385(7)
C(14)-C(19)	1.511(3)		
C(15)-C(16)	1.364(3)	N(1)-C(1)-C(2)	133.03(15)
C(16)-C(17)	1.377(3)	N(1)-C(1)-C(12)	120.08(14)
C(17)-C(18)	1.399(3)	C(2)-C(1)-C(12)	106.86(13)
C(18)-C(22)	1.515(3)	C(3)-C(2)-C(7)	119.40(15)
C(19)-C(20)	1.513(5)	C(3)-C(2)-C(1)	133.10(15)
C(19)-C(21)	1.524(5)	C(7)-C(2)-C(1)	107.48(14)
C(22)-C(23)	1.526(4)	C(4)-C(3)-C(2)	117.67(16)
C(22)-C(24)	1.527(4)	C(3)-C(4)-C(5)	122.20(16)
C(25)-C(26)	1.406(2)	C(6)-C(5)-C(4)	121.02(16)
C(25)-C(30)	1.410(2)	C(7)-C(6)-C(5)	116.02(15)
C(25)-N(2)	1.422(2)	C(7)-C(6)-C(8)	118.28(14)
C(26)-C(27)	1.397(3)	C(5)-C(6)-C(8)	125.69(15)
C(26)-C(31)	1.525(3)	C(6)-C(7)-C(2)	123.56(15)
C(27)-C(28)	1.376(3)	C(6)-C(7)-C(11)	123.59(14)
C(28)-C(29)	1.385(3)	C(2)-C(7)-C(11)	112.68(14)
C(29)-C(30)	1.397(3)	C(6)-C(8)-C(9)	110.73(13)
C(30)-C(34)	1.521(3)	C(6)-C(8)-C(37)	113.26(14)
C(31)-C(33)	1.526(3)	C(9)-C(8)-C(37)	113.00(13)
C(31)-C(32)	1.532(3)	O(1)-C(9)-C(10)	102.85(13)
C(34)-C(35)	1.526(3)	O(1)-C(9)-C(8)	111.61(13)
C(34)-C(36)	1.531(3)	C(10)-C(9)-C(8)	116.23(13)

C(11)-C(10)-C(9)	119.48(14)	C(25)-C(26)-C(31)	122.26(15)
C(10)-C(11)-C(7)	120.15(14)	C(28)-C(27)-C(26)	121.61(19)
C(10)-C(11)-C(12)	133.37(15)	C(27)-C(28)-C(29)	120.31(18)
C(7)-C(11)-C(12)	105.67(13)	C(28)-C(29)-C(30)	120.92(19)
N(2)-C(12)-C(11)	132.85(14)	C(29)-C(30)-C(25)	117.68(17)
N(2)-C(12)-C(1)	120.06(14)	C(29)-C(30)-C(34)	122.19(17)
C(11)-C(12)-C(1)	106.87(13)	C(25)-C(30)-C(34)	120.12(15)
C(14)-C(13)-C(18)	122.30(16)	C(26)-C(31)-C(33)	112.27(17)
C(14)-C(13)-N(1)	119.86(15)	C(26)-C(31)-C(32)	111.03(17)
C(18)-C(13)-N(1)	117.73(15)	C(33)-C(31)-C(32)	110.58(16)
C(13)-C(14)-C(15)	117.08(18)	C(30)-C(34)-C(35)	112.11(16)
C(13)-C(14)-C(19)	122.58(17)	C(30)-C(34)-C(36)	113.53(18)
C(15)-C(14)-C(19)	120.33(18)	C(35)-C(34)-C(36)	109.39(18)
C(16)-C(15)-C(14)	121.8(2)	C(39)-C(37)-C(40)	108.39(16)
C(15)-C(16)-C(17)	120.10(19)	C(39)-C(37)-C(38)	109.46(17)
C(16)-C(17)-C(18)	121.01(19)	C(40)-C(37)-C(38)	106.91(16)
C(13)-C(18)-C(17)	117.51(18)	C(39)-C(37)-C(8)	112.32(14)
C(13)-C(18)-C(22)	120.11(16)	C(40)-C(37)-C(8)	110.66(15)
C(17)-C(18)-C(22)	122.36(18)	C(38)-C(37)-C(8)	108.94(15)
C(14)-C(19)-C(20)	111.7(3)	C(1)-N(1)-C(13)	119.05(13)
C(14)-C(19)-C(21)	111.2(3)	C(12)-N(2)-C(25)	120.94(13)
C(20)-C(19)-C(21)	110.4(3)	C(46)-C(41)-C(42)	121.9(6)
C(18)-C(22)-C(23)	111.1(2)	C(46)-C(41)-C(47)	119.6(5)
C(18)-C(22)-C(24)	113.0(2)	C(42)-C(41)-C(47)	118.6(5)
C(23)-C(22)-C(24)	112.3(3)	C(43)-C(42)-C(41)	118.9(8)
C(26)-C(25)-C(30)	122.11(15)	C(42)-C(43)-C(44)	119.6(9)
C(26)-C(25)-N(2)	120.44(15)	C(43)-C(44)-C(45)	122.7(10)
C(30)-C(25)-N(2)	117.18(15)	C(44)-C(45)-C(46)	117.3(8)
C(27)-C(26)-C(25)	117.34(17)	C(41)-C(46)-C(45)	119.7(7)
C(27)-C(26)-C(31)	120.39(17)		

---



Table 25: Crystallographic Data and Structure Refinement of **4**.

Empirical formula	C <sub>38</sub> H <sub>46</sub> N <sub>2</sub>	
Formula weight	530.77	
Temperature	100(2) K	
Wavelength	0.71075 Å	
Crystal system	Triclinic	
Space group	P-1	
Unit cell dimensions	a = 13.782(3) Å	α = 95.165(2)°.
	b = 15.462(3) Å	β = 112.367(3)°.
	c = 17.085(3) Å	γ = 103.013(2)°.
Volume	3217.4(11) Å <sup>3</sup>	
Z	4	
Density (calculated)	1.096 Mg/m <sup>3</sup>	
Absorption coefficient	0.063 mm <sup>-1</sup>	
F(000)	1152	
Crystal size	0.25 x 0.16 x 0.13 mm <sup>3</sup>	
Theta range for data collection	1.38 to 25.00°.	
Index ranges	-16<=h<=16, -18<=k<=18, -20<=l<=20	
Reflections collected	49709	
Independent reflections	11348 [R(int) = 0.0442]	
Completeness to theta = 25.00°	100.0 %	
Absorption correction	Semi-empirical from equivalents	
Max. and min. transmission	1.00000 and 0.9322	
Refinement method	Full-matrix least-squares on F <sup>2</sup>	
Data / restraints / parameters	11348 / 0 / 762	
Goodness-of-fit on F <sup>2</sup>	1.114	
Final R indices [I>2sigma(I)]	R1 = 0.0619, wR2 = 0.1458	
R indices (all data)	R1 = 0.0709, wR2 = 0.1522	
Largest diff. peak and hole	0.316 and -0.213 e.Å <sup>-3</sup>	

Table 26: Atomic coordinates ( $\times 10^4$ ) and equivalent isotropic displacement parameters ( $\text{\AA}^2 \times 10^3$ ) for **4**.  $U(\text{eq})$  is defined as one third of the trace of the orthogonalized  $U^{\text{ij}}$  tensor.

	x	y	z	U(eq)
C(1)	5813(2)	2275(1)	2564(1)	30(1)
C(2)	5042(2)	1447(1)	2592(1)	29(1)
C(3)	3993(2)	1260(1)	2577(1)	33(1)
C(4)	3503(2)	382(1)	2615(1)	34(1)
C(5)	4011(2)	-311(1)	2638(1)	33(1)
C(6)	5041(2)	-140(1)	2628(1)	29(1)
C(7)	5542(2)	752(1)	2642(1)	27(1)
C(8)	5634(2)	-845(1)	2580(1)	31(1)
C(9)	6902(2)	-441(1)	3039(1)	30(1)
C(10)	7306(2)	512(1)	2917(1)	31(1)
C(11)	6666(2)	1064(1)	2731(1)	28(1)
C(12)	6856(2)	2036(1)	2670(1)	29(1)
C(13)	4691(2)	3229(1)	2306(1)	32(1)
C(14)	4573(2)	3665(1)	3003(1)	34(1)
C(15)	3569(2)	3822(1)	2860(1)	36(1)
C(16)	2691(2)	3552(1)	2060(1)	37(1)
C(17)	2852(2)	3146(1)	1377(1)	38(1)
C(18)	3844(2)	2991(1)	1477(1)	35(1)
C(19)	5511(2)	3933(2)	3880(1)	42(1)
C(20)	1601(2)	3708(2)	1933(2)	48(1)
C(21)	4012(2)	2578(2)	720(2)	48(1)
C(22)	8610(2)	2316(1)	2750(1)	31(1)
C(23)	9459(2)	2413(1)	3565(1)	34(1)
C(24)	10354(2)	2118(1)	3600(1)	37(1)
C(25)	10437(2)	1752(1)	2863(2)	38(1)
C(26)	9583(2)	1674(1)	2070(1)	36(1)

C(27)	8662(2)	1950(1)	1996(1)	34(1)
C(28)	9367(2)	2780(2)	4370(1)	44(1)
C(29)	11431(2)	1465(2)	2908(2)	49(1)
C(30)	7721(2)	1824(2)	1135(1)	42(1)
C(31)	5246(2)	-1363(1)	1628(1)	40(1)
C(32)	3992(2)	-1694(2)	1194(2)	48(1)
C(33)	5640(2)	-767(2)	1077(2)	50(1)
C(34)	5674(2)	-2203(2)	1654(2)	51(1)
C(35)	7406(2)	-501(1)	4025(1)	32(1)
C(36)	7275(2)	-1499(1)	4087(2)	43(1)
C(37)	8627(2)	-13(2)	4442(1)	44(1)
C(38)	6851(2)	-91(2)	4516(1)	41(1)
C(39)	7895(2)	2840(1)	7013(1)	29(1)
C(40)	8387(2)	3663(1)	6760(1)	30(1)
C(41)	7945(2)	4216(1)	6197(1)	37(1)
C(42)	8663(2)	4967(2)	6140(1)	41(1)
C(43)	9792(2)	5171(1)	6610(1)	35(1)
C(44)	10249(2)	4615(1)	7151(1)	30(1)
C(45)	9514(2)	3881(1)	7221(1)	27(1)
C(46)	11458(2)	4739(1)	7649(1)	31(1)
C(47)	11698(2)	4366(1)	8500(1)	32(1)
C(48)	10864(2)	3491(1)	8415(1)	29(1)
C(49)	9849(2)	3273(1)	7813(1)	25(1)
C(50)	8839(2)	2535(1)	7612(1)	27(1)
C(51)	6031(2)	2747(1)	6349(1)	29(1)
C(52)	5386(2)	2306(1)	5494(1)	30(1)
C(53)	4486(2)	2591(1)	5024(1)	32(1)
C(54)	4212(2)	3291(1)	5380(1)	31(1)
C(55)	4868(2)	3711(1)	6233(1)	31(1)
C(56)	5770(2)	3451(1)	6733(1)	30(1)
C(57)	5689(2)	1556(2)	5096(1)	40(1)
C(58)	3211(2)	3575(2)	4872(1)	39(1)

C(59)	6459(2)	3916(1)	7662(1)	40(1)
C(60)	9565(2)	1494(1)	8403(1)	30(1)
C(61)	10119(2)	1018(1)	8076(1)	35(1)
C(62)	10909(2)	685(1)	8648(2)	41(1)
C(63)	11146(2)	803(1)	9521(2)	42(1)
C(64)	10581(2)	1288(1)	9827(1)	40(1)
C(65)	9796(2)	1645(1)	9284(1)	34(1)
C(66)	9858(2)	863(2)	7122(2)	50(1)
C(67)	11970(2)	398(2)	10127(2)	60(1)
C(68)	9207(2)	2186(2)	9616(2)	48(1)
C(69)	11986(2)	4345(1)	7078(2)	40(1)
C(70)	11742(2)	4765(2)	6267(2)	46(1)
C(71)	13243(2)	4629(2)	7593(2)	56(1)
C(72)	11562(2)	3320(2)	6810(2)	49(1)
C(73)	11889(2)	5106(2)	9289(1)	44(1)
C(74)	12970(2)	5830(2)	9525(2)	61(1)
C(75)	12013(3)	4660(2)	10075(2)	68(1)
C(76)	10962(2)	5534(2)	9097(2)	56(1)
N(1)	5709(1)	3059(1)	2436(1)	35(1)
N(2)	7688(1)	2620(1)	2688(1)	33(1)
N(4)	8673(1)	1767(1)	7832(1)	30(1)
N(3)	6912(1)	2421(1)	6857(1)	31(1)

Table 27: Bond Lengths [ $\text{\AA}$ ] and Bond Angles [ $^\circ$ ] for **4**.

C(1)-N(1)	1.280(2)	C(6)-C(7)	1.389(3)
C(1)-C(2)	1.486(3)	C(6)-C(8)	1.517(3)
C(1)-C(12)	1.514(3)	C(7)-C(11)	1.458(3)
C(2)-C(7)	1.393(3)	C(8)-C(9)	1.561(3)
C(2)-C(3)	1.399(3)	C(8)-C(31)	1.575(3)
C(3)-C(4)	1.393(3)	C(9)-C(10)	1.516(3)
C(4)-C(5)	1.400(3)	C(9)-C(35)	1.580(3)
C(5)-C(6)	1.392(3)	C(10)-C(11)	1.336(3)

C(11)-C(12)	1.486(2)	C(40)-C(41)	1.402(3)
C(12)-N(2)	1.276(2)	C(41)-C(42)	1.384(3)
C(13)-C(14)	1.396(3)	C(42)-C(43)	1.395(3)
C(13)-C(18)	1.399(3)	C(43)-C(44)	1.390(3)
C(13)-N(1)	1.425(3)	C(44)-C(45)	1.390(3)
C(14)-C(15)	1.392(3)	C(44)-C(46)	1.511(3)
C(14)-C(19)	1.504(3)	C(45)-C(49)	1.459(2)
C(15)-C(16)	1.385(3)	C(46)-C(47)	1.558(3)
C(16)-C(17)	1.390(3)	C(46)-C(69)	1.576(3)
C(16)-C(20)	1.512(3)	C(47)-C(48)	1.520(3)
C(17)-C(18)	1.390(3)	C(47)-C(73)	1.585(3)
C(18)-C(21)	1.510(3)	C(48)-C(49)	1.325(3)
C(22)-C(27)	1.394(3)	C(49)-C(50)	1.486(3)
C(22)-C(23)	1.405(3)	C(50)-N(4)	1.275(2)
C(22)-N(2)	1.422(2)	C(51)-C(52)	1.395(3)
C(23)-C(24)	1.391(3)	C(51)-C(56)	1.404(3)
C(23)-C(28)	1.500(3)	C(51)-N(3)	1.427(2)
C(24)-C(25)	1.389(3)	C(52)-C(53)	1.389(3)
C(25)-C(26)	1.389(3)	C(52)-C(57)	1.508(3)
C(25)-C(29)	1.510(3)	C(53)-C(54)	1.387(3)
C(26)-C(27)	1.392(3)	C(54)-C(55)	1.387(3)
C(27)-C(30)	1.506(3)	C(54)-C(58)	1.509(3)
C(31)-C(33)	1.533(3)	C(55)-C(56)	1.384(3)
C(31)-C(32)	1.536(3)	C(56)-C(59)	1.509(3)
C(31)-C(34)	1.540(3)	C(60)-C(61)	1.394(3)
C(35)-C(38)	1.518(3)	C(60)-C(65)	1.399(3)
C(35)-C(37)	1.525(3)	C(60)-N(4)	1.427(2)
C(35)-C(36)	1.531(3)	C(61)-C(62)	1.392(3)
C(39)-N(3)	1.275(2)	C(61)-C(66)	1.512(3)
C(39)-C(40)	1.482(3)	C(62)-C(63)	1.386(3)
C(39)-C(50)	1.521(3)	C(63)-C(64)	1.394(3)
C(40)-C(45)	1.389(3)	C(63)-C(67)	1.516(3)

C(64)-C(65)	1.390(3)	C(10)-C(11)-C(12)	134.05(18)
C(65)-C(68)	1.501(3)	C(7)-C(11)-C(12)	105.96(16)
C(69)-C(72)	1.521(3)	N(2)-C(12)-C(11)	131.57(18)
C(69)-C(70)	1.536(3)	N(2)-C(12)-C(1)	121.65(17)
C(69)-C(71)	1.547(3)	C(11)-C(12)-C(1)	106.78(15)
C(73)-C(76)	1.509(3)	C(14)-C(13)-C(18)	121.29(19)
C(73)-C(74)	1.532(3)	C(14)-C(13)-N(1)	119.27(18)
C(73)-C(75)	1.533(3)	C(18)-C(13)-N(1)	119.39(19)
		C(15)-C(14)-C(13)	118.20(19)
N(1)-C(1)-C(2)	132.30(18)	C(15)-C(14)-C(19)	122.0(2)
N(1)-C(1)-C(12)	120.84(17)	C(13)-C(14)-C(19)	119.78(19)
C(2)-C(1)-C(12)	106.77(15)	C(16)-C(15)-C(14)	122.3(2)
C(7)-C(2)-C(3)	118.83(17)	C(15)-C(16)-C(17)	117.72(19)
C(7)-C(2)-C(1)	107.66(16)	C(15)-C(16)-C(20)	121.0(2)
C(3)-C(2)-C(1)	133.51(18)	C(17)-C(16)-C(20)	121.3(2)
C(4)-C(3)-C(2)	117.75(18)	C(16)-C(17)-C(18)	122.4(2)
C(3)-C(4)-C(5)	122.18(19)	C(17)-C(18)-C(13)	117.9(2)
C(6)-C(5)-C(4)	120.63(18)	C(17)-C(18)-C(21)	121.49(19)
C(7)-C(6)-C(5)	116.20(18)	C(13)-C(18)-C(21)	120.61(19)
C(7)-C(6)-C(8)	118.31(17)	C(27)-C(22)-C(23)	121.50(19)
C(5)-C(6)-C(8)	125.47(17)	C(27)-C(22)-N(2)	119.05(18)
C(6)-C(7)-C(2)	124.20(18)	C(23)-C(22)-N(2)	119.43(19)
C(6)-C(7)-C(11)	123.20(17)	C(24)-C(23)-C(22)	117.8(2)
C(2)-C(7)-C(11)	112.59(16)	C(24)-C(23)-C(28)	121.53(19)
C(6)-C(8)-C(9)	112.00(16)	C(22)-C(23)-C(28)	120.55(19)
C(6)-C(8)-C(31)	112.37(16)	C(25)-C(24)-C(23)	122.3(2)
C(9)-C(8)-C(31)	112.29(17)	C(24)-C(25)-C(26)	118.00(19)
C(10)-C(9)-C(8)	113.77(16)	C(24)-C(25)-C(29)	121.8(2)
C(10)-C(9)-C(35)	110.71(16)	C(26)-C(25)-C(29)	120.2(2)
C(8)-C(9)-C(35)	113.94(16)	C(25)-C(26)-C(27)	122.2(2)
C(11)-C(10)-C(9)	122.02(18)	C(26)-C(27)-C(22)	118.14(19)
C(10)-C(11)-C(7)	119.65(17)	C(26)-C(27)-C(30)	121.6(2)

C(22)-C(27)-C(30)	120.19(18)	C(48)-C(47)-C(73)	111.55(17)
C(33)-C(31)-C(32)	108.26(19)	C(46)-C(47)-C(73)	112.43(16)
C(33)-C(31)-C(34)	109.7(2)	C(49)-C(48)-C(47)	121.20(17)
C(32)-C(31)-C(34)	107.62(18)	C(48)-C(49)-C(45)	120.02(17)
C(33)-C(31)-C(8)	112.44(17)	C(48)-C(49)-C(50)	134.29(17)
C(32)-C(31)-C(8)	109.78(18)	C(45)-C(49)-C(50)	105.42(15)
C(34)-C(31)-C(8)	108.95(17)	N(4)-C(50)-C(49)	132.69(18)
C(38)-C(35)-C(37)	108.89(18)	N(4)-C(50)-C(39)	121.02(17)
C(38)-C(35)-C(36)	109.97(17)	C(49)-C(50)-C(39)	106.27(15)
C(37)-C(35)-C(36)	107.56(17)	C(52)-C(51)-C(56)	121.08(18)
C(38)-C(35)-C(9)	111.71(16)	C(52)-C(51)-N(3)	118.94(17)
C(37)-C(35)-C(9)	110.40(16)	C(56)-C(51)-N(3)	119.75(17)
C(36)-C(35)-C(9)	108.21(16)	C(53)-C(52)-C(51)	118.37(18)
N(3)-C(39)-C(40)	133.02(18)	C(53)-C(52)-C(57)	121.62(18)
N(3)-C(39)-C(50)	120.18(17)	C(51)-C(52)-C(57)	120.00(17)
C(40)-C(39)-C(50)	106.71(16)	C(54)-C(53)-C(52)	122.05(19)
C(45)-C(40)-C(41)	119.16(17)	C(55)-C(54)-C(53)	118.05(18)
C(45)-C(40)-C(39)	107.50(16)	C(55)-C(54)-C(58)	120.37(18)
C(41)-C(40)-C(39)	133.32(18)	C(53)-C(54)-C(58)	121.55(18)
C(42)-C(41)-C(40)	117.66(19)	C(56)-C(55)-C(54)	122.33(19)
C(41)-C(42)-C(43)	122.06(19)	C(55)-C(56)-C(51)	118.10(18)
C(44)-C(43)-C(42)	121.18(18)	C(55)-C(56)-C(59)	120.93(18)
C(45)-C(44)-C(43)	115.91(18)	C(51)-C(56)-C(59)	120.96(18)
C(45)-C(44)-C(46)	118.33(17)	C(61)-C(60)-C(65)	121.33(18)
C(43)-C(44)-C(46)	125.75(17)	C(61)-C(60)-N(4)	120.25(18)
C(40)-C(45)-C(44)	123.94(17)	C(65)-C(60)-N(4)	118.17(18)
C(40)-C(45)-C(49)	112.97(16)	C(62)-C(61)-C(60)	118.3(2)
C(44)-C(45)-C(49)	123.06(17)	C(62)-C(61)-C(66)	121.1(2)
C(44)-C(46)-C(47)	111.72(16)	C(60)-C(61)-C(66)	120.57(19)
C(44)-C(46)-C(69)	112.43(17)	C(63)-C(62)-C(61)	122.2(2)
C(47)-C(46)-C(69)	112.43(16)	C(62)-C(63)-C(64)	117.94(19)
C(48)-C(47)-C(46)	113.99(16)	C(62)-C(63)-C(67)	121.5(2)

C(64)-C(63)-C(67)	120.6(2)	C(76)-C(73)-C(74)	110.3(2)
C(65)-C(64)-C(63)	122.0(2)	C(76)-C(73)-C(75)	109.3(2)
C(64)-C(65)-C(60)	118.2(2)	C(74)-C(73)-C(75)	106.9(2)
C(64)-C(65)-C(68)	122.0(2)	C(76)-C(73)-C(47)	112.36(18)
C(60)-C(65)-C(68)	119.80(18)	C(74)-C(73)-C(47)	108.8(2)
C(72)-C(69)-C(70)	109.2(2)	C(75)-C(73)-C(47)	108.91(18)
C(72)-C(69)-C(71)	109.68(19)	C(1)-N(1)-C(13)	118.10(17)
C(70)-C(69)-C(71)	107.31(18)	C(12)-N(2)-C(22)	117.23(16)
C(72)-C(69)-C(46)	112.34(17)	C(50)-N(4)-C(60)	120.38(16)
C(70)-C(69)-C(46)	109.27(17)	C(39)-N(3)-C(51)	120.27(16)
C(71)-C(69)-C(46)	108.86(19)		

---



Table 28: Crystallographic Data and Structure Refinement of **5**.

Empirical formula	C <sub>28</sub> H <sub>24</sub> F <sub>2</sub> N <sub>2</sub>	
Formula weight	426.49	
Temperature	163(2) K	
Wavelength	0.71075 Å	
Crystal system	Monoclinic	
Space group	P2 <sub>1</sub> /c	
Unit cell dimensions	a = 9.612(2) Å	α = 90°.
	b = 10.093(2) Å	β = 95.446(5)°.
	c = 22.779(5) Å	γ = 90°.
Volume	2200.0(8) Å <sup>3</sup>	
Z	4	
Density (calculated)	1.288 Mg/m <sup>3</sup>	
Absorption coefficient	0.087 mm <sup>-1</sup>	
F(000)	896	
Crystal size	0.16 x 0.15 x 0.10 mm <sup>3</sup>	
Theta range for data collection	2.13 to 25.00°.	
Index ranges	-11<=h<=11, -12<=k<=12, -27<=l<=27	
Reflections collected	18770	
Independent reflections	3875 [R(int) = 0.0610]	
Completeness to theta = 25.00°	99.9 %	
Absorption correction	Semi-empirical from equivalents	
Max. and min. transmission	1.00000 and 0.587239	
Refinement method	Full-matrix least-squares on F <sup>2</sup>	
Data / restraints / parameters	3875 / 0 / 296	
Goodness-of-fit on F <sup>2</sup>	1.086	
Final R indices [I>2sigma(I)]	R1 = 0.0556, wR2 = 0.1192	
R indices (all data)	R1 = 0.0832, wR2 = 0.1354	
Largest diff. peak and hole	0.174 and -0.175 e.Å <sup>-3</sup>	

Table 29: Atomic coordinates ( $\times 10^4$ ) and equivalent isotropic displacement parameters ( $\text{\AA}^2 \times 10^3$ ) for **5**. U(eq) is defined as one third of the trace of the orthogonalized  $U^{ij}$  tensor.

	x	y	z	U(eq)
C(1)	7346(2)	7855(2)	8512(1)	35(1)
C(2)	7780(2)	6827(2)	8076(1)	37(1)
C(3)	8232(3)	6941(3)	7523(1)	49(1)
C(4)	8535(3)	5757(3)	7219(1)	56(1)
C(5)	8398(3)	4522(3)	7449(1)	53(1)
C(6)	7958(2)	4374(3)	8021(1)	43(1)
C(7)	7688(2)	5553(2)	8322(1)	35(1)
C(8)	7789(3)	3181(3)	8335(1)	50(1)
C(9)	7435(3)	3205(3)	8902(1)	45(1)
C(10)	7250(2)	4398(2)	9209(1)	38(1)
C(11)	7376(2)	5580(2)	8915(1)	32(1)
C(12)	7309(2)	6996(2)	9082(1)	31(1)
C(13)	9656(2)	8824(2)	8910(1)	35(1)
C(14)	10229(3)	9906(2)	9227(1)	43(1)
C(15)	11521(3)	9837(3)	9548(1)	46(1)
C(16)	12237(2)	8674(3)	9547(1)	40(1)
C(17)	11737(2)	7599(3)	9231(1)	43(1)
C(18)	10447(2)	7677(2)	8907(1)	40(1)
C(19)	7444(2)	6833(2)	10114(1)	32(1)
C(20)	8759(2)	6424(2)	10346(1)	38(1)
C(21)	8945(3)	5828(2)	10893(1)	40(1)
C(22)	7813(3)	5647(2)	11200(1)	37(1)
C(23)	6498(3)	6050(3)	10993(1)	43(1)
C(24)	6318(2)	6664(3)	10446(1)	41(1)
C(25)	5837(2)	8436(3)	8318(1)	41(1)
C(26)	5403(3)	9484(3)	8752(1)	50(1)

C(27)	5796(3)	9071(3)	7705(1)	57(1)
C(28)	4752(3)	7318(3)	8293(1)	47(1)
N(1)	8326(2)	8966(2)	8593(1)	39(1)
N(2)	7305(2)	7564(2)	9580(1)	34(1)
F(1)	13501(2)	8575(2)	9879(1)	56(1)
F(2)	7993(2)	5022(2)	11735(1)	53(1)

Table 30: Bond Lengths [ $\text{\AA}$ ] and Bond Angles [ $^\circ$ ] for **5**.

C(1)-N(1)	1.465(3)	C(17)-C(18)	1.385(3)
C(1)-C(2)	1.523(3)	C(19)-C(20)	1.386(3)
C(1)-C(12)	1.564(3)	C(19)-C(24)	1.389(3)
C(1)-C(25)	1.588(3)	C(19)-N(2)	1.419(3)
C(2)-C(3)	1.376(3)	C(20)-C(21)	1.379(3)
C(2)-C(7)	1.409(3)	C(21)-C(22)	1.362(3)
C(3)-C(4)	1.424(4)	C(22)-F(2)	1.368(3)
C(4)-C(5)	1.363(4)	C(22)-C(23)	1.368(3)
C(5)-C(6)	1.416(4)	C(23)-C(24)	1.388(3)
C(6)-C(7)	1.410(3)	C(25)-C(26)	1.533(4)
C(6)-C(8)	1.418(4)	C(25)-C(27)	1.533(3)
C(7)-C(11)	1.412(3)	C(25)-C(28)	1.534(3)
C(8)-C(9)	1.366(4)		
C(9)-C(10)	1.413(3)	N(1)-C(1)-C(2)	113.01(19)
C(10)-C(11)	1.379(3)	N(1)-C(1)-C(12)	112.65(18)
C(11)-C(12)	1.483(3)	C(2)-C(1)-C(12)	101.20(18)
C(12)-N(2)	1.270(3)	N(1)-C(1)-C(25)	108.13(19)
C(13)-C(18)	1.385(3)	C(2)-C(1)-C(25)	111.65(18)
C(13)-C(14)	1.392(3)	C(12)-C(1)-C(25)	110.13(18)
C(13)-N(1)	1.415(3)	C(3)-C(2)-C(7)	118.6(2)
C(14)-C(15)	1.382(4)	C(3)-C(2)-C(1)	132.2(2)
C(15)-C(16)	1.361(4)	C(7)-C(2)-C(1)	109.3(2)
C(16)-C(17)	1.363(3)	C(2)-C(3)-C(4)	118.1(3)
C(16)-F(1)	1.373(3)	C(5)-C(4)-C(3)	123.3(3)

C(4)-C(5)-C(6)	119.9(3)	C(17)-C(16)-F(1)	118.9(2)
C(7)-C(6)-C(5)	116.3(3)	C(16)-C(17)-C(18)	119.3(2)
C(7)-C(6)-C(8)	115.9(2)	C(17)-C(18)-C(13)	120.6(2)
C(5)-C(6)-C(8)	127.8(3)	C(20)-C(19)-C(24)	119.1(2)
C(2)-C(7)-C(6)	123.7(2)	C(20)-C(19)-N(2)	119.3(2)
C(2)-C(7)-C(11)	113.0(2)	C(24)-C(19)-N(2)	121.1(2)
C(6)-C(7)-C(11)	123.2(2)	C(21)-C(20)-C(19)	120.6(2)
C(9)-C(8)-C(6)	120.9(2)	C(22)-C(21)-C(20)	118.8(2)
C(8)-C(9)-C(10)	122.5(2)	C(21)-C(22)-F(2)	118.7(2)
C(11)-C(10)-C(9)	118.4(2)	C(21)-C(22)-C(23)	122.6(2)
C(10)-C(11)-C(7)	119.0(2)	F(2)-C(22)-C(23)	118.6(2)
C(10)-C(11)-C(12)	134.6(2)	C(22)-C(23)-C(24)	118.4(2)
C(7)-C(11)-C(12)	106.4(2)	C(23)-C(24)-C(19)	120.4(2)
N(2)-C(12)-C(11)	131.9(2)	C(26)-C(25)-C(27)	108.3(2)
N(2)-C(12)-C(1)	119.5(2)	C(26)-C(25)-C(28)	107.8(2)
C(11)-C(12)-C(1)	108.43(18)	C(27)-C(25)-C(28)	108.4(2)
C(18)-C(13)-C(14)	117.9(2)	C(26)-C(25)-C(1)	111.85(19)
C(18)-C(13)-N(1)	123.5(2)	C(27)-C(25)-C(1)	110.6(2)
C(14)-C(13)-N(1)	118.6(2)	C(28)-C(25)-C(1)	109.8(2)
C(15)-C(14)-C(13)	121.8(2)	C(13)-N(1)-C(1)	121.7(2)
C(16)-C(15)-C(14)	118.1(2)	C(12)-N(2)-C(19)	121.5(2)
C(15)-C(16)-C(17)	122.3(2)	C(1)-N(1)-H(1N)	109.7(17)
C(15)-C(16)-F(1)	118.9(2)		

---

Table 31: Crystallographic Data and Structure Refinement of 6.

Empirical formula	$C_{30}H_{30}N_2O_2$	
Formula weight	450.56	
Temperature	163(2) K	
Wavelength	0.71075 Å	
Crystal system	Triclinic	
Space group	P-1	
Unit cell dimensions	$a = 9.429(5)$ Å	$\alpha = 88.241(18)^\circ$ .
	$b = 10.021(5)$ Å	$\beta = 72.045(10)^\circ$ .
	$c = 13.394(7)$ Å	$\gamma = 82.134(17)^\circ$ .
Volume	$1192.5(11)$ Å <sup>3</sup>	
Z	2	
Density (calculated)	$1.255$ Mg/m <sup>3</sup>	
Absorption coefficient	$0.078$ mm <sup>-1</sup>	
F(000)	480	
Crystal size	$0.26 \times 0.13 \times 0.10$ mm <sup>3</sup>	
Theta range for data collection	1.60 to 25.00°.	
Index ranges	$-11 \leq h \leq 11$ , $-11 \leq k \leq 11$ , $-15 \leq l \leq 15$	
Reflections collected	10415	
Independent reflections	4171 [R(int) = 0.0560]	
Completeness to theta = 25.00°	99.5 %	
Absorption correction	Semi-empirical from equivalents	
Max. and min. transmission	1.00000 and 0.6873	
Refinement method	Full-matrix least-squares on F <sup>2</sup>	
Data / restraints / parameters	4171 / 0 / 316	
Goodness-of-fit on F <sup>2</sup>	1.238	
Final R indices [I > 2sigma(I)]	R1 = 0.0624, wR2 = 0.1438	
R indices (all data)	R1 = 0.1054, wR2 = 0.1813	
Largest diff. peak and hole	0.285 and -0.296 e.Å <sup>-3</sup>	

Table 32: Atomic coordinates ( $\times 10^4$ ) and equivalent isotropic displacement parameters ( $\text{\AA}^2 \times 10^3$ ) for **6**. U(eq) is defined as one third of the trace of the orthogonalized  $U^{ij}$  tensor.

	x	y	z	U(eq)
C(1)	6422(4)	7464(3)	6501(3)	34(1)
C(2)	4837(4)	7302(3)	6504(3)	32(1)
C(3)	4242(4)	7026(4)	5723(3)	40(1)
C(4)	2664(4)	7012(4)	5979(3)	42(1)
C(5)	1709(4)	7227(4)	6982(3)	40(1)
C(6)	2299(4)	7449(3)	7821(3)	36(1)
C(7)	3859(4)	7470(3)	7535(3)	32(1)
C(8)	1483(4)	7572(4)	8893(3)	42(1)
C(9)	2220(4)	7686(4)	9626(3)	39(1)
C(10)	3802(4)	7680(3)	9339(3)	37(1)
C(11)	4619(4)	7584(3)	8296(3)	32(1)
C(12)	6253(4)	7492(3)	7698(3)	33(1)
C(13)	7733(4)	5078(3)	6420(3)	35(1)
C(14)	6506(4)	4453(4)	6996(3)	50(1)
C(15)	6693(4)	3214(4)	7486(3)	48(1)
C(16)	8115(4)	2572(3)	7386(3)	38(1)
C(17)	9357(4)	3154(4)	6788(3)	40(1)
C(18)	9137(4)	4410(4)	6345(3)	40(1)
C(19)	9696(4)	689(4)	7804(3)	49(1)
C(20)	7322(4)	7356(4)	9070(3)	37(1)
C(21)	7084(4)	8550(4)	9659(3)	40(1)
C(22)	7097(4)	8507(4)	10689(3)	38(1)
C(23)	7344(4)	7279(3)	11162(3)	36(1)
C(24)	7595(4)	6087(4)	10581(3)	43(1)
C(25)	7599(4)	6136(4)	9547(3)	43(1)

C(26)	7541(5)	6055(4)	12682(3)	48(1)
C(27)	6896(4)	8850(4)	5987(3)	37(1)
C(28)	5830(4)	10024(3)	6642(3)	42(1)
C(29)	8508(4)	9025(4)	5953(3)	45(1)
C(30)	6804(4)	8948(4)	4865(3)	44(1)
N(1)	7563(3)	6349(3)	5929(2)	37(1)
N(2)	7429(3)	7371(3)	7989(2)	38(1)
O(1)	8212(3)	1350(2)	7888(2)	47(1)
O(2)	7310(3)	7330(3)	12190(2)	46(1)

Table 33: Bond Lengths [ $\text{\AA}$ ] angles [ $^\circ$ ] for **6**.

C(1)-N(1)	1.486(4)	C(15)-C(16)	1.374(5)
C(1)-C(2)	1.524(5)	C(16)-O(1)	1.385(4)
C(1)-C(12)	1.561(5)	C(16)-C(17)	1.391(5)
C(1)-C(27)	1.589(5)	C(17)-C(18)	1.392(5)
C(2)-C(3)	1.382(5)	C(19)-O(1)	1.437(5)
C(2)-C(7)	1.404(5)	C(20)-C(25)	1.392(5)
C(3)-C(4)	1.422(5)	C(20)-C(21)	1.407(5)
C(4)-C(5)	1.371(5)	C(20)-N(2)	1.419(5)
C(5)-C(6)	1.435(5)	C(21)-C(22)	1.383(5)
C(6)-C(8)	1.404(5)	C(22)-C(23)	1.391(5)
C(6)-C(7)	1.404(5)	C(23)-O(2)	1.370(4)
C(7)-C(11)	1.430(5)	C(23)-C(24)	1.399(5)
C(8)-C(9)	1.382(5)	C(24)-C(25)	1.384(5)
C(9)-C(10)	1.420(5)	C(26)-O(2)	1.440(5)
C(10)-C(11)	1.371(5)	C(27)-C(30)	1.532(5)
C(11)-C(12)	1.493(5)	C(27)-C(28)	1.536(5)
C(12)-N(2)	1.275(4)	C(27)-C(29)	1.540(5)
C(13)-C(18)	1.375(5)		
C(13)-C(14)	1.395(5)	N(1)-C(1)-C(2)	112.5(3)
C(13)-N(1)	1.427(5)	N(1)-C(1)-C(12)	112.6(3)
C(14)-C(15)	1.401(5)	C(2)-C(1)-C(12)	102.3(3)

N(1)-C(1)-C(27)	108.5(3)	C(16)-C(15)-C(14)	119.9(3)
C(2)-C(1)-C(27)	111.0(3)	C(15)-C(16)-O(1)	116.7(3)
C(12)-C(1)-C(27)	109.9(3)	C(15)-C(16)-C(17)	119.5(3)
C(3)-C(2)-C(7)	118.0(3)	O(1)-C(16)-C(17)	123.8(3)
C(3)-C(2)-C(1)	133.0(3)	C(16)-C(17)-C(18)	119.3(3)
C(7)-C(2)-C(1)	109.1(3)	C(13)-C(18)-C(17)	122.8(3)
C(2)-C(3)-C(4)	119.1(3)	C(25)-C(20)-C(21)	118.1(3)
C(5)-C(4)-C(3)	122.5(3)	C(25)-C(20)-N(2)	119.6(3)
C(4)-C(5)-C(6)	119.9(3)	C(21)-C(20)-N(2)	122.0(3)
C(8)-C(6)-C(7)	117.7(3)	C(22)-C(21)-C(20)	120.8(3)
C(8)-C(6)-C(5)	126.3(3)	C(21)-C(22)-C(23)	120.4(3)
C(7)-C(6)-C(5)	115.9(3)	O(2)-C(23)-C(22)	116.5(3)
C(2)-C(7)-C(6)	124.6(3)	O(2)-C(23)-C(24)	124.2(3)
C(2)-C(7)-C(11)	113.2(3)	C(22)-C(23)-C(24)	119.3(3)
C(6)-C(7)-C(11)	122.1(3)	C(25)-C(24)-C(23)	120.0(3)
C(9)-C(8)-C(6)	120.1(3)	C(24)-C(25)-C(20)	121.3(3)
C(8)-C(9)-C(10)	122.3(3)	C(30)-C(27)-C(28)	108.7(3)
C(11)-C(10)-C(9)	118.7(3)	C(30)-C(27)-C(29)	108.3(3)
C(10)-C(11)-C(7)	119.2(3)	C(28)-C(27)-C(29)	107.5(3)
C(10)-C(11)-C(12)	134.6(3)	C(30)-C(27)-C(1)	110.9(3)
C(7)-C(11)-C(12)	106.1(3)	C(28)-C(27)-C(1)	109.3(3)
N(2)-C(12)-C(11)	132.3(3)	C(29)-C(27)-C(1)	112.0(3)
N(2)-C(12)-C(1)	119.3(3)	C(13)-N(1)-C(1)	120.2(3)
C(11)-C(12)-C(1)	108.2(3)	C(12)-N(2)-C(20)	121.0(3)
C(18)-C(13)-C(14)	116.7(3)	C(16)-O(1)-C(19)	116.9(3)
C(18)-C(13)-N(1)	120.9(3)	C(23)-O(2)-C(26)	116.4(3)
C(14)-C(13)-N(1)	122.4(3)	C(1)-N(1)-H(1N)	111(2)
C(13)-C(14)-C(15)	121.7(3)		

---



Table 34: Crystallographic Data and Structure Refinement of 7.

Empirical formula	C <sub>34</sub> H <sub>40</sub> N <sub>2</sub> Si	
Formula weight	504.77	
Temperature	163(2) K	
Wavelength	0.71075 Å	
Crystal system	Monoclinic	
Space group	P2 <sub>1</sub> /c	
Unit cell dimensions	a = 16.0915(10) Å	α = 90°.
	b = 13.7972(8) Å	β = 93.402(2)°.
	c = 13.2201(8) Å	γ = 90°.
Volume	2929.9(3) Å <sup>3</sup>	
Z	4	
Density (calculated)	1.144 Mg/m <sup>3</sup>	
Absorption coefficient	0.104 mm <sup>-1</sup>	
F(000)	1088	
Crystal size	0.27 x 0.19 x 0.16 mm <sup>3</sup>	
Theta range for data collection	3.09 to 25.00°.	
Index ranges	-19<=h<=19, -16<=k<=16, -15<=l<=15	
Reflections collected	25234	
Independent reflections	5159 [R(int) = 0.0720]	
Completeness to theta = 25.00°	99.8 %	
Absorption correction	Semi-empirical from equivalents	
Max. and min. transmission	1.00000 and 0.7502	
Refinement method	Full-matrix least-squares on F <sup>2</sup>	
Data / restraints / parameters	5159 / 0 / 347	
Goodness-of-fit on F <sup>2</sup>	1.059	
Final R indices [I>2sigma(I)]	R1 = 0.0536, wR2 = 0.1192	
R indices (all data)	R1 = 0.0714, wR2 = 0.1286	
Largest diff. peak and hole	0.238 and -0.345 e.Å <sup>-3</sup>	

Table 35: Atomic coordinates ( $\times 10^4$ ) and equivalent isotropic displacement parameters ( $\text{\AA}^2 \times 10^3$ ) for 7. U(eq) is defined as one third of the trace of the orthogonalized  $U^{ij}$  tensor.

	x	y	z	U(eq)
C(1)	7621(1)	5531(2)	8325(2)	20(1)
C(2)	6778(1)	6011(2)	8229(2)	21(1)
C(3)	6366(1)	6510(2)	7452(2)	26(1)
C(4)	5570(2)	6898(2)	7608(2)	30(1)
C(5)	5200(2)	6808(2)	8512(2)	30(1)
C(6)	5617(1)	6330(2)	9342(2)	25(1)
C(7)	6401(1)	5934(2)	9164(2)	21(1)
C(8)	5343(2)	6209(2)	10332(2)	31(1)
C(9)	5834(2)	5739(2)	11059(2)	30(1)
C(10)	6622(1)	5350(2)	10872(2)	25(1)
C(11)	6901(1)	5445(2)	9913(2)	21(1)
C(12)	7688(1)	5185(2)	9447(2)	19(1)
C(13)	7331(1)	4578(2)	6697(2)	21(1)
C(14)	7841(1)	4672(2)	5877(2)	22(1)
C(15)	7482(2)	4624(2)	4895(2)	28(1)
C(16)	6635(2)	4485(2)	4696(2)	33(1)
C(17)	6153(2)	4340(2)	5514(2)	32(1)
C(18)	6484(1)	4361(2)	6509(2)	26(1)
C(19)	8772(2)	4766(2)	6020(2)	34(1)
C(20)	6264(2)	4446(3)	3621(2)	62(1)
C(21)	5935(2)	4094(2)	7355(2)	42(1)
C(22)	8436(1)	4323(2)	10758(2)	22(1)
C(23)	7987(1)	3484(2)	11005(2)	25(1)
C(24)	8174(2)	3039(2)	11938(2)	30(1)
C(25)	8780(2)	3389(2)	12630(2)	30(1)
C(26)	9206(1)	4220(2)	12372(2)	29(1)

C(27)	9058(1)	4689(2)	11446(2)	24(1)
C(28)	7317(2)	3065(2)	10287(2)	35(1)
C(29)	8991(2)	2873(2)	13623(2)	45(1)
C(30)	9549(2)	5578(2)	11191(2)	33(1)
C(31)	8324(1)	6247(2)	8111(2)	23(1)
C(32)	7786(2)	8387(2)	7869(2)	37(1)
C(33)	7966(2)	7589(2)	10000(2)	39(1)
C(34)	9497(2)	7843(2)	8797(2)	45(1)
N(1)	7653(1)	4608(1)	7728(1)	25(1)
N(2)	8347(1)	4751(1)	9778(1)	23(1)
Si(1)	8372(1)	7503(1)	8708(1)	24(1)

Table 36: Bond Lengths [ $\text{\AA}$ ] and Bond Angles [ $^\circ$ ] for **7**.

C(1)-N(1)	1.501(3)	C(13)-N(1)	1.430(3)
C(1)-C(2)	1.509(3)	C(14)-C(15)	1.390(3)
C(1)-C(31)	1.541(3)	C(14)-C(19)	1.505(3)
C(1)-C(12)	1.557(3)	C(15)-C(16)	1.386(3)
C(2)-C(3)	1.373(3)	C(16)-C(17)	1.382(4)
C(2)-C(7)	1.414(3)	C(16)-C(20)	1.510(4)
C(3)-C(4)	1.415(3)	C(17)-C(18)	1.390(3)
C(4)-C(5)	1.372(3)	C(18)-C(21)	1.512(3)
C(5)-C(6)	1.415(3)	C(22)-C(27)	1.406(3)
C(6)-C(7)	1.407(3)	C(22)-C(23)	1.412(3)
C(6)-C(8)	1.416(3)	C(22)-N(2)	1.423(3)
C(7)-C(11)	1.410(3)	C(23)-C(24)	1.394(3)
C(8)-C(9)	1.370(3)	C(23)-C(28)	1.508(3)
C(9)-C(10)	1.412(3)	C(24)-C(25)	1.384(3)
C(10)-C(11)	1.376(3)	C(25)-C(26)	1.388(3)
C(11)-C(12)	1.486(3)	C(25)-C(29)	1.514(3)
C(12)-N(2)	1.272(3)	C(26)-C(27)	1.393(3)
C(13)-C(14)	1.404(3)	C(27)-C(30)	1.508(3)
C(13)-C(18)	1.404(3)	C(31)-Si(1)	1.903(2)

C(32)-Si(1)	1.867(3)	C(14)-C(13)-N(1)	122.6(2)
C(33)-Si(1)	1.868(2)	C(18)-C(13)-N(1)	117.9(2)
C(34)-Si(1)	1.866(3)	C(15)-C(14)-C(13)	119.2(2)
		C(15)-C(14)-C(19)	118.5(2)
N(1)-C(1)-C(2)	112.76(18)	C(13)-C(14)-C(19)	122.2(2)
N(1)-C(1)-C(31)	113.55(18)	C(16)-C(15)-C(14)	122.2(2)
C(2)-C(1)-C(31)	111.69(17)	C(17)-C(16)-C(15)	117.6(2)
N(1)-C(1)-C(12)	103.73(16)	C(17)-C(16)-C(20)	121.4(2)
C(2)-C(1)-C(12)	103.12(17)	C(15)-C(16)-C(20)	120.9(2)
C(31)-C(1)-C(12)	111.20(17)	C(16)-C(17)-C(18)	122.4(2)
C(3)-C(2)-C(7)	118.6(2)	C(17)-C(18)-C(13)	119.1(2)
C(3)-C(2)-C(1)	132.5(2)	C(17)-C(18)-C(21)	119.2(2)
C(7)-C(2)-C(1)	108.86(18)	C(13)-C(18)-C(21)	121.7(2)
C(2)-C(3)-C(4)	118.8(2)	C(27)-C(22)-C(23)	120.0(2)
C(5)-C(4)-C(3)	122.4(2)	C(27)-C(22)-N(2)	117.9(2)
C(4)-C(5)-C(6)	120.5(2)	C(23)-C(22)-N(2)	121.7(2)
C(7)-C(6)-C(5)	116.1(2)	C(24)-C(23)-C(22)	118.5(2)
C(7)-C(6)-C(8)	116.2(2)	C(24)-C(23)-C(28)	119.8(2)
C(5)-C(6)-C(8)	127.7(2)	C(22)-C(23)-C(28)	121.7(2)
C(6)-C(7)-C(11)	123.2(2)	C(25)-C(24)-C(23)	122.6(2)
C(6)-C(7)-C(2)	123.5(2)	C(24)-C(25)-C(26)	117.7(2)
C(11)-C(7)-C(2)	113.21(19)	C(24)-C(25)-C(29)	121.4(2)
C(9)-C(8)-C(6)	120.3(2)	C(26)-C(25)-C(29)	120.9(2)
C(8)-C(9)-C(10)	123.0(2)	C(25)-C(26)-C(27)	122.6(2)
C(11)-C(10)-C(9)	118.0(2)	C(26)-C(27)-C(22)	118.6(2)
C(10)-C(11)-C(7)	119.3(2)	C(26)-C(27)-C(30)	120.7(2)
C(10)-C(11)-C(12)	133.8(2)	C(22)-C(27)-C(30)	120.7(2)
C(7)-C(11)-C(12)	106.85(18)	C(1)-C(31)-Si(1)	121.33(15)
N(2)-C(12)-C(11)	133.3(2)	C(13)-N(1)-C(1)	120.25(17)
N(2)-C(12)-C(1)	118.80(19)	C(12)-N(2)-C(22)	122.98(18)
C(11)-C(12)-C(1)	107.94(17)	C(34)-Si(1)-C(32)	109.08(13)
C(14)-C(13)-C(18)	119.3(2)	C(34)-Si(1)-C(33)	108.51(13)

C(32)-Si(1)-C(33)	108.04(12)	C(33)-Si(1)-C(31)	115.41(11)
C(34)-Si(1)-C(31)	105.70(12)	C(1)-N(1)-H(1N)	108.3(16)
C(32)-Si(1)-C(31)	109.96(11)		

---

Table 37: Crystallographic Data and Structure Refinement of **8a**.

Empirical formula	C <sub>28</sub> H <sub>26</sub> F <sub>2</sub> N <sub>2</sub> Si	
Formula weight	456.60	
Temperature	100(2) K	
Wavelength	0.71075 Å	
Crystal system	Triclinic	
Space group	P-1	
Unit cell dimensions	a = 11.163(2) Å	α = 78.474(12)°.
	b = 13.060(3) Å	β = 77.185(11)°.
	c = 18.647(4) Å	γ = 66.703(8)°.
Volume	2415.5(9) Å <sup>3</sup>	
Z	4	
Density (calculated)	1.256 Mg/m <sup>3</sup>	
Absorption coefficient	0.131 mm <sup>-1</sup>	
F(000)	960	
Crystal size	0.37 x 0.16 x 0.12 mm <sup>3</sup>	
Theta range for data collection	1.71 to 27.50°.	
Index ranges	-14 ≤ h ≤ 14, -16 ≤ k ≤ 16, -24 ≤ l ≤ 24	
Reflections collected	47961	
Independent reflections	10967 [R(int) = 0.0555]	
Completeness to theta = 27.50°	98.8 %	
Absorption correction	Semi-empirical from equivalents	
Max. and min. transmission	1.00000 and 0.9022	
Refinement method	Full-matrix least-squares on F <sup>2</sup>	
Data / restraints / parameters	10967 / 0 / 609	
Goodness-of-fit on F <sup>2</sup>	1.174	
Final R indices [I > 2σ(I)]	R1 = 0.0663, wR2 = 0.1442	
R indices (all data)	R1 = 0.0772, wR2 = 0.1506	
Largest diff. peak and hole	0.449 and -0.427 e.Å <sup>-3</sup>	

Table 38: Atomic coordinates ( $\times 10^4$ ) and equivalent isotropic displacement parameters ( $\text{\AA}^2 \times 10^3$ ) for **8a**. U(eq) is defined as one third of the trace of the orthogonalized  $U^{ij}$  tensor.

	x	y	z	U(eq)
C(1)	3098(2)	2224(2)	8568(1)	20(1)
C(2)	2104(2)	2114(2)	9259(1)	20(1)
C(3)	2083(2)	1233(2)	9795(1)	25(1)
C(4)	936(2)	1370(2)	10338(1)	27(1)
C(5)	-141(2)	2360(2)	10354(1)	26(1)
C(6)	-121(2)	3300(2)	9823(1)	22(1)
C(7)	1019(2)	3141(2)	9289(1)	20(1)
C(8)	-1114(2)	4396(2)	9784(1)	24(1)
C(9)	-922(2)	5240(2)	9252(1)	24(1)
C(10)	244(2)	5069(2)	8729(1)	22(1)
C(11)	1219(2)	4012(2)	8744(1)	19(1)
C(12)	2547(2)	3512(2)	8309(1)	19(1)
C(13)	4913(2)	2210(2)	9166(1)	21(1)
C(14)	6266(2)	1760(2)	9198(1)	26(1)
C(15)	6800(2)	2125(2)	9658(1)	28(1)
C(16)	5967(2)	2950(2)	10089(1)	26(1)
C(17)	4634(2)	3414(2)	10079(1)	26(1)
C(18)	4105(2)	3049(2)	9613(1)	23(1)
C(19)	2767(2)	5128(2)	7584(1)	20(1)
C(20)	2112(2)	5603(2)	6977(1)	26(1)
C(21)	1710(2)	6752(2)	6754(1)	29(1)
C(22)	1987(2)	7396(2)	7141(1)	29(1)
C(23)	2661(2)	6953(2)	7738(1)	29(1)
C(24)	3056(2)	5803(2)	7958(1)	24(1)
C(25)	3012(2)	1637(2)	7947(1)	23(1)
C(26)	1714(2)	-157(2)	8566(1)	32(1)

C(27)	4699(2)	-838(2)	8502(1)	31(1)
C(28)	3484(2)	-200(2)	7084(1)	34(1)
C(29)	6597(2)	3234(2)	6407(1)	22(1)
C(30)	7556(2)	3531(2)	5761(1)	24(1)
C(31)	7499(2)	4530(2)	5335(1)	30(1)
C(32)	8623(3)	4553(2)	4807(1)	34(1)
C(33)	9744(2)	3614(2)	4701(1)	33(1)
C(34)	9810(2)	2560(2)	5118(1)	27(1)
C(35)	8694(2)	2561(2)	5647(1)	23(1)
C(36)	10858(2)	1509(2)	5060(1)	33(1)
C(37)	10765(2)	559(2)	5501(1)	34(1)
C(38)	9633(2)	571(2)	6029(1)	27(1)
C(39)	8595(2)	1584(2)	6102(1)	23(1)
C(40)	7296(2)	1941(2)	6586(1)	21(1)
C(41)	5020(2)	2938(2)	5770(1)	24(1)
C(42)	3836(2)	2750(2)	5942(1)	27(1)
C(43)	3516(2)	2184(2)	5505(1)	36(1)
C(44)	4397(2)	1796(2)	4890(1)	37(1)
C(45)	5562(2)	1974(3)	4689(2)	44(1)
C(46)	5873(2)	2550(2)	5130(1)	40(1)
C(47)	7277(2)	191(2)	7178(1)	23(1)
C(48)	6951(2)	-404(2)	6757(1)	26(1)
C(49)	7381(2)	-1567(2)	6888(1)	28(1)
C(50)	8147(2)	-2115(2)	7434(1)	30(1)
C(51)	8507(2)	-1561(2)	7853(1)	30(1)
C(52)	8063(2)	-393(2)	7722(1)	27(1)
C(53)	6430(2)	3839(2)	7071(1)	25(1)
C(54)	8960(2)	2412(2)	7789(1)	39(1)
C(55)	6972(3)	4681(2)	8260(1)	39(1)
C(56)	8867(3)	4564(3)	6802(2)	44(1)
N(1)	4457(2)	1778(1)	8695(1)	21(1)
N(2)	3233(2)	3945(1)	7796(1)	21(1)



N(3)	5268(2)	3537(2)	6232(1)	24(1)
N(4)	6712(2)	1384(2)	7077(1)	23(1)
F(1)	6475(1)	3305(1)	10553(1)	36(1)
F(2)	1596(2)	8525(1)	6925(1)	42(1)
F(3)	4111(2)	1205(2)	4463(1)	57(1)
F(4)	8547(2)	-3257(1)	7571(1)	43(1)
Si(1)	3242(1)	100(1)	8058(1)	25(1)
Si(2)	7833(1)	3852(1)	7464(1)	28(1)

Table 39: Bond Lengths [Å] and Bond Angles [°] for **8a**.

C(1)-N(1)	1.450(3)	C(16)-F(1)	1.369(2)
C(1)-C(2)	1.526(3)	C(16)-C(17)	1.370(3)
C(1)-C(25)	1.549(3)	C(17)-C(18)	1.396(3)
C(1)-C(12)	1.558(3)	C(19)-C(20)	1.388(3)
C(2)-C(3)	1.370(3)	C(19)-C(24)	1.393(3)
C(2)-C(7)	1.408(3)	C(19)-N(2)	1.424(3)
C(3)-C(4)	1.418(3)	C(20)-C(21)	1.389(3)
C(4)-C(5)	1.374(3)	C(21)-C(22)	1.369(3)
C(5)-C(6)	1.420(3)	C(22)-F(2)	1.363(2)
C(6)-C(7)	1.402(3)	C(22)-C(23)	1.382(3)
C(6)-C(8)	1.421(3)	C(23)-C(24)	1.389(3)
C(7)-C(11)	1.420(3)	C(25)-Si(1)	1.894(2)
C(8)-C(9)	1.379(3)	C(26)-Si(1)	1.879(2)
C(9)-C(10)	1.410(3)	C(27)-Si(1)	1.857(2)
C(10)-C(11)	1.378(3)	C(28)-Si(1)	1.873(2)
C(11)-C(12)	1.482(3)	C(29)-N(3)	1.471(3)
C(12)-N(2)	1.273(3)	C(29)-C(30)	1.522(3)
C(13)-C(14)	1.398(3)	C(29)-C(53)	1.537(3)
C(13)-C(18)	1.399(3)	C(29)-C(40)	1.556(3)
C(13)-N(1)	1.404(3)	C(30)-C(31)	1.372(3)
C(14)-C(15)	1.389(3)	C(30)-C(35)	1.406(3)
C(15)-C(16)	1.376(3)	C(31)-C(32)	1.419(3)

C(32)-C(33)	1.372(4)	N(1)-C(1)-C(25)	108.33(16)
C(33)-C(34)	1.422(3)	C(2)-C(1)-C(25)	110.86(16)
C(34)-C(35)	1.407(3)	N(1)-C(1)-C(12)	114.46(16)
C(34)-C(36)	1.414(3)	C(2)-C(1)-C(12)	102.04(15)
C(35)-C(39)	1.413(3)	C(25)-C(1)-C(12)	106.69(16)
C(36)-C(37)	1.371(4)	C(3)-C(2)-C(7)	118.93(19)
C(37)-C(38)	1.416(3)	C(3)-C(2)-C(1)	132.35(19)
C(38)-C(39)	1.379(3)	C(7)-C(2)-C(1)	108.67(17)
C(39)-C(40)	1.479(3)	C(2)-C(3)-C(4)	118.6(2)
C(40)-N(4)	1.278(3)	C(5)-C(4)-C(3)	122.4(2)
C(41)-C(46)	1.394(3)	C(4)-C(5)-C(6)	120.0(2)
C(41)-C(42)	1.396(3)	C(7)-C(6)-C(5)	116.48(19)
C(41)-N(3)	1.406(3)	C(7)-C(6)-C(8)	116.28(19)
C(42)-C(43)	1.384(3)	C(5)-C(6)-C(8)	127.2(2)
C(43)-C(44)	1.370(3)	C(6)-C(7)-C(2)	123.44(19)
C(44)-C(45)	1.369(3)	C(6)-C(7)-C(11)	123.30(19)
C(44)-F(3)	1.373(3)	C(2)-C(7)-C(11)	113.20(18)
C(45)-C(46)	1.393(3)	C(9)-C(8)-C(6)	120.36(19)
C(47)-C(52)	1.391(3)	C(8)-C(9)-C(10)	122.53(19)
C(47)-C(48)	1.395(3)	C(11)-C(10)-C(9)	118.58(19)
C(47)-N(4)	1.422(3)	C(10)-C(11)-C(7)	118.93(18)
C(48)-C(49)	1.388(3)	C(10)-C(11)-C(12)	134.62(19)
C(49)-C(50)	1.375(3)	C(7)-C(11)-C(12)	106.44(17)
C(50)-F(4)	1.365(2)	N(2)-C(12)-C(11)	131.73(19)
C(50)-C(51)	1.374(3)	N(2)-C(12)-C(1)	119.85(17)
C(51)-C(52)	1.393(3)	C(11)-C(12)-C(1)	108.42(16)
C(53)-Si(2)	1.878(2)	C(14)-C(13)-C(18)	117.71(19)
C(54)-Si(2)	1.870(3)	C(14)-C(13)-N(1)	117.76(18)
C(55)-Si(2)	1.866(3)	C(18)-C(13)-N(1)	124.52(19)
C(56)-Si(2)	1.866(3)	C(15)-C(14)-C(13)	121.6(2)
		C(16)-C(15)-C(14)	118.6(2)
N(1)-C(1)-C(2)	114.16(17)	F(1)-C(16)-C(17)	118.7(2)

F(1)-C(16)-C(15)	119.34(19)	C(34)-C(35)-C(39)	123.3(2)
C(17)-C(16)-C(15)	121.9(2)	C(37)-C(36)-C(34)	120.8(2)
C(16)-C(17)-C(18)	119.1(2)	C(36)-C(37)-C(38)	122.6(2)
C(17)-C(18)-C(13)	120.96(19)	C(39)-C(38)-C(37)	118.1(2)
C(20)-C(19)-C(24)	119.85(19)	C(38)-C(39)-C(35)	119.17(19)
C(20)-C(19)-N(2)	120.67(18)	C(38)-C(39)-C(40)	134.2(2)
C(24)-C(19)-N(2)	119.32(19)	C(35)-C(39)-C(40)	106.60(18)
C(19)-C(20)-C(21)	120.4(2)	N(4)-C(40)-C(39)	131.7(2)
C(22)-C(21)-C(20)	118.4(2)	N(4)-C(40)-C(29)	119.80(18)
F(2)-C(22)-C(21)	118.7(2)	C(39)-C(40)-C(29)	108.46(17)
F(2)-C(22)-C(23)	118.3(2)	C(46)-C(41)-C(42)	117.6(2)
C(21)-C(22)-C(23)	123.0(2)	C(46)-C(41)-N(3)	123.7(2)
C(22)-C(23)-C(24)	118.2(2)	C(42)-C(41)-N(3)	118.71(19)
C(23)-C(24)-C(19)	120.2(2)	C(43)-C(42)-C(41)	121.8(2)
C(1)-C(25)-Si(1)	123.86(15)	C(44)-C(43)-C(42)	118.6(2)
N(3)-C(29)-C(30)	113.77(17)	C(45)-C(44)-C(43)	121.9(2)
N(3)-C(29)-C(53)	106.85(17)	C(45)-C(44)-F(3)	118.9(2)
C(30)-C(29)-C(53)	110.79(16)	C(43)-C(44)-F(3)	119.2(2)
N(3)-C(29)-C(40)	111.85(16)	C(44)-C(45)-C(46)	119.1(2)
C(30)-C(29)-C(40)	102.53(16)	C(45)-C(46)-C(41)	121.0(2)
C(53)-C(29)-C(40)	111.12(17)	C(52)-C(47)-C(48)	119.5(2)
C(31)-C(30)-C(35)	119.6(2)	C(52)-C(47)-N(4)	121.57(19)
C(31)-C(30)-C(29)	131.7(2)	C(48)-C(47)-N(4)	118.72(19)
C(35)-C(30)-C(29)	108.59(18)	C(49)-C(48)-C(47)	120.4(2)
C(30)-C(31)-C(32)	118.2(2)	C(50)-C(49)-C(48)	118.4(2)
C(33)-C(32)-C(31)	122.5(2)	F(4)-C(50)-C(51)	118.8(2)
C(32)-C(33)-C(34)	120.3(2)	F(4)-C(50)-C(49)	118.2(2)
C(35)-C(34)-C(36)	116.1(2)	C(51)-C(50)-C(49)	122.9(2)
C(35)-C(34)-C(33)	116.2(2)	C(50)-C(51)-C(52)	118.4(2)
C(36)-C(34)-C(33)	127.8(2)	C(47)-C(52)-C(51)	120.3(2)
C(30)-C(35)-C(34)	123.2(2)	C(29)-C(53)-Si(2)	124.50(15)
C(30)-C(35)-C(39)	113.52(19)	C(13)-N(1)-C(1)	123.37(17)

C(12)-N(2)-C(19)	120.10(17)	C(56)-Si(2)-C(55)	109.12(12)
C(41)-N(3)-C(29)	121.68(17)	C(56)-Si(2)-C(54)	107.58(13)
C(40)-N(4)-C(47)	119.85(18)	C(55)-Si(2)-C(54)	110.69(12)
C(27)-Si(1)-C(28)	110.05(11)	C(56)-Si(2)-C(53)	113.48(11)
C(27)-Si(1)-C(26)	110.62(11)	C(55)-Si(2)-C(53)	102.97(11)
C(28)-Si(1)-C(26)	107.01(11)	C(54)-Si(2)-C(53)	112.93(11)
C(27)-Si(1)-C(25)	112.91(10)	C(1)-N(1)-H(1N)	111.7(18)
C(28)-Si(1)-C(25)	103.81(10)	C(29)-N(3)-H(3N)	108.4(16)
C(26)-Si(1)-C(25)	112.06(10)		

---

Table 40: Crystallographic Data and Structure Refinement of **8b**.

Empirical formula	C <sub>28</sub> H <sub>26</sub> F <sub>2</sub> N <sub>2</sub> Si	
Formula weight	456.60	
Temperature	163(2) K	
Wavelength	0.71075 Å	
Crystal system	Triclinic	
Space group	P-1	
Unit cell dimensions	a = 10.845(7) Å	α = 107.901(3)°.
	b = 11.297(7) Å	β = 93.623(7)°.
	c = 11.508(7) Å	γ = 113.270(6)°.
Volume	1204.7(13) Å <sup>3</sup>	
Z	2	
Density (calculated)	1.259 Mg/m <sup>3</sup>	
Absorption coefficient	0.131 mm <sup>-1</sup>	
F(000)	480	
Crystal size	0.44 x 0.13 x 0.09 mm <sup>3</sup>	
Theta range for data collection	2.09 to 27.50°.	
Index ranges	-14<=h<=14, -14<=k<=14, -14<=l<=14	
Reflections collected	12861	
Independent reflections	5500 [R(int) = 0.0414]	
Completeness to theta = 27.50°	99.6 %	
Absorption correction	Semi-empirical from equivalents	
Max. and min. transmission	1.00000 and 0.7089	
Refinement method	Full-matrix least-squares on F <sup>2</sup>	
Data / restraints / parameters	5500 / 0 / 305	
Goodness-of-fit on F <sup>2</sup>	1.103	
Final R indices [I>2sigma(I)]	R1 = 0.0546, wR2 = 0.1366	
R indices (all data)	R1 = 0.0824, wR2 = 0.1694	
Largest diff. peak and hole	0.435 and -0.331 e.Å <sup>-3</sup>	

Table 41: Atomic coordinates ( $\times 10^4$ ) and equivalent isotropic displacement parameters ( $\text{\AA}^2 \times 10^3$ ) for **8b**.  $U(\text{eq})$  is defined as one third of the trace of the orthogonalized  $U^{ij}$  tensor.

	x	y	z	U(eq)
C(1)	454(2)	2937(2)	3985(2)	25(1)
C(2)	818(2)	1722(2)	3667(2)	25(1)
C(3)	167(2)	431(2)	3722(2)	33(1)
C(4)	744(3)	-513(2)	3316(2)	37(1)
C(5)	1918(2)	-194(2)	2859(2)	35(1)
C(6)	2617(2)	1136(2)	2786(2)	30(1)
C(7)	2024(2)	2055(2)	3193(2)	25(1)
C(8)	3853(2)	1648(2)	2364(2)	37(1)
C(9)	4422(2)	2972(3)	2367(2)	41(1)
C(10)	3809(2)	3884(2)	2783(2)	36(1)
C(11)	2604(2)	3424(2)	3200(2)	26(1)
C(12)	1693(2)	4050(2)	3707(2)	24(1)
C(13)	1186(2)	3741(2)	6362(2)	28(1)
C(14)	866(2)	4318(2)	7493(2)	34(1)
C(15)	1603(3)	4551(3)	8633(2)	40(1)
C(16)	2677(3)	4193(3)	8651(2)	40(1)
C(17)	3044(2)	3657(3)	7575(2)	40(1)
C(18)	2328(2)	3451(2)	6430(2)	36(1)
C(19)	2876(2)	6294(2)	3681(2)	28(1)
C(20)	3938(3)	7326(3)	4645(2)	45(1)
C(21)	4989(3)	8374(3)	4418(3)	55(1)
C(22)	4924(3)	8388(3)	3235(3)	44(1)
C(23)	3895(3)	7396(3)	2258(2)	42(1)
C(24)	2857(2)	6335(2)	2492(2)	37(1)
C(25)	-913(2)	2549(2)	3136(2)	27(1)

C(26)	-3040(2)	1527(3)	859(2)	44(1)
C(27)	-70(2)	2651(2)	601(2)	36(1)
C(28)	-1455(3)	-144(2)	900(2)	39(1)
N(1)	292(2)	3415(2)	5268(2)	28(1)
N(2)	1767(2)	5262(2)	3937(2)	28(1)
Si(1)	-1316(1)	1643(1)	1377(1)	29(1)
F(1)	3378(2)	4387(2)	9769(1)	61(1)
F(2)	5947(2)	9434(2)	3013(2)	72(1)

Table 42: Bond Lengths [Å] and Bond Angles [°] for **8b**.

C(1)-N(1)	1.456(3)	C(16)-C(17)	1.360(3)
C(1)-C(2)	1.520(3)	C(16)-F(1)	1.361(3)
C(1)-C(25)	1.545(3)	C(17)-C(18)	1.391(3)
C(1)-C(12)	1.567(3)	C(19)-C(20)	1.378(3)
C(2)-C(3)	1.371(3)	C(19)-C(24)	1.382(3)
C(2)-C(7)	1.406(3)	C(19)-N(2)	1.429(3)
C(3)-C(4)	1.416(3)	C(20)-C(21)	1.390(4)
C(4)-C(5)	1.366(3)	C(21)-C(22)	1.364(4)
C(5)-C(6)	1.422(3)	C(22)-C(23)	1.358(4)
C(6)-C(7)	1.406(3)	C(22)-F(2)	1.370(3)
C(6)-C(8)	1.418(3)	C(23)-C(24)	1.395(3)
C(7)-C(11)	1.418(3)	C(25)-Si(1)	1.897(2)
C(8)-C(9)	1.373(3)	C(26)-Si(1)	1.867(3)
C(9)-C(10)	1.417(3)	C(27)-Si(1)	1.866(2)
C(10)-C(11)	1.380(3)	C(28)-Si(1)	1.863(3)
C(11)-C(12)	1.479(3)		
C(12)-N(2)	1.280(3)	N(1)-C(1)-C(2)	113.68(17)
C(13)-N(1)	1.393(3)	N(1)-C(1)-C(25)	106.62(16)
C(13)-C(14)	1.398(3)	C(2)-C(1)-C(25)	110.80(16)
C(13)-C(18)	1.404(3)	N(1)-C(1)-C(12)	112.57(16)
C(14)-C(15)	1.384(3)	C(2)-C(1)-C(12)	102.13(16)
C(15)-C(16)	1.376(4)	C(25)-C(1)-C(12)	111.13(16)

C(3)-C(2)-C(7)	118.85(19)	C(17)-C(16)-F(1)	120.0(2)
C(3)-C(2)-C(1)	131.77(19)	C(17)-C(16)-C(15)	121.0(2)
C(7)-C(2)-C(1)	109.32(17)	F(1)-C(16)-C(15)	119.0(2)
C(2)-C(3)-C(4)	118.8(2)	C(16)-C(17)-C(18)	120.3(2)
C(5)-C(4)-C(3)	122.7(2)	C(17)-C(18)-C(13)	120.6(2)
C(4)-C(5)-C(6)	120.0(2)	C(20)-C(19)-C(24)	119.0(2)
C(7)-C(6)-C(8)	116.2(2)	C(20)-C(19)-N(2)	119.8(2)
C(7)-C(6)-C(5)	116.4(2)	C(24)-C(19)-N(2)	121.02(19)
C(8)-C(6)-C(5)	127.5(2)	C(19)-C(20)-C(21)	120.4(2)
C(2)-C(7)-C(6)	123.37(19)	C(22)-C(21)-C(20)	118.8(2)
C(2)-C(7)-C(11)	113.24(18)	C(23)-C(22)-C(21)	122.8(2)
C(6)-C(7)-C(11)	123.4(2)	C(23)-C(22)-F(2)	118.3(2)
C(9)-C(8)-C(6)	120.9(2)	C(21)-C(22)-F(2)	119.0(2)
C(8)-C(9)-C(10)	122.1(2)	C(22)-C(23)-C(24)	117.9(2)
C(11)-C(10)-C(9)	118.8(2)	C(19)-C(24)-C(23)	121.1(2)
C(10)-C(11)-C(7)	118.68(19)	C(1)-C(25)-Si(1)	123.16(14)
C(10)-C(11)-C(12)	134.6(2)	C(13)-N(1)-C(1)	128.15(18)
C(7)-C(11)-C(12)	106.71(17)	C(12)-N(2)-C(19)	120.83(17)
N(2)-C(12)-C(11)	132.00(19)	C(28)-Si(1)-C(27)	110.06(11)
N(2)-C(12)-C(1)	119.54(17)	C(28)-Si(1)-C(26)	108.23(12)
C(11)-C(12)-C(1)	108.46(16)	C(27)-Si(1)-C(26)	108.63(12)
N(1)-C(13)-C(14)	117.3(2)	C(28)-Si(1)-C(25)	112.83(10)
N(1)-C(13)-C(18)	125.6(2)	C(27)-Si(1)-C(25)	112.78(10)
C(14)-C(13)-C(18)	117.0(2)	C(26)-Si(1)-C(25)	103.98(10)
C(15)-C(14)-C(13)	122.0(2)	C(1)-N(1)-H(1N)	112.2(16)
C(16)-C(15)-C(14)	119.0(2)		

---



Table 43: Crystallographic Data and Structure Refinement of **9a**.

Empirical formula	$C_{30}H_{32}N_2O_2Si$	
Formula weight	480.66	
Temperature	100(2) K	
Wavelength	0.71075 Å	
Crystal system	Triclinic	
Space group	P-1	
Unit cell dimensions	$a = 11.1004(9)$ Å	$\alpha = 76.401(2)^\circ$ .
	$b = 11.3249(9)$ Å	$\beta = 83.103(2)^\circ$ .
	$c = 22.3211(18)$ Å	$\gamma = 74.218(3)^\circ$ .
Volume	$2619.8(4)$ Å <sup>3</sup>	
Z	4	
Density (calculated)	$1.219$ Mg/m <sup>3</sup>	
Absorption coefficient	$0.119$ mm <sup>-1</sup>	
F(000)	1024	
Crystal size	$0.32 \times 0.10 \times 0.08$ mm <sup>3</sup>	
Theta range for data collection	3.03 to 25.00°.	
Index ranges	$-13 \leq h \leq 10$ , $-13 \leq k \leq 13$ , $-26 \leq l \leq 26$	
Reflections collected	28748	
Independent reflections	9191 [R(int) = 0.0644]	
Completeness to theta = 25.00°	99.7 %	
Absorption correction	Semi-empirical from equivalents	
Max. and min. transmission	1.00000 and 0.6977	
Refinement method	Full-matrix least-squares on F <sup>2</sup>	
Data / restraints / parameters	9191 / 0 / 649	
Goodness-of-fit on F <sup>2</sup>	1.069	
Final R indices [I > 2sigma(I)]	R1 = 0.0621, wR2 = 0.1459	
R indices (all data)	R1 = 0.0891, wR2 = 0.1602	
Largest diff. peak and hole	0.473 and -0.284 e.Å <sup>-3</sup>	

Table 44: Atomic coordinates ( $\times 10^4$ ) and equivalent isotropic displacement parameters ( $\text{\AA}^2 \times 10^3$ ) for **9a**.  $U(\text{eq})$  is defined as one third of the trace of the orthogonalized  $U^{\text{ij}}$  tensor.

	x	y	z	U(eq)
C(1)	1601(2)	1460(2)	3041(1)	21(1)
C(2)	455(3)	931(3)	3193(1)	23(1)
C(3)	-792(3)	1498(3)	3160(1)	29(1)
C(4)	-1665(3)	750(3)	3352(1)	35(1)
C(5)	-1294(3)	-524(3)	3557(1)	38(1)
C(6)	-4(3)	-1145(3)	3589(1)	31(1)
C(7)	842(3)	-380(3)	3408(1)	25(1)
C(8)	538(3)	-2453(3)	3758(1)	36(1)
C(9)	1815(3)	-2914(3)	3748(1)	35(1)
C(10)	2660(3)	-2138(3)	3570(1)	31(1)
C(11)	2157(3)	-854(3)	3396(1)	24(1)
C(12)	2703(3)	248(2)	3158(1)	22(1)
C(13)	1594(2)	1815(2)	1873(1)	21(1)
C(14)	1651(2)	588(2)	1830(1)	23(1)
C(15)	1575(3)	295(3)	1268(1)	26(1)
C(16)	1435(3)	1221(3)	729(1)	24(1)
C(17)	1374(3)	2446(3)	764(1)	28(1)
C(18)	1453(2)	2727(3)	1324(1)	25(1)
C(19)	1608(3)	-237(3)	88(1)	39(1)
C(20)	4841(3)	-787(2)	3126(1)	25(1)
C(21)	5350(3)	-1261(3)	3699(1)	31(1)
C(22)	6378(3)	-2289(3)	3781(2)	37(1)
C(23)	6906(3)	-2857(3)	3288(2)	36(1)
C(24)	6391(3)	-2404(3)	2719(2)	36(1)
C(25)	5365(3)	-1360(3)	2639(1)	31(1)
C(26)	8366(3)	-4588(3)	2952(2)	58(1)

C(27)	1635(3)	2326(2)	3479(1)	24(1)
C(28)	1565(3)	3320(3)	4596(2)	41(1)
C(29)	-261(3)	1748(3)	4585(1)	40(1)
C(30)	2533(3)	496(3)	4719(1)	34(1)
C(31)	4917(2)	3368(2)	2051(1)	20(1)
C(32)	6105(3)	3827(2)	1887(1)	23(1)
C(33)	7337(3)	3217(3)	1950(1)	29(1)
C(34)	8258(3)	3890(3)	1723(2)	38(1)
C(35)	7952(3)	5143(3)	1441(2)	39(1)
C(36)	6680(3)	5811(3)	1378(1)	30(1)
C(37)	5786(2)	5119(2)	1605(1)	22(1)
C(38)	6190(3)	7114(3)	1136(1)	34(1)
C(39)	4925(3)	7630(3)	1128(1)	31(1)
C(40)	4041(3)	6913(2)	1357(1)	26(1)
C(41)	4475(3)	5641(2)	1591(1)	21(1)
C(42)	3869(2)	4603(2)	1873(1)	19(1)
C(43)	5017(3)	3080(2)	3215(1)	24(1)
C(44)	5087(3)	2186(3)	3774(1)	28(1)
C(45)	5415(3)	2407(3)	4298(1)	33(1)
C(46)	5715(3)	3521(3)	4295(1)	43(1)
C(47)	5573(3)	4446(3)	3762(1)	40(1)
C(48)	5222(3)	4239(3)	3228(1)	30(1)
C(49)	6649(5)	4656(4)	4799(2)	77(2)
C(50)	1758(2)	5728(2)	1836(1)	22(1)
C(51)	1241(3)	6139(2)	1259(1)	24(1)
C(52)	268(2)	7208(2)	1144(1)	24(1)
C(53)	-186(3)	7894(2)	1601(1)	26(1)
C(54)	323(3)	7505(3)	2175(1)	30(1)
C(55)	1290(3)	6417(3)	2287(1)	29(1)
C(56)	-1600(3)	9716(3)	1891(2)	36(1)
C(57)	4884(3)	2409(2)	1663(1)	21(1)
C(58)	4019(3)	3991(3)	377(1)	27(1)

C(59)	6805(3)	2835(3)	537(1)	30(1)
C(60)	5037(3)	1135(3)	647(1)	33(1)
N(1)	1619(2)	2216(2)	2416(1)	22(1)
N(2)	3828(2)	322(2)	3031(1)	24(1)
N(3)	4784(2)	2732(2)	2692(1)	24(1)
N(4)	2721(2)	4587(2)	1977(1)	22(1)
O(1)	1355(2)	1033(2)	151(1)	33(1)
O(2)	7942(2)	-3855(2)	3416(1)	52(1)
O(3)	6132(3)	3612(2)	4836(1)	65(1)
O(4)	-1165(2)	8941(2)	1445(1)	34(1)
Si(1)	1361(1)	1925(1)	4345(1)	29(1)
Si(2)	5196(1)	2639(1)	800(1)	23(1)

Table 45: Bond Lengths [Å] and Bond Angles [°] for **9a**.

C(1)-N(1)	1.455(3)	C(13)-C(18)	1.398(4)
C(1)-C(2)	1.519(4)	C(13)-C(14)	1.399(4)
C(1)-C(27)	1.550(4)	C(14)-C(15)	1.389(4)
C(1)-C(12)	1.562(4)	C(15)-C(16)	1.390(4)
C(2)-C(3)	1.362(4)	C(16)-O(1)	1.372(3)
C(2)-C(7)	1.410(4)	C(16)-C(17)	1.391(4)
C(3)-C(4)	1.420(4)	C(17)-C(18)	1.379(4)
C(4)-C(5)	1.368(4)	C(19)-O(1)	1.427(3)
C(5)-C(6)	1.416(4)	C(20)-C(25)	1.385(4)
C(6)-C(7)	1.408(4)	C(20)-C(21)	1.390(4)
C(6)-C(8)	1.416(4)	C(20)-N(2)	1.431(3)
C(7)-C(11)	1.411(4)	C(21)-C(22)	1.384(4)
C(8)-C(9)	1.370(4)	C(22)-C(23)	1.394(4)
C(9)-C(10)	1.416(4)	C(23)-O(2)	1.379(4)
C(10)-C(11)	1.387(4)	C(23)-C(24)	1.381(4)
C(11)-C(12)	1.493(4)	C(24)-C(25)	1.394(4)
C(12)-N(2)	1.268(3)	C(26)-O(2)	1.435(4)
C(13)-N(1)	1.398(3)	C(27)-Si(1)	1.886(3)

C(28)-Si(1)	1.872(3)	C(51)-C(52)	1.381(4)
C(29)-Si(1)	1.866(3)	C(52)-C(53)	1.391(4)
C(30)-Si(1)	1.868(3)	C(53)-O(4)	1.379(3)
C(31)-N(3)	1.451(3)	C(53)-C(54)	1.388(4)
C(31)-C(32)	1.520(4)	C(54)-C(55)	1.391(4)
C(31)-C(57)	1.551(3)	C(56)-O(4)	1.434(3)
C(31)-C(42)	1.560(4)	C(57)-Si(2)	1.884(3)
C(32)-C(33)	1.362(4)	C(58)-Si(2)	1.863(3)
C(32)-C(37)	1.414(4)	C(59)-Si(2)	1.868(3)
C(33)-C(34)	1.414(4)	C(60)-Si(2)	1.871(3)
C(34)-C(35)	1.376(4)		
C(35)-C(36)	1.415(4)	N(1)-C(1)-C(2)	112.2(2)
C(36)-C(37)	1.404(4)	N(1)-C(1)-C(27)	106.4(2)
C(36)-C(38)	1.423(4)	C(2)-C(1)-C(27)	111.3(2)
C(37)-C(41)	1.415(4)	N(1)-C(1)-C(12)	114.4(2)
C(38)-C(39)	1.367(4)	C(2)-C(1)-C(12)	102.3(2)
C(39)-C(40)	1.415(4)	C(27)-C(1)-C(12)	110.4(2)
C(40)-C(41)	1.382(4)	C(3)-C(2)-C(7)	119.1(3)
C(41)-C(42)	1.487(4)	C(3)-C(2)-C(1)	131.6(3)
C(42)-N(4)	1.273(3)	C(7)-C(2)-C(1)	109.3(2)
C(43)-N(3)	1.389(3)	C(2)-C(3)-C(4)	118.9(3)
C(43)-C(48)	1.400(4)	C(5)-C(4)-C(3)	122.2(3)
C(43)-C(44)	1.406(4)	C(4)-C(5)-C(6)	120.4(3)
C(44)-C(45)	1.363(4)	C(7)-C(6)-C(5)	116.4(3)
C(45)-C(46)	1.387(4)	C(7)-C(6)-C(8)	116.1(3)
C(46)-O(3)	1.380(4)	C(5)-C(6)-C(8)	127.5(3)
C(46)-C(47)	1.381(4)	C(6)-C(7)-C(2)	123.0(3)
C(47)-C(48)	1.383(4)	C(6)-C(7)-C(11)	123.5(3)
C(49)-O(3)	1.429(4)	C(2)-C(7)-C(11)	113.4(2)
C(50)-C(55)	1.384(4)	C(9)-C(8)-C(6)	120.5(3)
C(50)-C(51)	1.397(4)	C(8)-C(9)-C(10)	123.1(3)
C(50)-N(4)	1.432(3)	C(11)-C(10)-C(9)	117.7(3)

C(10)-C(11)-C(7)	119.2(3)	C(57)-C(31)-C(42)	110.9(2)
C(10)-C(11)-C(12)	134.3(3)	C(33)-C(32)-C(37)	118.9(2)
C(7)-C(11)-C(12)	106.5(2)	C(33)-C(32)-C(31)	131.7(2)
N(2)-C(12)-C(11)	131.5(3)	C(37)-C(32)-C(31)	109.3(2)
N(2)-C(12)-C(1)	120.1(2)	C(32)-C(33)-C(34)	118.9(3)
C(11)-C(12)-C(1)	108.3(2)	C(35)-C(34)-C(33)	122.3(3)
N(1)-C(13)-C(18)	117.3(2)	C(34)-C(35)-C(36)	120.2(3)
N(1)-C(13)-C(14)	125.9(2)	C(37)-C(36)-C(35)	116.3(3)
C(18)-C(13)-C(14)	116.8(2)	C(37)-C(36)-C(38)	115.7(3)
C(15)-C(14)-C(13)	121.3(3)	C(35)-C(36)-C(38)	127.9(3)
C(14)-C(15)-C(16)	120.7(3)	C(36)-C(37)-C(32)	123.3(3)
O(1)-C(16)-C(15)	125.4(2)	C(36)-C(37)-C(41)	123.8(2)
O(1)-C(16)-C(17)	115.9(2)	C(32)-C(37)-C(41)	112.9(2)
C(15)-C(16)-C(17)	118.7(3)	C(39)-C(38)-C(36)	120.9(3)
C(18)-C(17)-C(16)	120.2(3)	C(38)-C(39)-C(40)	122.5(3)
C(17)-C(18)-C(13)	122.3(3)	C(41)-C(40)-C(39)	118.6(3)
C(25)-C(20)-C(21)	119.2(3)	C(40)-C(41)-C(37)	118.5(2)
C(25)-C(20)-N(2)	120.3(3)	C(40)-C(41)-C(42)	134.7(3)
C(21)-C(20)-N(2)	120.4(3)	C(37)-C(41)-C(42)	106.8(2)
C(22)-C(21)-C(20)	120.4(3)	N(4)-C(42)-C(41)	131.5(2)
C(21)-C(22)-C(23)	120.1(3)	N(4)-C(42)-C(31)	120.0(2)
O(2)-C(23)-C(24)	124.8(3)	C(41)-C(42)-C(31)	108.5(2)
O(2)-C(23)-C(22)	115.3(3)	N(3)-C(43)-C(48)	125.3(3)
C(24)-C(23)-C(22)	119.9(3)	N(3)-C(43)-C(44)	117.5(2)
C(23)-C(24)-C(25)	119.7(3)	C(48)-C(43)-C(44)	117.1(3)
C(20)-C(25)-C(24)	120.7(3)	C(45)-C(44)-C(43)	121.5(3)
C(1)-C(27)-Si(1)	124.68(19)	C(44)-C(45)-C(46)	120.8(3)
N(3)-C(31)-C(32)	114.2(2)	O(3)-C(46)-C(47)	125.1(3)
N(3)-C(31)-C(57)	105.7(2)	O(3)-C(46)-C(45)	116.3(3)
C(32)-C(31)-C(57)	110.8(2)	C(47)-C(46)-C(45)	118.6(3)
N(3)-C(31)-C(42)	113.1(2)	C(46)-C(47)-C(48)	121.0(3)
C(32)-C(31)-C(42)	102.3(2)	C(47)-C(48)-C(43)	120.7(3)

C(55)-C(50)-C(51)	119.0(3)	C(46)-O(3)-C(49)	115.9(3)
C(55)-C(50)-N(4)	119.4(2)	C(53)-O(4)-C(56)	117.1(2)
C(51)-C(50)-N(4)	121.5(2)	C(29)-Si(1)-C(30)	109.98(15)
C(52)-C(51)-C(50)	120.5(3)	C(29)-Si(1)-C(28)	109.15(15)
C(51)-C(52)-C(53)	119.8(3)	C(30)-Si(1)-C(28)	108.82(15)
O(4)-C(53)-C(54)	123.8(3)	C(29)-Si(1)-C(27)	112.11(13)
O(4)-C(53)-C(52)	115.7(2)	C(30)-Si(1)-C(27)	112.96(13)
C(54)-C(53)-C(52)	120.4(3)	C(28)-Si(1)-C(27)	103.53(14)
C(53)-C(54)-C(55)	119.0(3)	C(58)-Si(2)-C(59)	109.21(13)
C(50)-C(55)-C(54)	121.2(3)	C(58)-Si(2)-C(60)	110.05(14)
C(31)-C(57)-Si(2)	125.12(18)	C(59)-Si(2)-C(60)	109.65(13)
C(13)-N(1)-C(1)	126.1(2)	C(58)-Si(2)-C(57)	112.23(12)
C(12)-N(2)-C(20)	120.4(2)	C(59)-Si(2)-C(57)	113.09(13)
C(43)-N(3)-C(31)	127.9(2)	C(60)-Si(2)-C(57)	102.42(13)
C(42)-N(4)-C(50)	120.1(2)	C(1)-N(1)-H(1N)	112(2)
C(16)-O(1)-C(19)	116.8(2)	C(31)-N(3)-H(3N)	112(2)
C(23)-O(2)-C(26)	116.1(3)		

---

Table 46: Crystallographic Data and Structure Refinement of **9b**.

Empirical formula	$C_{30}H_{32}N_2O_2Si$	
Formula weight	480.67	
Temperature	100(2) K	
Wavelength	0.71075 Å	
Crystal system	Monoclinic	
Space group	P2 <sub>1</sub> /c	
Unit cell dimensions	a = 11.174(4) Å	$\alpha = 90.000(5)^\circ$ .
	b = 43.677(10) Å	$\beta = 106.836(12)^\circ$ .
	c = 11.534(4) Å	$\gamma = 90.000(5)^\circ$ .
Volume	5388(3) Å <sup>3</sup>	
Z	8	
Density (calculated)	1.185 Mg/m <sup>3</sup>	
Absorption coefficient	0.116 mm <sup>-1</sup>	
F(000)	2048	
Crystal size	0.37 x 0.06 x 0.05 mm <sup>3</sup>	
Theta range for data collection	1.86 to 25.00°.	
Index ranges	-13 ≤ h ≤ 12, -51 ≤ k ≤ 51, -13 ≤ l ≤ 13	
Reflections collected	63581	
Independent reflections	9227 [R(int) = 0.1245]	
Completeness to theta = 25.00°	97.1 %	
Absorption correction	Semi-empirical from equivalents	
Max. and min. transmission	1.00000 and 0.6289	
Refinement method	Full-matrix least-squares on F <sup>2</sup>	
Data / restraints / parameters	9227 / 0 / 649	
Goodness-of-fit on F <sup>2</sup>	1.323	
Final R indices [I > 2σ(I)]	R1 = 0.1658, wR2 = 0.2660	
R indices (all data)	R1 = 0.1785, wR2 = 0.2720	
Largest diff. peak and hole	0.372 and -0.401 e.Å <sup>-3</sup>	



Table 47: Atomic coordinates ( $\times 10^4$ ) and equivalent isotropic displacement parameters ( $\text{\AA}^2 \times 10^3$ ) for **9b**.  $U(\text{eq})$  is defined as one third of the trace of the orthogonalized  $U^{ij}$  tensor.

	x	y	z	U(eq)
C(1)	-200(6)	1022(1)	9291(7)	25(2)
C(2)	-1352(6)	935(2)	9687(7)	28(2)
C(3)	-2612(7)	967(2)	9131(7)	34(2)
C(4)	-3488(7)	851(2)	9727(8)	43(2)
C(5)	-3125(7)	707(2)	10831(8)	39(2)
C(6)	-1830(7)	681(2)	11454(7)	32(2)
C(7)	-974(6)	796(1)	10853(7)	26(2)
C(8)	-1292(7)	558(2)	12643(7)	34(2)
C(9)	5(7)	558(2)	13154(8)	39(2)
C(10)	835(7)	676(2)	12510(7)	31(2)
C(11)	346(6)	792(2)	11365(7)	27(2)
C(12)	898(6)	936(2)	10440(7)	27(2)
C(13)	-364(7)	1605(2)	9622(7)	33(2)
C(14)	-420(7)	1894(2)	9044(9)	44(2)
C(15)	-679(8)	2158(2)	9586(11)	65(3)
C(16)	-895(8)	2147(2)	10718(12)	63(3)
C(17)	-790(7)	1867(2)	11331(9)	49(2)
C(18)	-518(7)	1597(2)	10783(7)	35(2)
C(19)	-2115(14)	2427(2)	11666(13)	116(6)
C(20)	3032(6)	919(2)	11535(7)	27(2)
C(21)	3453(7)	1145(2)	12411(8)	37(2)
C(22)	4437(7)	1089(2)	13447(7)	31(2)
C(23)	5015(6)	803(2)	13598(7)	32(2)
C(24)	4605(6)	571(2)	12732(7)	31(2)
C(25)	3617(6)	630(2)	11697(7)	30(2)
C(26)	6362(7)	943(2)	15542(8)	42(2)

C(27)	-133(7)	838(2)	8167(7)	30(2)
C(28)	-140(7)	335(2)	6440(7)	38(2)
C(29)	-1911(7)	267(2)	8077(7)	34(2)
C(30)	908(6)	193(2)	9171(7)	31(2)
C(31)	3052(6)	1504(2)	7800(7)	28(2)
C(32)	4179(6)	1582(1)	7309(7)	28(2)
C(33)	5449(7)	1569(2)	7874(7)	33(2)
C(34)	6282(7)	1669(2)	7199(9)	45(2)
C(35)	5850(7)	1774(2)	6016(9)	43(2)
C(36)	4532(7)	1783(2)	5407(7)	32(2)
C(37)	3726(7)	1690(2)	6122(7)	31(2)
C(38)	3943(8)	1865(2)	4200(8)	39(2)
C(39)	2637(8)	1855(2)	3740(8)	38(2)
C(40)	1865(7)	1762(2)	4465(7)	33(2)
C(41)	2400(7)	1678(2)	5632(7)	29(2)
C(42)	1919(6)	1562(1)	6647(7)	25(2)
C(43)	3198(6)	919(2)	7646(6)	25(2)
C(44)	3132(6)	905(2)	6421(7)	29(2)
C(45)	3277(6)	625(2)	5866(7)	30(2)
C(46)	3452(7)	355(1)	6525(7)	29(2)
C(47)	3494(7)	366(2)	7760(7)	33(2)
C(48)	3367(7)	644(1)	8307(7)	32(2)
C(49)	3367(7)	38(2)	4802(7)	40(2)
C(50)	-240(7)	1555(2)	5646(7)	34(2)
C(51)	-825(7)	1840(2)	5434(7)	35(2)
C(52)	-1831(6)	1884(2)	4411(7)	33(2)
C(53)	-2286(7)	1645(2)	3613(7)	37(2)
C(54)	-1705(7)	1354(2)	3832(8)	43(2)
C(55)	-687(7)	1313(2)	4865(7)	36(2)
C(56)	-3685(8)	1480(2)	1695(8)	55(2)
C(57)	3014(6)	1722(2)	8862(7)	28(2)
C(58)	3108(9)	2290(2)	10317(8)	54(2)

C(59)	4691(7)	2281(2)	8536(9)	46(2)
C(60)	1843(7)	2331(2)	7581(8)	38(2)
N(1)	-179(6)	1348(1)	8956(6)	31(2)
N(2)	2036(5)	987(1)	10462(6)	30(1)
N(3)	3130(6)	1192(1)	8294(6)	28(1)
N(4)	803(5)	1506(1)	6710(6)	32(2)
O(1)	-1187(6)	2417(1)	11213(9)	98(3)
O(2)	6001(5)	721(1)	14586(5)	39(1)
O(3)	3581(5)	64(1)	6083(5)	36(1)
O(4)	-3311(5)	1711(1)	2635(5)	47(2)
Si(1)	-325(2)	406(1)	7999(2)	29(1)
Si(2)	3169(2)	2157(1)	8783(2)	34(1)

Table 48: Bond Lengths [ $\text{\AA}$ ] and Bond Angles [ $^\circ$ ] for **9b**.

C(1)-N(1)	1.476(8)	C(13)-N(1)	1.411(9)
C(1)-C(2)	1.533(9)	C(13)-C(14)	1.422(10)
C(1)-C(27)	1.546(10)	C(14)-C(15)	1.379(12)
C(1)-C(12)	1.568(10)	C(15)-C(16)	1.397(15)
C(2)-C(3)	1.374(10)	C(16)-O(1)	1.389(10)
C(2)-C(7)	1.424(10)	C(16)-C(17)	1.398(13)
C(3)-C(4)	1.441(10)	C(17)-C(18)	1.413(10)
C(4)-C(5)	1.372(11)	C(19)-O(1)	1.290(12)
C(5)-C(6)	1.421(10)	C(20)-C(21)	1.391(10)
C(6)-C(7)	1.426(9)	C(20)-C(25)	1.410(9)
C(6)-C(8)	1.433(10)	C(20)-N(2)	1.436(9)
C(7)-C(11)	1.421(10)	C(21)-C(22)	1.391(10)
C(8)-C(9)	1.398(11)	C(22)-C(23)	1.395(10)
C(9)-C(10)	1.441(10)	C(23)-O(2)	1.384(9)
C(10)-C(11)	1.371(10)	C(23)-C(24)	1.403(10)
C(11)-C(12)	1.516(9)	C(24)-C(25)	1.395(10)
C(12)-N(2)	1.284(8)	C(26)-O(2)	1.436(9)
C(13)-C(18)	1.398(11)	C(27)-Si(1)	1.900(7)

C(28)-Si(1)	1.894(8)	C(51)-C(52)	1.387(10)
C(29)-Si(1)	1.900(7)	C(52)-C(53)	1.389(10)
C(30)-Si(1)	1.875(7)	C(53)-O(4)	1.387(9)
C(31)-N(3)	1.470(8)	C(53)-C(54)	1.414(11)
C(31)-C(57)	1.560(10)	C(54)-C(55)	1.400(11)
C(31)-C(32)	1.561(9)	C(56)-O(4)	1.451(10)
C(31)-C(42)	1.569(10)	C(57)-Si(2)	1.911(7)
C(32)-C(33)	1.380(10)	C(58)-Si(2)	1.883(9)
C(32)-C(37)	1.397(10)	C(59)-Si(2)	1.883(8)
C(33)-C(34)	1.444(10)	C(60)-Si(2)	1.874(8)
C(34)-C(35)	1.386(12)		
C(35)-C(36)	1.437(11)	N(1)-C(1)-C(2)	113.2(5)
C(36)-C(38)	1.403(11)	N(1)-C(1)-C(27)	105.9(6)
C(36)-C(37)	1.445(10)	C(2)-C(1)-C(27)	111.7(6)
C(37)-C(41)	1.425(10)	N(1)-C(1)-C(12)	112.6(5)
C(38)-C(39)	1.402(11)	C(2)-C(1)-C(12)	102.0(6)
C(39)-C(40)	1.425(10)	C(27)-C(1)-C(12)	111.6(5)
C(40)-C(41)	1.356(10)	C(3)-C(2)-C(7)	117.9(6)
C(41)-C(42)	1.510(10)	C(3)-C(2)-C(1)	132.2(7)
C(42)-N(4)	1.293(8)	C(7)-C(2)-C(1)	109.9(6)
C(43)-C(44)	1.394(10)	C(2)-C(3)-C(4)	119.2(7)
C(43)-C(48)	1.405(9)	C(5)-C(4)-C(3)	123.0(7)
C(43)-N(3)	1.421(9)	C(4)-C(5)-C(6)	119.3(7)
C(44)-C(45)	1.412(9)	C(5)-C(6)-C(7)	117.1(7)
C(45)-C(46)	1.386(10)	C(5)-C(6)-C(8)	126.6(7)
C(46)-O(3)	1.390(8)	C(7)-C(6)-C(8)	116.3(7)
C(46)-C(47)	1.412(10)	C(11)-C(7)-C(2)	112.8(6)
C(47)-C(48)	1.397(10)	C(11)-C(7)-C(6)	123.7(7)
C(49)-O(3)	1.432(9)	C(2)-C(7)-C(6)	123.5(6)
C(50)-C(55)	1.384(10)	C(9)-C(8)-C(6)	120.0(7)
C(50)-C(51)	1.394(10)	C(8)-C(9)-C(10)	121.7(8)
C(50)-N(4)	1.443(10)	C(11)-C(10)-C(9)	119.5(7)

C(10)-C(11)-C(7)	118.8(6)	C(32)-C(31)-C(42)	101.3(6)
C(10)-C(11)-C(12)	134.5(7)	C(33)-C(32)-C(37)	120.5(7)
C(7)-C(11)-C(12)	106.7(6)	C(33)-C(32)-C(31)	130.3(7)
N(2)-C(12)-C(11)	131.3(7)	C(37)-C(32)-C(31)	109.1(6)
N(2)-C(12)-C(1)	120.2(6)	C(32)-C(33)-C(34)	117.9(8)
C(11)-C(12)-C(1)	108.4(5)	C(35)-C(34)-C(33)	122.4(8)
C(18)-C(13)-N(1)	125.4(7)	C(34)-C(35)-C(36)	120.4(7)
C(18)-C(13)-C(14)	118.2(7)	C(38)-C(36)-C(35)	127.8(7)
N(1)-C(13)-C(14)	116.5(7)	C(38)-C(36)-C(37)	116.6(7)
C(15)-C(14)-C(13)	121.0(9)	C(35)-C(36)-C(37)	115.7(7)
C(14)-C(15)-C(16)	120.8(9)	C(32)-C(37)-C(41)	114.6(6)
O(1)-C(16)-C(15)	118.7(9)	C(32)-C(37)-C(36)	123.1(7)
O(1)-C(16)-C(17)	122.0(10)	C(41)-C(37)-C(36)	122.1(7)
C(15)-C(16)-C(17)	119.4(8)	C(39)-C(38)-C(36)	120.4(7)
C(16)-C(17)-C(18)	120.1(9)	C(38)-C(39)-C(40)	121.8(8)
C(13)-C(18)-C(17)	120.5(7)	C(41)-C(40)-C(39)	119.5(7)
C(21)-C(20)-C(25)	119.5(7)	C(40)-C(41)-C(37)	119.6(7)
C(21)-C(20)-N(2)	119.6(6)	C(40)-C(41)-C(42)	134.9(7)
C(25)-C(20)-N(2)	120.9(6)	C(37)-C(41)-C(42)	105.5(6)
C(20)-C(21)-C(22)	121.1(7)	N(4)-C(42)-C(41)	132.3(7)
C(21)-C(22)-C(23)	119.1(7)	N(4)-C(42)-C(31)	118.4(6)
O(2)-C(23)-C(22)	124.3(7)	C(41)-C(42)-C(31)	109.3(5)
O(2)-C(23)-C(24)	114.7(6)	C(44)-C(43)-C(48)	118.0(6)
C(22)-C(23)-C(24)	120.9(7)	C(44)-C(43)-N(3)	125.1(6)
C(25)-C(24)-C(23)	119.3(7)	C(48)-C(43)-N(3)	116.8(6)
C(24)-C(25)-C(20)	120.1(7)	C(43)-C(44)-C(45)	121.3(7)
C(1)-C(27)-Si(1)	124.8(5)	C(46)-C(45)-C(44)	120.3(7)
N(3)-C(31)-C(57)	105.8(6)	C(45)-C(46)-O(3)	126.1(7)
N(3)-C(31)-C(32)	112.2(5)	C(45)-C(46)-C(47)	118.9(6)
C(57)-C(31)-C(32)	111.2(5)	O(3)-C(46)-C(47)	115.1(6)
N(3)-C(31)-C(42)	114.9(6)	C(48)-C(47)-C(46)	120.5(7)
C(57)-C(31)-C(42)	111.6(5)	C(47)-C(48)-C(43)	121.0(7)

C(55)-C(50)-C(51)	120.3(7)	C(46)-O(3)-C(49)	116.6(6)
C(55)-C(50)-N(4)	119.4(7)	C(53)-O(4)-C(56)	117.0(6)
C(51)-C(50)-N(4)	120.2(7)	C(30)-Si(1)-C(28)	110.0(3)
C(52)-C(51)-C(50)	119.8(7)	C(30)-Si(1)-C(27)	112.5(3)
C(51)-C(52)-C(53)	120.6(7)	C(28)-Si(1)-C(27)	102.8(3)
O(4)-C(53)-C(52)	116.0(7)	C(30)-Si(1)-C(29)	107.9(3)
O(4)-C(53)-C(54)	124.2(7)	C(28)-Si(1)-C(29)	110.6(3)
C(52)-C(53)-C(54)	119.8(7)	C(27)-Si(1)-C(29)	113.1(3)
C(55)-C(54)-C(53)	119.0(7)	C(60)-Si(2)-C(58)	109.5(4)
C(50)-C(55)-C(54)	120.4(7)	C(60)-Si(2)-C(59)	109.1(4)
C(31)-C(57)-Si(2)	122.9(5)	C(58)-Si(2)-C(59)	109.5(4)
C(13)-N(1)-C(1)	127.5(6)	C(60)-Si(2)-C(57)	112.1(3)
C(12)-N(2)-C(20)	119.8(6)	C(58)-Si(2)-C(57)	103.5(4)
C(43)-N(3)-C(31)	125.5(6)	C(59)-Si(2)-C(57)	113.1(3)
C(42)-N(4)-C(50)	118.6(6)	C(1)-N(1)-H(1N)	115(4)
C(19)-O(1)-C(16)	120.6(8)	C(31)-N(1)-H(3N)	113(5)
C(23)-O(2)-C(26)	115.9(6)		

---

## Appendix B: X-Ray Diffraction Data for 10-21-DCM

Table 49: Crystallographic Data and Structure Refinement of 10.

Empirical formula	C <sub>26</sub> H <sub>20</sub> Cl <sub>2</sub> N <sub>2</sub> Zn	
Formula weight	496.71	
Temperature	100(2) K	
Wavelength	1.54184 Å	
Crystal system	Monoclinic	
Space group	I2/a	
Unit cell dimensions	a = 17.6901(6) Å	α = 90°.
	b = 11.7401(3) Å	β = 104.191(4)°.
	c = 23.2316(10) Å	γ = 90°.
Volume	4677.6(3) Å <sup>3</sup>	
Z	8	
Density (calculated)	1.411 Mg/m <sup>3</sup>	
Absorption coefficient	3.671 mm <sup>-1</sup>	
F(000)	2032	
Crystal size	0.32 x 0.15 x 0.06 mm <sup>3</sup>	
Theta range for data collection	3.93 to 74.79°.	
Index ranges	-22<=h<=15, -11<=k<=14, -28<=l<=28	
Reflections collected	17334	
Independent reflections	4733 [R(int) = 0.0367]	
Completeness to theta = 74.79°	98.4 %	
Absorption correction	Semi-empirical from equivalents	
Max. and min. transmission	1.00000 and 0.57675	
Refinement method	Full-matrix least-squares on F <sup>2</sup>	
Data / restraints / parameters	4733 / 0 / 282	
Goodness-of-fit on F <sup>2</sup>	1.054	
Final R indices [I>2sigma(I)]	R1 = 0.0508, wR2 = 0.1400	
R indices (all data)	R1 = 0.0603, wR2 = 0.1508	
Largest diff. peak and hole	0.823 and -0.921 e.Å <sup>-3</sup>	

Table 50: Atomic coordinates ( $\times 10^4$ ) and equivalent isotropic displacement parameters ( $\text{\AA}^2 \times 10^3$ ) for **10**. U(eq) is defined as one third of the trace of the orthogonalized  $U^{ij}$  tensor.

	x	y	z	U(eq)
C(1)	2078(2)	5218(2)	2252(1)	25(1)
C(2)	2245(2)	6095(2)	1848(1)	25(1)
C(3)	1837(2)	6574(3)	1322(1)	29(1)
C(4)	2195(2)	7466(3)	1071(1)	31(1)
C(5)	2927(2)	7870(3)	1336(1)	31(1)
C(6)	3353(2)	7417(3)	1886(1)	27(1)
C(7)	2997(2)	6526(2)	2128(1)	24(1)
C(8)	4096(2)	7779(2)	2226(1)	29(1)
C(9)	4432(2)	7280(2)	2764(2)	30(1)
C(10)	4061(2)	6381(2)	2998(1)	28(1)
C(11)	3348(2)	6001(2)	2679(1)	24(1)
C(12)	2778(2)	5154(2)	2779(1)	24(1)
C(13)	809(2)	4556(2)	1766(1)	26(1)
C(14)	91(2)	4796(3)	1875(1)	29(1)
C(15)	-573(2)	4777(3)	1407(2)	33(1)
C(16)	-531(2)	4488(3)	836(2)	34(1)
C(17)	194(2)	4211(3)	744(1)	34(1)
C(18)	865(2)	4242(3)	1203(1)	29(1)
C(19)	-1265(2)	4449(4)	335(2)	50(1)
C(20)	3355(2)	4240(2)	3707(1)	28(1)
C(21)	3181(2)	4181(3)	4262(2)	39(1)
C(22)	3757(2)	3878(3)	4759(2)	44(1)
C(23)	4507(2)	3621(3)	4715(2)	37(1)
C(24)	4665(2)	3654(3)	4159(2)	35(1)
C(25)	4092(2)	3958(3)	3655(2)	30(1)
C(26)	5128(2)	3285(3)	5260(2)	48(1)



Cl(1)	966(1)	4472(1)	3627(1)	30(1)
Cl(2)	1672(1)	1821(1)	2989(1)	42(1)
N(1)	1486(1)	4587(2)	2254(1)	25(1)
N(2)	2732(1)	4480(2)	3203(1)	25(1)
Zn(1)	1652(1)	3682(1)	3048(1)	26(1)

Table S1: Bond Lengths [Å] and Bond Angles [°] for **10**.

C(1)-N(1)	1.284(4)	C(20)-C(21)	1.399(5)
C(1)-C(2)	1.472(4)	C(20)-N(2)	1.426(4)
C(1)-C(12)	1.515(4)	C(21)-C(22)	1.386(5)
C(2)-C(3)	1.377(4)	C(22)-C(23)	1.389(5)
C(2)-C(7)	1.423(4)	C(23)-C(24)	1.386(5)
C(3)-C(4)	1.421(4)	C(23)-C(26)	1.511(5)
C(4)-C(5)	1.375(5)	C(24)-C(25)	1.396(4)
C(5)-C(6)	1.418(4)	Cl(1)-Zn(1)	2.2225(8)
C(6)-C(7)	1.407(4)	Cl(2)-Zn(1)	2.1896(9)
C(6)-C(8)	1.422(4)	N(1)-Zn(1)	2.085(2)
C(7)-C(11)	1.419(4)	N(2)-Zn(1)	2.079(2)
C(8)-C(9)	1.375(5)		
C(9)-C(10)	1.419(4)	N(1)-C(1)-C(2)	134.4(3)
C(10)-C(11)	1.372(4)	N(1)-C(1)-C(12)	118.3(3)
C(11)-C(12)	1.475(4)	C(2)-C(1)-C(12)	107.3(2)
C(12)-N(2)	1.282(4)	C(3)-C(2)-C(7)	119.3(3)
C(13)-C(14)	1.383(4)	C(3)-C(2)-C(1)	135.0(3)
C(13)-C(18)	1.384(4)	C(7)-C(2)-C(1)	105.6(3)
C(13)-N(1)	1.435(4)	C(2)-C(3)-C(4)	118.4(3)
C(14)-C(15)	1.393(4)	C(5)-C(4)-C(3)	122.4(3)
C(15)-C(16)	1.389(5)	C(4)-C(5)-C(6)	120.6(3)
C(16)-C(17)	1.391(5)	C(7)-C(6)-C(5)	116.6(3)
C(16)-C(19)	1.516(5)	C(7)-C(6)-C(8)	116.3(3)
C(17)-C(18)	1.389(4)	C(5)-C(6)-C(8)	127.1(3)
C(20)-C(25)	1.378(4)	C(6)-C(7)-C(11)	122.9(3)

C(6)-C(7)-C(2)	122.8(3)	C(25)-C(20)-N(2)	122.2(3)
C(11)-C(7)-C(2)	114.3(3)	C(21)-C(20)-N(2)	117.8(3)
C(9)-C(8)-C(6)	120.8(3)	C(22)-C(21)-C(20)	119.8(3)
C(8)-C(9)-C(10)	121.8(3)	C(21)-C(22)-C(23)	121.0(3)
C(11)-C(10)-C(9)	119.0(3)	C(24)-C(23)-C(22)	118.5(3)
C(10)-C(11)-C(7)	119.1(3)	C(24)-C(23)-C(26)	121.1(3)
C(10)-C(11)-C(12)	135.1(3)	C(22)-C(23)-C(26)	120.4(4)
C(7)-C(11)-C(12)	105.6(2)	C(23)-C(24)-C(25)	121.2(3)
N(2)-C(12)-C(11)	135.4(3)	C(20)-C(25)-C(24)	119.8(3)
N(2)-C(12)-C(1)	117.3(3)	C(1)-N(1)-C(13)	122.3(2)
C(11)-C(12)-C(1)	107.1(2)	C(1)-N(1)-Zn(1)	111.12(19)
C(14)-C(13)-C(18)	120.7(3)	C(13)-N(1)-Zn(1)	126.58(19)
C(14)-C(13)-N(1)	118.3(3)	C(12)-N(2)-C(20)	124.8(3)
C(18)-C(13)-N(1)	120.9(3)	C(12)-N(2)-Zn(1)	112.0(2)
C(13)-C(14)-C(15)	119.3(3)	C(20)-N(2)-Zn(1)	123.13(19)
C(16)-C(15)-C(14)	121.2(3)	N(1)-Zn(1)-N(2)	81.23(10)
C(15)-C(16)-C(17)	118.1(3)	N(2)-Zn(1)-Cl(2)	115.58(7)
C(15)-C(16)-C(19)	120.3(3)	N(1)-Zn(1)-Cl(2)	116.98(7)
C(17)-C(16)-C(19)	121.6(3)	N(2)-Zn(1)-Cl(1)	108.76(7)
C(18)-C(17)-C(16)	121.5(3)	N(1)-Zn(1)-Cl(1)	110.06(7)
C(13)-C(18)-C(17)	119.1(3)	Cl(1)-Zn(1)-Cl(2)	118.33(3)
C(25)-C(20)-C(21)	119.7(3)		

---

Table 52: Crystallographic Data and Structure Refinement of **11**.

Empirical formula	$C_{28}H_{24}Cl_2N_2Zn$	
Formula weight	524.76	
Temperature	100(2) K	
Wavelength	1.54184 Å	
Crystal system	Triclinic	
Space group	P-1	
Unit cell dimensions	$a = 11.4539(4)$ Å	$\alpha = 70.205(3)^\circ$ .
	$b = 13.9416(4)$ Å	$\beta = 75.906(3)^\circ$ .
	$c = 17.0847(5)$ Å	$\gamma = 88.921(3)^\circ$ .
Volume	$2483.64(13)$ Å <sup>3</sup>	
Z	4	
Density (calculated)	$1.403$ Mg/m <sup>3</sup>	
Absorption coefficient	$3.487$ mm <sup>-1</sup>	
F(000)	1080	
Crystal size	$0.27 \times 0.10 \times 0.06$ mm <sup>3</sup>	
Theta range for data collection	3.38 to 74.15°.	
Index ranges	$-14 \leq h \leq 11$ , $-14 \leq k \leq 17$ , $-21 \leq l \leq 20$	
Reflections collected	19816	
Independent reflections	9840 [R(int) = 0.0240]	
Completeness to theta = 74.15°	97.3 %	
Absorption correction	Semi-empirical from equivalents	
Max. and min. transmission	0.8181 and 0.4528	
Refinement method	Full-matrix least-squares on F <sup>2</sup>	
Data / restraints / parameters	9840 / 0 / 602	
Goodness-of-fit on F <sup>2</sup>	1.026	
Final R indices [I > 2sigma(I)]	R1 = 0.0322, wR2 = 0.0841	
R indices (all data)	R1 = 0.0396, wR2 = 0.0889	
Largest diff. peak and hole	0.539 and -0.366 e.Å <sup>-3</sup>	

Table 53: Atomic coordinates ( $\times 10^4$ ) and equivalent isotropic displacement parameters ( $\text{\AA}^2 \times 10^3$ ) for **11**. U(eq) is defined as one third of the trace of the orthogonalized  $U^{ij}$  tensor.

	x	y	z	U(eq)
C(1)	140(2)	1787(1)	373(1)	20(1)
C(2)	212(2)	1737(1)	-486(1)	23(1)
C(3)	1037(2)	2103(2)	-1278(1)	28(1)
C(4)	761(2)	1912(2)	-1981(1)	32(1)
C(5)	-273(2)	1366(2)	-1897(1)	30(1)
C(6)	-1123(2)	956(1)	-1084(1)	25(1)
C(7)	-851(2)	1168(1)	-397(1)	22(1)
C(8)	-2218(2)	365(2)	-894(1)	30(1)
C(9)	-2940(2)	4(2)	-71(1)	31(1)
C(10)	-2657(2)	214(2)	617(1)	25(1)
C(11)	-1618(2)	814(1)	446(1)	21(1)
C(12)	-1036(2)	1214(1)	960(1)	20(1)
C(13)	1962(2)	2695(1)	201(1)	22(1)
C(14)	2994(2)	2281(1)	431(1)	23(1)
C(15)	4123(2)	2740(2)	-64(1)	27(1)
C(16)	4187(2)	3645(2)	-756(1)	30(1)
C(17)	3162(2)	4090(2)	-969(1)	28(1)
C(18)	2032(2)	3603(2)	-484(1)	26(1)
C(19)	5254(2)	2260(2)	132(2)	37(1)
C(20)	3260(2)	5072(2)	-1723(1)	41(1)
C(21)	-2386(2)	613(1)	2330(1)	19(1)
C(22)	-2278(2)	-297(1)	2965(1)	21(1)
C(23)	-3312(2)	-892(1)	3516(1)	23(1)
C(24)	-4434(2)	-533(1)	3440(1)	23(1)
C(25)	-4548(2)	396(1)	2821(1)	22(1)
C(26)	-3505(2)	973(1)	2262(1)	22(1)

C(27)	-3213(2)	-1918(2)	4164(1)	35(1)
C(28)	-5779(2)	735(2)	2743(1)	33(1)
C(29)	1491(2)	6339(1)	3329(1)	20(1)
C(30)	250(2)	5914(1)	3532(1)	21(1)
C(31)	-344(2)	5346(1)	3208(1)	24(1)
C(32)	-1581(2)	5044(2)	3605(1)	28(1)
C(33)	-2199(2)	5285(1)	4304(1)	26(1)
C(34)	-1600(2)	5842(1)	4667(1)	22(1)
C(35)	-384(2)	6158(1)	4258(1)	20(1)
C(36)	-2100(2)	6107(1)	5405(1)	25(1)
C(37)	-1405(2)	6641(2)	5693(1)	27(1)
C(38)	-181(2)	6960(1)	5273(1)	25(1)
C(39)	328(2)	6723(1)	4548(1)	21(1)
C(40)	1542(2)	6861(1)	3974(1)	20(1)
C(41)	2532(2)	5802(1)	2189(1)	21(1)
C(42)	2040(2)	6197(2)	1488(1)	26(1)
C(43)	2139(2)	5683(2)	905(1)	26(1)
C(44)	2713(2)	4777(2)	1049(1)	26(1)
C(45)	3203(2)	4380(1)	1754(1)	26(1)
C(46)	3135(2)	4917(1)	2314(1)	23(1)
C(47)	1632(3)	6097(2)	128(2)	44(1)
C(48)	3764(3)	3368(2)	1925(2)	45(1)
C(49)	2691(2)	7748(1)	4526(1)	22(1)
C(50)	2145(2)	8655(1)	4486(1)	23(1)
C(51)	2304(2)	9162(2)	5033(1)	25(1)
C(52)	2999(2)	8731(2)	5614(1)	26(1)
C(53)	3544(2)	7821(2)	5658(1)	26(1)
C(54)	3407(2)	7339(1)	5089(1)	23(1)
C(55)	1728(2)	10152(2)	4997(1)	35(1)
C(56)	4267(2)	7367(2)	6309(1)	37(1)
CI(1)	1036(1)	686(1)	2778(1)	39(1)
CI(2)	-444(1)	3284(1)	2284(1)	59(1)

Cl(3)	5017(1)	5766(1)	3622(1)	41(1)
Cl(4)	4709(1)	8399(1)	1909(1)	45(1)
N(1)	826(1)	2162(1)	703(1)	21(1)
N(2)	-1297(1)	1168(1)	1746(1)	20(1)
N(3)	2479(1)	6319(1)	2791(1)	22(1)
N(4)	2568(1)	7239(1)	3944(1)	22(1)
Zn(1)	61(1)	1885(1)	2025(1)	24(1)
Zn(2)	3965(1)	6997(1)	2985(1)	25(1)

Table 54: Bond Lengths [Å] and Bond Angles [°] for **11**.

C(1)-N(1)	1.281(2)	C(16)-C(17)	1.387(3)
C(1)-C(2)	1.474(2)	C(17)-C(18)	1.396(3)
C(1)-C(12)	1.517(2)	C(17)-C(20)	1.512(3)
C(2)-C(3)	1.383(3)	C(21)-C(26)	1.385(3)
C(2)-C(7)	1.414(3)	C(21)-C(22)	1.389(3)
C(3)-C(4)	1.420(3)	C(21)-N(2)	1.435(2)
C(4)-C(5)	1.370(3)	C(22)-C(23)	1.393(3)
C(5)-C(6)	1.424(3)	C(23)-C(24)	1.390(3)
C(6)-C(7)	1.406(3)	C(23)-C(27)	1.506(3)
C(6)-C(8)	1.420(3)	C(24)-C(25)	1.395(3)
C(7)-C(11)	1.417(3)	C(25)-C(26)	1.395(3)
C(8)-C(9)	1.373(3)	C(25)-C(28)	1.501(3)
C(9)-C(10)	1.413(3)	C(29)-N(3)	1.279(2)
C(10)-C(11)	1.379(3)	C(29)-C(30)	1.465(2)
C(11)-C(12)	1.469(2)	C(29)-C(40)	1.525(2)
C(12)-N(2)	1.281(2)	C(30)-C(31)	1.377(3)
C(13)-C(14)	1.390(3)	C(30)-C(35)	1.421(2)
C(13)-C(18)	1.390(3)	C(31)-C(32)	1.416(3)
C(13)-N(1)	1.429(2)	C(32)-C(33)	1.376(3)
C(14)-C(15)	1.390(3)	C(33)-C(34)	1.418(3)
C(15)-C(16)	1.395(3)	C(34)-C(35)	1.401(2)
C(15)-C(19)	1.505(3)	C(34)-C(36)	1.418(3)

C(35)-C(39)	1.419(2)		
C(36)-C(37)	1.377(3)	N(1)-C(1)-C(2)	135.30(17)
C(37)-C(38)	1.412(3)	N(1)-C(1)-C(12)	117.69(15)
C(38)-C(39)	1.381(2)	C(2)-C(1)-C(12)	106.98(15)
C(39)-C(40)	1.466(2)	C(3)-C(2)-C(7)	119.38(17)
C(40)-N(4)	1.279(2)	C(3)-C(2)-C(1)	135.00(18)
C(41)-C(46)	1.381(3)	C(7)-C(2)-C(1)	105.62(15)
C(41)-C(42)	1.387(3)	C(2)-C(3)-C(4)	118.10(19)
C(41)-N(3)	1.432(2)	C(5)-C(4)-C(3)	122.55(19)
C(42)-C(43)	1.394(3)	C(4)-C(5)-C(6)	120.61(18)
C(43)-C(44)	1.387(3)	C(7)-C(6)-C(8)	116.62(18)
C(43)-C(47)	1.508(3)	C(7)-C(6)-C(5)	116.29(18)
C(44)-C(45)	1.392(3)	C(8)-C(6)-C(5)	127.09(18)
C(45)-C(46)	1.389(3)	C(6)-C(7)-C(2)	123.04(17)
C(45)-C(48)	1.506(3)	C(6)-C(7)-C(11)	122.42(17)
C(49)-C(54)	1.385(3)	C(2)-C(7)-C(11)	114.53(16)
C(49)-C(50)	1.389(3)	C(9)-C(8)-C(6)	120.53(18)
C(49)-N(4)	1.435(2)	C(8)-C(9)-C(10)	122.52(19)
C(50)-C(51)	1.393(3)	C(11)-C(10)-C(9)	118.17(18)
C(51)-C(52)	1.394(3)	C(10)-C(11)-C(7)	119.70(17)
C(51)-C(55)	1.507(3)	C(10)-C(11)-C(12)	134.67(17)
C(52)-C(53)	1.391(3)	C(7)-C(11)-C(12)	105.64(16)
C(53)-C(54)	1.394(3)	N(2)-C(12)-C(11)	134.93(17)
C(53)-C(56)	1.508(3)	N(2)-C(12)-C(1)	117.88(15)
Cl(1)-Zn(1)	2.2061(6)	C(11)-C(12)-C(1)	107.18(15)
Cl(2)-Zn(1)	2.1792(6)	C(14)-C(13)-C(18)	121.20(17)
Cl(3)-Zn(2)	2.2081(6)	C(14)-C(13)-N(1)	117.47(16)
Cl(4)-Zn(2)	2.1899(6)	C(18)-C(13)-N(1)	121.33(17)
N(1)-Zn(1)	2.1160(15)	C(15)-C(14)-C(13)	119.72(18)
N(2)-Zn(1)	2.0964(15)	C(14)-C(15)-C(16)	118.64(18)
N(3)-Zn(2)	2.1086(15)	C(14)-C(15)-C(19)	120.66(19)
N(4)-Zn(2)	2.1067(15)	C(16)-C(15)-C(19)	120.69(18)

C(17)-C(16)-C(15)	122.06(18)	C(37)-C(36)-C(34)	120.58(17)
C(16)-C(17)-C(18)	118.77(18)	C(36)-C(37)-C(38)	122.47(17)
C(16)-C(17)-C(20)	120.85(19)	C(39)-C(38)-C(37)	118.28(18)
C(18)-C(17)-C(20)	120.4(2)	C(38)-C(39)-C(35)	119.26(17)
C(13)-C(18)-C(17)	119.47(18)	C(38)-C(39)-C(40)	134.73(17)
C(26)-C(21)-C(22)	121.23(16)	C(35)-C(39)-C(40)	105.88(15)
C(26)-C(21)-N(2)	121.09(16)	N(4)-C(40)-C(39)	135.10(16)
C(22)-C(21)-N(2)	117.68(16)	N(4)-C(40)-C(29)	117.85(15)
C(21)-C(22)-C(23)	119.73(17)	C(39)-C(40)-C(29)	106.86(15)
C(24)-C(23)-C(22)	118.78(17)	C(46)-C(41)-C(42)	121.22(16)
C(24)-C(23)-C(27)	120.69(18)	C(46)-C(41)-N(3)	117.35(16)
C(22)-C(23)-C(27)	120.51(18)	C(42)-C(41)-N(3)	121.37(17)
C(23)-C(24)-C(25)	121.75(17)	C(41)-C(42)-C(43)	119.50(18)
C(24)-C(25)-C(26)	118.80(17)	C(44)-C(43)-C(42)	118.97(18)
C(24)-C(25)-C(28)	119.86(17)	C(44)-C(43)-C(47)	120.04(17)
C(26)-C(25)-C(28)	121.29(17)	C(42)-C(43)-C(47)	120.99(18)
C(21)-C(26)-C(25)	119.63(17)	C(43)-C(44)-C(45)	121.50(17)
N(3)-C(29)-C(30)	135.15(16)	C(46)-C(45)-C(44)	118.99(17)
N(3)-C(29)-C(40)	117.43(16)	C(46)-C(45)-C(48)	120.23(18)
C(30)-C(29)-C(40)	107.31(14)	C(44)-C(45)-C(48)	120.75(17)
C(31)-C(30)-C(35)	119.36(17)	C(41)-C(46)-C(45)	119.72(17)
C(31)-C(30)-C(29)	134.96(17)	C(54)-C(49)-C(50)	121.61(16)
C(35)-C(30)-C(29)	105.62(15)	C(54)-C(49)-N(4)	118.51(16)
C(30)-C(31)-C(32)	118.31(17)	C(50)-C(49)-N(4)	119.81(16)
C(33)-C(32)-C(31)	122.42(18)	C(49)-C(50)-C(51)	119.42(17)
C(32)-C(33)-C(34)	120.43(18)	C(50)-C(51)-C(52)	118.63(18)
C(35)-C(34)-C(33)	116.70(17)	C(50)-C(51)-C(55)	120.40(18)
C(35)-C(34)-C(36)	116.47(17)	C(52)-C(51)-C(55)	120.98(17)
C(33)-C(34)-C(36)	126.82(18)	C(53)-C(52)-C(51)	122.14(17)
C(34)-C(35)-C(39)	122.93(16)	C(52)-C(53)-C(54)	118.59(18)
C(34)-C(35)-C(30)	122.73(16)	C(52)-C(53)-C(56)	120.57(18)
C(39)-C(35)-C(30)	114.32(16)	C(54)-C(53)-C(56)	120.85(18)



C(49)-C(54)-C(53)	119.54(17)	N(1)-Zn(1)-N(2)	80.14(6)
C(1)-N(1)-C(13)	121.40(15)	N(2)-Zn(1)-Cl(2)	114.20(5)
C(1)-N(1)-Zn(1)	111.85(12)	N(1)-Zn(1)-Cl(2)	112.27(5)
C(13)-N(1)-Zn(1)	126.75(11)	N(2)-Zn(1)-Cl(1)	108.03(4)
C(12)-N(2)-C(21)	119.86(15)	N(1)-Zn(1)-Cl(1)	108.52(4)
C(12)-N(2)-Zn(1)	112.39(12)	Cl(1)-Zn(1)-Cl(2)	124.77(3)
C(21)-N(2)-Zn(1)	127.64(11)	N(4)-Zn(2)-N(3)	80.07(6)
C(29)-N(3)-C(41)	121.46(15)	N(4)-Zn(2)-Cl(4)	113.47(5)
C(29)-N(3)-Zn(2)	112.38(12)	N(3)-Zn(2)-Cl(4)	111.65(5)
C(41)-N(3)-Zn(2)	125.95(12)	N(4)-Zn(2)-Cl(3)	108.00(5)
C(40)-N(4)-C(49)	121.28(15)	N(3)-Zn(2)-Cl(3)	108.27(5)
C(40)-N(4)-Zn(2)	112.22(12)	Cl(4)-Zn(2)-Cl(3)	125.93(3)
C(49)-N(4)-Zn(2)	126.50(12)		

---

Table 55: Crystallographic Data and Structure Refinement of **12**.

Empirical formula	$C_{30}H_{28}Cl_2N_2Zn$	
Formula weight	552.81	
Temperature	147(2) K	
Wavelength	1.54184 Å	
Crystal system	Monoclinic	
Space group	P2 <sub>1</sub>	
Unit cell dimensions	$a = 8.8029(5)$ Å	$\alpha = 90^\circ$ .
	$b = 16.3249(9)$ Å	$\beta = 99.664(5)^\circ$ .
	$c = 9.4998(5)$ Å	$\gamma = 90^\circ$ .
Volume	1345.81(13) Å <sup>3</sup>	
Z	2	
Density (calculated)	1.364 Mg/m <sup>3</sup>	
Absorption coefficient	3.244 mm <sup>-1</sup>	
F(000)	572	
Crystal size	0.09 x 0.09 x 0.03 mm <sup>3</sup>	
Theta range for data collection	4.72 to 76.29°.	
Index ranges	-10 ≤ h ≤ 11, -20 ≤ k ≤ 20, -11 ≤ l ≤ 11	
Reflections collected	7253	
Independent reflections	7253 [R(int) = 0.0000]	
Completeness to theta = 76.29°	97.6 %	
Absorption correction	Semi-empirical from equivalents	
Max. and min. transmission	1.00000 and 0.89050	
Refinement method	Full-matrix least-squares on F <sup>2</sup>	
Data / restraints / parameters	7253 / 1 / 323	
Goodness-of-fit on F <sup>2</sup>	1.030	
Final R indices [I > 2σ(I)]	R1 = 0.0311, wR2 = 0.0806	
R indices (all data)	R1 = 0.0338, wR2 = 0.0817	
Largest diff. peak and hole	0.655 and -0.394 e.Å <sup>-3</sup>	

Table 56: Atomic coordinates ( $\times 10^4$ ) and equivalent isotropic displacement parameters ( $\text{\AA}^2 \times 10^3$ ) for **12**. U(eq) is defined as one third of the trace of the orthogonalized  $U^{ij}$  tensor.

	x	y	z	U(eq)
C(1)	1913(2)	5951(1)	2791(2)	23(1)
C(2)	529(2)	5707(1)	1796(2)	25(1)
C(3)	-512(3)	5072(2)	1748(3)	32(1)
C(4)	-1733(3)	5038(2)	568(3)	39(1)
C(5)	-1922(3)	5619(2)	-501(3)	36(1)
C(6)	-890(2)	6292(2)	-458(2)	28(1)
C(7)	327(2)	6310(2)	709(2)	24(1)
C(8)	-968(3)	6945(2)	-1439(2)	34(1)
C(9)	112(3)	7556(2)	-1254(3)	37(1)
C(10)	1346(3)	7570(2)	-76(2)	32(1)
C(11)	1438(2)	6942(1)	895(2)	24(1)
C(12)	2498(2)	6742(1)	2222(2)	23(1)
C(13)	2177(2)	4896(1)	4538(2)	22(1)
C(14)	1319(2)	4954(1)	5640(2)	24(1)
C(15)	940(2)	4226(2)	6262(2)	28(1)
C(16)	1401(3)	3462(2)	5817(2)	27(1)
C(17)	2250(3)	3440(1)	4716(2)	26(1)
C(18)	2645(3)	4147(2)	4053(2)	25(1)
C(19)	804(3)	5772(2)	6129(3)	33(1)
C(20)	984(3)	2686(2)	6534(3)	38(1)
C(21)	3535(3)	4099(2)	2827(3)	38(1)
C(22)	4322(2)	7812(1)	2413(2)	23(1)
C(23)	4097(2)	8558(1)	3078(2)	23(1)
C(24)	4726(3)	9258(1)	2565(2)	26(1)
C(25)	5564(3)	9233(2)	1461(2)	27(1)
C(26)	5781(3)	8472(2)	853(2)	28(1)

C(27)	5173(3)	7754(1)	1311(2)	25(1)
C(28)	3196(3)	8596(2)	4286(3)	34(1)
C(29)	6229(3)	9996(2)	910(3)	37(1)
C(30)	5448(3)	6943(2)	633(3)	35(1)
Cl(1)	4814(1)	6836(1)	6795(1)	52(1)
Cl(2)	6727(1)	5721(1)	4087(1)	60(1)
N(1)	2666(2)	5646(1)	3937(2)	23(1)
N(2)	3694(2)	7078(1)	2925(2)	23(1)
Zn(1)	4671(1)	6332(1)	4646(1)	32(1)

Table 57: Bond Lengths [Å] and Bond Angles [°] for **12**.

C(1)-N(1)	1.277(3)	C(14)-C(19)	1.508(3)
C(1)-C(2)	1.466(3)	C(15)-C(16)	1.399(3)
C(1)-C(12)	1.523(3)	C(16)-C(17)	1.384(3)
C(2)-C(3)	1.380(3)	C(16)-C(20)	1.512(3)
C(2)-C(7)	1.416(3)	C(17)-C(18)	1.388(3)
C(3)-C(4)	1.417(3)	C(18)-C(21)	1.510(4)
C(4)-C(5)	1.379(4)	C(22)-C(27)	1.389(3)
C(5)-C(6)	1.422(4)	C(22)-C(23)	1.401(3)
C(6)-C(7)	1.407(2)	C(22)-N(2)	1.438(3)
C(6)-C(8)	1.410(4)	C(23)-C(24)	1.393(3)
C(7)-C(11)	1.413(3)	C(23)-C(28)	1.502(3)
C(8)-C(9)	1.369(4)	C(24)-C(25)	1.381(3)
C(9)-C(10)	1.423(3)	C(25)-C(26)	1.396(3)
C(10)-C(11)	1.371(3)	C(25)-C(29)	1.507(3)
C(11)-C(12)	1.473(3)	C(26)-C(27)	1.389(3)
C(12)-N(2)	1.273(3)	C(27)-C(30)	1.509(3)
C(13)-C(18)	1.393(3)	Cl(1)-Zn(1)	2.1848(7)
C(13)-C(14)	1.393(3)	Cl(2)-Zn(1)	2.2082(8)
C(13)-N(1)	1.445(3)	N(1)-Zn(1)	2.1030(17)
C(14)-C(15)	1.393(3)	N(2)-Zn(1)	2.1038(17)

		C(17)-C(16)-C(15)	118.2(2)
N(1)-C(1)-C(2)	134.5(2)	C(17)-C(16)-C(20)	121.4(2)
N(1)-C(1)-C(12)	118.38(19)	C(15)-C(16)-C(20)	120.4(2)
C(2)-C(1)-C(12)	107.16(18)	C(16)-C(17)-C(18)	122.0(2)
C(3)-C(2)-C(7)	119.8(2)	C(17)-C(18)-C(13)	118.0(2)
C(3)-C(2)-C(1)	134.5(2)	C(17)-C(18)-C(21)	120.6(2)
C(7)-C(2)-C(1)	105.71(19)	C(13)-C(18)-C(21)	121.4(2)
C(2)-C(3)-C(4)	117.9(2)	C(27)-C(22)-C(23)	122.3(2)
C(5)-C(4)-C(3)	122.5(2)	C(27)-C(22)-N(2)	119.03(19)
C(4)-C(5)-C(6)	120.9(2)	C(23)-C(22)-N(2)	118.65(19)
C(7)-C(6)-C(8)	116.8(2)	C(24)-C(23)-C(22)	117.4(2)
C(7)-C(6)-C(5)	115.9(2)	C(24)-C(23)-C(28)	121.7(2)
C(8)-C(6)-C(5)	127.2(2)	C(22)-C(23)-C(28)	120.9(2)
C(6)-C(7)-C(11)	122.2(2)	C(25)-C(24)-C(23)	122.4(2)
C(6)-C(7)-C(2)	123.1(2)	C(24)-C(25)-C(26)	117.9(2)
C(11)-C(7)-C(2)	114.66(17)	C(24)-C(25)-C(29)	121.8(2)
C(9)-C(8)-C(6)	120.7(2)	C(26)-C(25)-C(29)	120.2(2)
C(8)-C(9)-C(10)	122.3(2)	C(27)-C(26)-C(25)	122.3(2)
C(11)-C(10)-C(9)	118.0(2)	C(22)-C(27)-C(26)	117.6(2)
C(10)-C(11)-C(7)	119.99(19)	C(22)-C(27)-C(30)	121.8(2)
C(10)-C(11)-C(12)	134.3(2)	C(26)-C(27)-C(30)	120.6(2)
C(7)-C(11)-C(12)	105.66(19)	C(1)-N(1)-C(13)	121.37(18)
N(2)-C(12)-C(11)	134.6(2)	C(1)-N(1)-Zn(1)	110.68(15)
N(2)-C(12)-C(1)	118.61(18)	C(13)-N(1)-Zn(1)	127.83(13)
C(11)-C(12)-C(1)	106.80(18)	C(12)-N(2)-C(22)	120.86(18)
C(18)-C(13)-C(14)	122.4(2)	C(12)-N(2)-Zn(1)	110.60(15)
C(18)-C(13)-N(1)	119.19(19)	C(22)-N(2)-Zn(1)	127.99(13)
C(14)-C(13)-N(1)	118.33(19)	N(1)-Zn(1)-N(2)	81.26(7)
C(13)-C(14)-C(15)	117.4(2)	N(1)-Zn(1)-Cl(1)	114.46(5)
C(13)-C(14)-C(19)	121.3(2)	N(2)-Zn(1)-Cl(1)	117.36(6)
C(15)-C(14)-C(19)	121.3(2)	N(1)-Zn(1)-Cl(2)	111.12(6)
C(14)-C(15)-C(16)	122.0(2)	N(2)-Zn(1)-Cl(2)	108.61(6)

Cl(1)-Zn(1)-Cl(2)      118.28(3)

---

Table 58: Crystallographic Data and Structure Refinement of **13**.

Empirical formula	C <sub>26</sub> H <sub>20</sub> Cl <sub>2</sub> N <sub>2</sub> Zn	
Formula weight	496.71	
Temperature	147(2) K	
Wavelength	0.71075 Å	
Crystal system	Orthorhombic	
Space group	P2 <sub>1</sub> 2 <sub>1</sub> 2 <sub>1</sub>	
Unit cell dimensions	a = 11.5832(3) Å	α = 90°.
	b = 11.9827(4) Å	β = 90°.
	c = 16.3451(5) Å	γ = 90°.
Volume	2268.67(12) Å <sup>3</sup>	
Z	4	
Density (calculated)	1.454 Mg/m <sup>3</sup>	
Absorption coefficient	1.334 mm <sup>-1</sup>	
F(000)	1016	
Crystal size	0.44 x 0.28 x 0.07 mm <sup>3</sup>	
Theta range for data collection	2.11 to 26.64°.	
Index ranges	-14 ≤ h ≤ 14, -11 ≤ k ≤ 14, -20 ≤ l ≤ 20	
Reflections collected	12178	
Independent reflections	4373 [R(int) = 0.0315]	
Completeness to theta = 26.64°	97.0 %	
Absorption correction	Semi-empirical from equivalents	
Max. and min. transmission	1.00000 and 0.40095	
Refinement method	Full-matrix least-squares on F <sup>2</sup>	
Data / restraints / parameters	4373 / 396 / 415	
Goodness-of-fit on F <sup>2</sup>	1.078	
Final R indices [I > 2σ(I)]	R1 = 0.0499, wR2 = 0.1345	
R indices (all data)	R1 = 0.0568, wR2 = 0.1428	
Largest diff. peak and hole	0.448 and -0.565 e.Å <sup>-3</sup>	

Table 59: Atomic coordinates ( $\times 10^4$ ) and equivalent isotropic displacement parameters ( $\text{\AA}^2 \times 10^3$ ) for **13**.  $U(\text{eq})$  is defined as one third of the trace of the orthogonalized  $U^{\text{ij}}$  tensor.

	x	y	z	U(eq)
C(1)	1795(3)	2502(4)	6439(2)	39(1)
C(2)	1536(4)	1360(4)	6193(3)	43(1)
C(3)	1035(5)	879(5)	5507(3)	54(1)
C(4)	989(5)	-292(5)	5466(3)	65(1)
C(5)	1379(5)	-960(5)	6093(4)	69(2)
C(6)	1873(4)	-500(4)	6797(3)	56(1)
C(7)	1939(3)	661(3)	6828(3)	45(1)
C(8)	2351(5)	-1082(4)	7472(4)	72(2)
C(9)	2840(6)	-521(5)	8113(4)	81(2)
C(10)	2908(4)	665(4)	8137(3)	59(1)
C(11)	2446(4)	1248(3)	7490(3)	44(1)
C(12)	2376(4)	2433(3)	7276(2)	41(1)
C(13)	1091(17)	3620(20)	5337(7)	49(2)
C(14)	1702(9)	3603(11)	4615(7)	50(2)
C(15)	1113(11)	3758(9)	3871(6)	52(2)
C(16)	-52(9)	4012(10)	3892(6)	62(2)
C(17)	-682(10)	4077(11)	4637(6)	69(2)
C(18)	-70(11)	3887(14)	5372(7)	59(2)
C(19)	2951(9)	3436(11)	4649(6)	61(2)
C(13A)	1306(18)	3520(30)	5284(8)	50(3)
C(14A)	163(12)	3760(16)	5125(7)	57(2)
C(15A)	-193(11)	3905(12)	4308(7)	61(2)
C(16A)	603(11)	3763(11)	3686(6)	56(2)
C(17A)	1782(11)	3526(10)	3850(6)	53(2)
C(18A)	2124(12)	3407(13)	4672(7)	50(2)
C(19A)	-631(10)	3892(14)	5824(7)	81(3)



C(20)	3404(7)	3303(10)	8355(4)	40(2)
C(21)	2822(7)	3517(9)	9092(6)	48(2)
C(22)	3486(9)	3499(7)	9813(5)	52(2)
C(23)	4634(7)	3312(7)	9790(5)	56(2)
C(24)	5191(8)	3095(8)	9046(5)	57(2)
C(25)	4576(7)	3104(9)	8323(5)	51(2)
C(26)	1575(7)	3704(9)	9094(5)	66(2)
C(20A)	3059(12)	3330(20)	8460(9)	44(3)
C(21A)	4248(14)	3152(19)	8545(9)	52(3)
C(22A)	4728(13)	3199(16)	9333(9)	57(2)
C(23A)	4051(15)	3404(15)	9986(8)	55(3)
C(24A)	2863(15)	3575(14)	9889(9)	56(3)
C(25A)	2360(14)	3549(19)	9124(10)	50(3)
C(26A)	4964(13)	2962(18)	7822(10)	70(4)
Cl(1)	4055(1)	5281(2)	6420(1)	80(1)
Cl(2)	1033(1)	5935(1)	7245(1)	65(1)
N(1)	1683(3)	3451(3)	6115(2)	43(1)
N(2)	2691(3)	3340(3)	7620(2)	44(1)
Zn(1)	2365(1)	4720(1)	6867(1)	58(1)

Table 60: Bond Lengths [ $\text{\AA}$ ] and Bond Angles [ $^\circ$ ] for **13**.

C(1)-N(1)	1.261(6)	C(8)-C(9)	1.368(8)
C(1)-C(2)	1.456(6)	C(9)-C(10)	1.424(7)
C(1)-C(12)	1.527(5)	C(10)-C(11)	1.376(6)
C(2)-C(3)	1.389(6)	C(11)-C(12)	1.464(6)
C(2)-C(7)	1.413(7)	C(12)-N(2)	1.277(5)
C(3)-C(4)	1.405(8)	C(13)-C(14)	1.377(17)
C(4)-C(5)	1.377(8)	C(13)-C(18)	1.384(19)
C(5)-C(6)	1.398(7)	C(13)-N(1)	1.459(10)
C(6)-C(7)	1.395(6)	C(14)-C(15)	1.407(12)
C(6)-C(8)	1.418(8)	C(14)-C(19)	1.461(12)
C(7)-C(11)	1.418(6)	C(15)-C(16)	1.383(13)

C(16)-C(17)	1.422(12)	N(1)-C(1)-C(12)	118.0(4)
C(17)-C(18)	1.412(13)	C(2)-C(1)-C(12)	106.7(4)
C(13A)-C(14A)	1.379(17)	C(3)-C(2)-C(7)	119.0(4)
C(13A)-C(18A)	1.38(2)	C(3)-C(2)-C(1)	134.3(5)
C(13A)-N(1)	1.429(11)	C(7)-C(2)-C(1)	106.6(4)
C(14A)-C(15A)	1.409(13)	C(2)-C(3)-C(4)	117.9(5)
C(14A)-C(19A)	1.475(13)	C(5)-C(4)-C(3)	122.2(5)
C(15A)-C(16A)	1.383(13)	C(4)-C(5)-C(6)	121.1(5)
C(16A)-C(17A)	1.421(13)	C(7)-C(6)-C(5)	116.5(5)
C(17A)-C(18A)	1.408(13)	C(7)-C(6)-C(8)	116.2(5)
C(20)-C(25)	1.379(11)	C(5)-C(6)-C(8)	127.3(5)
C(20)-C(21)	1.404(10)	C(6)-C(7)-C(2)	123.2(5)
C(20)-N(2)	1.460(8)	C(6)-C(7)-C(11)	123.0(5)
C(21)-C(22)	1.407(11)	C(2)-C(7)-C(11)	113.8(4)
C(21)-C(26)	1.462(11)	C(9)-C(8)-C(6)	121.1(5)
C(22)-C(23)	1.349(12)	C(8)-C(9)-C(10)	122.3(5)
C(23)-C(24)	1.401(11)	C(11)-C(10)-C(9)	117.7(5)
C(24)-C(25)	1.379(11)	C(10)-C(11)-C(7)	119.7(4)
C(20A)-C(25A)	1.379(13)	C(10)-C(11)-C(12)	134.3(4)
C(20A)-C(21A)	1.401(13)	C(7)-C(11)-C(12)	106.0(4)
C(20A)-N(2)	1.438(15)	N(2)-C(12)-C(11)	134.8(4)
C(21A)-C(22A)	1.404(13)	N(2)-C(12)-C(1)	118.3(4)
C(21A)-C(26A)	1.462(13)	C(11)-C(12)-C(1)	106.9(3)
C(22A)-C(23A)	1.346(13)	C(14)-C(13)-C(18)	122.6(9)
C(23A)-C(24A)	1.401(13)	C(14)-C(13)-N(1)	120.2(13)
C(24A)-C(25A)	1.380(13)	C(18)-C(13)-N(1)	117.0(13)
Cl(1)-Zn(1)	2.1952(15)	C(13)-C(14)-C(15)	119.3(10)
Cl(2)-Zn(1)	2.2082(16)	C(13)-C(14)-C(19)	118.6(10)
N(1)-Zn(1)	2.110(3)	C(15)-C(14)-C(19)	122.1(11)
N(2)-Zn(1)	2.095(3)	C(16)-C(15)-C(14)	118.7(10)
		C(15)-C(16)-C(17)	122.3(9)
N(1)-C(1)-C(2)	135.2(4)	C(18)-C(17)-C(16)	117.5(10)

C(13)-C(18)-C(17)	119.3(10)	C(20A)-C(21A)-C(22A)	118.3(11)
C(14A)-C(13A)-C(18A)	122.8(9)	C(20A)-C(21A)-C(26A)	120.1(12)
C(14A)-C(13A)-N(1)	119.0(14)	C(22A)-C(21A)-C(26A)	121.6(13)
C(18A)-C(13A)-N(1)	118.1(14)	C(23A)-C(22A)-C(21A)	120.3(12)
C(13A)-C(14A)-C(15A)	119.0(10)	C(22A)-C(23A)-C(24A)	120.6(11)
C(13A)-C(14A)-C(19A)	118.3(11)	C(25A)-C(24A)-C(23A)	120.9(12)
C(15A)-C(14A)-C(19A)	122.6(12)	C(20A)-C(25A)-C(24A)	118.0(12)
C(16A)-C(15A)-C(14A)	119.1(11)	C(1)-N(1)-C(13A)	118.8(14)
C(15A)-C(16A)-C(17A)	121.8(9)	C(1)-N(1)-C(13)	122.6(12)
C(18A)-C(17A)-C(16A)	118.1(10)	C(1)-N(1)-Zn(1)	111.6(3)
C(13A)-C(18A)-C(17A)	119.2(11)	C(13A)-N(1)-Zn(1)	128.8(14)
C(25)-C(20)-C(21)	122.5(6)	C(13)-N(1)-Zn(1)	125.7(12)
C(25)-C(20)-N(2)	122.1(6)	C(12)-N(2)-C(20A)	120.0(12)
C(21)-C(20)-N(2)	115.4(6)	C(12)-N(2)-C(20)	119.8(6)
C(20)-C(21)-C(22)	117.0(7)	C(12)-N(2)-Zn(1)	111.3(3)
C(20)-C(21)-C(26)	120.3(7)	C(20A)-N(2)-Zn(1)	128.2(12)
C(22)-C(21)-C(26)	122.7(8)	C(20)-N(2)-Zn(1)	127.6(5)
C(23)-C(22)-C(21)	121.2(8)	N(1)-Zn(1)-N(2)	80.80(14)
C(22)-C(23)-C(24)	120.6(7)	N(2)-Zn(1)-Cl(1)	106.04(12)
C(25)-C(24)-C(23)	120.3(8)	N(1)-Zn(1)-Cl(1)	111.11(11)
C(20)-C(25)-C(24)	118.5(8)	N(2)-Zn(1)-Cl(2)	118.82(11)
C(25A)-C(20A)-C(21A)	121.9(11)	N(1)-Zn(1)-Cl(2)	112.12(12)
C(25A)-C(20A)-N(2)	125.2(11)	Cl(1)-Zn(1)-Cl(2)	120.97(7)
C(21A)-C(20A)-N(2)	112.8(10)		

---

Table 61: Crystallographic Data and Structure Refinement of **10-CHCl<sub>3</sub>**.

Empirical formula	C <sub>28</sub> H <sub>22</sub> Cl <sub>8</sub> N <sub>2</sub> Zn	
Formula weight	735.45	
Temperature	133(2) K	
Wavelength	1.54184 Å	
Crystal system	Monoclinic	
Space group	P2 <sub>1</sub> /c	
Unit cell dimensions	a = 11.80690(10) Å	α = 90°.
	b = 23.7064(3) Å	β = 98.4180(10)°.
	c = 11.05040(10) Å	γ = 90°.
Volume	3059.67(5) Å <sup>3</sup>	
Z	4	
Density (calculated)	1.597 Mg/m <sup>3</sup>	
Absorption coefficient	7.725 mm <sup>-1</sup>	
F(000)	1480	
Crystal size	0.34 x 0.21 x 0.20 mm <sup>3</sup>	
Theta range for data collection	3.73 to 74.16°.	
Index ranges	-11<=h<=14, -27<=k<=29, -13<=l<=9	
Reflections collected	12057	
Independent reflections	6064 [R(int) = 0.0307]	
Completeness to theta = 74.16°	97.2 %	
Absorption correction	Semi-empirical from equivalents	
Max. and min. transmission	1.00000 and 0.72643	
Refinement method	Full-matrix least-squares on F <sup>2</sup>	
Data / restraints / parameters	6064 / 0 / 354	
Goodness-of-fit on F <sup>2</sup>	1.069	
Final R indices [I>2sigma(I)]	R1 = 0.0330, wR2 = 0.0894	
R indices (all data)	R1 = 0.0355, wR2 = 0.0931	
Largest diff. peak and hole	0.490 and -0.587 e.Å <sup>-3</sup>	

Table 62: Atomic coordinates ( $\times 10^4$ ) and equivalent isotropic displacement parameters ( $\text{\AA}^2 \times 10^3$ ) for **10-CHCl<sub>3</sub>**. U(eq) is defined as one third of the trace of the orthogonalized  $U^{ij}$  tensor.

	x	y	z	U(eq)
C(1)	2314(2)	4857(1)	4292(2)	12(1)
C(2)	1499(2)	4402(1)	4437(2)	13(1)
C(3)	1021(2)	3960(1)	3719(2)	16(1)
C(4)	155(2)	3629(1)	4135(2)	19(1)
C(5)	-227(2)	3733(1)	5230(2)	19(1)
C(6)	233(2)	4185(1)	5986(2)	14(1)
C(7)	1101(2)	4507(1)	5562(2)	11(1)
C(8)	-119(2)	4359(1)	7104(2)	18(1)
C(9)	361(2)	4828(1)	7707(2)	18(1)
C(10)	1220(2)	5152(1)	7268(2)	14(1)
C(11)	1604(2)	4986(1)	6201(2)	12(1)
C(12)	2401(2)	5221(1)	5434(2)	11(1)
C(13)	2917(2)	4716(1)	2347(2)	13(1)
C(14)	2749(2)	5014(1)	1248(2)	17(1)
C(15)	2788(2)	4727(1)	160(2)	20(1)
C(16)	3006(2)	4150(1)	141(2)	18(1)
C(17)	3221(2)	3867(1)	1253(2)	19(1)
C(18)	3181(2)	4144(1)	2354(2)	16(1)
C(19)	3028(2)	3850(1)	-1060(2)	28(1)
C(20)	3289(2)	5978(1)	6607(2)	12(1)
C(21)	3135(2)	6560(1)	6548(2)	16(1)
C(22)	3349(2)	6876(1)	7614(2)	18(1)
C(23)	3743(2)	6624(1)	8738(2)	19(1)
C(24)	3933(2)	6043(1)	8764(2)	20(1)
C(25)	3710(2)	5719(1)	7709(2)	17(1)
C(26)	4001(2)	6974(1)	9889(2)	27(1)

C(27)	811(2)	6754(1)	271(2)	24(1)
C(28)	3097(2)	2996(1)	6143(2)	19(1)
Cl(1)	5577(1)	5707(1)	3898(1)	22(1)
Cl(2)	2781(1)	6509(1)	2926(1)	18(1)
Cl(3)	359(1)	6097(1)	-376(1)	50(1)
Cl(4)	-164(1)	6995(1)	1206(1)	36(1)
Cl(5)	970(1)	7244(1)	-884(1)	36(1)
Cl(6)	3144(1)	2852(1)	4587(1)	31(1)
Cl(7)	4314(1)	2722(1)	7058(1)	28(1)
Cl(8)	1848(1)	2706(1)	6587(1)	32(1)
N(1)	2869(1)	5025(1)	3440(2)	12(1)
N(2)	3065(1)	5650(1)	5511(2)	11(1)
Zn(1)	3723(1)	5784(1)	3888(1)	11(1)

Table 63: Bond Lengths [ $\text{\AA}$ ] and Bond Angles [ $^\circ$ ] for **10-CHCl<sub>3</sub>**.

C(1)-N(1)	1.287(3)	C(13)-C(14)	1.394(3)
C(1)-C(2)	1.470(3)	C(13)-N(1)	1.422(3)
C(1)-C(12)	1.521(3)	C(14)-C(15)	1.388(3)
C(2)-C(3)	1.383(3)	C(15)-C(16)	1.392(3)
C(2)-C(7)	1.414(3)	C(16)-C(17)	1.390(3)
C(3)-C(4)	1.418(3)	C(16)-C(19)	1.509(3)
C(4)-C(5)	1.374(3)	C(17)-C(18)	1.389(3)
C(5)-C(6)	1.416(3)	C(20)-C(25)	1.390(3)
C(6)-C(7)	1.412(3)	C(20)-C(21)	1.392(3)
C(6)-C(8)	1.421(3)	C(20)-N(2)	1.431(2)
C(7)-C(11)	1.419(3)	C(21)-C(22)	1.387(3)
C(8)-C(9)	1.375(3)	C(22)-C(23)	1.396(3)
C(9)-C(10)	1.414(3)	C(23)-C(24)	1.393(3)
C(10)-C(11)	1.381(3)	C(23)-C(26)	1.512(3)
C(11)-C(12)	1.466(3)	C(24)-C(25)	1.389(3)
C(12)-N(2)	1.279(3)	C(27)-Cl(4)	1.753(2)
C(13)-C(18)	1.391(3)	C(27)-Cl(5)	1.756(3)

C(27)-Cl(3)	1.763(3)	C(11)-C(12)-C(1)	106.98(16)
C(28)-Cl(7)	1.755(2)	C(18)-C(13)-C(14)	120.17(19)
C(28)-Cl(8)	1.760(2)	C(18)-C(13)-N(1)	122.38(18)
C(28)-Cl(6)	1.761(2)	C(14)-C(13)-N(1)	117.36(18)
Cl(1)-Zn(1)	2.1961(5)	C(15)-C(14)-C(13)	119.1(2)
Cl(2)-Zn(1)	2.2292(5)	C(14)-C(15)-C(16)	121.6(2)
N(1)-Zn(1)	2.0858(16)	C(17)-C(16)-C(15)	118.1(2)
N(2)-Zn(1)	2.0805(17)	C(17)-C(16)-C(19)	121.7(2)
		C(15)-C(16)-C(19)	120.2(2)
N(1)-C(1)-C(2)	136.00(19)	C(18)-C(17)-C(16)	121.4(2)
N(1)-C(1)-C(12)	116.81(17)	C(17)-C(18)-C(13)	119.5(2)
C(2)-C(1)-C(12)	106.99(17)	C(25)-C(20)-C(21)	120.46(19)
C(3)-C(2)-C(7)	118.57(19)	C(25)-C(20)-N(2)	119.96(18)
C(3)-C(2)-C(1)	135.4(2)	C(21)-C(20)-N(2)	119.50(18)
C(7)-C(2)-C(1)	105.83(17)	C(22)-C(21)-C(20)	119.3(2)
C(2)-C(3)-C(4)	119.1(2)	C(21)-C(22)-C(23)	121.3(2)
C(5)-C(4)-C(3)	122.0(2)	C(24)-C(23)-C(22)	118.26(19)
C(4)-C(5)-C(6)	120.6(2)	C(24)-C(23)-C(26)	120.9(2)
C(7)-C(6)-C(5)	116.6(2)	C(22)-C(23)-C(26)	120.8(2)
C(7)-C(6)-C(8)	116.69(19)	C(25)-C(24)-C(23)	121.3(2)
C(5)-C(6)-C(8)	126.7(2)	C(24)-C(25)-C(20)	119.4(2)
C(6)-C(7)-C(2)	123.10(19)	Cl(4)-C(27)-Cl(5)	111.18(13)
C(6)-C(7)-C(11)	122.59(19)	Cl(4)-C(27)-Cl(3)	109.95(14)
C(2)-C(7)-C(11)	114.23(18)	Cl(5)-C(27)-Cl(3)	110.36(13)
C(9)-C(8)-C(6)	120.3(2)	Cl(7)-C(28)-Cl(8)	110.09(12)
C(8)-C(9)-C(10)	122.6(2)	Cl(7)-C(28)-Cl(6)	110.54(13)
C(11)-C(10)-C(9)	118.59(19)	Cl(8)-C(28)-Cl(6)	110.08(12)
C(10)-C(11)-C(7)	119.21(18)	C(1)-N(1)-C(13)	123.30(17)
C(10)-C(11)-C(12)	134.64(19)	C(1)-N(1)-Zn(1)	111.98(13)
C(7)-C(11)-C(12)	105.91(17)	C(13)-N(1)-Zn(1)	124.69(13)
N(2)-C(12)-C(11)	134.72(19)	C(12)-N(2)-C(20)	121.59(17)
N(2)-C(12)-C(1)	118.23(18)	C(12)-N(2)-Zn(1)	111.50(13)

C(20)-N(2)-Zn(1)	126.92(13)	N(2)-Zn(1)-Cl(2)	107.81(5)
N(1)-Zn(1)-N(2)	81.07(7)	N(1)-Zn(1)-Cl(2)	111.19(5)
N(2)-Zn(1)-Cl(1)	118.73(5)	Cl(1)-Zn(1)-Cl(2)	119.60(2)
N(1)-Zn(1)-Cl(1)	112.07(5)		

---



Table 64: Crystallographic Data and Structure Refinement of **10-THF**.

Empirical formula	C <sub>30</sub> H <sub>28</sub> Cl <sub>2</sub> N <sub>2</sub> OZn	
Formula weight	568.81	
Temperature	133(2) K	
Wavelength	1.54184 Å	
Crystal system	Monoclinic	
Space group	C2/c	
Unit cell dimensions	a = 16.9142(9) Å	α = 90°.
	b = 15.5131(7) Å	β = 110.811(6)°.
	c = 21.6462(12) Å	γ = 90°.
Volume	5309.2(5) Å <sup>3</sup>	
Z	8	
Density (calculated)	1.423 Mg/m <sup>3</sup>	
Absorption coefficient	3.335 mm <sup>-1</sup>	
F(000)	2352	
Crystal size	0.49 x 0.18 x 0.17 mm <sup>3</sup>	
Theta range for data collection	3.99 to 74.07°.	
Index ranges	-19<=h<=20, -14<=k<=19, -23<=l<=26	
Reflections collected	9926	
Independent reflections	5252 [R(int) = 0.0300]	
Completeness to theta = 74.07°	97.2 %	
Absorption correction	Semi-empirical from equivalents	
Max. and min. transmission	1.00000 and 0.63989	
Refinement method	Full-matrix least-squares on F <sup>2</sup>	
Data / restraints / parameters	5252 / 214 / 374	
Goodness-of-fit on F <sup>2</sup>	1.000	
Final R indices [I>2sigma(I)]	R1 = 0.0381, wR2 = 0.1047	
R indices (all data)	R1 = 0.0409, wR2 = 0.1075	
Largest diff. peak and hole	0.646 and -0.704 e.Å <sup>-3</sup>	

Table 65: Atomic coordinates ( $\times 10^4$ ) and equivalent isotropic displacement parameters ( $\text{\AA}^2 \times 10^3$ ) for **10-THF**.  $U(\text{eq})$  is defined as one third of the trace of the orthogonalized  $U^{ij}$  tensor.

	x	y	z	U(eq)
C(1)	6111(1)	3370(1)	5079(1)	17(1)
C(2)	6850(1)	3019(1)	5608(1)	18(1)
C(3)	6979(1)	2412(1)	6100(1)	21(1)
C(4)	7819(1)	2218(1)	6514(1)	24(1)
C(5)	8509(1)	2592(1)	6433(1)	23(1)
C(6)	8403(1)	3194(1)	5915(1)	21(1)
C(7)	7565(1)	3400(1)	5520(1)	17(1)
C(8)	9049(1)	3582(1)	5738(1)	25(1)
C(9)	8852(1)	4117(1)	5198(1)	26(1)
C(10)	8008(1)	4326(1)	4806(1)	22(1)
C(11)	7365(1)	3977(1)	4977(1)	18(1)
C(12)	6439(1)	3991(1)	4684(1)	18(1)
C(13)	4901(1)	2727(1)	5210(1)	19(1)
C(14)	4279(1)	2153(1)	4840(1)	26(1)
C(15)	3877(2)	1630(2)	5153(1)	33(1)
C(16)	4063(2)	1678(2)	5833(1)	35(1)
C(17)	4663(2)	2277(2)	6191(1)	31(1)
C(18)	5078(1)	2806(1)	5888(1)	24(1)
C(19)	3612(2)	1106(2)	6169(2)	55(1)
C(20)	6163(1)	5015(1)	3826(1)	20(1)
C(21)	5967(1)	4906(2)	3149(1)	28(1)
C(22)	6196(2)	5547(2)	2796(1)	35(1)
C(23)	6603(1)	6289(2)	3096(1)	30(1)
C(24)	6793(1)	6384(1)	3775(1)	28(1)
C(25)	6570(1)	5755(1)	4138(1)	25(1)
C(26)	6822(2)	6999(2)	2703(2)	45(1)

O(1)	1333(5)	4151(4)	1980(4)	76(2)
C(27)	2066(7)	4543(9)	2442(6)	48(2)
C(28)	1720(19)	5349(15)	2638(9)	54(2)
C(29)	822(7)	4826(6)	1598(5)	75(2)
C(30)	1095(7)	5677(5)	2000(5)	67(2)
O(1A)	1604(2)	4498(3)	1652(2)	54(1)
C(27A)	1947(7)	4460(7)	2352(4)	61(2)
C(28A)	1717(11)	5302(9)	2591(5)	49(2)
C(29A)	1000(5)	5167(5)	1453(3)	70(2)
C(30A)	843(5)	5456(5)	2096(4)	71(2)
Cl(1)	3758(1)	4909(1)	4069(1)	31(1)
Cl(2)	4243(1)	3051(1)	3155(1)	29(1)
N(1)	5305(1)	3251(1)	4874(1)	17(1)
N(2)	5903(1)	4372(1)	4185(1)	19(1)
Zn(1)	4676(1)	3941(1)	4010(1)	18(1)

Table 66: Bond Lengths [ $\text{\AA}$ ] and Bond Angles [ $^\circ$ ] for **10-THF**.

C(1)-N(1)	1.288(2)	C(12)-N(2)	1.281(3)
C(1)-C(2)	1.468(3)	C(13)-C(14)	1.394(3)
C(1)-C(12)	1.517(3)	C(13)-C(18)	1.394(3)
C(2)-C(3)	1.380(3)	C(13)-N(1)	1.419(3)
C(2)-C(7)	1.419(3)	C(14)-C(15)	1.382(3)
C(3)-C(4)	1.416(3)	C(15)-C(16)	1.394(4)
C(4)-C(5)	1.370(3)	C(16)-C(17)	1.391(4)
C(5)-C(6)	1.421(3)	C(16)-C(19)	1.515(3)
C(6)-C(7)	1.407(3)	C(17)-C(18)	1.386(3)
C(6)-C(8)	1.414(3)	C(20)-C(25)	1.386(3)
C(7)-C(11)	1.419(3)	C(20)-C(21)	1.393(3)
C(8)-C(9)	1.375(3)	C(20)-N(2)	1.427(3)
C(9)-C(10)	1.415(3)	C(21)-C(22)	1.391(3)
C(10)-C(11)	1.377(3)	C(22)-C(23)	1.379(4)
C(11)-C(12)	1.467(3)	C(23)-C(24)	1.396(3)

C(23)-C(26)	1.516(3)	C(9)-C(8)-C(6)	120.67(19)
C(24)-C(25)	1.386(3)	C(8)-C(9)-C(10)	122.4(2)
O(1)-C(29)	1.421(9)	C(11)-C(10)-C(9)	118.2(2)
O(1)-C(27)	1.423(10)	C(10)-C(11)-C(7)	119.45(18)
C(27)-C(28)	1.504(8)	C(10)-C(11)-C(12)	134.60(19)
C(28)-C(30)	1.498(11)	C(7)-C(11)-C(12)	105.68(17)
C(29)-C(30)	1.559(9)	N(2)-C(12)-C(11)	134.18(18)
O(1A)-C(29A)	1.412(7)	N(2)-C(12)-C(1)	118.53(17)
O(1A)-C(27A)	1.418(9)	C(11)-C(12)-C(1)	107.24(16)
C(27A)-C(28A)	1.505(6)	C(14)-C(13)-C(18)	119.86(19)
C(28A)-C(30A)	1.503(10)	C(14)-C(13)-N(1)	118.21(18)
C(29A)-C(30A)	1.571(7)	C(18)-C(13)-N(1)	121.84(18)
Cl(1)-Zn(1)	2.1961(5)	C(15)-C(14)-C(13)	119.7(2)
Cl(2)-Zn(1)	2.2150(6)	C(14)-C(15)-C(16)	121.4(2)
N(1)-Zn(1)	2.0891(16)	C(17)-C(16)-C(15)	118.0(2)
N(2)-Zn(1)	2.0827(16)	C(17)-C(16)-C(19)	121.1(2)
		C(15)-C(16)-C(19)	120.8(2)
N(1)-C(1)-C(2)	135.99(19)	C(18)-C(17)-C(16)	121.6(2)
N(1)-C(1)-C(12)	116.81(17)	C(17)-C(18)-C(13)	119.3(2)
C(2)-C(1)-C(12)	107.13(16)	C(25)-C(20)-C(21)	120.33(19)
C(3)-C(2)-C(7)	118.66(18)	C(25)-C(20)-N(2)	120.61(18)
C(3)-C(2)-C(1)	135.49(18)	C(21)-C(20)-N(2)	119.00(18)
C(7)-C(2)-C(1)	105.70(17)	C(22)-C(21)-C(20)	118.9(2)
C(2)-C(3)-C(4)	118.79(19)	C(23)-C(22)-C(21)	121.8(2)
C(5)-C(4)-C(3)	122.52(19)	C(22)-C(23)-C(24)	118.3(2)
C(4)-C(5)-C(6)	120.32(18)	C(22)-C(23)-C(26)	121.5(2)
C(7)-C(6)-C(8)	116.52(19)	C(24)-C(23)-C(26)	120.2(2)
C(7)-C(6)-C(5)	116.56(19)	C(25)-C(24)-C(23)	121.0(2)
C(8)-C(6)-C(5)	126.88(18)	C(20)-C(25)-C(24)	119.7(2)
C(6)-C(7)-C(11)	122.62(18)	C(29)-O(1)-C(27)	107.0(7)
C(6)-C(7)-C(2)	123.07(18)	O(1)-C(27)-C(28)	103.0(10)
C(11)-C(7)-C(2)	114.24(17)	C(30)-C(28)-C(27)	103.9(9)

O(1)-C(29)-C(30)	107.5(6)	C(12)-N(2)-C(20)	121.38(16)
C(28)-C(30)-C(29)	101.5(8)	C(12)-N(2)-Zn(1)	111.44(13)
C(29A)-O(1A)-C(27A)	109.5(5)	C(20)-N(2)-Zn(1)	127.17(12)
O(1A)-C(27A)-C(28A)	105.9(7)	N(1)-Zn(1)-N(2)	81.01(6)
C(30A)-C(28A)-C(27A)	101.7(6)	N(2)-Zn(1)-Cl(1)	116.72(5)
O(1A)-C(29A)-C(30A)	105.7(5)	N(1)-Zn(1)-Cl(1)	116.33(5)
C(28A)-C(30A)-C(29A)	98.9(8)	N(2)-Zn(1)-Cl(2)	111.41(5)
C(1)-N(1)-C(13)	123.32(17)	N(1)-Zn(1)-Cl(2)	109.91(5)
C(1)-N(1)-Zn(1)	112.01(13)	Cl(1)-Zn(1)-Cl(2)	116.37(2)
C(13)-N(1)-Zn(1)	124.65(12)		

---

Table 67: Crystallographic Data and Structure Refinement of **10-DCM**.

Empirical formula	$C_{27}H_{22}Cl_4N_2Zn$	
Formula weight	581.64	
Temperature	133(2) K	
Wavelength	1.54184 Å	
Crystal system	Monoclinic	
Space group	$P2_1/c$	
Unit cell dimensions	$a = 12.8103(2)$ Å	$\alpha = 90^\circ$ .
	$b = 11.8043(2)$ Å	$\beta = 105.731(2)^\circ$ .
	$c = 17.9425(4)$ Å	$\gamma = 90^\circ$ .
Volume	$2611.58(8)$ Å <sup>3</sup>	
Z	4	
Density (calculated)	$1.479$ Mg/m <sup>3</sup>	
Absorption coefficient	$5.213$ mm <sup>-1</sup>	
F(000)	1184	
Crystal size	$0.38 \times 0.36 \times 0.16$ mm <sup>3</sup>	
Theta range for data collection	3.58 to 74.22°.	
Index ranges	$-14 \leq h \leq 15$ , $-14 \leq k \leq 8$ , $-22 \leq l \leq 18$	
Reflections collected	9963	
Independent reflections	5173 [R(int) = 0.0229]	
Completeness to theta = 74.22°	97.3 %	
Absorption correction	Semi-empirical from equivalents	
Max. and min. transmission	1.00000 and 0.57328	
Refinement method	Full-matrix least-squares on F <sup>2</sup>	
Data / restraints / parameters	5173 / 75 / 338	
Goodness-of-fit on F <sup>2</sup>	1.000	
Final R indices [I > 2sigma(I)]	R1 = 0.0407, wR2 = 0.1108	
R indices (all data)	R1 = 0.0441, wR2 = 0.1144	
Largest diff. peak and hole	0.576 and -0.750 e.Å <sup>-3</sup>	

Table 68: Atomic coordinates ( $\times 10^4$ ) and equivalent isotropic displacement parameters ( $\text{\AA}^2 \times 10^3$ ) for **10-DCM**.  $U(\text{eq})$  is defined as one third of the trace of the orthogonalized  $U^{ij}$  tensor.

	x	y	z	U(eq)
C(1)	-327(2)	7626(2)	5228(2)	23(1)
C(2)	-1102(2)	8473(2)	4806(2)	23(1)
C(3)	-2086(2)	8874(2)	4865(2)	28(1)
C(4)	-2586(2)	9769(2)	4370(2)	31(1)
C(5)	-2113(2)	10256(2)	3842(2)	29(1)
C(6)	-1092(2)	9865(2)	3775(2)	25(1)
C(7)	-614(2)	8969(2)	4267(2)	22(1)
C(8)	-509(2)	10287(2)	3268(2)	28(1)
C(9)	483(2)	9832(2)	3271(2)	28(1)
C(10)	960(2)	8935(2)	3773(2)	25(1)
C(11)	411(2)	8501(2)	4272(2)	22(1)
C(12)	637(2)	7640(2)	4889(2)	22(1)
C(13)	-1174(2)	6857(2)	6137(2)	26(1)
C(14)	-1057(3)	7145(3)	6902(2)	33(1)
C(15)	-1926(3)	6977(3)	7220(2)	40(1)
C(16)	-2886(3)	6496(3)	6791(2)	39(1)
C(17)	-2979(3)	6203(3)	6025(2)	36(1)
C(18)	-2134(2)	6382(2)	5688(2)	31(1)
C(19)	-3804(4)	6233(4)	7148(3)	60(1)
C(20)	2378(2)	6948(2)	4916(2)	23(1)
C(21)	3376(2)	7245(3)	5411(2)	30(1)
C(22)	4288(3)	7260(3)	5136(2)	39(1)
C(23)	4228(3)	6935(3)	4379(2)	37(1)
C(24)	3232(2)	6591(3)	3905(2)	31(1)
C(25)	2309(2)	6600(2)	4165(2)	28(1)
C(26)	5218(3)	6977(4)	4073(3)	58(1)

Cl(1)	2240(1)	6999(1)	7214(1)	35(1)
Cl(2)	1131(1)	4294(1)	6190(1)	39(1)
Cl(3)	4893(1)	1011(1)	2954(1)	57(1)
Cl(4)	3884(3)	-53(3)	4051(2)	72(1)
C(27)	3653(4)	429(5)	3088(3)	62(2)
Cl(3A)	4440(7)	555(8)	2731(5)	81(2)
Cl(4A)	4165(10)	165(13)	4224(7)	66(3)
C(27A)	3293(12)	160(30)	3185(9)	65(5)
N(1)	-272(2)	6979(2)	5812(1)	24(1)
N(2)	1440(2)	6986(2)	5204(1)	22(1)
Zn(1)	1209(1)	6151(1)	6167(1)	24(1)

Table 69: Bond Lengths [ $\text{\AA}$ ] and Bond Angles [ $^\circ$ ] for **10-DCM**.

C(1)-N(1)	1.284(4)	C(14)-C(15)	1.396(4)
C(1)-C(2)	1.467(4)	C(15)-C(16)	1.383(5)
C(1)-C(12)	1.517(3)	C(16)-C(17)	1.390(5)
C(2)-C(3)	1.376(4)	C(16)-C(19)	1.516(4)
C(2)-C(7)	1.414(4)	C(17)-C(18)	1.392(4)
C(3)-C(4)	1.417(4)	C(20)-C(25)	1.388(4)
C(4)-C(5)	1.380(4)	C(20)-C(21)	1.391(4)
C(5)-C(6)	1.423(4)	C(20)-N(2)	1.432(3)
C(6)-C(7)	1.406(4)	C(21)-C(22)	1.387(4)
C(6)-C(8)	1.416(4)	C(22)-C(23)	1.394(5)
C(7)-C(11)	1.422(4)	C(23)-C(24)	1.388(5)
C(8)-C(9)	1.378(4)	C(23)-C(26)	1.512(4)
C(9)-C(10)	1.417(4)	C(24)-C(25)	1.383(4)
C(10)-C(11)	1.379(4)	Cl(1)-Zn(1)	2.2190(7)
C(11)-C(12)	1.473(4)	Cl(2)-Zn(1)	2.1961(8)
C(12)-N(2)	1.288(3)	Cl(3)-C(27)	1.806(6)
C(13)-C(14)	1.382(4)	Cl(4)-C(27)	1.766(6)
C(13)-C(18)	1.392(4)	Cl(3A)-C(27A)	1.922(11)
C(13)-N(1)	1.436(3)	Cl(4A)-C(27A)	1.895(11)



N(1)-Zn(1)	2.074(2)	C(16)-C(15)-C(14)	121.3(3)
N(2)-Zn(1)	2.079(2)	C(15)-C(16)-C(17)	118.5(3)
		C(15)-C(16)-C(19)	121.6(3)
N(1)-C(1)-C(2)	134.9(2)	C(17)-C(16)-C(19)	119.9(4)
N(1)-C(1)-C(12)	117.6(2)	C(18)-C(17)-C(16)	121.5(3)
C(2)-C(1)-C(12)	107.3(2)	C(13)-C(18)-C(17)	118.6(3)
C(3)-C(2)-C(7)	119.6(2)	C(25)-C(20)-C(21)	120.0(3)
C(3)-C(2)-C(1)	134.6(3)	C(25)-C(20)-N(2)	121.5(2)
C(7)-C(2)-C(1)	105.8(2)	C(21)-C(20)-N(2)	118.5(2)
C(2)-C(3)-C(4)	118.5(3)	C(22)-C(21)-C(20)	119.5(3)
C(5)-C(4)-C(3)	122.1(3)	C(21)-C(22)-C(23)	121.0(3)
C(4)-C(5)-C(6)	120.5(3)	C(24)-C(23)-C(22)	118.4(3)
C(7)-C(6)-C(8)	116.9(2)	C(24)-C(23)-C(26)	120.7(3)
C(7)-C(6)-C(5)	116.4(3)	C(22)-C(23)-C(26)	120.9(3)
C(8)-C(6)-C(5)	126.7(3)	C(25)-C(24)-C(23)	121.3(3)
C(6)-C(7)-C(2)	122.9(2)	C(24)-C(25)-C(20)	119.6(3)
C(6)-C(7)-C(11)	122.7(2)	Cl(4)-C(27)-Cl(3)	109.4(3)
C(2)-C(7)-C(11)	114.4(2)	Cl(4A)-C(27A)-Cl(3A)	95.8(8)
C(9)-C(8)-C(6)	120.5(3)	C(1)-N(1)-C(13)	121.3(2)
C(8)-C(9)-C(10)	122.2(3)	C(1)-N(1)-Zn(1)	111.97(18)
C(11)-C(10)-C(9)	118.8(3)	C(13)-N(1)-Zn(1)	126.72(17)
C(10)-C(11)-C(7)	119.0(2)	C(12)-N(2)-C(20)	120.6(2)
C(10)-C(11)-C(12)	135.5(3)	C(12)-N(2)-Zn(1)	111.86(17)
C(7)-C(11)-C(12)	105.5(2)	C(20)-N(2)-Zn(1)	127.46(17)
N(2)-C(12)-C(11)	135.6(2)	N(1)-Zn(1)-N(2)	81.14(9)
N(2)-C(12)-C(1)	117.2(2)	N(1)-Zn(1)-Cl(2)	115.72(7)
C(11)-C(12)-C(1)	107.0(2)	N(2)-Zn(1)-Cl(2)	120.42(7)
C(14)-C(13)-C(18)	121.0(3)	N(1)-Zn(1)-Cl(1)	109.42(7)
C(14)-C(13)-N(1)	119.7(3)	N(2)-Zn(1)-Cl(1)	107.64(6)
C(18)-C(13)-N(1)	119.1(3)	Cl(1)-Zn(1)-Cl(2)	116.98(3)
C(13)-C(14)-C(15)	119.1(3)		

Table 70: Crystallographic Data and Structure Refinement of **10-MeCN**.

Empirical formula	$C_{28}H_{23}Cl_2N_3Zn$	
Formula weight	537.76	
Temperature	133(2) K	
Wavelength	1.54184 Å	
Crystal system	Monoclinic	
Space group	$P2_1/c$	
Unit cell dimensions	$a = 12.7775(5)$ Å	$\alpha = 90^\circ$ .
	$b = 11.6266(2)$ Å	$\beta = 101.166(2)^\circ$ .
	$c = 17.4931(4)$ Å	$\gamma = 90^\circ$ .
Volume	$2549.56(12)$ Å <sup>3</sup>	
Z	4	
Density (calculated)	$1.401$ Mg/m <sup>3</sup>	
Absorption coefficient	$3.424$ mm <sup>-1</sup>	
F(000)	1104	
Crystal size	$0.12 \times 0.08 \times 0.04$ mm <sup>3</sup>	
Theta range for data collection	3.53 to 74.23°.	
Index ranges	$-15 \leq h \leq 13$ , $-14 \leq k \leq 9$ , $-21 \leq l \leq 21$	
Reflections collected	10438	
Independent reflections	5041 [R(int) = 0.0240]	
Completeness to theta = 74.23°	97.1 %	
Absorption correction	Semi-empirical from equivalents	
Max. and min. transmission	1.00000 and 0.82178	
Refinement method	Full-matrix least-squares on F <sup>2</sup>	
Data / restraints / parameters	5041 / 39 / 325	
Goodness-of-fit on F <sup>2</sup>	1.269	
Final R indices [I > 2sigma(I)]	R1 = 0.0505, wR2 = 0.1172	
R indices (all data)	R1 = 0.0534, wR2 = 0.1200	
Largest diff. peak and hole	0.369 and -0.408 e.Å <sup>-3</sup>	

Table 71: Atomic coordinates ( $\times 10^4$ ) and equivalent isotropic displacement parameters ( $\text{\AA}^2 \times 10^3$ ) for **10-MeCN**.  $U(\text{eq})$  is defined as one third of the trace of the orthogonalized  $U^{\text{ij}}$  tensor.

	x	y	z	U(eq)
C(1)	4388(3)	2661(3)	10106(2)	21(1)
C(2)	4588(3)	3542(3)	10724(2)	21(1)
C(3)	4014(3)	3993(3)	11240(2)	25(1)
C(4)	4478(3)	4882(3)	11752(2)	27(1)
C(5)	5474(3)	5309(3)	11742(2)	27(1)
C(6)	6089(3)	4869(3)	11211(2)	25(1)
C(7)	5624(3)	3980(3)	10714(2)	21(1)
C(8)	7124(3)	5236(3)	11137(2)	29(1)
C(9)	7626(3)	4731(3)	10586(2)	30(1)
C(10)	7140(3)	3838(3)	10090(2)	27(1)
C(11)	6145(3)	3467(3)	10158(2)	22(1)
C(12)	5374(3)	2627(3)	9742(2)	22(1)
C(13)	2645(3)	1962(3)	10116(2)	23(1)
C(14)	1684(3)	2171(3)	9615(2)	29(1)
C(15)	744(3)	2144(4)	9898(2)	36(1)
C(16)	742(3)	1855(4)	10675(2)	33(1)
C(17)	1712(3)	1622(3)	11158(2)	29(1)
C(18)	2661(3)	1672(3)	10889(2)	26(1)
C(19)	-291(4)	1833(5)	10975(3)	52(1)
C(20)	6284(3)	1831(3)	8807(2)	24(1)
C(21)	6248(3)	2140(3)	8037(2)	28(1)
C(22)	7147(3)	1984(3)	7714(2)	31(1)
C(23)	8076(3)	1498(3)	8142(2)	32(1)
C(24)	8083(3)	1173(3)	8910(2)	30(1)
C(25)	7193(3)	1340(3)	9245(2)	28(1)
C(26)	9050(4)	1291(5)	7784(3)	50(1)

N(3)	10236(7)	3871(8)	8113(5)	56(2)
C(28)	9566(7)	4322(8)	8306(5)	42(2)
C(27)	8716(11)	4910(13)	8571(8)	72(4)
N(4)	9612(8)	4764(10)	9453(7)	71(3)
C(28A)	9208(9)	4768(11)	8827(7)	51(3)
C(27A)	8683(2)	4759(3)	8006(1)	69(4)
N(1)	3606(1)	2010(1)	9815(1)	22(1)
N(2)	5358(1)	1969(1)	9147(1)	22(1)
Cl(1)	3973(1)	-747(1)	8831(1)	37(1)
Cl(2)	2910(1)	1992(1)	7806(1)	34(1)
Zn(1)	3898(1)	1141(1)	8830(1)	23(1)

Table 72: Bond Lengths [ $\text{\AA}$ ] and Bond Angles [ $^\circ$ ] for **10-MeCN**.

C(1)-N(1)	1.278(3)	C(14)-C(15)	1.386(5)
C(1)-C(2)	1.476(5)	C(15)-C(16)	1.401(6)
C(1)-C(12)	1.519(5)	C(16)-C(17)	1.385(6)
C(2)-C(3)	1.371(5)	C(16)-C(19)	1.512(6)
C(2)-C(7)	1.421(5)	C(17)-C(18)	1.384(5)
C(3)-C(4)	1.420(5)	C(20)-C(25)	1.386(5)
C(4)-C(5)	1.368(5)	C(20)-C(21)	1.387(5)
C(5)-C(6)	1.422(5)	C(20)-N(2)	1.433(3)
C(6)-C(7)	1.406(5)	C(21)-C(22)	1.386(5)
C(6)-C(8)	1.419(5)	C(22)-C(23)	1.394(6)
C(7)-C(11)	1.413(5)	C(23)-C(24)	1.394(6)
C(8)-C(9)	1.387(5)	C(23)-C(26)	1.517(5)
C(9)-C(10)	1.417(5)	C(24)-C(25)	1.391(5)
C(10)-C(11)	1.370(5)	N(3)-C(28)	1.111(11)
C(11)-C(12)	1.476(5)	C(28)-C(27)	1.434(12)
C(12)-N(2)	1.288(3)	N(4)-C(28A)	1.117(13)
C(13)-C(14)	1.386(5)	C(28A)-C(27A)	1.464(11)
C(13)-C(18)	1.389(5)	N(1)-Zn(1)	2.089(2)
C(13)-N(1)	1.428(3)	N(2)-Zn(1)	2.077(6)

Cl(1)-Zn(1)	2.1969(20)	C(14)-C(15)-C(16)	121.2(4)
Cl(2)-Zn(1)	2.2147(19)	C(17)-C(16)-C(15)	118.0(4)
		C(17)-C(16)-C(19)	121.6(4)
N(1)-C(1)-C(2)	135.6(3)	C(15)-C(16)-C(19)	120.4(4)
N(1)-C(1)-C(12)	117.7(3)	C(18)-C(17)-C(16)	121.6(3)
C(2)-C(1)-C(12)	106.6(3)	C(17)-C(18)-C(13)	119.6(3)
C(3)-C(2)-C(7)	119.3(3)	C(25)-C(20)-C(21)	120.7(3)
C(3)-C(2)-C(1)	135.1(3)	C(25)-C(20)-N(2)	119.1(3)
C(7)-C(2)-C(1)	105.6(3)	C(21)-C(20)-N(2)	120.1(3)
C(2)-C(3)-C(4)	118.8(3)	C(22)-C(21)-C(20)	119.2(4)
C(5)-C(4)-C(3)	122.1(3)	C(21)-C(22)-C(23)	121.4(4)
C(4)-C(5)-C(6)	120.8(3)	C(24)-C(23)-C(22)	118.3(4)
C(7)-C(6)-C(8)	117.0(3)	C(24)-C(23)-C(26)	120.1(4)
C(7)-C(6)-C(5)	116.5(3)	C(22)-C(23)-C(26)	121.6(4)
C(8)-C(6)-C(5)	126.5(3)	C(25)-C(24)-C(23)	121.0(4)
C(6)-C(7)-C(11)	122.4(3)	C(20)-C(25)-C(24)	119.4(4)
C(6)-C(7)-C(2)	122.6(3)	N(3)-C(28)-C(27)	178.7(12)
C(11)-C(7)-C(2)	114.9(3)	N(4)-C(28A)-C(27A)	179.3(14)
C(9)-C(8)-C(6)	120.0(3)	C(1)-N(1)-C(13)	122.5(2)
C(8)-C(9)-C(10)	122.0(4)	C(1)-N(1)-Zn(1)	111.37(16)
C(11)-C(10)-C(9)	118.7(3)	C(13)-N(1)-Zn(1)	126.04(14)
C(10)-C(11)-C(7)	119.8(3)	C(12)-N(2)-C(20)	121.1(2)
C(10)-C(11)-C(12)	135.0(3)	C(12)-N(2)-Zn(1)	111.36(16)
C(7)-C(11)-C(12)	105.1(3)	C(20)-N(2)-Zn(1)	127.50(14)
N(2)-C(12)-C(11)	134.2(3)	N(1)-Zn(1)-N(2)	81.3(2)
N(2)-C(12)-C(1)	118.0(3)	N(2)-Zn(1)-Cl(1)	115.22(17)
C(11)-C(12)-C(1)	107.7(3)	N(1)-Zn(1)-Cl(1)	119.40(17)
C(14)-C(13)-C(18)	120.1(3)	N(2)-Zn(1)-Cl(2)	110.50(17)
C(14)-C(13)-N(1)	118.6(3)	N(1)-Zn(1)-Cl(2)	106.61(16)
C(18)-C(13)-N(1)	121.2(3)	Cl(1)-Zn(1)-Cl(2)	117.69(8)
C(13)-C(14)-C(15)	119.5(4)		

Table 73: Crystallographic Data and Structure Refinement of **11-CHCl<sub>3</sub>**.

Empirical formula	C <sub>29</sub> H <sub>25</sub> Cl <sub>5</sub> N <sub>2</sub> Zn	
Formula weight	644.13	
Temperature	133(2) K	
Wavelength	1.54184 Å	
Crystal system	Monoclinic	
Space group	P2 <sub>1</sub> /c	
Unit cell dimensions	a = 8.92570(10) Å	α = 90°.
	b = 12.49020(10) Å	β = 99.0280(10)°.
	c = 25.9339(2) Å	γ = 90°.
Volume	2855.39(5) Å <sup>3</sup>	
Z	4	
Density (calculated)	1.498 Mg/m <sup>3</sup>	
Absorption coefficient	5.668 mm <sup>-1</sup>	
F(000)	1312	
Crystal size	0.62 x 0.52 x 0.21 mm <sup>3</sup>	
Theta range for data collection	3.45 to 74.15°.	
Index ranges	-10 ≤ h ≤ 11, -15 ≤ k ≤ 10, -32 ≤ l ≤ 29	
Reflections collected	20482	
Independent reflections	5739 [R(int) = 0.0206]	
Completeness to theta = 74.15°	98.9 %	
Absorption correction	Semi-empirical from equivalents	
Max. and min. transmission	1.00000 and 0.64729	
Refinement method	Full-matrix least-squares on F <sup>2</sup>	
Data / restraints / parameters	5739 / 0 / 338	
Goodness-of-fit on F <sup>2</sup>	1.050	
Final R indices [I > 2σ(I)]	R1 = 0.0391, wR2 = 0.0978	
R indices (all data)	R1 = 0.0397, wR2 = 0.0988	
Largest diff. peak and hole	1.084 and -1.254 e.Å <sup>-3</sup>	

Table 74: Atomic coordinates ( $\times 10^4$ ) and equivalent isotropic displacement parameters ( $\text{\AA}^2 \times 10^3$ ) for **11-CHCl<sub>3</sub>**. U(eq) is defined as one third of the trace of the orthogonalized  $U^{ij}$  tensor.

	x	y	z	U(eq)
C(1)	464(2)	8389(2)	5773(1)	14(1)
C(2)	-868(2)	9046(2)	5580(1)	16(1)
C(3)	-1708(2)	9791(2)	5802(1)	19(1)
C(4)	-2861(2)	10355(2)	5471(1)	23(1)
C(5)	-3166(2)	10183(2)	4942(1)	24(1)
C(6)	-2327(2)	9414(2)	4704(1)	21(1)
C(7)	-1176(2)	8861(2)	5033(1)	17(1)
C(8)	-2486(3)	9164(2)	4165(1)	26(1)
C(9)	-1541(3)	8438(2)	3984(1)	28(1)
C(10)	-376(3)	7898(2)	4319(1)	23(1)
C(11)	-200(2)	8114(2)	4847(1)	17(1)
C(12)	905(2)	7801(2)	5304(1)	15(1)
C(13)	958(2)	8713(2)	6689(1)	15(1)
C(14)	2033(2)	9358(2)	6985(1)	18(1)
C(15)	1718(3)	9805(2)	7450(1)	22(1)
C(16)	355(3)	9545(2)	7616(1)	22(1)
C(17)	-685(3)	8844(2)	7339(1)	19(1)
C(18)	-391(2)	8441(2)	6863(1)	17(1)
C(19)	2866(3)	10524(2)	7770(1)	34(1)
C(20)	-2065(3)	8479(2)	7558(1)	28(1)
C(21)	2613(2)	6599(2)	4982(1)	16(1)
C(22)	4091(2)	6753(2)	4888(1)	17(1)
C(23)	4659(3)	6113(2)	4523(1)	19(1)
C(24)	3755(3)	5295(2)	4279(1)	22(1)
C(25)	2287(3)	5116(2)	4379(1)	23(1)
C(26)	1708(3)	5791(2)	4730(1)	21(1)

C(27)	6238(3)	6296(2)	4407(1)	29(1)
C(28)	1366(3)	4186(2)	4133(1)	35(1)
C(29)	3180(3)	8232(2)	2919(1)	30(1)
Cl(1)	5348(1)	8154(1)	6196(1)	27(1)
Cl(2)	2947(1)	5815(1)	6599(1)	28(1)
Cl(3)	1694(1)	7840(1)	3240(1)	93(1)
Cl(4)	3920(1)	9460(1)	3179(1)	32(1)
Cl(5)	4591(1)	7258(1)	2966(1)	66(1)
N(1)	1318(2)	8267(1)	6216(1)	14(1)
N(2)	2101(2)	7223(1)	5382(1)	15(1)
Zn(1)	3187(1)	7291(1)	6162(1)	15(1)

Table 75: Bond Lengths [ $\text{\AA}$ ] and Bond Angles [ $^\circ$ ] for **11-CHCl<sub>3</sub>**.

C(1)-N(1)	1.284(3)	C(14)-C(15)	1.395(3)
C(1)-C(2)	1.466(3)	C(15)-C(16)	1.392(3)
C(1)-C(12)	1.523(3)	C(15)-C(19)	1.510(3)
C(2)-C(3)	1.376(3)	C(16)-C(17)	1.392(3)
C(2)-C(7)	1.420(3)	C(17)-C(18)	1.394(3)
C(3)-C(4)	1.419(3)	C(17)-C(20)	1.506(3)
C(4)-C(5)	1.373(3)	C(21)-C(26)	1.390(3)
C(5)-C(6)	1.419(4)	C(21)-C(22)	1.391(3)
C(6)-C(7)	1.409(3)	C(21)-N(2)	1.428(3)
C(6)-C(8)	1.416(3)	C(22)-C(23)	1.394(3)
C(7)-C(11)	1.413(3)	C(23)-C(24)	1.391(3)
C(8)-C(9)	1.371(4)	C(23)-C(27)	1.505(3)
C(9)-C(10)	1.416(3)	C(24)-C(25)	1.393(3)
C(10)-C(11)	1.380(3)	C(25)-C(26)	1.397(3)
C(11)-C(12)	1.472(3)	C(25)-C(28)	1.507(3)
C(12)-N(2)	1.278(3)	C(29)-Cl(5)	1.741(3)
C(13)-C(14)	1.389(3)	C(29)-Cl(3)	1.743(3)
C(13)-C(18)	1.392(3)	C(29)-Cl(4)	1.761(3)
C(13)-N(1)	1.430(2)	Cl(1)-Zn(1)	2.1992(6)



Cl(2)-Zn(1)	2.1932(6)	C(16)-C(15)-C(14)	118.6(2)
N(1)-Zn(1)	2.0886(17)	C(16)-C(15)-C(19)	121.2(2)
N(2)-Zn(1)	2.1035(17)	C(14)-C(15)-C(19)	120.2(2)
		C(17)-C(16)-C(15)	122.0(2)
N(1)-C(1)-C(2)	134.92(19)	C(16)-C(17)-C(18)	118.8(2)
N(1)-C(1)-C(12)	117.73(18)	C(16)-C(17)-C(20)	120.9(2)
C(2)-C(1)-C(12)	107.21(16)	C(18)-C(17)-C(20)	120.2(2)
C(3)-C(2)-C(7)	119.63(19)	C(13)-C(18)-C(17)	119.39(19)
C(3)-C(2)-C(1)	134.58(19)	C(26)-C(21)-C(22)	120.98(19)
C(7)-C(2)-C(1)	105.58(18)	C(26)-C(21)-N(2)	120.59(19)
C(2)-C(3)-C(4)	118.3(2)	C(22)-C(21)-N(2)	118.15(18)
C(5)-C(4)-C(3)	122.6(2)	C(21)-C(22)-C(23)	119.69(19)
C(4)-C(5)-C(6)	120.4(2)	C(24)-C(23)-C(22)	119.0(2)
C(7)-C(6)-C(8)	116.2(2)	C(24)-C(23)-C(27)	120.9(2)
C(7)-C(6)-C(5)	116.9(2)	C(22)-C(23)-C(27)	120.1(2)
C(8)-C(6)-C(5)	126.9(2)	C(23)-C(24)-C(25)	121.8(2)
C(6)-C(7)-C(11)	123.0(2)	C(24)-C(25)-C(26)	118.7(2)
C(6)-C(7)-C(2)	122.3(2)	C(24)-C(25)-C(28)	120.8(2)
C(11)-C(7)-C(2)	114.59(18)	C(26)-C(25)-C(28)	120.5(2)
C(9)-C(8)-C(6)	120.8(2)	C(21)-C(26)-C(25)	119.8(2)
C(8)-C(9)-C(10)	122.5(2)	Cl(5)-C(29)-Cl(3)	111.46(17)
C(11)-C(10)-C(9)	118.2(2)	Cl(5)-C(29)-Cl(4)	111.03(14)
C(10)-C(11)-C(7)	119.3(2)	Cl(3)-C(29)-Cl(4)	109.24(13)
C(10)-C(11)-C(12)	134.8(2)	C(1)-N(1)-C(13)	122.75(17)
C(7)-C(11)-C(12)	105.70(17)	C(1)-N(1)-Zn(1)	112.13(14)
N(2)-C(12)-C(11)	135.57(19)	C(13)-N(1)-Zn(1)	125.04(13)
N(2)-C(12)-C(1)	117.48(17)	C(12)-N(2)-C(21)	123.33(17)
C(11)-C(12)-C(1)	106.87(17)	C(12)-N(2)-Zn(1)	112.04(13)
C(14)-C(13)-C(18)	121.35(19)	C(21)-N(2)-Zn(1)	124.62(14)
C(14)-C(13)-N(1)	118.15(18)	N(1)-Zn(1)-N(2)	80.56(7)
C(18)-C(13)-N(1)	120.34(18)	N(1)-Zn(1)-Cl(2)	108.19(5)
C(13)-C(14)-C(15)	119.6(2)	N(2)-Zn(1)-Cl(2)	113.34(5)

N(1)-Zn(1)-Cl(1)	114.61(5)	Cl(1)-Zn(1)-Cl(2)	123.12(3)
N(2)-Zn(1)-Cl(1)	109.18(5)		

---

Table 76: Crystallographic Data and Structure Refinement of **11-THF**.

Empirical formula	C <sub>32</sub> H <sub>32</sub> Cl <sub>2</sub> N <sub>2</sub> OZn	
Formula weight	596.87	
Temperature	133(2) K	
Wavelength	1.54184 Å	
Crystal system	Monoclinic	
Space group	P2 <sub>1</sub> /c	
Unit cell dimensions	a = 8.11540(10) Å	α = 90°.
	b = 17.4717(2) Å	β = 99.2520(10)°.
	c = 20.2868(3) Å	γ = 90°.
Volume	2839.04(6) Å <sup>3</sup>	
Z	4	
Density (calculated)	1.396 Mg/m <sup>3</sup>	
Absorption coefficient	3.144 mm <sup>-1</sup>	
F(000)	1240	
Crystal size	0.24 x 0.12 x 0.10 mm <sup>3</sup>	
Theta range for data collection	3.36 to 74.22°.	
Index ranges	-9<=h<=9, -21<=k<=14, -22<=l<=24	
Reflections collected	11237	
Independent reflections	5590 [R(int) = 0.0215]	
Completeness to theta = 74.22°	96.9 %	
Absorption correction	Semi-empirical from equivalents	
Max. and min. transmission	1.00000 and 0.93531	
Refinement method	Full-matrix least-squares on F <sup>2</sup>	
Data / restraints / parameters	5590 / 0 / 347	
Goodness-of-fit on F <sup>2</sup>	1.065	
Final R indices [I>2sigma(I)]	R1 = 0.0286, wR2 = 0.0747	
R indices (all data)	R1 = 0.0313, wR2 = 0.0825	
Largest diff. peak and hole	0.294 and -0.388 e.Å <sup>-3</sup>	

Table 77: Atomic coordinates ( $\times 10^4$ ) and equivalent isotropic displacement parameters ( $\text{\AA}^2 \times 10^3$ ) for **11-THF**.  $U(\text{eq})$  is defined as one third of the trace of the orthogonalized  $U^{\text{ij}}$  tensor.

	x	y	z	U(eq)
C(1)	4704(2)	8644(1)	4180(1)	14(1)
C(2)	3691(2)	8983(1)	4641(1)	15(1)
C(3)	3231(2)	8754(1)	5234(1)	18(1)
C(4)	2328(2)	9272(1)	5576(1)	20(1)
C(5)	1890(2)	9995(1)	5332(1)	18(1)
C(6)	2350(2)	10245(1)	4721(1)	17(1)
C(7)	3259(2)	9728(1)	4391(1)	15(1)
C(8)	2021(2)	10974(1)	4420(1)	19(1)
C(9)	2624(2)	11154(1)	3841(1)	21(1)
C(10)	3573(2)	10633(1)	3522(1)	18(1)
C(11)	3886(2)	9914(1)	3796(1)	16(1)
C(12)	4894(2)	9252(1)	3657(1)	15(1)
C(13)	5231(2)	7398(1)	4604(1)	16(1)
C(14)	6603(2)	7131(1)	5041(1)	19(1)
C(15)	6390(2)	6556(1)	5495(1)	22(1)
C(16)	4811(2)	6236(1)	5472(1)	24(1)
C(17)	3438(2)	6481(1)	5016(1)	21(1)
C(18)	3653(2)	7077(1)	4582(1)	18(1)
C(19)	7838(3)	6292(1)	6003(1)	38(1)
C(20)	1746(2)	6108(1)	4990(1)	30(1)
C(21)	6193(2)	9613(1)	2734(1)	16(1)
C(22)	7831(2)	9821(1)	2692(1)	18(1)
C(23)	8143(2)	10308(1)	2182(1)	20(1)
C(24)	6796(2)	10569(1)	1724(1)	20(1)
C(25)	5161(2)	10344(1)	1750(1)	18(1)
C(26)	4865(2)	9855(1)	2260(1)	17(1)

C(27)	9906(2)	10521(1)	2116(1)	31(1)
C(28)	3727(2)	10625(1)	1241(1)	23(1)
C(29)	7527(3)	2836(2)	3386(1)	46(1)
C(30)	7982(3)	2177(1)	2970(1)	36(1)
C(31)	8049(3)	2563(1)	2305(1)	32(1)
C(32)	8758(3)	3341(1)	2517(1)	34(1)
Cl(1)	9651(1)	8180(1)	4059(1)	26(1)
Cl(2)	6772(1)	7286(1)	2592(1)	29(1)
N(1)	5461(2)	8005(1)	4152(1)	15(1)
N(2)	5924(2)	9105(1)	3255(1)	16(1)
O(1)	8190(2)	3516(1)	3134(1)	42(1)
Zn(1)	7130(1)	8046(1)	3461(1)	16(1)

Table 78: Bond Lengths [ $\text{\AA}$ ] and Bond Angles [ $^\circ$ ] for **11-THF**.

C(1)-N(1)	1.281(2)	C(13)-N(1)	1.433(2)
C(1)-C(2)	1.466(2)	C(14)-C(15)	1.392(2)
C(1)-C(12)	1.525(2)	C(15)-C(16)	1.392(3)
C(2)-C(3)	1.376(2)	C(15)-C(19)	1.506(3)
C(2)-C(7)	1.420(2)	C(16)-C(17)	1.395(3)
C(3)-C(4)	1.415(2)	C(17)-C(18)	1.392(2)
C(4)-C(5)	1.383(2)	C(17)-C(20)	1.513(2)
C(5)-C(6)	1.419(2)	C(21)-C(26)	1.390(2)
C(6)-C(7)	1.404(2)	C(21)-C(22)	1.394(2)
C(6)-C(8)	1.419(2)	C(21)-N(2)	1.425(2)
C(7)-C(11)	1.421(2)	C(22)-C(23)	1.393(2)
C(8)-C(9)	1.379(2)	C(23)-C(24)	1.393(3)
C(9)-C(10)	1.415(2)	C(23)-C(27)	1.506(2)
C(10)-C(11)	1.382(2)	C(24)-C(25)	1.393(2)
C(11)-C(12)	1.470(2)	C(25)-C(26)	1.393(2)
C(12)-N(2)	1.284(2)	C(25)-C(28)	1.508(2)
C(13)-C(14)	1.389(2)	C(29)-O(1)	1.432(3)
C(13)-C(18)	1.392(2)	C(29)-C(30)	1.509(3)

C(30)-C(31)	1.518(3)	C(14)-C(13)-C(18)	121.55(15)
C(31)-C(32)	1.511(3)	C(14)-C(13)-N(1)	118.91(15)
C(32)-O(1)	1.436(3)	C(18)-C(13)-N(1)	119.52(15)
Cl(1)-Zn(1)	2.2168(5)	C(13)-C(14)-C(15)	119.55(16)
Cl(2)-Zn(1)	2.1880(5)	C(16)-C(15)-C(14)	118.60(16)
N(1)-Zn(1)	2.1014(14)	C(16)-C(15)-C(19)	120.85(17)
N(2)-Zn(1)	2.1024(14)	C(14)-C(15)-C(19)	120.54(17)
		C(15)-C(16)-C(17)	122.19(16)
N(1)-C(1)-C(2)	134.60(15)	C(18)-C(17)-C(16)	118.65(16)
N(1)-C(1)-C(12)	118.30(14)	C(18)-C(17)-C(20)	120.33(17)
C(2)-C(1)-C(12)	107.00(13)	C(16)-C(17)-C(20)	121.02(16)
C(3)-C(2)-C(7)	119.56(15)	C(17)-C(18)-C(13)	119.35(16)
C(3)-C(2)-C(1)	134.41(15)	C(26)-C(21)-C(22)	121.31(15)
C(7)-C(2)-C(1)	105.86(14)	C(26)-C(21)-N(2)	120.54(15)
C(2)-C(3)-C(4)	118.51(16)	C(22)-C(21)-N(2)	118.02(15)
C(5)-C(4)-C(3)	122.19(16)	C(23)-C(22)-C(21)	119.54(16)
C(4)-C(5)-C(6)	120.37(15)	C(24)-C(23)-C(22)	118.63(16)
C(7)-C(6)-C(5)	116.82(15)	C(24)-C(23)-C(27)	120.95(16)
C(7)-C(6)-C(8)	116.64(15)	C(22)-C(23)-C(27)	120.37(16)
C(5)-C(6)-C(8)	126.52(16)	C(23)-C(24)-C(25)	122.14(16)
C(6)-C(7)-C(2)	122.54(15)	C(26)-C(25)-C(24)	118.71(16)
C(6)-C(7)-C(11)	123.08(15)	C(26)-C(25)-C(28)	120.17(16)
C(2)-C(7)-C(11)	114.33(14)	C(24)-C(25)-C(28)	121.13(15)
C(9)-C(8)-C(6)	120.26(15)	C(21)-C(26)-C(25)	119.58(15)
C(8)-C(9)-C(10)	122.52(16)	O(1)-C(29)-C(30)	107.09(18)
C(11)-C(10)-C(9)	118.58(15)	C(29)-C(30)-C(31)	101.83(19)
C(10)-C(11)-C(7)	118.89(15)	C(32)-C(31)-C(30)	102.32(17)
C(10)-C(11)-C(12)	135.30(15)	O(1)-C(32)-C(31)	106.20(17)
C(7)-C(11)-C(12)	105.57(14)	C(1)-N(1)-C(13)	120.29(14)
N(2)-C(12)-C(11)	135.90(15)	C(1)-N(1)-Zn(1)	111.37(11)
N(2)-C(12)-C(1)	116.80(14)	C(13)-N(1)-Zn(1)	128.07(10)
C(11)-C(12)-C(1)	107.06(13)	C(12)-N(2)-C(21)	122.66(14)

C(12)-N(2)-Zn(1)	112.32(11)	N(2)-Zn(1)-Cl(2)	112.12(4)
C(21)-N(2)-Zn(1)	125.02(10)	N(1)-Zn(1)-Cl(1)	105.98(4)
C(29)-O(1)-C(32)	109.05(16)	N(2)-Zn(1)-Cl(1)	112.03(4)
N(1)-Zn(1)-N(2)	80.40(5)	Cl(1)-Zn(1)-Cl(2)	119.753(19)
N(1)-Zn(1)-Cl(2)	120.01(4)		

---

Table 79: Crystallographic Data and Structure Refinement of **11-DCM**.

Empirical formula	C <sub>29</sub> H <sub>26</sub> Cl <sub>4</sub> N <sub>2</sub> Zn	
Formula weight	609.69	
Temperature	133(2) K	
Wavelength	1.54184 Å	
Crystal system	Monoclinic	
Space group	P2 <sub>1</sub> /c	
Unit cell dimensions	a = 8.23390(10) Å	α = 90°.
	b = 18.2260(2) Å	β = 98.6430(10)°.
	c = 19.0885(2) Å	γ = 90°.
Volume	2832.10(6) Å <sup>3</sup>	
Z	4	
Density (calculated)	1.430 Mg/m <sup>3</sup>	
Absorption coefficient	4.833 mm <sup>-1</sup>	
F(000)	1248	
Crystal size	0.38 x 0.36 x 0.16 mm <sup>3</sup>	
Theta range for data collection	3.37 to 74.27°.	
Index ranges	-10<=h<=9, -22<=k<=16, -23<=l<=20	
Reflections collected	11042	
Independent reflections	5611 [R(int) = 0.0220]	
Completeness to theta = 74.27°	97.2 %	
Absorption correction	Semi-empirical from equivalents	
Max. and min. transmission	1.00000 and 0.77598	
Refinement method	Full-matrix least-squares on F <sup>2</sup>	
Data / restraints / parameters	5611 / 0 / 329	
Goodness-of-fit on F <sup>2</sup>	1.068	
Final R indices [I>2sigma(I)]	R1 = 0.0365, wR2 = 0.0971	
R indices (all data)	R1 = 0.0393, wR2 = 0.0990	
Largest diff. peak and hole	0.534 and -0.646 e.Å <sup>-3</sup>	



Table 80: Atomic coordinates ( $\times 10^4$ ) and equivalent isotropic displacement parameters ( $\text{\AA}^2 \times 10^3$ ) for **11-DCM**.  $U(\text{eq})$  is defined as one third of the trace of the orthogonalized  $U^{ij}$  tensor.

	x	y	z	U(eq)
C(1)	9843(2)	5712(1)	8645(1)	14(1)
C(2)	8938(2)	5051(1)	8797(1)	13(1)
C(3)	8763(2)	4348(1)	8522(1)	16(1)
C(4)	7844(2)	3830(1)	8854(1)	17(1)
C(5)	7152(2)	3999(1)	9448(1)	16(1)
C(6)	7347(2)	4707(1)	9755(1)	14(1)
C(7)	8218(2)	5221(1)	9410(1)	13(1)
C(8)	6784(2)	4943(1)	10385(1)	16(1)
C(9)	7098(2)	5645(1)	10634(1)	17(1)
C(10)	7962(2)	6164(1)	10278(1)	16(1)
C(11)	8516(2)	5950(1)	9660(1)	13(1)
C(12)	9531(2)	6290(1)	9183(1)	13(1)
C(13)	11213(2)	5371(1)	7687(1)	15(1)
C(14)	12844(3)	5187(1)	7665(1)	18(1)
C(15)	13212(3)	4686(1)	7157(1)	22(1)
C(16)	11939(3)	4408(1)	6668(1)	23(1)
C(17)	10307(3)	4614(1)	6670(1)	20(1)
C(18)	9957(2)	5101(1)	7185(1)	17(1)
C(19)	14975(3)	4474(2)	7127(2)	37(1)
C(20)	8948(3)	4316(1)	6124(1)	30(1)
C(21)	9936(2)	7496(1)	9635(1)	15(1)
C(22)	11269(3)	7781(1)	10083(1)	17(1)
C(23)	11015(3)	8323(1)	10570(1)	20(1)
C(24)	9431(3)	8587(1)	10573(1)	22(1)
C(25)	8097(3)	8328(1)	10101(1)	20(1)
C(26)	8359(3)	7773(1)	9628(1)	19(1)

C(27)	12438(3)	8620(1)	11082(1)	32(1)
C(28)	6395(3)	8641(1)	10102(1)	34(1)
C(29)	6610(4)	7391(2)	7475(2)	44(1)
Cl(1)	14378(1)	6911(1)	8944(1)	32(1)
Cl(2)	11038(1)	7701(1)	7530(1)	41(1)
Cl(3)	6598(1)	6427(1)	7402(1)	51(1)
Cl(4)	6043(1)	7807(1)	6641(1)	56(1)
N(1)	10855(2)	5872(1)	8217(1)	14(1)
N(2)	10218(2)	6919(1)	9157(1)	15(1)
Zn(1)	11811(1)	6937(1)	8400(1)	18(1)

Table 81: Bond Lengths [Å] and Bond Angles [°] for **11-DCM**.

C(1)-N(1)	1.285(3)	C(15)-C(16)	1.390(3)
C(1)-C(2)	1.468(3)	C(15)-C(19)	1.513(3)
C(1)-C(12)	1.521(2)	C(16)-C(17)	1.396(3)
C(2)-C(3)	1.384(3)	C(17)-C(18)	1.386(3)
C(2)-C(7)	1.423(3)	C(17)-C(20)	1.510(3)
C(3)-C(4)	1.417(3)	C(21)-C(22)	1.387(3)
C(4)-C(5)	1.378(3)	C(21)-C(26)	1.391(3)
C(5)-C(6)	1.417(3)	C(21)-N(2)	1.435(2)
C(6)-C(7)	1.403(3)	C(22)-C(23)	1.393(3)
C(6)-C(8)	1.419(3)	C(23)-C(24)	1.390(3)
C(7)-C(11)	1.421(3)	C(23)-C(27)	1.509(3)
C(8)-C(9)	1.377(3)	C(24)-C(25)	1.395(3)
C(9)-C(10)	1.417(3)	C(25)-C(26)	1.394(3)
C(10)-C(11)	1.383(3)	C(25)-C(28)	1.513(3)
C(11)-C(12)	1.463(3)	C(29)-Cl(3)	1.761(3)
C(12)-N(2)	1.283(3)	C(29)-Cl(4)	1.763(3)
C(13)-C(18)	1.390(3)	Cl(1)-Zn(1)	2.2117(6)
C(13)-C(14)	1.391(3)	Cl(2)-Zn(1)	2.1868(6)
C(13)-N(1)	1.427(2)	N(1)-Zn(1)	2.1022(16)
C(14)-C(15)	1.397(3)	N(2)-Zn(1)	2.0927(16)

		C(14)-C(15)-C(19)	120.2(2)
N(1)-C(1)-C(2)	135.19(18)	C(15)-C(16)-C(17)	121.93(19)
N(1)-C(1)-C(12)	117.60(17)	C(18)-C(17)-C(16)	118.48(19)
C(2)-C(1)-C(12)	106.99(15)	C(18)-C(17)-C(20)	120.5(2)
C(3)-C(2)-C(7)	118.67(18)	C(16)-C(17)-C(20)	121.0(2)
C(3)-C(2)-C(1)	135.44(18)	C(17)-C(18)-C(13)	120.20(19)
C(7)-C(2)-C(1)	105.69(16)	C(22)-C(21)-C(26)	121.43(18)
C(2)-C(3)-C(4)	118.74(18)	C(22)-C(21)-N(2)	118.60(18)
C(5)-C(4)-C(3)	122.18(18)	C(26)-C(21)-N(2)	119.94(18)
C(4)-C(5)-C(6)	120.60(18)	C(21)-C(22)-C(23)	119.49(19)
C(7)-C(6)-C(5)	116.63(18)	C(24)-C(23)-C(22)	118.90(19)
C(7)-C(6)-C(8)	116.83(18)	C(24)-C(23)-C(27)	120.70(19)
C(5)-C(6)-C(8)	126.52(18)	C(22)-C(23)-C(27)	120.4(2)
C(6)-C(7)-C(11)	122.73(17)	C(23)-C(24)-C(25)	121.86(19)
C(6)-C(7)-C(2)	123.12(18)	C(26)-C(25)-C(24)	118.77(19)
C(11)-C(7)-C(2)	114.10(17)	C(26)-C(25)-C(28)	120.5(2)
C(9)-C(8)-C(6)	120.37(18)	C(24)-C(25)-C(28)	120.7(2)
C(8)-C(9)-C(10)	122.52(18)	C(21)-C(26)-C(25)	119.42(19)
C(11)-C(10)-C(9)	118.25(18)	Cl(3)-C(29)-Cl(4)	111.09(17)
C(10)-C(11)-C(7)	119.28(18)	C(1)-N(1)-C(13)	121.82(16)
C(10)-C(11)-C(12)	134.71(18)	C(1)-N(1)-Zn(1)	111.55(13)
C(7)-C(11)-C(12)	105.78(16)	C(13)-N(1)-Zn(1)	126.63(12)
N(2)-C(12)-C(11)	134.40(17)	C(12)-N(2)-C(21)	121.07(16)
N(2)-C(12)-C(1)	118.16(17)	C(12)-N(2)-Zn(1)	111.54(13)
C(11)-C(12)-C(1)	107.35(16)	C(21)-N(2)-Zn(1)	127.29(12)
C(18)-C(13)-C(14)	121.02(18)	N(1)-Zn(1)-N(2)	80.93(6)
C(18)-C(13)-N(1)	120.30(18)	N(2)-Zn(1)-Cl(2)	113.12(5)
C(14)-C(13)-N(1)	118.62(17)	N(1)-Zn(1)-Cl(2)	113.76(5)
C(13)-C(14)-C(15)	119.32(19)	N(2)-Zn(1)-Cl(1)	109.23(5)
C(16)-C(15)-C(14)	118.9(2)	N(1)-Zn(1)-Cl(1)	111.48(5)
C(16)-C(15)-C(19)	120.8(2)	Cl(1)-Zn(1)-Cl(2)	121.24(3)

Table 82: Crystallographic Data and Structure Refinement of **11-MeCN**.

Empirical formula	$C_{30}H_{27}Cl_2N_3Zn$	
Formula weight	565.82	
Temperature	133(2) K	
Wavelength	1.54184 Å	
Crystal system	Monoclinic	
Space group	$P2_1/n$	
Unit cell dimensions	$a = 8.2649(2)$ Å	$\alpha = 90^\circ$ .
	$b = 18.4330(4)$ Å	$\beta = 102.417(3)^\circ$ .
	$c = 18.5506(5)$ Å	$\gamma = 90^\circ$ .
Volume	$2760.02(12)$ Å <sup>3</sup>	
Z	4	
Density (calculated)	$1.362$ Mg/m <sup>3</sup>	
Absorption coefficient	$3.189$ mm <sup>-1</sup>	
F(000)	1168	
Crystal size	$0.27 \times 0.13 \times 0.07$ mm <sup>3</sup>	
Theta range for data collection	3.42 to 74.16°.	
Index ranges	$-8 \leq h \leq 10, -13 \leq k \leq 22, -23 \leq l \leq 22$	
Reflections collected	12690	
Independent reflections	5467 [R(int) = 0.0234]	
Completeness to theta = 74.16°	97.3 %	
Absorption correction	Semi-empirical from equivalents	
Max. and min. transmission	1.00000 and 0.82178	
Refinement method	Full-matrix least-squares on F <sup>2</sup>	
Data / restraints / parameters	5467 / 0 / 330	
Goodness-of-fit on F <sup>2</sup>	1.038	
Final R indices [I > 2sigma(I)]	R1 = 0.0306, wR2 = 0.0811	
R indices (all data)	R1 = 0.0340, wR2 = 0.0837	
Largest diff. peak and hole	0.312 and -0.337 e.Å <sup>-3</sup>	

Table 83: Atomic coordinates ( $\times 10^4$ ) and equivalent isotropic displacement parameters ( $\text{\AA}^2 \times 10^3$ ) for **11-MeCN**.  $U(\text{eq})$  is defined as one third of the trace of the orthogonalized  $U^{\text{ij}}$  tensor.

	x	y	z	U(eq)
C(1)	4972(2)	6293(1)	4128(1)	19(1)
C(2)	6345(2)	5949(1)	4646(1)	19(1)
C(3)	7426(2)	6165(1)	5285(1)	22(1)
C(4)	8540(2)	5648(1)	5676(1)	24(1)
C(5)	8590(2)	4939(1)	5443(1)	23(1)
C(6)	7476(2)	4699(1)	4796(1)	20(1)
C(7)	6369(2)	5215(1)	4413(1)	19(1)
C(8)	7340(2)	3983(1)	4506(1)	24(1)
C(9)	6132(2)	3816(1)	3893(1)	24(1)
C(10)	5001(2)	4339(1)	3520(1)	22(1)
C(11)	5128(2)	5044(1)	3777(1)	19(1)
C(12)	4161(2)	5713(1)	3586(1)	18(1)
C(13)	5010(2)	7495(1)	4567(1)	20(1)
C(14)	4041(2)	7774(1)	5024(1)	22(1)
C(15)	4687(2)	8304(1)	5541(1)	26(1)
C(16)	6278(2)	8563(1)	5562(1)	29(1)
C(17)	7231(2)	8306(1)	5085(1)	28(1)
C(18)	6591(2)	7760(1)	4582(1)	24(1)
C(19)	3685(3)	8581(1)	6068(1)	40(1)
C(20)	8949(2)	8605(1)	5118(1)	44(1)
C(21)	2002(2)	5376(1)	2587(1)	20(1)
C(22)	348(2)	5214(1)	2549(1)	23(1)
C(23)	-454(2)	4718(1)	2023(1)	27(1)
C(24)	419(2)	4418(1)	1532(1)	29(1)
C(25)	2065(2)	4599(1)	1552(1)	26(1)
C(26)	2858(2)	5086(1)	2087(1)	22(1)

C(27)	-2255(2)	4536(1)	1979(1)	40(1)
C(28)	2987(3)	4279(1)	1011(1)	41(1)
C(29)	1326(3)	8143(1)	7428(1)	44(1)
C(30)	1537(3)	7361(1)	7399(2)	56(1)
Cl(1)	22(1)	6968(1)	3857(1)	37(1)
Cl(2)	2033(1)	7684(1)	2338(1)	43(1)
N(1)	4324(2)	6925(1)	4069(1)	20(1)
N(2)	2816(2)	5881(1)	3132(1)	19(1)
N(3)	1185(3)	8751(1)	7462(1)	59(1)
Zn(1)	2099(1)	6951(1)	3272(1)	23(1)

Table 84: Bond Lengths [ $\text{\AA}$ ] and Bond Angles [ $^\circ$ ] for **11-MeCN**.

C(1)-N(1)	1.278(2)	C(15)-C(16)	1.391(2)
C(1)-C(2)	1.464(2)	C(15)-C(19)	1.501(2)
C(1)-C(12)	1.5201(19)	C(16)-C(17)	1.388(3)
C(2)-C(3)	1.382(2)	C(17)-C(18)	1.397(2)
C(2)-C(7)	1.421(2)	C(17)-C(20)	1.512(2)
C(3)-C(4)	1.412(2)	C(21)-C(22)	1.385(2)
C(4)-C(5)	1.379(2)	C(21)-C(26)	1.389(2)
C(5)-C(6)	1.418(2)	C(21)-N(2)	1.4319(18)
C(6)-C(7)	1.402(2)	C(22)-C(23)	1.397(2)
C(6)-C(8)	1.420(2)	C(23)-C(24)	1.392(3)
C(7)-C(11)	1.422(2)	C(23)-C(27)	1.511(2)
C(8)-C(9)	1.377(2)	C(24)-C(25)	1.394(2)
C(9)-C(10)	1.416(2)	C(25)-C(26)	1.393(2)
C(10)-C(11)	1.380(2)	C(25)-C(28)	1.504(2)
C(11)-C(12)	1.471(2)	C(29)-N(3)	1.129(3)
C(12)-N(2)	1.2807(19)	C(29)-C(30)	1.454(3)
C(13)-C(14)	1.384(2)	Cl(1)-Zn(1)	2.2192(5)
C(13)-C(18)	1.390(2)	Cl(2)-Zn(1)	2.1885(5)
C(13)-N(1)	1.4333(18)	N(1)-Zn(1)	2.0970(12)
C(14)-C(15)	1.393(2)	N(2)-Zn(1)	2.0920(12)

		C(14)-C(15)-C(19)	120.23(16)
N(1)-C(1)-C(2)	134.67(13)	C(17)-C(16)-C(15)	121.81(15)
N(1)-C(1)-C(12)	117.84(13)	C(16)-C(17)-C(18)	119.10(16)
C(2)-C(1)-C(12)	107.40(12)	C(16)-C(17)-C(20)	120.40(16)
C(3)-C(2)-C(7)	119.16(14)	C(18)-C(17)-C(20)	120.49(17)
C(3)-C(2)-C(1)	134.86(14)	C(13)-C(18)-C(17)	119.10(15)
C(7)-C(2)-C(1)	105.77(12)	C(22)-C(21)-C(26)	121.51(14)
C(2)-C(3)-C(4)	118.37(14)	C(22)-C(21)-N(2)	118.95(13)
C(5)-C(4)-C(3)	122.64(14)	C(26)-C(21)-N(2)	119.46(13)
C(4)-C(5)-C(6)	120.20(14)	C(21)-C(22)-C(23)	119.36(15)
C(7)-C(6)-C(5)	116.84(14)	C(24)-C(23)-C(22)	118.90(15)
C(7)-C(6)-C(8)	116.65(14)	C(24)-C(23)-C(27)	121.27(15)
C(5)-C(6)-C(8)	126.49(14)	C(22)-C(23)-C(27)	119.80(16)
C(6)-C(7)-C(2)	122.77(13)	C(23)-C(24)-C(25)	121.83(15)
C(6)-C(7)-C(11)	123.04(14)	C(26)-C(25)-C(24)	118.67(15)
C(2)-C(7)-C(11)	114.14(13)	C(26)-C(25)-C(28)	120.00(16)
C(9)-C(8)-C(6)	120.31(14)	C(24)-C(25)-C(28)	121.33(15)
C(8)-C(9)-C(10)	122.43(14)	C(21)-C(26)-C(25)	119.64(15)
C(11)-C(10)-C(9)	118.67(14)	N(3)-C(29)-C(30)	178.7(3)
C(10)-C(11)-C(7)	118.86(14)	C(1)-N(1)-C(13)	120.84(12)
C(10)-C(11)-C(12)	135.20(14)	C(1)-N(1)-Zn(1)	111.68(10)
C(7)-C(11)-C(12)	105.72(12)	C(13)-N(1)-Zn(1)	127.08(9)
N(2)-C(12)-C(11)	135.31(13)	C(12)-N(2)-C(21)	121.15(12)
N(2)-C(12)-C(1)	117.55(13)	C(12)-N(2)-Zn(1)	112.02(10)
C(11)-C(12)-C(1)	106.90(12)	C(21)-N(2)-Zn(1)	126.79(9)
C(14)-C(13)-C(18)	121.51(14)	N(1)-Zn(1)-N(2)	80.64(5)
C(14)-C(13)-N(1)	117.80(14)	N(2)-Zn(1)-Cl(2)	116.25(4)
C(18)-C(13)-N(1)	120.69(14)	N(1)-Zn(1)-Cl(2)	116.19(4)
C(13)-C(14)-C(15)	119.68(15)	N(2)-Zn(1)-Cl(1)	110.06(4)
C(16)-C(15)-C(14)	118.70(15)	N(1)-Zn(1)-Cl(1)	108.02(4)
C(16)-C(15)-C(19)	121.07(15)	Cl(1)-Zn(1)-Cl(2)	119.24(2)

Table 85: Crystallographic Data and Structure Refinement of **14**.

Empirical formula	C <sub>32</sub> H <sub>32</sub> Cl <sub>2</sub> N <sub>2</sub> O <sub>2</sub> Zn	
Formula weight	612.87	
Temperature	100(2) K	
Wavelength	1.54184 Å	
Crystal system	Monoclinic	
Space group	I2/a	
Unit cell dimensions	a = 18.3252(3) Å	α = 90°.
	b = 11.6963(2) Å	β = 97.0670(10)°.
	c = 26.7400(4) Å	γ = 90°.
Volume	5687.83(16) Å <sup>3</sup>	
Z	8	
Density (calculated)	1.431 Mg/m <sup>3</sup>	
Absorption coefficient	3.182 mm <sup>-1</sup>	
F(000)	2544	
Crystal size	0.03 x 0.05 x 0.38 mm <sup>3</sup>	
Theta range for data collection	3.33 to 76.26°.	
Index ranges	-22<=h<=22, -14<=k<=13, -33<=l<=33	
Reflections collected	27764	
Independent reflections	5871 [R(int) = 0.0342]	
Completeness to theta = 76.26°	98.3 %	
Absorption correction	Semi-empirical from equivalents	
Max. and min. transmission	1.00000 and 0.49341	
Refinement method	Full-matrix least-squares on F <sup>2</sup>	
Data / restraints / parameters	5871 / 0 / 354	
Goodness-of-fit on F <sup>2</sup>	1.055	
Final R indices [I>2sigma(I)]	R1 = 0.0335, wR2 = 0.0889	
R indices (all data)	R1 = 0.0365, wR2 = 0.0918	
Largest diff. peak and hole	0.466 and -0.521 e.Å <sup>-3</sup>	



Table 86: Atomic coordinates ( $\times 10^4$ ) and equivalent isotropic displacement parameters ( $\text{\AA}^2 \times 10^3$ ) for **14**. U(eq) is defined as one third of the trace of the orthogonalized  $U^{ij}$  tensor.

	x	y	z	U(eq)
C(1)	7303(1)	5168(1)	7577(1)	17(1)
C(2)	7636(1)	6072(2)	7914(1)	19(1)
C(3)	7445(1)	6620(2)	8336(1)	21(1)
C(4)	7892(1)	7535(2)	8542(1)	25(1)
C(5)	8502(1)	7897(2)	8336(1)	26(1)
C(6)	8703(1)	7368(2)	7895(1)	22(1)
C(7)	8258(1)	6460(2)	7695(1)	20(1)
C(8)	9291(1)	7689(2)	7626(1)	26(1)
C(9)	9399(1)	7146(2)	7184(1)	25(1)
C(10)	8945(1)	6233(2)	6986(1)	22(1)
C(11)	8378(1)	5879(2)	7246(1)	19(1)
C(12)	7773(1)	5051(1)	7151(1)	17(1)
C(13)	6292(1)	4527(1)	7968(1)	18(1)
C(14)	5541(1)	4707(2)	7869(1)	19(1)
C(15)	5110(1)	4773(2)	8263(1)	20(1)
C(16)	5440(1)	4606(2)	8755(1)	21(1)
C(17)	6187(1)	4341(2)	8850(1)	22(1)
C(18)	6615(1)	4304(2)	8459(1)	21(1)
C(19)	4327(1)	5046(2)	9100(1)	24(1)
C(20)	4085(1)	5139(2)	9619(1)	27(1)
C(21)	3272(1)	5454(2)	9599(1)	28(1)
C(22)	3107(1)	6682(2)	9441(1)	33(1)
C(23)	8031(1)	4124(2)	6414(1)	19(1)
C(24)	7769(1)	4316(2)	5912(1)	27(1)
C(25)	8232(1)	4144(2)	5547(1)	31(1)
C(26)	8947(1)	3752(2)	5675(1)	23(1)

C(27)	9198(1)	3516(2)	6176(1)	22(1)
C(28)	8736(1)	3700(2)	6543(1)	23(1)
C(29)	10109(1)	3311(2)	5395(1)	25(1)
C(30)	10420(1)	3182(2)	4901(1)	28(1)
C(31)	11247(1)	2962(2)	4984(1)	33(1)
C(32)	11545(1)	2572(3)	4503(1)	47(1)
Cl(1)	6510(1)	1746(1)	7031(1)	23(1)
Cl(2)	5643(1)	4305(1)	6368(1)	27(1)
N(1)	6725(1)	4546(1)	7561(1)	17(1)
N(2)	7567(1)	4338(1)	6797(1)	17(1)
Zn(1)	6555(1)	3602(1)	6895(1)	17(1)
O(1)	5077(1)	4662(1)	9169(1)	25(1)
O(2)	9348(1)	3612(1)	5283(1)	29(1)

Table 87: Bond Lengths [ $\text{\AA}$ ] and Bond Angles [ $^\circ$ ] for **14**.

C(1)-N(1)	1.283(2)	C(13)-C(18)	1.397(2)
C(1)-C(2)	1.472(2)	C(13)-N(1)	1.422(2)
C(1)-C(12)	1.516(2)	C(14)-C(15)	1.393(2)
C(2)-C(3)	1.380(3)	C(15)-C(16)	1.393(3)
C(2)-C(7)	1.418(3)	C(16)-O(1)	1.362(2)
C(3)-C(4)	1.416(3)	C(16)-C(17)	1.397(3)
C(4)-C(5)	1.372(3)	C(17)-C(18)	1.382(3)
C(5)-C(6)	1.420(3)	C(19)-O(1)	1.437(2)
C(6)-C(7)	1.405(2)	C(19)-C(20)	1.514(2)
C(6)-C(8)	1.417(3)	C(20)-C(21)	1.529(3)
C(7)-C(11)	1.421(3)	C(21)-C(22)	1.517(3)
C(8)-C(9)	1.378(3)	C(23)-C(24)	1.386(3)
C(9)-C(10)	1.416(3)	C(23)-C(28)	1.387(3)
C(10)-C(11)	1.382(3)	C(23)-N(2)	1.432(2)
C(11)-C(12)	1.471(2)	C(24)-C(25)	1.386(3)
C(12)-N(2)	1.284(2)	C(25)-C(26)	1.391(3)
C(13)-C(14)	1.386(2)	C(26)-O(2)	1.362(2)

C(26)-C(27)	1.389(3)	N(2)-C(12)-C(11)	134.61(17)
C(27)-C(28)	1.388(3)	N(2)-C(12)-C(1)	118.06(15)
C(29)-O(2)	1.434(2)	C(11)-C(12)-C(1)	107.27(14)
C(29)-C(30)	1.509(3)	C(14)-C(13)-C(18)	120.18(16)
C(30)-C(31)	1.527(3)	C(14)-C(13)-N(1)	119.13(15)
C(31)-C(32)	1.528(3)	C(18)-C(13)-N(1)	120.67(16)
Cl(1)-Zn(1)	2.2044(5)	C(13)-C(14)-C(15)	120.51(16)
Cl(2)-Zn(1)	2.2090(5)	C(14)-C(15)-C(16)	119.02(16)
N(1)-Zn(1)	2.0865(14)	O(1)-C(16)-C(15)	124.31(17)
N(2)-Zn(1)	2.0895(14)	O(1)-C(16)-C(17)	115.39(16)
		C(15)-C(16)-C(17)	120.29(17)
N(1)-C(1)-C(2)	134.93(16)	C(18)-C(17)-C(16)	120.31(17)
N(1)-C(1)-C(12)	117.91(15)	C(17)-C(18)-C(13)	119.40(17)
C(2)-C(1)-C(12)	107.09(14)	O(1)-C(19)-C(20)	106.68(15)
C(3)-C(2)-C(7)	119.09(17)	C(19)-C(20)-C(21)	112.22(16)
C(3)-C(2)-C(1)	134.96(17)	C(22)-C(21)-C(20)	113.44(17)
C(7)-C(2)-C(1)	105.72(15)	C(24)-C(23)-C(28)	120.03(17)
C(2)-C(3)-C(4)	118.44(18)	C(24)-C(23)-N(2)	119.83(16)
C(5)-C(4)-C(3)	122.52(18)	C(28)-C(23)-N(2)	120.12(16)
C(4)-C(5)-C(6)	120.41(17)	C(25)-C(24)-C(23)	119.27(18)
C(7)-C(6)-C(8)	116.71(18)	C(24)-C(25)-C(26)	120.96(18)
C(7)-C(6)-C(5)	116.57(18)	O(2)-C(26)-C(27)	125.00(18)
C(8)-C(6)-C(5)	126.67(18)	O(2)-C(26)-C(25)	115.51(17)
C(6)-C(7)-C(2)	122.94(17)	C(27)-C(26)-C(25)	119.47(17)
C(6)-C(7)-C(11)	122.70(17)	C(28)-C(27)-C(26)	119.54(18)
C(2)-C(7)-C(11)	114.32(16)	C(23)-C(28)-C(27)	120.63(17)
C(9)-C(8)-C(6)	120.76(17)	O(2)-C(29)-C(30)	107.58(15)
C(8)-C(9)-C(10)	121.90(18)	C(29)-C(30)-C(31)	111.35(17)
C(11)-C(10)-C(9)	118.81(18)	C(30)-C(31)-C(32)	112.27(19)
C(10)-C(11)-C(7)	119.07(17)	C(1)-N(1)-C(13)	121.33(15)
C(10)-C(11)-C(12)	135.08(17)	C(1)-N(1)-Zn(1)	111.32(11)
C(7)-C(11)-C(12)	105.59(15)	C(13)-N(1)-Zn(1)	127.34(11)

C(12)-N(2)-C(23)	119.67(15)	N(1)-Zn(1)-Cl(2)	111.66(4)
C(12)-N(2)-Zn(1)	111.10(12)	N(2)-Zn(1)-Cl(2)	112.32(4)
C(23)-N(2)-Zn(1)	129.21(11)	Cl(1)-Zn(1)-Cl(2)	115.555(19)
N(1)-Zn(1)-N(2)	81.28(6)	C(16)-O(1)-C(19)	117.65(14)
N(1)-Zn(1)-Cl(1)	112.61(4)	C(26)-O(2)-C(29)	118.04(15)
N(2)-Zn(1)-Cl(1)	118.60(4)		

---

Table 88: Crystallographic Data and Structure Refinement of **15**.

Empirical formula	$C_{28}H_{24}Cl_2N_2O_4Zn$	
Formula weight	588.76	
Temperature	153(2) K	
Wavelength	1.54184 Å	
Crystal system	Monoclinic	
Space group	$P2_1/c$	
Unit cell dimensions	$a = 12.4510(3)$ Å	$\alpha = 90^\circ$ .
	$b = 11.7454(3)$ Å	$\beta = 95.969(2)^\circ$ .
	$c = 17.4508(4)$ Å	$\gamma = 90^\circ$ .
Volume	$2538.20(11)$ Å <sup>3</sup>	
Z	4	
Density (calculated)	$1.541$ Mg/m <sup>3</sup>	
Absorption coefficient	$3.603$ mm <sup>-1</sup>	
F(000)	1208	
Crystal size	$0.14 \times 0.09 \times 0.07$ mm <sup>3</sup>	
Theta range for data collection	3.57 to 74.33°.	
Index ranges	$-12 \leq h \leq 15$ , $-12 \leq k \leq 14$ , $-19 \leq l \leq 21$	
Reflections collected	9920	
Independent reflections	5030 [R(int) = 0.0284]	
Completeness to theta = 74.33°	97.0 %	
Absorption correction	Semi-empirical from equivalents	
Max. and min. transmission	1.00000 and 0.74906	
Refinement method	Full-matrix least-squares on F <sup>2</sup>	
Data / restraints / parameters	5030 / 0 / 341	
Goodness-of-fit on F <sup>2</sup>	1.037	
Final R indices [I > 2sigma(I)]	R1 = 0.0320, wR2 = 0.0837	
R indices (all data)	R1 = 0.0365, wR2 = 0.0872	
Largest diff. peak and hole	0.476 and -0.425 e.Å <sup>-3</sup>	

Table 89: Atomic coordinates ( $\times 10^4$ ) and equivalent isotropic displacement parameters ( $\text{\AA}^2 \times 10^3$ ) for **15**. U(eq) is defined as one third of the trace of the orthogonalized  $U^{ij}$  tensor.

	x	y	z	U(eq)
C(1)	9328(1)	2375(2)	5182(1)	17(1)
C(2)	9484(2)	1496(2)	5785(1)	18(1)
C(3)	8863(2)	1061(2)	6326(1)	20(1)
C(4)	9287(2)	145(2)	6798(1)	22(1)
C(5)	10290(2)	-313(2)	6732(1)	22(1)
C(6)	10939(2)	108(2)	6173(1)	20(1)
C(7)	10514(2)	1011(2)	5709(1)	18(1)
C(8)	11979(2)	-292(2)	6038(1)	23(1)
C(9)	12516(2)	194(2)	5470(1)	24(1)
C(10)	12070(2)	1098(2)	4999(1)	22(1)
C(11)	11064(1)	1508(2)	5121(1)	18(1)
C(12)	10318(1)	2359(2)	4745(1)	17(1)
C(13)	7626(2)	3234(2)	5341(1)	19(1)
C(14)	6614(2)	3199(2)	4919(1)	21(1)
C(15)	5686(2)	3397(2)	5280(1)	23(1)
C(16)	5776(2)	3650(2)	6064(1)	20(1)
C(17)	6792(2)	3708(2)	6481(1)	21(1)
C(18)	7714(2)	3500(2)	6123(1)	21(1)
C(19)	3860(2)	3774(2)	6077(1)	29(1)
C(20)	11220(2)	3087(2)	3715(1)	18(1)
C(21)	11082(2)	2901(2)	2920(1)	20(1)
C(22)	11966(2)	2961(2)	2501(1)	21(1)
C(23)	12980(2)	3249(2)	2863(1)	22(1)
C(24)	13101(2)	3502(2)	3649(1)	22(1)
C(25)	12218(2)	3420(2)	4071(1)	21(1)
C(26)	14885(2)	3311(2)	2776(1)	31(1)

C(27)	4325(2)	252(2)	3963(1)	23(1)
C(28)	3758(2)	454(2)	3178(1)	28(1)
Cl(1)	7766(1)	3092(1)	2992(1)	22(1)
Cl(2)	9053(1)	5736(1)	3921(1)	24(1)
N(1)	8560(1)	3063(1)	4948(1)	17(1)
N(2)	10306(1)	2988(1)	4142(1)	17(1)
O(1)	4924(1)	3867(1)	6473(1)	25(1)
O(2)	13803(1)	3249(1)	2405(1)	27(1)
O(3)	4419(1)	-821(1)	4162(1)	33(1)
O(4)	4660(1)	1038(1)	4387(1)	30(1)
Zn(1)	8865(1)	3873(1)	3931(1)	17(1)

Table 90: Bond Lengths [ $\text{\AA}$ ] and Bond Angles [ $^\circ$ ] for **15**.

C(1)-N(1)	1.286(2)	C(14)-C(15)	1.391(3)
C(1)-C(2)	1.471(3)	C(15)-C(16)	1.392(3)
C(1)-C(12)	1.516(2)	C(16)-O(1)	1.364(2)
C(2)-C(3)	1.379(3)	C(16)-C(17)	1.394(3)
C(2)-C(7)	1.422(3)	C(17)-C(18)	1.384(3)
C(3)-C(4)	1.423(3)	C(19)-O(1)	1.434(2)
C(4)-C(5)	1.375(3)	C(20)-C(25)	1.387(3)
C(5)-C(6)	1.417(3)	C(20)-C(21)	1.396(3)
C(6)-C(7)	1.404(3)	C(20)-N(2)	1.428(2)
C(6)-C(8)	1.420(3)	C(21)-C(22)	1.385(3)
C(7)-C(11)	1.418(3)	C(22)-C(23)	1.394(3)
C(8)-C(9)	1.375(3)	C(23)-O(2)	1.364(2)
C(9)-C(10)	1.420(3)	C(23)-C(24)	1.396(3)
C(10)-C(11)	1.380(3)	C(24)-C(25)	1.389(3)
C(11)-C(12)	1.471(2)	C(26)-O(2)	1.435(2)
C(12)-N(2)	1.284(2)	C(27)-O(4)	1.228(2)
C(13)-C(14)	1.391(3)	C(27)-O(3)	1.310(3)
C(13)-C(18)	1.394(3)	C(27)-C(28)	1.493(3)
C(13)-N(1)	1.424(2)	Cl(1)-Zn(1)	2.2203(5)

Cl(2)-Zn(1)	2.2016(5)	C(14)-C(15)-C(16)	119.62(18)
N(1)-Zn(1)	2.0838(15)	O(1)-C(16)-C(15)	124.57(17)
N(2)-Zn(1)	2.0730(15)	O(1)-C(16)-C(17)	115.47(17)
		C(15)-C(16)-C(17)	119.95(17)
N(1)-C(1)-C(2)	134.95(17)	C(18)-C(17)-C(16)	120.37(17)
N(1)-C(1)-C(12)	117.68(16)	C(17)-C(18)-C(13)	119.80(17)
C(2)-C(1)-C(12)	107.28(15)	C(25)-C(20)-C(21)	120.09(17)
C(3)-C(2)-C(7)	119.31(17)	C(25)-C(20)-N(2)	120.93(17)
C(3)-C(2)-C(1)	135.02(17)	C(21)-C(20)-N(2)	118.90(16)
C(7)-C(2)-C(1)	105.58(15)	C(22)-C(21)-C(20)	119.64(18)
C(2)-C(3)-C(4)	118.41(17)	C(21)-C(22)-C(23)	120.33(18)
C(5)-C(4)-C(3)	122.18(18)	O(2)-C(23)-C(22)	115.79(17)
C(4)-C(5)-C(6)	120.59(18)	O(2)-C(23)-C(24)	124.41(18)
C(7)-C(6)-C(5)	116.85(17)	C(22)-C(23)-C(24)	119.80(17)
C(7)-C(6)-C(8)	116.71(18)	C(25)-C(24)-C(23)	119.73(18)
C(5)-C(6)-C(8)	126.44(18)	C(20)-C(25)-C(24)	120.21(18)
C(6)-C(7)-C(11)	123.16(17)	O(4)-C(27)-O(3)	123.20(19)
C(6)-C(7)-C(2)	122.64(17)	O(4)-C(27)-C(28)	122.17(19)
C(11)-C(7)-C(2)	114.20(16)	O(3)-C(27)-C(28)	114.62(18)
C(9)-C(8)-C(6)	120.17(18)	C(1)-N(1)-C(13)	123.59(16)
C(8)-C(9)-C(10)	122.52(18)	C(1)-N(1)-Zn(1)	111.22(12)
C(11)-C(10)-C(9)	118.54(18)	C(13)-N(1)-Zn(1)	125.19(12)
C(10)-C(11)-C(7)	118.89(17)	C(12)-N(2)-C(20)	122.17(15)
C(10)-C(11)-C(12)	135.17(18)	C(12)-N(2)-Zn(1)	111.74(12)
C(7)-C(11)-C(12)	105.84(15)	C(20)-N(2)-Zn(1)	125.99(12)
N(2)-C(12)-C(11)	135.17(17)	C(16)-O(1)-C(19)	117.58(15)
N(2)-C(12)-C(1)	117.67(16)	C(23)-O(2)-C(26)	117.54(16)
C(11)-C(12)-C(1)	106.99(15)	N(1)-Zn(1)-N(2)	81.42(6)
C(14)-C(13)-C(18)	119.93(17)	N(2)-Zn(1)-Cl(2)	114.15(4)
C(14)-C(13)-N(1)	118.81(16)	N(1)-Zn(1)-Cl(2)	119.28(4)
C(18)-C(13)-N(1)	121.15(16)	N(2)-Zn(1)-Cl(1)	112.33(4)
C(15)-C(14)-C(13)	120.31(17)	N(1)-Zn(1)-Cl(1)	106.69(4)



Cl(1)-Zn(1)-Cl(2)

117.554(19)

---

Table 91: Crystallographic Data and Structure Refinement of **16**.

Empirical formula	C <sub>28</sub> H <sub>24</sub> Cl <sub>2</sub> N <sub>2</sub> O <sub>2</sub> S <sub>2</sub> Zn	
Formula weight	620.88	
Temperature	100(2) K	
Wavelength	1.54184 Å	
Crystal system	Monoclinic	
Space group	P2 <sub>1</sub> /c	
Unit cell dimensions	a = 13.036(3) Å	α = 90°.
	b = 11.7210(15) Å	β = 98.657(16)°.
	c = 17.716(2) Å	γ = 90°.
Volume	2676.1(8) Å <sup>3</sup>	
Z	4	
Density (calculated)	1.541 Mg/m <sup>3</sup>	
Absorption coefficient	4.813 mm <sup>-1</sup>	
F(000)	1272	
Crystal size	0.070 x 0.030 x 0.010 mm <sup>3</sup>	
Theta range for data collection	3.429 to 67.484°.	
Index ranges	-15 ≤ h ≤ 15, -10 ≤ k ≤ 14, -21 ≤ l ≤ 20	
Reflections collected	16148	
Independent reflections	16148 [R(int) = 0.0000]	
Completeness to theta = 67.684°	99.4 %	
Absorption correction	Semi-empirical from equivalents	
Max. and min. transmission	1.00000 and 0.60099	
Refinement method	Full-matrix least-squares on F <sup>2</sup>	
Data / restraints / parameters	16148 / 528 / 338	
Goodness-of-fit on F <sup>2</sup>	1.088	
Final R indices [I > 2σ(I)]	R1 = 0.1556, wR2 = 0.3454	
R indices (all data)	R1 = 0.3689, wR2 = 0.3854	
Largest diff. peak and hole	0.690 and -0.858 e.Å <sup>-3</sup>	

Table 92: Atomic coordinates ( $\times 10^4$ ) and equivalent isotropic displacement parameters ( $\text{\AA}^2 \times 10^3$ ) for **16**. U(eq) is defined as one third of the trace of the orthogonalized  $U^{ij}$  tensor.

	x	y	z	U(eq)
C(1)	5460(30)	2690(30)	4714(19)	34(6)
C(2)	6140(30)	3530(30)	5098(18)	36(7)
C(3)	7070(30)	4000(30)	4971(19)	44(8)
C(4)	7530(20)	4890(30)	5466(17)	35(7)
C(5)	7070(30)	5250(30)	6016(18)	43(8)
C(6)	6080(30)	4920(20)	6135(19)	39(7)
C(7)	5640(20)	3930(30)	5665(18)	36(7)
C(8)	5470(20)	5260(30)	6690(17)	33(7)
C(9)	4520(20)	4830(30)	6740(18)	42(8)
C(10)	4100(30)	3910(30)	6270(18)	42(8)
C(11)	4650(30)	3570(30)	5730(19)	40(7)
C(12)	4490(30)	2640(30)	5108(19)	37(7)
C(13)	6290(30)	1950(30)	3664(19)	32(6)
C(14)	6070(30)	2180(20)	2893(18)	34(7)
C(15)	6900(20)	2110(20)	2508(18)	28(7)
C(16)	7870(30)	1790(30)	2863(19)	35(7)
C(17)	8020(20)	1540(20)	3635(17)	30(7)
C(18)	7210(20)	1640(20)	4052(18)	28(6)
C(19)	10100(20)	1910(30)	2947(17)	45(9)
C(20)	2840(30)	1770(20)	5224(18)	31(6)
C(21)	1880(20)	1840(20)	4767(18)	32(7)
C(22)	980(30)	1620(20)	5118(18)	42(8)
C(23)	1160(30)	1310(30)	5885(17)	37(7)
C(24)	2130(20)	1270(20)	6313(18)	33(7)
C(25)	2980(30)	1490(20)	5986(18)	32(7)
C(26)	-1070(20)	1300(30)	5733(18)	52(10)

C(27)	9250(30)	4840(30)	3950(20)	43(8)
C(28)	8710(20)	4740(30)	3162(17)	42(8)
N(1)	5390(20)	2060(20)	4064(16)	41(6)
N(2)	3712(19)	1989(19)	4835(13)	24(5)
S(1)	8875(7)	1686(8)	2275(5)	46(3)
S(2)	84(7)	1026(8)	6393(5)	46(3)
Cl(1)	2984(7)	1995(7)	2863(5)	40(2)
Cl(2)	4061(8)	-679(6)	3901(5)	46(3)
Zn(1)	3994(4)	1182(4)	3847(3)	36(1)
O(1)	9530(20)	5916(17)	4188(12)	46(6)
O(2)	9530(20)	4027(18)	4392(14)	55(7)

Table 93: Bond Lengths [ $\text{\AA}$ ] and Bond Angles [ $^\circ$ ] for **16**.

C(1)-N(1)	1.36(4)	C(14)-C(15)	1.36(4)
C(1)-C(2)	1.43(4)	C(15)-C(16)	1.37(4)
C(1)-C(12)	1.53(4)	C(16)-C(17)	1.39(4)
C(2)-C(7)	1.36(4)	C(16)-S(1)	1.80(3)
C(2)-C(3)	1.38(4)	C(17)-C(18)	1.39(4)
C(3)-C(4)	1.44(4)	C(19)-S(1)	1.86(3)
C(4)-C(5)	1.29(4)	C(20)-C(25)	1.37(4)
C(5)-C(6)	1.40(4)	C(20)-C(21)	1.39(4)
C(6)-C(8)	1.41(4)	C(20)-N(2)	1.44(4)
C(6)-C(7)	1.49(4)	C(21)-C(22)	1.43(4)
C(7)-C(11)	1.37(4)	C(22)-C(23)	1.39(4)
C(8)-C(9)	1.36(4)	C(23)-C(24)	1.37(4)
C(9)-C(10)	1.41(4)	C(23)-S(2)	1.81(3)
C(10)-C(11)	1.35(4)	C(24)-C(25)	1.35(4)
C(11)-C(12)	1.54(4)	C(26)-S(2)	1.79(3)
C(12)-N(2)	1.30(4)	C(27)-O(2)	1.25(4)
C(13)-C(18)	1.34(4)	C(27)-O(1)	1.36(3)
C(13)-C(14)	1.38(4)	C(27)-C(28)	1.47(4)
C(13)-N(1)	1.46(4)	N(1)-Zn(1)	2.08(3)

N(2)-Zn(1)	2.07(2)	C(14)-C(15)-C(16)	122(3)
Cl(1)-Zn(1)	2.232(9)	C(15)-C(16)-C(17)	120(3)
Cl(2)-Zn(1)	2.185(8)	C(15)-C(16)-S(1)	117(3)
		C(17)-C(16)-S(1)	123(3)
N(1)-C(1)-C(2)	137(3)	C(18)-C(17)-C(16)	120(3)
N(1)-C(1)-C(12)	114(3)	C(13)-C(18)-C(17)	117(3)
C(2)-C(1)-C(12)	108(3)	C(25)-C(20)-C(21)	124(3)
C(7)-C(2)-C(3)	121(3)	C(25)-C(20)-N(2)	121(3)
C(7)-C(2)-C(1)	105(3)	C(21)-C(20)-N(2)	115(3)
C(3)-C(2)-C(1)	134(3)	C(20)-C(21)-C(22)	118(3)
C(2)-C(3)-C(4)	119(3)	C(23)-C(22)-C(21)	116(3)
C(5)-C(4)-C(3)	120(3)	C(24)-C(23)-C(22)	124(3)
C(4)-C(5)-C(6)	125(3)	C(24)-C(23)-S(2)	116(2)
C(5)-C(6)-C(8)	131(3)	C(22)-C(23)-S(2)	120(3)
C(5)-C(6)-C(7)	115(3)	C(25)-C(24)-C(23)	120(3)
C(8)-C(6)-C(7)	114(3)	C(24)-C(25)-C(20)	118(3)
C(2)-C(7)-C(11)	121(3)	O(2)-C(27)-O(1)	118(3)
C(2)-C(7)-C(6)	120(3)	O(2)-C(27)-C(28)	126(3)
C(11)-C(7)-C(6)	119(3)	O(1)-C(27)-C(28)	116(3)
C(9)-C(8)-C(6)	124(3)	C(1)-N(1)-C(13)	120(3)
C(8)-C(9)-C(10)	121(3)	C(1)-N(1)-Zn(1)	112(2)
C(11)-C(10)-C(9)	116(3)	C(13)-N(1)-Zn(1)	127(2)
C(10)-C(11)-C(7)	125(3)	C(12)-N(2)-C(20)	123(3)
C(10)-C(11)-C(12)	133(3)	C(12)-N(2)-Zn(1)	111(2)
C(7)-C(11)-C(12)	101(3)	C(20)-N(2)-Zn(1)	125(2)
N(2)-C(12)-C(1)	120(3)	C(16)-S(1)-C(19)	104.4(15)
N(2)-C(12)-C(11)	134(3)	C(26)-S(2)-C(23)	106.3(15)
C(1)-C(12)-C(11)	105(3)	N(1)-Zn(1)-N(2)	83.0(10)
C(18)-C(13)-C(14)	126(3)	N(2)-Zn(1)-Cl(2)	115.5(7)
C(18)-C(13)-N(1)	120(3)	N(1)-Zn(1)-Cl(2)	117.3(8)
C(14)-C(13)-N(1)	114(3)	N(2)-Zn(1)-Cl(1)	107.8(7)
C(15)-C(14)-C(13)	115(3)	N(1)-Zn(1)-Cl(1)	109.3(8)

Cl(1)-Zn(1)-Cl(2)      118.4(4)

---

Table 94: Crystallographic Data and Structure Refinement of 17.

Empirical formula	$C_{36}H_{24}Cl_2N_2O_2Zn$	
Formula weight	652.84	
Temperature	100(2) K	
Wavelength	1.54184 Å	
Crystal system	Monoclinic	
Space group	$P2_1/c$	
Unit cell dimensions	$a = 14.0015(9)$ Å	$\alpha = 90^\circ$ .
	$b = 11.7228(9)$ Å	$\beta = 91.996(6)^\circ$ .
	$c = 17.9471(12)$ Å	$\gamma = 90^\circ$ .
Volume	$2944.0(4)$ Å <sup>3</sup>	
Z	4	
Density (calculated)	$1.473$ Mg/m <sup>3</sup>	
Absorption coefficient	$3.122$ mm <sup>-1</sup>	
F(000)	1336	
Crystal size	$0.10 \times 0.03 \times 0.02$ mm <sup>3</sup>	
Theta range for data collection	4.506 to 76.612°.	
Index ranges	$-17 \leq h \leq 17$ , $-14 \leq k \leq 14$ , $-22 \leq l \leq 21$	
Reflections collected	33186	
Independent reflections	6070 [R(int) = 0.1948]	
Completeness to theta = 67.684°	99.9 %	
Absorption correction	Semi-empirical from equivalents	
Max. and min. transmission	1.00000 and 0.89282	
Refinement method	Full-matrix least-squares on F <sup>2</sup>	
Data / restraints / parameters	6070 / 0 / 388	
Goodness-of-fit on F <sup>2</sup>	1.409	
Final R indices [I > 2sigma(I)]	R1 = 0.1160, wR2 = 0.3155	
R indices (all data)	R1 = 0.2048, wR2 = 0.3473	
Largest diff. peak and hole	0.512 and -0.877 e.Å <sup>-3</sup>	

Table 95: Atomic coordinates ( $\times 10^4$ ) and equivalent isotropic displacement parameters ( $\text{\AA}^2 \times 10^3$ ) for **17**.  $U(\text{eq})$  is defined as one third of the trace of the orthogonalized  $U^{ij}$  tensor.

	x	y	z	U(eq)
C(1)	4642(7)	2256(8)	4661(6)	27(2)
C(2)	3972(7)	1387(8)	4927(6)	28(2)
C(3)	3143(8)	900(9)	4649(6)	33(3)
C(4)	2716(8)	38(8)	5065(6)	33(3)
C(5)	3097(8)	-353(8)	5744(7)	37(3)
C(6)	3973(8)	111(8)	6028(6)	31(3)
C(7)	4386(8)	984(8)	5614(6)	27(2)
C(8)	4465(8)	-220(9)	6702(6)	34(3)
C(9)	5330(8)	280(8)	6902(6)	32(3)
C(10)	5742(8)	1153(8)	6476(6)	30(2)
C(11)	5269(7)	1504(8)	5832(6)	28(2)
C(12)	5469(7)	2313(7)	5229(5)	23(2)
C(13)	3894(8)	2901(8)	3544(6)	32(3)
C(14)	4037(8)	2609(8)	2805(6)	28(2)
C(15)	3266(8)	2596(9)	2295(6)	34(3)
C(16)	2364(8)	2904(8)	2529(6)	31(3)
C(17)	2241(8)	3271(8)	3252(6)	32(3)
C(18)	3007(8)	3266(8)	3769(6)	31(3)
C(19)	1537(8)	2223(9)	1443(6)	31(3)
C(20)	1334(8)	2719(9)	761(6)	36(3)
C(21)	1222(8)	2023(10)	130(6)	37(3)
C(22)	1330(8)	851(10)	194(7)	42(3)
C(23)	1539(9)	375(10)	886(7)	43(3)
C(24)	1648(9)	1058(9)	1507(6)	39(3)
C(25)	6978(7)	3151(8)	5573(6)	28(2)
C(26)	7889(8)	2950(9)	5299(7)	38(3)



C(27)	8679(8)	3224(9)	5748(6)	36(3)
C(28)	8559(8)	3706(9)	6445(6)	36(3)
C(29)	7674(8)	3870(9)	6715(6)	32(3)
C(30)	6870(8)	3596(9)	6279(6)	33(3)
C(31)	9521(8)	4108(10)	7557(6)	36(3)
C(32)	10033(9)	5024(11)	7867(8)	49(4)
C(33)	10252(10)	5026(11)	8619(8)	55(4)
C(34)	9954(10)	4135(12)	9063(8)	58(4)
C(35)	9455(9)	3252(12)	8752(7)	48(3)
C(36)	9243(8)	3225(10)	7996(7)	39(3)
Cl(1)	6922(2)	3073(2)	3213(2)	33(1)
Cl(2)	5741(2)	5647(2)	4070(2)	37(1)
N(1)	4685(6)	2868(6)	4077(5)	26(2)
N(2)	6172(6)	2963(7)	5071(5)	27(2)
O(1)	1560(5)	2928(6)	2061(4)	41(2)
O(2)	9401(6)	4118(8)	6789(5)	51(2)
Zn(1)	5954(1)	3787(1)	4047(1)	29(1)

Table 96: Bond Lengths [ $\text{\AA}$ ] and Bond Angles [ $^\circ$ ] for **17**.

C(1)-N(1)	1.273(12)	C(10)-C(11)	1.375(13)
C(1)-C(2)	1.475(14)	C(11)-C(12)	1.474(14)
C(1)-C(12)	1.517(12)	C(12)-N(2)	1.284(13)
C(2)-C(3)	1.371(14)	C(13)-C(18)	1.385(15)
C(2)-C(7)	1.425(13)	C(13)-C(14)	1.391(15)
C(3)-C(4)	1.403(15)	C(13)-N(1)	1.439(12)
C(4)-C(5)	1.392(14)	C(14)-C(15)	1.391(13)
C(5)-C(6)	1.420(14)	C(15)-C(16)	1.392(15)
C(6)-C(7)	1.402(14)	C(16)-O(1)	1.381(11)
C(6)-C(8)	1.425(14)	C(16)-C(17)	1.385(15)
C(7)-C(11)	1.421(14)	C(17)-C(18)	1.393(13)
C(8)-C(9)	1.382(14)	C(19)-C(20)	1.376(14)
C(9)-C(10)	1.412(14)	C(19)-C(24)	1.378(14)

C(19)-O(1)	1.382(12)	C(5)-C(4)-C(3)	123.1(10)
C(20)-C(21)	1.400(14)	C(4)-C(5)-C(6)	119.2(10)
C(21)-C(22)	1.386(15)	C(7)-C(6)-C(5)	117.2(9)
C(22)-C(23)	1.384(16)	C(7)-C(6)-C(8)	116.9(10)
C(23)-C(24)	1.377(15)	C(5)-C(6)-C(8)	125.9(10)
C(25)-C(30)	1.384(14)	C(6)-C(7)-C(11)	122.5(9)
C(25)-C(26)	1.404(16)	C(6)-C(7)-C(2)	122.5(9)
C(25)-N(2)	1.436(11)	C(11)-C(7)-C(2)	114.9(10)
C(26)-C(27)	1.383(14)	C(9)-C(8)-C(6)	120.0(10)
C(27)-C(28)	1.388(16)	C(8)-C(9)-C(10)	122.4(9)
C(28)-C(29)	1.361(16)	C(11)-C(10)-C(9)	118.6(10)
C(28)-O(2)	1.398(12)	C(10)-C(11)-C(7)	119.5(10)
C(29)-C(30)	1.386(13)	C(10)-C(11)-C(12)	135.4(10)
C(31)-C(36)	1.366(15)	C(7)-C(11)-C(12)	105.0(9)
C(31)-O(2)	1.383(13)	N(2)-C(12)-C(11)	135.3(9)
C(31)-C(32)	1.396(16)	N(2)-C(12)-C(1)	116.8(9)
C(32)-C(33)	1.373(17)	C(11)-C(12)-C(1)	107.8(8)
C(33)-C(34)	1.39(2)	C(18)-C(13)-C(14)	120.9(9)
C(34)-C(35)	1.357(18)	C(18)-C(13)-N(1)	119.5(10)
C(35)-C(36)	1.379(15)	C(14)-C(13)-N(1)	119.5(10)
Cl(1)-Zn(1)	2.217(3)	C(15)-C(14)-C(13)	119.7(11)
Cl(2)-Zn(1)	2.201(3)	C(14)-C(15)-C(16)	119.4(11)
N(1)-Zn(1)	2.080(8)	O(1)-C(16)-C(17)	116.0(10)
N(2)-Zn(1)	2.089(8)	O(1)-C(16)-C(15)	123.4(10)
		C(17)-C(16)-C(15)	120.5(9)
N(1)-C(1)-C(2)	134.8(9)	C(16)-C(17)-C(18)	120.3(11)
N(1)-C(1)-C(12)	118.1(9)	C(13)-C(18)-C(17)	119.0(10)
C(2)-C(1)-C(12)	107.0(8)	C(20)-C(19)-C(24)	120.7(10)
C(3)-C(2)-C(7)	119.4(10)	C(20)-C(19)-O(1)	117.3(9)
C(3)-C(2)-C(1)	135.2(10)	C(24)-C(19)-O(1)	121.8(10)
C(7)-C(2)-C(1)	105.3(8)	C(19)-C(20)-C(21)	119.2(10)
C(2)-C(3)-C(4)	118.6(10)	C(22)-C(21)-C(20)	120.1(11)

C(23)-C(22)-C(21)	119.6(11)	C(35)-C(34)-C(33)	119.9(13)
C(24)-C(23)-C(22)	120.3(11)	C(34)-C(35)-C(36)	120.8(13)
C(23)-C(24)-C(19)	120.1(10)	C(31)-C(36)-C(35)	119.6(12)
C(30)-C(25)-C(26)	120.9(9)	C(1)-N(1)-C(13)	120.3(9)
C(30)-C(25)-N(2)	121.7(10)	C(1)-N(1)-Zn(1)	112.2(6)
C(26)-C(25)-N(2)	117.3(9)	C(13)-N(1)-Zn(1)	127.4(7)
C(27)-C(26)-C(25)	118.4(11)	C(12)-N(2)-C(25)	122.9(9)
C(26)-C(27)-C(28)	120.0(11)	C(12)-N(2)-Zn(1)	112.3(6)
C(29)-C(28)-C(27)	121.3(10)	C(25)-N(2)-Zn(1)	124.6(7)
C(29)-C(28)-O(2)	123.9(11)	C(16)-O(1)-C(19)	118.1(8)
C(27)-C(28)-O(2)	114.4(11)	C(31)-O(2)-C(28)	120.6(9)
C(28)-C(29)-C(30)	119.8(11)	N(1)-Zn(1)-N(2)	80.6(3)
C(25)-C(30)-C(29)	119.5(11)	N(1)-Zn(1)-Cl(2)	113.3(2)
C(36)-C(31)-O(2)	123.7(10)	N(2)-Zn(1)-Cl(2)	117.2(2)
C(36)-C(31)-C(32)	120.3(11)	N(1)-Zn(1)-Cl(1)	111.4(2)
O(2)-C(31)-C(32)	115.7(11)	N(2)-Zn(1)-Cl(1)	110.2(2)
C(33)-C(32)-C(31)	119.1(12)	Cl(1)-Zn(1)-Cl(2)	118.23(12)
C(32)-C(33)-C(34)	120.2(12)		

---

Table 97: Crystallographic Data and Structure Refinement of **18**.

Empirical formula	C <sub>24</sub> H <sub>14</sub> Cl <sub>2</sub> F <sub>2</sub> N <sub>2</sub> Zn	
Formula weight	504.64	
Temperature	100(2) K	
Wavelength	0.71075 Å	
Crystal system	Monoclinic	
Space group	P2 <sub>1</sub> /c	
Unit cell dimensions	a = 9.984(3) Å	α = 90°.
	b = 11.965(4) Å	β = 101.504(5)°.
	c = 17.609(7) Å	γ = 90°.
Volume	2061.3(13) Å <sup>3</sup>	
Z	4	
Density (calculated)	1.626 Mg/m <sup>3</sup>	
Absorption coefficient	1.483 mm <sup>-1</sup>	
F(000)	1016	
Crystal size	0.110 x 0.090 x 0.050 mm <sup>3</sup>	
Theta range for data collection	2.071 to 24.999°.	
Index ranges	-9<=h<=11, -14<=k<=14, -20<=l<=20	
Reflections collected	21742	
Independent reflections	3627 [R(int) = 0.0626]	
Completeness to theta = 24.999°	99.9 %	
Absorption correction	Semi-empirical from equivalents	
Max. and min. transmission	1.00000 and 0.7659	
Refinement method	Full-matrix least-squares on F <sup>2</sup>	
Data / restraints / parameters	3627 / 0 / 280	
Goodness-of-fit on F <sup>2</sup>	1.245	
Final R indices [I>2sigma(I)]	R1 = 0.0506, wR2 = 0.0868	
R indices (all data)	R1 = 0.0539, wR2 = 0.0881	
Largest diff. peak and hole	0.444 and -0.516 e.Å <sup>-3</sup>	

Table 98: Atomic coordinates ( $\times 10^4$ ) and equivalent isotropic displacement parameters ( $\text{\AA}^2 \times 10^3$ ) for **18**. U(eq) is defined as one third of the trace of the orthogonalized  $U^{ij}$  tensor.

	x	y	z	U(eq)
C(1)	4271(3)	2639(3)	4678(2)	14(1)
C(2)	4465(4)	3521(3)	4125(2)	15(1)
C(3)	3691(4)	3954(3)	3451(2)	18(1)
C(4)	4214(4)	4878(3)	3093(2)	18(1)
C(5)	5453(4)	5362(3)	3399(2)	19(1)
C(6)	6258(4)	4960(3)	4102(2)	16(1)
C(7)	5734(4)	4039(3)	4448(2)	15(1)
C(8)	7533(4)	5396(3)	4497(2)	21(1)
C(9)	8187(4)	4937(3)	5190(2)	18(1)
C(10)	7639(4)	4027(3)	5538(2)	18(1)
C(11)	6411(4)	3566(3)	5161(2)	16(1)
C(12)	5499(3)	2688(3)	5345(2)	14(1)
C(13)	2212(4)	1629(3)	4131(2)	15(1)
C(14)	975(4)	1359(3)	4345(2)	19(1)
C(15)	-146(4)	1038(3)	3784(2)	20(1)
C(16)	19(4)	973(3)	3027(2)	20(1)
C(17)	1237(4)	1194(3)	2800(2)	19(1)
C(18)	2349(4)	1518(3)	3364(2)	18(1)
C(19)	6667(4)	1921(3)	6549(2)	17(1)
C(20)	6454(4)	2006(3)	7301(2)	20(1)
C(21)	7554(4)	1856(3)	7925(2)	23(1)
C(22)	8806(4)	1594(3)	7761(2)	23(1)
C(23)	9045(4)	1512(3)	7022(2)	21(1)
C(24)	7956(4)	1667(3)	6405(2)	18(1)
N(1)	3347(3)	1901(2)	4732(2)	15(1)
N(2)	5516(3)	2024(2)	5925(2)	16(1)

F(1)	-1071(2)	652(2)	2473(1)	27(1)
F(2)	9868(2)	1397(2)	8367(1)	31(1)
Cl(1)	2379(1)	1918(1)	6529(1)	21(1)
Cl(2)	3786(1)	-725(1)	5854(1)	24(1)
Zn(1)	3716(1)	1116(1)	5811(1)	15(1)

Table 99: Bond Lengths [Å] and Bond Angles [°] for **18**.

C(1)-N(1)	1.293(4)	C(19)-C(24)	1.395(5)
C(1)-C(2)	1.475(5)	C(19)-N(2)	1.428(5)
C(1)-C(12)	1.521(5)	C(20)-C(21)	1.401(5)
C(2)-C(3)	1.381(5)	C(21)-C(22)	1.375(6)
C(2)-C(7)	1.424(5)	C(22)-F(2)	1.367(4)
C(3)-C(4)	1.424(5)	C(22)-C(23)	1.373(5)
C(4)-C(5)	1.375(5)	C(23)-C(24)	1.388(5)
C(5)-C(6)	1.419(5)	N(1)-Zn(1)	2.086(3)
C(6)-C(7)	1.409(5)	N(2)-Zn(1)	2.075(3)
C(6)-C(8)	1.423(5)	Cl(1)-Zn(1)	2.2305(11)
C(7)-C(11)	1.419(5)	Cl(2)-Zn(1)	2.2042(12)
C(8)-C(9)	1.378(5)		
C(9)-C(10)	1.412(5)	N(1)-C(1)-C(2)	136.6(3)
C(10)-C(11)	1.387(5)	N(1)-C(1)-C(12)	116.6(3)
C(11)-C(12)	1.468(5)	C(2)-C(1)-C(12)	106.9(3)
C(12)-N(2)	1.292(5)	C(3)-C(2)-C(7)	118.8(3)
C(13)-C(18)	1.391(5)	C(3)-C(2)-C(1)	135.3(3)
C(13)-C(14)	1.399(5)	C(7)-C(2)-C(1)	105.7(3)
C(13)-N(1)	1.425(5)	C(2)-C(3)-C(4)	118.7(3)
C(14)-C(15)	1.392(5)	C(5)-C(4)-C(3)	122.3(3)
C(15)-C(16)	1.377(5)	C(4)-C(5)-C(6)	120.5(3)
C(16)-F(1)	1.364(4)	C(7)-C(6)-C(5)	116.6(3)
C(16)-C(17)	1.380(5)	C(7)-C(6)-C(8)	116.6(3)
C(17)-C(18)	1.388(5)	C(5)-C(6)-C(8)	126.7(3)
C(19)-C(20)	1.387(5)	C(6)-C(7)-C(11)	122.8(3)

C(6)-C(7)-C(2)	123.0(3)	C(20)-C(19)-N(2)	118.4(3)
C(11)-C(7)-C(2)	114.1(3)	C(24)-C(19)-N(2)	120.6(3)
C(9)-C(8)-C(6)	120.4(3)	C(19)-C(20)-C(21)	119.6(4)
C(8)-C(9)-C(10)	122.4(3)	C(22)-C(21)-C(20)	117.9(4)
C(11)-C(10)-C(9)	118.7(3)	F(2)-C(22)-C(23)	118.3(4)
C(10)-C(11)-C(7)	119.0(3)	F(2)-C(22)-C(21)	118.1(4)
C(10)-C(11)-C(12)	134.9(3)	C(23)-C(22)-C(21)	123.6(4)
C(7)-C(11)-C(12)	105.9(3)	C(22)-C(23)-C(24)	118.4(4)
N(2)-C(12)-C(11)	134.7(3)	C(23)-C(24)-C(19)	119.6(4)
N(2)-C(12)-C(1)	117.9(3)	C(1)-N(1)-C(13)	125.1(3)
C(11)-C(12)-C(1)	107.3(3)	C(1)-N(1)-Zn(1)	112.0(2)
C(18)-C(13)-C(14)	120.1(3)	C(13)-N(1)-Zn(1)	122.9(2)
C(18)-C(13)-N(1)	121.7(3)	C(12)-N(2)-C(19)	122.9(3)
C(14)-C(13)-N(1)	117.8(3)	C(12)-N(2)-Zn(1)	111.8(2)
C(15)-C(14)-C(13)	120.0(3)	C(19)-N(2)-Zn(1)	125.3(2)
C(16)-C(15)-C(14)	117.9(3)	N(1)-Zn(1)-N(2)	81.06(11)
F(1)-C(16)-C(15)	118.5(3)	N(2)-Zn(1)-Cl(2)	119.96(9)
F(1)-C(16)-C(17)	118.0(3)	N(1)-Zn(1)-Cl(2)	118.72(9)
C(15)-C(16)-C(17)	123.5(3)	N(2)-Zn(1)-Cl(1)	108.91(9)
C(16)-C(17)-C(18)	118.1(3)	N(1)-Zn(1)-Cl(1)	107.81(8)
C(17)-C(18)-C(13)	120.2(3)	Cl(1)-Zn(1)-Cl(2)	115.35(4)
C(20)-C(19)-C(24)	120.9(3)		

---

Table 100: Crystallographic Data and Structure Refinement of **20**.

Empirical formula	C <sub>26</sub> H <sub>14</sub> Cl <sub>2</sub> F <sub>6</sub> N <sub>2</sub> O <sub>2</sub> Zn	
Formula weight	636.66	
Temperature	100(2) K	
Wavelength	1.54184 Å	
Crystal system	Triclinic	
Space group	P-1	
Unit cell dimensions	a = 8.1932(8) Å	α = 112.425(13)°.
	b = 12.0306(16) Å	β = 91.392(9)°.
	c = 14.760(2) Å	γ = 109.799(10)°.
Volume	1245.5(3) Å <sup>3</sup>	
Z	2	
Density (calculated)	1.698 Mg/m <sup>3</sup>	
Absorption coefficient	4.024 mm <sup>-1</sup>	
F(000)	636	
Crystal size	0.080 x 0.040 x 0.030 mm <sup>3</sup>	
Theta range for data collection	4.189 to 76.579°.	
Index ranges	-10<=h<=10, -15<=k<=10, -12<=l<=18	
Reflections collected	9457	
Independent reflections	4945 [R(int) = 0.0417]	
Completeness to theta = 67.684°	99.3 %	
Absorption correction	Semi-empirical from equivalents	
Max. and min. transmission	1.00000 and 0.90542	
Refinement method	Full-matrix least-squares on F <sup>2</sup>	
Data / restraints / parameters	4945 / 0 / 352	
Goodness-of-fit on F <sup>2</sup>	1.051	
Final R indices [I>2sigma(I)]	R1 = 0.0480, wR2 = 0.0984	
R indices (all data)	R1 = 0.0672, wR2 = 0.1062	
Largest diff. peak and hole	0.597 and -0.599 e.Å <sup>-3</sup>	



Table 101: Atomic coordinates ( $\times 10^4$ ) and equivalent isotropic displacement parameters ( $\text{\AA}^2 \times 10^3$ ) for **20**.  $U(\text{eq})$  is defined as one third of the trace of the orthogonalized  $U^{ij}$  tensor.

	x	y	z	U(eq)
C(1)	-259(4)	2095(3)	-468(2)	16(1)
C(2)	-1752(4)	899(3)	-603(2)	19(1)
C(3)	-3086(4)	-49(3)	-1384(3)	22(1)
C(4)	-4246(5)	-1124(3)	-1240(3)	27(1)
C(5)	-4088(5)	-1265(3)	-367(3)	24(1)
C(6)	-2709(4)	-317(3)	441(3)	22(1)
C(7)	-1583(4)	750(3)	291(2)	18(1)
C(8)	-2336(5)	-336(3)	1380(3)	24(1)
C(9)	-914(5)	645(3)	2087(3)	24(1)
C(10)	197(5)	1713(3)	1932(3)	23(1)
C(11)	-141(4)	1775(3)	1039(2)	18(1)
C(12)	721(4)	2667(3)	593(2)	17(1)
C(13)	-569(4)	2308(3)	-1975(2)	18(1)
C(14)	235(5)	2002(3)	-2802(3)	24(1)
C(15)	-672(5)	1650(4)	-3743(3)	28(1)
C(16)	-2352(5)	1652(3)	-3823(3)	24(1)
C(17)	-3147(5)	2005(3)	-2998(3)	23(1)
C(18)	-2253(4)	2326(3)	-2071(3)	21(1)
C(19)	-2789(5)	1108(4)	-5572(3)	28(1)
C(20)	2781(4)	4392(3)	1954(2)	18(1)
C(21)	4501(4)	4568(3)	2257(3)	21(1)
C(22)	5225(5)	5201(3)	3273(3)	24(1)
C(23)	4212(5)	5652(3)	3946(3)	23(1)
C(24)	2492(5)	5472(3)	3654(3)	22(1)
C(25)	1777(4)	4838(3)	2644(3)	20(1)
C(26)	6461(5)	7153(4)	5345(3)	30(1)

Cl(1)	4653(1)	3623(1)	-1028(1)	18(1)
Cl(2)	1881(1)	5712(1)	-774(1)	21(1)
N(1)	363(3)	2688(3)	-1010(2)	17(1)
N(2)	2023(3)	3768(3)	911(2)	15(1)
O(1)	-3421(3)	1334(3)	-4722(2)	29(1)
O(2)	4809(3)	6278(2)	4993(2)	28(1)
Zn(1)	2694(1)	4467(1)	-200(1)	17(1)
F(1)	-4047(3)	909(2)	-6272(2)	35(1)
F(2)	-1354(3)	2106(2)	-5520(2)	35(1)
F(3)	-2357(3)	64(2)	-5876(2)	36(1)
F(4)	6904(3)	8001(2)	4940(2)	42(1)
F(5)	7669(3)	6621(2)	5232(2)	41(1)
F(6)	6582(3)	7802(2)	6325(2)	40(1)

Table 102: Bond Lengths [ $\text{\AA}$ ] and Bond Angles [ $^\circ$ ] for **20**.

C(1)-N(1)	1.273(4)	C(13)-C(18)	1.392(5)
C(1)-C(2)	1.477(4)	C(13)-N(1)	1.427(4)
C(1)-C(12)	1.520(4)	C(14)-C(15)	1.396(5)
C(2)-C(3)	1.384(4)	C(15)-C(16)	1.380(5)
C(2)-C(7)	1.407(5)	C(16)-C(17)	1.385(5)
C(3)-C(4)	1.417(5)	C(16)-O(1)	1.416(4)
C(4)-C(5)	1.370(5)	C(17)-C(18)	1.383(5)
C(5)-C(6)	1.422(5)	C(19)-F(1)	1.333(4)
C(6)-C(7)	1.405(5)	C(19)-O(1)	1.335(4)
C(6)-C(8)	1.421(5)	C(19)-F(3)	1.336(4)
C(7)-C(11)	1.431(4)	C(19)-F(2)	1.341(4)
C(8)-C(9)	1.381(5)	C(20)-C(25)	1.388(5)
C(9)-C(10)	1.405(5)	C(20)-C(21)	1.388(4)
C(10)-C(11)	1.375(5)	C(20)-N(2)	1.439(4)
C(11)-C(12)	1.460(5)	C(21)-C(22)	1.400(5)
C(12)-N(2)	1.288(4)	C(22)-C(23)	1.379(5)
C(13)-C(14)	1.385(5)	C(23)-C(24)	1.383(5)

C(23)-O(2)	1.422(4)	C(10)-C(11)-C(12)	134.7(3)
C(24)-C(25)	1.392(4)	C(7)-C(11)-C(12)	105.7(3)
C(26)-F(4)	1.325(5)	N(2)-C(12)-C(11)	134.2(3)
C(26)-F(5)	1.332(4)	N(2)-C(12)-C(1)	118.4(3)
C(26)-F(6)	1.338(4)	C(11)-C(12)-C(1)	107.4(3)
C(26)-O(2)	1.339(4)	C(14)-C(13)-C(18)	120.2(3)
Cl(1)-Zn(1)	2.3135(9)	C(14)-C(13)-N(1)	120.3(3)
Cl(1)-Zn(1)#1	2.5562(10)	C(18)-C(13)-N(1)	119.4(3)
Cl(2)-Zn(1)	2.2411(9)	C(13)-C(14)-C(15)	120.2(3)
N(1)-Zn(1)	2.197(3)	C(16)-C(15)-C(14)	118.6(4)
N(2)-Zn(1)	2.117(3)	C(15)-C(16)-C(17)	121.9(3)
Zn(1)-Cl(1)#1	2.5562(10)	C(15)-C(16)-O(1)	125.0(3)
		C(17)-C(16)-O(1)	113.1(3)
N(1)-C(1)-C(2)	136.0(3)	C(18)-C(17)-C(16)	119.1(3)
N(1)-C(1)-C(12)	117.2(3)	C(17)-C(18)-C(13)	120.0(3)
C(2)-C(1)-C(12)	106.7(3)	F(1)-C(19)-O(1)	107.5(3)
C(3)-C(2)-C(7)	119.1(3)	F(1)-C(19)-F(3)	108.0(3)
C(3)-C(2)-C(1)	134.9(3)	O(1)-C(19)-F(3)	113.4(3)
C(7)-C(2)-C(1)	105.9(3)	F(1)-C(19)-F(2)	108.0(3)
C(2)-C(3)-C(4)	118.2(3)	O(1)-C(19)-F(2)	113.1(3)
C(5)-C(4)-C(3)	122.7(3)	F(3)-C(19)-F(2)	106.7(3)
C(4)-C(5)-C(6)	120.3(3)	C(25)-C(20)-C(21)	120.8(3)
C(7)-C(6)-C(8)	116.5(3)	C(25)-C(20)-N(2)	118.9(3)
C(7)-C(6)-C(5)	116.3(3)	C(21)-C(20)-N(2)	120.3(3)
C(8)-C(6)-C(5)	127.3(3)	C(20)-C(21)-C(22)	119.4(3)
C(6)-C(7)-C(2)	123.4(3)	C(23)-C(22)-C(21)	118.9(3)
C(6)-C(7)-C(11)	122.3(3)	C(22)-C(23)-C(24)	122.3(3)
C(2)-C(7)-C(11)	114.2(3)	C(22)-C(23)-O(2)	123.2(3)
C(9)-C(8)-C(6)	120.6(3)	C(24)-C(23)-O(2)	114.4(3)
C(8)-C(9)-C(10)	122.4(3)	C(23)-C(24)-C(25)	118.5(3)
C(11)-C(10)-C(9)	118.6(3)	C(20)-C(25)-C(24)	120.0(3)
C(10)-C(11)-C(7)	119.5(3)	F(4)-C(26)-F(5)	107.3(3)

F(4)-C(26)-F(6)	108.4(3)	C(19)-O(1)-C(16)	120.9(3)
F(5)-C(26)-F(6)	106.8(3)	C(26)-O(2)-C(23)	118.6(3)
F(4)-C(26)-O(2)	113.6(3)	N(1)-Zn(1)-N(2)	78.07(10)
F(5)-C(26)-O(2)	113.3(3)	N(2)-Zn(1)-Cl(2)	135.57(8)
F(6)-C(26)-O(2)	107.2(3)	N(1)-Zn(1)-Cl(2)	95.83(7)
Zn(1)-Cl(1)-Zn(1)#1	92.00(3)	N(2)-Zn(1)-Cl(1)	109.09(8)
C(1)-N(1)-C(13)	121.2(3)	N(1)-Zn(1)-Cl(1)	94.47(8)
C(1)-N(1)-Zn(1)	112.3(2)	Cl(1)-Zn(1)-Cl(2)	115.27(4)
C(13)-N(1)-Zn(1)	125.8(2)	N(2)-Zn(1)-Cl(1)#1	90.27(7)
C(12)-N(2)-C(20)	118.1(3)	N(1)-Zn(1)-Cl(1)#1	168.27(8)
C(12)-N(2)-Zn(1)	113.6(2)	Cl(1)-Zn(1)-Cl(2)#1	93.46(3)
C(20)-N(2)-Zn(1)	128.3(2)	Cl(1)-Zn(1)-Cl(1)#1	88.00(3)

---

Table 103: Crystallographic Data and Structure Refinement of **21**.

Empirical formula	$C_{52}H_{28}Cl_4F_{12}N_4Zn_2$	
Formula weight	1209.32	
Temperature	100(2) K	
Wavelength	1.54184 Å	
Crystal system	Triclinic	
Space group	P-1	
Unit cell dimensions	$a = 11.9861(17)$ Å	$\alpha = 99.188(9)^\circ$ .
	$b = 14.4270(17)$ Å	$\beta = 102.008(11)^\circ$ .
	$c = 16.0295(14)$ Å	$\gamma = 114.266(13)^\circ$ .
Volume	$2376.4(5)$ Å <sup>3</sup>	
Z	2	
Density (calculated)	$1.690$ Mg/m <sup>3</sup>	
Absorption coefficient	$4.116$ mm <sup>-1</sup>	
F(000)	1208	
Crystal size	$0.10 \times 0.04 \times 0.03$ mm <sup>3</sup>	
Theta range for data collection	2.931 to 67.498°.	
Index ranges	$-14 \leq h \leq 14$ , $-17 \leq k \leq 12$ , $-19 \leq l \leq 19$	
Reflections collected	17656	
Independent reflections	8564 [R(int) = 0.1294]	
Completeness to theta = 67.498°	99.8 %	
Absorption correction	Semi-empirical from equivalents	
Max. and min. transmission	1.00000 and 0.44297	
Refinement method	Full-matrix least-squares on F <sup>2</sup>	
Data / restraints / parameters	8564 / 0 / 667	
Goodness-of-fit on F <sup>2</sup>	1.082	
Final R indices [I > 2sigma(I)]	R1 = 0.1127, wR2 = 0.2856	
R indices (all data)	R1 = 0.1975, wR2 = 0.3387	
Largest diff. peak and hole	0.851 and -1.056 e.Å <sup>-3</sup>	

Table 104: Atomic coordinates ( $\times 10^4$ ) and equivalent isotropic displacement parameters ( $\text{\AA}^2 \times 10^3$ ) for **21**. U(eq) is defined as one third of the trace of the orthogonalized  $U^{ij}$  tensor.

	x	y	z	U(eq)
C(1)	-2452(12)	557(10)	6055(9)	30(3)
C(2)	-3405(13)	944(11)	6082(8)	32(3)
C(3)	-3513(17)	1833(13)	5966(10)	50(4)
C(4)	-4625(17)	1899(14)	5993(11)	58(5)
C(5)	-5596(15)	1144(12)	6191(11)	47(4)
C(6)	-5554(15)	205(12)	6319(10)	44(4)
C(7)	-4458(14)	100(11)	6231(10)	39(3)
C(8)	-6504(16)	-698(15)	6484(11)	58(5)
C(9)	-6339(15)	-1560(13)	6534(11)	49(4)
C(10)	-5233(15)	-1620(12)	6452(9)	44(4)
C(11)	-4262(13)	-768(11)	6311(10)	36(3)
C(12)	-3020(14)	-551(10)	6189(9)	34(3)
C(13)	-679(13)	2024(9)	5941(10)	33(3)
C(14)	-478(14)	2212(10)	5145(10)	36(3)
C(15)	230(15)	3226(12)	5119(11)	46(4)
C(16)	716(15)	4043(11)	5875(10)	41(3)
C(17)	492(14)	3850(11)	6669(10)	42(4)
C(18)	-208(15)	2851(10)	6691(10)	39(3)
C(19)	1606(17)	5173(11)	5886(12)	49(4)
C(20)	-2768(15)	-2077(12)	6285(10)	44(4)
C(21)	-3064(15)	-2944(11)	5605(11)	47(4)
C(22)	-3367(16)	-3903(11)	5795(10)	47(4)
C(23)	-3399(15)	-3995(11)	6664(11)	44(4)
C(24)	-3065(16)	-3114(11)	7315(10)	46(4)
C(25)	-2759(14)	-2146(10)	7127(9)	37(3)
C(26)	-3776(18)	-5045(13)	6844(14)	60(5)

C(27)	3036(12)	983(9)	8785(9)	28(3)
C(28)	4288(13)	1309(10)	8647(9)	31(3)
C(29)	5170(12)	2211(10)	8522(9)	33(3)
C(30)	6332(14)	2245(11)	8411(10)	40(3)
C(31)	6649(14)	1442(10)	8493(10)	38(3)
C(32)	5773(13)	504(11)	8627(9)	35(3)
C(33)	4611(13)	471(9)	8700(9)	32(3)
C(34)	5951(14)	-365(11)	8740(9)	38(3)
C(35)	5021(15)	-1224(12)	8891(10)	42(4)
C(36)	3842(15)	-1267(11)	8929(10)	40(3)
C(37)	3596(13)	-437(9)	8817(8)	27(3)
C(38)	2561(14)	-152(10)	8843(9)	33(3)
C(39)	2651(13)	2471(10)	8838(10)	34(3)
C(40)	2783(15)	3202(11)	9567(10)	42(4)
C(41)	3151(15)	4237(10)	9554(10)	41(3)
C(42)	3290(15)	4525(10)	8789(10)	43(4)
C(43)	3087(15)	3784(10)	8037(10)	41(3)
C(44)	2732(14)	2728(10)	8052(9)	37(3)
C(45)	3699(17)	5634(12)	8762(12)	53(4)
C(46)	912(13)	-1764(9)	8841(10)	33(3)
C(47)	785(13)	-2089(9)	9594(9)	30(3)
C(48)	277(14)	-3170(11)	9525(9)	38(3)
C(49)	-69(15)	-3882(11)	8706(10)	39(3)
C(50)	35(15)	-3543(11)	7971(10)	42(3)
C(51)	562(14)	-2463(10)	8043(10)	39(3)
C(52)	-572(17)	-5051(12)	8647(11)	51(4)
Cl(1)	-1355(3)	-1139(3)	4408(2)	37(1)
Cl(2)	590(4)	-593(3)	6876(2)	41(1)
Cl(3)	-721(3)	850(3)	8228(2)	34(1)
Cl(4)	1316(3)	1111(2)	10619(2)	33(1)
F(1)	2854(10)	5442(8)	6224(8)	73(3)
F(2)	1383(11)	5888(7)	6371(7)	67(3)

F(3)	1459(10)	5312(7)	5067(7)	59(3)
F(4)	-3456(11)	-4998(7)	7685(7)	65(3)
F(5)	-3211(11)	-5571(7)	6441(8)	69(3)
F(6)	-5024(10)	-5704(7)	6480(7)	64(3)
F(7)	2838(10)	5822(7)	8278(8)	79(4)
F(8)	4721(12)	6008(8)	8437(9)	89(4)
F(9)	4127(12)	6323(7)	9558(7)	76(4)
F(10)	-1291(10)	-5664(6)	7823(6)	55(2)
F(11)	-1243(11)	-5331(7)	9221(7)	63(3)
F(12)	412(10)	-5308(7)	8881(7)	64(3)
N(1)	-1355(11)	929(8)	5973(8)	35(3)
N(2)	-2366(12)	-1041(9)	6126(8)	37(3)
N(3)	2319(11)	1414(8)	8902(7)	30(2)
N(4)	1419(10)	-649(8)	8891(7)	28(2)
Zn(1)	-563(2)	-143(1)	5889(1)	34(1)
Zn(2)	508(2)	317(1)	9081(1)	33(1)

Table 105: Bond Lengths [ $\text{\AA}$ ] and Bond Angles [ $^\circ$ ] for **21**.

C(1)-N(1)	1.245(16)	C(11)-C(12)	1.453(19)
C(1)-C(2)	1.468(18)	C(12)-N(2)	1.261(17)
C(1)-C(12)	1.529(17)	C(13)-C(18)	1.377(19)
C(2)-C(3)	1.378(19)	C(13)-C(14)	1.395(18)
C(2)-C(7)	1.445(19)	C(13)-N(1)	1.465(15)
C(3)-C(4)	1.38(2)	C(14)-C(15)	1.368(18)
C(4)-C(5)	1.37(2)	C(15)-C(16)	1.37(2)
C(5)-C(6)	1.42(2)	C(16)-C(17)	1.40(2)
C(6)-C(7)	1.42(2)	C(16)-C(19)	1.53(2)
C(6)-C(8)	1.44(2)	C(17)-C(18)	1.348(19)
C(7)-C(11)	1.385(19)	C(19)-F(1)	1.342(19)
C(8)-C(9)	1.35(2)	C(19)-F(2)	1.340(18)
C(9)-C(10)	1.40(2)	C(19)-F(3)	1.345(19)
C(10)-C(11)	1.39(2)	C(20)-C(25)	1.368(19)



C(20)-C(21)	1.38(2)	C(42)-C(45)	1.480(18)
C(20)-N(2)	1.452(17)	C(43)-C(44)	1.409(18)
C(21)-C(22)	1.381(19)	C(45)-F(7)	1.30(2)
C(22)-C(23)	1.43(2)	C(45)-F(9)	1.335(19)
C(23)-C(24)	1.36(2)	C(45)-F(8)	1.37(2)
C(23)-C(26)	1.49(2)	C(46)-C(47)	1.378(18)
C(24)-C(25)	1.391(18)	C(46)-C(51)	1.36(2)
C(26)-F(4)	1.31(2)	C(46)-N(4)	1.448(15)
C(26)-F(6)	1.33(2)	C(47)-C(48)	1.397(17)
C(26)-F(5)	1.38(2)	C(48)-C(49)	1.39(2)
C(27)-N(3)	1.278(16)	C(49)-C(50)	1.355(18)
C(27)-C(28)	1.453(18)	C(49)-C(52)	1.519(19)
C(27)-C(38)	1.523(17)	C(50)-C(51)	1.394(18)
C(28)-C(29)	1.376(17)	C(52)-F(10)	1.340(19)
C(28)-C(33)	1.422(18)	C(52)-F(11)	1.347(17)
C(29)-C(30)	1.423(19)	C(52)-F(12)	1.37(2)
C(30)-C(31)	1.376(19)	Cl(1)-Zn(1)	2.337(4)
C(31)-C(32)	1.414(19)	Cl(1)-Zn(1)#1	2.484(4)
C(32)-C(34)	1.388(19)	Cl(2)-Zn(1)	2.234(4)
C(32)-C(33)	1.403(19)	Cl(3)-Zn(2)	2.249(4)
C(33)-C(37)	1.448(17)	Cl(4)-Zn(2)	2.350(4)
C(34)-C(35)	1.38(2)	Cl(4)-Zn(2)#2	2.512(4)
C(35)-C(36)	1.40(2)	N(1)-Zn(1)	2.121(11)
C(36)-C(37)	1.375(17)	N(2)-Zn(1)	2.166(12)
C(37)-C(38)	1.464(18)	N(3)-Zn(2)	2.209(10)
C(38)-N(4)	1.283(17)	N(4)-Zn(2)	2.117(10)
C(39)-C(44)	1.380(18)	Zn(1)-Cl(1)#1	2.484(4)
C(39)-C(40)	1.376(19)	Zn(2)-Cl(4)#2	2.512(4)
C(39)-N(3)	1.437(15)		
C(40)-C(41)	1.377(18)	N(1)-C(1)-C(2)	135.1(12)
C(41)-C(42)	1.38(2)	N(1)-C(1)-C(12)	118.1(12)
C(42)-C(43)	1.38(2)	C(2)-C(1)-C(12)	106.8(11)

C(3)-C(2)-C(7)	119.2(14)	F(1)-C(19)-F(3)	106.1(14)
C(3)-C(2)-C(1)	135.8(14)	F(2)-C(19)-F(3)	106.8(12)
C(7)-C(2)-C(1)	104.9(11)	F(1)-C(19)-C(16)	112.9(12)
C(2)-C(3)-C(4)	119.4(16)	F(2)-C(19)-C(16)	111.7(13)
C(5)-C(4)-C(3)	122.4(16)	F(3)-C(19)-C(16)	112.2(13)
C(4)-C(5)-C(6)	121.3(14)	C(25)-C(20)-C(21)	122.0(14)
C(7)-C(6)-C(5)	116.5(15)	C(25)-C(20)-N(2)	118.1(14)
C(7)-C(6)-C(8)	114.0(14)	C(21)-C(20)-N(2)	119.8(14)
C(5)-C(6)-C(8)	129.4(14)	C(22)-C(21)-C(20)	118.1(15)
C(11)-C(7)-C(6)	124.8(13)	C(21)-C(22)-C(23)	120.6(14)
C(11)-C(7)-C(2)	114.2(13)	C(24)-C(23)-C(22)	119.1(13)
C(6)-C(7)-C(2)	120.9(14)	C(24)-C(23)-C(26)	121.3(15)
C(9)-C(8)-C(6)	121.6(15)	C(22)-C(23)-C(26)	119.6(15)
C(8)-C(9)-C(10)	122.2(15)	C(23)-C(24)-C(25)	120.4(14)
C(11)-C(10)-C(9)	119.4(15)	C(20)-C(25)-C(24)	119.7(14)
C(10)-C(11)-C(7)	118.0(13)	F(4)-C(26)-F(6)	108.6(15)
C(10)-C(11)-C(12)	134.9(13)	F(4)-C(26)-F(5)	107.1(14)
C(7)-C(11)-C(12)	107.1(12)	F(6)-C(26)-F(5)	102.7(15)
N(2)-C(12)-C(11)	137.1(13)	F(4)-C(26)-C(23)	114.1(16)
N(2)-C(12)-C(1)	115.9(12)	F(6)-C(26)-C(23)	113.1(15)
C(11)-C(12)-C(1)	106.9(11)	F(5)-C(26)-C(23)	110.4(14)
C(18)-C(13)-C(14)	120.5(12)	N(3)-C(27)-C(28)	136.5(11)
C(18)-C(13)-N(1)	120.6(12)	N(3)-C(27)-C(38)	116.4(11)
C(14)-C(13)-N(1)	118.8(12)	C(28)-C(27)-C(38)	107.0(11)
C(15)-C(14)-C(13)	119.6(14)	C(29)-C(28)-C(33)	118.1(12)
C(14)-C(15)-C(16)	119.5(14)	C(29)-C(28)-C(27)	134.8(12)
C(17)-C(16)-C(15)	120.7(14)	C(33)-C(28)-C(27)	107.1(11)
C(17)-C(16)-C(19)	118.6(14)	C(28)-C(29)-C(30)	118.7(12)
C(15)-C(16)-C(19)	120.6(14)	C(31)-C(30)-C(29)	122.4(12)
C(18)-C(17)-C(16)	119.7(14)	C(30)-C(31)-C(32)	120.5(13)
C(17)-C(18)-C(13)	120.0(14)	C(34)-C(32)-C(33)	116.1(13)
F(1)-C(19)-F(2)	106.7(14)	C(34)-C(32)-C(31)	127.7(13)

C(33)-C(32)-C(31)	116.1(12)	C(46)-C(47)-C(48)	118.5(12)
C(32)-C(33)-C(28)	124.1(12)	C(49)-C(48)-C(47)	119.4(12)
C(32)-C(33)-C(37)	123.3(12)	C(50)-C(49)-C(48)	120.9(13)
C(28)-C(33)-C(37)	112.6(12)	C(50)-C(49)-C(52)	120.2(14)
C(35)-C(34)-C(32)	121.7(13)	C(48)-C(49)-C(52)	118.9(12)
C(34)-C(35)-C(36)	121.7(13)	C(49)-C(50)-C(51)	119.6(14)
C(37)-C(36)-C(35)	119.8(13)	C(46)-C(51)-C(50)	119.8(13)
C(36)-C(37)-C(33)	117.2(12)	F(10)-C(52)-F(11)	109.8(13)
C(36)-C(37)-C(38)	136.9(13)	F(10)-C(52)-F(12)	106.5(13)
C(33)-C(37)-C(38)	105.7(11)	F(11)-C(52)-F(12)	104.6(13)
N(4)-C(38)-C(37)	133.9(12)	F(10)-C(52)-C(49)	112.1(13)
N(4)-C(38)-C(27)	118.7(11)	F(11)-C(52)-C(49)	111.9(13)
C(37)-C(38)-C(27)	107.4(12)	F(12)-C(52)-C(49)	111.6(14)
C(44)-C(39)-C(40)	120.8(12)	Zn(1)-Cl(1)-Zn(1)#1	90.04(13)
C(44)-C(39)-N(3)	121.3(12)	Zn(2)-Cl(4)-Zn(2)#2	92.94(13)
C(40)-C(39)-N(3)	117.7(12)	C(1)-N(1)-C(13)	121.8(11)
C(41)-C(40)-C(39)	120.1(14)	C(1)-N(1)-Zn(1)	114.8(9)
C(40)-C(41)-C(42)	120.0(14)	C(13)-N(1)-Zn(1)	123.4(8)
C(41)-C(42)-C(43)	120.3(12)	C(12)-N(2)-C(20)	121.2(12)
C(41)-C(42)-C(45)	121.0(14)	C(12)-N(2)-Zn(1)	114.0(9)
C(43)-C(42)-C(45)	118.6(14)	C(20)-N(2)-Zn(1)	124.6(9)
C(42)-C(43)-C(44)	119.8(14)	C(27)-N(3)-C(39)	121.4(11)
C(39)-C(44)-C(43)	118.6(13)	C(27)-N(3)-Zn(2)	112.6(8)
F(7)-C(45)-F(9)	105.3(14)	C(39)-N(3)-Zn(2)	125.8(9)
F(7)-C(45)-F(8)	104.5(14)	C(38)-N(4)-C(46)	118.7(11)
F(9)-C(45)-F(8)	103.0(14)	C(38)-N(4)-Zn(2)	113.9(8)
F(7)-C(45)-C(42)	116.3(15)	C(46)-N(4)-Zn(2)	127.3(8)
F(9)-C(45)-C(42)	114.0(14)	N(1)-Zn(1)-N(2)	77.0(4)
F(8)-C(45)-C(42)	112.4(14)	N(1)-Zn(1)-Cl(2)	134.8(3)
C(47)-C(46)-C(51)	121.8(11)	N(2)-Zn(1)-Cl(2)	94.9(3)
C(47)-C(46)-N(4)	119.6(12)	N(1)-Zn(1)-Cl(1)	106.7(3)
C(51)-C(46)-N(4)	118.6(12)	N(2)-Zn(1)-Cl(1)	91.9(3)

Cl(1)-Zn(1)-Cl(2)	118.11(14)	N(4)-Zn(2)-Cl(4)	103.3(3)
N(1)-Zn(1)-Cl(1)#1	92.3(3)	N(3)-Zn(2)-Cl(4)	90.8(3)
N(2)-Zn(1)-Cl(1)#1	169.2(3)	Cl(3)-Zn(2)-Cl(4)	118.84(13)
Cl(1)-Zn(1)-Cl(2)#1	93.60(14)	N(4)-Zn(2)-Cl(4)#2	92.5(3)
Cl(1)-Zn(1)-Cl(1)#1	89.96(13)	N(3)-Zn(2)-Cl(4)#2	169.2(3)
N(4)-Zn(2)-N(3)	77.7(4)	Cl(3)-Zn(2)-Cl(4)#2	95.68(13)
N(4)-Zn(2)-Cl(3)	137.4(3)	Cl(4)-Zn(2)-Cl(4)#2	87.06(13)
N(3)-Zn(2)-Cl(3)	94.7(3)		

---

Table 106: Crystallographic Data and Structure Refinement of **14-DCM**.

Empirical formula	$C_{33}H_{34}Cl_4N_2O_2Zn$	
Formula weight	697.79	
Temperature	100(2) K	
Wavelength	0.71075 Å	
Crystal system	Monoclinic	
Space group	$P2_1/n$	
Unit cell dimensions	$a = 17.490(3)$ Å	$\alpha = 90^\circ$ .
	$b = 11.6120(17)$ Å	$\beta = 117.505(3)^\circ$ .
	$c = 17.926(3)$ Å	$\gamma = 90^\circ$ .
Volume	$3229.2(8)$ Å <sup>3</sup>	
Z	4	
Density (calculated)	$1.435$ Mg/m <sup>3</sup>	
Absorption coefficient	$1.124$ mm <sup>-1</sup>	
F(000)	1440	
Crystal size	$0.560 \times 0.220 \times 0.200$ mm <sup>3</sup>	
Theta range for data collection	3.105 to 24.996°.	
Index ranges	$-20 \leq h \leq 20$ , $-13 \leq k \leq 13$ , $-21 \leq l \leq 21$	
Reflections collected	27165	
Independent reflections	5671 [R(int) = 0.0660]	
Completeness to theta = 25.242°	97.4 %	
Absorption correction	Semi-empirical from equivalents	
Max. and min. transmission	1.00000 and 0.7151	
Refinement method	Full-matrix least-squares on F <sup>2</sup>	
Data / restraints / parameters	5671 / 93 / 409	
Goodness-of-fit on F <sup>2</sup>	1.000	
Final R indices [I > 2sigma(I)]	R1 = 0.0761, wR2 = 0.1944	
R indices (all data)	R1 = 0.0826, wR2 = 0.2013	
Largest diff. peak and hole	2.068 and -2.158 e.Å <sup>-3</sup>	

Table 107: Atomic coordinates ( $\times 10^4$ ) and equivalent isotropic displacement parameters ( $\text{\AA}^2 \times 10^3$ ) for **14-DCM**.  $U(\text{eq})$  is defined as one third of the trace of the orthogonalized  $U^{\text{ij}}$  tensor.

	x	y	z	U(eq)
C(1)	4843(3)	2662(4)	9546(3)	17(1)
C(2)	5426(3)	3565(4)	9511(3)	18(1)
C(3)	5552(3)	4066(4)	8878(3)	21(1)
C(4)	6151(3)	4989(5)	9091(3)	24(1)
C(5)	6604(3)	5402(5)	9899(4)	24(1)
C(6)	6472(3)	4921(4)	10559(3)	19(1)
C(7)	5879(3)	4001(4)	10346(3)	17(1)
C(8)	6864(3)	5285(4)	11413(3)	22(1)
C(9)	6651(3)	4761(4)	11985(3)	22(1)
C(10)	6051(3)	3846(4)	11755(3)	20(1)
C(11)	5665(3)	3456(4)	10936(3)	18(1)
C(12)	4984(3)	2607(4)	10445(3)	17(1)
C(13)	4111(3)	1978(4)	8137(3)	21(1)
C(14)	3298(3)	2223(5)	7497(3)	22(1)
C(15)	3142(4)	2229(5)	6660(3)	25(1)
C(16)	3808(4)	1938(5)	6476(3)	25(1)
C(17)	4618(4)	1633(5)	7122(3)	27(1)
C(18)	4772(4)	1658(5)	7950(3)	24(1)
C(19)	2933(4)	2366(6)	5011(4)	39(2)
C(20)	3038(6)	2391(9)	4221(4)	63(2)
C(21)	2266(8)	2733(12)	3458(6)	92(4)
C(22)	2059(7)	3952(11)	3495(7)	84(3)
C(23)	4601(3)	1754(4)	11429(3)	20(1)
C(24)	3885(4)	1867(5)	11577(4)	30(1)
C(25)	3995(4)	1733(6)	12390(4)	40(2)
C(26)	4806(4)	1453(6)	13049(4)	33(1)

C(27)	5504(4)	1266(5)	12888(3)	26(1)
C(28)	5398(3)	1425(4)	12075(3)	21(1)
C(29)	5698(5)	1272(7)	14539(4)	49(2)
C(30)	5595(7)	1555(10)	15329(5)	74(3)
C(31)	6374(10)	1813(17)	16069(8)	130(6)
C(32)	6898(8)	833(16)	16313(10)	136(7)
N(1)	4257(3)	2015(4)	8995(3)	18(1)
N(2)	4486(3)	1936(4)	10599(3)	19(1)
O(1)	3731(3)	1927(4)	5678(2)	36(1)
O(2)	4851(3)	1386(5)	13831(3)	46(1)
Cl(2)	3635(1)	-762(1)	9510(1)	29(1)
Cl(1)	2268(1)	1908(1)	9038(1)	28(1)
Zn(1)	3573(1)	1133(1)	9507(1)	17(1)
Cl(3)	4156(5)	5258(5)	5167(3)	105(2)
C(34)	4553(14)	5210(20)	6191(11)	95(4)
Cl(5)	5578(7)	4639(10)	6884(5)	152(3)
Cl(4)	4339(4)	4707(8)	6503(4)	111(2)
C(33)	5113(9)	5622(13)	6783(9)	48(3)
Cl(6)	6108(5)	5088(12)	6905(6)	172(4)

Table 108: Bond Lengths [ $\text{\AA}$ ] and Bond Angles [ $^\circ$ ] for **14-DCM**.

C(1)-N(1)	1.287(7)	C(8)-C(9)	1.383(8)
C(1)-C(2)	1.483(7)	C(9)-C(10)	1.414(7)
C(1)-C(12)	1.516(7)	C(10)-C(11)	1.379(7)
C(2)-C(3)	1.380(7)	C(11)-C(12)	1.482(7)
C(2)-C(7)	1.425(7)	C(12)-N(2)	1.290(7)
C(3)-C(4)	1.422(8)	C(13)-C(14)	1.382(7)
C(4)-C(5)	1.376(8)	C(13)-C(18)	1.395(7)
C(5)-C(6)	1.421(7)	C(13)-N(1)	1.438(6)
C(6)-C(7)	1.413(7)	C(14)-C(15)	1.396(7)
C(6)-C(8)	1.423(7)	C(15)-C(16)	1.391(8)
C(7)-C(11)	1.423(7)	C(16)-O(1)	1.374(6)

C(16)-C(17)	1.400(8)	C(7)-C(2)-C(1)	105.4(4)
C(17)-C(18)	1.381(8)	C(2)-C(3)-C(4)	118.3(5)
C(19)-O(1)	1.448(7)	C(5)-C(4)-C(3)	122.6(5)
C(19)-C(20)	1.510(9)	C(4)-C(5)-C(6)	120.3(5)
C(20)-C(21)	1.465(12)	C(7)-C(6)-C(5)	116.9(5)
C(21)-C(22)	1.470(16)	C(7)-C(6)-C(8)	116.4(5)
C(23)-C(28)	1.392(7)	C(5)-C(6)-C(8)	126.6(5)
C(23)-C(24)	1.401(8)	C(6)-C(7)-C(11)	123.2(5)
C(23)-N(2)	1.423(6)	C(6)-C(7)-C(2)	122.4(5)
C(24)-C(25)	1.387(8)	C(11)-C(7)-C(2)	114.5(4)
C(25)-C(26)	1.401(9)	C(9)-C(8)-C(6)	120.3(5)
C(26)-O(2)	1.369(7)	C(8)-C(9)-C(10)	122.2(5)
C(26)-C(27)	1.396(9)	C(11)-C(10)-C(9)	119.3(5)
C(27)-C(28)	1.393(7)	C(10)-C(11)-C(7)	118.6(5)
C(29)-O(2)	1.444(9)	C(10)-C(11)-C(12)	135.6(5)
C(29)-C(30)	1.543(10)	C(7)-C(11)-C(12)	105.6(4)
C(30)-C(31)	1.427(16)	N(2)-C(12)-C(11)	135.4(5)
C(31)-C(32)	1.40(2)	N(2)-C(12)-C(1)	117.3(4)
N(1)-Zn(1)	2.083(4)	C(11)-C(12)-C(1)	107.1(4)
N(2)-Zn(1)	2.088(4)	C(14)-C(13)-C(18)	120.3(5)
Cl(2)-Zn(1)	2.2026(15)	C(14)-C(13)-N(1)	119.2(5)
Cl(1)-Zn(1)	2.2265(14)	C(18)-C(13)-N(1)	120.5(5)
Cl(3)-C(34)	1.636(18)	C(13)-C(14)-C(15)	120.6(5)
C(34)-Cl(5)	1.772(16)	C(16)-C(15)-C(14)	118.9(5)
Cl(4)-C(33)	1.608(16)	O(1)-C(16)-C(15)	124.0(5)
C(33)-Cl(6)	1.763(14)	O(1)-C(16)-C(17)	115.7(5)
		C(15)-C(16)-C(17)	120.3(5)
N(1)-C(1)-C(2)	134.4(5)	C(18)-C(17)-C(16)	120.2(5)
N(1)-C(1)-C(12)	118.2(4)	C(17)-C(18)-C(13)	119.5(5)
C(2)-C(1)-C(12)	107.3(4)	O(1)-C(19)-C(20)	107.0(6)
C(3)-C(2)-C(7)	119.4(5)	C(21)-C(20)-C(19)	114.9(8)
C(3)-C(2)-C(1)	134.9(5)	C(22)-C(21)-C(20)	111.1(10)



C(28)-C(23)-C(24)	120.4(5)	C(13)-N(1)-Zn(1)	127.0(3)
C(28)-C(23)-N(2)	121.0(5)	C(12)-N(2)-C(23)	122.0(4)
C(24)-C(23)-N(2)	118.5(5)	C(12)-N(2)-Zn(1)	111.6(3)
C(25)-C(24)-C(23)	119.1(5)	C(23)-N(2)-Zn(1)	126.3(3)
C(24)-C(25)-C(26)	120.5(6)	C(16)-O(1)-C(19)	116.8(5)
O(2)-C(26)-C(27)	124.1(6)	C(26)-O(2)-C(29)	117.1(5)
O(2)-C(26)-C(25)	115.7(5)	N(1)-Zn(1)-N(2)	81.24(16)
C(27)-C(26)-C(25)	120.2(5)	N(1)-Zn(1)-Cl(2)	117.04(12)
C(28)-C(27)-C(26)	119.3(5)	N(2)-Zn(1)-Cl(2)	115.36(12)
C(27)-C(28)-C(23)	120.4(5)	N(1)-Zn(1)-Cl(1)	109.42(12)
O(2)-C(29)-C(30)	106.3(7)	N(2)-Zn(1)-Cl(1)	112.35(12)
C(31)-C(30)-C(29)	115.7(9)	Cl(1)-Zn(1)-Cl(2)	116.43(5)
C(32)-C(31)-C(30)	109.0(15)	Cl(3)-C(34)-Cl(5)	124.6(13)
C(1)-N(1)-C(13)	121.6(4)	Cl(4)-C(33)-Cl(6)	116.6(9)
C(1)-N(1)-Zn(1)	111.4(3)		

---

Table 109: Crystallographic Data and Structure Refinement of **15-DCM**.

Empirical formula	$C_{27}H_{22}Cl_4N_2O_2Zn$	
Formula weight	613.63	
Temperature	153(2) K	
Wavelength	0.71075 Å	
Crystal system	Monoclinic	
Space group	$P2_1/c$	
Unit cell dimensions	$a = 13.840(5)$ Å	$\alpha = 90^\circ$ .
	$b = 11.647(4)$ Å	$\beta = 111.446(4)^\circ$ .
	$c = 17.844(6)$ Å	$\gamma = 90^\circ$ .
Volume	$2677.2(15)$ Å <sup>3</sup>	
Z	4	
Density (calculated)	$1.522$ Mg/m <sup>3</sup>	
Absorption coefficient	$1.345$ mm <sup>-1</sup>	
F(000)	1248	
Crystal size	0.140 x 0.090 x 0.070 mm <sup>3</sup>	
Theta range for data collection	2.136 to 27.474°.	
Index ranges	-17<=h<=17, -13<=k<=15, -22<=l<=23	
Reflections collected	20087	
Independent reflections	6116 [R(int) = 0.0522]	
Completeness to theta = 25.242°	99.8 %	
Absorption correction	Semi-empirical from equivalents	
Max. and min. transmission	1.00000 and 0.5110	
Refinement method	Full-matrix least-squares on F <sup>2</sup>	
Data / restraints / parameters	6116 / 0 / 327	
Goodness-of-fit on F <sup>2</sup>	1.045	
Final R indices [I>2sigma(I)]	R1 = 0.0348, wR2 = 0.0888	
R indices (all data)	R1 = 0.0389, wR2 = 0.0918	
Largest diff. peak and hole	0.688 and -0.649 e.Å <sup>-3</sup>	

Table 110: Atomic coordinates ( $\times 10^4$ ) and equivalent isotropic displacement parameters ( $\text{\AA}^2 \times 10^3$ ) for **15-DCM**.  $U(\text{eq})$  is defined as one third of the trace of the orthogonalized  $U^{\text{ij}}$  tensor.

	x	y	z	U(eq)
C(1)	4499(1)	2602(2)	5110(1)	14(1)
C(2)	4700(1)	3464(2)	5752(1)	14(1)
C(3)	4169(1)	3857(2)	6223(1)	16(1)
C(4)	4578(2)	4796(2)	6749(1)	18(1)
C(5)	5488(2)	5335(2)	6800(1)	18(1)
C(6)	6047(1)	4969(2)	6315(1)	16(1)
C(7)	5633(1)	4027(2)	5804(1)	14(1)
C(8)	6963(1)	5473(2)	6280(1)	18(1)
C(9)	7393(2)	5059(2)	5746(1)	19(1)
C(10)	6967(1)	4121(2)	5232(1)	17(1)
C(11)	6089(1)	3593(2)	5267(1)	14(1)
C(12)	5389(1)	2673(2)	4808(1)	13(1)
C(13)	2924(1)	1664(2)	5006(1)	15(1)
C(14)	1919(1)	1626(2)	4434(1)	19(1)
C(15)	1091(1)	1409(2)	4674(1)	23(1)
C(16)	1269(2)	1192(2)	5481(1)	19(1)
C(17)	2275(2)	1157(2)	6045(1)	17(1)
C(18)	3101(1)	1397(2)	5804(1)	16(1)
C(19)	531(2)	957(2)	6496(1)	28(1)
C(20)	6216(1)	1984(2)	3950(1)	14(1)
C(21)	6029(1)	2202(2)	3144(1)	16(1)
C(22)	6852(1)	2225(2)	2869(1)	18(1)
C(23)	7852(1)	2000(2)	3405(1)	17(1)
C(24)	8032(1)	1726(2)	4207(1)	18(1)
C(25)	7215(1)	1717(2)	4479(1)	17(1)
C(26)	8562(2)	2298(2)	2378(1)	28(1)

C(27)	1138(2)	-115(2)	1326(2)	32(1)
N(1)	3760(1)	1902(1)	4745(1)	13(1)
N(2)	5365(1)	2015(1)	4224(1)	14(1)
O(1)	398(1)	1017(1)	5659(1)	25(1)
O(2)	8717(1)	2027(1)	3199(1)	24(1)
Cl(1)	3962(1)	-767(1)	3766(1)	24(1)
Cl(2)	2940(1)	1881(1)	2610(1)	19(1)
Cl(3)	243(1)	176(1)	1793(1)	51(1)
Cl(4)	1093(1)	928(1)	599(1)	40(1)
Zn(1)	3968(1)	1122(1)	3771(1)	14(1)

Table 111: Bond Lengths [Å] and Bond Angles [°] for **15-DCM**.

C(1)-N(1)	1.284(2)	C(15)-C(16)	1.394(3)
C(1)-C(2)	1.471(2)	C(16)-O(1)	1.370(2)
C(1)-C(12)	1.518(2)	C(16)-C(17)	1.388(3)
C(2)-C(3)	1.380(2)	C(17)-C(18)	1.389(3)
C(2)-C(7)	1.420(3)	C(19)-O(1)	1.437(2)
C(3)-C(4)	1.417(3)	C(20)-C(21)	1.387(3)
C(4)-C(5)	1.381(3)	C(20)-C(25)	1.395(3)
C(5)-C(6)	1.419(3)	C(20)-N(2)	1.432(2)
C(6)-C(7)	1.408(3)	C(21)-C(22)	1.396(2)
C(6)-C(8)	1.420(3)	C(22)-C(23)	1.390(3)
C(7)-C(11)	1.421(2)	C(23)-O(2)	1.376(2)
C(8)-C(9)	1.381(3)	C(23)-C(24)	1.395(3)
C(9)-C(10)	1.410(3)	C(24)-C(25)	1.385(3)
C(10)-C(11)	1.383(3)	C(26)-O(2)	1.435(2)
C(11)-C(12)	1.475(3)	C(27)-Cl(3)	1.761(2)
C(12)-N(2)	1.285(2)	C(27)-Cl(4)	1.762(2)
C(13)-C(18)	1.389(3)	N(1)-Zn(1)	2.0725(16)
C(13)-C(14)	1.393(2)	N(2)-Zn(1)	2.0800(16)
C(13)-N(1)	1.424(2)	Cl(1)-Zn(1)	2.2000(9)
C(14)-C(15)	1.384(3)	Cl(2)-Zn(1)	2.2225(7)

		O(1)-C(16)-C(17)	124.22(18)
N(1)-C(1)-C(2)	135.93(16)	O(1)-C(16)-C(15)	115.44(17)
N(1)-C(1)-C(12)	116.96(16)	C(17)-C(16)-C(15)	120.34(17)
C(2)-C(1)-C(12)	106.96(15)	C(16)-C(17)-C(18)	119.40(17)
C(3)-C(2)-C(7)	118.74(17)	C(13)-C(18)-C(17)	120.34(17)
C(3)-C(2)-C(1)	135.09(17)	C(21)-C(20)-C(25)	120.41(16)
C(7)-C(2)-C(1)	105.95(15)	C(21)-C(20)-N(2)	118.93(15)
C(2)-C(3)-C(4)	119.11(17)	C(25)-C(20)-N(2)	120.65(16)
C(5)-C(4)-C(3)	121.85(17)	C(20)-C(21)-C(22)	120.00(17)
C(4)-C(5)-C(6)	120.72(18)	C(23)-C(22)-C(21)	119.35(17)
C(7)-C(6)-C(5)	116.42(17)	O(2)-C(23)-C(22)	123.84(17)
C(7)-C(6)-C(8)	116.87(17)	O(2)-C(23)-C(24)	115.61(16)
C(5)-C(6)-C(8)	126.69(18)	C(22)-C(23)-C(24)	120.55(16)
C(6)-C(7)-C(2)	123.14(17)	C(25)-C(24)-C(23)	119.88(17)
C(6)-C(7)-C(11)	122.59(17)	C(24)-C(25)-C(20)	119.68(17)
C(2)-C(7)-C(11)	114.20(16)	Cl(3)-C(27)-Cl(4)	111.94(13)
C(9)-C(8)-C(6)	120.22(18)	C(1)-N(1)-C(13)	123.27(15)
C(8)-C(9)-C(10)	122.44(18)	C(1)-N(1)-Zn(1)	112.06(12)
C(11)-C(10)-C(9)	118.72(17)	C(13)-N(1)-Zn(1)	124.62(12)
C(10)-C(11)-C(7)	119.13(17)	C(12)-N(2)-C(20)	120.74(15)
C(10)-C(11)-C(12)	135.05(17)	C(12)-N(2)-Zn(1)	111.03(12)
C(7)-C(11)-C(12)	105.60(15)	C(20)-N(2)-Zn(1)	128.21(12)
N(2)-C(12)-C(11)	134.47(16)	C(16)-O(1)-C(19)	117.26(16)
N(2)-C(12)-C(1)	118.16(16)	C(23)-O(2)-C(26)	117.26(15)
C(11)-C(12)-C(1)	107.27(15)	N(1)-Zn(1)-N(2)	81.34(6)
C(18)-C(13)-C(14)	119.94(16)	N(1)-Zn(1)-Cl(1)	116.09(5)
C(18)-C(13)-N(1)	121.27(16)	N(2)-Zn(1)-Cl(1)	120.18(5)
C(14)-C(13)-N(1)	118.65(16)	N(1)-Zn(1)-Cl(2)	111.65(5)
C(15)-C(14)-C(13)	119.77(17)	N(2)-Zn(1)-Cl(2)	110.55(5)
C(14)-C(15)-C(16)	119.99(17)	Cl(1)-Zn(1)-Cl(2)	113.20(2)

Table 112: Crystallographic Data and Structure Refinement of **16-DCM**.

Empirical formula	$C_{27}H_{22}Cl_4N_2S_2Zn$	
Formula weight	645.75	
Temperature	100(2) K	
Wavelength	0.71075 Å	
Crystal system	Monoclinic	
Space group	P2 <sub>1</sub> /c	
Unit cell dimensions	a = 13.2610(2) Å	$\alpha = 90^\circ$ .
	b = 12.02200(10) Å	$\beta = 109.1270(10)^\circ$ .
	c = 18.1350(2) Å	$\gamma = 90^\circ$ .
Volume	2731.54(6) Å <sup>3</sup>	
Z	4	
Density (calculated)	1.570 Mg/m <sup>3</sup>	
Absorption coefficient	1.464 mm <sup>-1</sup>	
F(000)	1312	
Crystal size	0.180 x 0.170 x 0.050 mm <sup>3</sup>	
Theta range for data collection	1.625 to 26.554°.	
Index ranges	-16<=h<=16, -14<=k<=14, -22<=l<=22	
Reflections collected	16166	
Independent reflections	5505 [R(int) = 0.0318]	
Completeness to theta = 25.242°	99.6 %	
Absorption correction	Semi-empirical from equivalents	
Max. and min. transmission	1.00000 and 0.77049	
Refinement method	Full-matrix least-squares on F <sup>2</sup>	
Data / restraints / parameters	5505 / 294 / 356	
Goodness-of-fit on F <sup>2</sup>	1.237	
Final R indices [I>2sigma(I)]	R1 = 0.0711, wR2 = 0.1747	
R indices (all data)	R1 = 0.0718, wR2 = 0.1750	
Largest diff. peak and hole	0.543 and -0.945 e.Å <sup>-3</sup>	

Table 113: Atomic coordinates ( $\times 10^4$ ) and equivalent isotropic displacement parameters ( $\text{\AA}^2 \times 10^3$ ) for **16-DCM**.  $U(\text{eq})$  is defined as one third of the trace of the orthogonalized  $U^{\text{ij}}$  tensor.

	x	y	z	U(eq)
C(1)	461(4)	2611(5)	10353(3)	14(1)
C(2)	253(4)	3438(5)	10883(3)	15(1)
C(3)	785(5)	3798(5)	11634(3)	16(1)
C(4)	369(5)	4719(5)	11930(3)	19(1)
C(5)	-550(5)	5261(5)	11499(3)	18(1)
C(6)	-1109(4)	4920(5)	10725(3)	16(1)
C(7)	-691(4)	4009(5)	10439(3)	13(1)
C(8)	-2034(5)	5429(5)	10199(3)	18(1)
C(9)	-2481(4)	5028(5)	9447(3)	19(1)
C(10)	-2060(4)	4102(5)	9171(3)	17(1)
C(11)	-1158(4)	3589(5)	9665(3)	15(1)
C(12)	-459(4)	2677(5)	9589(3)	13(1)
C(13)	2081(4)	1711(5)	11086(3)	15(1)
C(14)	3126(5)	1751(5)	11066(3)	20(1)
C(15)	3962(5)	1518(6)	11740(4)	22(1)
C(16)	3770(4)	1210(5)	12426(3)	17(1)
C(17)	2719(4)	1136(5)	12426(3)	17(1)
C(18)	1877(4)	1380(5)	11756(3)	15(1)
C(19)	4358(5)	959(6)	14041(4)	27(1)
C(20)	-1293(4)	2020(5)	8305(3)	15(1)
C(21)	-1067(4)	2271(5)	7619(3)	17(1)
C(22)	-1879(5)	2286(5)	6912(3)	19(1)
C(23)	-2924(4)	2032(5)	6869(3)	15(1)
C(24)	-3134(5)	1730(5)	7549(4)	20(1)
C(25)	-2334(5)	1732(5)	8263(3)	18(1)
C(26)	-3427(6)	2590(8)	5303(4)	38(2)

N(1)	1224(4)	1943(4)	10381(3)	14(1)
N(2)	-444(4)	2032(4)	9029(3)	14(1)
S(1)	4891(1)	914(2)	13248(1)	25(1)
S(2)	-4015(1)	2064(1)	5994(1)	21(1)
Cl(1)	1969(1)	2035(1)	8686(1)	20(1)
Cl(2)	995(1)	-647(1)	9286(1)	23(1)
Zn(1)	1001(1)	1178(1)	9312(1)	22(1)
Cl(3)	6166(4)	-902(4)	12195(3)	38(1)
C(27)	6418(13)	-12(13)	11524(10)	47(4)
Cl(4)	5519(4)	-229(4)	10565(3)	64(1)
Cl(5)	6833(2)	309(3)	12129(2)	17(1)
C(27A)	5870(30)	-960(40)	12020(30)	86(13)
Cl(6)	4957(3)	-1027(3)	11351(2)	35(1)

Table 114: Bond Lengths [Å] and Bond Angles [°] for **16-DCM**.

C(1)-N(1)	1.281(7)	C(13)-C(14)	1.400(8)
C(1)-C(2)	1.472(8)	C(13)-N(1)	1.432(7)
C(1)-C(12)	1.519(7)	C(14)-C(15)	1.382(8)
C(2)-C(3)	1.382(8)	C(15)-C(16)	1.399(8)
C(2)-C(7)	1.424(8)	C(16)-C(17)	1.397(8)
C(3)-C(4)	1.418(8)	C(16)-S(1)	1.762(6)
C(4)-C(5)	1.377(8)	C(17)-C(18)	1.385(8)
C(5)-C(6)	1.417(8)	C(19)-S(1)	1.798(7)
C(6)-C(7)	1.400(8)	C(20)-C(25)	1.401(8)
C(6)-C(8)	1.423(8)	C(20)-C(21)	1.405(8)
C(7)-C(11)	1.428(7)	C(20)-N(2)	1.422(7)
C(8)-C(9)	1.384(8)	C(21)-C(22)	1.378(8)
C(9)-C(10)	1.409(8)	C(22)-C(23)	1.396(8)
C(10)-C(11)	1.383(8)	C(23)-C(24)	1.398(8)
C(11)-C(12)	1.471(8)	C(23)-S(2)	1.763(6)
C(12)-N(2)	1.281(7)	C(24)-C(25)	1.379(8)
C(13)-C(18)	1.386(8)	C(26)-S(2)	1.793(7)



N(1)-Zn(1)	2.078(5)	N(2)-C(12)-C(1)	118.3(5)
N(2)-Zn(1)	2.085(5)	C(11)-C(12)-C(1)	107.2(4)
Cl(1)-Zn(1)	2.2257(15)	C(18)-C(13)-C(14)	120.8(5)
Cl(2)-Zn(1)	2.1937(16)	C(18)-C(13)-N(1)	120.9(5)
Cl(3)-C(27)	1.727(16)	C(14)-C(13)-N(1)	118.2(5)
C(27)-Cl(4)	1.774(17)	C(15)-C(14)-C(13)	119.0(5)
Cl(4)-Cl(4)#1	2.135(9)	C(14)-C(15)-C(16)	120.8(5)
Cl(5)-C(27A)	1.91(6)	C(17)-C(16)-C(15)	119.3(5)
C(27A)-Cl(6)	1.57(6)	C(17)-C(16)-S(1)	123.5(4)
		C(15)-C(16)-S(1)	117.2(4)
N(1)-C(1)-C(2)	135.5(5)	C(18)-C(17)-C(16)	120.3(5)
N(1)-C(1)-C(12)	117.2(5)	C(17)-C(18)-C(13)	119.8(5)
C(2)-C(1)-C(12)	107.2(4)	C(25)-C(20)-C(21)	119.8(5)
C(3)-C(2)-C(7)	118.5(5)	C(25)-C(20)-N(2)	121.4(5)
C(3)-C(2)-C(1)	135.3(5)	C(21)-C(20)-N(2)	118.8(5)
C(7)-C(2)-C(1)	105.9(5)	C(22)-C(21)-C(20)	120.0(5)
C(2)-C(3)-C(4)	118.7(5)	C(21)-C(22)-C(23)	120.5(5)
C(5)-C(4)-C(3)	122.5(5)	C(22)-C(23)-C(24)	119.2(5)
C(4)-C(5)-C(6)	120.1(5)	C(22)-C(23)-S(2)	123.5(4)
C(7)-C(6)-C(5)	116.9(5)	C(24)-C(23)-S(2)	117.3(4)
C(7)-C(6)-C(8)	116.6(5)	C(25)-C(24)-C(23)	121.0(5)
C(5)-C(6)-C(8)	126.5(5)	C(24)-C(25)-C(20)	119.5(5)
C(6)-C(7)-C(2)	123.2(5)	C(1)-N(1)-C(13)	122.9(5)
C(6)-C(7)-C(11)	122.9(5)	C(1)-N(1)-Zn(1)	111.8(4)
C(2)-C(7)-C(11)	113.8(5)	C(13)-N(1)-Zn(1)	125.2(4)
C(9)-C(8)-C(6)	120.5(5)	C(12)-N(2)-C(20)	121.6(5)
C(8)-C(9)-C(10)	122.2(5)	C(12)-N(2)-Zn(1)	110.8(4)
C(11)-C(10)-C(9)	118.8(5)	C(20)-N(2)-Zn(1)	127.4(4)
C(10)-C(11)-C(7)	118.9(5)	C(16)-S(1)-C(19)	103.1(3)
C(10)-C(11)-C(12)	135.2(5)	C(23)-S(2)-C(26)	102.8(3)
C(7)-C(11)-C(12)	105.8(5)	N(1)-Zn(1)-N(2)	81.35(18)
N(2)-C(12)-C(11)	134.3(5)	N(1)-Zn(1)-Cl(2)	117.43(14)

N(2)-Zn(1)-Cl(2)	119.41(14)	Cl(3)-C(27)-Cl(4)	111.5(9)
N(1)-Zn(1)-Cl(1)	109.97(13)	C(27)-Cl(4)-Cl(4)#1	156.6(6)
N(2)-Zn(1)-Cl(1)	106.47(14)	Cl(6)-C(27A)-Cl(5)	113(3)
Cl(1)-Zn(1)-Cl(2)	116.80(6)		

---

Table 115: Crystallographic Data and Structure Refinement of **17-DCM**.

Empirical formula	$C_{36.37}H_{24.74}Cl_{2.74}N_2O_2Zn$	
Formula weight	1369.38	
Temperature	100(2) K	
Wavelength	0.71075 Å	
Crystal system	Monoclinic	
Space group	I2/a	
Unit cell dimensions	$a = 17.442(7)$ Å	$\alpha = 90^\circ$ .
	$b = 11.790(5)$ Å	$\beta = 104.238(7)^\circ$ .
	$c = 31.054(15)$ Å	$\gamma = 90^\circ$ .
Volume	$6190(5)$ Å <sup>3</sup>	
Z	4	
Density (calculated)	$1.469$ Mg/m <sup>3</sup>	
Absorption coefficient	$1.068$ mm <sup>-1</sup>	
F(000)	2798	
Crystal size	$0.05 \times 0.21 \times 0.27$ mm <sup>3</sup>	
Theta range for data collection	1.855 to 24.998°.	
Index ranges	$-20 \leq h \leq 20$ , $-14 \leq k \leq 13$ , $-36 \leq l \leq 36$	
Reflections collected	39380	
Independent reflections	5446 [R(int) = 0.0481]	
Completeness to theta = 25.242°	97.1 %	
Absorption correction	Semi-empirical from equivalents	
Max. and min. transmission	1.00000 and 0.7810	
Refinement method	Full-matrix least-squares on F <sup>2</sup>	
Data / restraints / parameters	5446 / 879 / 527	
Goodness-of-fit on F <sup>2</sup>	1.225	
Final R indices [I > 2sigma(I)]	R1 = 0.0637, wR2 = 0.1751	
R indices (all data)	R1 = 0.0675, wR2 = 0.1788	
Largest diff. peak and hole	1.510 and -0.574 e.Å <sup>-3</sup>	

Table 116: Atomic coordinates ( $\times 10^4$ ) and equivalent isotropic displacement parameters ( $\text{\AA}^2 \times 10^3$ ) for **17-DCM**.  $U(\text{eq})$  is defined as one third of the trace of the orthogonalized  $U^{\text{ij}}$  tensor.

	x	y	z	U(eq)
C(1)	12778(3)	162(4)	7597(2)	39(1)
C(2)	12609(3)	1043(4)	7900(2)	42(1)
C(3)	13012(3)	1502(4)	8301(2)	51(1)
C(4)	12649(4)	2418(4)	8472(2)	62(1)
C(5)	11944(4)	2868(4)	8264(2)	59(1)
C(6)	11515(3)	2435(4)	7849(2)	53(1)
C(7)	11866(3)	1505(3)	7675(2)	44(1)
C(8)	10788(3)	2819(4)	7585(2)	58(1)
C(9)	10444(3)	2338(4)	7183(2)	57(1)
C(10)	10796(3)	1397(4)	7011(2)	51(1)
C(11)	11507(3)	985(4)	7260(2)	43(1)
C(12)	12074(2)	91(4)	7201(2)	38(1)
C(13)	14026(3)	-569(3)	7980(2)	39(1)
C(14)	14795(3)	-450(4)	7931(2)	41(1)
C(15)	15432(3)	-507(4)	8298(2)	47(1)
C(16)	15299(3)	-733(4)	8709(2)	54(1)
C(17)	14532(3)	-908(5)	8756(2)	59(1)
C(18)	13898(3)	-836(4)	8394(2)	49(1)
C(19)	11447(3)	-852(4)	6521(2)	42(1)
C(20)	10695(3)	-1096(4)	6575(2)	43(1)
C(21)	10087(3)	-1352(4)	6211(2)	49(1)
C(22)	10229(3)	-1390(5)	5796(2)	61(1)
C(23)	10979(4)	-1185(7)	5738(2)	81(2)
C(24)	11594(3)	-917(6)	6103(2)	66(2)
C(25)	16590(3)	-208(5)	9153(2)	53(2)
C(26)	16595(3)	907(5)	9015(2)	54(2)

C(27)	17272(4)	1555(5)	9139(2)	66(2)
C(28)	17956(3)	1090(6)	9406(2)	75(2)
C(29)	17955(4)	-22(7)	9540(2)	94(3)
C(36)	17278(4)	-663(5)	9417(2)	82(2)
C(25A)	16673(6)	-629(18)	9202(7)	72(6)
C(26A)	16858(9)	447(16)	9098(7)	66(5)
C(27A)	17647(11)	768(14)	9199(7)	77(6)
C(28A)	18226(7)	7(18)	9400(7)	77(6)
C(29A)	18021(9)	-1074(16)	9500(7)	86(6)
C(36A)	17234(10)	-1397(14)	9400(7)	76(6)
C(30)	9698(4)	-2077(5)	5046(2)	51(2)
C(31)	9965(4)	-3130(5)	4975(2)	57(2)
C(32)	10063(5)	-3424(6)	4556(2)	65(2)
C(33)	9892(7)	-2656(9)	4221(2)	84(5)
C(34)	9623(7)	-1581(7)	4295(3)	112(4)
C(35)	9518(6)	-1298(6)	4708(3)	97(3)
C(30A)	8939(4)	-960(7)	5276(3)	47(2)
C(31A)	8771(5)	80(8)	5440(3)	47(2)
C(32A)	8044(6)	585(7)	5280(3)	56(3)
C(33A)	7478(5)	55(8)	4955(4)	70(3)
C(34A)	7633(5)	-970(8)	4788(3)	58(3)
C(35A)	8360(6)	-1481(7)	4947(3)	58(3)
Cl(1A)	9905(3)	-3951(5)	4828(2)	91(1)
Cl(2A)	9738(4)	-2478(5)	4084(2)	87(2)
C(1AA)	10328(11)	-2774(17)	4624(6)	73(4)
N(1)	13379(2)	-479(3)	7599(1)	36(1)
N(2)	12100(2)	-625(3)	6895(1)	38(1)
O(1)	15895(3)	-878(4)	9092(1)	78(1)
O(2)	9603(2)	-1672(4)	5444(1)	75(1)
Cl(1)	13352(1)	-3258(1)	7130(1)	40(1)
Cl(2)	13824(1)	-692(1)	6526(1)	47(1)
Zn(1)	13211(1)	-1416(1)	7014(1)	35(1)

Table 117: Bond Lengths [ $\text{\AA}$ ] and Bond Angles [ $^\circ$ ] for **17-DCM**.

C(1)-N(1)	1.291(5)	C(23)-C(24)	1.392(8)
C(1)-C(2)	1.478(6)	C(25)-C(26)	1.383(7)
C(1)-C(12)	1.512(7)	C(25)-C(36)	1.386(6)
C(2)-C(3)	1.381(7)	C(26)-C(27)	1.380(7)
C(2)-C(7)	1.421(7)	C(27)-C(28)	1.387(7)
C(3)-C(4)	1.421(7)	C(28)-C(29)	1.375(7)
C(4)-C(5)	1.349(9)	C(29)-C(36)	1.374(7)
C(5)-C(6)	1.417(8)	C(25A)-O(1)	1.347(8)
C(6)-C(8)	1.404(8)	C(25A)-C(36A)	1.364(8)
C(6)-C(7)	1.424(6)	C(25A)-C(26A)	1.367(8)
C(7)-C(11)	1.427(7)	C(26A)-C(27A)	1.386(8)
C(8)-C(9)	1.368(8)	C(27A)-C(28A)	1.380(8)
C(9)-C(10)	1.432(7)	C(28A)-C(29A)	1.380(8)
C(10)-C(11)	1.377(7)	C(29A)-C(36A)	1.384(8)
C(11)-C(12)	1.489(6)	C(30)-C(31)	1.361(7)
C(12)-N(2)	1.279(5)	C(30)-C(35)	1.372(7)
C(13)-C(14)	1.394(6)	C(31)-C(32)	1.399(7)
C(13)-C(18)	1.395(6)	C(32)-C(33)	1.355(8)
C(13)-N(1)	1.423(6)	C(33)-C(34)	1.390(8)
C(14)-C(15)	1.384(7)	C(34)-C(35)	1.379(7)
C(15)-C(16)	1.376(7)	C(30A)-C(31A)	1.387(8)
C(16)-O(1)	1.383(6)	C(30A)-C(35A)	1.390(8)
C(16)-C(17)	1.398(8)	C(30A)-O(2)	1.422(7)
C(17)-C(18)	1.372(8)	C(31A)-C(32A)	1.376(8)
C(19)-C(24)	1.385(6)	C(32A)-C(33A)#1	1.194(14)
C(19)-C(20)	1.392(6)	C(32A)-C(33A)	1.378(8)
C(19)-N(2)	1.437(6)	C(33A)-C(33A)#1	0.27(3)
C(20)-C(21)	1.380(7)	C(33A)-C(32A)#1	1.194(14)
C(21)-C(22)	1.370(7)	C(33A)-C(34A)	1.367(8)
C(22)-O(2)	1.383(7)	C(33A)-C(34A)#1	1.486(15)
C(22)-C(23)	1.385(8)	C(34A)-C(35A)	1.381(8)

C(34A)-C(33A)#1	1.486(15)	C(11)-C(12)-C(1)	106.9(4)
C(34A)-C(34A)#1	1.50(2)	C(14)-C(13)-C(18)	119.9(4)
Cl(1A)-C(1AA)	1.76(2)	C(14)-C(13)-N(1)	119.4(4)
Cl(2A)-C(1AA)	1.771(19)	C(18)-C(13)-N(1)	120.6(4)
N(1)-Zn(1)	2.085(4)	C(15)-C(14)-C(13)	120.4(4)
N(2)-Zn(1)	2.100(3)	C(16)-C(15)-C(14)	119.2(5)
Cl(1)-Zn(1)	2.2048(14)	C(15)-C(16)-O(1)	123.9(5)
Cl(2)-Zn(1)	2.2282(13)	C(15)-C(16)-C(17)	120.6(5)
		O(1)-C(16)-C(17)	115.3(5)
N(1)-C(1)-C(2)	134.2(4)	C(18)-C(17)-C(16)	120.3(5)
N(1)-C(1)-C(12)	117.8(4)	C(17)-C(18)-C(13)	119.4(5)
C(2)-C(1)-C(12)	107.9(4)	C(24)-C(19)-C(20)	119.8(5)
C(3)-C(2)-C(7)	119.5(4)	C(24)-C(19)-N(2)	118.3(4)
C(3)-C(2)-C(1)	135.4(5)	C(20)-C(19)-N(2)	121.6(4)
C(7)-C(2)-C(1)	105.0(4)	C(21)-C(20)-C(19)	120.2(4)
C(2)-C(3)-C(4)	117.4(5)	C(22)-C(21)-C(20)	119.8(5)
C(5)-C(4)-C(3)	123.8(6)	C(21)-C(22)-O(2)	117.6(5)
C(4)-C(5)-C(6)	120.7(5)	C(21)-C(22)-C(23)	120.7(5)
C(8)-C(6)-C(5)	127.9(5)	O(2)-C(22)-C(23)	121.7(5)
C(8)-C(6)-C(7)	115.9(5)	C(22)-C(23)-C(24)	119.8(5)
C(5)-C(6)-C(7)	116.2(5)	C(19)-C(24)-C(23)	119.5(5)
C(2)-C(7)-C(6)	122.3(5)	C(26)-C(25)-C(36)	118.8(4)
C(2)-C(7)-C(11)	115.1(4)	C(27)-C(26)-C(25)	120.7(4)
C(6)-C(7)-C(11)	122.6(5)	C(26)-C(27)-C(28)	119.9(5)
C(9)-C(8)-C(6)	121.9(5)	C(29)-C(28)-C(27)	119.5(5)
C(8)-C(9)-C(10)	121.9(5)	C(36)-C(29)-C(28)	120.4(5)
C(11)-C(10)-C(9)	118.3(5)	C(29)-C(36)-C(25)	120.7(5)
C(10)-C(11)-C(7)	119.3(4)	O(1)-C(25A)-C(36A)	122.4(15)
C(10)-C(11)-C(12)	135.6(5)	O(1)-C(25A)-C(26A)	115.1(14)
C(7)-C(11)-C(12)	105.0(4)	C(36A)-C(25A)-C(26A)	122.5(6)
N(2)-C(12)-C(11)	134.8(4)	C(25A)-C(26A)-C(27A)	118.7(5)
N(2)-C(12)-C(1)	118.1(4)	C(28A)-C(27A)-C(26A)	119.9(6)

C(27A)-C(28A)-C(29A)	120.1(6)	C(34A)-C(33A)-C(34A)#1	63.1(8)
C(28A)-C(29A)-C(36A)	120.1(6)	C(32A)-C(33A)-C(34A)#1	98.0(8)
C(25A)-C(36A)-C(29A)	118.7(6)	C(33A)-C(34A)-C(35A)	120.0(5)
C(31)-C(30)-C(35)	120.7(5)	C(33A)-C(34A)-C(33A)#1	9.9(8)
C(30)-C(31)-C(32)	120.0(5)	C(35A)-C(34A)-C(33A)#1	1113.0(7)
C(33)-C(32)-C(31)	119.7(5)	C(33A)-C(34A)-C(34A)#1	62.3(5)
C(32)-C(33)-C(34)	120.1(5)	C(35A)-C(34A)-C(34A)#1	98.1(7)
C(35)-C(34)-C(33)	120.1(5)	C(33A)#1-C(34A)-C(34A)#1	154.5(7)
C(30)-C(35)-C(34)	119.4(5)	C(34A)-C(35A)-C(30A)	120.5(5)
C(31A)-C(30A)-C(35A)	118.6(5)	Cl(1A)-C(1AA)-Cl(2A)	107.4(11)
C(31A)-C(30A)-O(2)	127.9(7)	C(1)-N(1)-C(13)	121.6(4)
C(35A)-C(30A)-O(2)	112.8(7)	C(1)-N(1)-Zn(1)	111.5(3)
C(32A)-C(31A)-C(30A)	120.6(5)	C(13)-N(1)-Zn(1)	126.7(3)
C(33A)#1-C(32A)-C(31A)	119.3(7)	C(12)-N(2)-C(19)	123.8(4)
C(33A)#1-C(32A)-C(33A)	9.0(12)	C(12)-N(2)-Zn(1)	111.2(3)
C(31A)-C(32A)-C(33A)	119.9(5)	C(19)-N(2)-Zn(1)	125.0(3)
C(33A)#1-C(33A)-C(32A)#1	128(4)	C(25A)-O(1)-C(16)	133.5(10)
C(33A)#1-C(33A)-C(34A)	110.9(14)	C(22)-O(2)-C(30A)	124.1(5)
C(32A)#1-C(33A)-C(34A)	115.1(12)	N(1)-Zn(1)-N(2)	81.01(14)
C(33A)#1-C(33A)-C(32A)	43(3)	N(1)-Zn(1)-Cl(1)	113.15(10)
C(32A)#1-C(33A)-C(32A)	120.9(10)	N(2)-Zn(1)-Cl(1)	121.78(10)
C(34A)-C(33A)-C(32A)	120.4(6)	N(1)-Zn(1)-Cl(2)	113.76(10)
C(33A)#1-C(33A)-C(34A)#1	159.2(17)	N(2)-Zn(1)-Cl(2)	106.64(10)
C(32A)#1-C(33A)-C(34A)#1	125.0(11)	Cl(1)-Zn(1)-Cl(2)	115.82(4)

---



Table 118: Crystallographic Data and Structure Refinement of **18-THF**.

Empirical formula	$C_{30}H_{26}Cl_2F_2N_2O_{1.5}Zn$	
Formula weight	1225.59	
Temperature	153(2) K	
Wavelength	0.71075 Å	
Crystal system	Monoclinic	
Space group	$P2_1/c$	
Unit cell dimensions	$a = 14.3180(15)$ Å	$\alpha = 90^\circ$ .
	$b = 11.7050(8)$ Å	$\beta = 112.958(4)^\circ$ .
	$c = 17.7720(18)$ Å	$\gamma = 90^\circ$ .
Volume	$2742.5(4)$ Å <sup>3</sup>	
Z	2	
Density (calculated)	$1.484$ Mg/m <sup>3</sup>	
Absorption coefficient	$1.133$ mm <sup>-1</sup>	
F(000)	1256	
Crystal size	0.230 x 0.110 x 0.090 mm <sup>3</sup>	
Theta range for data collection	2.139 to 27.500°.	
Index ranges	-18 ≤ h ≤ 18, -15 ≤ k ≤ 15, -23 ≤ l ≤ 22	
Reflections collected	28653	
Independent reflections	6289 [R(int) = 0.0641]	
Completeness to theta = 25.242°	99.7 %	
Absorption correction	Semi-empirical from equivalents	
Max. and min. transmission	1.00000 and 0.7994	
Refinement method	Full-matrix least-squares on F <sup>2</sup>	
Data / restraints / parameters	6289 / 672 / 417	
Goodness-of-fit on F <sup>2</sup>	1.070	
Final R indices [I > 2σ(I)]	R1 = 0.0518, wR2 = 0.1089	
R indices (all data)	R1 = 0.0732, wR2 = 0.1248	
Largest diff. peak and hole	0.448 and -0.494 e.Å <sup>-3</sup>	

Table 119: Atomic coordinates ( $\times 10^4$ ) and equivalent isotropic displacement parameters ( $\text{\AA}^2 \times 10^3$ ) for **18-THF**.  $U(\text{eq})$  is defined as one third of the trace of the orthogonalized  $U^{\text{ij}}$  tensor.

	x	y	z	U(eq)
C(1)	4466(2)	2702(3)	5007(2)	27(1)
C(2)	4671(2)	3532(3)	5675(2)	27(1)
C(3)	4151(3)	3923(3)	6132(2)	32(1)
C(4)	4594(3)	4791(3)	6718(2)	35(1)
C(5)	5530(3)	5239(3)	6852(2)	35(1)
C(6)	6087(2)	4860(3)	6390(2)	31(1)
C(7)	5640(2)	4008(3)	5810(2)	28(1)
C(8)	7054(3)	5256(3)	6460(2)	38(1)
C(9)	7497(3)	4823(3)	5957(2)	38(1)
C(10)	7031(2)	3974(3)	5365(2)	35(1)
C(11)	6097(2)	3558(3)	5293(2)	27(1)
C(12)	5366(2)	2727(3)	4756(2)	26(1)
C(13)	2871(2)	1897(3)	4826(2)	30(1)
C(14)	1919(3)	2151(4)	4250(2)	47(1)
C(15)	1074(3)	1987(4)	4446(3)	62(1)
C(16)	1225(3)	1558(4)	5201(3)	52(1)
C(17)	2155(3)	1302(3)	5780(2)	43(1)
C(18)	2999(3)	1473(3)	5590(2)	35(1)
C(19)	6167(2)	2028(3)	3906(2)	28(1)
C(20)	6036(2)	2330(3)	3118(2)	32(1)
C(21)	6853(3)	2264(3)	2877(2)	39(1)
C(22)	7751(3)	1853(3)	3431(2)	42(1)
C(23)	7899(3)	1517(3)	4210(2)	42(1)
C(24)	7086(2)	1608(3)	4449(2)	36(1)
O(1)	403(6)	3707(6)	2714(4)	88(2)
C(25)	-51(8)	4694(8)	2215(7)	108(3)

C(26)	-1065(7)	4311(8)	1621(6)	88(3)
C(27)	-980(8)	3037(8)	1605(7)	61(3)
C(28)	66(5)	2792(7)	2221(4)	59(2)
O(1A)	100(8)	4046(13)	2824(7)	90(4)
C(25A)	272(11)	3537(18)	2145(10)	94(5)
C(26A)	-754(14)	3050(20)	1601(15)	91(7)
C(27A)	-1461(10)	3853(17)	1768(10)	99(5)
C(28A)	-868(10)	4368(14)	2574(9)	93(4)
N(2)	5320(2)	2110(2)	4147(2)	27(1)
N(1)	3725(2)	2038(2)	4607(2)	28(1)
F(1)	395(2)	1376(3)	5390(2)	84(1)
F(2)	8554(2)	1758(2)	3196(2)	64(1)
Cl(2)	2910(1)	1898(1)	2474(1)	41(1)
Cl(1)	4186(1)	-662(1)	3785(1)	46(1)
Zn(1)	3955(1)	1199(1)	3656(1)	29(1)
O(2)	9865(13)	5617(18)	4491(9)	197(7)
C(30)	9393(12)	4842(18)	4877(11)	149(6)
C(31)	10143(15)	4710(30)	5752(12)	190(8)
C(32)	11128(11)	5068(16)	5699(10)	151(6)
C(33)	10795(12)	5868(13)	5002(10)	121(5)

Table 120: Bond Lengths [ $\text{\AA}$ ] and Bond Angles [ $^\circ$ ] for **18-THF**.

C(1)-N(1)	1.282(4)	C(7)-C(11)	1.422(4)
C(1)-C(2)	1.473(4)	C(8)-C(9)	1.378(5)
C(1)-C(12)	1.520(4)	C(9)-C(10)	1.412(5)
C(2)-C(3)	1.376(4)	C(10)-C(11)	1.382(4)
C(2)-C(7)	1.424(4)	C(11)-C(12)	1.473(4)
C(3)-C(4)	1.416(5)	C(12)-N(2)	1.282(4)
C(4)-C(5)	1.371(5)	C(13)-C(14)	1.380(5)
C(5)-C(6)	1.421(5)	C(13)-C(18)	1.390(4)
C(6)-C(7)	1.398(4)	C(13)-N(1)	1.432(4)
C(6)-C(8)	1.419(5)	C(14)-C(15)	1.396(5)

C(15)-C(16)	1.368(6)	N(1)-C(1)-C(2)	135.2(3)
C(16)-C(17)	1.363(6)	N(1)-C(1)-C(12)	117.5(3)
C(16)-F(1)	1.371(4)	C(2)-C(1)-C(12)	107.3(2)
C(17)-C(18)	1.389(5)	C(3)-C(2)-C(7)	119.0(3)
C(19)-C(24)	1.384(4)	C(3)-C(2)-C(1)	135.3(3)
C(19)-C(20)	1.384(4)	C(7)-C(2)-C(1)	105.7(3)
C(19)-N(2)	1.439(4)	C(2)-C(3)-C(4)	118.9(3)
C(20)-C(21)	1.394(4)	C(5)-C(4)-C(3)	121.9(3)
C(21)-C(22)	1.367(5)	C(4)-C(5)-C(6)	120.7(3)
C(22)-F(2)	1.372(4)	C(7)-C(6)-C(8)	116.7(3)
C(22)-C(23)	1.374(5)	C(7)-C(6)-C(5)	116.7(3)
C(23)-C(24)	1.390(5)	C(8)-C(6)-C(5)	126.6(3)
O(1)-C(28)	1.346(9)	C(6)-C(7)-C(11)	123.2(3)
O(1)-C(25)	1.452(10)	C(6)-C(7)-C(2)	122.7(3)
C(25)-C(26)	1.488(12)	C(11)-C(7)-C(2)	114.1(3)
C(26)-C(27)	1.492(11)	C(9)-C(8)-C(6)	120.2(3)
C(27)-C(28)	1.503(11)	C(8)-C(9)-C(10)	122.7(3)
O(1A)-C(28A)	1.336(10)	C(11)-C(10)-C(9)	118.5(3)
O(1A)-C(25A)	1.454(11)	C(10)-C(11)-C(7)	118.8(3)
C(25A)-C(26A)	1.510(14)	C(10)-C(11)-C(12)	135.3(3)
C(26A)-C(27A)	1.481(12)	C(7)-C(11)-C(12)	105.9(3)
C(27A)-C(28A)	1.482(13)	N(2)-C(12)-C(11)	135.1(3)
N(2)-Zn(1)	2.094(2)	N(2)-C(12)-C(1)	117.8(3)
N(1)-Zn(1)	2.089(2)	C(11)-C(12)-C(1)	107.0(2)
Cl(2)-Zn(1)	2.2066(9)	C(14)-C(13)-C(18)	121.2(3)
Cl(1)-Zn(1)	2.2019(9)	C(14)-C(13)-N(1)	118.4(3)
O(2)-C(33)	1.330(10)	C(18)-C(13)-N(1)	120.4(3)
O(2)-C(30)	1.461(11)	C(13)-C(14)-C(15)	119.1(4)
C(30)-C(31)	1.500(15)	C(16)-C(15)-C(14)	118.4(4)
C(31)-C(32)	1.489(14)	C(17)-C(16)-C(15)	123.7(3)
C(32)-C(33)	1.486(12)	C(17)-C(16)-F(1)	117.8(4)
		C(15)-C(16)-F(1)	118.5(4)

C(16)-C(17)-C(18)	118.1(3)	C(28A)-C(27A)-C(26A)	105.0(11)
C(17)-C(18)-C(13)	119.6(3)	O(1A)-C(28A)-C(27A)	110.5(9)
C(24)-C(19)-C(20)	120.9(3)	C(12)-N(2)-C(19)	121.2(3)
C(24)-C(19)-N(2)	119.9(3)	C(12)-N(2)-Zn(1)	111.8(2)
C(20)-C(19)-N(2)	119.2(3)	C(19)-N(2)-Zn(1)	126.82(19)
C(19)-C(20)-C(21)	119.8(3)	C(1)-N(1)-C(13)	121.9(3)
C(22)-C(21)-C(20)	117.8(3)	C(1)-N(1)-Zn(1)	112.1(2)
C(21)-C(22)-F(2)	118.4(3)	C(13)-N(1)-Zn(1)	125.9(2)
C(21)-C(22)-C(23)	123.9(3)	N(1)-Zn(1)-N(2)	80.71(10)
F(2)-C(22)-C(23)	117.7(3)	N(1)-Zn(1)-Cl(1)	116.42(8)
C(22)-C(23)-C(24)	117.9(3)	N(2)-Zn(1)-Cl(1)	112.53(7)
C(19)-C(24)-C(23)	119.7(3)	N(1)-Zn(1)-Cl(2)	109.47(7)
C(28)-O(1)-C(25)	105.6(6)	N(2)-Zn(1)-Cl(2)	112.59(7)
O(1)-C(25)-C(26)	105.5(7)	Cl(1)-Zn(1)-Cl(2)	119.00(4)
C(25)-C(26)-C(27)	105.4(8)	C(33)-O(2)-C(30)	107.1(9)
C(26)-C(27)-C(28)	103.2(9)	O(2)-C(30)-C(31)	106.8(10)
O(1)-C(28)-C(27)	109.2(6)	C(32)-C(31)-C(30)	104.8(12)
C(28A)-O(1A)-C(25A)	108.6(8)	C(33)-C(32)-C(31)	101.4(12)
O(1A)-C(25A)-C(26A)	104.4(10)	O(2)-C(33)-C(32)	110.7(9)
C(27A)-C(26A)-C(25A)	103.3(11)		

---

Table 121: Crystallographic Data and Structure Refinement of **19-DCM**.

Empirical formula	C <sub>25</sub> H <sub>16</sub> Br <sub>2</sub> Cl <sub>4</sub> N <sub>2</sub> Zn	
Formula weight	711.39	
Temperature	100(2) K	
Wavelength	1.54184 Å	
Crystal system	Monoclinic	
Space group	P2 <sub>1</sub> /c	
Unit cell dimensions	a = 13.10500(10) Å	α = 90°.
	b = 11.84230(10) Å	β = 110.0250(10)°.
	c = 17.5235(2) Å	γ = 90°.
Volume	2555.12(4) Å <sup>3</sup>	
Z	4	
Density (calculated)	1.849 Mg/m <sup>3</sup>	
Absorption coefficient	8.994 mm <sup>-1</sup>	
F(000)	1392	
Crystal size	0.140 x 0.060 x 0.030 mm <sup>3</sup>	
Theta range for data collection	3.590 to 76.359°.	
Index ranges	-16<=h<=16, -14<=k<=13, -21<=l<=21	
Reflections collected	25415	
Independent reflections	5292 [R(int) = 0.0273]	
Completeness to theta = 67.684°	100.0 %	
Absorption correction	Semi-empirical from equivalents	
Max. and min. transmission	1.00000 and 0.59098	
Refinement method	Full-matrix least-squares on F <sup>2</sup>	
Data / restraints / parameters	5292 / 0 / 307	
Goodness-of-fit on F <sup>2</sup>	1.086	
Final R indices [I>2sigma(I)]	R1 = 0.0250, wR2 = 0.0682	
R indices (all data)	R1 = 0.0260, wR2 = 0.0691	
Largest diff. peak and hole	0.511 and -0.432 e.Å <sup>-3</sup>	

Table 122: Atomic coordinates ( $\times 10^4$ ) and equivalent isotropic displacement parameters ( $\text{\AA}^2 \times 10^3$ ) for **19-DCM**.  $U(\text{eq})$  is defined as one third of the trace of the orthogonalized  $U^{\text{ij}}$  tensor.

	x	y	z	U(eq)
C(1)	5506(1)	2352(2)	5351(1)	15(1)
C(2)	5318(1)	1494(2)	5893(1)	16(1)
C(3)	5907(2)	1102(2)	6660(1)	18(1)
C(4)	5476(2)	189(2)	6976(1)	20(1)
C(5)	4501(2)	-315(2)	6545(1)	19(1)
C(6)	3885(1)	66(2)	5750(1)	17(1)
C(7)	4319(1)	970(2)	5445(1)	15(1)
C(8)	2883(2)	-385(2)	5228(1)	19(1)
C(9)	2398(2)	51(2)	4460(1)	20(1)
C(10)	2851(2)	959(2)	4157(1)	18(1)
C(11)	3813(1)	1424(2)	4653(1)	16(1)
C(12)	4550(1)	2305(2)	4559(1)	15(1)
C(13)	7139(1)	3199(2)	6153(1)	16(1)
C(14)	8190(2)	2916(2)	6211(1)	19(1)
C(15)	9024(2)	3027(2)	6953(1)	21(1)
C(16)	8788(2)	3443(2)	7611(1)	20(1)
C(17)	7754(2)	3789(2)	7548(1)	19(1)
C(18)	6917(2)	3661(2)	6810(1)	19(1)
C(19)	3662(1)	3024(2)	3241(1)	15(1)
C(20)	3808(2)	2754(2)	2512(1)	18(1)
C(21)	2933(2)	2807(2)	1788(1)	20(1)
C(22)	1934(2)	3172(2)	1808(1)	19(1)
C(23)	1785(2)	3481(2)	2525(1)	19(1)
C(24)	2661(2)	3400(2)	3250(1)	17(1)
C(26)	9385(2)	4775(2)	3821(1)	37(1)
Br(1)	9909(1)	3519(1)	8640(1)	30(1)

Br(2)	749(1)	3264(1)	810(1)	29(1)
Cl(1)	6035(1)	5715(1)	4320(1)	23(1)
Cl(2)	7108(1)	3057(1)	3719(1)	21(1)
Cl(3)	9002(1)	4763(1)	2750(1)	37(1)
Cl(4)	10788(1)	4541(1)	4303(1)	34(1)
N(1)	6271(1)	3047(1)	5400(1)	15(1)
N(2)	4568(1)	2965(1)	3982(1)	16(1)
Zn(1)	6046(1)	3860(1)	4307(1)	15(1)

Table 123: Bond Lengths [Å] and Bond Angles [°] for **19-DCM**.

C(1)-N(1)	1.278(2)	C(16)-Br(1)	1.8977(18)
C(1)-C(2)	1.469(2)	C(17)-C(18)	1.388(3)
C(1)-C(12)	1.519(2)	C(19)-C(24)	1.391(3)
C(2)-C(3)	1.381(3)	C(19)-C(20)	1.392(3)
C(2)-C(7)	1.418(2)	C(19)-N(2)	1.431(2)
C(3)-C(4)	1.418(3)	C(20)-C(21)	1.391(3)
C(4)-C(5)	1.377(3)	C(21)-C(22)	1.390(3)
C(5)-C(6)	1.422(3)	C(22)-C(23)	1.385(3)
C(6)-C(7)	1.401(3)	C(22)-Br(2)	1.9031(18)
C(6)-C(8)	1.422(3)	C(23)-C(24)	1.394(3)
C(7)-C(11)	1.423(2)	C(26)-Cl(4)	1.762(3)
C(8)-C(9)	1.377(3)	C(26)-Cl(3)	1.769(2)
C(9)-C(10)	1.417(3)	Cl(1)-Zn(1)	2.1974(5)
C(10)-C(11)	1.377(3)	Cl(2)-Zn(1)	2.2098(5)
C(11)-C(12)	1.470(2)	N(1)-Zn(1)	2.0720(15)
C(12)-N(2)	1.284(2)	N(2)-Zn(1)	2.1079(15)
C(13)-C(14)	1.387(3)		
C(13)-C(18)	1.392(3)	N(1)-C(1)-C(2)	134.78(16)
C(13)-N(1)	1.428(2)	N(1)-C(1)-C(12)	117.88(16)
C(14)-C(15)	1.389(3)	C(2)-C(1)-C(12)	107.29(15)
C(15)-C(16)	1.383(3)	C(3)-C(2)-C(7)	119.61(17)
C(16)-C(17)	1.384(3)	C(3)-C(2)-C(1)	134.45(17)



C(7)-C(2)-C(1)	105.81(15)	C(17)-C(16)-Br(1)	118.69(15)
C(2)-C(3)-C(4)	118.15(17)	C(16)-C(17)-C(18)	118.84(18)
C(5)-C(4)-C(3)	122.29(17)	C(17)-C(18)-C(13)	119.37(17)
C(4)-C(5)-C(6)	120.62(17)	C(24)-C(19)-C(20)	120.78(16)
C(7)-C(6)-C(8)	116.55(17)	C(24)-C(19)-N(2)	119.84(16)
C(7)-C(6)-C(5)	116.55(17)	C(20)-C(19)-N(2)	119.30(16)
C(8)-C(6)-C(5)	126.89(17)	C(21)-C(20)-C(19)	119.78(17)
C(6)-C(7)-C(2)	122.78(17)	C(22)-C(21)-C(20)	118.71(17)
C(6)-C(7)-C(11)	123.10(16)	C(23)-C(22)-C(21)	122.14(17)
C(2)-C(7)-C(11)	114.10(16)	C(23)-C(22)-Br(2)	119.62(14)
C(9)-C(8)-C(6)	120.25(17)	C(21)-C(22)-Br(2)	118.23(14)
C(8)-C(9)-C(10)	122.55(17)	C(22)-C(23)-C(24)	118.74(17)
C(11)-C(10)-C(9)	118.51(17)	C(19)-C(24)-C(23)	119.77(17)
C(10)-C(11)-C(7)	119.03(17)	Cl(4)-C(26)-Cl(3)	112.18(13)
C(10)-C(11)-C(12)	135.04(17)	C(1)-N(1)-C(13)	120.11(15)
C(7)-C(11)-C(12)	105.84(15)	C(1)-N(1)-Zn(1)	112.14(12)
N(2)-C(12)-C(11)	135.25(16)	C(13)-N(1)-Zn(1)	127.75(12)
N(2)-C(12)-C(1)	117.76(16)	C(12)-N(2)-C(19)	120.76(15)
C(11)-C(12)-C(1)	106.94(15)	C(12)-N(2)-Zn(1)	110.84(12)
C(14)-C(13)-C(18)	121.23(17)	C(19)-N(2)-Zn(1)	128.41(12)
C(14)-C(13)-N(1)	119.58(16)	N(1)-Zn(1)-N(2)	80.98(6)
C(18)-C(13)-N(1)	119.15(16)	N(1)-Zn(1)-Cl(1)	117.01(5)
C(13)-C(14)-C(15)	119.26(17)	N(2)-Zn(1)-Cl(1)	119.78(4)
C(16)-C(15)-C(14)	119.03(18)	N(1)-Zn(1)-Cl(2)	108.57(4)
C(15)-C(16)-C(17)	122.09(18)	N(2)-Zn(1)-Cl(2)	108.95(4)
C(15)-C(16)-Br(1)	119.20(15)	Cl(1)-Zn(1)-Cl(2)	116.240(19)

---

Table 124: Crystallographic Data and Structure Refinement of **20-DCM**.

Empirical formula	$C_{27}H_{16}Cl_4F_6N_2O_2Zn$	
Formula weight	721.59	
Temperature	100(2) K	
Wavelength	1.54184 Å	
Crystal system	Triclinic	
Space group	P-1	
Unit cell dimensions	$a = 11.8689(6)$ Å	$\alpha = 107.262(7)^\circ$ .
	$b = 14.1948(11)$ Å	$\beta = 92.978(5)^\circ$ .
	$c = 17.6232(16)$ Å	$\gamma = 94.504(5)^\circ$ .
Volume	$2817.8(4)$ Å <sup>3</sup>	
Z	4	
Density (calculated)	$1.701$ Mg/m <sup>3</sup>	
Absorption coefficient	$5.342$ mm <sup>-1</sup>	
F(000)	1440	
Crystal size	$0.10 \times 0.25 \times 0.38$ mm <sup>3</sup>	
Theta range for data collection	3.530 to 76.980°.	
Index ranges	$-14 \leq h \leq 12$ , $-17 \leq k \leq 17$ , $-21 \leq l \leq 21$	
Reflections collected	17297	
Independent reflections	17297 [R(int) = 0.0000]	
Completeness to theta = 67.684°	99.8 %	
Absorption correction	Semi-empirical from equivalents	
Max. and min. transmission	1.00000 and 0.45025	
Refinement method	Full-matrix least-squares on F <sup>2</sup>	
Data / restraints / parameters	17297 / 702 / 758	
Goodness-of-fit on F <sup>2</sup>	1.060	
Final R indices [I > 2sigma(I)]	R1 = 0.0877, wR2 = 0.2289	
R indices (all data)	R1 = 0.1073, wR2 = 0.2449	
Largest diff. peak and hole	2.192 and -1.217 e.Å <sup>-3</sup>	

Table 125: Atomic coordinates ( $\times 10^4$ ) and equivalent isotropic displacement parameters ( $\text{\AA}^2 \times 10^3$ ) for **20-DCM**.  $U(\text{eq})$  is defined as one third of the trace of the orthogonalized  $U^{\text{ij}}$  tensor.

	x	y	z	U(eq)
C(1)	7317(6)	4485(4)	4669(4)	21(1)
C(2)	6465(6)	4673(5)	4103(4)	23(1)
C(3)	6034(6)	4159(5)	3341(4)	25(1)
C(4)	5154(6)	4558(5)	2993(4)	27(1)
C(5)	4717(6)	5433(5)	3397(4)	26(1)
C(6)	5144(6)	5954(5)	4186(4)	23(1)
C(7)	6036(6)	5570(4)	4513(4)	21(1)
C(8)	4751(6)	6833(5)	4691(4)	27(1)
C(9)	5221(6)	7241(5)	5457(4)	28(1)
C(10)	6130(6)	6845(5)	5778(4)	25(1)
C(11)	6529(6)	6012(5)	5298(4)	23(1)
C(12)	7380(6)	5361(5)	5429(4)	23(1)
C(13)	7938(6)	2916(5)	4016(4)	23(1)
C(14)	7643(6)	2001(5)	4098(4)	28(1)
C(15)	7674(7)	1153(5)	3459(4)	33(2)
C(16)	8060(7)	1254(5)	2756(4)	30(2)
C(17)	8376(6)	2167(5)	2664(4)	30(2)
C(18)	8319(6)	3010(5)	3302(4)	26(1)
C(19)	7509(9)	142(6)	1480(5)	45(2)
C(20)	8211(6)	6204(5)	6717(4)	25(1)
C(21)	7952(7)	6080(6)	7448(4)	30(2)
C(22)	8047(7)	6892(6)	8124(5)	34(2)
C(23)	8456(7)	7807(6)	8075(5)	37(2)
C(24)	8757(7)	7941(5)	7362(5)	33(2)
C(25)	8631(6)	7118(5)	6683(4)	30(2)
C(26)	8837(14)	9454(10)	8904(8)	85(3)

C(27)	7600(6)	4554(5)	-321(4)	22(1)
C(28)	8453(6)	4696(5)	-854(4)	23(1)
C(29)	8786(6)	4132(5)	-1564(4)	26(1)
C(30)	9722(6)	4510(5)	-1891(4)	28(1)
C(31)	10291(6)	5415(5)	-1525(4)	27(1)
C(32)	9979(6)	6022(5)	-781(4)	24(1)
C(33)	9054(6)	5626(5)	-461(4)	23(1)
C(34)	10493(6)	6964(5)	-324(4)	29(1)
C(35)	10111(6)	7450(5)	397(4)	30(2)
C(36)	9196(6)	7045(5)	720(4)	29(1)
C(37)	8670(6)	6121(5)	288(4)	23(1)
C(38)	7744(6)	5457(5)	416(4)	23(1)
C(39)	6492(6)	3045(5)	-1025(4)	24(1)
C(40)	6388(7)	2090(5)	-965(4)	31(2)
C(41)	5996(7)	1297(5)	-1636(5)	36(2)
C(42)	5679(7)	1491(5)	-2337(4)	32(2)
C(43)	5748(6)	2446(5)	-2395(4)	28(1)
C(44)	6160(6)	3228(5)	-1736(4)	26(1)
C(45)	5797(9)	310(6)	-3588(5)	49(2)
C(46)	7182(6)	6284(5)	1691(4)	23(1)
C(47)	7450(6)	6144(5)	2420(4)	28(1)
C(48)	7565(7)	6949(5)	3111(4)	31(2)
C(49)	7378(6)	7866(5)	3046(4)	27(1)
C(50)	7054(7)	8015(5)	2328(4)	29(2)
C(51)	6950(6)	7215(5)	1644(4)	28(1)
C(52)	7250(12)	8798(7)	4379(6)	60(2)
C(53)	5507(13)	8252(11)	8681(9)	89(4)
C(54)	9390(11)	10957(8)	6393(8)	72(3)
CI(1)	7953(2)	3070(1)	6410(1)	29(1)
CI(2)	10664(2)	4179(1)	5800(1)	36(1)
CI(3)	4259(2)	4067(1)	748(1)	28(1)
CI(4)	6953(2)	3221(1)	1428(1)	29(1)

Cl(5)	5512(3)	8421(2)	7746(2)	78(1)
Cl(6)	5852(5)	9301(4)	9435(2)	125(2)
Cl(7)	9757(3)	9725(2)	6102(3)	90(1)
Cl(8)	9425(5)	11425(3)	7427(2)	123(2)
F(1)	6403(6)	29(5)	1643(4)	68(2)
F(2)	7559(6)	787(4)	1086(3)	54(1)
F(3)	7740(6)	-723(3)	1015(3)	54(1)
F(4)	8145(9)	9824(6)	8401(5)	105(3)
F(5)	8759(8)	10015(5)	9619(4)	102(3)
F(6)	9856(9)	9651(8)	8684(5)	142(4)
F(7)	6256(6)	981(4)	-3892(3)	63(2)
F(8)	5136(6)	-352(3)	-4143(3)	56(2)
F(9)	6645(6)	-133(5)	-3369(4)	75(2)
F(10)	7356(6)	9726(4)	4836(3)	64(2)
F(11)	6020(6)	8519(5)	4226(4)	74(2)
F(12)	7490(7)	8222(4)	4776(3)	72(2)
N(1)	7912(5)	3780(4)	4685(3)	23(1)
N(2)	8067(5)	5366(4)	6022(3)	24(1)
N(3)	6829(5)	3858(4)	-337(3)	23(1)
N(4)	7110(5)	5452(4)	992(3)	22(1)
O(1)	8171(6)	373(4)	2149(3)	43(1)
O(2)	8505(7)	8566(5)	8800(4)	57(2)
O(3)	5161(5)	703(4)	-2980(3)	38(1)
O(4)	7569(6)	8744(4)	3694(3)	42(1)
Zn(1)	8810(1)	4035(1)	5791(1)	23(1)
Zn(2)	6120(1)	4110(1)	756(1)	23(1)

Table 126: Bond Lengths [Å] and Bond Angles [°] for **20-DCM**.

C(1)-N(1)	1.275(7)	C(2)-C(7)	1.414(7)
C(1)-C(2)	1.479(7)	C(3)-C(4)	1.421(8)
C(1)-C(12)	1.528(7)	C(4)-C(5)	1.390(8)
C(2)-C(3)	1.374(7)	C(5)-C(6)	1.413(8)

C(6)-C(7)	1.402(7)	C(27)-N(3)	1.286(7)
C(6)-C(8)	1.429(8)	C(27)-C(28)	1.458(8)
C(7)-C(11)	1.411(7)	C(27)-C(38)	1.521(7)
C(8)-C(9)	1.370(8)	C(28)-C(29)	1.367(8)
C(9)-C(10)	1.421(8)	C(28)-C(33)	1.411(7)
C(10)-C(11)	1.370(8)	C(29)-C(30)	1.419(8)
C(11)-C(12)	1.475(7)	C(30)-C(31)	1.360(8)
C(12)-N(2)	1.289(7)	C(31)-C(32)	1.425(7)
C(13)-C(14)	1.370(7)	C(32)-C(34)	1.412(8)
C(13)-C(18)	1.400(8)	C(32)-C(33)	1.411(8)
C(13)-N(1)	1.428(7)	C(33)-C(37)	1.416(7)
C(14)-C(15)	1.387(8)	C(34)-C(35)	1.371(8)
C(15)-C(16)	1.385(9)	C(35)-C(36)	1.413(8)
C(16)-C(17)	1.379(8)	C(36)-C(37)	1.385(7)
C(16)-O(1)	1.404(7)	C(37)-C(38)	1.461(8)
C(17)-C(18)	1.387(8)	C(38)-N(4)	1.296(7)
C(19)-F(2)	1.302(8)	C(39)-C(40)	1.387(7)
C(19)-F(3)	1.318(8)	C(39)-C(44)	1.395(8)
C(19)-O(1)	1.324(9)	C(39)-N(3)	1.417(7)
C(19)-F(1)	1.362(10)	C(40)-C(41)	1.397(8)
C(20)-C(25)	1.371(8)	C(41)-C(42)	1.384(9)
C(20)-C(21)	1.398(8)	C(42)-C(43)	1.385(8)
C(20)-N(2)	1.422(7)	C(42)-O(3)	1.408(7)
C(21)-C(22)	1.381(8)	C(43)-C(44)	1.383(7)
C(22)-C(23)	1.379(9)	C(45)-F(8)	1.312(8)
C(23)-C(24)	1.387(10)	C(45)-F(7)	1.323(8)
C(23)-O(2)	1.404(7)	C(45)-F(9)	1.324(10)
C(24)-C(25)	1.395(8)	C(45)-O(3)	1.350(8)
C(26)-O(2)	1.266(14)	C(46)-C(47)	1.383(8)
C(26)-F(5)	1.299(10)	C(46)-C(51)	1.397(7)
C(26)-F(6)	1.300(13)	C(46)-N(4)	1.424(6)
C(26)-F(4)	1.412(16)	C(47)-C(48)	1.394(8)

C(48)-C(49)	1.377(8)	C(5)-C(6)-C(8)	126.6(5)
C(49)-C(50)	1.382(8)	C(6)-C(7)-C(11)	122.7(5)
C(49)-O(4)	1.412(6)	C(6)-C(7)-C(2)	122.7(5)
C(50)-C(51)	1.382(8)	C(11)-C(7)-C(2)	114.4(5)
C(52)-F(12)	1.247(10)	C(9)-C(8)-C(6)	120.2(5)
C(52)-O(4)	1.259(9)	C(8)-C(9)-C(10)	122.7(5)
C(52)-F(10)	1.319(8)	C(11)-C(10)-C(9)	117.8(5)
C(52)-F(11)	1.501(14)	C(10)-C(11)-C(7)	120.1(5)
C(53)-Cl(6)	1.684(13)	C(10)-C(11)-C(12)	133.5(5)
C(53)-Cl(5)	1.730(11)	C(7)-C(11)-C(12)	106.2(5)
C(54)-Cl(8)	1.746(11)	N(2)-C(12)-C(11)	134.7(5)
C(54)-Cl(7)	1.768(9)	N(2)-C(12)-C(1)	118.5(5)
Cl(1)-Zn(1)	2.2102(14)	C(11)-C(12)-C(1)	106.7(4)
Cl(2)-Zn(1)	2.1931(16)	C(14)-C(13)-C(18)	120.6(5)
Cl(3)-Zn(2)	2.2042(15)	C(14)-C(13)-N(1)	119.5(5)
Cl(4)-Zn(2)	2.2205(14)	C(18)-C(13)-N(1)	119.8(5)
N(1)-Zn(1)	2.091(4)	C(13)-C(14)-C(15)	120.3(5)
N(2)-Zn(1)	2.088(5)	C(16)-C(15)-C(14)	118.6(5)
N(3)-Zn(2)	2.087(5)	C(17)-C(16)-C(15)	122.2(5)
N(4)-Zn(2)	2.077(4)	C(17)-C(16)-O(1)	121.2(6)
		C(15)-C(16)-O(1)	116.6(5)
N(1)-C(1)-C(2)	136.3(5)	C(16)-C(17)-C(18)	118.7(5)
N(1)-C(1)-C(12)	116.9(5)	C(17)-C(18)-C(13)	119.6(5)
C(2)-C(1)-C(12)	106.6(4)	F(2)-C(19)-F(3)	109.3(6)
C(3)-C(2)-C(7)	119.9(5)	F(2)-C(19)-O(1)	115.8(6)
C(3)-C(2)-C(1)	134.0(5)	F(3)-C(19)-O(1)	108.7(6)
C(7)-C(2)-C(1)	106.0(4)	F(2)-C(19)-F(1)	106.4(7)
C(2)-C(3)-C(4)	117.8(5)	F(3)-C(19)-F(1)	106.7(6)
C(5)-C(4)-C(3)	122.5(5)	O(1)-C(19)-F(1)	109.6(6)
C(4)-C(5)-C(6)	119.8(5)	C(25)-C(20)-C(21)	119.8(5)
C(7)-C(6)-C(5)	117.1(5)	C(25)-C(20)-N(2)	121.1(5)
C(7)-C(6)-C(8)	116.3(5)	C(21)-C(20)-N(2)	119.1(5)

C(22)-C(21)-C(20)	119.8(6)	C(36)-C(37)-C(38)	135.0(5)
C(23)-C(22)-C(21)	119.3(6)	C(33)-C(37)-C(38)	105.9(4)
C(22)-C(23)-C(24)	121.9(6)	N(4)-C(38)-C(37)	135.7(5)
C(22)-C(23)-O(2)	113.7(6)	N(4)-C(38)-C(27)	117.7(5)
C(24)-C(23)-O(2)	124.3(6)	C(37)-C(38)-C(27)	106.5(4)
C(23)-C(24)-C(25)	117.8(6)	C(40)-C(39)-C(44)	120.9(5)
C(20)-C(25)-C(24)	121.2(6)	C(40)-C(39)-N(3)	119.6(5)
O(2)-C(26)-F(5)	111.2(12)	C(44)-C(39)-N(3)	119.2(5)
O(2)-C(26)-F(6)	115.5(12)	C(39)-C(40)-C(41)	119.4(6)
F(5)-C(26)-F(6)	109.3(8)	C(42)-C(41)-C(40)	118.9(5)
O(2)-C(26)-F(4)	108.0(9)	C(41)-C(42)-C(43)	122.0(5)
F(5)-C(26)-F(4)	106.6(10)	C(41)-C(42)-O(3)	118.3(5)
F(6)-C(26)-F(4)	105.6(13)	C(43)-C(42)-O(3)	119.3(6)
N(3)-C(27)-C(28)	134.9(5)	C(44)-C(43)-C(42)	119.1(5)
N(3)-C(27)-C(38)	117.4(5)	C(43)-C(44)-C(39)	119.7(5)
C(28)-C(27)-C(38)	107.6(4)	F(8)-C(45)-F(7)	108.8(6)
C(29)-C(28)-C(33)	119.6(5)	F(8)-C(45)-F(9)	108.6(6)
C(29)-C(28)-C(27)	134.8(5)	F(7)-C(45)-F(9)	106.8(7)
C(33)-C(28)-C(27)	105.5(5)	F(8)-C(45)-O(3)	107.5(7)
C(28)-C(29)-C(30)	118.6(5)	F(7)-C(45)-O(3)	112.5(6)
C(31)-C(30)-C(29)	122.2(5)	F(9)-C(45)-O(3)	112.6(7)
C(30)-C(31)-C(32)	120.9(5)	C(47)-C(46)-C(51)	120.7(5)
C(34)-C(32)-C(33)	116.4(5)	C(47)-C(46)-N(4)	118.6(5)
C(34)-C(32)-C(31)	127.7(5)	C(51)-C(46)-N(4)	120.7(5)
C(33)-C(32)-C(31)	116.0(5)	C(46)-C(47)-C(48)	119.9(5)
C(28)-C(33)-C(32)	122.7(5)	C(49)-C(48)-C(47)	118.3(5)
C(28)-C(33)-C(37)	114.5(5)	C(48)-C(49)-C(50)	122.7(5)
C(32)-C(33)-C(37)	122.8(5)	C(48)-C(49)-O(4)	122.8(5)
C(35)-C(34)-C(32)	120.9(5)	C(50)-C(49)-O(4)	114.4(5)
C(34)-C(35)-C(36)	122.5(5)	C(51)-C(50)-C(49)	118.8(5)
C(37)-C(36)-C(35)	118.3(5)	C(50)-C(51)-C(46)	119.5(5)
C(36)-C(37)-C(33)	119.1(5)	F(12)-C(52)-O(4)	126.9(9)



F(12)-C(52)-F(10)	111.8(7)	C(46)-N(4)-Zn(2)	128.1(3)
O(4)-C(52)-F(10)	110.6(6)	C(19)-O(1)-C(16)	119.6(5)
F(12)-C(52)-F(11)	98.1(7)	C(26)-O(2)-C(23)	124.6(8)
O(4)-C(52)-F(11)	101.8(8)	C(45)-O(3)-C(42)	117.5(5)
F(10)-C(52)-F(11)	103.2(9)	C(52)-O(4)-C(49)	122.9(5)
Cl(6)-C(53)-Cl(5)	113.6(6)	N(1)-Zn(1)-N(2)	81.26(17)
Cl(8)-C(54)-Cl(7)	110.5(5)	N(2)-Zn(1)-Cl(2)	115.02(14)
C(1)-N(1)-C(13)	122.9(5)	N(1)-Zn(1)-Cl(2)	116.24(14)
C(1)-N(1)-Zn(1)	112.2(4)	N(2)-Zn(1)-Cl(1)	109.86(14)
C(13)-N(1)-Zn(1)	124.8(3)	N(1)-Zn(1)-Cl(1)	107.74(13)
C(12)-N(2)-C(20)	120.1(5)	Cl(1)-Zn(1)-Cl(2)	120.13(6)
C(12)-N(2)-Zn(1)	110.8(4)	N(4)-Zn(2)-N(3)	81.46(17)
C(20)-N(2)-Zn(1)	129.2(3)	N(4)-Zn(2)-Cl(3)	120.39(13)
C(27)-N(3)-C(39)	123.4(5)	N(3)-Zn(2)-Cl(3)	117.55(14)
C(27)-N(3)-Zn(2)	111.4(3)	N(4)-Zn(2)-Cl(4)	107.51(13)
C(39)-N(3)-Zn(2)	125.1(4)	N(3)-Zn(2)-Cl(4)	108.01(13)
C(38)-N(4)-C(46)	120.6(4)	Cl(3)-Zn(2)-Cl(4)	116.52(6)
C(38)-N(4)-Zn(2)	111.3(3)		

---

Table 127: Crystallographic Data and Structure Refinement of **21-DCM**.

Empirical formula	$C_{27}H_{16}Cl_4F_6N_2Zn$	
Formula weight	689.59	
Temperature	100(2) K	
Wavelength	1.54184 Å	
Crystal system	Monoclinic	
Space group	P2 <sub>1</sub> /c	
Unit cell dimensions	$a = 13.7395(5)$ Å	$\alpha = 90^\circ$ .
	$b = 11.9489(3)$ Å	$\beta = 111.023(4)^\circ$ .
	$c = 17.6137(5)$ Å	$\gamma = 90^\circ$ .
Volume	2699.19(16) Å <sup>3</sup>	
Z	4	
Density (calculated)	1.697 Mg/m <sup>3</sup>	
Absorption coefficient	5.486 mm <sup>-1</sup>	
F(000)	1376	
Crystal size	0.420 x 0.090 x 0.080 mm <sup>3</sup>	
Theta range for data collection	4.575 to 76.256°.	
Index ranges	-17<=h<=11, -13<=k<=14, -15<=l<=21	
Reflections collected	10491	
Independent reflections	5421 [R(int) = 0.0313]	
Completeness to theta = 67.684°	99.4 %	
Absorption correction	Semi-empirical from equivalents	
Max. and min. transmission	1.00000 and 0.50168	
Refinement method	Full-matrix least-squares on F <sup>2</sup>	
Data / restraints / parameters	5421 / 366 / 390	
Goodness-of-fit on F <sup>2</sup>	0.980	
Final R indices [I>2sigma(I)]	R1 = 0.0415, wR2 = 0.1110	
R indices (all data)	R1 = 0.0458, wR2 = 0.1160	
Largest diff. peak and hole	0.434 and -0.688 e.Å <sup>-3</sup>	

Table 128: Atomic coordinates ( $\times 10^4$ ) and equivalent isotropic displacement parameters ( $\text{\AA}^2 \times 10^3$ ) for **21-DCM**.  $U(\text{eq})$  is defined as one third of the trace of the orthogonalized  $U^{\text{ij}}$  tensor.

	x	y	z	U(eq)
C(1)	5522(2)	2349(2)	5383(1)	18(1)
C(2)	5339(2)	1496(2)	5918(1)	18(1)
C(3)	5893(2)	1111(2)	6692(1)	20(1)
C(4)	5478(2)	205(2)	7000(1)	22(1)
C(5)	4545(2)	-295(2)	6551(1)	20(1)
C(6)	3964(2)	80(2)	5750(1)	19(1)
C(7)	4382(2)	976(2)	5453(1)	18(1)
C(8)	3011(2)	-376(2)	5212(2)	22(1)
C(9)	2548(2)	59(2)	4440(2)	23(1)
C(10)	2980(2)	961(2)	4152(1)	22(1)
C(11)	3898(2)	1424(2)	4662(1)	18(1)
C(12)	4602(2)	2306(2)	4582(1)	17(1)
C(13)	7125(2)	3171(2)	6180(1)	20(1)
C(14)	8116(2)	2907(2)	6204(2)	27(1)
C(15)	8961(2)	3040(3)	6928(2)	33(1)
C(16)	8804(2)	3454(2)	7610(2)	27(1)
C(17)	7813(2)	3753(2)	7576(1)	24(1)
C(18)	6965(2)	3610(2)	6858(1)	22(1)
C(19)	9708(2)	3631(3)	8385(2)	37(1)
C(20)	3768(2)	3008(2)	3251(1)	19(1)
C(21)	3962(2)	2748(2)	2546(1)	23(1)
C(22)	3149(2)	2780(2)	1798(1)	26(1)
C(23)	2165(2)	3103(2)	1759(2)	27(1)
C(24)	1976(2)	3400(2)	2462(2)	26(1)
C(25)	2783(2)	3351(2)	3211(1)	22(1)
C(26)	1299(2)	3172(2)	936(2)	34(1)

Cl(1)	5936(1)	5682(1)	4322(1)	29(1)
Cl(2)	7018(1)	3037(1)	3754(1)	25(1)
F(1)	10006(1)	4716(2)	8489(1)	49(1)
F(2)	10555(1)	3054(2)	8411(1)	49(1)
F(3)	9488(2)	3349(2)	9039(1)	57(1)
F(4)	1486(2)	2545(2)	387(1)	80(1)
F(5)	1187(1)	4209(2)	637(1)	45(1)
F(6)	375(2)	2904(2)	966(1)	71(1)
N(1)	6260(2)	3034(2)	5438(1)	18(1)
N(2)	4613(1)	2962(2)	4011(1)	18(1)
Zn(1)	6023(1)	3850(1)	4340(1)	18(1)
C(27)	10771(8)	5327(10)	6166(5)	56(2)
Cl(3)	9384(3)	5351(2)	5856(2)	61(1)
Cl(4)	11355(3)	5107(3)	7219(2)	72(1)
C(27')	10860(20)	5580(30)	6230(20)	99(14)
Cl(4')	11465(7)	4773(9)	7044(6)	95(3)
Cl(3')	9549(8)	5263(11)	5845(9)	139(6)

Table 129: Bond Lengths [ $\text{\AA}$ ] and Bond Angles [ $^\circ$ ] for **21-DCM**.

C(1)-N(1)	1.280(3)	C(10)-C(11)	1.375(3)
C(1)-C(2)	1.469(3)	C(11)-C(12)	1.472(3)
C(1)-C(12)	1.521(3)	C(12)-N(2)	1.279(3)
C(2)-C(3)	1.380(3)	C(13)-C(14)	1.384(3)
C(2)-C(7)	1.418(3)	C(13)-C(18)	1.392(3)
C(3)-C(4)	1.419(3)	C(13)-N(1)	1.426(3)
C(4)-C(5)	1.377(3)	C(14)-C(15)	1.392(3)
C(5)-C(6)	1.421(3)	C(15)-C(16)	1.386(4)
C(6)-C(7)	1.402(3)	C(16)-C(17)	1.387(4)
C(6)-C(8)	1.420(3)	C(16)-C(19)	1.495(3)
C(7)-C(11)	1.416(3)	C(17)-C(18)	1.389(3)
C(8)-C(9)	1.380(3)	C(19)-F(3)	1.333(4)
C(9)-C(10)	1.411(3)	C(19)-F(2)	1.339(4)

C(19)-F(1)	1.352(4)	C(8)-C(6)-C(5)	126.6(2)
C(20)-C(25)	1.391(3)	C(6)-C(7)-C(11)	123.0(2)
C(20)-C(21)	1.395(3)	C(6)-C(7)-C(2)	122.6(2)
C(20)-N(2)	1.425(3)	C(11)-C(7)-C(2)	114.4(2)
C(21)-C(22)	1.389(3)	C(9)-C(8)-C(6)	120.1(2)
C(22)-C(23)	1.384(4)	C(8)-C(9)-C(10)	122.5(2)
C(23)-C(24)	1.399(4)	C(11)-C(10)-C(9)	118.5(2)
C(23)-C(26)	1.512(3)	C(10)-C(11)-C(7)	119.2(2)
C(24)-C(25)	1.387(3)	C(10)-C(11)-C(12)	134.8(2)
C(26)-F(4)	1.321(4)	C(7)-C(11)-C(12)	105.84(19)
C(26)-F(6)	1.328(4)	N(2)-C(12)-C(11)	135.1(2)
C(26)-F(5)	1.333(3)	N(2)-C(12)-C(1)	117.96(19)
Cl(1)-Zn(1)	2.1924(6)	C(11)-C(12)-C(1)	106.86(18)
Cl(2)-Zn(1)	2.2127(6)	C(14)-C(13)-C(18)	121.1(2)
N(1)-Zn(1)	2.0845(18)	C(14)-C(13)-N(1)	119.3(2)
N(2)-Zn(1)	2.0991(19)	C(18)-C(13)-N(1)	119.6(2)
C(27)-Cl(4)	1.760(9)	C(13)-C(14)-C(15)	119.4(2)
C(27)-Cl(3)	1.783(13)	C(16)-C(15)-C(14)	119.8(2)
C(27')-Cl(4')	1.68(3)	C(15)-C(16)-C(17)	120.7(2)
C(27')-Cl(3')	1.73(3)	C(15)-C(16)-C(19)	120.3(2)
		C(17)-C(16)-C(19)	119.0(2)
N(1)-C(1)-C(2)	135.1(2)	C(16)-C(17)-C(18)	119.8(2)
N(1)-C(1)-C(12)	117.62(19)	C(17)-C(18)-C(13)	119.2(2)
C(2)-C(1)-C(12)	107.19(18)	F(3)-C(19)-F(2)	107.7(3)
C(3)-C(2)-C(7)	119.5(2)	F(3)-C(19)-F(1)	106.0(3)
C(3)-C(2)-C(1)	134.7(2)	F(2)-C(19)-F(1)	105.8(2)
C(7)-C(2)-C(1)	105.67(19)	F(3)-C(19)-C(16)	112.5(2)
C(2)-C(3)-C(4)	118.4(2)	F(2)-C(19)-C(16)	112.7(2)
C(5)-C(4)-C(3)	122.0(2)	F(1)-C(19)-C(16)	111.7(2)
C(4)-C(5)-C(6)	120.6(2)	C(25)-C(20)-C(21)	120.9(2)
C(7)-C(6)-C(8)	116.6(2)	C(25)-C(20)-N(2)	120.6(2)
C(7)-C(6)-C(5)	116.8(2)	C(21)-C(20)-N(2)	118.4(2)

C(22)-C(21)-C(20)	119.5(2)	C(1)-N(1)-Zn(1)	111.91(15)
C(23)-C(22)-C(21)	119.6(2)	C(13)-N(1)-Zn(1)	126.78(14)
C(22)-C(23)-C(24)	121.0(2)	C(12)-N(2)-C(20)	121.79(19)
C(22)-C(23)-C(26)	118.9(2)	C(12)-N(2)-Zn(1)	111.27(15)
C(24)-C(23)-C(26)	120.1(2)	C(20)-N(2)-Zn(1)	126.89(14)
C(25)-C(24)-C(23)	119.5(2)	N(1)-Zn(1)-N(2)	80.89(7)
C(24)-C(25)-C(20)	119.5(2)	N(1)-Zn(1)-Cl(1)	118.06(5)
F(4)-C(26)-F(6)	109.3(3)	N(2)-Zn(1)-Cl(1)	117.44(6)
F(4)-C(26)-F(5)	105.2(2)	N(1)-Zn(1)-Cl(2)	108.11(5)
F(6)-C(26)-F(5)	105.3(3)	N(2)-Zn(1)-Cl(2)	108.22(5)
F(4)-C(26)-C(23)	112.2(2)	Cl(1)-Zn(1)-Cl(2)	118.10(2)
F(6)-C(26)-C(23)	112.6(2)	Cl(4)-C(27)-Cl(3)	111.0(6)
F(5)-C(26)-C(23)	111.7(2)	Cl(4')-C(27')-Cl(3')	109(2)
C(1)-N(1)-C(13)	121.32(19)		

---

## References

- (1) Matei, I.; Lixandru, T.; Comanita, E. *Bul. Inst. Politeh. Iasi*. **1960**, *6*, 171–176.
- (2) Matei, I.; Lixandru, T.; Comanita, E. *Acad. Rep. Populare Romine, Filiala Iasi, Studii Cercetari Stiint. Chim.* **1960**, *11*, 281–289.
- (3) Matei, I.; Lixandru, T. *Bul. Inst. Politeh. Iasi*. **1967**, *13*, 245–255.
- (4) Dvolaitzky, M. *C. R. Acad. Sci. Ser. C* **1969**, *268*, 1811–1813.
- (5) Van Asselt, R.; Elsevier, C. J.; Smeets, W. J.; Spek, A. L.; Benedix, R. *Recl. Trav. Chim. Pays-Bas* **1994**, *113*, 88–98.
- (6) Johnson, L. K.; Killian, C. M.; Brookhart, M. *J. Am. Chem. Soc.* **1995**, *117*, 6414–6415.
- (7) Fedushkin, I. L.; Morozov, A. G.; Chudakova, V. A.; Fukin, G. K.; Cherkasov, V. K. *Eur. J. Inorg. Chem.* **2009**, *2009*, 4995–5003.
- (8) Rosa, V.; Carabineiro, S. A.; Avilés, T.; Gomes, P. T.; Welter, R.; Campos, J. M.; Ribeiro, M. R. *J. Organomet. Chem.* **2008**, *693*, 769–775.
- (9) Bomfim, J. A. S.; Dias, M. L.; Filgueiras, C. A. L.; Peruch, F.; Deffieux, A. *Catal. Today* **2008**, *133–135*, 879–885.
- (10) Amoroso, F.; Zangrando, E.; Carfagna, C.; Müller, C.; Vogt, D.; Hagar, M.; Ragaini, F.; Milani, B. *Dalton Trans.* **2013**, *42*, 14583–14602.
- (11) Gao, B.; Gao, W.; Wu, Q.; Luo, X.; Zhang, J.; Su, Q.; Mu, Y. *Organometallics* **2011**, *30*, 5480–5486.
- (12) Fliedel, C.; Rosa, V.; Santos, C. I. M.; Gonzalez, P. J.; Almeida, R. M.; Gomes, C. S. B.; Gomes, P. T.; Lemos, M. A. N. D. A.; Aullón, G.; Welter, R.; Avilés, T. *Dalton Trans.* **2014**, *43*, 13041–13054.
- (13) Fedushkin, I. L.; Nikipelov, A. S.; Morozov, A. G.; Skatova, A. A.; Cherkasov, A. V.; Abakumov, G. A. *Chem. – Eur. J.* **2012**, *18*, 255–266.
- (14) Gasperini, M.; Ragaini, F.; Cenini, S. *Organometallics* **2002**, *21*, 2950–2957.
- (15) Fedushkin, I. L.; Skatova, A. A.; Chudakova, V. A.; Fukin, G. K. *Angew. Chem. Int. Ed.* **2003**, *42*, 3294–3298.
- (16) Fedushkin, I. L.; Skatova, A. A.; Lukoyanov, A. N.; Chudakova, V. A.; Dechert, S.; Hummert, M.; Schumann, H. *Russ. Chem. Bull.* **2004**, *53*, 2751–2762.
- (17) Fedushkin, I. L.; Makarov, V. M.; Rosenthal, E. C. E.; Fukin, G. K. *Eur. J. Inorg. Chem.* **2006**, *2006*, 827–832.
- (18) Fedushkin, I. L.; Hummert, M.; Schumann, H. *Eur. J. Inorg. Chem.* **2006**, *2006*, 3266–3273.
- (19) Fedushkin, I. L.; Tishkina, A. N.; Fukin, G. K.; Hummert, M.; Schumann, H. *Eur. J. Inorg. Chem.* **2008**, *2008*, 483–489.
- (20) Tishkina, A. N.; Lukoyanov, A. N.; Morozov, A. G.; Fukin, G. K.; Lyssenko, K. A.; Fedushkin, I. L. *Russ. Chem. Bull.* **2010**, *58*, 2250–2257.
- (21) Fedushkin, I. L.; Lukoyanov, A. N.; Tishkina, A. N.; Maslov, M. O.; Ketkov, S. Y.; Hummert, M. *Organometallics* **2011**, *30*, 3628–3636.
- (22) Bonello, O.; Jones, C.; Stasch, A.; Woodul, W. D. *Organometallics* **2010**, *29*, 4914–4922.

- (23) Dange, D.; Choong, S. L.; Schenk, C.; Stasch, A.; Jones, C. *Dalton Trans.* **2012**, 41, 9304–9315.
- (24) Fedushkin, I. L.; Lukoyanov, A. N.; Ketkov, S. Y.; Hummert, M.; Schumann, H. *Chem. – Eur. J.* **2007**, 13, 7050–7056.
- (25) Jones, C.; Rose, R. P.; Stasch, A. *Dalton Trans.* **2007**, 2997–2999.
- (26) Fedushkin, I. L.; Lukoyanov, A. N.; Fukin, G. K.; Ketkov, S. Y.; Hummert, M.; Schumann, H. *Chem. – Eur. J.* **2008**, 14, 8465–8468.
- (27) Romain, C.; Rosa, V.; Fliedel, C.; Bier, F.; Hild, F.; Welter, R.; Dagorne, S.; Avilés, T. *Dalton Trans.* **2012**, 41, 3377–3379.
- (28) Fedushkin, I. L.; Nikipelov, A. S.; Lyssenko, K. A. *J. Am. Chem. Soc.* **2010**, 132, 7874–7875.
- (29) Fedushkin, I. L.; Moskalev, M. V.; Lukoyanov, A. N.; Tishkina, A. N.; Baranov, E. V.; Abakumov, G. A. *Chem. – Eur. J.* **2012**, 18, 11264–11276.
- (30) Fedushkin, I. L.; Moskalev, M. V.; Baranov, E. V.; Abakumov, G. A. *J. Organomet. Chem.* **2013**, 747, 235–240.
- (31) Arévalo, R.; Pérez, J.; Riera, L. *Inorg. Chem.* **2013**, 52, 6785–6787.
- (32) Fedushkin, I. L.; Skatova, A. A.; Dodonov, V. A.; Chudakova, V. A.; Bazyakina, N. L.; Piskunov, A. V.; Demeshko, S. V.; Fukin, G. K. *Inorg. Chem.* **2014**, 53, 5159–5170.
- (33) Arrowsmith, M.; Hill, M. S.; Kociok-Köhn, G. *Organometallics* **2011**, 30, 1291–1294.
- (34) Arrowsmith, M.; Hill, M. S.; Kociok-Köhn, G. *Organometallics* **2014**, 33, 206–216.
- (35) Evans, D. A.; Cowley, A. H. *J. Am. Chem. Soc.* **2012**, 134, 15672–15675.
- (36) Fedushkin, I. L.; Chudakova, V. A.; Fukin, G. K.; Dechert, S.; Hummert, M.; Schumann, H. *Russ. Chem. Bull.* **2004**, 53, 2744–2750.
- (37) López Ortiz, F.; Iglesias, M. J.; Fernández, I.; Andújar Sánchez, C. M.; Ruiz Gómez, G. *Chem. Rev.* **2007**, 107, 1580–1691.
- (38) Evans, D. A.; Vargas-Baca, I.; Cowley, A. H. *J. Am. Chem. Soc.* **2013**, 135, 13939–13946.
- (39) Parr, R. G.; Yang, W. *J. Am. Chem. Soc.* **1984**, 106, 4049–4050.
- (40) Yang, W.; Parr, R. G.; Pucci, R. *J. Chem. Phys.* **1984**, 81, 2862–2863.
- (41) Dastgir, S.; Coleman, K. S.; Cowley, A. R.; Green, M. L. H. *Organometallics* **2010**, 29, 4858–4870.
- (42) Sprengers, J. W.; de Greef, M.; Duin, M. A.; Elsevier, C. J. *Eur. J. Inorg. Chem.* **2003**, 2003, 3811–3819.
- (43) Gasperini, M.; Ragaini, F. *Organometallics* **2004**, 23, 995–1001.
- (44) Sheldrick, G. M. *Acta Crystallogr. A* **2008**, 64, 112–122.
- (45) Spek, A. L. *Acta Crystallogr. A* **1990**, 46, 34–34.
- (46) Te Velde, G.; Bickelhaupt, F. M.; Baerends, E. J.; Fonseca Guerra, C.; van Gisbergen, S. J. A.; Snijders, J. G.; Ziegler, T. *J. Comput. Chem.* **2001**, 22, 931–967.



- (47) Guerra, C. F.; Snijders, J. G.; Velde, G. te; Baerends, E. J. *Theor. Chem. Acc.* **1998**, *99*, 391–403.
- (48) ADF 2013.01, SCM, Theoretical Chemistry, Vrije Universiteit, Amsterdam, The Netherlands, <http://www.scm.com>.
- (49) Visser, O.; Leyronnas, P.; van Zeist, W. J.; Luppi, M. GUI 2013, SCM, Amsterdam, The Netherlands, <http://www.scm.com>.
- (50) Knör, G.; Leirer, M.; Keyes, T. E.; Vos, J. G. *Eur. J. Inorg. Chem.* **2000**, *2000*, 749–751.
- (51) Adams, C. J.; Fey, N.; Weinstein, J. A. *Inorg. Chem.* **2006**, *45*, 6105–6107.
- (52) Adams, C. J.; Fey, N.; Harrison, Z. A.; Sazanovich, I. V.; Towrie, M.; Weinstein, J. A. *Inorg. Chem.* **2008**, *47*, 8242–8257.
- (53) Singh, S. K.; Dubey, S. K.; Pandey, R.; Mishra, L.; Zou, R.-Q.; Xu, Q.; Pandey, D. S. *Polyhedron* **2008**, *27*, 2877–2882.
- (54) Kern, T.; Monkowius, U.; Zabel, M.; Knör, G. *Inorg. Chim. Acta* **2011**, *374*, 632–636.
- (55) Tang, C. W.; VanSlyke, S. A. *Appl. Phys. Lett.* **1987**, *51*, 913.
- (56) Xu, H.; Chen, R.; Sun, Q.; Lai, W.; Su, Q.; Huang, W.; Liu, X. *Chem. Soc. Rev.* **2014**, *43*, 3259–3302.
- (57) Kamtekar, K. T.; Monkman, A. P.; Bryce, M. R. *Adv. Mater.* **2010**, *22*, 572–582.
- (58) Friend, R. H.; Gymer, R. W.; Holmes, A. B.; Burroughes, J. H.; Marks, R. N.; Taliani, C.; Bradley, D. D. C.; Santos, D. A. D.; Brédas, J. L.; Lögdlund, M.; Salaneck, W. R. *Nature* **1999**, *397*, 121–128.
- (59) Birks, J. B. *Photophysics of Aromatic Molecules*; Wiley: London, 1970.
- (60) Wang, J.; Zhao, Y.; Dou, C.; Sun, H.; Xu, P.; Ye, K.; Zhang, J.; Jiang, S.; Li, F.; Wang, T. *J. Phys. Chem. B* **2007**, *111*, 5082–5589.
- (61) Luo, J.; Xie, Z.; Lam, J. W. Y.; Cheng, L.; Chen, H.; Qiu, C.; Kwok, H. S.; Zhan, X.; Liu, Y.; Zhu, D.; Tang, B. Z. *Chem. Commun.* **2001**, 1740–1741.
- (62) Hong, Y.; Lam, J. W. Y.; Tang, B. Z. *Chem. Commun.* **2009**, 4332–4353.
- (63) Hong, Y.; Lam, J. W. Y.; Tang, B. Z. *Chem. Soc. Rev.* **2011**, *40* (11), 5361–5388.
- (64) Chen, J.; Law, C. C. W.; Lam, J. W. Y.; Dong, Y.; Lo, S. M. F.; Williams, I. D.; Zhu, D.; Tang, B. Z. *Chem. Mater.* **2003**, *15*, 1535–1546.
- (65) Fan, X.; Sun, J.; Wang, F.; Chu, Z.; Wang, P.; Dong, Y.; Hu, R.; Tang, B. Z.; Zou, D. *Chem. Commun.* **2008**, 2989–2991.
- (66) Li, S.; Wang, Q.; Qian, Y.; Wang, S.; Li, Y.; Yang, G. *J. Phys. Chem. A* **2007**, *111*, 11793–11800.
- (67) He, L.; Xiong, F.; Li, S.; Gan, Q.; Zhang, G.; Li, Y.; Zhang, B.; Chen, B.; Yang, G. *J. Phys. Chem. B* **2004**, *108*, 7092–7097.
- (68) Mei, J.; Hong, Y.; Lam, J. W. Y.; Qin, A.; Tang, Y.; Tang, B. Z. *Adv. Mater.* **2014**, *26*, 5429–5479.
- (69) Reineke, S.; Thomschke, M.; Lüssem, B.; Leo, K. *Rev. Mod. Phys.* **2013**, *85*, 1245–1293.
- (70) Yang, S.-H.; Shih, P.-J.; Wu, W.-J.; Huang, Y.-H. *J. Lumin.* **2013**, *142*, 86–91.

- (71) Tong, H.; Hong, Y.; Dong, Y.; Ren, Y.; Häußler, M.; Lam, J. W. Y.; Wong, K. S.; Tang, B. Z. *J. Phys. Chem. B* **2007**, *111*, 2000–2007.
- (72) Kokado, K.; Chujo, Y. *J. Org. Chem.* **2011**, *76*, 316–319.
- (73) Rajagopal, S. K.; Philip, A. M.; Nagarajan, K.; Hariharan, M. *Chem. Commun.* **2014**, *50*, 8644–8647.
- (74) Varghese, S.; Das, S. *J. Phys. Chem. Lett.* **2011**, *2*, 863–873.
- (75) Zhang, H. Y.; Zhang, Z. L.; Ye, K. Q.; Zhang, J. Y.; Wang, Y. *Adv. Mater.* **2006**, *18*, 2369–2372.
- (76) Ye, K.; Wang, J.; Sun, H.; Liu, Y.; Mu, Z.; Li, F.; Jiang, S.; Zhang, J.; Zhang, H.; Wang, Y.; Che, C.-M. *J. Phys. Chem. B* **2005**, *109*, 8008–8016.
- (77) Kitamura, C.; Ohara, T.; Kawatsuki, N.; Yoneda, A.; Kobayashi, T.; Naito, H.; Komatsu, T.; Kitamura, T. *CrystEngComm* **2007**, *9*, 644–647.
- (78) Fan, Y.; Zhao, Y.; Ye, L.; Li, B.; Yang, G.; Wang, Y. *Cryst. Growth Des.* **2009**, *9*, 1421–1430.
- (79) Quartapelle Procopio, E.; Mauro, M.; Panigati, M.; Donghi, D.; Mercandelli, P.; Sironi, A.; D'Alfonso, G.; De Cola, L. *J. Am. Chem. Soc.* **2010**, *132*, 14397–14399.
- (80) Dong, Y.; Xu, B.; Zhang, J.; Tan, X.; Wang, L.; Chen, J.; Lv, H.; Wen, S.; Li, B.; Ye, L.; Zou, B.; Tian, W. *Angew. Chem. Int. Ed.* **2012**, *51*, 10782–10785.
- (81) Galer, P.; Korošec, R. C.; Vidmar, M.; Šket, B. *J. Am. Chem. Soc.* **2014**, *136*, 7383–7394.
- (82) Evans, D. A.; Lee, L. M.; Vargas-Baca, I.; Cowley, A. H. *Organometallics* **2015**.
- (83) Rosa, V.; Santos, C. I. M.; Welter, R.; Aullón, G.; Lodeiro, C.; Avilés, T. *Inorg. Chem.* **2010**, *49*, 8699–8708.
- (84) Paulovicova, A.; El-Ayaan, U.; Shibayama, K.; Morita, T.; Fukuda, Y. *Eur. J. Inorg. Chem.* **2001**, *2001*, 2641–2646.
- (85) Hasan, K.; Zysman-Colman, E. *J. Phys. Org. Chem.* **2013**, *26*, 274–279.
- (86) Hansch, C.; Leo, A.; Taft, R. W. *Chem. Rev.* **1991**, *91*, 165–195.
- (87) Ragaini, F.; Cenini, S.; Tollari, S. *J. Mol. Catal.* **1993**, *85*, L1–L5.
- (88) Shirakawa, E.; Yoshida, H.; Nakao, Y.; Hiyama, T. *J. Am. Chem. Soc.* **1999**, *121*, 4290–4291.
- (89) CrysAlisPro, version 1.171.37.31; Agilent Technologies UK Ltd., Oxford, UK, 2013.
- (90) Perdew, J. P.; Burke, K.; Ernzerhof, M. *Phys. Rev. Lett.* **1996**, *77*, 3865–3868.
- (91) Grimme, S. *J. Comput. Chem.* **2006**, *27*, 1787–1799.
- (92) van Lenthe, E.; Baerends, E. J.; Snijders, J. G. *J. Chem. Phys.* **1993**, *99*, 4597–4610.
- (93) van Lenthe, E.; Baerends, E. J.; Snijders, J. G. *J. Chem. Phys.* **1994**, *101*, 9783–9792.
- (94) van Lenthe, E.; Snijders, J. G.; Baerends, E. J. *J. Chem. Phys.* **1996**, *105*, 6505–6516.
- (95) van Lenthe, E.; van Leeuwen, R.; Baerends, E. J.; Snijders, J. G. *Int. J. Quantum Chem.* **1996**, *57*, 281–293.

- (96) van Lenthe, E.; Ehlers, A.; Baerends, E. J. *J. Chem. Phys.* **1999**, *110*, 8943-8953.
- (97) van Gisbergen, S. J. A.; Snijders, J. G.; Baerends, E. J. *Comput. Phys. Commun.* **1999**, *118*, 119-138.
- (98) Rosa, A.; Baerends, E. J.; van Gisbergen, S. J. A.; van Lenthe, E.; Groeneveld, J. A.; Snijders, J. G. *J. Am. Chem. Soc.* **1999**, *121*, 10356-10365.
- (99) Gritsenko, O. V.; Schipper, P. R. T.; Baerends, E. J. *Chem. Phys. Lett.* **1999**, *302*, 199-207.
- (100) Gritsenko, O. V.; Schipper, P. R. T.; Baerends, E. J. *Int. J. Quantum Chem.* **2000**, *76*, 407-419.
- (101) Schipper, P. R. T.; Gritsenko, O. V.; van Gisbergen, S. J. A.; Baerends, E. J. *J. Chem. Phys.* **2000**, *112*, 1344-1352.
- (102) Razeghi, M.; Choi, Y. H.; He, X.; Sun, C. J. *Mater. Sci. Technol.* **1995**, *11*, 3-30.
- (103) Perri, J. A.; La Placa, S.; Post, B. *Acta Crystallogr.* **1958**, *11*, 310-310.
- (104) Lindsay, L.; Broido, D. A.; Reinecke, T. L. *Phys. Rev. Lett.* **2013**, *111*, 025901-025905.
- (105) Wei, L.; Kuo, P. K.; Thomas, R. L.; Anthony, T. R.; Banholzer, W. F. *Phys. Rev. Lett.* **1993**, *70*, 3764-3767.
- (106) Slack, G. A. *J. Phys. Chem. Solids* **1973**, *34*, 321-335.
- (107) Ball, P. *Nature* **2012**, *492*, 174-176.
- (108) Hart, G. L. W.; Zunger, A. *J. Phys-Condens. Mat.* **2000**, *62*, 13522-13537.
- (109) Boudjemline, A.; Islam, M. M.; Louail, L.; Diawara, B. *Phys. B Condens. Matter* **2011**, *406*, 4272-4277.
- (110) Lv, B.; Lan, Y.; Wang, X.; Zhang, Q.; Hu, Y.; Jacobson, A. J.; Broido, D.; Chen, G.; Ren, Z.; Chu, C.-W. *Appl. Phys. Lett.* **2015**, *106*, 074105-074109.
- (111) Wang, S.; Swingle, S. F.; Ye, H.; Fan, F.-R. F.; Cowley, A. H.; Bard, A. J. *J. Am. Chem. Soc.* **2012**, *134*, 11056-11059.
- (112) Callmer, B. *Acta Crystallogr. B* **1977**, *33*, 1951-1954.
- (113) Greene, R. G.; Luo, H.; Ruoff, A. L.; Trail, S. S.; DiSalvo, F. J. *Phys. Rev. Lett.* **1994**, *73*, 2476-2479.
- (114) Naritsuka, S.; Mori, M.; Takeuchi, Y.; Monno, Y.; Maruyama, T. *Phys. Status Solidi C* **2011**, *8*, 291-293.
- (115) Shi, L.; Li, D.; Yu, C.; Jang, W.; Kim, D.; Yao, Z.; Kim, P.; Majumdar, A. *J. Heat Transf.* **2003**, *125*, 881-888.
- (116) Kim, J.; Ou, E.; Sellan, D. P.; Shi, L. *Rev. Sci. Instrum.* **2015**.